hydralab+

Adaptation For Climate Change

Trans-national Access in Hydralab+
Proceedings of the Joint User Meeting

Bucharest - May 23, 2019

Status: Final

Version: v2

Date: May 10, 2019

DOCUMENT INFORMATION

Title	Proceedings of the HYDRALAB+ Joint User Meeting
Editors	Pierre-Yves Henry, Mark Klein Breteler
Authors	Transnational Access Users of Hydralab+
Distribution	Final
Document Reference	

LICENSE

This report is licenced under the Creative Commons Attribution-ShareAlike 4.0 International License.
To view a copy of this license, visit http://creativecommons.org/licenses/by-sa/4.0/

ACKNOWLEDGEMENT

DISCLAIMER

RECOMMENDED CITATION STYLE

Paper authors; Paper title; in P.-Y. Henry & M. Klein Breteler (Eds.) Proceedings of the HYDRALAB+ Joint User Meeting, Bucharest, Romania, 22-23 May 2019 (pp. XXX-XXX).

TABLE OF CONTENT

INTRODUCTION

HYDRALAB is an Integrated Infrastructure Initiative, financially supported by the EC, to optimise the use of unique facilities for laboratory experiments in the field of Hydraulics, Geophysical Hydrodynamics, Environmental Fluid Dynamics and Ice Engineering. One of the three main activities of Hydralab was enabling international groups of researchers to conduct hydraulic research in selected large and unique facilities, which is called 'transnational access'. A detailed description of Transnational Access is given in Appendix A.

The contract period of Hydralab+ is from September 2015 to August 2019. Hydralab+ is financially supported by the European Union's Horizon 2020 Research and Innovation programme (grant agreement 654110).

The Joint User Meeting is the final event of four years of Transnational Access in the framework of Hydralab. It is a mini conference in which the results of 31 research projects are presented. These projects have been carried out by international groups of researchers in a large and unique facility of Hydralab, to which they normally do not have access to.

The joint user meeting is held on May 23, 2019, in Bucharest (Romania).

About each project a paper is available, describing the main results of the research. These are given in these proceedings. These are also available on the website of Hydralab:
https://hydralab.eu/taking-part/Hydralab-Bucharest-Event/programme-and-papers/

The papers are grouped per host institute where the project took place (provider):

I. Aalto University, Finland (Ice Tank)
II. CNRS, France (CoriolisII Rotating Platform)
III. Deltares, the Netherlands (Delta Flume and Delta Basin)
IV. DHI, Denmark (Offshore Wave Basin and Shallow Water Basin)
V. Leibniz University Hannover (LUH), Germany (Large Wave Flume and Multi-directional Wave and Current Basin)
VI. HSVA, Germany (Arctic Environmental Test Basin and Large Ice Model Basin)
VII. University of Hull, UK (Total Environment Simulator)
VIII. NTNU, Norway (Marine Ecohydraulics Field Station, Sletvik)
IX. Universitat Politècnica de Catalunya (UPC), Spain (CIEM)
X. HR Wallingford, UK (Fast Flow Facility)

I – AALTO - ICE TANK

The Aalto Ice Tank is part of the Department of Mechanical Engineering of Aalto University. The tank has a 40m x 40m lateral area and a depth of 2.8m, which is unique in Europe. The basin has a movable bridge which spans over the basin. Below the bridge is a carriage which can move along the bridge. Consequently, objects mounted to the carriage can be moved in any path through the basin, while e.g. forces and path are measured. At the front, the bridge has 4 pushing plates of 10 m length, which can be lowered individually or together to push ice against fixed installations, while measuring forces.

The model-scale ice is produced by spraying fine water mist (seeding) layer by layer onto the cooled surface, which produces a fine-grained structure. The spray water is doped with 0.3% of ethanol to weaken the produced ice artificially. The properties of the ice sheets range from 20 mm – 80 mm thickness and from 15 kPa – 120 kPa bending strength.

The basin dimensions also allow extraordinary tests as in HYDRALAB IV, where floating icebergs have been towed against floating structures. Furthermore, the laboratory has a model of an ice-going tanker which can be used and instrumented (see also HYDRALAB IV) for research tests.

The basin has an affiliated workshop for wood and metal that allows manufacturing custom equipment. In addition to this, several other special workshops are located nearby on the campus.

See also: http://icetank.aalto.fi/en/
https://twitter.com/#!/AaltoIceTank

WAVES–IN–ICE: WAVE ATTENUATION AND ICE BREAKUP

Alessandro Toffoli (1,2) and Jaak Monbaliu (1)

(1) KU Leuven, Belgium, E-mail: toffoli.alessandro@gmail.com and jaak.monbaliu@kuleuven.be
(2) The University of Melbourne, Australia, E-mail: alessandro.toffoli@unimelb.edu.au

A small scale waves-in-ice flume is used to conduct a pilot project to investigate the hydroelastic interactions between water waves of different periods and amplitudes and freshwater floating ice. It is shown that only incident waves with long period and large amplitudes can break up the ice cover and that the extent of the break up increases with increasing period and amplitude. The proportion of the incident wave that propagates through the ice-covered water grows as the period and amplitude increase, indicating the existence of a positive feedback loop between ice break up and increased wave propagation. Results are limited by the brittle nature of the fresh water ice, which is more fragile than sea ice, and the small dimensions of the flume. To achieve a more comprehensive insight of the waves-in-ice problem, an experimental model is planned in a substantially larger wave facility with feature-controlled sea ice model in the wave-ice tank of Aalto University, within the framework of Hydralab+.

1.   INTRODUCTION

Sea ice acts as a refrigerator for the world. Its bright surface reflects solar heat, which would otherwise be absorbed by the dark ocean it conceals, and the salt it expels during the freezing process drives thermohaline circulation, which transports cold water towards the equator. As a result, sea ice plays a crucial role in our climate system.

Waves penetrate deep into the ice-covered ocean and impact the ice cover (e.g. Liu and Mollo-Christensen, 1988). Concomitantly, the ice cover attenuates the wave energy over distance, so that wave impacts die out eventually (e.g. Wadhams et al., 1988). The most heralded effect is the ability of waves to break up the ice cover into floes with diameters comparable to the prevailing wavelengths. Asplin et al. (e.g. 2012) report wave-induced breakup 250 km into the Beaufort Sea; Kohout et al. (2014) observed breakup events over 300km into the Antarctic sea ice. The resulting region covered by broken floes, which sits between the open ocean and the quasi-continuous pack ice, is known as the marginal ice zone (MIZ). Following the breakup, waves herd floes (Wadhams, 1983), introduce warm water and overwash the floes, thus accelerating ice melt (Wadhams et al., 1979), and cause the floes to collide, which erodes the floes and influences the large-scale deformation of the ice field via momentum transfer (Shen et al., 1987). Waves, therefore, have a substantial role in controlling the ice extent.

Accounts of wave-induced breakup in the literature are serendipitous and rarely accompanied by data, due to the difficulties in making measurements in the harsh and dynamic MIZ conditions. Models of ice breakup, which are based on strains imposed by waves exceeding a specified failure strain, are embedded into operational climate models (e.g. Williams et al., 2013, and reference therein). These further include the crucial process of wave energy attenuation over distance due to the presence of ice cover. Attenuation dictates the spatial distribution of wave energy in the ice-covered ocean, and hence the region susceptible to breakup. Therefore, an accurate model of attenuation undergirds breakup models and, in turn, climate models.

A series of pioneering experiments were conducted in the Arctic Ocean in the 1970s to early 1980s (e.g. Wadhams et al., 1988). The experiments were a catalyst for development of mathematical attenuation models. The models are conventionally based on an accumulation of scattering events (e.g. Masson and LeBlond, 1989) and/or parameterised viscous dissipation (e.g. Wang and Shen, 2010). Notably, they are also based on linear theories, i.e. the attenuation rate is independent of

wave amplitude. Field observations (Kohout et al., 2014) confirm a linear regime exists for attenuation of small-amplitude waves. However, there is a transition in attenuation rates as wave amplitude increases (this is substantiated by a number of field and laboratory experiments, see e.g. Meylan et al., 2014; Bennetts et al., 2015; Bennetts and Williams, 2015). Thus, the linear model is inaccurate for large-amplitude waves (Toffoli et al., 2015), and, consequently, erroneously predicts wave-induced breakup by up to hundreds of kilometres.

Field experiments are dominated by the natural environment and thus no control is possible, leaving a number of open questions in the interpretation of observations. Laboratory experiments, on the other hand, offer a controlled environment. However, previous tests have been limited to wave attenuation as induced by plastic or wooden plates (e.g. Bennetts and Williams, 2015; Bennetts et al., 2015; Toffoli et al., 2015) due to the difficulties to access proper ice tank facilities. Current knowledge of waves-in-ice is therefore impaired by a backdrop of uncertainties. Here we describe a first attempt to investigate experimentally the interaction between waves and real ice. Results are used to plan a larger scale experiment in the wave-ice tank at Aalto University.

2.   A PHYSICAL MODEL IN A SMALL SCALE WAVE-ICE FLUME

Preliminary laboratory experiments were undertaken at the University of Melbourne in a facility consisting of a wave flume housed inside a refrigerated chamber, where air temperatures can be reduced to −15 ℃ (figure 1). The flume is made out of glass supported by a wooden frame, ensuring optical access and that the structure experiences minimal contraction or expansion during freezing and defrosting. The flume is 14 m long, is 0.76 m wide, and was filled with fresh water 0.45 m deep. It is bounded at one end by a computer-controlled cylindrical wave-maker and at the opposite end by a linear beach with slope 1:6, which absorbs incoming wave energy (95% energy-effective for waves tested).
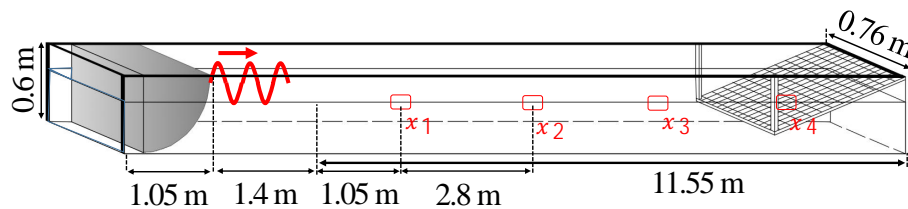
Figure 1: Schematic of the wave flume. The light-blue is the water, and the dark blue is the ice cover. Red rectangles indicate the camera locations.

Regular incident wave fields were generated with different periods, $T = 0.8$, 1, and 1.2 s (corresponding wavelengths $\lambda = 1$, 1.56, and 2.1 m), and amplitudes, a, so that the wave steepness $ka = 0.04$, 0.06, and 0.1, where $k = 2\pi/\lambda$ is the wavenumber. For each incident wave, a floating ice cover was grown, beginning with the water temperature being reduced to 0 ℃ by keeping the air temperature at −1 ℃ for 24 h. The freezing process was then initiated by dropping the air temperature to −12 ℃ for 5 h, at the end of which the ice cover was ≈0.01 m thick and covered the water surface along the full flume length. Tests were executed at an air temperature of −1 ℃. To allow wave generation in open water, ice in the initial 1.4 m of the flume was removed. With the ice at the desired initial condition, the wave maker was used to generate the specified wave field for 60 s (including a 5 s run-up). In all tests, the incident waves forced a layer of water 3 to 50 mm deep onto the surface of the ice at the leading ice edge (this is normally known as overwash, Nelli et al, 2017). Four cameras with a sampling rate of 60 Hz and a resolution of 1280 × 720 pixels were deployed at distances $x_1 = 1.05$m, $x_2 = 3.85$m, $x_3 = 6.65$m, and $x_4 = 9.45$ m from the wave maker. An image processing technique was used to extract the oscillatory vertical displacements of the surface (water or ice) in contact with air. Ice displacements were also recorded by tracking red markers embedded in the ice. Note that both techniques return the same displacements in the absence of overwash, while differences are notable in presence of an overwash flow on top of the ice cover.

3. ICE BREAK UP AND WAVE ATTENUATION

Figure 2 shows the amplitudes corresponding to the displacements obtained from the image processing and markers, denoted as a_{im} and a_{mk}, respectively, normalised with respect to the incident wave amplitude, a_0, as measured in the absence of ice. It also shows the ice configuration (broken/unbroken) at the end of each test. A more detailed description of this experiment can be found in Dolatshah et al. (2018).
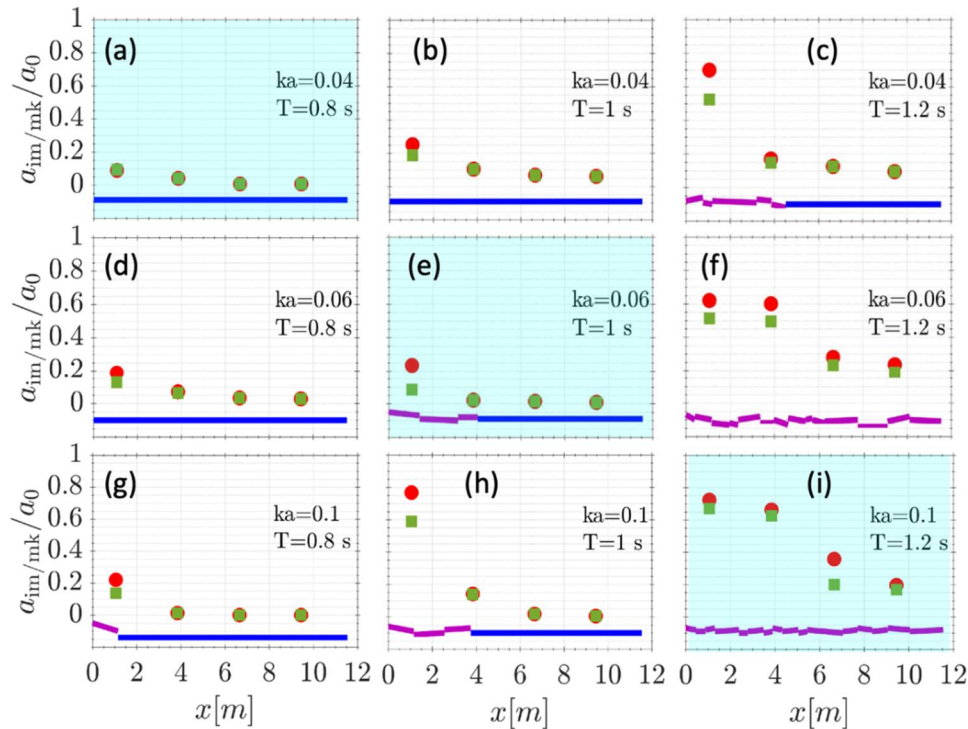
Figure 2: Mean ice (green filled square) and wave/ice-air interface (red filled circle) amplitudes as a function of distance from the wave maker. The continuous (blue thick line) and jagged (pink thick line) lines at the bottom of panels indicate the unbroken and broken status of the ice cover, respectively, at end of each tests; the lengths of broken ice floes are the measured dimension, while vertical displacements are arbitrary.

For the least steep and shortest period incident wave tested, ka = 0.04 and t = 0.8 s, the ice surface undulates with waves and the overwash is shallow, meaning that the amplitudes obtained from the image processing (a_{im}) and the markers in the ice cover (a_{mk}) are identical. The amplitudes are reduced significantly at the first observation point compared with the incident wave amplitude, with $a_{im}/a_0 \approx a_{mk}/a_0 \approx 0.09$. It then reduces steadily along the tank, with $a_{im}/a_0 \approx a_{mk}/a_0 \approx 0.01$ at the last observation point and without breaking the ice.

For the larger steepness, ka = 0.06 in fig. 2(d), the overwash is deeper, and the amplitude a_{im} is slightly greater than a_{mk} at the first observation point. The reduction at the first observation point is less than for the smallest steepness, but nonetheless significant, with $a_{im}/a_0 \approx 0.19$, which is ≈1.5 times greater than a_{mk}/a_0. Moreover, the reduction along the ice cover is rapid so that, at the last observation point, $a_{im}/a_0 \approx 0.03$. The waves do not break the ice but do produce a crack approximately half way along the ice cover.

For the largest steepness, ka = 0.1 in Fig. 2(g), the ice breaks close to its leading edge after 5 s, creating a 1.15 m-long floe, i.e., slightly greater than the incident wavelength. The wave amplitude at the first observation point, in the vicinity of the wave-induced breakup, is larger than for the smaller steepness, with $a_{im}/a_0 \approx 0.22$, which is ≈1.6 times greater than a_{mk}/a_0, due to the presence of overwash. Note that the large bending moments induced by the wave motion cause breakup,

while the increase of overwash depth is a consequence of breakup rather than a cause. The amplitudes measured at the subsequent observation points, in the continuous ice cover, are significantly reduced, with $a_{im}/a_0 \approx 0.01$, 0.00, and 0.00, respectively.

For the intermediate wave period, T = 1 s, the two steepest incident waves, ka = 0.06 in Fig. 2(E) and 0.1 in Fig. 2(F), break the ice into multiple floes at the leading edge, over a distance slightly greater than two incident wavelengths. The breakup for ka = 0.06 is relatively slow in comparison to ka = 0.1, for which the breakup occurs in <10 s, i.e., 10 wave periods. For all steepnesses, the amplitudes are greater than in the corresponding tests with the shortest period, particularly at the first observation point where the increase is up to a factor of 3.5 (for the largest steepness). Amplitudes a_{im} are 1.3, 2.8, and 1.3 times larger than the a_{mk} for ka = 0.04, 0.06, and 0.1, respectively. For all steepnesses, by the third observation point, $a_{im}/a_0 < 0.10$ and by the fourth observation point, $a_{im}/a_0 \approx 0.06$.

For the longest incident period, T = 1.2 s, the extent of wave-induced breakup significantly increases. For even the smallest steepness, ka = 0.04 in Fig. 2(c), and ice is broken for $\approx 2/5$ of the ice cover, i.e., slightly greater than two incident wavelengths. The first floe broke away from the edge after <5 s $\approx$ 4 T, but the next breaking event did not occur until ≈ 30 s = 25 T. Between the first two breaking events, the overwash reaches the second observation point so that the overwash amplitude is slightly larger there.

The two steepest waves, ka = 0.06 and 0.1 in Figs. 2(F) and 2(I), respectively, break up the entire ice cover, and the breakup reached the far end of the ice cover after only 5–10 s ($\approx$ 4–9 wave periods), noting that further breakup occurred following this. The wave amplitudes at the second, third, and fourth observation points are substantially greater than the smallest steepness case, with the amplitudes at the second observation point similar to those at the first observation point, and non-negligible amplitudes, $a_{im}/a_0 > a_{mk}/a_0 > 0.15$, at the fourth observation point. Moreover, the overwash was intense, getting deeper as the tests progressed, generally ≈ 30 mm but up to 50 mm, and reaching the fourth observation point after $\approx$ 40 s. The overwash depth is up to 5 times the ice thickness and ≈ 1.5 times the incident amplitude, a $\approx$ 35 mm.

4.   AN EXPERIMENTAL MODEL WITH MODEL ICE IN A LARGER FACILITY

The experiments described in Sections 2 and 3 are affected by a number of limitations. These include the use of fresh water ice, which is a more brittle form of ice than the natural sea ice, and two-dimensional physics, which does not describe the full extent of ice break up and thus ice response. To achieve a better understanding of wave-ice interaction, the large wave-ice tank at Aalto University will be accessed within the framework of Hydralab+. The tank is 40 m wide and 40 m long and it is equipped with a directional wave maker at one side and a beach at the other (the basin has been recently refurbished). The advantage of this facility is the availability of model ice, which is a property-controlled material generated by "doping" the water surface with a concentration of ethanol (mechanical properties of ice depends on ethanol concentration), and the large dimensions, which allow ice to break in more natural manner. The experiment will consist of tracing the attenuation rate of incident regular and irregular waves with varying dominant periods and amplitudes and monitoring the concurrent, wave-induced ice breakup.

The initial set up will be a continuous ice sheet with thickness of 0.02m, covering the entire basin. About one third of the ice cover in front of the wave maker will be used to measure mechanical properties using destructive tests and it will be be removed before running the tests. An operational ice surface covering two third of the tank (see figure 3) allows enough space to monitor the incident wave in open water, while leaving enough space for assessing the propagation of waves in ice. Wave propagation and transformation will be monitored in terms of water surface elevation at different distances from the wave maker, using five pressure sensors. The advantage of the pressure sensors is that they are below the water surface and thus are not subjected to collision with ice floes, which would otherwise happen with standard surface sensors. The response of the

ice cover will be measured with motion sensors that will be distributed evenly on the surface (see figure 3). Infrared cameras will track the instantaneous positions of the sensors and return their accelerations. The instrumentation is complemented with an industrial camera to monitor the temporal evolution of the ice break up and statistical distribution of the ice floe size distribution.

Tests will run with different initial regular and irregular wave configurations. Wave periods will be T = 1.4, 1.6, and 1.8 s (wavelengths of 3, 4 and 5 m). The wave amplitude will be chosen to have wave steepness ka = 0.08, where k is the wavenumber associated to the wave period and a is the wave amplitude defined as half the wave height. The irregular wave fields defined by a JONSWAP spectral form (Komen et al. 1994), with peak period identical to the period selected for monochromatic waves and significant wave height to ensure an average wave steepness of 0.08. Each test will last 1 hour to allow the ice floe distribution to reach a steady condition. This large run time will allow an estimation of the temporal evolution of wave attenuation as a function of the extent of ice break up and the evaluation of the temporal evolution of floe size distribution.
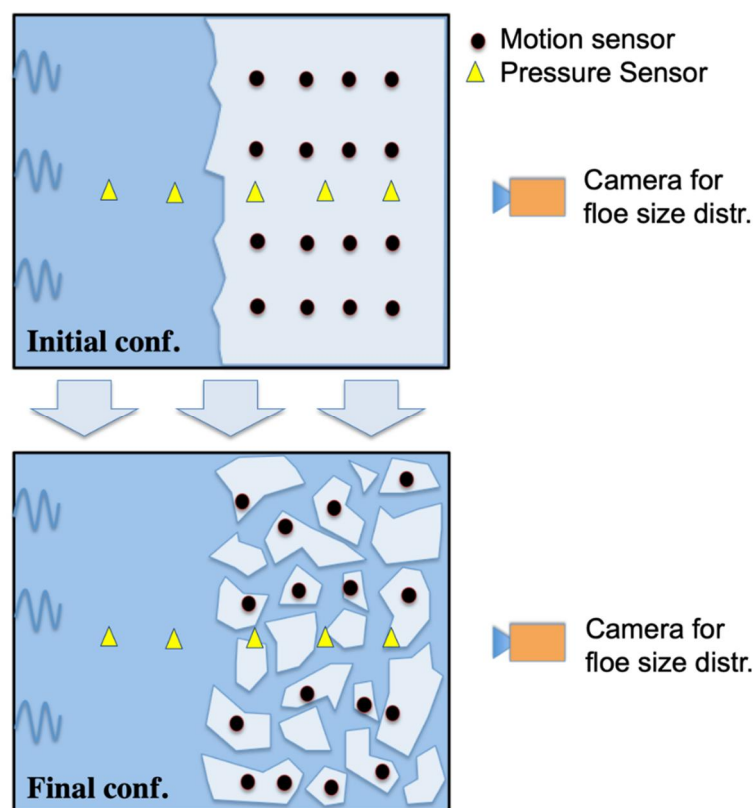
Figure 3: Schematic of the experimental set up in the wave-ice tank at Aalto University

4.   CONCLUSIONS

Preparatory tests in a small scale wave-ice flume are reported to explore the interaction between waves and a compact sheet of freshwater ice. Results show that short-period small-steepness incident waves travel only a short distance into the ice-covered water without breaking the ice. As the incident waves get longer and steeper, the waves propagate farther into the ice cover and rapidly break up the ice cover over an increasing distance. Consequently, a sharp transition was noted to rapid breakup of the entire ice cover and wave propagation along the full length of ice-covered water, indicating the existence of a positive feedback loop between increased breakup and increased propagation. Results from this pilot project are limited by the brittle properties of the freshwater ice and the small dimensions of the flume. An experimental model in the large wave-ice tank at Aalto University is planned to validate preliminary results.

REFERENCES

Asplin, M. G., Galley, R., Barber, D. G. and Prinsenberg, S. (2012). Fracture of summer perennial sea ice by ocean swell as a result of Arctic storms. *J. Geophys. Res.* 117 (C06025).

Bennetts, L. G., Alberello, A., Meylan, M. H., Cavaliere, C., Babanin, A. V. and Toffoli, A. (2015). An idealised experimental model of ocean surface wave transmission by an ice floe. *Ocean Modelling* 96, 85–92.

Bennetts, L. G. and Williams, T. D. (2015). Water wave transmission by an array of floating discs. *Proc. R. Soc. A* 471 (2173), 20140698.

Dolatshah, A., Nelli, F., Bennetts, L.G., Alberello, A., Meylan, M.H., Monty, J.P., Toffoli, A. (2018). Hydroelastic interactions between water waves and floating freshwater ice. *Physics of Fluids*, 30(9), 091702.

Khon, V. C., Mokhov, I. I., Pogarskiy, F. A., Babanin, A., Dethloff, K., Rinke, A., Matthes, H. (2014). Wave heights in the 21st century Arctic Ocean simulated with a regional climate model. *Geophys. Res. Lett.* 41, 2956–2961.

Kohout, A. L., Williams, M. J. M., Dean, S. M. and Meylan, M. H. 2014 Storm-induced sea ice breakup and the implications for ice extent. Nature pp. 604–607.

Komen, G. J., Cavaleri, L., Donelan, M., Hasselmann, K., Hasselmann, H., Janssen, P. A. E. M. (1994). Dynamics and Modelling of Ocean Waves. *Cambridge University Press*.

Liu, A. K., Mollo-Christensen, E. (1988). Wave propagation in a solid ice pack. *J. Phys. Oceanogr*. 18 (11), 1702–1712.

Masson, D., LeBlond, P. H. (1989). Spectral evolution of wind-generated surface gravity waves in a dispersed ice field. *J. Fluid Mech.* 202, 43–81.

Meylan, M. H., Bennetts, L. G., Kohout, A. L. (2014). In-situ measurements and analysis of ocean waves in the Antarctic marginal ice zone. *Geophys. Res. Lett*. 41, 5046–5051.

Richter-Menge, J., Walsh, J. E., Thomas, K. (2012). Seasonal-to-decadal predictions of Arctic Sea Ice: Challenges and strategies. Tech. Rep. Polar Research Board, National Academy of Sciences, ISBN: 978-0-309-26526-3.

Shen, H. H., Hibler, W. D., Lepparanta, M. (1987). The role of floe collisions in sea ice rheology. *J. Geophys. Res.* 92 (C7), 7085–7096.

Thomson, J., Rogers, W. E. (2014). Swell and sea in the emerging Arctic Ocean. *Geophys. Res. Lett.* 41, 3136–3140.

Toffoli, A., Bennetts, L. G., Meylan, M. H., Cavaliere, C., Alberello, A., Elsnab, J., Monty, J. P. (2015) Sea ice floes dissipate the energy of steep ocean waves*. Geophys. Res. Lett.* 42 (20), 8547–8554.

Wadhams, P. (1983) A mechanism for the formation of ice edge bands*. J. Geophys. Res.* 88 (C5), 2813–2818.

Wadhams, P., Gill, A. E., Linden, P. F. (1979). Transects by submarine of the east Greenland polar front. Deep Sea Research Part A. *Oceanographic Research Papers* 26 (12), 1311–1327.

Wadhams, P., Squire, V. A., Goodman, D. J., Cowan, A. M., Moore, S. C. (1988). The attenuation rates of ocean waves in the marginal ice zone. *J. Geophys. Res.* 93 (C6), 6799–6818.

Wang, R., Shen, H. (2010). Gravity waves propagating into an ice-covered ocean: A viscoelastic model. *J. Geophys. Res.* 115 (C06024).

Williams, T. D., Bennetts, L. G., Dumont, D., Squire, V. A., Bertino, L. (2013). Wave-ice interactions in the marginal ice zone. Part 1: Theoretical foundations. *Ocean Model.* 71, 81–91..

SCALE-MODEL RIDGES AND INTERACTION WITH NARROW STRUCTURES

Aleksey Shestov (1), Jaakko Heinonen (2), Knut V.Høyland (3), Evgenii Salganik (3), Marnix van den Berg (3), Mark Shortt (4), Åse Ervik (5), Ilkka Perälä (2)

(1) UNIS, Norway
(2) VTT, Finland
(3) NTNU, Norway, E-mail: knut.hoyland@ntnu.no, Evgenii.salganik@ntnu.no
(4) UCL, Great Britain
(5) Multiconsult, Norway

An experimental campaign to investigate sea ice ridge interaction with bottom-fixed structures has been designed. We aim to investigate a) the scaled ridge properties, b) the processes during testing and c) the scaling of ridge forces with respect to a cylindrical and conical structures at the water line. Full-scale ridge structure interaction data is available for the Norstrtrömsgrund lighthouse so we will use its size in scaling the tests. We will assume that gravity/buoyancy forces contribute and combine Froude and Strength scaling with a geometric scale-factor of 15. The initial ice temperature and accumulated air temperatures during consolidation (FDD) will be varied to investigate how reasonably scaled ridge properties can be achieved. Finally, structures with cylindrical an conical different waterlines will be used.

1.   INTRODUCTION

Ice action from first-year ice ridges remains one of the key challenges in design of structures (offshore wind, aids for navigation and oil/gas), mooring systems and ships in a warming Arctic and sub-Arctic marine and coastal environment. There is a relatively high uncertainty in the prediction of ridge loads, in the most recent review the world-wide expert estimation of ridge loads ranged from 120 to 605 MN (Timco and Croasdale, 2006). In shallow water without tide such as the Baltic conical structures are often used. But, the effect of cones, and in particularly narrow cones, on ice ridge interaction is not well known or documented. Basin tests are often carried out in relation to design of structures, but the validation of these experiments is lacking, and there is no general agreement on how to scale and produce first-year ridges in ice basins (Repetto-Llamazares, 2010).

Due to climate change the Arctic sea ice cover is changing, it becomes thinner (Kwok et al., 2009; Kwok and Rothrock, 2009; Haas et al., 2008; Giles et al., 2008) and younger (Maslanik et al., 2007, 2011; Wadhams et al., 2011). It gives longer ice-free summers, lighter ice condition and a larger fraction of the Arctic sea ice cover becomes *First-year ice*. This will probably cause increased Arctic sea transport, both through Arctic waters (e.g. Northeast passage), and to and from Arctic settlements. It will also increase the exploitation of mineral resources. Much of this increased activity will take place in areas with predominantly first-year ice, such as all sub-Arctic seas (the Baltic Sea, the Sea of Okhotsk, the Caspian Sea and the Sea of Bohai), and many shallow Arctic areas where *First-year ice ridges* give the Ultimate Limit State quasi-static design ice load. Even though the ice conditions get lighter it is not obvious that the extreme events are reduced. Cammaert et al. (2008) used a probabilistic approach and included a warming climate, but found negligible effect on a 100 year ice load. One important application is the development of European offshore wind power in the Baltic Sea, where one promising way to decrease the costs in the sub-structure part is to use a slightly conical structures. However, this will lead the ice load design outside the guidelines (*e.g.* ISO 19906).

2.   BACKGROUND AND THEORY

We wish to examine

- The scaled ridge properties
- The processes during testing

- The scaling of ridge forces with respect to a cylindrical and conical structures at the water line.

The scaling of measured ridge forces can be done by assuming that the gravity/buoyancy give vital contributions to the force, or by assuming that these can be neglected. We assume that during the ridge interaction with the structure the effects of inertia, gravity/buoyancy and ice breaking are the three essential force contributions. The geometric and strength variables are both scaled - according to the Froude scaling law - with the same factor λ, the velocity is scaled with $\lambda^{1/2}$, and the forces with λ^3. However, there is considerable disagreement in the ice community about scaling of ice-structure interaction dominated by crushing, see Määttänen (1979) for derivation of scaling without gravity/buoyancy effects. The most important ridge properties are the thickness and the strength of the consolidated layer. It may easily become too thick and strong and seems to be very sensitive to the temperature of the ice used to produce the ridge (Høyland, 2010). Thermo-dynamics play an essential role and we wish to quantify the effect of initial ice temperature and FDD on the thickness and strength of consolidated layer. This will enable a controlled way to scale the consolidated layer.

During process of interaction the ice rubble surcharge and effect of level ice confinement behind the ridge affects the force on the structure. The present ISO standard disregards the effect of surcharge, and, tacitly assumes full level ice confinement behind the ridge. However, the study of Serré and Liferov (2010) indicate that the surcharge may significantly affect the ridge action. Further Dalane et al. (2009) suggest a significant reduction of ridge force for unconfined ridges. We will quantify the mechanical (including volumetric) properties of the ice unconsolidated layer (rubble) by critical state theory, and study the rubble surcharge during tests with a scaled version of the Norströmsgrund lighthouse (LOLEIF / STRICE data). We will also quantify the reduction of ridge force with level ice confinement. In this project, we wish to scale, produce and characterize first-year ice ridges and measure their interaction with a scaled model of the Norströmsgrund lighthouse. Full-scale measurements of first-year ice ridge action on the Norströmsgrund lighthouse has been thoroughly measured through the EU projects LOLEIF and STRICE (1997-2003) and gives a rare base for the comparison of measured full-scale ice ridge action and a scale-model test.

3.   EXPERIMENTAL PLAN

3.1 Scaling

We assume that during the ridge interaction with the structure the effects of inertia, gravity/buoyancy and ice breaking are the three essential force contributions so that the geometric and strength variables are both scaled with the same factor λ, and the velocity is scaled with $\lambda^{1/2}$. We choose a scale factor $\lambda=15$. The deepest measured ice ridge keel in the Baltic ever was 28 m (Palosuo, 1975), but no ridges deeper than 9 m were observed in the LOLEIF/STRICE programs to interact with the Norströmsgrund lighthouse, so we choose a full-scale value of ridge keel depth of 10 m. Palosuo (1975) report that block thickness in the Baltic ridges range from 0.15 to 1.2 m so we choose a full-scale initial level ice thickness of 0.75 m. We will not study ice-induced vibrations so the scaled structure will be as stiff as possible. Further, there is little proof that ice drift velocity affects the ice ridge action, and most high load events on the Norströmsgrund occurred with drift velocities between 0.1 and 0.2 m/s, so we choose a full-scale ice drift velocity of 0.15 m/s. Table 1 gives the geometric properties. The mechanical properties of the ridges is a function of the geometry and the thermodynamic processes and will be measured, not predetermined.

Table 1. Scaling of properties, full-scale and model-scale (scale factor $\lambda=15$).

	Ice thickness	Keel depth	Structure diameter	Ice drift velocity
Full-scale	0.75 m	10 m	7.5 m	0.15 m/s
Model-scale	0.05 m	0.67 m	0.50 m	0.04 m/s

3.2 Test matrix and parameter variation

The experimental program consists of four steps (see next paragraph) and we aim at letting the following three variables have two levels (high / low) as detailed in Table 2: a) The initial temperature of the level ice going into the ridge ($T_{i,0}$), b) Degree of consolidation measured by the *Freezing Degree Days (FDD)* and c) the level ice confinement in the interaction experiments. Høyland et al. (2001) showed that $T_{i,0}$ may have considerable effect of the thickness of the consolidated layer, a change of $T_{i,0}$ from -1.3 C to -1.8 C increased the thickness of the consolidated layer from about 0.08 m to 0.12 m. With a low *FDD* the initial phase of consolidation will dominate (Høyland, 2010) but with higher FDDs the main phase becomes more important so our experiments will allow for a quantification of this effect. Finally, Dalane et al. (2009) showed that the ridge load can be reduced considerably if the level ice behind the ridge is broken. This means that ice ridges embedded in a large ice sheet will give higher ridge action than ridges without a surrounding confining level ice sheet. The main features in the experimental program are:

1. Ridge production where the initial temperature ($T_{i,0}$) and the thickness (h_i) of the level ice are the variable parameters. These will be measured manually.
2. Consolidation where the air temperature (T_a) and the consolidation time (Δt_{cons}) give the *Freezing Degree Days (FDD)* that will be the variable parameter. The development of the consolidated layer will be monitored with thermistor-strings installed through the ridges.
3. Measure mechanical properties and geometry prior to interaction experiments. The strength of the ice ridge consolidated layer and ice rubble fragments is measured as explained below. To accurately measure the ice ridge profile, an upward looking sonar will be utilized.
4. Run ridge interaction experiments with a cylindrical and conical structures. The cylindrical will be the base as comparison can be done with full-scale data from the EU projects LOLEIF and STRICE. The cone angle will be 75°.
5.

Table 2. Ridge production and parameter variability. Two ridges will be made from each ice sheet. T_f is the freezing point of the basin-water

	Sheet	Ridge #	$T_{i,0}$	FDD	Structure
Week 1 Cylindrical structure , Base case Norströmsgrund to allow for comparison with full-scale data	1	R11	T_f - 1.5°C	-5°C·Days	Cylindrical
	1	R12	T_f	-5°C·Days	Cylindrical
	2	R21	T_f - 1.5°C	No cooling	Cylindrical
	2	R22	T_f	No cooling	Cylindrical
Week 2 Conical structure	3	R31	T_f - 1.5°C	-5°C·Days	Conical
	3	R32	T_f	-5°C·Days	Conical
	4	R41	T_f - 1.5°C	No cooling	Conical
	4	R42	T_f	No cooling	Conical

3.3 Testing of mechanical properties

The mechanical properties of the consolidated layer and the ice rubble (unconsolidated part) will be measured separately. In the consolidated layer the uniaxial tensile and compressive strength and bi-axial compressive strength should be measured. The uniaxial tensile strength will be measured through bending tests (Jensen et al., 2001).

The ice rubble mechanical properties will be measured through punch shear tests, in which the ridge keel is penetrated vertically by a cylinder. The punch force and corresponding cylinder displacement is measured. Possible areas for punch tests are indicated in Fig 1a. The force and displacement of the platen is measured with video recordings (above and underwater). Before the keel is loaded, the consolidated layer is cut free from the surrounding ice field along the perimeter of cylinder. This test data is then further analysed to evaluate the material parameters of the ice rubble.

The ice rubble elastic behavior is assumed isotropic so it will be characterized by two elastic constants (K and G). The plastic behavior is modelled by the combination of critical state concept (see e.g. Muir Wood, 1990) which requires a frictional resistance constant (M) and breakage mechanics concept which takes three parameters (p_c, ω, and v) (Einav, 2007).

3.4 Measurements during interaction testing

A schematic drawing of a ridge interaction test is shown in Fig. 1a. The structures, shown in Fig. 1b, are fixed to the main carriage of the ice basin. The carriage is moved with a constant velocity through the ridges. We will measure the forces, displacements and use tactile sensors to measure the contact pressure of ice. The experiments will be filmed above the water level and underwater. In addition, the ridge keel interaction will be continuously scanned with a sonar so that careful studies on the deformation mechanisms in the ridges can be studied.
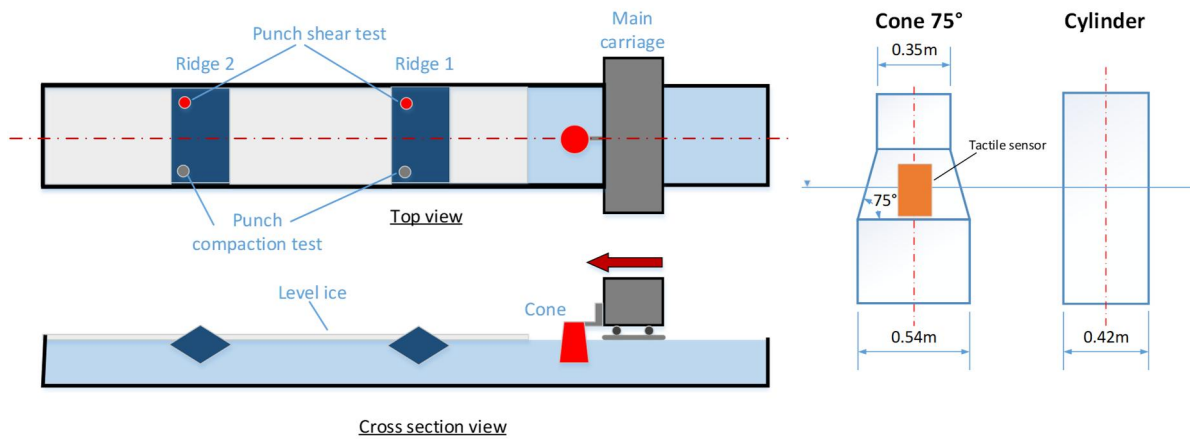
Figure 1. a) Schematic drawing of ridge penetration tests, b) Shape and main dimensions of the test structures in the model scale.

ACKNOWLEDGEMENT

REFERENCES

Cammaert, G., Trumars, J. and Eide, L.I. 2008. A probabilistic approach to design ice loads for an Arctic jack-up drilling platform, Proc. of the 27 OMAE, Estoril, Portugal, OMAE2008-57519.

Dalane, O., Aksnes, V., Løset, S. and Aarsnes, J.V. (2009). A moored arctic floater in first-year sea ice ridges, Proc. of the 28 OMAE, Honolulu, USA, OMAE2009-79945.

Einav, I., 2007. Breakage mechanics-Part II: Modelling granular materials. Journal of the Mechanics and Physics of Solids 55, 1298–1320. doi:10.1016/j.jmps.2006.11.004

ISO (2010). Petroleum and natural gas industries - Arctic offshore structures, ISO/FDIS/19906, ISO TC 67/SC 7. Final Draft, International Standard, International Standardization organization, Geneva, Switzerland, 434 p.

Giles, K. A., S. W. Laxon, and A. L. Ridout (2008), Circumpolar thinning of Arctic sea ice following the 2007 record ice extent minimum, Geophys. Res. Lett., 35, L22502, doi:10.1029/2008GL035710.

Haas, C., S. Hendricks, H. Eicken, and A. Herber (2010), Synoptic airborne thickness surveys reveal state of Arctic sea ice cover, Geophys. Res. Lett., 37, L09501, doi:10.1029/2010GL042652.

Høyland, K.V. (2010). Thermal aspects of model basin ridges, Proc. of 20 Int. Symp. on Ice (IAHR), Lahti, Finland, Paper \#66.

Høyland, K.V., Jensen, A., Liferov, P., Heinonen, J., Evers, K-U., Løset, S., and Määttänen, M. (2001). Physical modelling of first-year ice ridges - Part I: Production, consolidation and physical properties, Proc. of the 16th Int. Conf. on Port and Ocean Eng. under Arctic Conditions (POAC), Ottawa, Canada, 3: pp. 1483-1492.

Jensen, A., Løset, S., Høyland, K.V., Liferov, P., Heinonen, J., Evers, K-U., and Määttänen, M. (2001). Physical modelling of first-year ice ridges - Part II: Mechanical properties, Proc. of the 16th Int. Conf. on Port and Ocean Eng. under Arctic Conditions (POAC), Ottawa, Canada, 3: pp. 1493-1502.

Kulyakhtin, S. and Høyland, K.V. (2015). Ice rubble frictional resistance by critical state theories. Cold Regions Science and Technology, 119, 145-150.

Kwok, R., and D. A. Rothrock (2009), Decline in Arctic sea ice thickness from submarine and ICESat records: 1958–2008, geophys. Res. Lett., 36, L15501, doi:10.1029/2009GL039035.

Kwok, R., G. F. Cunningham, M. Wensnahan, I. Rigor, H. J. Zwally, and D. Yi (2009), Thinning and volume loss of the Arctic Ocean sea ice cover: 2003–2008, J. Geophys. Res., 114, C07005, doi:10.1029/2009JC005312.

Lindbjør-Nilsen, H. and Høyland, K.V. (2016), FEM-CEL simulations of full scale and model scale punch tests on ice rubble with the Modified Cam clay model, Proc. of the 23 Int. Symp. on Ice (IAHR), Ann Arbor, USA, Paper 4877586.

Maslanik, J. A., J. Stroeve, C. Fowler, and W. Emery (2011), Distribution and trends in Arctic sea ice age through spring 2011, Geophys. Res. Lett.,38, L13502, doi:10.1029/2011GL047735.

Muir Wood, D., (1990). Soil behaviour and critical state soil mechanics. Cambridge University Press, New York.

Repetto-Llamazares, A.h.W. (2010). Review in model basin ridges, Proc. of the 20th Ice Symp. (IAHR), Lahti, Finland, Paper \#154.

Palosuo, E. (1975) Formation and structure of ice ridges in the Baltic, University of Helsinki / Finish board of navigation, Helsinki, Winter navigation research board, rep no. 12, 54 p.

Pustogvar, A., Kulyakhtin, S. and Høyland, K.V. (2014). Laboratory Oedometer Tests on Rubble Ice,

Proc. of the 22 Int. Symp. on Ice (IAHR), Singapore, Paper \#1166.

Serré, N. and Liferov, P. (2010). Loads from ice ridge keels - experimental vs. numerical vs. analytical,

Proc. of the 20 Int. Symp. on Ice (IAHR), Lahti, Finland, paper 92.

Timco, G.W. and Croasdale K. (2006). How well can we predict ice loads? Proc. of the 18th Ice Symp. (IAHR), Sapporo, Japan, pp 167-174.

Wadhams, P., N. Hughes, and J. Rodrigues (2011), Arctic sea ice thickness characteristics in winter 2004 and 2007 from submarine sonar transects, J. Geophys. Res., 116, C00E02, doi:10.1029/2011JC006982.

II – CNRS - CORIOLIS II

The « Coriolis » rotating platform, 14 m in diameter, is the largest turntable in the world. Its total weight is 150 tons and it supports an extra load of 180 tons. The axis of rotation is vertical with an accuracy ± 3.10-6 rad. Its rotation period can be set with high stability (dT/T = 10-4) between 30 and 1000 s and can be modulated by computer control in order to generate permanent or oscillating circular flows, so to simulate tidal effects for instance.

The platform is equipped with a tank of 13 m diameter and 1.2 m height. It can be filled with homogeneous or density stratified water with any vertical profile (e.g. multilayer or linear). The stratification is made by filling the tank through the bottom with increasingly salty water, obtained by computer controlled mixing from two underground tanks with specified salinity and temperature (within 1C). Various fixed or moving obstacles can be installed in the tank (transverse channel 10 m long and 4 m wide, annular shelf, oscillating plates, towed cylinder, cylindrical plunger …). All the instruments, including lasers and computers, stay on the platform, where electricity, water and computer network are available, like in an ordinary laboratory. Researchers can stay on the platform during rotation. Many operations are then easier than in a small rotating tank.

Thanks to the large dimensions, large Reynolds number (inertia/viscous friction) can be reached, and Rossby numbers (inertia/rotation) as low as 10-3 -10-2, like in natural geophysical or environmental flows. This is obtained with negligible centrifugal effects, e.g. small curvature of isopycnals.

The facility is equipped with continuous Argon laser (8 W) and Yag solid laser, and use highly transparent water for illumination along a large scale laser sheet. Particle Imaging Velocimetry (PIV) systems provide time resolved velocity fields in both horizontal and vertical planes of up to 3 m x 4 m in size, with a relative precision 2%. The laser sheet position is scanned by a computer controlled system, so that image correlation for PIV can be made in a volume. Both vorticity and divergence fields can be computed from the PIV data and directly compared with numerical computations.

Various techniques of flow visualization are available, with dye, hydrogen bubbles or tin oxyde electrolytically released from a wire. Illumination devices and high quality video cameras are available. Tracking of float motion by image processing is available to record lagrangian trajectories in a plane.

THE DYNAMICS OF BI-DRIECTIONAL EXCHANGE FLOWS: IMPLICATIONS FOR MORPHODYNAMIC CHANGES WITHIN ESTUARIES

Claudia Adduce (1), Maria Chiara De Falco (1), Alan Cuthbertson (2), Janek Laanearu (3), Daniela Malcangio (4), Katrin Kaur (3), Eletta Negretti (5), Joel Sommeria (5), Thomas Valrha (5) & Samuel Viboud (5)

(1) University Roma Tre, Italy, E-mail: claudia.adduce@uniroma3.it
(2) University of Dundee, School of Science and Engineering, UK, E-mail: a.j.s.cuthbertson@dundee.ac.uk
(3) Tallinn University of Technology, Estonia, E-mail: janek.laanearu@taltech.ee
(4) Polytechnic University of Bari, Italy, E-mail: daniela.malcangio@poliba.it
(5) Laboratory of Geophysical and Industrial Flows, France, E-mail: joel.sommeria@univ-grenoble-alpes.fr

An experimental study has been conducted at the CNRS Coriolis Rotating Platform at LEGI, Grenoble, in a trapezoidal cross section channel, to investigate uni and bi-directional exchange flows. Both rotating and non rotating experiments, with a non-erodible and erodible bed layer were considered. Experimental measurements focused on obtaining high-resolution velocity and density fields in different vertical planes spanning the width of the channel using 2D Particle Image Velocimetry, Laser Induced Fluorescence, ADV and micro-conductivity probes in several channel sections. Preliminary results from the study are presented herein and consider the exchange flow dynamics at the interface, with particular focus on the observed cross-channel variations in the counter-flowing water masses and layer thickness. Further analyses are ongoing to improve understanding of the interfacial mixing and entrainment/detrainment processes, along with the bed-morphological changes initiated by interaction mechanisms between the erodible bottom boundary and the uni- or bi-directional exchange flows.

1. INTRODUCTION

Uni-directional gravity currents and bi-directional exchange flows occur within estuaries, tidal inlets and sea straits when horizontal density differences (i.e. baroclinic forcing) and/or pressure gradients (i.e. barotropic forcing) are present between the adjacent water bodies. The nature of these buoyancy-driven flows depends on whether Coriolis effects due to the Earth's rotation play a significant role in the internal flow dynamics (depending on the scale of the environmental/geophysical flow under consideration), as well as the strong topographic controls imposed by seafloor bathymetry and channel shape. These factors are known to exert significant influence on both internal mixing and secondary circulations generated by exchange flows (e.g. Kõuts and Omstedt, 1993; Johnson and Ohlson, 1994; Andrejev et al., 2004; Laanearu et al., 2014). In such cases, the flow dynamics of the dense lower layer depend primarily on the volumetric flux and channel cross-sectional shape, while the stratified interfacial flow mixing characteristics, leading to fluid entrainment/detrainment, are also dependent on the buoyancy flux and motion within the upper (lower density) water mass (i.e. bi-directional exchange flow). Furthermore, when submerged channels are relatively wide in comparison to the internal Rossby radius of deformation, Earth rotation effects introduce geostrophic adjustment of these internal fluid motions (e.g. Cuthbertson et al, 2011) that can suppress turbulent mixing generated at the interface (e.g. Maxworthy, 1985) and result in the development of Ekman layers that induce secondary, cross-channel circulations (e.g. Johnson and Ohlson, 1994; Cossu et al., 2010), even within straight, rectangular channels.

Understanding of these uni- and bi-directional flow processes is particularly relevant in coastal regions, where water and nutrient exchanges between both tidal and non-tidal inlets (e.g. estuaries, lagoons) and open marine waters are strongly regulated by channel topography and bathymetric features (Cuthbertson et al., 2006). This has significant implications for the intrusion of saline marine waters and flushing of semi-enclosed estuarine impoundments, fjords and regional

seas (Matthäus and Lass, 1995; Farmer and Armi, 1999). Furthermore, as many tidal inlets and estuaries exhibit complex morphological patterns consisting of channels and shoals with strong spatial and temporal variability (e.g. Schramkowski and de Smart, 2002), it is important to understand how the evolution of these topographical features produces an associated feedback on internal flow dynamics. Specifically, the interaction between channel bathymetry and exchange flows under the influence of boundary friction and earth rotation has been shown analytically (Valle-Levinson et al., 2003) to result in transverse asymmetries in the structure of the along-estuary flows, which disappear under strongly frictional (i.e. high Ekman number) conditions. In addition, the cross-channel structure of secondary flows, controlled by the balance between pressure gradient and friction, can reverse in direction under very weak friction, reflecting Coriolis deflection of along-estuary flows (i.e. geostrophic adjustment). It is therefore expected that, for both uni-directional currents and bi-directional exchange flows generated over deformable channels (e.g. estuaries), the physical interactions between the lower dense water flow and the erodible bed will have a strong influence in reshaping channel morphology (e.g. Schramkowski and de Swart, 2002). This changing morphology is thus expected to have associated feedback on transverse asymmetries associated with uni-directional currents and bi-directional exchange flows (e.g. velocity distributions; maximum velocity thalweg; secondary flow circulations), as well as on their internal flow stability (e.g. stratification; interfacial mixing; entrainment) (e.g. Valle-Levinson et al., 2003).

In the current study, the behaviour of uni-directional gravity currents and bi-directional exchange flows along a trapezoidal-shaped channel with a rigid and erodible bottom topography is investigated to determine the relative influence of the channel geometry and Coriolis forces on the lateral distribution of the (counter-)flowing water masses, interfacial mixing and secondary flow generation, as well as the feedback from bed deformation on these internal flow processes. Recent studies (e.g. Cuthbertson et al, 2011; 2014; Laanearu et al, 2014) of uni-directional, dense gravity currents generated in rotating and non-rotating systems indicated that a rigid, V-shaped channel topography had a strong influence on both flow distribution and associated interfacial mixing characteristics along the channel. Similar topographic controls on bi-directional exchange flows in rotating and non-rotating systems, along with their impact on (and feedback from) deformable channel bed conditions have not yet been fully resolved.

The current paper reports initial findings from a parametric experimental study conducted at the Coriolis Rotating Platform at LEGI Grenoble in Spring/Summer 2018, which was aimed at filling existing knowledge gaps associated with enhanced understanding of (i) the physical nature of exchange flow-bathymetry feedback within deformable channels; (ii) interfacial mixing, secondary flow circulations and near-bed boundary dynamics; and (iii) the external parametric influences of tidal/freshwater forcing, density differences, bed friction and Coriolis effects on these exchange flow-topography interactions

2.   EXPERIMENTAL APPARATUS

Laboratory experiments were conducted in the CNRS Coriolis Rotating Platform at Laboratoire des Ecoulements Geophisiques et Industriels (LEGI) in Grenoble, which consists of a 13 m diameter and 1.2 m deep circular tank that can be rotated at a constant angular velocity. For the current experimental configuration, a trapezoidal cross-section channel of length 6.5 m (Figure 1) was positioned in the tank. This channel was constructed from transparent Plexiglas to facilitate flow visualization along its length.

Entry and exit slopes (α_b **= 26.57°**) connected the main channel section to the inlet basin (B) and outlet basin (A). The trapezoidal section had a 2 m top width, 1 m bottom width and 0.5 m total depth, with side slopes of α_s **= 45°**. A 0.1 m deep sediment trap, running the full length of the channel, was built into the trapezoidal channel arrangement to perform the experiments with an erodible bed layer, while a rigid Plexiglas bottom was used for the non-erodible bed experiments. The sediments used were polystyrene particles with representative nominal diameter D_n **= 310** μm, density ρ_s **= 1040** kg/m^3 and settling velocity of the particles v_s **= 0.15** cm/s based on

Stokes law for an isolated spherical grain. Before commencing the erodible bed experiments, the sediment bed layer contained within the trap was leveled manually in order to provide the same initial boundary condition as for the equivalent non-erodible bed experiments. At the beginning of each experiment the circular tank was filled with freshwater at density ρ_2, to a total depth $H = 0.9\ m$, with a corresponding submergence depth in the channel $h = 0.4\ m$. For the rotating experiments, the platform was spun-up slowly to reach a fixed angular velocity and attain a state of rigid body rotation after several hours.
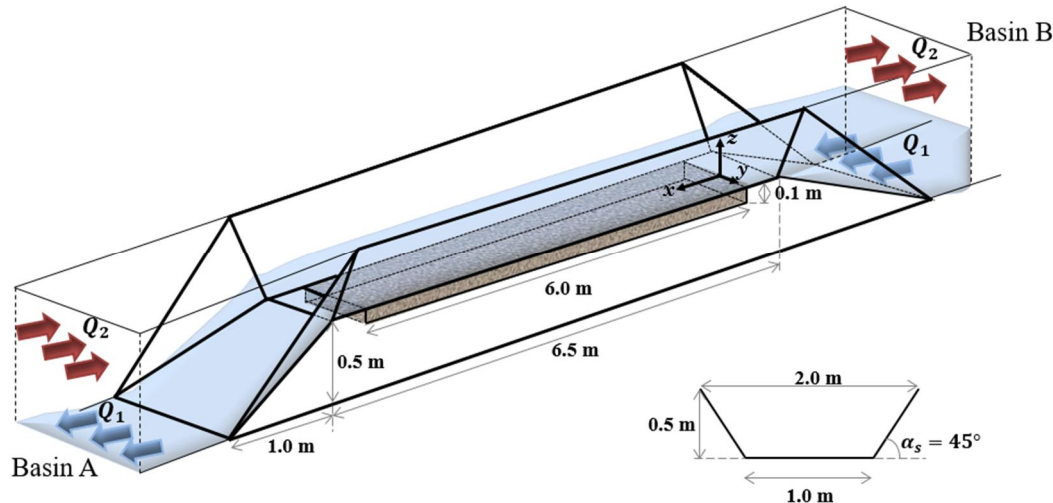
Figure 1 Schematic representation of the experimental apparatus in the LEGI Coriolis Platform

The saline water at density ρ_1 was delivered through a gravity feed system to the bottom of Basin B, via a rectangular manifold, filling up basin B slowly (to minimize mixing) until the dense water interface reached the elevation of the channel bottom. At this point, a prescribed, constant saline water discharge Q_1 was fed into basin B to establish a stable, uni-directional flow along the trapezoidal channel. The same flow rate was extracted from outside of the channel (through the drainage system in the circular tank) to ensure the water depth in the channel remained constant. Two water pumps in the upper part of Basin B provided a constant fresh water flux Q_2 within the channel to generate a bi-directional exchange flow, once the saline water outflow was fully established.

Experimental measurements were targeted at obtaining high temporal and spatial resolution density and velocity fields across the channel, particularly within a central 1 m-long section of the 6.5 m long trapezoidal channel (i.e. away from the converging and upsloping approaches from basins A and B). This central section was selected to ensure that the exchange flow conditions generated through the channel at this location could be assumed to be fully geostrophically-adjusted. To this aim, two-dimensional Particle Image Velocimetry (PIV) and Laser Induced Fluorescence (LIF) were used to obtain measurements in vertical (XZ) planes along this central region of the trapezoidal channel (Figure 2a).

A 6 W YAG laser, mounted on a traverse system on the side of the tank, provided a movable vertical laser sheet, aligned along the x-direction, spanning the channel width. This set-up allowed velocity and density fields to be obtained in 11 vertical sections (XZ) at lateral positions ranging between -79.2 cm < y < 20.8 cm (Figure 2b), at lateral intervals of 10 cm. These velocity (PIV) and density (LIF) fields were acquired by two PCO high-speed, digital cameras with a spatial resolution of 2560x2160 pixels and frame rate set at 10 Hz. For the LIF and flow visualization, Rhodamine 6G was added to the saline water at a constant concentration.

The PIV and LIF measurements were obtained by scanning the 11 vertical sections 3 times over a 30 second duration for each field. Moreover, rapid-deploying measurements were performed by profiling probes positioned on a transect arm across the trapezoidal channel and overlapping the central area of interest and PIV-LIF fields [at 3 locations, namely Section D, E and F (Figure 2a,c)].

In particular, 6 micro-conductivity probes distributed on the cross-section (Figure 2c) were used to measure the instantaneous density profiles, while one side-looking and one down-looking Acoustic Doppler Velocimeter (ADV) were positioned with their sampling volumes at an equivalent vertical elevation to the micro-conductivity probes tips to collect coupled velocity profiles. An additional ADV profiler was positioned at a fixed elevation to measure the near bed velocity field.
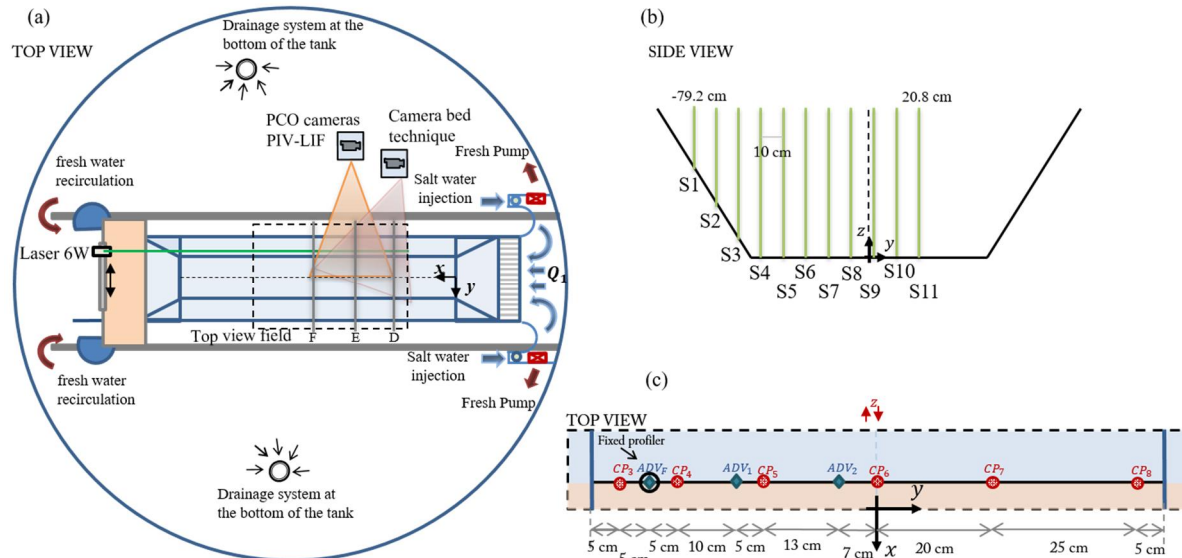
Figure 2 Schematic representation of (a) top view configuration of the channel and experimental set-up in the circular tank, (b) side view of the PIV planes and (c) top view of the ADV measurement locations.

A bottom-boundary visualisation technique, using the vertical laser sheet, was implemented to measure deformations in the erodible bed. A digital camera (resolution 4096 x 3072 pixels) placed outside the trapezoidal channel was used to acquire at a frame rate of 20 Hz the bed-shape before and after each experiment, in the central region of the channel, 2.8 m long and 0.9 m thick. A geometrical calibration was applied and allowed to evaluate the bed surface elevations from the initial undisturbed conditions. Finally, an additional camera positioned on the top of the circular tank provided a global field of the experimental runs.

3. LABORATORY EXPERIMENTS

Four experimental configurations were considered in the project:

- Case 1: uni / bi-directional exchange flows in a non-rotating, rigid-bottom channel.
- Case 2: uni / bi-directional exchange flows in a rotating, rigid-bottom channel
- Case 3: uni / bi-directional exchange flows in a non-rotating channel with an erodible bed.
- Case 4: uni / bi-directional exchange flows in a rotating channel with an erodible bed.

Within all experiments, the flow rate of the salty water Q_2 was kept constant (Q_2 **= 4.4** l/s), while the flow rate of the fresh water Q_1 was increased over a range of values (Q_1 **= 0, 8, 20** l/s). The rotation of the Coriolis Platform was varied with four angular velocities Ω tested (i.e. Ω = **0, 0.05, 0.1, 0.2** rad/s). The density difference of fresh and saline water flows was maintained constant and equal to $\Delta\rho$ **= 10** kg/m^3 for most of the experiments, with a limited number of experiments with the erodible bed layer performed at a higher density difference $\Delta\rho$ **= 20** kg/m^3. The main parameters investigated in the experimental runs are thus (i) the relative magnitude of fresh and saline water volume fluxes $q^* = Q_1/Q_2$, (ii) the density difference $\Delta\rho$ and (iii) the angular velocity Ω of the rotating circular tank, both with a rigid bottom channel (Case 1-2) and an erodible bed layer (Case 3-4).

4. PRELIMINARY RESULTS

In this section an overview of the preliminary results of the experiments with the rigid-bottom condition is presented. In particular, the PIV measurements permit us to obtain detailed information on the spatial flow structure of the upper and lower layers. Figure 3 shows, for $\Omega = 0\ rad/s$, the time averaged velocity vector field, while the background color map details the absolute value of the horizontal time-averaged velocity component at PIV section S9 (i.e. $y = 0.8\ m$, approximately along the channel centerline). Here, the initial gravity current experiment (i.e. $q^* = 0$, Figure3a) and the subsequent bi-directional exchange flow condition ($q^* = 1.8$, Figure3b) are compared to highlight the effect of the upper fresh water volume flux Q_1. Indeed, for the same Ω, the increase of the upper layer flux Q_1 results in a reduction of the lower saline layer thickness h_c, defined by $u = 0\ cm/s$ interface, and a slight increase of the velocity of the lower saline flow u_2. Moreover, a constant increase of the time averaged velocity u_1 in the upper layer flow is observed, as a consequence of the increasing upper fresh water flow Q_1.

In Figure 4, the effect of the rotation rate on the gravity current development along the trapezoidal channel is shown (i.e. $q^* = 0$). The non-rotating experiment (i.e. $\Omega = 0\ rad/s$, Figure 4a-b) and the rotating case with $\Omega = 0.05\ rad/s$ (Figure 4c-d) are compared in Sections S3 ($y = -59.2\ cm$) and S4 ($y = -49.2\ cm$) located on the side slope of the trapezoidal section and on the horizontal bottom of the channel, respectively.
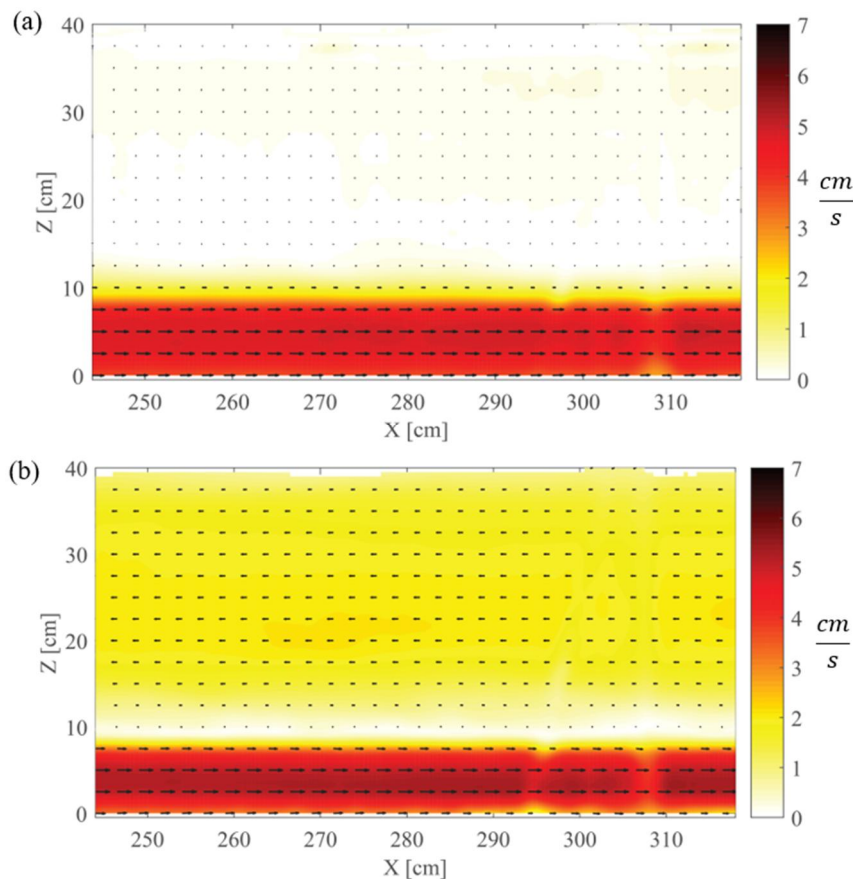
Figure 3 PIV velocity fields at section S9 and colormap of the absolute value of u for Ω=0 rad/s and (a) q*=0, (b) q*=1.4.
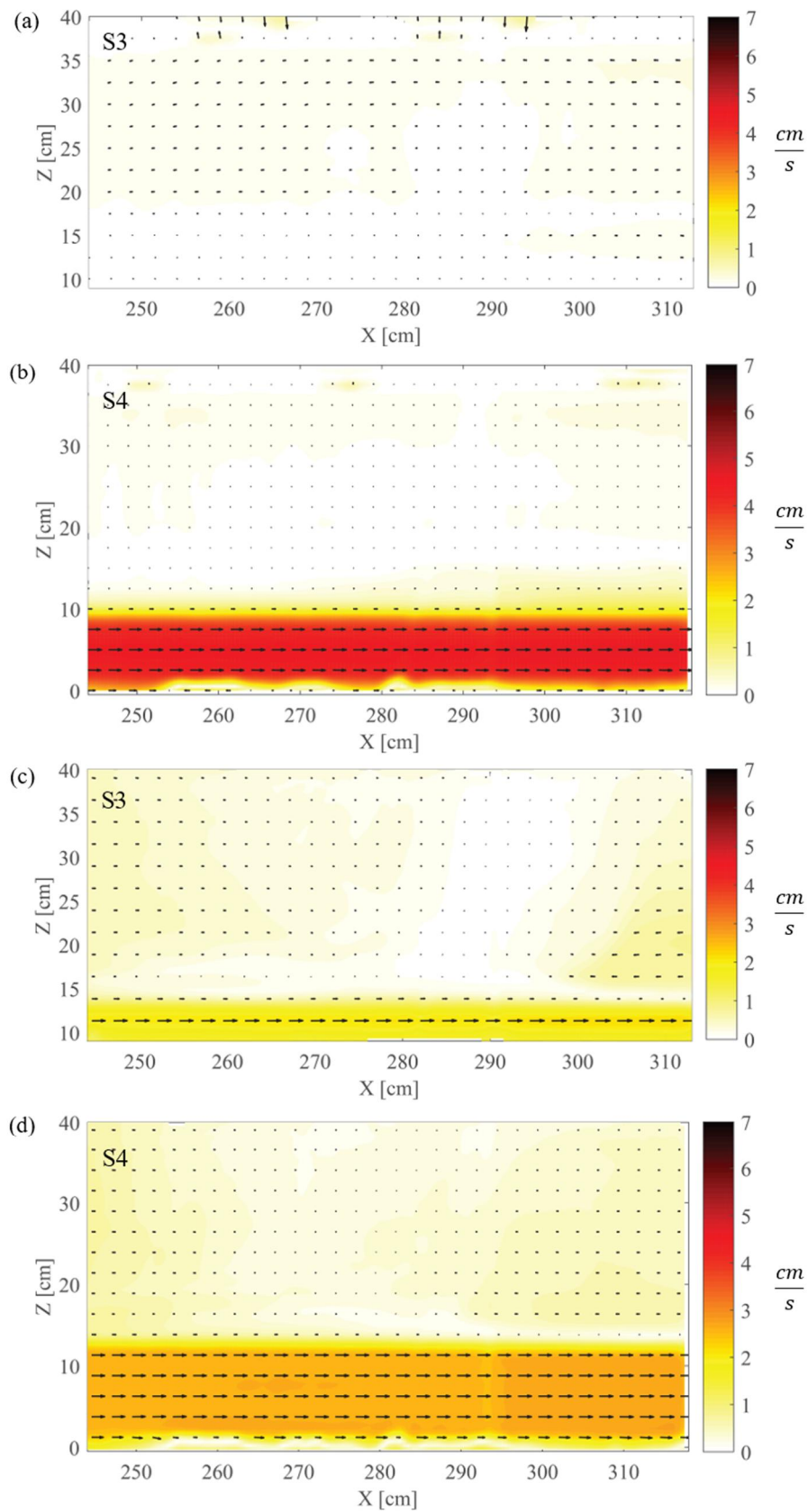
Figure 4 PIV velocity fields and colormap of the absolute value of u for gravity current experiments, i.e. q*=0, for Ω=0 rad/s in PIV Section (a) S3 (i.e. y=-59.2 cm) and (b) S4 (i.e. y=-59.2 cm) and for Ω=0.05 rad/s in PIV Section (c) S3 and (d) S4.

In Figures 4a & 4c, the time averaged velocity vector field and the color map of the magnitude of the horizontal time-averaged velocity component u, are shown at section S3 for the $\Omega = 0\ rad/s$ and $\Omega = 0.05\ rad/s$, respectively. These indicate the clear inclination of the cross-channel interface between the upper fresh and lower saline layers, induced by the non-zero angular velocity. Indeed, for the non-rotating case (Figure 4a), the absence of lower saline layer from the velocity field indicates that the saline layer has a thickness lower than the minimum z elevation of PIV section S3 on the sloping side wall ($z = 9.2\ cm$). By contrast, in the rotating case (Figure 4c), the elevation of the $u = 0\ cm/s$ interface lower saline and upper fresh water fluxes is observed at $h_c = 14\ cm$, indicating that the saline flow is directed to the right side of the channel (in the direction of the saline flow) due to the non-zero angular rotation of the channel. Furthermore, in PIV section S4 (Figures 4b & 4d), an increase in the thickness of the saline flow layer is observed, with a corresponding decrease in the lower layer velocity u_2.

The cross channel variation in the $u = 0\ cm/s$ interface elevation is shown in Figure 5 in the measured PIV sections for the three q^* values tested. The non-rotating experiments (Figure 5a) are compared with the experiments with an angular velocity $\Omega = 0.05\ rad/s$ (Figure 5b) to highlight the influence of the rotation on the internal fluid motions. In particular for $\Omega = 0\ rad/s$, the effect of the increasing upper fresh water flow (i.e. increasing q^*) is to reduce the lower layer thickness. Whereas, when the angular rotation Ω plays a key role in the counter-flowing water masses (i.e. for $\Omega = 0.05\ rad/s$, Figure 5b), a tilt in the interface is observed and is coupled with the effect of the increasing q^*, causing a significant deflection of the saline outflow on the right hand side of the trapezoidal channel.
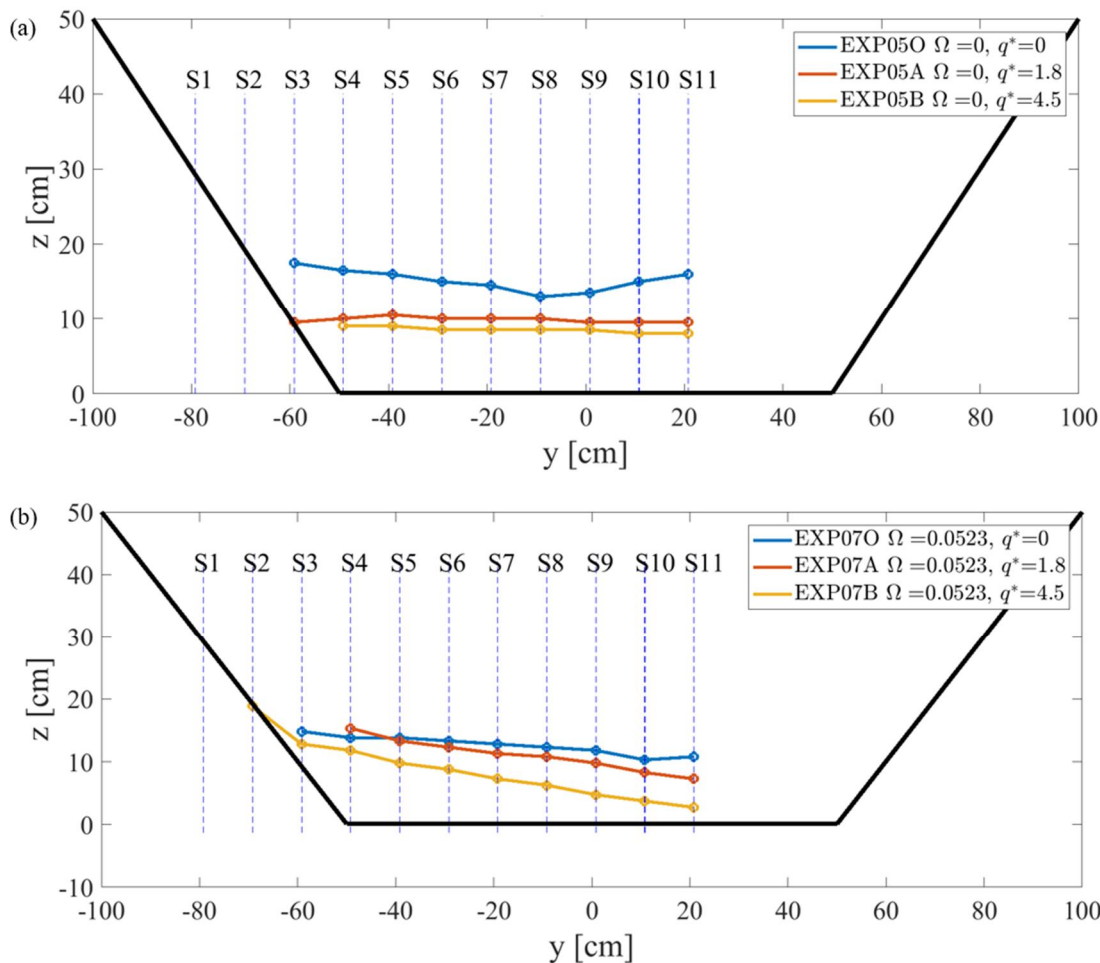
Figure 5 Cross channel $u = 0\ cm/s$ velocity interface in all the measured PIV sections, for increasing q* and angular velocity (a) $\Omega = 0\ rad/s$ and (b) $\Omega = 0.05\ rad/s$

CONCLUSIONS AND FUTURE DEVELOPMENTS

The present work deals with the initial analysis and preliminary findings from an experimental study conducted in the Coriolis Rotating Platform at LEGI Grenoble. Data analysis is ongoing to investigate how the channel cross-sectional shape influences the flow distribution, interfacial mixing and entrainment, secondary flow circulations, and near-bed dynamics in both uni and bi-directional, stratified, exchange flows, as well as to study the reciprocal feedback mechanisms generated between these exchange flow and the evolution of channel topography with an erodible bottom boundary. Access granted to the LEGI Coriolis Platform through the Hydralab+ Initiative has allowed a unique opportunity to conduct large-scale experiments on stratified, non-rotating and rotating exchange flows on both rigid-bottom and erodible bottom channels, within a wide parametric range of relevant geophysical conditions.

ACKNOWLEDGEMENT

REFERENCES

Andrejev, Myrberg, Alenius & Lundberg (2004). Mean circulation and water exchange in the Gulf of Finland – a study based on the three-dimensional modelling. Boreal Env. Res., 9, 1-16.

Cossu, Wells & Wåhlin (2010). Influence of the Coriolis force on the velocity structure of gravity currents in straight submarine channel systems, J. Geophy. Res., 115, C11016.

Cuthbertson A J S, Laanearu J & Davies P A (2006). Buoyancy-driven two-layer exchange flows across a slowly submerging barrier. Environ. Fluid Mech., 6, 133-151.

Cuthbertson A J S, Laanearu J, Wåhlin A K & Davies P A (2011). Experimental and analytical investigation of dense gravity currents in a rotating, up-sloping and converging channel. Dyn. Atmos. Oceans, 52(3), 386-409.

Cuthbertson A J S, Lundberg P, Davies P A & Laanearu J (2014). Gravity Currents in Rotating, Wedge-Shaped Adverse Channels. Environ. Fluid Mech., 14, 1251-1273.

Farmer & Armi (1999). Stratified flow over topography: the role of small-scale entrainment and mixing in flow establishment. Proc. Roy. Soc. A, 455, 3221-3258.

Johnson & Ohlson (1994). Frictionally modified rotating hydraulic channel exchange and ocean outflows. J. Phys. Ocean., 24(1), 66-78.

Kõuts & Omstedt (1993). Deep-water exchange in the Baltic Proper. Tellus A, 45, 311-324.

Laanearu J, Cuthbertson A J S & Davies P A (2014). Dynamics of dense gravity currents and mixing in an up-sloping and converging vee-shaped channel. J. Hyd. Res., 52(1), 67-80.

Matthäus & Lass (1995). The recent salt inflow into the Baltic Sea. J. Phys. Ocean., 25(2), 280-286.

Maxworthy (1985). On turbulent mixing across a density interface in the presence of rotation. J. Phys. Ocean., 16, 1136-1137.

Schramkowski & de Swart (2002). Morphodynamic equilibrium in straight tidal channels: Combined effects of Coriolis force and external overtides, J. Geophy. Res., 107(C12), 3227.

Valle-Levinson, Reyes & Sanay (2003). Effects of Bathymetry, Friction, and Rotation on Estuary–Ocean Exchange. J. Phys. Ocean., 33, 2375-2393.

TOPOGRAPHIC BARRIERS AND WARM OCEAN CURRENTS CONTROLLING ANTARCTIC ICE SHELF MELTING

Elin Derelius (1), et al…

JET INTERACTING WITH VEGETATION IN A ROTATING BASIN

Francesca De Serio (1), Elvira Armenio (2), Gualtiero Badin (3), Alice Di Leonardo (4), Roni Hilel Goldsmith (5), Dan Liberzon (5), Michele Mossa (2), Eletta Negretti (6), Giuseppe R. Pisaturo (7), Maurizio Righetti (7), Joel Sommeria (6), Donatella Termini (4), Thomas Valran (6), Bart Vermeulen (8) & Samuel Viboud (6)

(1) CoNISMa, National Interuniversity Consortium for Marine Sciences, Italy, E-mail: francesca.deserio@poliba.it
(2) Polytechnic University of Bari, Italy, E-mail: elvira.armenio@poliba.it; michele.mossa@poliba.it
(3) Universitat Hamburg, Germany, E-mail: gualtiero.badin@uni-hamburg.de
(4) University of Palermo, Italy, E-mail: alice.dileonardo@unipa.it; donatella.termini@unipa.it
(5) Technion, Israel, E-mail: ronihilel@gmail.com; liberzon@technion.ac.il
(6) LEGI-Grenoble, France, E-mail: joel.sommeria@legi.cnrs.fr; Maria-Eletta.Negretti@legi.cnrs.fr; samuel.viboud@legi.grenoble-inp.fr; Thomas.Valran@legi.cnrs.fr;
(7) University of Bozen, Italy, E-mail: gr.pisaturo@unitn.it; Maurizio.Righetti@unibz.it
(8) University of Twente, The Netherlands, E-mail: b.vermeulen@utwente.nl

Contaminants, nutrients and sediment particles flow into inland and coastal water bodies often forming turbulent jets. The aim of the present research is to improve our capability to describe how jets interact with the environment they discharge into, providing useful insights for possible mitigation of undesired and harmful impacts. Here, we focus on the case of a jet interacting with an obstructed flow under the effect of the Coriolis force as is often the case with large scale rivers discharging into the sea in vegetated environments.

1. INTRODUCTION

Rivers and waste water flowing into lakes and coastal waters have a profound effect on aquatic ecosystems, due to transport of turbulence, scalars (tracers) and sediment particles. The mixing and spreading of the outflow have an even greater impact when vegetation canopies or mussel cultivation farms occupy the receiving site. Thus, a thorough knowledge of the interaction between effluents and receiving environments is required, to mitigate undesired impacts and to develop best environmental management practices, also highlighted in the recent EU Marine Strategy Framework Directive (2015).

Mixing processes induced by the inflow of unobstructed jets are rather well understood, and are mainly governed by the initial jet characteristics, the boundary conditions and the hydrodynamic features of the ambient current (Nepf, 2012; Smith & Mungal, 1998; Liberzon & Fernando, 2014). When discharging in the presence of rotation, the Coriolis force changes the orientation of turbulent eddies, affecting the energy cascading process (Lin & Atkinson, 1999). For density driven jets (Thomas & Linden, 2007; Cenedese & Adduce, 2008), mixing and entrainment depend on bottom slope, Froude and Reynolds numbers.

Our knowledge of the effect of vegetation on flows in general is rather extensive. The vegetation canopy, characterized particularly by its density and geometry (Oldham & Sturman, 2001; Nepf et al. 1997; Ghisalberti & Nepf, 2005; Poggi et al., 2009; Nepf, 2012; Termini, 2015), interacts with the mean and turbulent flow, perturbing both advection and dispersion (Raupach & Thom, 1981; Ben Meftah et al., 2015; De Serio et al., 2018; Righetti, 2008). For canopy flows, the formation of coherent structures has been studied also numerically by e.g. Bailey & Stoll (2016). Momentum jets obstructed by vegetation have been investigated only recently (Ben Meftah et al., 2015; Ben Meftah & Mossa, 2016). It is well known that, when released in an unobstructed flow, the momentum jet experiences entrainment, while detrainment is observed for density jets. Results by Mossa & De Serio (2016) and Mossa et al. (2017) showed that the vegetation canopy is capable of inducing detrainment for momentum jets, which is an unexpected behavior. Although there is quite a good understanding of turbulent jets interacting with rotating frames and with vegetation in

isolation, to the best of our knowledge experimental investigation of jets released in a vegetated pattern under the effect of the Coriolis force was never reported. This motivated the present study.

In the ocean, the direct effect of rotation on turbulence induced by an obstructed pattern should be quite negligible, because of its small scale. Nevertheless, the mean flow is modified by rotation and consequently the transport and spreading of turbulent kinetic energy and tracers by the mean flow is modified in a rotating frame (Godeferd & Moisy, 2015). Furthermore, the rotational effects are manifested through the development of Ekman boundary layers, effectively increasing friction. Hence, the interplay between rotation and turbulence due to obstacles deserves a thorough study.

It is worth noting that obstructions for the jet discharge are not only representative of vegetated canopies, but also include mussels or oyster cultivation farms and mangrove forests in coastal regions. Therefore, the results of such experiments are expected to support environmental planning. Here, we report the experimental setup and methods and the very preliminary results, focusing on the average velocity, vorticity and turbulence as observed under various experimental conditions.

2.   EXPERIMENTAL SETUP

The experiments were carried out in the Coriolis rotating platform at LEGI-Grenoble. In this large-scale facility, two different kinds of experiments were executed, discharging a horizontal momentum jet 1) in the unobstructed tank; 2) in the tank partially obstructed by a canopy made of rigid rods. In the first case, the jet (mimicking a generic discharge) spread and transport in a rotating background were examined. In the second case, the outflow spread through the obstructed pattern in a rotating background was investigated. Both experiments were conducted under identical rotation parameters expressed by T, the rotation period of the tank: $T=\infty$ (no rotation), $T=60s$ $T=90s$, $T=120s$ and $T=180s$. Some parameters, such as the spacing s between the rods and the jet initial flowrate q_j, were varied during the tests to evaluate their effects on the jet behavior. In this report, we show the preliminary results of some of the experimental runs.

The LEGI tank has a diameter of $D=13m$, the working water depth was set at $H=0.80m$. A dedicated pipework, installed in the tank, was used to release the momentum jet. The pipe outlet O was 0.10m in diameter, rigidly fixed at 0.40m depth. The outlet ensured a horizontal release of a jet with an initial diameter of $d_j=0.08m$ (internal diameter of the pipe) oriented horizontally. A specially designed canopy was placed in the tank for the obstructed configuration. The rigid, emergent vegetation stems were mimicked by plastic transparent (Plexiglass made) rods of diameter $d=0.02m$, arranged on a 2m x 2m panel fixed at the bottom of the tank. The rods were manually mounted on the panel inside pre-drilled holes, thus assuring a regular pattern with a center-to-center distance s. The panel was placed in the tank as shown in Figure 1, between the carriage supports, which also proved a positioning platform for the instruments. The center of the jet outlet (O) was 1m away from the upstream edge of the panel and 0.77m from its external edge.

The instantaneous measurements of the velocity field at several pre-selected horizontal planes were principally made using a PIV (Particle Image Velocimetry) system. The laser source of the PIV system was mounted in the center of the tank, and the system included three synchronized recording cameras mounted on the top of the tank. The laser used in our experiments was a continuous Yag laser (532 nm wavelength) providing 25 Watts of power, illuminating a large area of the rotating tank by a horizontal sheet. A Powell prism produced the 5mm thick sheet. In the measurements discussed here, the laser sheet was set in a horizontal plane spanning an area of more than 3x3 m^2, with a 60° opening angle. Orgasol neutrally buoyant particles with a 60µm diameter were used to seed the flow. To map the velocity fields in the examined volume of water a "multi-level" approach was adopted, acquiring several images and consequently the 2D velocity fields at each horizontal layer of interest. See Figure 2 to have a view of the set up. Figure 3 shows, as an example, the six horizontal layers measured by the PIV during each experiment. These are

named as 0, m1, m2, 1, 2, 3, respectively for z=0m, -0.10m, -0.2m, 0.1m, 0.2m, 0.3m, being z the vertical axis, positive upward, with origin at the jet outlet. The rigid rods are also sketched in this figure.

The three cameras, named PCO1, PCO2 and Falcon, were fixed on rigid supports located at 4.29m, 4.74m, and 4.87m from the bottom, respectively. PCO1 and PCO2 filmed at 2560 x 2160 pixels resolution using a 35 mm objective lens (Samyang F1.4). The FALCON provided images at 2432 x 1728 pixels resolution using a 20mm objective lens (Sigma F1.8). Orientation of the cameras ensured the three fields of view partially overlapped, in order to ensure full coverage of the deviated jet (Figure 4).
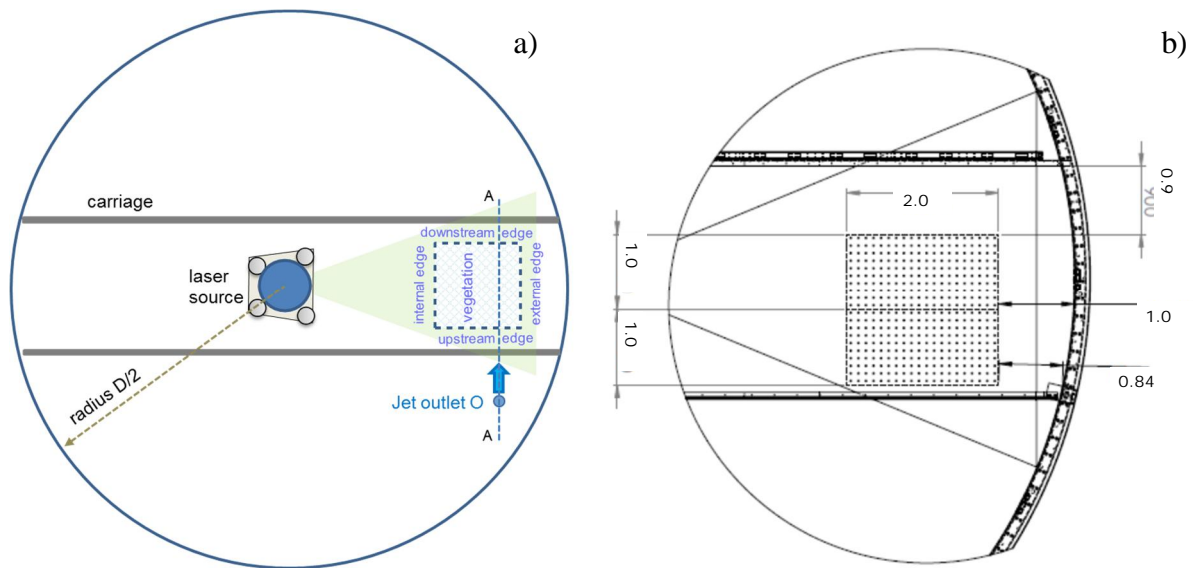
Figure 1. a) Plan view: sketch of the location of jet outlet and vegetation panel in the LEGI tank.
b) Detail of the vegetated panel with distances (in m) from the carriage and the tank wall
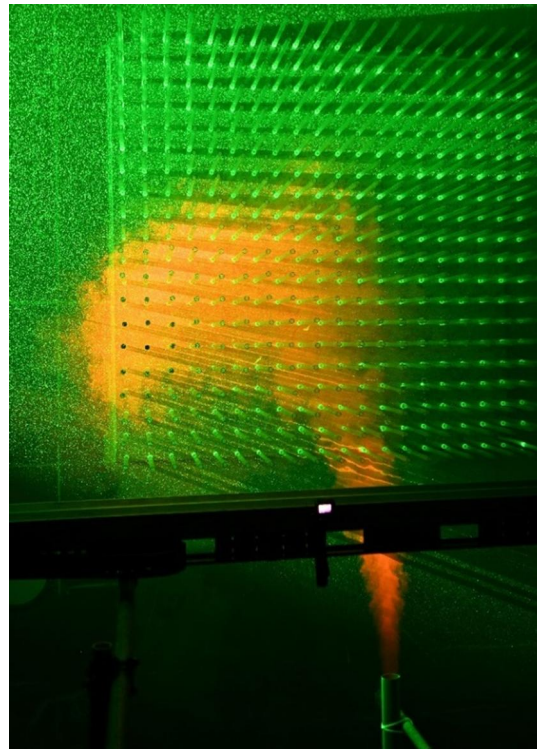
Figure 2. Top view of the experiment set up: dyed jet spreading in the obstructed panel, illuminating by the laser. Jet outlet position as in Fig.1a)
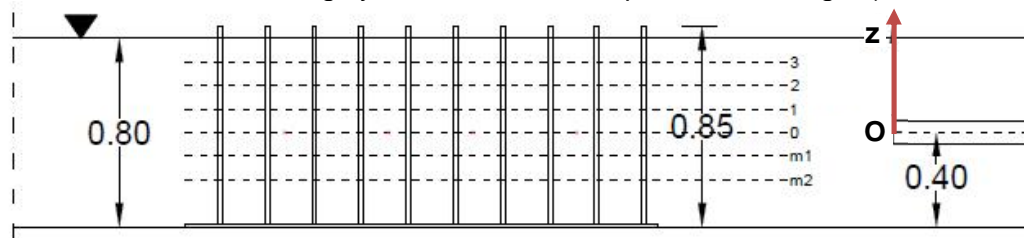
Figure 3. View in the vertical plane (AA dotted line in Fig.1a) of the investigated layers at different depths (measurements in m). Dashed lines are reciprocally distant 0.10m

In addition to the PIV system described above, some velocity measurements were also carried out by means of two 3D Acoustic Doppler Velocimeters (3D-ADV), a bottom-looking one and a side-looking one. The ADVs provided velocity measurements with accuracy of ±0.5% of measured value ±1 mm/s. Settled with a sampling frequency of 50Hz, the ADVs required a measurement time equal to 2-3 minutes to obtain a satisfactory signal. Independently from the obstacles, such measurement times were not possible as the released jet travels through the entire tank coming back to its origin, thus overlapping with itself. This behavior was noted at preliminary testing using a dyed jet visualization. In both unobstructed and obstructed cases, the ADV measurements at several locations at selected depths were hence used to check the spreading of the jet in the still water, to compare it with the expected theoretical trend and previous research result, which were confirmed.

Table 1 lists the experimental parameters (not significant EXPs are not listed). After the preliminary tests (denoted as EXP1 to EXP13), the main 14 experimental runs were conducted (EXP14 to EX27) using the PIV system as described above. Five additional experiments (denoted EXP28 to EX32) were conducted implementing the volume scanning technique. Here the LIF (Laser Induced Fluorescence) system scanned the target volume rapidly, recording images of the water motion

seeded with a fluorescent dye (Rhodamine 6G). The laser was scanning vertically in order to provide detection of the jet volume and to support reconstruction the jet three-dimensional shape. These results will not be reported here as the data is yet to be processed.
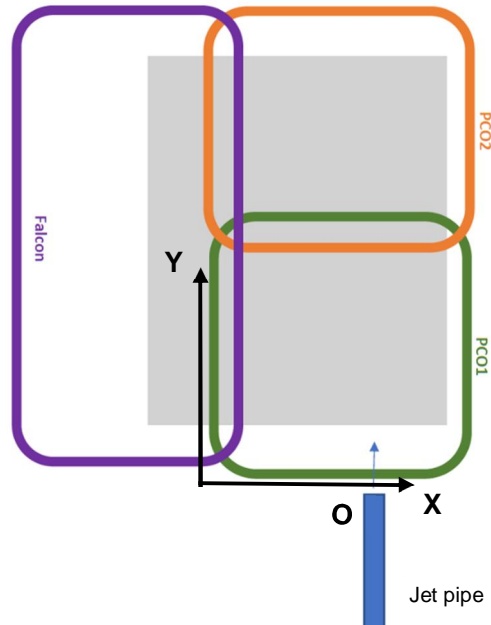
Figure 4. Sketch of the frames in the horizontal plane covered by the three top cameras used in the PIV system. Coordinate reference system for PCO1 shown.

Table 1. List of the principal executed experiments, with different configurations

EXP number	T [s]	Vegetation spacing s [cm]	Jet flowrate q_j [m^3/h]	Instruments used
EXP2	No rotation	unobstructed	20.7	ADVs
EXP7	No rotation	20	20.7	ADVs
EXP9	60	20	20.7	ADVs
EXP13	90	unobstructed	20.7	PIV
EXP14	No rotation	unobstructed	20.7	PIV
EXP15	90	Unobstructed	20.7	PIV
EXP16	60	Unobstructed	20.7	PIV
EXP17	No rotation	20	20.7	PIV
EXP18	60	20	20.7	PIV
EXP19	90	20	20.7	PIV
EXP20	120	20	10.8	PIV
EXP21	No rotation	20	20.7	PIV
EXP22	No rotation	10	20.7	PIV
EXP23	90	10	20.7	PIV
EXP24	60	10	20.7	PIV
EXP25	120	10	10.8	PIV + ADVs
EXP26	180	10	10.8	PIV + ADVs
EXP27	No rotation	10	10.8	PIV + ADVs
EXP28	No rotation	10	20.7	LIF
EXP29	90	10	20.7	LIF
EXP32	60	10	20.7	LIF

3. DATA PROCESSING

The mode of operation for each of the PIV supported experiments was as follows. The horizontal layer under consideration was illuminated with the laser sheet, and simultaneously filmed by the three PIV cameras. Each camera was filming at 33Hz (i.e. frame time of 0.03s) for the duration of 1 minute, thus providing a total of 2000 images. The images were successively coupled and correlated, to obtain the PIV measured velocity field in the horizontal plane. As for the PIV images, we adopt a coordinate reference system (X,Y) which refers to the frame, with the X axis aligned with the panel upstream edge and positive outwards, while the Y axis is aligned with the internal edge and positive in the jet direction (see Fig. 4). Velocities in the X direction are named u, while those in the Y direction are named v.

The open source ParaPIV software (Wang, 2017) running in Matlab 2017b was used to process the acquired images. Extensive parallelization (16 cores) was implemented to reduce computational times. The PIV results presented below were obtained using a 16 X 16 pixels interrogation window. The calibration coefficients were estimated taking EXP 27 as a reference (see Table 1) and are shown in Table 2. For each horizontal layer of each experiment a time series of velocity data on a grid with 159x134 points in the case of both PCO1 and PCO2 and 151x107 points in the case of Falcon camera were obtained.

Table 2. Velocity calibration coefficients

Layer	PCO1 [cm px^{-1} s^{-1}]	PCO2 [cm px^{-1} s^{-1}]	Falcon [cm px^{-1} s^{-1}]
0	2.1667	2.4567	3.9633
1	2.1233	2.4267	3.9167
2	2.0933	2.3900	3.8467
3	2.0400	2.3533	3.7767
m1	2.2133	2.5000	4.0433
m2	2.2533	2.5467	4.1033

4. FIRST RESULTS AND CONCLUSION

Large number of experimental runs have provided us with a massive data set, which is being processed. Here we present and discuss in brief only the initial results of few selected cases, as acquired by the PCO1 camera only. Specifically, the experiments addressed here are:

- EXP14 - no rotation, no obstructions, jet with q_j=20.7m^3/h;
- EXP21 - no rotation, obstructions spaced at s=20cm, jet with q_j=20.7m^3/h;
- EXP16 - rotation at T=60s, no obstructions, jet with q_j=20.7m^3/h;
- EXP18 - rotation at T=60s, obstructions spaced at s=20cm, jet with q_j=20.7m^3/h.

Figure 5 presents the average velocity distribution (averaged over the total acquisition time of 1 minute) for the four different EXPs listed above. The results are for the horizontal plane at z=0, i.e. halfway the tank's water depth. The velocity fields are quite typical for the different configurations examined. The jet appears being fully developed along the panel, considering the distance of the jet relative to the panel (and thus to the measurement area) being larger than 10d_j.

In EXP14 the jet is well defined and undisturbed. The jet travels through still water, exhibiting a quite symmetrical spread in the X direction while propagating along Y. In the first half of the panel length, the velocity magnitude along the centerline of the jet is initially lower than expected, since the investigated layer (z=0) is slightly shifted upward with respect to the axis of symmetry of the jet. In the second half, higher velocity values are observed in the fully developed condition and they gradually decrease along the jet path, as expected in the free jet case, due to the entrainment of ambient water.

In EXP16 rotation is present and the jet is released in water in solid body rotation, thus the curvature of the jet path is evident. The structure of the flow remains quite symmetrical relatively to the jet centerline, but the velocity magnitude is slightly lower in the central part than in EXP14. Lateral circulations can be noted, specifically a weak anticlockwise one spanning the outer part of the frame, and a flow drawn by the bending jet in the inner part of the frame, due to entrainment.

Both cases with obstructions (EXP18 and 21) show significant (up to twofold) reduction in jet mean velocity magnitude due to flow blockage by the rods, confirming previous results (Mossa et al., 2017; De Serio et al., 2018). Also worth noting is the smoothing of velocity in the lateral areas. Cases with obstructions, represented by vertical rods, showed harmonic fluctuations of velocity. Origin and nature of such fluctuations are yet to be determined, with vortex shedding or other wake effects being a possible explanation requiring further investigation.

The time-averaged vorticity distributions are presented in Figure 6, following the same scheme of Fig. 5. The typical vortical structure of jets is observed for the unobstructed cases (EXP14 and EXP16), especially along the second part of the panel, with positive and negative vorticity respectively dominating half of the jet and contributing to entrainment. On the contrary, in EXP21 and EXP18 cases, the presence of vertical rods alters the vorticity distribution and, even if the jet pattern is still identifiable, local concentrations of vorticity around and behind the rods seem more pronounced and prevailing. Furthermore, the oscillating velocity induces a disturbance also in these cases.

In Figure 7, the distribution of the time-averaged turbulent Reynolds stresses $\overline{u'v'}$ (apart from $-\rho$, with ρ water density) is shown for the same four experimental cases. In all cases, it is consistent with the map of the time-averaged velocity, presenting higher values of $\overline{u'v'}$ at locations of higher drag, namely in the initial portion of the flow, also confirming previous works (e.g. Ben Meftah et al. 2018). The presence of the rods (EXP21 and EXP18) reduces the Reynolds stresses magnitude with approximately 30%.

It is evident the different behavior of the jet in obstructed/unobstructed configurations as well as in rotating/not rotating mode. Further analysis is ongoing to highlight with more detail the reciprocal effects of jet, obstructions and rotation.
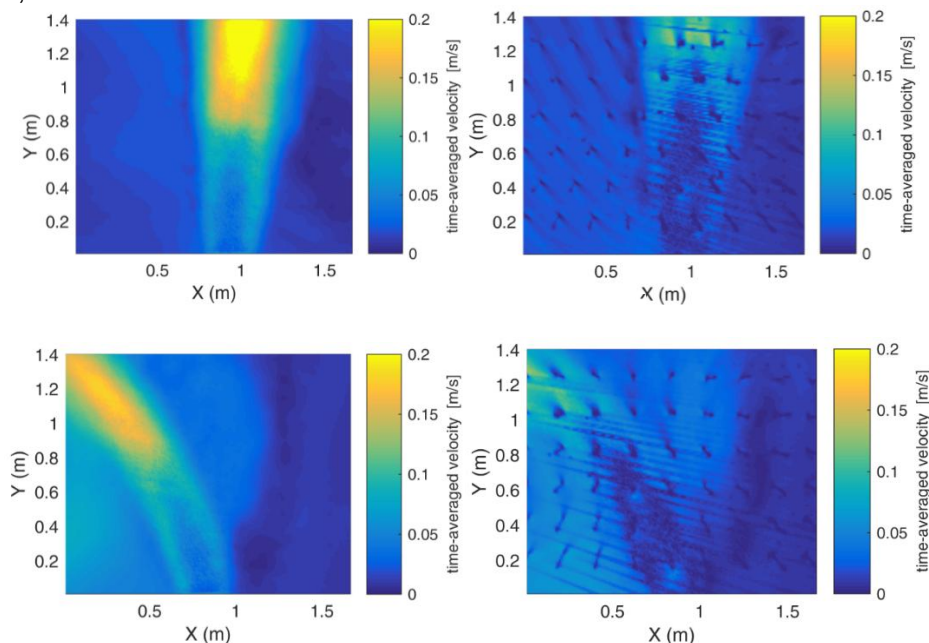

Figure 5. Time-averaged velocities in the horizontal layer at z=0: top line no rotation; left column no obstructions
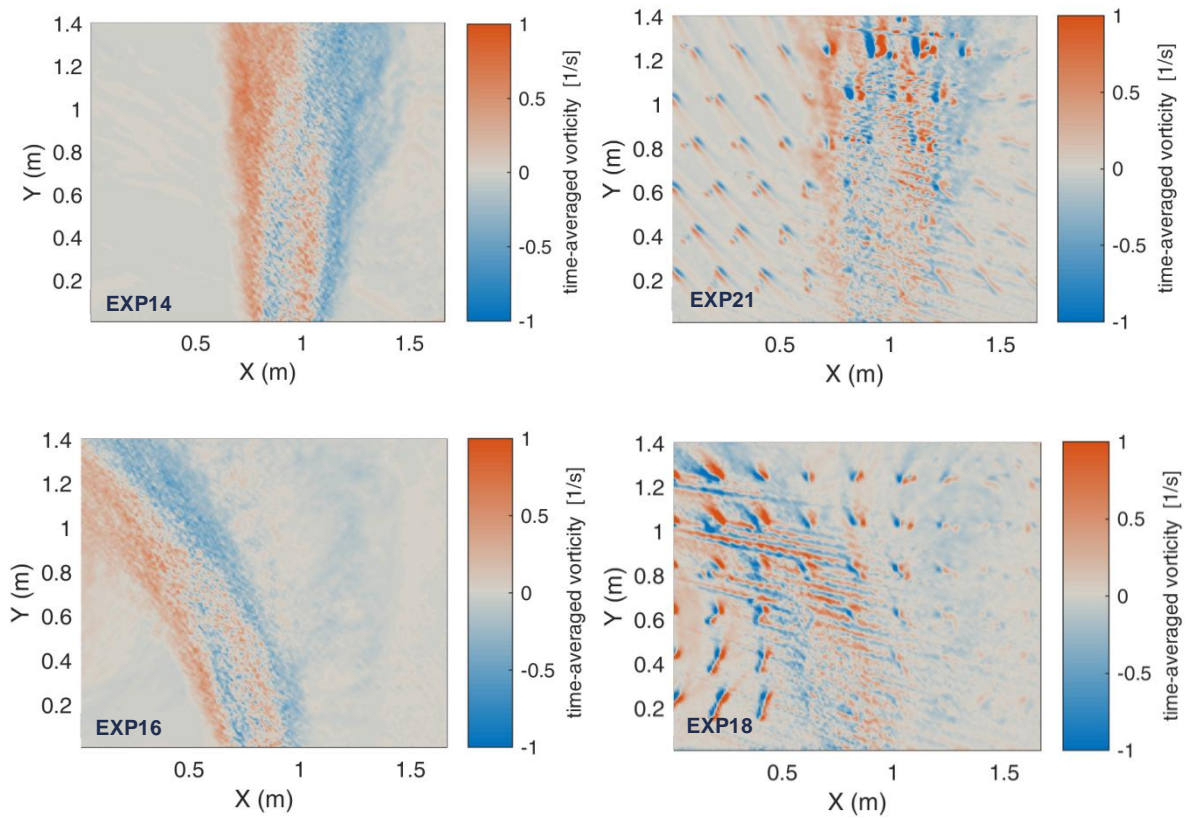
Figure 6. Time-averaged vorticity in the horizontal layer at z=0: top line no rotation; left column no obstructions
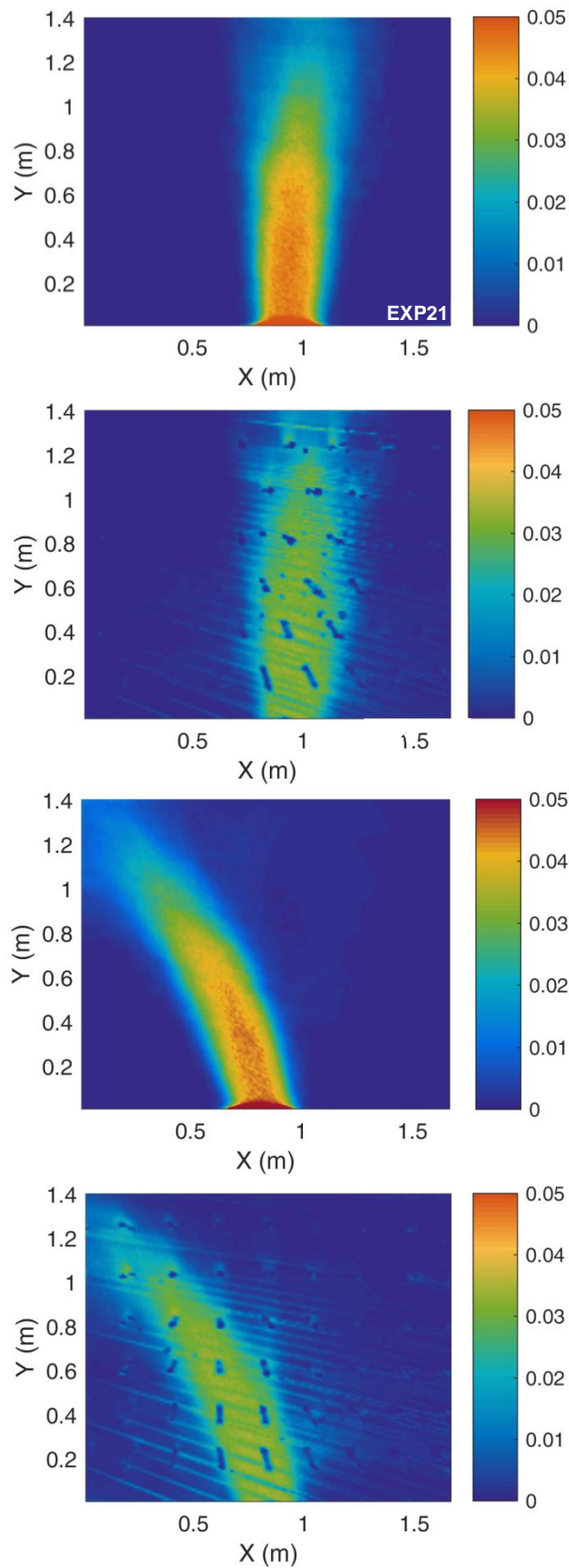
Figure 7. Time-averaged turbulent Reynolds stresses $\overline{u'v'}$ [m²/s²] in the horizontal layer at z=0: top line no rotation; left column no obstructions

References

Bailey, B.N, and Stoll, R. (2016). The creation and evolution of coherent structures in plant canopy flows and their role in turbulent transport, *J. Fluid Mech.*, 789, 425-460.

Ben Meftah, M., De Serio, F., Malcangio, D., Mossa, M. and Petrillo, A.F. (2015). Experimental study of a vertical jet in a vegetated crossflow, *J. Env. Management,* 9.

Ben Meftah, M. and Mossa, M. (2016). Partially obstructed channel: Contraction ratio effect on the flow hydrodynamic structure and prediction of the transversal mean velocity profile. *Journal of Hydrology,* 542.

Cenedese, C. and Adduce, C. (2008). Mixing in a density-driven current flowing down a slope in a rotating fluid, *J. Fluid Mech.*, 604, 369–388.

De Serio, F., Ben Meftah, M., Mossa, M. and Termini, D. (2018). Experimental investigation on dispersion mechanisms in rigid and flexible vegetated beds, *Advances in Water Resources*, 120, 98-113.

Ghisalberti, M. and Nepf, H. (2005). Mass transfer in vegetated shear flows. *Environ. Fluid Mech.*, 5(6), 527-551.

Godeferd, F.S. and Moisy, F. (2015). Structure and Dynamics of Rotating Turbulence: A Review of Recent Experimental and Numerical Results, *Applied Mechanics Reviews*, 67, 030802-1.

Liberzon, D. and Fernando, H.J.S. (2014). Pressure distribution in confined jet flow, *Journal of Fluids Eng.*, 136, 3, 031202.

Lin, G., Atkinson, J.F. (1999). A Mechanism for Offshore Transport across the Gulf Stream, *J. Phys. Ocean.*, 30, 226-232.

Mossa, M. and De Serio, F. (2016). Rethinking the process of detrainment: jets in obstructed natural flows, *Scient. Rep.*, 3910.

Mossa, M., Ben Meftah, M., De Serio, F. and Nepf, H. (2017). How vegetation in flows modifies the turbulent mixing and spreading of jets, *Scient. Rep.*,7, 6587.

Nepf, H., Mugnier, C. and Zavistoski, R. (1997). The effects of vegetation on longitudinal dispersion, *Est. Coast. Shelf Science,* 44, 675-684.

Nepf, H. (2012). Hydrodynamics of vegetated channels, *J. Hydraul. Res.*, 50(3), 262–279.

Oldham, C.E. and Sturman, J.J. (2001). The effect of emergent vegetation on convective flushing in shallow wetlands: Scaling and experiments, *Limnol. Oceanogr.*, 46(6), 1486–1493.

Poggi, D., Krug, C. and Katul, G.G. (2009). Hydraulic resistance of submerged rigid vegetation derived from first-order closure models, *Water Resource Research*, 45, W10442.

Raupach, M.R. and Thom, A.S. (1981). Turbulence in and above plant canopies, *Annual Rev. Fluid Mech.*, 13, 97–129.

Righetti, M. (2008). Flow analysis in a channel with flexible vegetation using double-averaging method, *Acta Geophysica,* 56(3), 801–823.

Smith, S.H. and Mungal, M.G. (1998). Mixing, structure and scaling of the jet in crossflow, *J. Fluid Mech., 357, 83-122.*

Termini, D. (2015). Flexible Vegetation Behavior and Effects on Flow Conveyance: Experimental Observations. *Int. Jour. of River Basin Manag.*, doi:10.1080/15715124.2015.1012519.

Thomas, P.J. and Linden, P.F. (2007). Rotating gravity currents: small-scale and large-scale laboratory experiments and a geostrophic model, *J. Fluid Mech.,* 578, 35–65.

Wang, C.S. (2017). ParaPIV: PIVlab in Parallel, Technical Report, https://doi.org/10.13140/rg.2.2.30705.79203.

A ROTATING TANK MODEL OF THE NORTH IONIAN GYRE INVERSIONS PRODUCED BY DENSE WATER FLOWS

M. Gačić (1), M. Bensi (1), V. Kovačević (1), E. Negretti (2), A. Rubino (3), J. Sommeria (2), M. Menna (1), R. Viana (3), L. Ursella (1), G. Civitarese (1), G. Siena (1), V. Cardin (1), B. Petelin (4), S. Vibaud (2), T. Valran (2)

(1) Istituto Nazionale di Oceanografia e di Geofisica Sperimentale - OGS, Italy, E-mail: mgacic@inogs.it
(2) CNRS/Grenoble-INP/UJF-Grenoble1, LEGI UMR 5519, France, E-mail: Maria-Eletta.Negretti@legi.cnrs.fr
(3) Università Ca' Foscari, Venice, Italy, E-mail: rubino@unive.it
(4) Marine Biological Station, Piran, Slovenia, E-mail: Boris.Petelin@nib.si

Results of the analysis of a rotating tank experiment simulating the response of a two-layer basin to dense-water injection are presented. The temporal evolution of the near-surface vorticity field inverts its polarity as a response to the dense water discharge, passing from weak cyclonic to strong anticyclonic. Similarities with the oceanic conditions found in the Northern Ionian Sea, which shows multiyear surface vorticity inversions are discussed. In particular, the winter 2012 situation in the Adriatic Sea, characterized by harsh meteorological conditions leading to the formation of very dense water, which was then discharged into the Ionian, is considered. In this case, the dense water of Adriatic origin caused an unusually fast inversion of the Ionian cyclonic circulation into an anticyclonic one. A comparison between the experimental results and a theoretical temporal evolution of the vorticity based on potential vorticity conservation equation shows an excellent agreement.

1. INTRODUCTION

The circulation of the upper layer of the Northern Ionian Sea is subject to periodical reversals on a decadal scale. A reversal from anticyclonic to cyclonic circulation was observed already in 1997 (Manca et al., 2003) and was associated by Borzelli et al. (2009) with the spreading of dense Cretan Sea Outflow Water (CSOW) toward the central abyssal portion of the Ionian, during the second phase of the Eastern Mediterranean Transient (EMT, Roether et al., 1996).

The available altimetric data records show that, until now, other reversals took place in 2006, 2011, and 2017, indicating that this phenomenon generally occurred every about five years, except for the post-EMT period when the cyclonic regime lasted about nine years. In the seminal paper by Gačić et al. (2010), the phenomenon of the periodical inversions of the Northern Ionian Gyre (NIG, Gačić et al., 2011) found its full explanation in terms of a complex feedback mechanism, baptized Adriatic-Ionian Bimodal Oscillating System (BiOS), which is qualitatively explained below.

Associated with the anticyclonic/cyclonic circulation mode of the NIG, less salty/saltier Atlantic Water (AW)/Levantine Intermediate Water (LIW) is advected into the Adriatic (Fig. 1). This water then contributes to shape the Adriatic winter convection, thus determining variations in density of the newly formed Adriatic Dense Water (AdDW). In the post-convection period, the AdDW spreads toward the Ionian abyss. Depending on its density, which from year to year can be larger/smaller than the ambient Ionian deep water density, it determines the horizontal pressure gradient orientation.
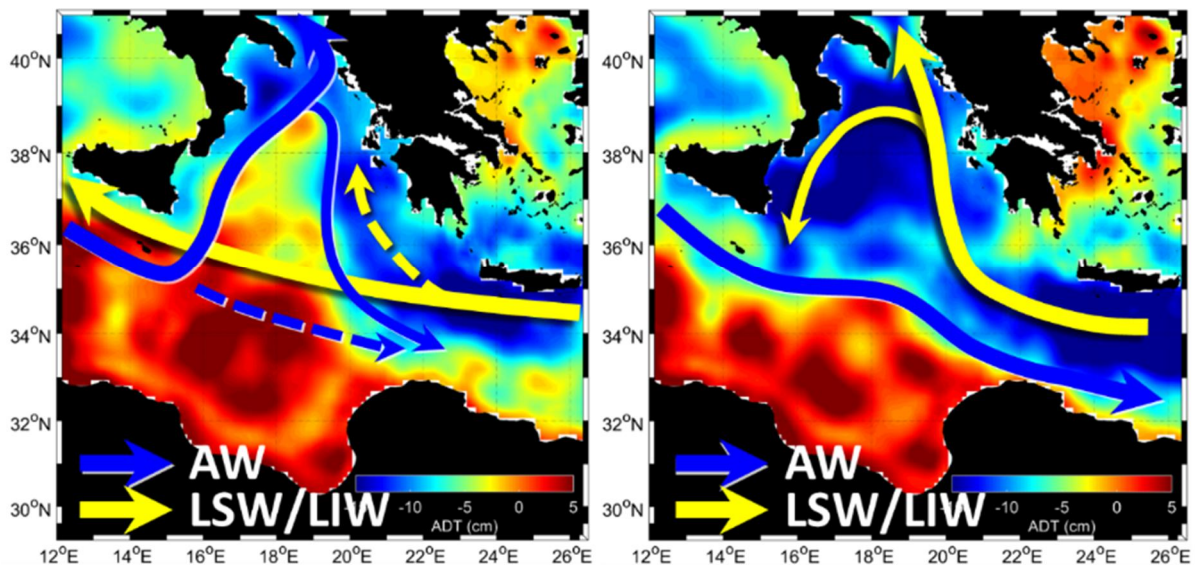
Figure 1. Schematic presentation of the flow inversions in the Ionian Sea (as from Menna et al., 2019).
For the water mass acronyms see text.

During the cyclonic mode, the high-density AdDW spreads along the western continental slope in the Ionian. This results in the lowering of the sea level along the AdDW path, which creates a surface pressure gradient toward the coast and the resulting northward surface geostrophic flow. The cyclonic circulation weakens and, eventually, the anticyclonic flow takes place. Conversely, during the anticyclonic mode, relatively fresh AW enters the Adriatic causing the decrease of the AdDW density. In this situation, along the AdDW path in the Ionian (western border) the sea-level becomes higher than in the center, producing the sea surface pressure gradient responsible for the southward geostrophic flow, which eventually overwhelms the northward branch of the Ionian anticyclone creating the cyclonic basin-wide meander. In deeper layers (the layer above the vein), the northward geostrophic flow is generated due to the pressure gradient in the opposite direction. As can be seen from these considerations, the Ionian behaves as a two-layer system.

Since the Ionian interior is the crossroads of transiting Mediterranean ubiquitous waters like AW and LIW, changes in the NIG circulation pattern have also an important impact on the distribution of many oceanographic properties (Gačić et al., 2011; Gačić et al., 2014; Mihanović et al., 2015, Ozer et al., 2017). As a result, biogeochemical and biological processes occurring in the Ionian, Adriatic and Levantine seas are affected by the BiOS (Civitarese et al., 2010; Batistić et al., 2014; Vilibić et al., 2015; Ozer et al., 2017; Lavigne et al., 2018).

Due to this multifaceted impacts exerted by the NIG inversions on the marine environment, studies focusing on the BiOS mechanism, its influence and behavior, especially in the context of changes in the climatic conditions, are now flourishing.

As noted above, the cyclic inversions of the NIG show typical time scales of about five years, although sudden interruptions of the cyclonic or anticyclonic modes are possible due to particularly strong events, such as the sudden production of high-density waters in the Adriatic. Here, background conditions become the prevailing factor generating, during harsh winters, very cold high-density AdDW. This water can then invert the bottom pressure gradient in the Ionian and change the surface circulation from cyclonic to anticyclonic. Indeed, such an event was recorded in 2012 (Gačić et al., 2014) when the extremely rigid winter over the Adriatic resulted in a formation of very cold and dense AdDW. Probably not only the density of the AdDW played an important role in this inversion, but also the amount of water produced, which very likely was much larger than usual.

Generally, the BiOS-CRoPEx (Adriatic-Ionian Bimodal Oscillating System – Coriolis Rotating Platform Experiment) project was designed to broaden our understanding of the BiOS mechanism

and to demonstrate the capability of internal processes to dictate the circulation in the upper thermocline.

One of the specific aims of the BiOS-CRoPEx project was to try to simulate the 2012 situation, when exceptionally dense AdDW outflow in spring 2012 inverted temporarily the NIG circulation pattern. In this paper, we will compare the *in situ* oceanographic and experimental data, and discuss differences and similarities between the physical model and the real ocean. This exercise will give us the opportunity to study in more details the mechanism responsible for the circulation inversions and the impact of climatic conditions on the cyclical variations of the circulation in the Ionian Sea.

2. EXPERIMENTAL DESIGN, MEASUREMENT TECHNIQUES AND DATA ANALYSIS

Experiments were conducted at the Coriolis rotating platform at LEGI, in a circular tank of 13 m diameter and 1 m depth. The experimental setup is shown in Figure 2. The slope was realized using an axisymmetric conical-shaped boundary descending toward the center of the tank with a slope s of 0.1. The total width of the slope was 4 m. It gradually descended from the tank edge, where its height was 40 cm, down to the tank bottom. Hence, the central (deep) portion of the tank with constant depth had a diameter of 5 m.

Figure 2. Experimental setup (two-layer system).

The tank, put on constant anticlockwise (cyclonic) rotation, was initially filled with two layers of different densities. The filling lasted several hours, in order to assure a minimum interface thickness and reach a solid-body rotation. Saline solutions were injected through specifically designed devices, which consisted of a tube ending on a rigid plate and a flexible plastic cover,

fixed at the two sides to the bottom plate, 50 cm wide and 2 m long. This configuration enables the saline current to adjust geostrophically within the tube without mixing with the fresh ambient water during the adjustment phase. The flow rate Q and dimensions of the injector (L, h_j) were estimated prior to the experiment. The scope was to obtain velocities of the order of the Nof speed u = g' s/f (a theoretical along-slope speed of a geostrophically balanced dense water fluid; Nof, 1983), where f = 4π/T, T is the rotation period, s is the slope, and Q = uh_jL. With this balance, the injection systems S1 and S2 positioned 1 m from the top of the slope area, generated a density current in the direction of rotation 50 cm wide (L) and maximum 2 cm high (h_j) at the device outlet (Fig. 2). The flow rate, ranging between 0.4 and 1.6 l s^{-1}, was controlled by a pump with a maximum capacity of 4 l s^{-1}. Outlets were opened beyond the conical slope at the tank bottom to keep the total water depth constant throughout the experiment duration and allow discharging the fresh water by the thin gap around the upper circular end of the slope, assuring also the minimal disturbance to the flow in the central part of the tank.

Polyamide particles (Orgasol) with a mean diameter of 60 μm and a density of 1.016 g cm^{-3} were added to both the salt and the fresh water layers and to the injected saline solutions as tracers for velocity measurements with particle image velocimetry (PIV). A 25 W Yag laser operating with wavelength λ = 514 nm was used as a continuous light source. The beam was transmitted through different mirrors within a glass cylinder with a diameter of 30 cm in the center of the tank where a rotating mirror optical system generated a horizontal laser sheet of 130 m^2 and a thickness of roughly 5 mm. The systems moved vertically through a Labview controlled linear axis to permit a scan of the depth with 12 different levels equidistant by 4 cm, the highest and lowest levels being at 51 cm and 7 cm from the bottom, respectively. Images of 13 m × 9 m were taken with a Nikon Camera (D850 SLR, 45MPx) at a frame rate of 1 Hz, synchronized with the laser system. With the use of an optical lens of 14 mm on the camera, the spatial resolution was 1 mm pixel^{-1}. With the software UVMAT developed at LEGI, the velocity fields were computed using a cross-correlation PIV algorithm. For this purpose, an adaptive multi-pass routine was used, starting with an interrogation window of 35×35 pixels and a final window size of 20×20 pixels, with 70 % overlap. Each vector of the resulting vector field represented an area of roughly 0.5×0.5 cm. The velocity vectors were post-processed using a local median filter. Given the velocities encountered in the experiments, the experimental error in the instantaneous velocity was estimated to be approximately 3% and in ∂u/∂x approximately 10% maximum.

The velocity and the density at the outlet were monitored by means of an Acoustic Doppler Velocimetry Profiler (ADVP, Vectrino) and a conductivity probe. Both instruments were mounted 1 m downstream of the injector outlet S1 on a traversing system that enabled continuous periodic measurements on a radial section of 1 m length. Three velocity components were measured in a vertical section within the layer 3.5 cm wide and parallel to the bottom slope, while the density was calculated from conductivity values recorded at a distance of 1 cm from the bottom. An additional acoustic Doppler velocimeter (Vectrino) and a conductivity probe, mounted 4 m downstream of the injector outlet S1, were used to capture velocities and densities 1 cm from the bottom. A conductivity probe was positioned in the central (deep) part of the tank and mounted on a third traverse system enabling to take continuously vertical density profiles during the experiments.

The initial condition for the chosen experiment was a two-layer system, with ρ_{top} = 999.5 kg m^{-3}, ρ_{bottom} = 1014.7 kg m^{-3} and respective heights h$_{top}$ = 21 cm and h$_0$ = 36 cm. The rotation period T was set to 120 s. Two sources of saline injections were used, the first, S1, injecting ρ_1 = 1010 kg m^{-3} at a rather low flow rate of 0.4 ls^{-1} from the beginning of the experiment, the second, S2, positioned 180 degrees downstream from the first outlet with ρ_2 = 1019.8 kg m^{-3} at a flow rate of 1.6 ls^{-1}. The second source was switched on 90 minutes (45 experimental "days", i.e. rotation periods) after the beginning of the experiment. It was then switched off after 180 minutes, when the flow rate of the S1 source was doubled to 0.8 l s^{-1}. Discharge from S1 continued for 60 minutes more. In total, the experiment lasted 270 minutes (i.e., 135 "days").

The altimetric data used for the study of the evolution of the Ionian surface circulation were the gridded (1/8° Mercator projection grid), daily Absolute Dynamic Topography (ADT) and the corresponding Absolute Geostrophic Velocities (AGV) distributed by CMEMS-Copernicus Marine Environment Monitoring Service (SEALEVEL_MED_PHY_L4_REP_OBSERVATIONS_008_051). Vorticity was averaged over the rectangular area of the Northern Ionian (37-39 °N, 17-19 °E) and

normalized by a Coriolis parameter (10^{-4} s^{-1}). Similarly, the vorticity from the PIV measurements was normalized by the Coriolis parameter of the tank (10^{-1} s^{-1} – 120 s rotational period) and averaged within the plain deep central area.

3.   PREDICTIONS OF MEAN CIRCULATION AND TIME SCALES

In order to show that internal processes, compressing the upper freshwater layer, induce the circulation in the upper layer, we consider the equation of conservation of potential vorticity, with ζ representing the relative vorticity, h is a time dependent depth of the bottom layer. The variation in depth $\partial h/\partial t$ is related to the injected flow rate as: $\partial h/\partial t = Q/(\pi\ R(t)^2)$, where $R(t)=R_0+h(t)/s$ being the radius of the interfacial layer which depends on time t, s is a slope and R_0 is the radius of the central (deep) region. This gives thus

$$\frac{\partial \zeta}{\partial t} = \frac{f}{h}\ \frac{\partial h}{\partial t} = \frac{f}{h}\ \frac{Q}{\pi(R0+h/s)^{\wedge}2}\ .$$

Figure 3c shows the variation of the vorticity, spatially averaged within the central region (with a radius of 2.5 m), whereas different colors indicate the various horizontal layers in the vertical. The start of the injection of deep salty water (the S2 source) is highlighted at t/T=45 and cessation at t/T=90. We see that once the dense water source is switched on, the circulation in the upper layer quickly changes sign, from slightly cyclonic (due to weak residual motions in the tank) to anticyclonic shortly after t/T=45. The vorticity reaches a minimum value around -0.0175 s^{-1}, roughly in correspondence with the switching off the second source. Monotonous decrease of the anticyclonic vorticity then takes place until the end of the experiment. We believe that the reversal to the cyclonic vorticity was not observed due to the relatively short experiment duration. The vorticity in the deepest layers was close to zero during the entire experiment duration except for the period immediately after the beginning of the dense water injection when the clear cyclonic vorticity appeared. We compared the experimental results with the theoretical prediction of the vorticity variations in time as given in the equation of the potential vorticity conservation, obtaining an excellent agreement.

4.   RESULTS AND DISCUSSION

Surface circulation was weakly cyclonic before the injection of the dense water (ρ_2) due to a residual initial flow (Fig. 3a). After the injection of the dense water, the surface circulation turned into the rather strong and persistent anticyclonic flow (Fig. 3b). At the beginning of the dense water injection, the vorticity in the bottom layer (Fig. 3c) was slightly positive, but of smaller absolute values than the surface anticyclonic vorticity. It is important to notice that, generally, the anticyclonic vorticity was stronger than the cyclonic one, i.e., the systems shows a preference for the water column to rotate anticyclonically. This result differs from previous studies, which are however related to processes characterized by large Rossby numbers (≥ 1, see Rudnyck, 2001), and show a preference for cyclonic circulation. In our experiment, instead, the Rossby number was O(0.1).
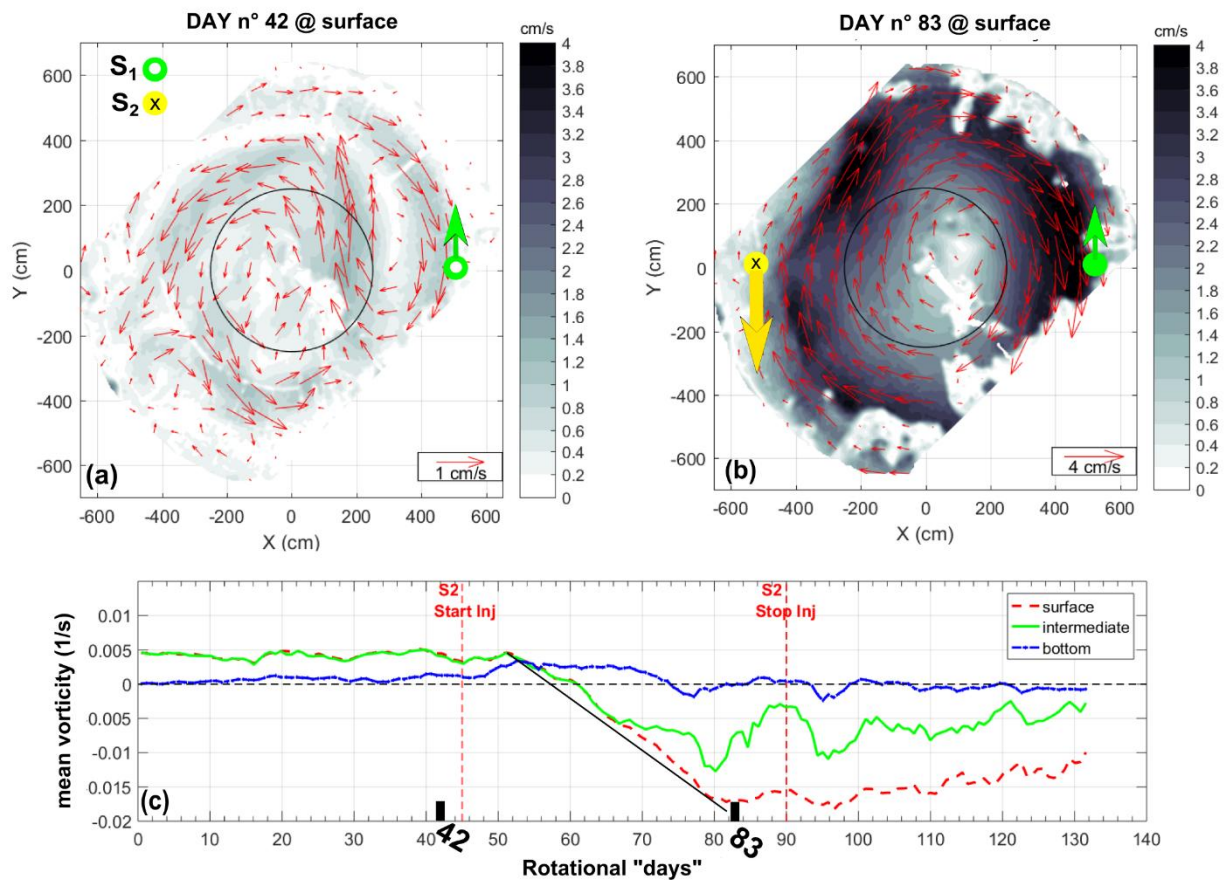
Figure 3. Horizontal distribution of the flow and vorticity field in the uppermost level at "rotational day" 42, before S2 source injection (a) and at "day" 83 (b). Panel c shows the time evolution of the spatially averaged vorticity within the deep portion of the tank in three layers: surface (including levels 2-4), intermediate (level 7) and bottom (including levels 10-12). The black solid line represents the theoretical prediction of vorticity variations using equations of the potential vorticity conservation.

The vorticity evolution in the upper layer of the rotating tank (Fig. 3) shows quite a quick response of the vorticity field to the dense water injections (day 45); after about ten days (day 55) there is a sudden switch to anticyclonic vorticity with its progressive intensification. Finally, the curve flattens out after about another twenty days (day 80). The intermediate level (close to the interface) shows anticyclonic vorticity as well. However, it is less intense than for the upper layers and fluctuates in such a way that minimum values occur about every ten days. This behavior corresponds to the passage of cyclonic eddies through the central plain area. The mesoscale cyclones are evident at almost all levels (not shown) with the largest amplitude at the interface, between days 80 and 100, which suggests that they might be subsurface intensified structures. The horizontal distribution of the flow field (not shown) indeed confirms the formation or the passage of these subsurface intensified cyclones. The temporal evolution of the bottom layer vorticity reveals an increase of the cyclonic vorticity from the beginning of the dense water injection, which reduces to zero rather soon (Fig. 3c).

Winter 2012, which was characterized by the formation of an extremely dense water in the Adriatic, resulted, during spring 2012, in a spreading of this newly formed water into the Ionian, which caused a transient inversion of the Ionian cyclonic circulation (Gačić et al., 2014). This physical situation should be similar to the analyzed experiment in the rotating tank. In the paper of Gačić et al. (2014), the start of the very dense AdDW discharge into the Ionian was determined with rather satisfactory precision and we are thus able to compare the evolution of the *in situ* vorticity and the rotating tank vorticity, starting from the moment of the dense water injection (Fig. 4). The *in situ* geostrophic flow is determined from altimetric data and thus the associated surface

vorticity field represents the geostrophic vorticity; therefore, the two vorticity fields are not fully comparable. However, as in the case of the rotating tank, the response of the Ionian near-surface geostrophic vorticity field was quite fast (on the order of a month); differences appeared instead in the time needed to reach the quasi-steady state, which in the Ionian is about two times longer than in the rotating tank. Differences in the response time between the rotating tank experiment and the Ionian Sea case can be estimated from the non-dimensional number, i.e. the ratio between the inertial period and the residence time, which we show to be almost twice as large in the real ocean than for the tank experiment.
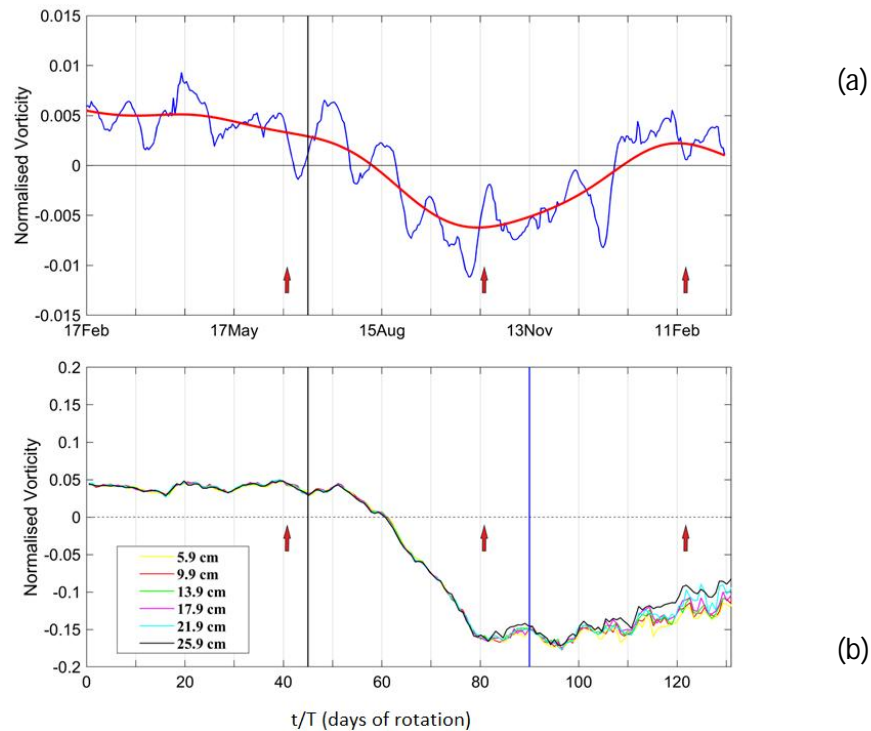

Figure 4. Normalized vorticity for the Northern Ionian Sea (a) and for the tank experiment (b). Red arrows indicate the elapsed times corresponding to the histograms shown in Fig. 5.

The histograms of vorticity distribution (Fig. 5) at all levels show, generally, a shape close to the Gaussian distribution. The histograms for the surface layer reveal clearly the evolution of the flow field before and after the start of the dense water discharge. Vorticity inverts into the anticyclonic mode after the 45th day of the experiment. After the dense water injection ceases, a secondary maximum occurs at positive vorticity values. The asymmetry is also evident at the density interface where during the injection period two peaks occur: one in the anticyclonic and one in the cyclonic part. As expected, the vorticity histogram for the interface deviates largely from the Gaussian distribution (Fig. 5e) during the dense water discharge due to heterogeneous velocity field and the presence of both cyclonic and anticyclonic mesoscale structures. After ceasing of the S2 dense water injection, while the S1 light water injection continues, there is a slow decrease of the absolute values of the anticyclonic vorticity in the surface layer. Indeed, on the 123th day a secondary weak maximum at positive (cyclonic) vorticity values shows up. However, a complete reversal could not have been reached, due to a relatively short experiment duration after the cessation of the dense water injection.
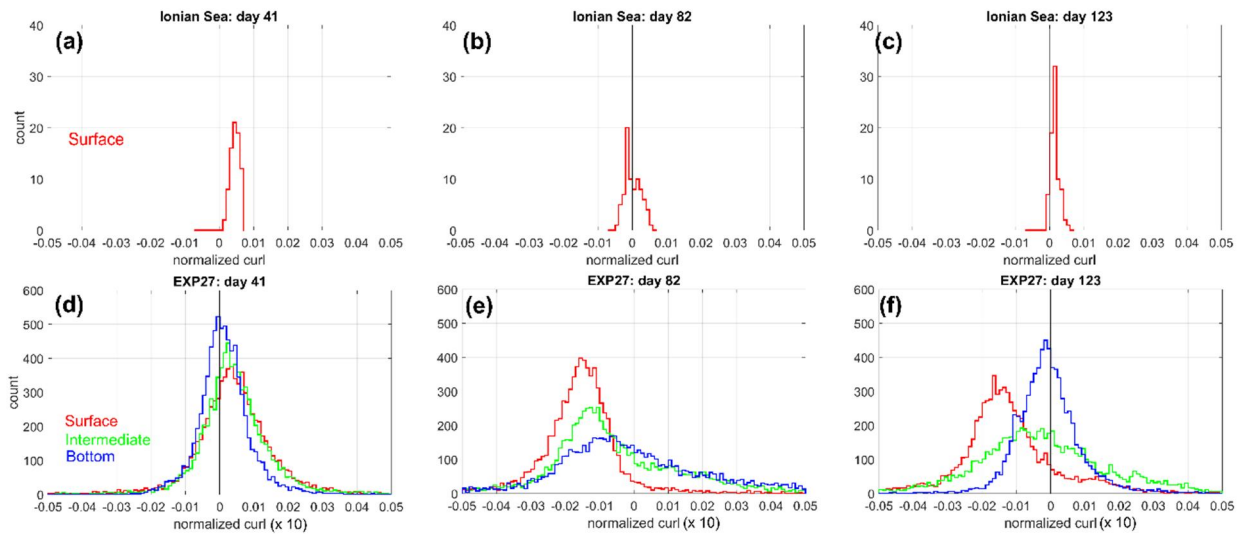
Figure 5. Histograms of the mean normalized vorticity in three different moments: before, after and during dense water injection. Upper panels (a, b, c) refer to the surface layer in the Ionian Sea, while lower panels (d, e, f) refer to the central part of the rotating tank at three measurement levels (surface level 1, intermediate level 7, and bottom level 12). The days in the upper panels indicate time scaled by a factor 0.5 (see text) in order to obtain the same slope of both Ionian and tank vorticity curves.

We discuss the *in situ* vorticity distribution at the same days when we choose the rotating tank vorticity distribution. However, in order to have similar physical conditions in both data sets we had to rescale the time axis of the *in situ* data by multiplying the time interval of the Ionian Sea vorticity evolution by a factor of 0.5, as seen above. We have also to consider that before the start of the AdDW injection into the Ionian, the background *in situ* conditions were characterized by a cyclonic circulation, different from the case in the rotating tank. In fact, on the 41st day a peak of the vorticity histogram is at the positive vorticity value and then on the 82nd day (during the AdDW discharge) the peak moves toward negative values, showing anticyclonic circulation. The histogram of the 88th day is highly asymmetric, with the maximum at anticyclonic vorticity values (not shown). On the 123rd day the peak returns back to a positive vorticity value meaning that the impact of the AdDW weakened appreciably and the system went back to the initial cyclonic circulation.

5.   CONCLUSIONS

In this paper, we discuss results of the analysis of an experiment, which was conducted at the Coriolis rotating platform at LEGI in the framework of the CroPEx project. The experiment consisted of three phases; in the first phase, relatively light water (1015 kg m^{-3}) was injected for about one-third of the experiment duration into the two-layer system. Then, a second source was added and very dense water (1020 kg m^{-3}, denser than the deep-layer density) was injected for 45 rotations (days) and, finally, after the cessation of the dense water injection, the light water continued discharging for about 50 days at a double discharge rate with respect to its initial injection rate. The experiment was thought to be dynamically similar to the situation occurred in the Ionian basin after winter 2012. Climatic conditions in the area were characterized by an extremely harsh winter over the region and, consequently, the Adriatic Sea produced very dense water, which was then discharged into the Ionian Sea and was able to invert temporarily the Ionian circulation from cyclonic to the anticyclonic one.

The evolution of the vorticity field in the rotating platform shows strong similarities with the *in situ* situation; quite a sudden inversion of the surface circulation from the cyclonic to the anticyclonic took place both in the Ionian Sea and in the rotating platform after the dense water injection. However, differences in the response time scale are evident and the response is almost twice as fast in the physical experiment than in the Ionian. This relationship between the response time in the Ionian and in the rotating tank is obtained from a non-dimensional number, i.e. the ratio

between the inertial period and the residence time of the receiving basin (the Ionian Sea or the central plain area of the rotating tank). It can be shown that the response time is larger for the tank experiment than for the Ionian Sea. Starting from the equation of conservation of potential vorticity, we showed quite a good agreement between the experimental data and theoretical estimates of the rate of change of the vorticity. After about 20 (rescaled) days from the beginning of the dense water discharge, the anticyclonic vorticity reaches a plateau in both the real ocean and in the rotating tank. From the field observations, it can be seen that the flow after some time returns to the cyclonic mode when probably the Adriatic dense water impact weakens. In the rotating tank, after the cessation of the dense water injection, the anticyclonic vorticity started to weaken but did not come back to the cyclonic flow probably due to the relatively short duration of the experiment. With this experiment and comparison with *in situ* data, we thus show how climatic conditions responsible for a sudden increase of the bottom water density in the Adriatic can change the "internally" dictated rhythm of the circulation inversions in the Ionian Sea, definitely confirming the robustness of the BiOS mechanism.

ACKNOWLEDGMENTS

REFERENCES

Batistić M., Garić, R., Molinero J.C. (2014). Interannual variations in Adriatic Sea zooplankton mirror shifts in circulation regimes in the Ionian Sea. Clim. Res., Vol. 61: 231–240, doi: 10.3354/cr01248.

Borzelli, G. L. E., Gačić, M., Cardin, V. and Civitarese, G. (2009). Eastern Mediterranean Transient and reversal of the Ionian Sea circulation, Geophys. Res. Lett., 36, L15108, doi:10.1029/2009GL039261.

Civitarese, G., Gačić, M. Lipizer, M. and Eusebi Borzelli, G. L. (2010). On the impact of the Bimodal Oscillating System (BiOS) on the biogeochemistry and biology of the Adriatic and Ionian Seas (Eastern Mediterranean), Biogeosciences, 7, 3987–3997, doi:10.5194/bg-7-3987-2010.

Gačić, M., Eusebi Borzelli, G.L. Civitarese, G. Cardin V. and Yari, S. (2010). Can internal processes sustain reversals of the ocean upper circulation? The Ionian Sea example, Geophys. Res. Lett., 37, 10 L09608, doi:10.1029/2010GL043216.

Gačić, M., Civitarese, G., Kovačević, V., Poulain, P-M., Theocharis, A., Menna, M., Catucci, A., Zarokanellos, N. (2011). On the relationship between the decadal oscillations of the Northern Ionian Sea and the salinity distributions in the Eastern Mediterranean. J. Geoph. Res.; 116. C12002, doi:10.1029/2011JC007280.

Gačić, M., Civitarese, G., Kovačević, V., Ursella, L., Bensi, M., Menna, M., Cardin, V., Poulain, P.-M., Cosoli, S., Notarstefano, G., and Pizzi, C. (2014). Extreme winter 2012 in the Adriatic: an example of climatic effect on the BiOS rhythm, Ocean Sci., 10, 513-522, https://doi.org/10.5194/os-10-513-2014.

Lavigne, H., Civitarese, G., Gačić, M., and D'Ortenzio, F. (2018). Impact of decadal reversals of the north Ionian circulation on phytoplankton phenology, Biogeosciences, 15, 4431-4445, https://doi.org/10.5194/bg-15-4431-2018.

Manca, B.B., Budillon, G. Scarazzato, P. and Ursella, L. (2003). Evolution of dynamics in the eastern Mediterranean affecting water mass structures and properties in the Ionian and Adriatic seas, J. Geophys. Res., 108(C9), 8102, doi:10.1029/2002JC001664..

Menna, M., Reyes Suarez, N.C., Civitarese, G., Gačić, M., Rubino, A., Poulain, P.-M. (2019). Decadal variations of circulation in the Central Mediterranean and its interactions with mesoscale gyres. Deep Sea Res. II, 2019, doi:10.1016/dsr2.2019.02.004.

Mihanović, H., Vilibić, I., Dunić, N. and Šepić, J. (2015). Mapping of decadal middle Adriatic oceanographic variability and its relation to the BiOS regime, J. Geophys. Res. Oceans, 120, 5615–5630, doi:10.1002/5JC010725.

Nof, D. (1983). The translation of isolated cold eddies on a sloping bottom. Deep-Sea Res. **30**, 171–182.

Ozer, T., Gertman, I., Kress, N., Silverman, J., and Herut, B. (2017). Interannual thermohaline (1979–2014) and nutrient (2002–2014) dynamics in the Levantine surface and intermediate water masses, SE Mediterranean Sea. Global and Planetary Change 151, 60–67.

Roether, W., Manca, B.B., Klein, B., Bregant, D., Georgopoulos, D., Beitzel, V., Kovačević, V., and Luchetta, A. (1996). Recent Changes in Eastern Mediterranean Deep Waters. Science, 271, 333-335.

Rudnyck, D.L. (2001). On the skewness of vorticity in the upper ocean. Geophys. Res. Lett., Vol. 28, 10, 2045-2048, https://doi.org/10.1029/2000GL012265

Vilibić I., Mihanović H., Kušpilić G., Ivčević A., and Milun, V. (2015). Mapping of oceanographic properties along a middle Adriatic transect using Self-Organising Maps, Estuarine, Coastal and Shelf Science, 163, 84-92.

LABORATORY MODELING OF GAP-LEAPING AND INTRUDING WESTERN BOUNDARY CURRENTS UNDER DIFFERENT CLIMATE CHANGE SCENARIOS

Stefano Pierini (1), Paola de Ruggiero (1), Henk A. Dijkstra (2), Ilana Schiller-Weiss (2), Julia Weiffenbach (2), Eletta Negretti (3) & Joël Sommeria (3)

(1) Department of Science and Technology, Parthenope University of Naples, Italy
E-mail: stefano.pierini@uniparthenope.it
(2) Department of Physics and Astronomy, Utrecht University, The Netherlands
(3) LEGI-CNRS, Grenoble, France

Western boundary currents (WBCs), such as, for example, the Kuroshio and the Gulf Stream, are very intense currents flowing along the western boundaries of the oceans. WBCs -and their respective extensions- have an important effect on climate because of their huge heat transports, the corresponding air–sea interactions and the role they play in sustaining the global conveyor belt. It is therefore very relevant to analyze WBC dynamics not only through observations and numerical modelling, but also by means of laboratory experiments; to this respect several rotating tank experiments have been performed in recent years. In this paper we describe the new laboratory experiments proposed for the Hydralab+ 19GAPWEBS project, which are aimed at analyzing the interactions of a WBC with gaps located along the western coast. Examples of such processes include the Gulf Stream leaping from the Yucatan to Florida and the Kuroshio leaping, and partly penetrating, through the South and East China Seas and through the wider gap separating Taiwan to Japan. In the experiments (that will be carried out with the 13-m diameter Coriolis rotating tank at LEGI-CNRS in Grenoble in June-July 2019) a WBC is produced by a horizontally unsheared current flowing over a topographic beta slope; along the western lateral boundary a sequence of gaps of different widths simulate the openings present in the above mentioned locations.

1.   INTRODUCTION AND MOTIVATION

WBCs are very intense currents flowing along the western boundaries of the oceans and owe their peculiar structure to the sphericity of the earth, which generates the so-called planetary beta effect (e.g., Pedlosky, 1987). The Kuroshio and Gulf Stream (GS) are notable examples of WBCs belonging to the subtropical gyres of the North Pacific and Atlantic Oceans, respectively. The very important effect that WBCs -and their respective extensions- have on climate is known to be due to their huge heat transports, to the corresponding air–sea interactions and to the role they play in sustaining the global conveyor belt (e.g., Qiu, 2000, 2003; Ganopolski & Rahmstorf, 2002; Kelly et al., 2010). Some of the proposers have developed several numerical model studies with different degrees of complexity to investigate basic aspects of WBC dynamics (e.g., Dijkstra & Katsman, 1997; Schmeits & Dijkstra, 2000, 2001; Pierini, 2006, 2010, 2011, 2014, 2015; Pierini & Dijkstra, 2009; Pierini et al., 2009, 2014; Kramer et al., 2012; Quattrocchi et al., 2012).

One of the most interesting and intriguing WBC phenomena of climate relevance is the interaction of the jet with a gap located along the western coast. Examples include the GS leaping from the Yucatan to Florida, and the Kuroshio leaping, and partly penetrating through the South and East China Seas (SCS and ECS, Fig. 1a). The Kuroshio carrying the northwestern Pacific water intrudes partially into the SCS through the Luzon Strait (Fig. 1c), significantly affecting the hydrology, circulation and mixing in the SCS (e.g., Nan et al., 2015). A similar phenomenon occurs through the wider gap separating Taiwan to Japan (Fig. 1b, e.g., Liu et al., 2014).

Inferred from the satellite and in situ hydrographic data from the 1990s and 2000s, Nan et al. (2013) found that the Kuroshio intrusion into the SCS had a weakening trend over the past two decades, so that the Kuroshio loop and eddy activity southwest of Taiwan became weaker. The same authors noticed that the Kuroshio transport east of Luzon Island also had a negative trend, and suggested that this might have caused the weakening of the Kuroshio intrusion because of the decreased inertia of the jet. A similar hypothesis was put forward also by Liu et al. (2014) to

explain the observed relation between the changes of the Kuroshio intrusion across the ECS and those of the Kuroshio volume transport. To support their hypothesis, these authors invoked the rotating tank experiments of Pierini et al. (2011), in which the different but related process of WBC separation due to inertial overshooting, and its critical behavior, was investigated for varying jet intensity.

The gap-leaping and intruding WBC phenomena are manifestations of an oceanographically generic problem, i.e., that of the interaction of a boundary current with a gap along the coast. This was investigated in several observational (e.g., Centurioni & Niiler, 2004; Liu et al., 2014; Lu & Liu, 2013; Nan et al., 2013, 2015) and numerical model studies (e.g., Sheremet, 2001; Xue et al., 2004; Sheu et al., 2010).
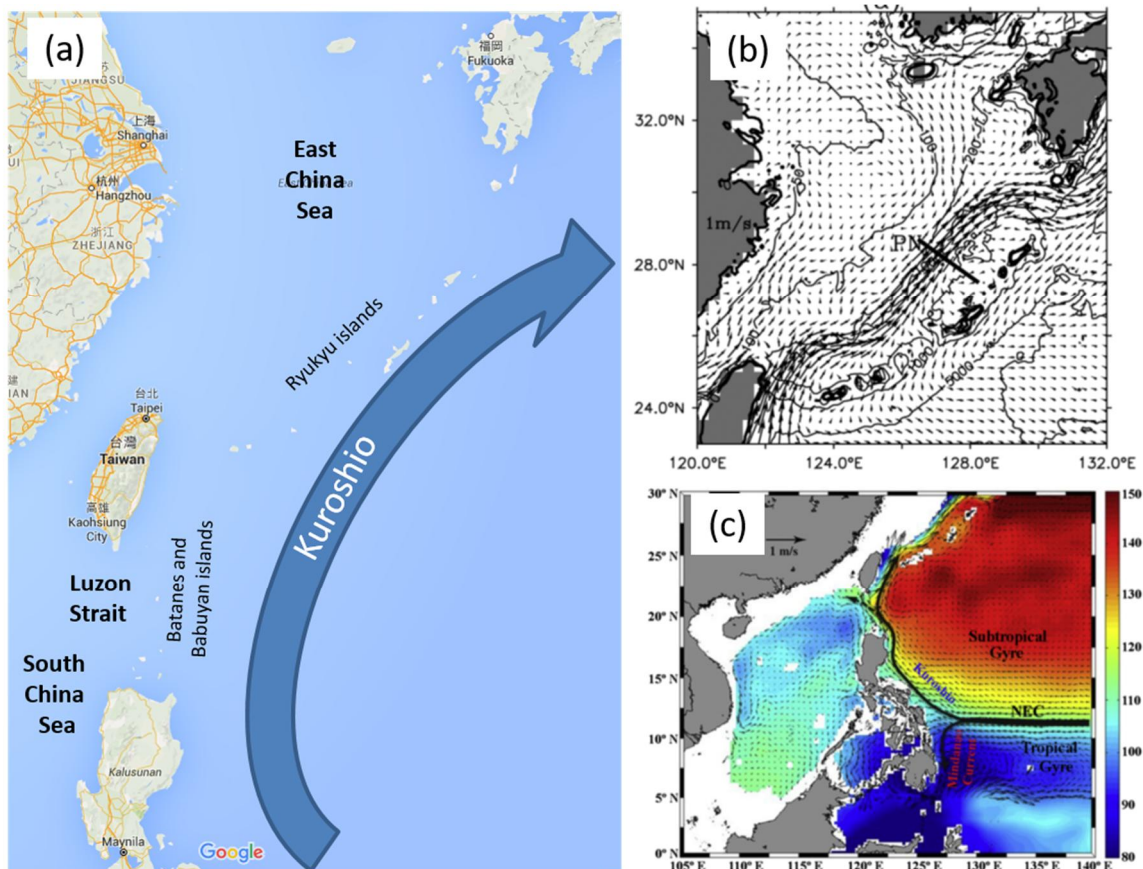
Fig. 1. (a) Schema of the Kuroshio flowing along the gaps connecting the Pacific with the South and East China Seas. Maps of the Kuroshio intrusion into the East [(b), from Liu et al., 2014] and South [(c), from Nan et al., 2015] China Seas.

Laboratory experiments were also performed in a cylindrical tank on a one-meter rotating table by Sheremet & Kuehl (2007) and Kuehl & Sheremet (2009). The great relevance of the problem calls for further laboratory experiments accounting for variations in WBC intensity related to climate change scenarios, but this requires larger scale simulations and, in turn, a larger rotating tank facility.

This motivates the present project, which is based on a substantial extension of three previous laboratory experiments performed by one of the proposers with the 13-m diameter Coriolis rotating tank of CNRS in Grenoble (Pierini et al., 1999; 2002) and with the 5-m diameter Coriolis rotating tank of SINTEF in Trondheim (Pierini et al., 2008; 2010; 2011). The proposed experiments are described in sect. 2; in sects. 3 and 4 the dynamic similarity with the full-scale phenomenon and the synergy effect with mathematical models are respectively discussed.

2. EXPERIMENTAL SETUP AND PROPOSED EXPERIMENTS

The setup proposed to study the problem described in Sect. 1 is reported in Fig. 2. A pumping system located in channel C produces a current of speed u_p that, following the lateral boundaries, generates a virtually unsheared flow at the entrance of the slope Σ_1, which in turn provides the topographic beta-effect β^* necessary for the intensification (this imposes the use of homogeneous water).
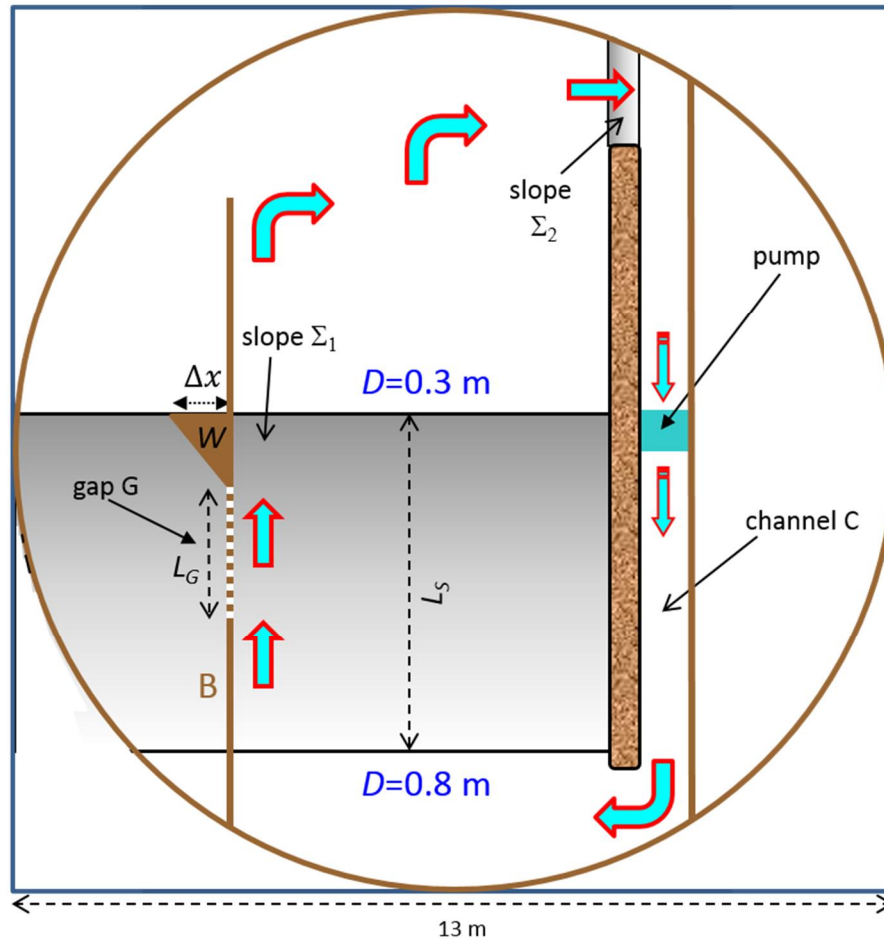

Fig. 2. The proposed setup.

This part of the setup is basically the same as the one adopted by Pierini (2008; 2011): this insures the feasibility of the project. Three substantial improvements are now present:

(i) The motion will be introduced in the channel C by a pumping system rather than through a moving piston. This will allow for experiments with, in principle, unlimited duration (and corresponding very long time series) also for strong WBCs, for which a large u_p is required (see Pierini et al., 2008, 2011, for a discussion on the limited duration of the experiments when a moving paddle is used). The large length of channel C is required to reduce the turbulence at its lower end.

(ii) The length L_S of the slope Σ_1 is $L_S = 2L_{S\_old}$ (L_{S_old} is the corresponding length in the setup used by Pierini et al., 2008; 2011) while the inclination of the slope is the same (this requires the water depth to be doubled, which has also the positive consequence of reducing the effect of the free surface deformation): thus, $\beta^* = \beta^*_{old}/2$. The inertial WBC length scale $\delta_I \approx \sqrt{u_p / \beta^*}$ (see sect. 3) is therefore greater by a factor $\sqrt{2}$, so a better WBC resolution is achieved. Moreover, the parameter $\sigma = L_S/\delta_I$ measuring the effective length of the WBC is $\sigma = \sqrt{2}\,\sigma_{old}$: thus, a longer effective WBC is achieved as well. This will therefore allow us to obtain WBCs whose spatial resolution is the highest ever attained in rotating tank experiments. On the other hand, such high

resolution is needed to study the intrusion of WBCs through the gaps: this justifies the use a large scale facility such as the 13-m diameter Coriolis rotating tank of CNRS in Grenoble.

(iii) The completely new part of the setup, specifically designed to analyze the phenomenon under investigation, includes the introduction of the gap G along the "western" boundary B. G will also include smaller gaps to represent islands (e.g., see Fig. 1a). A wedge-shaped obstacle W of width Δx simulating an island (e.g., Taiwan, see Fig. 1c) is also introduced.

Experiments will be carried out by varying: (a) the rotation period T; (b) u_p (and so the intensity of the WBCs) by taking into account both the various dynamical ranges (see Sect. 3 of Pierini et al. 2011) and the climate change scenarios described by Nan et al. (2013); (c) the length L_G of the gap; (d) the number and width of the islands inside G; (e) the width Δx of the obstacle W.

The measuring technique will be provided by the Particle Imaging Velocimetry (PIV) covering the area of the slope Σ_1. The results will be published in an outstanding scientific journal, the dissemination will be provided by means of an ad hoc web site and through presentations to major international conferences and, finally, the data will be stored in a server of the principal investigator's department and will be made available through the internet to the researchers outside the research team according to the HDRALAB+ rules.

3. DYNAMIC SIMILARITY AND DIMENSIONLESS PARAMETERS

To study the dynamic similarity between the proposed experiments and the full-scale phenomenon one can rely on the evolution equation of potential vorticity in the quasigeostrophic approximation (valid for our experiments because the Rossby number ε_R for a typical simulated WBC is $\varepsilon_R \approx$ **0.05** $\ll$ **1**) in its steady and dimensionless form. For this specific problem one has (Pierini et al., 2008):

$$\varepsilon(uv_{xx} - vu_{xx}) + v = Ev_{xxx} - Bv_x \tag{1}$$

Here, (x, y) and (u, v) are the dimensionless zonal and meridional coordinates and velocity components, respectively, and the dimensionless parameters

$$\varepsilon = \frac{U}{\beta\ell^2} = \left(\frac{\delta_I}{\ell}\right)^2 ; \quad E = \frac{A_H}{\beta\ell^3} = \left(\frac{\delta_M}{\ell}\right)^3 ; \quad B = \frac{r}{\beta\ell} = \frac{\delta_s}{\ell} \tag{2}$$

measure the importance of nonlinearities and lateral and bottom friction, respectively (the Reynolds number is $Re = \varepsilon/E$). U and ℓ are typical zonal velocity and length scales, β is the meridional gradient of the Coriolis parameter f (in our experiments it is given by β^*), A_H is either a constant lateral eddy viscosity coefficient in a full-scale schematization of WBCs or the molecular viscosity of water in our experiments, r is the inverse of the spin-down time due to bottom friction, and δ_I, δ_M, and δ_s represent the boundary layer length scales for purely inertial and purely viscous Munk and Stommel flows, respectively. In the derivation of (1), a boundary layer approximation has been made: x is scaled through the width ℓ of the western boundary layer and y through the meridional width L of the low-latitude region where the current flows toward the western boundary, respectively, with $\ell \ll L$ (again, see Pierini et al., 2008, for a detailed explanation; in particular see Sect. 3b, Fig. 7 and Table 2 therein, but see also Sect. 3 and Fig. 5 in Pierini et al., 2011).

The WBC scaling adopted in Pierini et al. (2008; 2011) applies to the proposed experiments as well, but with one difference: as discussed above, now $\beta^* = \beta^*_{old}/2$. From (2) one can see that the relative weights of ε, E and B do not change, nor does Re. On the other hand, the inertial length scale δ_I (the relevant one for simulated WBCs that are dynamically similar to the real ones) increases by a factor $\sqrt{2}$, with the positive consequences pointed out in Sect. 2. Typical values that will be used in the experiments are: $T =$ **30 ÷ 60** s, $u_p =$ **1 ÷ 6** $cm\ s^{-1}$. The width L_G of the gap G will be modified according to the WBC width ℓ.

4. SYNERGY EFFECTS WITH MATHEMATICAL MODELS

The interplay between experimental research and mathematical/numerical modeling is quite a subtle issue. As noted by Van Os (1999) in his contribution to the HYDRALAB workshop held in

Hannover in 1999, in the '70s and '80s, experimental and numerical hydraulic researches were often seen as competitors; in the '90s experimental research was rather seen as supporting process research for the improvement of mathematical models, but the latter could in turn assist the experimental facility. In a more challenging approach, the integrated use of physical models, numerical models, theoretical analysis and field experiments can provide the best advancements in our understanding of the hydraulic processes under investigation. Thus, according to Van Os (1999), the real challenge is to achieve a two-way cooperation between experimental research and mathematical modeling so as "to migrate from competition to synergy".

According to this view, numerical modeling (based on the same shallow water model used by Pierini and collaborators in their studies on the Kuroshio Extension, see sect. 1) was carried out in synergy with the laboratory experiments performed to analyze Rossby normal modes (Pierini et al., 1999; 2002) and western boundary currents (Pierini et al., 2008).

Following the same approach, in the present project we will implement the Princeton Ocean Model (POM) to a domain that closely represents the experimental setup. It is worth stressing that one of the proposers is an expert in the application of POM to coastal circulation modeling (e.g., de Ruggiero et al., 2016, 2018). In addition, numerical bifurcation studies on a discretized shallow water model will also be performed (as in Schmeits & Dijkstra, 2001) to study the possible flow patterns (versus parameters) and their variability in the laboratory configuration.

ACKNOWLEDGEMENT

REFERENCES

Centurioni, L. and P. P. Niiler (2004). Observations of Inflow of Philippine Sea Surface Water into the South China Sea through the Luzon Strait. *J. Phys. Oceanogr.*, 34, 113-121.

De Ruggiero, P., E. Napolitano, R. Iacono and S. Pierini (2016). A high-resolution modelling study of the circulation along the Campania coastal system, with a special focus on the Gulf of Naples. *Cont. Shelf Res.*, 122, 85-101.

De Ruggiero, P., E. Napolitano, R. Iacono, S. Pierini and G. Spezie (2018). A baroclinic coastal trapped wave event in the Gulf of Naples (Tyrrhenian Sea). *Ocean Dyn.*, 68, 1-12.

Dijkstra, H. A, and C. A. Katsman (1997). Temporal variability of the wind- driven quasi-geostrophic double gyre ocean circulation: Basic bifurcation diagrams. *Geophys. Astrophys. Fluid Dyn.*, 85, 195-232.

Ganopolski, A. and S. Rahmstorf (2002). Abrupt glacial climate changes due to stochastic resonance. *Phys. Rev. Lett.*, 88, 038501.

Kelly, K. A., R. J. Small, R. M. Samelson, B. Qiu, T. M. Joyce, Y. Kwon and M. F. Cronin (2010). Western boundary currents and frontal air–sea interaction: Gulf Stream and Kuroshio Extension. *J. Climate*, 23, 5644–5667.

Kramer, W., H. A. Dijkstra, S. Pierini and P. J. van Leeuwen (2012). Measuring the impact of observations on the predictability of the Kuroshio Extension in a shallow-water model. *J. Phys. Oceanogr.*, 42, 3-17.

Kuehl, J.J. and V. A. Sheremet (2009). Identification of a cusp catastrophe in a gap-leaping western boundary current. *J. Mar. Res.*, 67, 25–42.

Liu, C., F. Wang, X. Chen and J.-S. von Storch (2014). Interannual variability of the Kuroshio onshore intrusion along the East China Sea shelf break: Effect of the Kuroshio volume transport. *J. Geophys. Res.*, 119, 6190-6209.

Lu, J. and Q. Liu (2013). Gap-leaping Kuroshio and blocking westward-propagating Rossby wave and eddy in the Luzon Strait. *J. Geophys. Res.*, 118, 1170–1181.

Nan, F., H. Xue, F. Chai D. Wang, F. Yu, M. Shi, P. Guo and P. Xiu (2013). Weakening of the Kuroshio Intrusion into the South China Sea over the Past Two Decades. *J. Climate*, 26, 8097-8110.

Nan, F., H. Xue and F. Yu (2015). Kuroshio intrusion into the South China Sea: A review. *Progr. Oceanogr.*, 137, 314-333.

Pedlosky, J. (1987). *Geophysical Fluid Dynamics*. Springer-Verlag, 710 pp.

Pierini, S. (2006). A Kuroshio Extension system model study: Decadal chaotic self-sustained oscillations. *J. Phys. Oceanogr.*, 36, 1605–1625.

Pierini, S. (2010). Coherence resonance in a double-gyre model of the Kuroshio Extension. *J. Phys. Oceanogr.*, 40, 238–248.

Pierini, S. (2011). Low-frequency variability, coherence resonance and phase selection in a low-order model of the wind-driven ocean circulation. *J. Phys. Oceanogr.*, 41, 1585–1604.

Pierini, S. (2014). Kuroshio Extension bimodality and the North Pacific Oscillation: A case of intrinsic variability paced by external forcing. *J. Climate*, 27, 448–454.

Pierini, S. (2015). A comparative analysis of Kuroshio Extension indices from a modeling perspective. *J. Climate*, 28, 5873-5881.

Pierini, S. and H. A. Dijkstra (2009). Low-frequency variability of the Kuroshio Extension. *Nonlin. Processes Geophys.*, 16, 665-675.

Pierini, S., H. A. Dijkstra and A. Riccio (2009). A nonlinear theory of the Kuroshio Extension bimodality. *J. Phys. Oceanogr.*, 39, 2212–2229.

Pierini S., H. A. Dijkstra and M. Mu (2014). Intrinsic low-frequency variability and predictability of the Kuroshio Current and of its extension. *Adv. Oceanogr. Limnol.*, 5, 1-44.

Pierini, S., P. Falco, G. Zambardino, T. A. McClimans and I. Ellingsen (2010). Laboratory simulation of western boundary currents over shelf topography and of their extensions. In Proceedings of the HYDRALAB III Joint Transnational Access User Meeting, Hannover, J. Grüne and M. K. Breteler (Editors). Forschungszentrum Küste FZK (ISBN-978-3-00-030141-4), 131-134.

Pierini, S., P. Falco, G. Zambardino, T. A. McClimans and I. Ellingsen (2011). A laboratory study of nonlinear western boundary currents, with application to the Gulf Stream separation due to inertial overshooting, *J. Phys. Oceanogr.*, 41, 2063–2079.

Pierini, S., A. M. Fincham, D. Renouard, M. R. D'Ambrosio and H. Didelle (1999). Topographic Rossby normal modes simulated in the Coriolis rotating tank and by means of a mathematical model. In Proceedings of the HYDRALAB Workshop: *Experimental Research and Synergy Effects with Mathematical Models*. K.U. Evers, J. Grüne and A. Van Os (Editors). Forschungszentrum Küste FZK (ISBN-3-00-004942-8), 171-180.

Pierini, S., A. M. Fincham, D. Renouard, M. R. D'Ambrosio and H. Didelle (2002). Laboratory modeling of topographic Rossby normal modes. *Dyn. Atmos. Oceans,* 35, 205–225.

Pierini, S., V. Malvestuto, G. Siena, T. A. McClimans and S. M. Løvås (2008). A laboratory study of the zonal structure of western boundary currents. *J. Phys. Oceanogr.*, 38, 1073–1090.

Qiu, B. (2000). Interannual variability of the Kuroshio Extension system and its impact on the wintertime SST field. *J. Phys. Oceanogr.*, 30, 1486–1502.

Qiu, B. (2003). Kuroshio Extension variability and forcing of the Pacific decadal oscillations: Responses and potential feedback. *J. Phys. Oceanogr.*, 33, 2465–2482.

Quattrocchi, G., S. Pierini and H. A. Dijkstra (2012). Intrinsic low-frequency variability of the Gulf Stream. *Nonlin. Processes Geophys.*, 19, 155-164.

Schmeits, M. J. and H. A. Dijkstra (2000). Physics of the 9-month variability in the Gulf Stream region: Combining data and dynamical systems analyses. *J. Phys. Oceanogr.*, 30, 1967-1987.

Schmeits, M. J. and H. A. Dijkstra (2001). Bimodal behavior of the Kuroshio and the Gulf Stream. *J. Phys. Oceanogr.*, 31, 3435-3456.

Sheremet, V. A. (2001). Hysteresis of a Western Boundary Current Leaping across a Gap. *J. Phys. Oceanogr.*, 31, 1247-1259.

Sheremet, V. A. and J. Kuehl (2007). Gap-Leaping Western Boundary Current in a Circular Tank Model. *J. Phys. Oceanogr.*, 37, 1488-1495.

Sheu, W.-J., C.-R. Wu and L.-Y. Oey (2010). Blocking and westward passage of eddies in the Luzon Strait. *Deep-Sea Res. II*, 57, 1783–1791.

Van Os, A. G. (1999). The role of HYDRALAB in European research. In Proceedings of the HYDRALAB Workshop: *Experimental Research and Synergy Effects with Mathematical*

Models. K.U. Evers, J. Grüne and A. Van Os (Editors). Forschungszentrum Küste FZK (ISBN-3-00-004942-8), 1-5.

Xue, H. J., F. Chai, N. R. Pettigrew, D. Y. Xu, M. C. Shi and J. P. Xu (2004). Kuroshio intrusion and the circulation in the South China Sea. *J. Geophys. Res.*, 109, C02017.

III – Deltares - Delta Flume and Basin

The Delta Flume is a wave flume which is unique because of its dimensions. The flume has a length of 300 m, a width of 5 m and a depth of 9.5 m. A flume with these dimensions allows for physical models on a scale which is close to prototype. This means that there are hardly any scale effects to take into account. The state-of -the-art Delta Flume is capable of generating both regular (periodic) and irregular (random) waves, which are higher than any facility in Europe. The wave generator is equipped with online Active Reflection Compensation, which effectively eliminates re-reflections of waves from the wave board. In this way they do not disturb the measurements. Also wave board control for random second-order waves is operational to compensate for spurious waves.

Because of the size of the Delta Flume there is a wide range of applications in which we are involved. Several breakwaters have been tested in the Delta Flume. The stability of the armour layer and the overtopping discharge are typical measurements in such tests. Typical measurements carried out in the Delta Flume include wave height, pressures, flow velocities, overtopping volumes and profiles.

Tests related to erosion of sediments are difficult to investigate on a smaller scale. Problems regarding grain size are difficult to solve in a small scale model. The Delta flume makes it possible to solve some of those problems because for instance the grain size can be one that is really found in nature. The Delta Flume is a versatile and indispensable facility which can be put to use in numerous projects.

The Delta Basin (50 x 50 m) is a multidirectional wave basin, equipped with 2 multidirectional wave generators, placed at a right angle to each other. The wave generators are capable of generating both regular (periodic) as irregular (random) long-crested or short-crested waves according to both well-known frequency-directional distributions. Both wave generators are equipped with online Active Reflection Compensation, which effectively eliminates re-reflections of waves from the wave board. Also wave board control for random second-order waves is operational to compensate for spurious waves. The Dalrymple Method generates a wave train at a specified location, which effectively increases the model area which can be used.

The influence of 3D wave attack on structures can be substantial. To study phenomena related to such conditions the Delta basin is very suitable, because of its large dimensions and the 2 multidirectional wave generators. Both waves, current and a combination of these can be generated.

The Delta basin is used for coastal and offshore related projects. In all of these studies, aspects of armour stability, hydraulic performance, wave impact loading and the determination of the relevant hydraulic conditions for design purposes were of primary interest.

OVERTOPPED WAVE LOADS ON WALLS (WALOWA) – NUMERICAL AND PHYSICAL MODELLING OF LARGE-SCALE EXPERIMENTS IN THE DELTA FLUME

Maximilian Streicher (1) & Andreas Kortenhaus (1) & Vincent Gruwez (1) & Tomohiro Suzuki (2) & Corrado Altomare (3) & Alessandra Saponieri (4) & Davide Pasquali (5) & Nico Valentini (4) & Giuseppe Tripepi (6) & Daniele Celli (6) & Marcello Di Risio (5) & Francesco Aristodemo (6) & Leonardo Damiani (4) & Lorenzo Cappietti (7) & Mark Klein Breteler (8) & Dorothea Kaste (8)

(1) Ghent University, Belgium, E-mail: Maximilian.Streicher@UGent.be
(2) Flanders Hydraulics Research, Belgium, E-mail: tomohiro.suzuki@mow.vlaanderen.be
(3) Universitat Politecnica de Catalunya, Spain, E-mail: corrado.altomare@upc.edu
(4) Politecnico di Bari, Italy, E-mail: alessandra.saponieri@poliba.it
(5) Università degli Studi dell'Aquila, Italy, E-mail: da-vide.pasquali@univaq.it
(6) Università della Calabria, Italy, E-mail: giuseppe.tripepi@unical.it
(7) Università degli Studi di Firenze, Italy, E-mail: lorenzo.cappietti@unifi.it
(8) Deltares, The Netherlands, E-mail: Mark.KleinBreteler@deltares.nl

Large-scale experiments on overtopping wave impact loads on dike mounted walls were conducted in the Deltares Delta Flume for mildly sloping foreshore and shallow water conditions. The experiments were accompanied by a set of numerical model tools in order to help design the experimental set-up, extend the measured data by the high resolution output of the numerical models and to numerically remodel a change in geometry. The methods used for the hybrid modelling approach and first results are herein discussed.

1.   INTRODUCTION AND OBJECTIVES

For the research project WALOWA (WAve LOads on WAlls), carried out within the EU program HYDRALAB+, model tests in the Deltares Delta Flume in Delft (The Netherlands) were conducted in March 2017. The project was a cooperation of Ghent University (Belgium), TU Delft (The Netherlands), RWTH Aachen (Germany), Polytechnic University of Bari, University of L'Aquila, University of Calabria, University of Florence (Italy) and Flanders Hydraulics Research (Belgium). It was the aim to study overtopping wave impacts on storm walls and buildings situated on top of a dike and for mild foreshore conditions. A major second objective was to use the measured data and validate numerical models in terms of water surface elevation over the mild foreshore (SWASH), morphological foreshore evolution (XBeach) and wave impact forces and pressures on the wall (SWASH, DualSPHysics and OpenFOAM). Furthermore a detailed simulation of the overtopped flow field formation, in terms of flow layer thickness and velocity, on the promenade and the complex interaction between incoming and reflected flow, should be enabled with the numerical model results from SWASH, DualSPHysics and OpenFOAM. The detailed objectives regarding the hybrid modelling approach involved:

1. To study the morphology bed evolution of the sandy foreshore before the experiment with the numerical model XBeach in order to estimate the expected profile changes and erosion depth at the dike toe. To measure the profile change during the experiment and validate the XBeach model with the measured data.
2. To calibrate the numerical model SWASH based on the surface elevation measurements from the wave gauges and perform numerical simulations for a situation without the dike present in order to obtain the incident wave conditions (without reflections from the dike or wall).
3. To re-model the water surface elevation at the dike toe and the flow field formation on the promenade in high-resolution with the numerical models SWASH, DualSPHysics and OpenFOAM. To validate the results with the measurements from the physical model and enable an inter-comparison between the models.

2.   EXPERIMENTAL SET-UP

The model geometry was divided into four parts (see Figure 1): (1) A sandy foreshore with a combined slope $\cot(n) = 10$ at the beginning and $\cot(\theta) = 35$ seaward of the toe of the dike, along
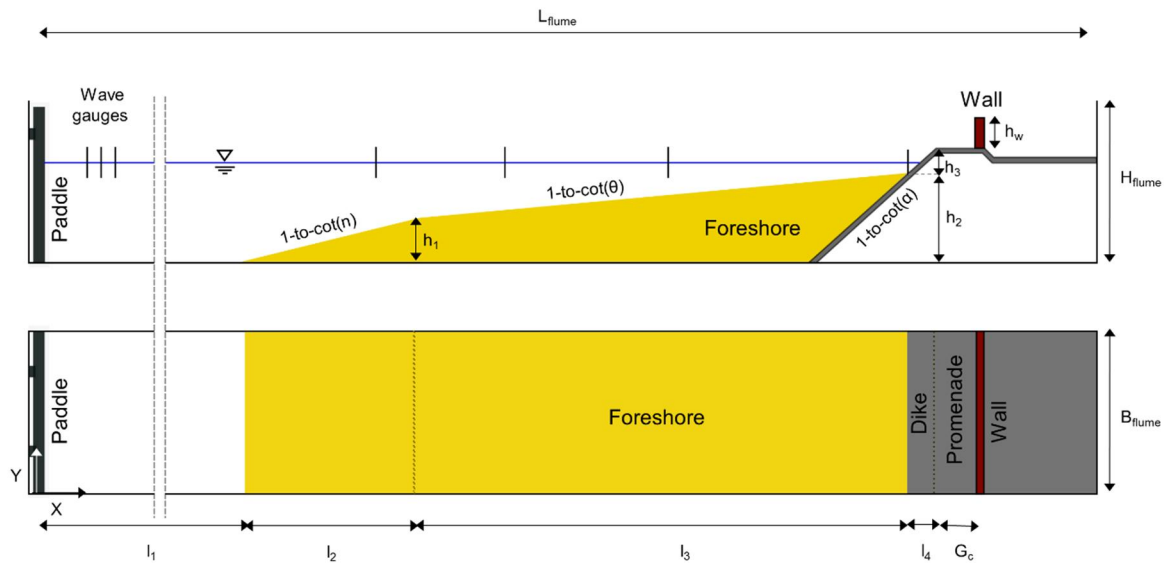
Figure 1: WALOWA model geometry as a side-view (upper figure) and a top-view (lower figure) drawing.

reaches of 19.5 m and 61.6 m, respectively. The total foreshore volume was comprised of ~1000 m³ of sand spread over the 5 m flume width. (2) Attached to the foreshore a concrete dike with a cot(α) = 2 slope and (3) a 2.35 m-wide promenade with an offshore slope of 1-to-100 to drain the water. (4) At the end of the promenade a vertical 1.6 m-high steel wall was built to measure the impact loads with pressure sensors and load cells. The model dimensions were given in model scale using Froude similarity and length scale factor 1-to-4.3 (see Table 1). A more detailed description of the model and measurement set-up was given by Streicher et al. (2017).

Table 1: Geometrical parameters for WALOWA model set-up

Model scale	L; H; B	cot(n); cot(θ); cot(α)	l_1; l_2; l_3; l_4	h_1, h_2; h_3; h_w	G_c
-	m	°	m	m	m
1-to-4.3	275.5; 9.5; 5	10; 35; 2	93.98; 19.5; 61.6; 1.07	1.95; 3.73; 0.53; 1.6	2.35

The test program in chronological order is given in Table 2. The asterix behind the testID indicates after which test a profile measurement was carried out. The profile measurements are numbered accordingly from 0-16, with 0 as the initial conditions before the test.

3.   STUDY OF MORPHOLOGICAL SAND BED EVOLUTION

The numerical model XBeach was used to design the physical experiment and to estimate the scour depth at the dike toe and the profile evolution of the sandy foreshore in front of the dike in a first step. Profile measurements were taken during the physical experiments and the morphological evolution in front of the storm seawall was discussed in terms of bed scour at the dike toe and its temporal evolution. In order to analyze the performance of the XBeach model in simulating bed evolution in front of the dike in such particular foreshore conditions, the measured data were used and compared to the numerical results in a second step. A more detailed description of the procedure can be found in Saponieri et al. 2018.

3.1 Measurement of sand bed profile evolution
Cross-shore bed profiles were measured by means of a mechanical profiler after 16 tests (see superscript number for the testID in Table 2). Five sections were considered, along the centerline and at 0.2 m and 0.4 m to both sides of the centerline. The mechanical profiler (see Figure 2, left),

developed by Deltares, consisted of a wheel which was attached to a measurement hinge/arm fixed to the measurement carriage, moving in both long-shore and cross-shore directions. The wheel, with a diameter equal to 10 cm, was able to measure the bed profile by moving with a low and constant velocity along the selected section. Both cross-shore distances and relative bed elevations were acquired.

Table 2: Test program for WALOWA experiments with measured parameters (model scale) in chronological order. Superscripts for the testID indicate that after this test a profile measurement of the foreshore was carried out.

testID	Waves	h_{paddle}	h_{toe}	A_c	$H_{m0,off}$	$H_{m0,toe}$	$T_{m-1,0,off}$	$T_{m-1,0,toe}$	$h_{toe}/H_{m0,off}$
-	-	m	m	m	m	m	s	s	-
Bi_1_4	~18	3.99	0.28	0.25	1.11	0.36	6.76	19.89	0.25
Bi_1_5*[2]	~18	4.00	0.29	0.24	1.29	0.42	6.99	21.55	0.22
Bi_1_6	~18	4.01	0.30	0.23	1.23	0.40	7.40	21.44	0.24
Bi_2_4*[3]	~18	4.13	0.42	0.11	1.17	0.44	6.10	19.36	0.36
Irr_1_F*[4]	~1000	3.99	0.28	0.25	1.05	0.30	5.80	12.30	0.27
Irr_2_F*[5]	~3000	4.00	0.29	0.24	0.92	0.29	5.36	10.39	0.32
Irr_2_S*[6]	~3000	3.99	0.28	0.25	0.92	0.29	5.38	9.35	0.30
Irr_3_F*[7]	~3000	4.12	0.41	0.12	0.92	0.36	5.36	7.98	0.45
Bi_2_5	~18	4.14	0.43	0.10	1.27	0.49	6.16	17.31	0.34
Bi_2_6	~18	4.14	0.43	0.10	1.30	0.51	6.24	17.14	0.33
Bi_2_6_R*[8]	~18	4.14	0.43	0.10	1.31	0.50	6.19	17.26	0.33
Irr_8_F*[9]	~1000	4.13	0.42	0.11	0.49	0.35	3.83	4.85	0.86
Irr_4_F*[10]	~1000	3.79	0.08	0.45	0.87	0.22	5.41	12.05	0.09
Irr_5_F*[11]	~1000	3.78	0.07	0.46	1.05	0.26	5.82	13.55	0.07
Irr_1_F_R*[12]	~1000	4.01	0.30	0.23	1.06	0.35	5.80	10.43	0.28
Irr_7_F*[13]	~1000	4.00	0.29	0.24	0.65	0.29	4.65	7.00	0.45
Irr_2_F_R*[14]	~3000	4.01	0.30	0.23	0.92	0.32	5.36	8.55	0.33
Bi_1_6_R	~18	4.01	0.30	0.23	1.34	0.48	6.07	17.50	0.22
Bi_3_6	~18	3.77	0.06	0.47	1.05	0.31	6.52	22.79	0.05
Bi_3_6_1	~18	3.77	0.06	0.47	1.16	0.34	6.64	21.71	0.05
Bi_3_6_2*[15]	~18	3.76	0.05	0.48	1.28	0.35	6.36	19.59	0.04
Irr_6_F*[16]	~1000	3.77	0.06	0.47	0.65	0.19	4.68	10.05	0.09

The location in x-direction (flume main axis direction) was determined by using a laser distance meter targeting to a fixed point at the end of the flume. After each test, the foreshore was not restored to its initial configuration. For the purpose of clarity, the sketch of the scour and the main geometrical parameters used for the analyses were shown in Figure 2 (right). In the following, S (m) and L_s (m) refer to the maximum scour depth from the initial profile (scour trough) and its horizontal extension, respectively. The parameter Δz_{mean} [m] was used to describe the mean scour depth. A_e (m^2) is the scour area, D_d (m) is the distance of the scour trough from the dike toe, β indicates the bed slope, d (cm) is the initial offshore water depth. Analyses was carried out by comparing the measured initial and final profiles before and after the test. Morphodynamic evolution of the beach profiles was investigated by observing scour formation at the dike toe induced by the different wave conditions tested during the campaign. With reference to WALOWA tests program (see Table 2), there was a temporal mixing between monochromatic and irregular waves, not suitable for studying long-term morphodynamics. The analysis of bed profiles was therefore carried out for transient conditions.
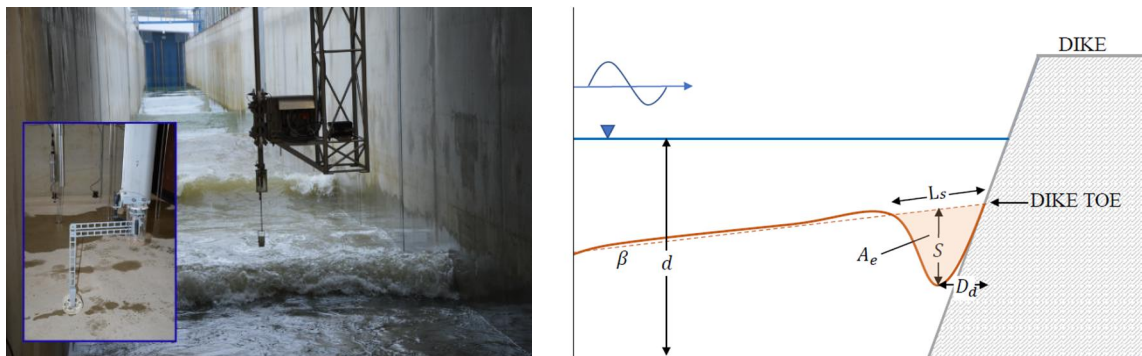
Figure 2: *Mechanical profiler deployed in the Delta Flume (left figure). Sketch of parameter definitions for scour evolution at the dike toe (right figure).*
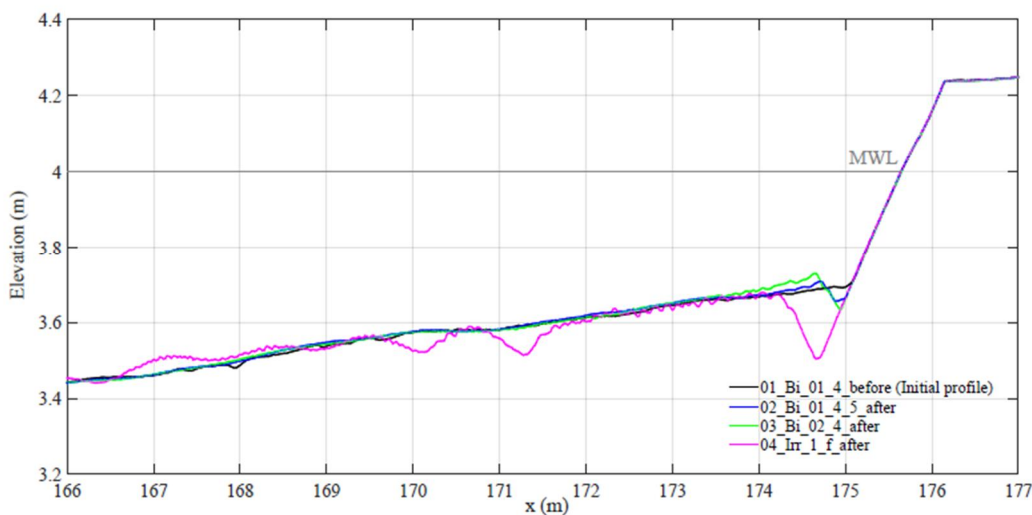

Figure 3: *Example of bottom foreshore evolution for the first 4 tests from the test program (see Table 2).*

Figure 3 shows an example of bed profile evolution evaluated for the central flume section, after the first 4 tests of the test program (3 bi-chromatic and 1 irregular wave test). A rough estimate of the maximum scour depth was 0.3 m for the WALOWA laboratory scale, corresponding to a prototype depth of about 1.3 m. The scour velocity of the erosion process at the dike toe was higher at the beginning of the experiments, mainly during irregular wave attacks. Then, the buildup of the scour hole decelerated. Despite the transient wave conditions, the scour geometry reached a quasi-equilibrium state, after 11 h of wave forcing. The final area affected by scour has a cross-shore length of $L_s = 9$ m, a relative mean scour depth of $\Delta z_{mean} = 0.2$ m and the eroded volume is about 8 m^3.

3.2 Numerical modelling of sand bed profile evolution with XBeach

Numerical modeling was employed in two steps. In the first step, the XBeach model was used to support the design of the experiments and estimate the expected amount and location of erosion/ accretion (Step-1). Then, the same XBeach model set-up was used with the boundary conditions from the physical experiment and the results compared to the measurements (Step-2). In Step-1 a sensitivity analysis of the model morphodynamics predictive skills was performed by varying both grid spatial discretization and boundary conditions. The simulations were carried out by imposing stationary wave boundary conditions (STAT) and wave groups based on JONSWAP spectra (VAR). The offshore and inshore boundary conditions were set absorbing and impermeable. The

duration of each simulation was selected to be equal to the foreseen experimental one. Only for wave group simulations (VAR) a 15 minutes warm-up interval was used during which the whole domain was considered as a fixed bottom. During the large-scale physical experiments it was expected that the bed profile could not be re-profiled after each test. Hence, an extended series of simulations were performed with XBeach, to estimate the cumulative erosion/accretion pattern and scour depth at the dike toe without (numerically) re-profiling at the end of each simulation in both stationary and wave group conditions. In Step-2 the numerical model XBeach was further validated with the obtained profile measurements from the physical experiments, by setting the model according to the outcomes derived from the sensitivity analysis. A 2D uniform computational grid was used with a spatial discretization equal to 0.20 m, forced with a non-stationary JONSWAP (or bi-chromatic) wave boundary condition with a warm-up time of 900 s, imposing as absorbing both offshore and inshore boundaries. A validation of the XBeach model for such particular conditions, characterized by frequent occurrence of breaking waves, suspension mode of sediment transport and presence of very shallow to extremely shallow foreshore, was achieved in two steps. First, the test program for the XBeach model was set equal with that detailed in Table 2. Secondly, the profile evolution between numerical model and measurement was studied and the maximum S and mean Δz_{mean} scour depth at the dike toe compared (see Figure 5). The x-label in the figure indicates the measured profile number (superscripts for testID in Table 2). It was observed that the XBeach model was able to catch the general trend of the scour evolution over time and was able to correctly reproduce the magnitude of long term scour evolution (more than 18000 waves).
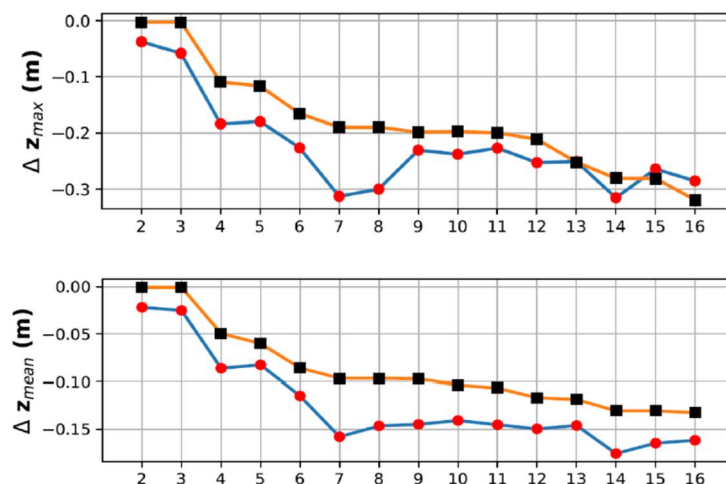

Figure 5: Scour evolution related to profile number in terms of maximum (S) and relative mean (Δz_{mean}) depth. The solid line with circles refers to experimental results and the orange line with squares to the numerical results.

4. STUDY OF WATER SURFACE ELEVATION AND WAVE PARAMETERS

For the purpose of design guidance the incident wave parameters at the dike toe are of key importance. To eliminate most of the reflection occurring from the dike and wall, often experiments featuring the same wave train were conducted but removing the dike, promenade and wall in the experimental set-up. Due to cost and construction constraints this was not feasible in the physical large-scale experiment in the Delta Flume. It was decided to use the numerical SWASH model to calculate the incident wave parameters, which was already successfully applied for the computation of spectral wave parameters in shallow water and mild foreshore conditions (Suzuki et al. 2014). The SWASH model was calibrated based on the wave measurements in test Bi_2_6 from the test program (see Table 2) in a first step. In a second step the calibrated SWASH model was used to artificially remove the dike, promenade and wall in the numerical simulation and derive the incident spectral wave parameters for the dike toe location (without reflections from the dike and wall).

4.1 Measurement of water surface elevation

The water surface elevation was measured with wave gauges WG1-WG7 at several locations along the flume (see Table 4). A first location was in the flat bottom part of the flume, close to the wave paddle, to measure the deep water surface elevation. This was done with 3 wave gauges (WG1-WG3), to allow for reflection analysis of the signal using the method of Mansard and Funke (1980). Along the foreshore 3 wave gauges (WG4-WG6) were deployed. They mainly served to monitor the change in wave parameters, wave breaking and shift in spectral wave energy towards lower frequency components (Hofland et al. 2017). Lastly, a wave gauge was deployed just 0.35m in front of the at the dike toe (WG7), to measure the incident water surface elevation at the dike toe.

Table 4: Location of wave gauges in flume length direction, with the origin (x=0) at the wave paddle

Paddle	WG1	WG2	WG3	WG4	WG5	WG6	WG7	Dike toe
m	m	m	m	m	m	m	m	m
0	43.5	49.5	61.5	107.89	126.42	155.66	174.73	175.08

In-house made resistive type wave gauges were installed at the right flume wall, when looking towards the paddle. A reference electrode was used to compensate for changes in the water conductivity due to salinity or temperature during the experiment. Wave analysis of the measured water surface elevation was carried out using Wavelab Version 3.7. The time-series of the incident water surface elevation and incident spectral wave parameters $H_{m0,o}$ [m] and $T_{m-1,0}$ [s] at the WG1-WG3 location were obtained using the method of Mansard and Funke (1980), to distinguish incident and reflected components. A spectra independent high-pass filter at 0.03Hz and a spectra dependent low-pass filter at $3/T_p$ Hz were used. Additionally, the fft block size was selected automatically and the taper width and overlap set to 20%. Furthermore a number of data points were skipped at the beginning and end of each time-series to focus the wave analysis on a fully developed wave field. Next, the measured time-series and spectral wave parameters for the other wave gauges were derived by simply analyzing the signal of each individual wave gauge (no separation of incident and reflected waves was possible). The calibrated numerical model SWASH was then used to calculate the incident water surface elevation and incident wave parameters at the dike toe, key for the design of coastal structures.

4.2 Numerical modelling of water surface elevation with SWASH

The input at the wave boundary of SWASH was the incident wave time-series obtained by the reflection analysis of Mansard and Funke (1980) method (see Section 4.1). Note, that the distance of the three wave gauges (WG1-WG3) was not optimized for the bichromaic wave Bi_2_6 test. Still, a reasonable time-series was achieved after reflection analysis. The SWASH domain was modelled from x=43.5 to 206.4 m flume length (see Figure 1). The grid size of dx=0.2 m was used. The vertical wall was modelled by activating BOTCel SHIFT mode in SWASH, so that the wall was expressed correctly (i.e. no interpolation). As stated above, the boundary input came from time-series of water surface elevation, and the type of the wave boundary in SWASH was the weakly reflective boundary condition which was functioning the same as an Active Wave Absorption Systems (AWAS). The Manning bottom friction parameter n=0.019 m$^{-1/3}$s was applied for the entire domain, for both sand bottom and dike. The used SWASH version was 4.01.
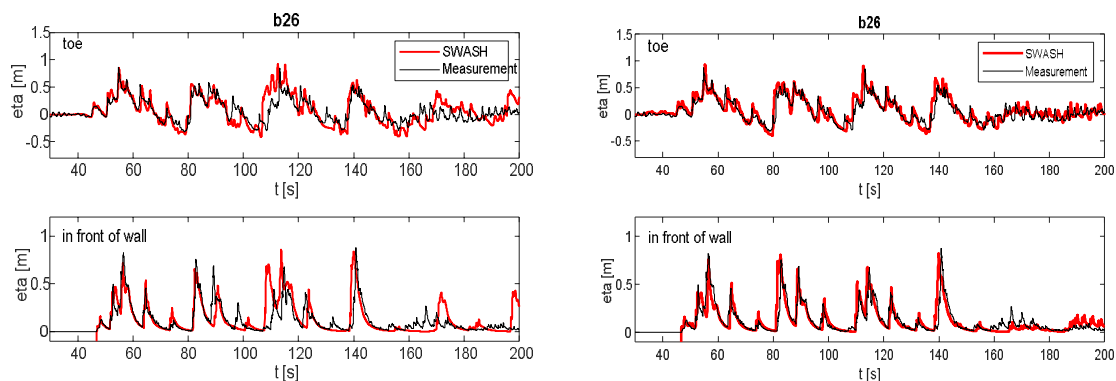
Figure 6: Sensitivity analysis on time-series input (left: time-series from the wave gauge at x=43.5 m, right: time-series of incident waves). One layer and dx=0.2 was applied to this analysis.

The number of layers in SWASH was selected by the kh value (where k is wavenumber and h is depth at the three wave gauge location). In this condition the kh value was below 1, and therefore one layer approach was used as a standard case. The setting described above was decided based on sensitivity analyses. Firstly, the sensitivity analysis was focused on the incident wave time-series: one time-series was taken as the measured time-series from wave gauge WG1 at x=43.5 m (Figure 6, left) and the other time-series was taken from the time-series obtained after reflection analysis (Figure 6, right). The former was less accurate compared to the measurements. A possible reason for this could be that the raw time-series at one wave gauge still contained the reflection from the foreshore. Even though the reflection coefficient was small, the influence of the reflected waves on the time-series was not negligible. Secondly, a sensitivity analysis for the grid size was conducted. Grid sizes in flume length direction of dx=0.1, 0.2, 0.4 and 0.8 m were tested. Grid size dx=0.2 m resulted in the best fit comparison between measured and computed water surface elevation and was selected for the simulation. Wave transformation wise, the dx=0.1 and 0.2 m cases gave similar results, so dx=0.2 m was used as it is computationally faster. Finally, a sensitivity analysis of the number of layers used for the computation was conducted. Both, one layer and two layer approach gave similar results. This was explained by the kh number as stated above; One layer calculation was considered accurate enough for the wave propagation and selected for the computation.

5.   STUDY OF OVERTOPPING FLOW THICKNESS AND VELOCITY

Overtopping flow thicknesses η [m] and velocities u [m/s] were measured on top of the promenade. The measurement of overtopping flow thickness and velocity is extremely difficult in alternating wet and dry conditions and for highly turbulent and aerated flows. None of the conventional devices to measure water surface elevations (wave gauges, ultra-sonic distance sensors) or velocities (paddle wheels, micro propellers, acoustic doppler velocimeter, electro-magnetic current meter) was designed to measure in this conditions. Hence, a redundant measurement set-up was aimed for. Furthermore, it was the objective to use calibrated numerical models to compute the high-resolution flow parameters along the promenade until the wall. In this way a study of the flow field and transformation of the flow field along the promenade was enabled. Numerical modelling of the overtopping flow parameters for the same bichromatic wave test investigated in Section 4 (Bi_2_6) was done using SWASH, DualSPHysics and OpenFOAM. The SWASH numerical model and model setup was described in Section 4.2. The remaining models and model setups were discussed in Section 5.2 together with the first results.

5.1 Measurement of flow thickness and velocity

The overtopping flow parameters thickness η [m] and velocity u [m/s] were measured by instruments attached to a wooden frame installed 1m above of the promenade on the right flume side when looking towards the paddle (see Figure 8, left). The flow thickness was obtained by 4 resistance-type wave gauges (WLDM1-WLDM4). The measurement principle was similar to the water surface elevation measurement along the foreshore (see Section 4.1), measuring the change in conductivity between two metal electrodes according to the water level. The wave gauge foot with the reference electrode was submerged 5cm below the elevation of the promenade, in a 12cm deep bucket of water. The flow velocity was obtained by 4 Airmar S300 ow meter paddle wheels (PW1-PW4), measuring only the incoming flow velocity. Two paddles attached to a
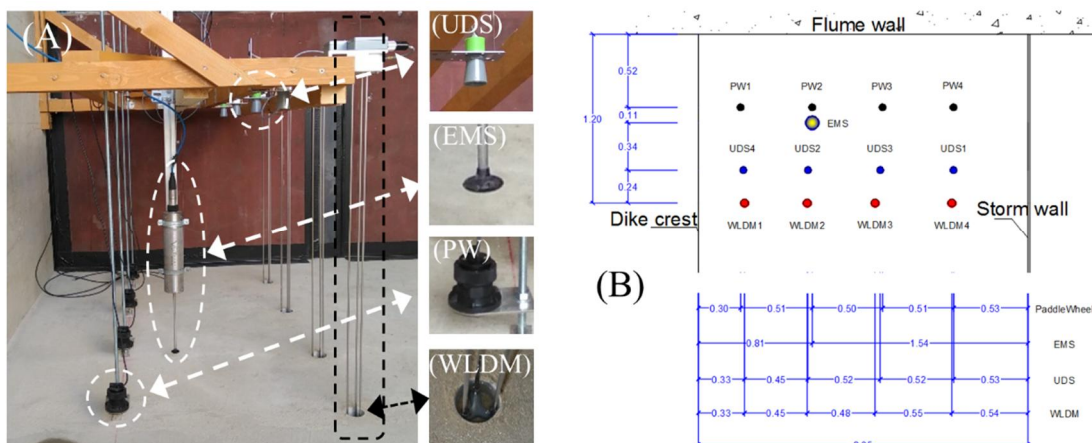

Figure 8: The measurement of flow thickness and velocity on the promenade in the Deltares Delta Flume. Ultrasonic distance sensors (UDS) and resistive type wave gauges (WLDM) were used to measure the flow thickness and electro-magnetic current meter (EMS) and paddle wheel (PW) to measure the flow velocities.

rotational axis and mounted in a half open housing were rotated by the incoming overtopping flow. Depending on the rotation speed the flow velocity was derived. The paddle wheels were measuring at 0.03m above the promenade. Both types of instruments (WLDM and PW) were installed in two lines parallel to the flume wall 0.24m apart from each other. Detailed locations of the measurement devices measuring the flow parameters on the promenade can be found in Cappietti et al. (2018). Additionally, an electromagnetic current meter (Valeport 802) was installed to measure the flow velocity and 4 ultra-sonic distance sensor (3 MaxSonar HRXL, 1 Honeywell 943 M18), to obtain a non-intrusive measurement of the flow thickness. The ultra-sonic distance sensors often lost the signal, due to spray which would touch the sensor surface. The time-series of the wave gauges installed on the promenade was used to determine the flow layer thicknesses on the promenade. It was further noted that the overtopping flow at location 1 was often affected by the overtopping splash. Hence, it was decided to use the measurements from WLDM2 (see Figure 8, right), to compare to the numerical model simulations.

5.2 Numerical modelling of layer thickness with OpenFOAM, DualSPHysics and SWASH

OpenFOAM® (Weller *et al.*, 1998) is a library of applications and solvers including interFoam, a Navier-Stokes equations solver following an Eulerian mesh-based method for two incompressible, isothermal immiscible fluids using a Volume-of-Fluid (VOF) phase-fraction based interface capturing approach. In this work OpenFOAM v6 was applied, using the solver interFoam (for a detailed description it is referred to Larsen et al. 2018) with the boundary conditions for wave generation and absorption provided by olaFlow (Higuera, 2017), hereafter simply referred to as OpenFOAM. Turbulence was modelled by the Reynolds-Averaged Navier-Stokes equations (RANS) coupled with the turbulence closure model k-ω SST (k is the turbulent kinetic energy density, ω is the specific dissipation rate). The k-ω SST model that was stabilized in nearly potential flow regions by Larsen and Fuhrman (2018) was used. The OpenFOAM model domain started at the wave paddle zero position, and included the foreshore and dike geometry as

measured in the experiment up to the vertical wall. The model was run in a vertical two-dimensional (2DV) configuration (cross-shore section of the wave flume). To optimise the computational time, a variable grid resolution was applied. The structured mesh had a grid resolution of 0.18 m in the air phase and 0.09 m in the water phase. The mesh was further refined in the zone of the surface elevation up to the dike toe (dx = dz = 0.045 m) and on the dike up to the wall (dx = dz = 0.0225 m), which led to a grid with 314,482 cells. Waves were generated by applying a Dirichlet-type boundary condition: the experimental wave paddle displacement was first converted to a wave paddle velocity, which was then applied to the water phase at the stationary boundary (x = 0 m). Active wave absorption (as implemented in olaFlow) was activated to prevent re-reflection of reflected waves.

DualSPHysics is a numerical model based on the Smoothed Particle Hydrodynamics (SPH) method (for a detailed description it is referred to Crespo *et al.*, 2015). SPH is a Lagrangian and mesh-less method where the fluid is discretised into a set of particles that are nodal points where physical quantities (such as position, velocity, density, pressure) are computed as an interpolation of the values of the neighbouring particles. The contribution of these neighbours is weighted using a kernel function (*W*) that measures that contribution starting from the initial particle spacing. This distance between particles is normalized using the smoothing length (h_{SPH}), which is the characteristic length that defines the area of influence of the kernel. The kernel presents compact support, so that the contribution of particles beyond a cut-off distance (here $2h_{SPH}$) is not considered. The DualSPHysics 2DV model domain also extended from the wave paddle, over the foreshore up to the vertical wall on top of the dike and promenade. However, only the water phase was modelled, with an initial particle spacing of $d_p = 0.01$ m, leading to a total of 5,245,337 particles in the model domain. Waves were generated by a moving boundary, which exactly reproduced the recorded experimental wave paddle displacement, including active wave absorption.

A comparison of model performance for the modelling of the surface elevation at the dike toe and on the promenade (i.e. flow layer thickness) is shown in Figure 8.
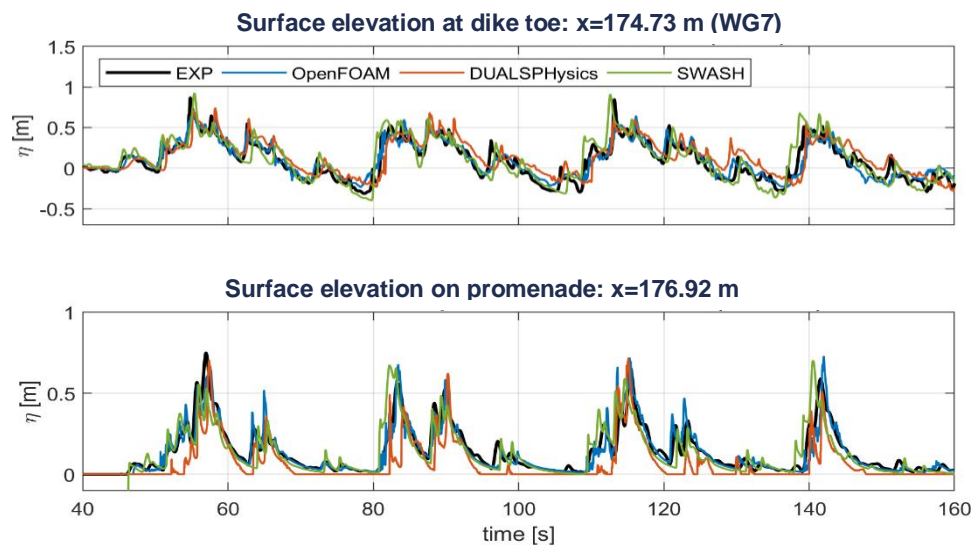

Figure 8: Comparison between the numerical model results (SWASH: green line, DualSPHysics: red line, OpenFOAM: blue line) and the experiment (black line) of the surface elevation at the dike toe wave gauge location (WG7) in the upper figure and for the second gauge (WLDM2) on the promenade in the lower figure.

A quantitative comparison was done as well (see Table 5) by means of the normalized bias $B^* = \frac{\bar{m}-\bar{r}}{\sigma_r}$. Where the asterisk indicates normalization by σ_r, the overbars indicate the mean, *m* and *r* are the surface elevation time-series of the numerical model and experiment respectively, and σ is the standard deviation. Furthermore, the normalised centered Root-Mean-Square Deviation was

investigated with $RMSD_c^* = \frac{\sqrt{\frac{1}{N}\sum_{n=1}^{N}[(m_n-\bar{m})-(r_n-\bar{r})]^2}}{\sigma_r}$. Finally, the linear correlation coefficient $R = \frac{\frac{1}{N}\sum_{n=1}^{N}(m_n-\bar{m})(r_n-\bar{r})}{\sigma_m\sigma_r}$ was calculated, where N is the number of samples in the surface elevation time-series. The mean surface elevation at the dike toe (i.e. wave setup), indicated by *B**, was slightly overestimated by all numerical models and the mean layer thickness was underestimated on the promenade. The *RMSD* was comparable between SWASH and DualSPHysics, while OpenFOAM showed lower values both at the dike toe and on top of the promenade.

Table 5: Comparison between the numerical model results and experiment: the normalised bias, B*, the normalised centered Root-Mean-Square Difference, RMSD*c, and the linear correlation coefficient, R.

Model	B* [%]		RMSD$_c$* [%]		R [%]	
	WG7	WLDM2	WG7	WLDM2	WG7	WLDM2
SWASH	7.4	-10.9	57.3	61.8	86.4	81.3
DualSPHysics	19.5	-53.9	57.4	62.7	82.5	78.5
OpenFOAM	4.2	-5.1	40.7	39.7	91.3	92.3

The correlation coefficient was lowest for DualSPHysics and highest for OpenFOAM. Although all considered numerical models showed a very good correspondence to the experiment, DualSPHysics seemed to perform the least of the three. This was mostly attributed to the fact that DualSPHysics suffered most from a phase lag with the experiments, most likely a result from the weakly compressible nature of DualSPHysics, which affected the wave breaking and consequently the broken wave propagation and interaction with the dike. Further investigation will be performed to analyse the influence of the fluid compressibility on wave breaking, propagation of broken waves and wave-structure interaction. Overall, OpenFOAM achieved the best correspondence with the experiment of the surface elevations at the dike. However, this came at the cost of the highest computational and model setup time required of all three models. Finally, the remarkable performance of SWASH has to be noted. This depth-averaged model managed to obtain an accuracy that was comparable to fully 2DV flow models, even for the complex flows of broken and overtopped waves on the promenade, while having a significantly lower computational cost.

6. CONCLUSIONS AND OUTLOOK

In this study a hybrid modelling approach was carried out to complement the measured data from laboratory large-scale experiments in the Deltares Delta Flume by a chain of numerical modelling tools. The numerical tools were used (1) to help design the experiment in terms of the sandy morphological foreshore evolution with XBeach; (2) to study the wave parameters along the foreshore in high-resolution and obtain the incident wave parameters at the dike toe location with SWASH and (3) to model the high resolution flow field on top of the promenade with SWASH, DualSPHysics and OpenFOAM for a detailed study of the flow transformation along the promenade. As a next step, the numerical models SWASH, DualSPHysics and OpenFOAM will be used to derive the flow field at the moment of impact at the wall and finally to model the total impact force and pressure distribution over the wall height. It is the purpose to further use the model results to obtain parameters such as the vertical and horizontal velocities of the flow at the moment of impact, which could not be measured during the experiment, to validate theoretical impact load prediction approaches. Furthermore, the numerical model XBeach will be further validated using the measured bed profile evolution.

REFERENCES

Cappietti, L., Simonetti, I., Esposito, A., Streicher, M., Kortenhaus, A., Scheres, B., Schuettrumpf, H., Hirt, M., Hofland, B., Chen, X. (2018). Large-scale experiments of wave-overtopping loads on walls: Layer thicknesses and velocities, *Proceedings of the 37th International conference on ocean, offshore and arctic engineering*, Madrid, Spain, 6 pp.

Crespo, A.J.C., Domínguez, J.M., Rogers, B.D., Gómez-Gesteira, M., Longshaw, S., Canelas, R., Vacondio, R., Barreiro, A., García-Feal, O. (2015). DualSPHysics: open-source parallel CFD solver on Smoothed Particle Hydrodynamics (SPH), *Computer Physics Communications*, 187: 204-216, 13pp.

Higuera, P. (2017). olaFlow: CFD for waves, https://doi.org/10.5281/zenodo.1297013.

Hofland, B., Chen, X., Altomare, C., Oosterlo, P. (2017). Prediction formula for the spectral period Tm-1,0 on mildly sloping shallow foreshores, *Coastal Engineering* 123, 21-28.

Larsen, B.E., Fuhrman, D.R., Roenby, J. (2018). Performance of interFoam on the simulation of progressive waves, *arXiv:1804.01158v1 [physics.flu-dyn],* 03 April 2018, 18pp.

Larsen, B.E. and Fuhrman, D.R. (2018). On the over-production of turbulence beneath surface waves in Reynolds-averaged Navier–Stokes models, *Journal of Fluid Mechanics*, 853:419-460, 42pp.

Mansard, E.P.D. and Funke, E.R. (1980). The measurement of incident and reflected spectra using a least squares method, *Proceedings of 17th International conference on coastal engineering*, Hamburg, Germany, 154-169, 16pp.

Saponieri, A., Di Risio, M., Pasquali, D., Valentini, N., Aristodemo, F., Tripepi, G., Celli, D., Streicher, M., Damiani, L. (2018). Beach profile evolution in front of storm seawalls: A physical and numerical study, *Proceedings of 36th International conference on coastal engineering*, Baltimore, US, 13pp.

Streicher, M., A. Kortenhaus, C. Altomare, V. Gruwez, B. Hofland, X. Chen, K. Marinov, B. Scheres, H. Schüttrumpf, M. Hirt, L. Cappietti, A. Esposito, A. Saponieri, N. Valentini, G. Tripepi, D. Pasquali, M. D. Risio, F. Aristodemo, L. Damiani, M. Willems., D. Vanneste, T.Suzuki, M. Klein Breteler, D. Kaste. (2017). WALOWA (Wave Loads on Walls) – Large-scale experiments in the Delta Flume, *Proceedings of the 8th SCACR conference*, Santander, Spain, 2017, 11pp, doi: 10.5281/zenodo.834874.

Suzuki, T. Altomare, C., Verwaest, T., Trouw, K., Zijlema, M. (2015). Two-dimensional wave overtopping calculation over a dike in shallow foreshore by SWASH, *Proceedings of the 34th International Conference on Coastal Engineering*, Seoul, South-Korea, 12pp, doi=10.9753/icce.v34.forward.1

Weller, H.G., Tabor, G., Jasak, H., Fureby, C. (1998). A tensorial approach to computational continuum mechanics using object-oriented techniques, *Computers in Physics*, 12:620-631, 12pp.

LARGE-SCALE ICEBERG-TSUNAMI EXPERIMENTS

Valentin Heller (1), Tommaso Attili (2), Fan Chen (3), Markus Brühl (4), Roman Gabl (5), Xuexue Chen (6), Guido Wolters (7) & Helge Fuchs (8)

(1) University of Nottingham, UK, Email: valentin.heller@nottingham.ac.uk
(2) University of Nottingham, UK & University of Pisa, Italy, Email: t.attili@studenti.unipi.it
(3) University of Nottingham, UK, Email: fan.chen@nottingham.ac.uk
(4) Technische Universität Braunschweig, Germany, Email: m.bruehl@tu-braunschweig.de
(5) University of Edinburgh, UK & University of Innsbruck, Austria, Email: roman.gabl@ed.ac.uk
(6) Royal HaskoningDHV, The Netherlands, Email: xuexue.cheung@gmail.com
(7) Deltares, The Netherlands, Email: guido.wolters@deltares.nl
(8) ETH Zurich, Switzerland, Email: fuchs@vaw.baug.ethz.ch

Iceberg calving at outlet glaciers contributes to global sea-level rise in the context of climate change. This study investigates tsunamis generated by iceberg calving, so-called *iceberg-tsunamis*. Such tsunamis reached amplitudes of 50 m in the recent past and endanger human beings and coastal infrastructure. 73 unique large-scale experiments have been conducted in the 50 m ✕ 50 m Delta Basin at Deltares. These experiments involved the five iceberg calving mechanisms: A: capsizing, B: gravity-dominated fall, C: buoyancy-dominated fall, D: gravity-dominated overturning and E: buoyancy-dominated overturning. Gravity-dominated icebergs essentially fall into the water body whereas buoyancy-dominated icebergs essentially rise to the water surface. The iceberg-tsunamis from gravity-dominated mechanisms (B and D) are roughly an order of magnitude larger than from mechanisms A, C and E. The maximum wave heights and amplitudes and their decay with distance from the calving locations are correlated with six dimensionless parameters, with the Froude number, the relative iceberg width and the relative released energy identified as the most important ones. Empirical equations for initial iceberg-tsunami hazard assessment were derived predicting the wave features reasonably well, considering the variety of the underlying physics involved in the iceberg calving mechanisms. Ongoing and future work aims to analyse the wave parameters in more detail, investigate the wave features with a novel wave component decomposition method, compare iceberg- with landslide-tsunamis and investigate iceberg-tsunamis numerically.

1.   INTRODUCTION

Iceberg calving accounts for a significant part of the mass losses of the Antarctic and Greenland Ice Sheets and contributes to global sea-level rise in the context of climate change (Hanna et al., 2013; Enderlin et al., 2014). Iceberg calving generates so-called *iceberg-tsunamis* (Heller et al., 2019). Significant iceberg-tsunamis have been observed in Greenland at the Eqip Sermia glacier where a wave amplitude of 50 m destroyed some infrastructure in 2014 (Lüthi & Vieli, 2016) and at the Helheim outlet glacier where approximately 25 km from the glacier front the measured wave was still 24 cm large (Vaňková & Holland, 2016). An iceberg-tsunami was also observed at the mountain glacier Tasman Glacier in New Zealand in 2011 (Dykes et al., 2016) and iceberg-tsunamis generated by capsizing icebergs destroyed a Greenlandic harbour in 1995 (N24, 2009).

   Figure 1(a,b) shows iceberg calving events in nature. The icebergs interact with the surrounding water via different iceberg calving mechanisms (Benn et al., 2007; Heller et al., 2019; Massel & Przyborska, 2013; Minowa et al., 2018). Five idealised mechanisms have been investigated in this work as illustrated in Fig. 1(c): A: capsizing, B: gravity-dominated fall, C: buoyancy-dominated fall, D: gravity-dominated overturning and E: buoyancy-dominated overturning. Gravity-dominated icebergs essentially fall into the water body whereas buoyancy-dominated icebergs essentially rise to the water surface. The current understanding of iceberg-tsunamis is limited and only small-scale flume experiments (Burton et al., 2012) have been conducted thus far.

The tsunamigenic potentials of mechanisms A to E have been investigated within a HYDRALAB+ funded test campaign at Deltares in Delft. The five main objectives of the test campaign were (Heller, 2019):

I. Conduct large-scale iceberg-tsunami experiments in the 50 m × 50 m large Delta Basin under variation of the iceberg calving mechanisms (capsizing, fall, overturning) as well as the iceberg volume and kinematics

II. Quantify the tsunami features (height, length, velocity) and cross-compare the tsunamigenic potentials from the five different iceberg calving mechanisms

III. Relate the new findings to an established landslide-tsunami hazard assessment method to potentially transfer knowledge

IV. Analyse the new data using the highly promising new wave component decomposition method Korteweg-de Vries equations in combination with the nonlinear Fourier transform

V. Provide benchmark test cases to the numerical modelling community and apply the test cases to calibrate and validate numerical simulations of members of the project team to investigate additional iceberg-tsunami scenarios

This article provides a general overview about the experiments and presents some key results and empirical equations to predict the most relevant iceberg-tsunami parameters.
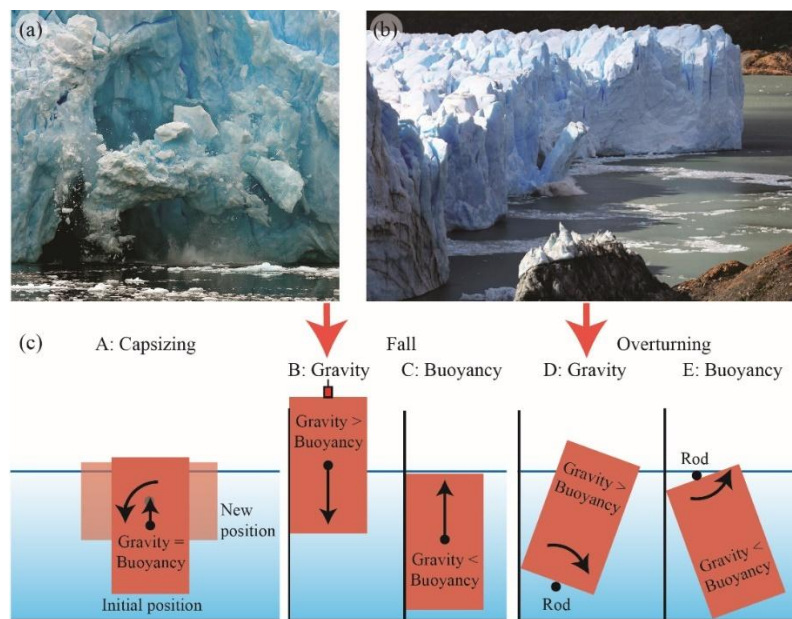

Figure 1: Real and idealised iceberg calving and iceberg-tsunami generation: (a) falling iceberg at Neko Harbour, Antarctica (courtesy of Alek Komarnitsky - www.komar.org), (b) overturning iceberg at Perito Moreno Glacier, Argentina (courtesy of Victor Qixiang Chen - http://photo.qyer.com/7259134/allphoto), (c) sketches of investigated idealised iceberg calving mechanisms from left to right: A: capsizing, B: gravity-dominated fall, C: buoyancy-dominated fall, D: gravity-dominated overturning and E: buoyancy-dominated overturning (Heller et al., 2019).

2. EXPERIMENTAL METHOD

2.1 Experimental Procedure

The experiments have been conducted under Froude similarity in the 50 m × 50 m basin shown in Fig. 2. Two blocks consisting of polypropylene homopolymer with a density similar to ice (≈920 kg/m^3) were released offshore (capsizing, Fig. 1c) and at the vertical boundary of the basin (fall, overturning, Figs. 1c and 2). The sizes of the two blocks were 0.800 m × 0.500 m × 0.500 m (block type 1) and 0.800 m × 0.500 m × 0.250 m (block type 2, Fig. 2) and they weighted up to 187 kg.

The experimental programme is shown in Table 1 and included 73 experiments (62 individual tests plus 11 repetitions) and two water depths h = 1.000 and 0.750 m. The capsizing mechanism

involved 16 experiments, the fall mechanism 30 (21 gravity- and 9 buoyancy-dominated), the overturning mechanism 20 (14 gravity- and 6 buoyancy-dominated) experiments and 7 fall experiments were conducted with a sphere, which will not be further addressed herein and are also excluded from the data analysis and specified parameter ranges. Videos of the experiments are included in Heller et al. (2019).
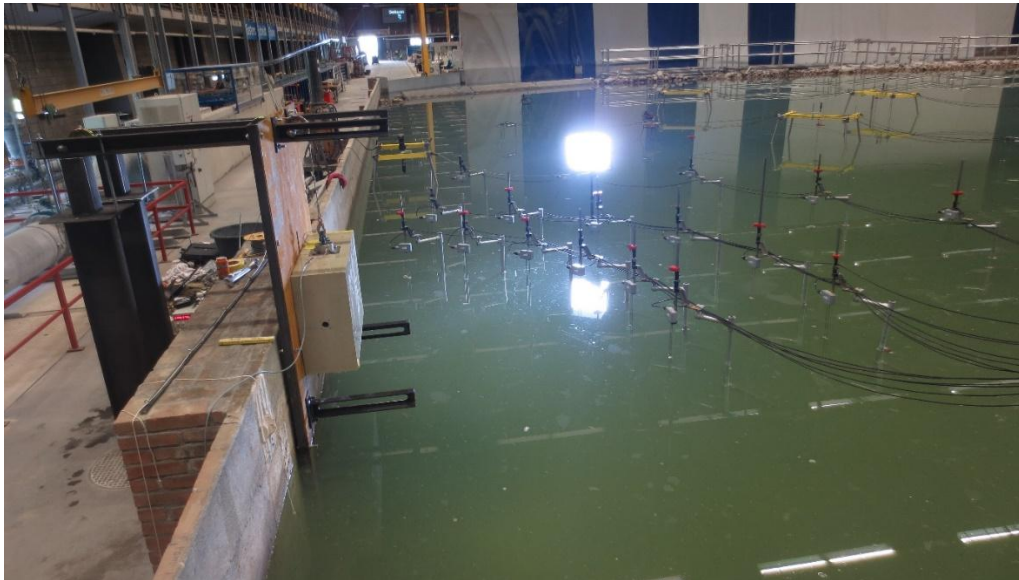

Figure 2: Picture of a gravity-dominated fall experiment (mechanism B) at the wall of the basin with block type 2 in the initial position and some of the 35 wave probes on the right-hand side.

Table 1: Experimental parameters of all 73 conducted experiments involving the five iceberg calving mechanisms A to E; the number of tests marked with [+] included repetitions. SWL = still water level and Neut. = Neutrally.

Block parameters	(i) Capsizing (mechanism A)			(iii) Overturning (mechanism D and E)			
Block release location	Offshore	Offshore	Offshore	At shore	At shore	At shore	At shore
Block type	1	2	2	1	2	2	2
Block length l (m)	0.800	0.800	0.500	0.800	0.800	0.500	0.500
Block width b (m)	0.500	0.500	0.800	0.500	0.500	0.800	0.800
Block thickness s (m)	0.500	0.250	0.250	0.500	0.250	0.250	0.250
Block volume $\forall_s$ (m^3)	0.200	0.100	0.100	0.200	0.100	0.100	0.100
Block density ρ_s (kg/m^3)	929	924	924	936/923	912	912	936/912
Block mass m_s (kg)	185.8	92.4	92.3	187.1/184.6	91.2	91.2	93.6/91.2
Water depth h (m)	1.000	1.000	1.000	1.000	1.000	1.000	0.750
Release position above SWL (cm)	Neut. buoyant	Neut. buoyant	Neut. buoyant	15, 0, −30, −60, −90	15, 0, −30, −60, −90	15, 0, −30, −60	15, 0, −30, −60
(0 cm corresponds to the SWL)							
Number of runs (73 in total)	5[+]	6[+]	5[+]	5	5	4	6[+]

Block parameters	(ii) Fall (mechanism B and C)						
Block release location	At shore	At shore	At shore	At shore	At shore	At shore	At shore
Block type	1	2	1	1	2	2	sphere
Block length l (m)	0.800	0.800	0.500	0.500	0.500	0.500	0.215
Block width b (m)	0.500	0.500	0.800	0.800	0.800	0.800	0.215
Block thickness s (m)	0.500	0.250	0.500	0.500	0.250	0.250	0.215
Block volume $\forall_s$ (m^3)	0.200	0.100	0.200	0.200	0.100	0.100	0.005
Block density ρ_s (kg/m^3)	936/923	936/912	936/923	936/923	936/912	936/912	922
Block mass m_s (kg)	187.1/184.6	93.6/91.2	187.1/184.6	187.1/184.6	93.6/91.2	93.6/91.2	4.8
Water depth h (m)	1.000	1.000	1.000	0.750	1.000	0.750	0.750
Release position above SWL (cm)	0, −30, −60, −84	0, −30, −60, −83	30, 0, −30, −60, −70, −83	30, 0, −30, −60	30, 0, −30, −60, −83	30, 0, −30, −60	54, 32, 11, 0, −11, −32, −43
(0 cm corresponds to the SWL)							
Number of runs (73 in total)	6[+]	4	7[+]	4	5	4	7

The experimental procedures for the five calving mechanisms (Fig. 1c) were as follows: Capsizing (mechanism A in Fig. 1c): The blocks in the capsizing case were hold in position with a wooden rod guided through the centre of the blocks. This rod was hold in position on both sides with steel profiles and was able to move in the vertical direction (but not sideward or forward) and

rotate. The rotation of the block was initiated in most cases by removing a fitting which stabilised the block. Block type 1 had to be slightly pushed by hand, with a force in the order of 1 N, to capsize. In some tests the blocks were pushed harder to investigate the effect of an increased rotation speed on the wave features.

Fall (mechanisms B and C in Fig. 1c): The blocks were hold in position with an electromagnet prior to release, which was connected to a rope as shown in Fig. 2. The supporting frame for this electromagnet and the blocks was fixed to a steel plate at the basin wall. The blocks were moved in vertical direction with a winch system which was fixed to a support structure outside the wave basin (Fig. 2). For the fall buoyancy case, the block was pulled under water with a rope attached to the centre of the block bottom to oppose the buoyancy force of up to 150 N. For some buoyancy-dominated tests the block had to be stabilised in addition with a steel beam from above and both the steel beam and the rope were then released simultaneously.

Overturning (mechanisms D and E in Fig. 1c): The blocks rotated around a fixed steel rod of 30 mm diameter. This rod was fed through two ball bearings fixed to the block surface. This ensured that the blocks underwent a pure rotation and no translation. The rod was hold in position on the sides with steel profiles (Fig. 2). The rod was located either below (gravity-dominated) or above (buoyancy-dominated) the block. For some buoyancy dominated tests the block had to be stabilised in addition with a steel beam from above and the blocks started to move once the steel beam was removed.

2.2 Measurement System

The block kinematics was recorded with a sampling rate of ≈74 Hz with a 9 Degree of Freedom motion sensor (Adafruit BNO055). The sensor was located in a black enclosure and attached to the block surface. Two cameras (5 MP PointGrey ZBR2-PGEHD-50S5C-CS (which recorded at 15 Hz) and 2 MP IOIndustries Flare 2M280-CXP (at 100 Hz)) were used for general observations. The wave features were recorded at 100 Hz in different directions on one side of the block axis, given that the wave field is symmetric, with up to 35 resistance type wave probes.

Table 2: Name and locations of wave probes and cameras.

Iceberg calving mechanism	Device	Water depth h (m)	Locations in function of the radial distance r (m) and the wave propagation angle γ (°) (Fig. 3a,c)
Capsizing	Wave probes	1.000	A1 (2, 0); A10 (3, 0); A19 (5, 0); A28 (10, 0); A32 (15, 0); A2 (2, −15); A11 (3, −15); A20 (5, −15); A29 (10, −15); A3 (2, −30); A12 (3, −30); A21 (5, −30); A4 (2, −60); A13 (3, −60); A22 (5, −60); A5 (2, −90); A14 (3, −90); A23 (5, −90); A6 (2, −120); A15 (3, −120); A24 (5, −120); A7 (2, −150); A16 (3, −150); A25 (5, −150); A8 (2, −165); A17 (3, −165); A26 (5, −165); A30 (10, −165); A9 (2, −180); A18 (3, −180); A27 (5, −180); A31 (10, −180); A33 (15, −180)
Capsizing	Cameras	1.000	5 MP at 15 Hz: (6, −45); 2 MP at 100 Hz: (6, −95)
Fall/ overturning	Wave probes	1.000	B1 (2, 0); B7 (3, 0); B13 (5, 0); B19 (10, 0); B25 (15, 0); B31 (22.5, 0); B34 (35, 0); B2 (2, −15); B8 (3, −15); B14 (5, −15); B20 (10, −15); B26 (15, −15); B32 (22.5, −15); B35 (35, −15); B3 (2, −30); B9 (3, −30); B15 (5, −30); B21 (10, −30); B27 (15, −30); B33 (22.5, −30); B4 (2, −45); B10 (3, −45); B16 (5, −45); B22 (10, −45); B28 (15, −45); B5 (2, −60); B11 (3, −60); B17 (5, −60); B23 (10, −60); B29 (15, −60); B6 (2, −75); B12 (3, −75); B18 (5, −75); B24 (10, −75); B30 (15, −75)
Fall/ overturning	Wave probes	0.750	C1 (1.5, 0); C7 (2.25, 0); C13 (3.75, 0); C19 (7.5, 0); C25 (11.25, 0); C31 (16.875, 0); C34 (26.25, 0); C2 (1.5, −15); C8 (2.25, −15); C14 (3.75, −15); C20 (7.5, −15); C26 (11.25, −15); C32 (16.875, −15); C35 (26.25, −15); C3 (1.5, −30); C9 (2.25, −30); C15 (3.75, −30); C21 (7.5, −30); C27 (11.25, −30); C33 (16.875, −30); C4 (1.5, −45); C10 (2.25, −45); C16 (3.75, −45); C22 (7.5, −45); C28 (11.25, −45); C5 (1.5, −60); C11 (2.25, −60); C17 (3.75, −60); C23 (7.5, −60); C29 (11.25, −60); C6 (1.5, −75); C12 (2.25, −75); C18 (3.75, −75); C24 (7.5, −75); C30 (11.25, −75)
Fall/ overturning	Cameras	1.000 and 0.750	2 MP at 100 Hz: (6, −85); 5 MP at 15 Hz: (6, 45)

The coordinate origins of the cylindrical coordinate systems (r, z, γ) are shown in Fig. 3. The origins are located for all calving mechanisms in vertical direction z on the water surface. In the horizontal plan the origin is located at the block centre for the capsizing case (Fig. 3a) and at the front of the steel plate in the centre of the block in cross-shore direction for all other calving mechanisms (Fig. 3c). The wave propagation angle γ (angular angle) is defined positive in clockwise direction. The wave probes are numbered anti-clockwise starting at $\gamma = 0°$ and from smaller to higher radial distance r (Fig. 3a,c). Table 2 shows the locations of all wave probes.

The time in all experiments was adjusted such that $t = 0$ s corresponds to when the blocks started to move for experiments where they were initially in contact with the surrounding water, or when the blocks reached the water surface when they were initially located above the water body. The raw data of the motion sensor were further analysed in Matlab to transform the accelerations in global coordinates and to derive the block velocities and positions. The wave probe time series were individually shortened to remove data affected by reflection from the basin boundaries. The wave probe data were then filtered with a low-pass filter with a cut off frequency at 9 to 11 Hz. For wave probes A9, A17 and A25 in the capsizing experiments and B21/C21, B24/C24 and B32/C32 for all fall and overturning experiments a low-pass filter with a cut off frequency at 3.0 or 3.5 Hz was applied to remove large high-frequency noise. For 3 locations out of all 2278 wave probe locations the wave probe signals remained noisy after filtering given that the waves were extremely small. These 3 data series were excluded from further analysis.
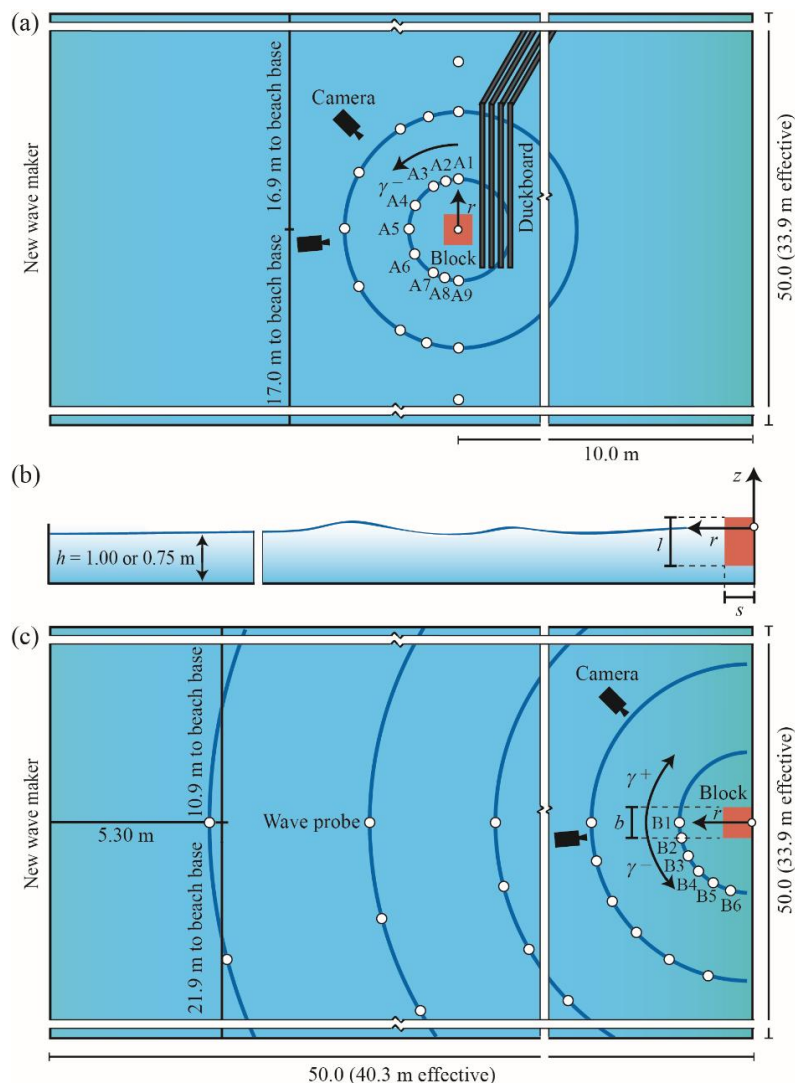

Figure 3: Sketches of experimental set-ups with some wave probes: (a) plan view of capsizing case, (b) side view of a gravity-dominated fall experiment and (c) plan view of a gravity-dominated fall experiment (Heller, 2019).

2.3 Governing Parameters

The following nine governing parameters were considered in the correlations of the iceberg-tsunami features such as the maximum wave heights and amplitudes and their decay with r and γ:

- Released energy E
- Water depth h
- Iceberg velocity V_s
- Iceberg thickness s
- Iceberg width b
- Iceberg volume V_s
- Iceberg density ρ_s
- Water density ρ_w
- Gravitational acceleration g

A wider variation of s and b was achieved by changing the orientation of the two block types 1 and 2 in the initial position (Table 1). The velocity V_s corresponds to the fastest moving section of the block and was derived based on the motion sensor data as 0.27 to 4.17 m/s over all block experiments. The density ρ_s changed slightly with the attachments to the block (Table 1). The additional parameter E was introduced after the test campaign varying between 6 and 980 J over all block experiments making this parameter instrumental to correlate very large and very small waves. This energy corresponds to the energy difference of the iceberg between the initial and final positions and is thus the maximum available energy to be transferred into tsunami energy. The theoretical expressions and values for E were derived by Heller et al. (2019) in function of the iceberg calving mechanism, iceberg geometry and initial position relative to the water surface.

The nine governing parameters can be expressed in dimensionless form based on the reference quantities g, h and ρ_w. This results in the following six dimensionless parameters and ranges covered by the block experiments (Attili, 2019):

- Relative released energy: $0.0006 \le E_r = E/(\rho_w gh^4) \le 0.3157$
- Froude number: $0.09 \le F = V_s/(gh)^{1/2} \le 1.33$
- Relative iceberg thickness: $0.25 \le S = s/h \le 0.67$
- Relative iceberg width: $0.50 \le B = b/h \le 1.07$
- Relative iceberg volume: $0.10 \le V = V_s/h^3 \le 0.47$
- Relative density: $0.91 \le D = \rho_s/\rho_w \le 0.94$

Scale effects due to the kinematic viscosity ν_w and surface tension σ_w were neglected in this Froude scaling experiments given that the Weber number $W = \rho_w gh^2/\sigma_w \ge 75{,}552$ and Reynolds number $R = g^{1/2}h^{3/2}/\nu_w \ge 2{,}033{,}835$ in the experiments were large and satisfied the limitations $W \ge 5{,}000$ and $R \ge 300{,}000$ applicable for the physically closely related subaerial landslide-tsunamis (Heller et al., 2008). The absolute and relative measurement errors of most dimensional and dimensionless parameters are given in Heller et al. (2019). The six dimensionless parameters are used in the *Results and Discussion* section to correlate the maximum wave heights and amplitudes.

3. RESULTS AND DISCUSSION

Figure 4 shows the free water surface η versus time t of five selected experiments involving all five iceberg calving mechanisms. These wave profiles were all measured at relative radial distance r/h = 2 (Fig. 3 and Table 2). The scales on the y-axes in Fig. 4 vary by up to a factor of 20. The wave magnitudes significantly differ for the mechanisms A to E; the gravity-dominated overturning mechanism D results in the largest tsunamis followed by the gravity-dominated fall mechanism B. The three remaining mechanisms resulted in up to a factor of 27 smaller waves (Heller et al., 2019). Further, the wave trains consist of several nonlinear waves for all mechanisms, similar as for subaerial landslide-tsunamis (Heller & Spinneken, 2015). The largest wave amplitude is observed in the middle of the wave train for the slower moving mechanisms A, C and E. For the gravity-dominated mechanisms B and D the largest wave is observed earlier in the wave train.

Figure 5 shows the relative maximum wave heights (Fig. 5a) and the relative maximum wave amplitudes (Fig. 5b) for all 66 block experiments and iceberg calving mechanisms combined in function of the six dimensionless parameters. The best correlations were found with a regression analysis based on the least-square approach with the Matlab function *lsqcurvefit*. Some restrictions were imposed on the exponents (e.g. > 0) to obtain physical meaningful results. The corresponding empirical equations and coefficients of determination R^2 are

$$\frac{H_M}{h} = \mathbf{0.26}\big(E_r^{0.20}\mathbf{F}^{1.72}S^{0.53}B^{1.10}V^{0.20}D^{0.10}\big)^{\mathbf{0.50}} \qquad (R^2 = 0.92) \qquad (1)$$

$$\frac{a_M}{h} = \mathbf{0.14}\big(E_r^{0.20}\mathbf{F}^{2.07}S^{0.10}B^{1.20}V^{0.20}D^{0.40}\big)^{\mathbf{0.50}} \qquad (R^2 = 0.91) \qquad (2)$$

The most important parameter in Eqn. (1) and (2) is F with an exponent of approximately 2. Further important are the relative slide width B, with an exponent slightly larger than 1, as well as E_r. E_r is influential due to the combination of the exponent 0.20 with the large range of E_r over nearly three orders of magnitude. The influences of S, V and D on the maximum wave parameters are significantly smaller. Figure 5 confirms that the tsunami heights generated by mechanisms B and D (gravity-dominated) were roughly an order of magnitude larger than for mechanisms A, C and E over all conducted experiments. Most data lie within the ±40% bounds, however, the inserts in Fig. 5 reveal that Eqn. (1) and (2) tend to overpredict the buoyancy-dominated and capsizing mechanisms and therefore operate on the save side.
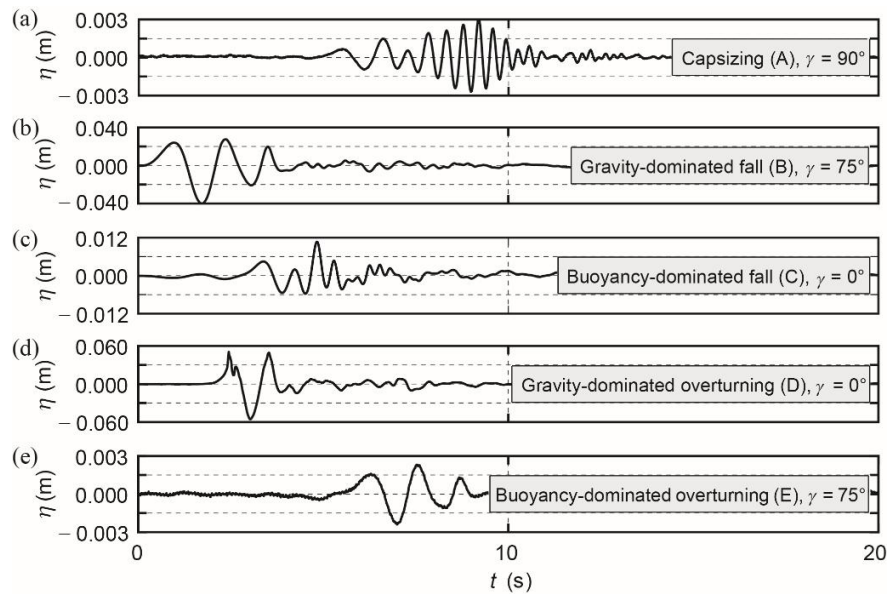
Figure 4: One selected iceberg-tsunami profile for each calving mechanism A to E. These tsunami profiles were recorded at ($r/h = 2$, γ) where the maximum wave height H_M was measured. (a) Capsizing, (b) gravity-dominated fall, (c) buoyancy-dominated fall, (d) gravity-dominated overturning and (e) buoyancy-dominated overturning mechanism. The scales on the *y*-axes change by up to a factor of 20 (Heller et al., 2019).
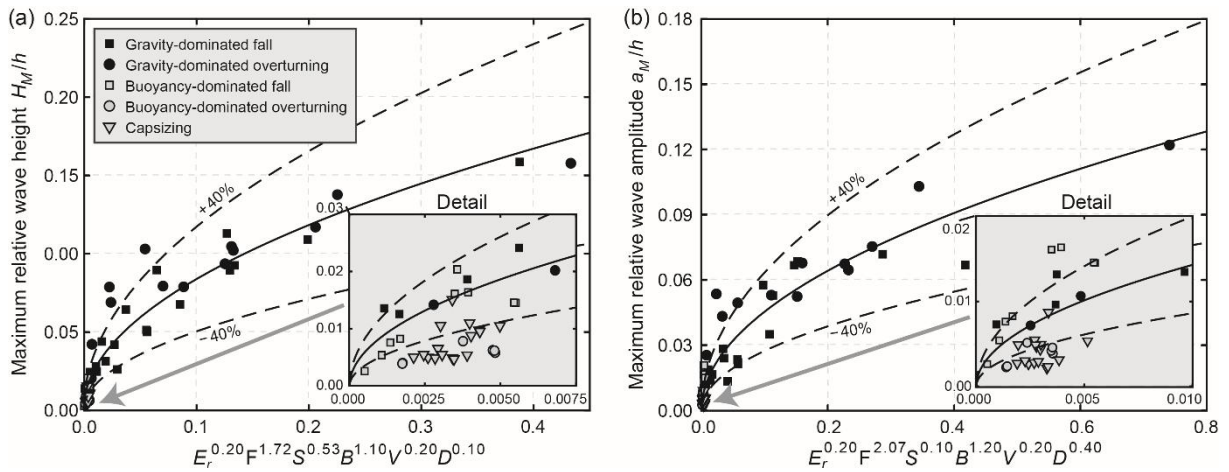
Figure 5: Maximum wave parameters for all calving mechanisms: (a) maximum relative wave height H_M/h versus a combination of the dimensionless parameters and Eq. (1) plotted as (—) with ±40% deviation as (- -) ($R^2 = 0.92$) and (b) maximum relative wave amplitude a_M/h versus a combination of the dimensionless parameters and Eq. (2) plotted as (—) with ±40% deviation as (- -) ($R^2 = 0.91$). The inserts show the smallest waves in more detail.
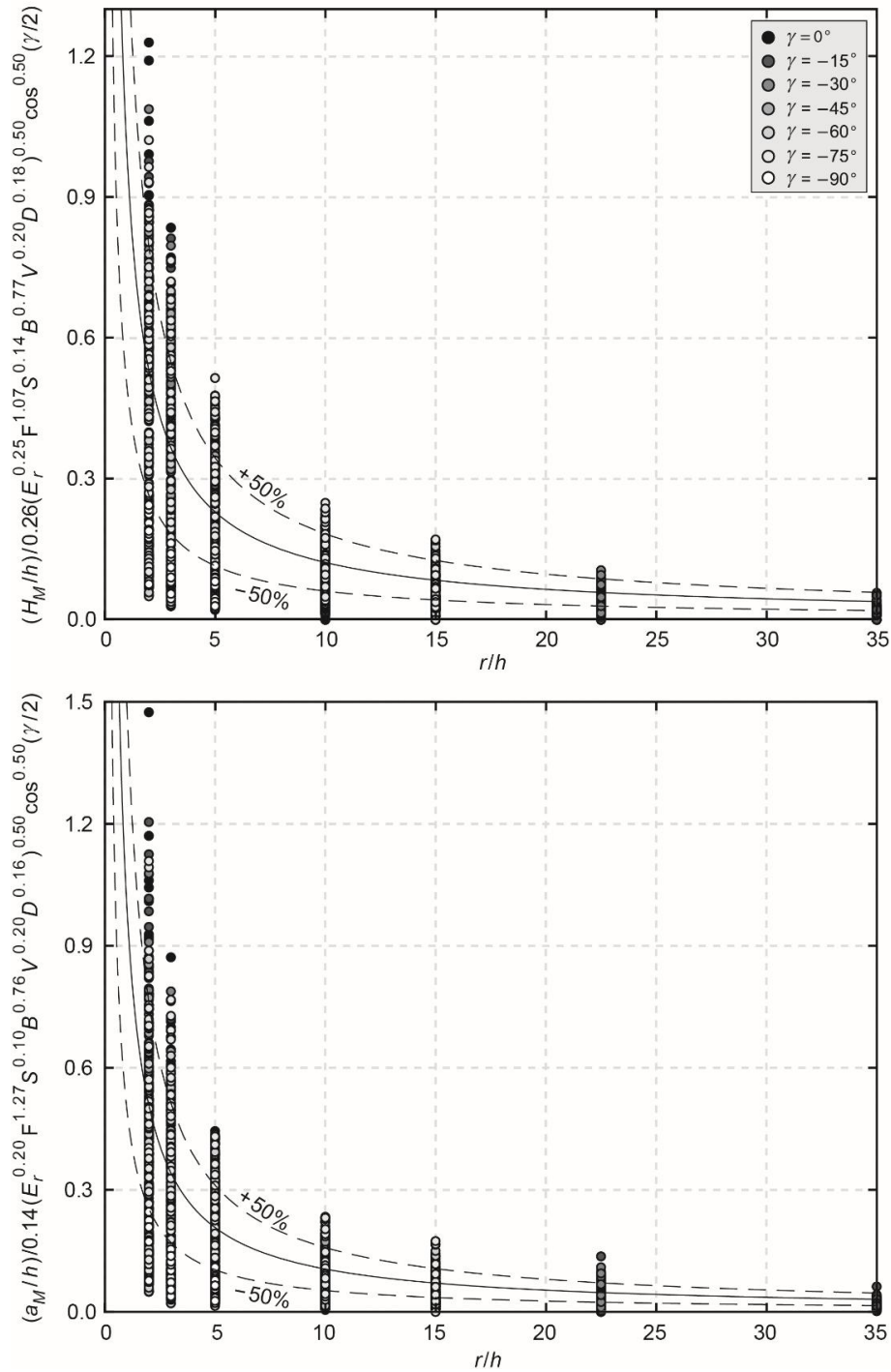
Figure 6: Maximum wave parameter decays for all calving mechanisms: (a) normalised wave heights versus the relative distance r/h and Eq. (3) plotted as (—) with ±50% deviation as (--) ($R^2 = 0.80$) and (b) normalised wave amplitude versus the relative distance r/h and Eq. (4) plotted as (—) with ±50% deviation as (--) ($R^2 = 0.78$).

The decays of the relative maximum wave heights and amplitudes for all 66 block experiments and iceberg calving mechanisms combined are represented by

$$\frac{H_M}{h}\left(\frac{r}{h}, \gamma\right) = \mathbf{0.26}\big(E_r^{0.25}\mathbf{F}^{1.07}S^{0.14}B^{0.77}V^{0.20}D^{0.18}\big)^{0.50}\left(\frac{r}{h}\right)^{-0.91}\mathbf{cos}^{0.5}\left(\frac{\gamma}{2}\right) \qquad (R^2 = 0.80) \qquad (3)$$

$$\frac{a_M}{h}\left(\frac{r}{h}, \gamma\right) = \mathbf{0.14}\big(E_r^{0.20}\mathbf{F}^{1.27}S^{0.10}B^{0.76}V^{0.20}D^{0.16}\big)^{0.50}\left(\frac{r}{h}\right)^{-0.98}\mathbf{cos}^{0.5}\left(\frac{\gamma}{2}\right) \qquad (R^2 = 0.78) \qquad (4)$$

The parameters F, *B* and E_r are also dominant in Eqn. (3) and (4) and *S*, *V* and *D* play a less significant roll. The wave decay is close to $(r/h)^{-1.0}$, corresponding both to the theoretically expected decay for a wave created by a point source propagating on a spatial water surface (Kranzer & Keller, 1959) and the decay previously found for landslide-tsunami experiments conducted in a wave basin (Heller & Spinneken, 2015). Figure 6 represents these empirical correlations. It shows the relative wave heights H_M/h and amplitudes a_M/h divided by the dimensionless parameter combinations of Eqn. (3) and (4) on the *y*-axes versus the relative distance r/h on the *x*-axes. The data follow the predictions based on Eqn. (3) and (4) reasonably well, considering the variety of underlying physics involved in the five iceberg calving mechanisms. However, the data scatter is particularly large in proximity of the iceberg calving location where water splashes reached the wave probes at $r/h = 2$ in some of the experiments.

4. CONCLUSIONS AND OUTLOOK

Unique large-scale experiments have been conducted in the 50 m × 50 m Delta Basin at Deltares within a HYDRALAB+ test campaign. 73 iceberg-tsunami experiments with up to 187 kg heavy blocks under variation of the iceberg volume, geometry, kinematics and initial position relative to the water surface have been conducted. The blocks interacted with the surrounding water through five iceberg calving mechanisms namely: A: capsizing, B: gravity-dominated fall, C: buoyancy-dominated fall, D: gravity-dominated overturning and E: buoyancy-dominated overturning. The main conclusions of this study are summarised as follows:

- The tsunami magnitudes generated by mechanisms B and D (gravity-dominated) are roughly an order of magnitude larger than from mechanisms A, C and E. Icebergs of a given volume and geometry released above the water surface are therefore significantly more hazardous in terms of tsunami generation than neutrally buoyant icebergs or icebergs released underwater.

- The tsunami features were expressed in function of six dimensionless parameters where the slide Froude number F, the relative iceberg width *B* and the relative released energy E_r are the most dominant ones.

- Empirical equations for the maximum wave heights and amplitudes and their decay with propagation distance *r* and wave propagation angle γ are presented which are useful for initial iceberg-tsunami hazard assessment.

Ongoing and future work aims to resolve all objectives (I) to (V) mentioned in the *Introduction* by correlating the wave parameters for each iceberg calving mechanism individually (Attili, 2019) and by applying the highly promising new wave component decomposition method Korteweg-de Vries equations in combination with the nonlinear Fourier transform to iceberg-tsunamis (Brühl & Becker, 2018). The iceberg-tsunamis will also be compared in more detail with landslide-tsunamis (Heller & Spinneken, 2015) and a numerical model is under development which, in principle, is capable of simulating all five iceberg calving mechanisms and iceberg-tsunamis (Chen et al., 2019).

ACKNOWLEDGEMENT

REFERENCES

Attili, T. (2019). Analysis of iceberg-tsunamis from large-scale experiments. *MSc thesis*. University of Pisa, Italy.

Benn, D.I., Warren, C.R. and Mottram, R.H. (2007). Calving processes and the dynamics of calving glaciers. *Earth-Science Reviews* 82, 143-179.

Burton, J.C., Amundson, J.M., Abbot, D.S., Boghosian, A., Cathles, L.M., Correa-Legisos, S., Darnell, K.N., Guttenberg, N., Holland, D.M. and MacAyeal, D.R. (2012). Laboratory investigations of iceberg capsize dynamics, energy dissipation and tsunamigenesis. *Journal of Geophysical Research* 117(F01007).

Brühl, M. and Becker, M. (2018). Analysis of subaerial landslide data using nonlinear Fourier transform based on Korteweg-deVries equations (KdV-NLFT). *Journal of Earthquake and Tsunami* 12(2), 1-21.

Chen, F., Heller, V. and Briganti, R. (2019). Numerical modelling of tsunamis generated by iceberg calving validated with large-scale laboratory experiments (in preparation).

Dykes, R.C., Brook, M.S. and Lube, G. (2016). A major ice-calving event at Tasman Glacier terminus, Southern Alps, 22 February 2011. *Journal of the Royal Society of New Zealand* 47(4), 336-343.

Enderlin, E.M., Howat, I.M., Jeong, S., Noh, M.-J., van Angelen, J.H. and van den Broeke, M.R. (2014). An improved mass budget for the Greenland ice sheet. *Geophysical Research Letters* 41, 866-872.

Hanna, E., Navarro, F.J., Pattyn, F., Domingues, C.M., Fettweis, X., Ivins, E.R., Nicholls, R.J., Ritz, C., Smith, B., Tulaczyk, S., Whitehouse, P.L. and Zwally, H.J. (2013). Ice-sheet mass balance and climate change. *Nature* 498, 51-59.

Heller, V. (2019). Tsunamis due to ice masses - Different calving mechanisms and linkage to landslide-tsunamis – Data storage report. *Data storage report of HYDRALAB+ test campaign* (online http://hydralab.eu/research--results/ta-projects/project/hydralab-plus/11/, 10.5281/zenodo.2556614).

Heller, V., Chen, F., Brühl, M., Gabl, R., Chen, X., Wolters, G. and Fuchs, H. (2019). Large-scale experiments into the tsunamigenic potential of different iceberg calving mechanisms. *Scientific Reports* 9:861.

Heller, V., Hager, W.H. and Minor, H.-E. (2008). Scale effects in subaerial landslide generated impulse waves. *Experiments in Fluids* 44(5), 691-703.

Heller, V. and Spinneken, J. (2015). On the effect of the water body geometry on landslide-tsunamis: physical insight from laboratory tests and 2D to 3D wave parameter transformation. *Coastal Engineering* 104(10), 113-134.

Kranzer, H.C. and Keller, J.B. (1959). Water waves produced by explosions. *Journal of Applied Physics* 30(3), 398-407.

Lüthi, M.P. and Vieli, A. (2016). Multi-method observation and analysis of a tsunami caused by glacier calving. *The Cryosphere* 10, 995-1002.

Massel, S.R. and Przyborska, A. (2013). Surface wave generation due to glacier calving. *Oceanologia* 55(1), 101-127.

Minowa, M., Podolskiy, E.A., Sugiyama, S., Sakakibara, D. and Skvarca, P. (2018). Glacier calving observed with time-lapse imagery and tsunami waves at Glaciar Perito Moreno, Patagonia. *Journal of Glaciology* 64(245), 362-376.

N24 (2009). Tsunami Greenland - Tsunami Groelândia 1995. Online under https://www.youtube.com/watch?v=z8LWSOPwkn8 (in German).

Vaňková, I. and Holland, D.M. (2016). Calving signature in ocean waves at Helheim Glacier and Sermilik Fjord, East Greenland. *Journal of Physical Oceanography* 46(10), 2925-2941.

THE "CROSSOVER" PROJECT:
WAVE OVERTOPPING UNDER DIRECTIONALLY BIMODAL WAVE ATTACK

Tom Bruce (1), Leopoldo Franco (2), Alessandro Romano (2), Melisa Menendez (3),
Liliana Pinheiro (4), Maria Teresa Reis (4), Jentsje van der Meer (5)

(1) University of Edinburgh, UK, E-mail: Tom.Bruce@ed.ac.uk
(2) University of Rome TRE, Italy, E-mail: Leopoldo.franco@uniroma3.it
(3) Cantabria University, Spain, E-mail: melisa.menendez@unican.es
(4) National Laboratory for Civil Engineering (LNEC), Portugal,
E-mails: treis@lnec.pt, lpinheiro@lnec.pt
(5) Van der Meer Consulting bv & UNESCO IHE Delft, The Netherlands,
E-mail: jm@vandermeerconsulting.nl

It is common for the local sea state in coastal waters to be a complex combination of waves due to local and recent wind (the "sea") and long period waves from earlier weather systems, which have travelled many 100s of km with little attenuation (the "swell"). Sea and swell may have very different directions and periods. The *CrossOver* project was born out of the recognition that there is an absence of guidance on the influence of directionally-bimodal (or bidirectional, or 'crossing') seas upon wave overtopping at a coastal defence. The basis of the project was a physical model study in the Delta Basin at Deltares, utilising its two banks of wave generators set at 90 degrees to each other. The structure was a simple 1:3 smooth dike. 170 tests were carried out over a four-week period. Tests included "sea-only" and "swell-only" calibration tests, and tests with sea and swell crossing, with sea obliquities ranging from -85° to +60°, and swells from -75° to +60°. Analysis of the wave (sea and swell) conditions using the directional wave gauge data acquired and processed at the time has presented anomalous results. The raw data from the directional wave gauges and from an 'Edinburgh array' of wave gauges has been reanalysed at LNEC, offering some improved confidence in many cases. With 24 of the calibration tests remaining in the 'low confidence' class, further exploration of this problem including new analysis using the Edinburgh SPAIR method is in progress. Until the incident conditions are established with good confidence, there is no value in exploring the overtopping data. Once the overtopping data is analysed, it is anticipated that the findings will contribute to "EurOtop Live" first round update in 2019.

1. INTRODUCTION

It is common for the local sea state in coastal waters to be a complex combination of waves due to local and recent wind – the "sea" – and long period waves resulting from earlier weather systems, which have travelled many 100s of km with little attenuation of these very long waves – the "swell" (shown schematically in Figure 1). Sea and swell may have very different directions and periods.
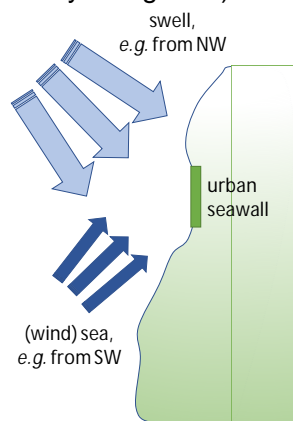
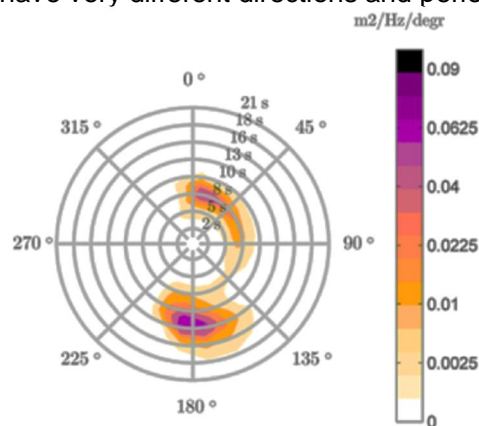Figure 1: Schematic representation of a seawall exposed to crossing sea and swell.

Figure 2: Bidirectional spectrum simulated from weather records, southern Brazilian coast.

Bidirectional seas are well-reported in the oceanographic literature, but few studies in coastal waters are found. Alves & Melo (1999) report reconstructed bidirectional seas at the coast at Santa Catarina state, Brazil (Figure 2) – a study being revisited by researchers at University of Cantabria at the time of writing. Also in a coastal setting, Long & Resio (2007) report measured bidirectional spectra off the North Carolina coast, USA. More recently, investigation into damage at the Civitavecchia breakwater has included bidirectional seas (Artelia, 2012).

Defences whose geometry is simple can be analysed by using formulae from *e.g.* EurOtop (2018). For more complex structures, the CLASH Artificial Neural Network (ANN) (Van Gent *et al.*, 2007) is a key tool. The ANN is based upon the CLASH database of *c.*10500 laboratory measurements of overtopping (Van der Meer *et al.*, 2009), but these are not distributed uniformly across the range of conditions found at real coastlines (Table 1).

Table 1: Indicative numbers of overtopping tests in the CLASH database according to sea conditions. The highlighted cells correspond to the most common situations in nature.

	long-crested seas	short-crested seas	bidirectional
2-d	9200	n/a	n/a
3-d	1300	40	0

The paucity of testing under the more realistic conditions is due to the fact that their reproduction in wave basins has hitherto been limited to a very few facilities, and has been almost impossible for very large angle differences between swell and wind seas. The Delta Basin at Deltares with its two banks of wavemakers set at 90 degrees to each other is ideally suited to enabling the filling of this gap in the knowledge. Prior to this project, the basin had been used to explore overtopping with crossing sea and swell at $\pm 45°$ obliquities (Van der Werf & Van Gent, 2018), with a prediction method proposed tentatively.

Awarded access to the Delta Basin by the EC *Hydralab+* project, *CrossOver*'s aim was to explore the influence of crossing seas upon wave overtopping responses. The project's specific objectives were:
- to design a test set up and matrix which would allow the generation of a wide range of combined, oblique sea and swell conditions;
- to calibrate these incident conditions, including situations with long-and short-crested seas and swells;
- to measure mean and wave-by-wave overtopping at a 1:3 slope under combined directionally-bimodal swell and sea conditions with (i) just the swell oblique, (ii) just the sea oblique and (iii) with both sea and swell oblique and crossing at variable angles;
- to determine the influence of very high obliquities on wave overtopping for sea-only and swell-only conditions and to support or revise existing guidance;
- to determine the influence of short-crestedness on wave overtopping under oblique wave attack for sea-only and swell-only conditions and to support or revise existing guidance;
- to synthesise practical guidance giving corrections / influence factors for estimation of overtopping resulting from crossing seas. The guidance, subject to peer-review, should be suitable as an addition to EurOtop (2018) in the first "EurOtop Live" update round.

2. METHODOLOGY

2.1 Basin layout
The layout of the sloping structure in the Delta Basin is sketched in Figure 3. The structure is set at a 30° angle across that basin rather than at 45° in order that head on (zero obliquity) seas and swells could be generated. The structure is a 40m long, 1:3 simple slope with its crest at elevation 1.15m. The majority of the tests were in a water depth of 0.95m, with some larger sea cases at a

lower depth of 0.90m. The newer 100-paddle bank of wave makers is used to generate bidirectional sea and swell for all but the most extreme obliquities. The older 80-paddle bank of wave makers is used to generate sea and swell from -60º, -75º and -85º. For all other tests, this paddle bank is nevertheless active in absorption mode.
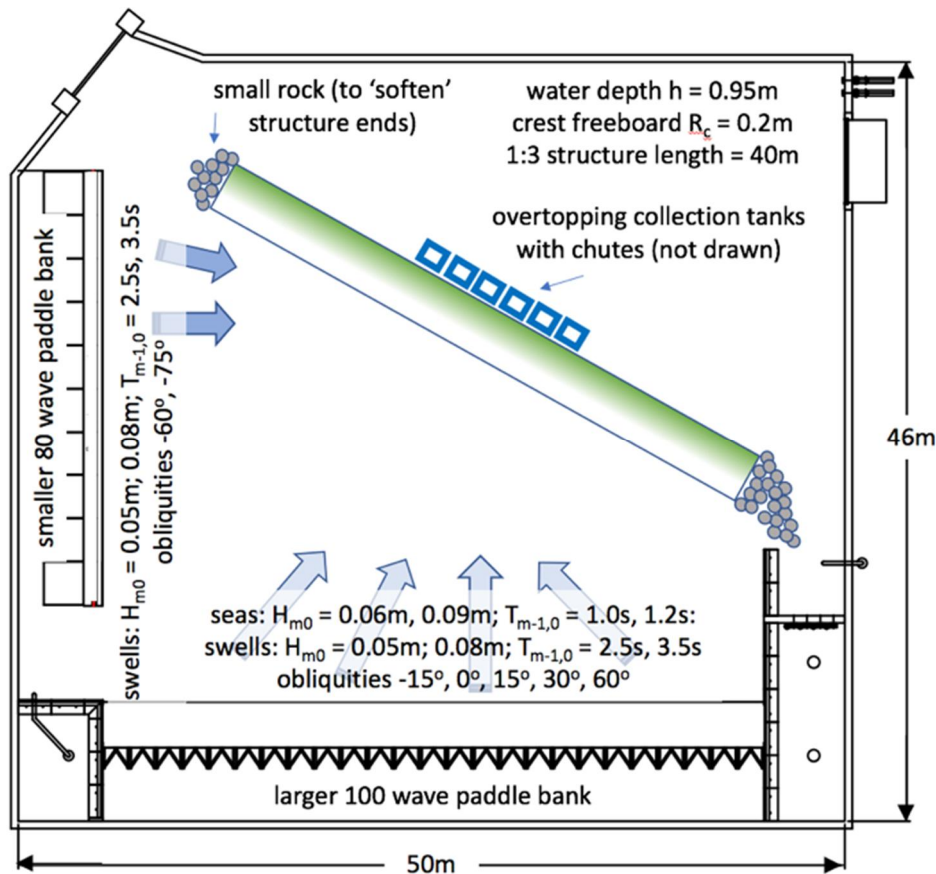

Figure 3: Sketch of the layout of the structure in the Delta Basin. Not to scale. Wave directions indicated are those originally proposed. Larger obliquities of up to -85º were subsequently explored.

Six overtopping collection tanks are arranged along the central 10m run of the structure, equi-spaced at 2 m (centre to centre) intervals. Mean discharge is measured using elevation probes in each collection tank. In addition, one tank has an extra probe mounted at the crest as an overtopping event detector. Figure 4 shows the just-completed structure, and the detailing of the overtopping collection tanks and chutes. Preliminary analysis of the collected overtopping volumes in the six boxes shows a fairly uniform longitudinal distribution of the mean discharge, even for large wave obliquities.
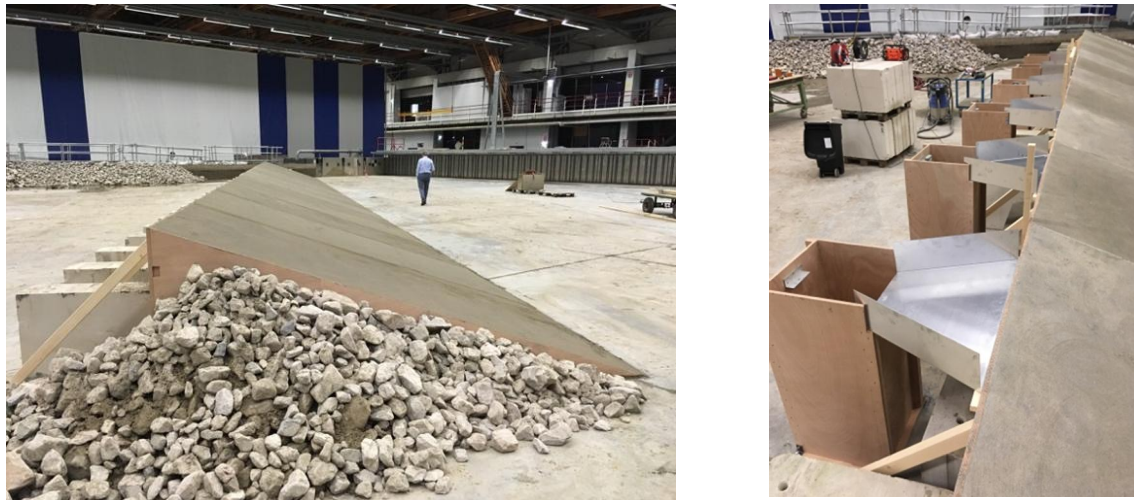
Figure 4: Right, the just completed smooth slope and left, the detail of the overtopping collection via chutes from the structure crest to the collection tank.

2.2   Instrumentation

The instrumentation deployed is shown in Figure 5. Each of the six overtopping collection tanks had a simple resistance wave gauge mounted inside to measure the water elevation within the tank. One of the two centrally-located collection tanks was designated the 'super-box' and was additionally instrumented with a second wave gauge in the box to give a sense of the uniformity or otherwise of the water surfaces in the collection tanks, and also with a third gauge right at the structure crest, at the entrance to the chute. This gauge acted as an 'overtopping event detector', showing a voltage spike every time water passed by. This voltage was not used in any quantitative (calibrated) way, but it provided valuable markers when examining the time histories of the water levels in the collection tanks to extract the overtopping volumes (V) associated with individual events.

Three Deltares directional wave gauges ("GRSMs") were deployed; one in front of each paddle bank and one 4m offshore from the toe of the structure. Finally, an array of eight simple wave gauges was deployed close to the central GRSM. These were arranged in an "Edinburgh array" configuration to enable subsequent analysis by the SPAIR method (Draycott *et al.*, 2016).
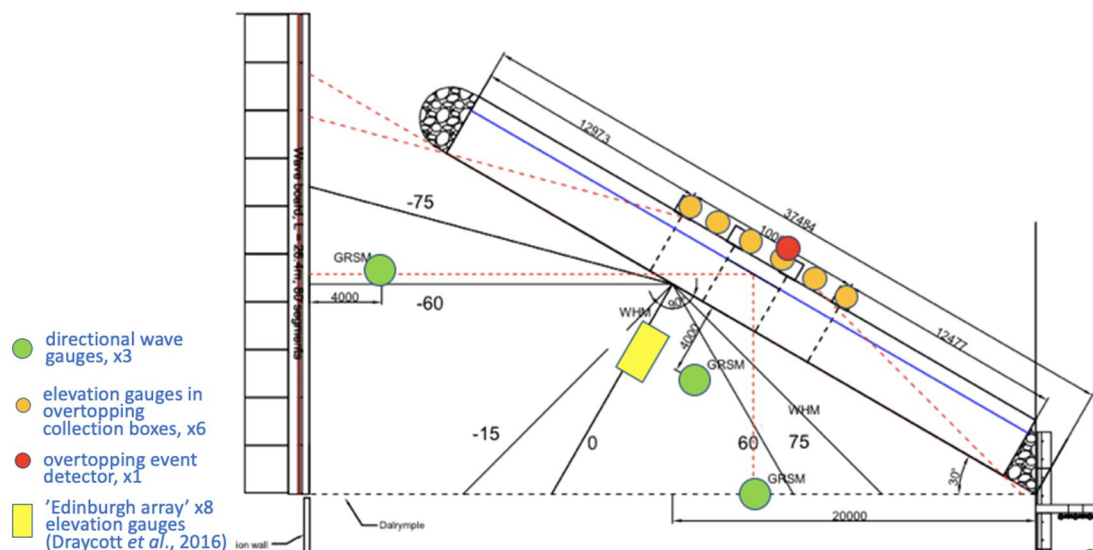

Figure 5: Instrumentation deployed. In addition, all tests were video recorded from the elevated balcony above the basin, from two viewpoints – one looking head on to structure, and one looking along its length. Note that the wave directions shown here are not those tested, which are described in Section 2.3.

2.3 Wave generation and test matrix

The two wave paddle banks are shown in Figure 6. The general strategy was to use the newer paddle bank (along the lower side of the basin as seen in Figure 5) to generate sea-only, swell-only *and* combined sea and swell (bimodal) conditions for sea and swell obliquities ranging from -15º to +60º. The older paddle bank was only brought into use as a wave *generator* for the high, negative obliquities of -60º and greater.
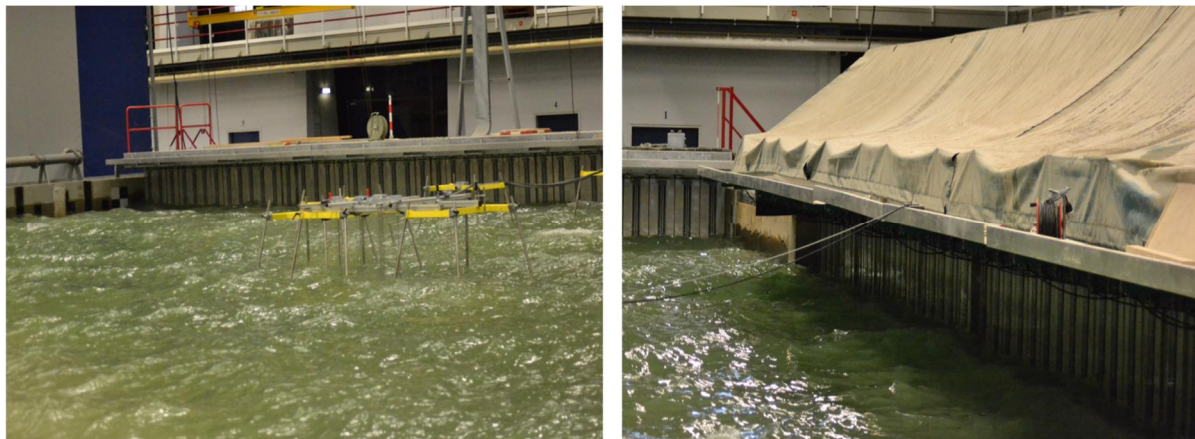

Figure 6: The newer, 100-paddle bank (left) and older, 80-paddle bank of wave generators.

A core set of sea and swell conditions was defined (Table 2). The selection of the maximum wave heights was constrained by the limitation that when generating *both* swell *and* sea, the wave heights that could be generated were significantly reduced from those which could be generated for sea-only or swell-only cases.

Table 2: Core test conditions; nominal / target values.

	wave height, H_{m0} (m)	wave period, $T_{m-1,0}$ (s)	wave steepness, $s_{m-1,0}$ (-)	spreading σ (º)	
sea	0.09	1.2	0.04	30	plus some $\sigma = 0º$ tests
sea	0.065	1.0	0.04	30	plus some $\sigma = 0º$ tests
swell	0.08	3.5	0.004	10	plus some $\sigma = 0º$ tests
swell	0.05	3.5	0.003	10	plus some $\sigma = 0º$ tests
swell	0.08	2.5	0.008	10	plus some $\sigma = 0º$ tests

The seas and swells were calibrated separately. After calibration tests, 44 tests were carried out in the first phase of testing:

- sea and swell from same direction (12 tests)
- sea normal, swell oblique (8)
- swell normal, sea oblique (8)
- crossing; sea and swell oblique and opposed (16)

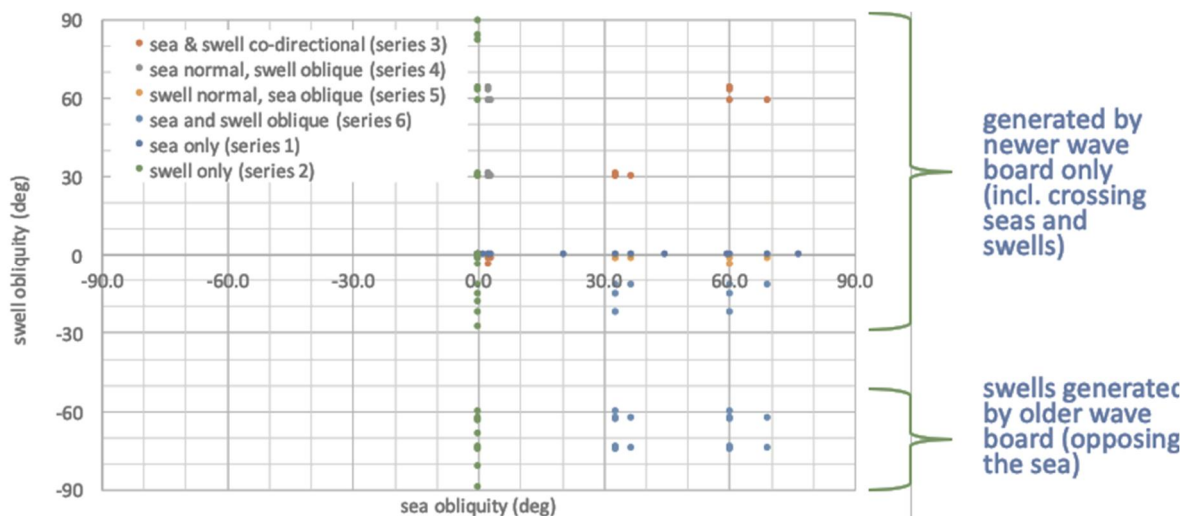This core test matrix is shown diagrammatically in Figure 7.

Figure 7: The core test matrix, as originally devised at the outset of testing.

A view of the structure and instrumentation during testing is given in Figure 8.

Figure 8: The basin view during testing.

3. RESULTS

Before any meaningful analysis of the overtopping can be done, the incident wave conditions need to be determined with confidence. The strategy was to determine the incident wave conditions for the sea-only and swell-only tests individually, and then to assume that these incident conditions were well recreated when generated as one component of a crossing condition. The Deltares directional wave gauge data was processed by the in-house AUKE software. Outputs were supplied in both tabular and graphical forms.

In appraising the outputs in detail, it became apparent that while many calibration tests gave results which were wholly self-consistent, with incident wave heights, reflection coefficient, incident and reflected wave directions all being close to the desired values, there were a number of cases where the analysed wave data did not appear to be reliable. In order to explore these conditions very carefully, *CrossOver* partner LNEC reanalysed some of the problematic data using their IMLM method. Then, test by test, the Deltares and LNEC outputs were compared, graphically and in tabular form. An example of a case where good agreement is found between anticipated conditions, Deltares and LNEC is given first (Figure 9), followed by an example of a more problematic case (Figure 10).
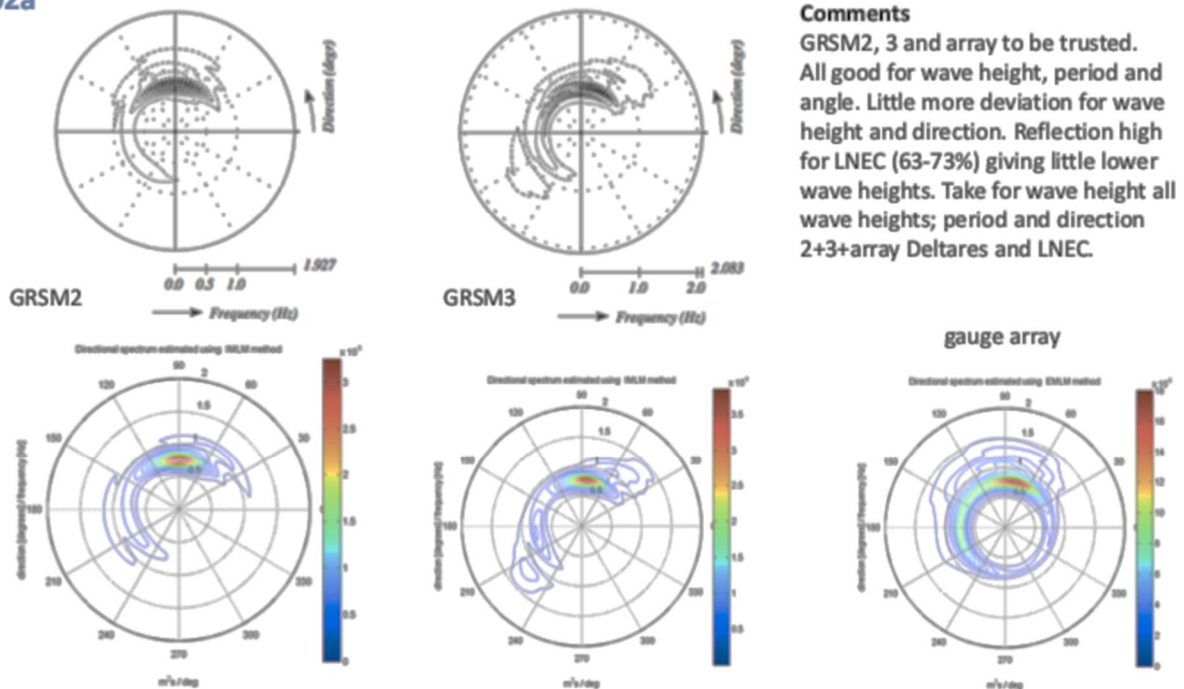
102a

Comments
GRSM2, 3 and array to be trusted. All good for wave height, period and angle. Little more deviation for wave height and direction. Reflection high for LNEC (63-73%) giving little lower wave heights. Take for wave height all wave heights; period and direction 2+3+array Deltares and LNEC.

Figure 9. Calibration test "102a", sea only; larger sea ($H_{m0} = 0.09$m); $\beta = 30°$ incidence. The upper polar plots are the Deltares AUKE outputs, and the lower ones from LNEC's reanalysis. Directional wave gauge GRSM2 is located in front of the 100-paddle wavemaker bank, and GRSM3 approximately 4m in front of the toe of the structure (see Figure 5). The structure is oriented along a "10 o'clock to 4 o'clock" line in the plots.

208

Comments
GRSM2, 3 and array to be trusted. Total wave heights GRSM 2 versus 3 and array differ, 0.078 versus 0.096. Why, standing wave? Reflection very low for Deltares3 (10%) and 94% for LNEC3, giving differences in wave heights. Wave height not reliable. Periods ok. Directions: ok, not for Deltares3.
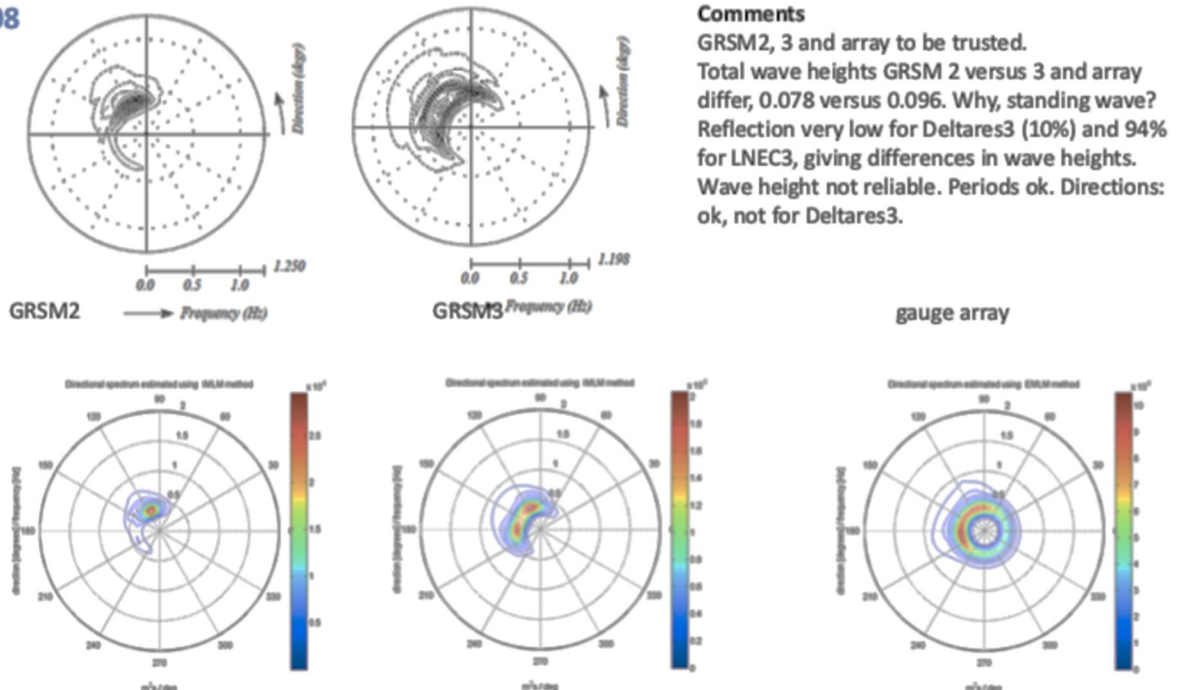
Figure 10. Calibration test "208", swell only; shorter, larger swell ($H_{m0} = 0.08$m, $T_{m-1,0} = 2.5$s); oblique $\beta = 60°$ incidence.

The case in Figure 9 gives outputs deemed 'reliable'. The incident wave heights derived from both independent analyses are close to each other. Overtopping (not shown here) is close to that

predicted by standard methods (EurOtop, 2018). The direction of the incident and reflected waves are identified at the expected angles.

The example shown in Figure 10 presents much more difficulty, however. The outputs of the Deltares and LNEC analyses differ significantly, e.g. in estimation of reflection coefficient, resulting in a high degree of uncertainty in establishing the critical parameter of the incident wave height. At the time of writing, 24 of the 77 calibration (simple, sea only and swell only) tests remained in this 'no reliable conditions determined' category.

Detailed work in progress suggests that the location of the key wave measurement (GRSM3 and the wave gauge array) are in the zone most strongly affected by reflection and possibly standing waves. Work is on-going to explore and understand the differences between the quantities derived by the different analyses, and a third approach is also being explored, using the "SPAIR" method (Draycott *et al.*, 2016).

4. CONCLUSIONS

The Delta Basin's special directional capability due to its wave paddle configuration has enabled a unique and exciting series of tests to have been carried out exploring the realistic but hitherto hardly studied problem of the influence of directionally-bimodal (or "crossing") seas on the overtopping response of a simple 1:3 smooth sloping breakwater.

170 tests were carried out over a four-week period. Tests included "sea-only" and "swell-only" calibration tests, and tests with sea and swell crossing, with sea obliquities ranging from -85° to +60°, and swells from -75° to +60°.

Analysis of the wave (sea and swell) conditions using the directional wave gauge data acquired and processed at the time has presented anomalous results. The raw data from the directional wave gauges and from an 'Edinburgh array' of wave gauges has been reanalysed at LNEC, offering some improved confidence in many cases. With 24 of the calibration tests remaining in the 'low confidence' class, further exploration of this problem including new analysis using the Edinburgh SPAIR method is in progress.

Until the incident conditions are established with good confidence, there is no value in exploring the overtopping data. Once the overtopping data is analysed, it is anticipated that the findings will contribute to "EurOtop Live" first round update in 2019.

REFERENCES
Alves, J.H.G.M. & Melo, E. (1999), On the measurement of directional wave spectra at the southern Brazil coast, Appl. Ocean Res. **21**, pp295-309
Artelia (2012), Diga di Civitavecchia, Etude de la digue en modèle physique, report date 31.7.2012 (in Italian)

Draycott, S., Davey, T., Ingram, D.M., Day, A. & Johanning, L. (2016), The SPAIR method: Isolating incident and reflected directional wave spectra in multidirectional wave basins, Coastal Engineering, **114**, pp265-283

EurOtop (2018), Manual on wave overtopping of sea defences and related structures: An overtopping manual largely based on European research, but for worldwide application, *Second Edition,* Van der Meer, J.W., Allsop, N.W.H., Bruce, T., De Rouck, J., Kortenhaus, A., Pullen, T., Schüttrumpf, H., Troch, P. & Zanuttigh, B. www.overtopping-manual.com

Long, C.E. & Resio, D.T. (2007), Wind wave spectral observations in Currituck Sound, North Carolina, J. Geophys. Res, **112**, C5

Van Gent, M.R.A, Van den Boogaard, H.F.P., Pozueta, B. & Medina, J.R. (2007), Neural network modelling of wave overtopping at coastal structures, Coastal Engineering, **54**, 8, pp586-593

Van der Meer, J.W., Verhaege, H. & Steendam, G.J. (2009), The new wave overtopping database for coastal structures, Coastal Engineering, **56**, 2, pp108-120

Van der Werf & Van Gent (2018), Wave overtopping over dikes with oblique wind and swell waves, Proc. 7th Int. Conf. Appl. of Physical Modelling in Coastal & Port Eng. & Sci. ("Coastlab18")

IV – DHI – Offshore Wave & Shallow Water Basins

The Offshore Wave Basin is 20 m long and 30 m wide with an overall depth of 3 m and a 12 m pit. Short-crested (3D) waves and swell are generated by 60 individually controlled flaps. A parabolic wave absorber located opposite the wavemakers minimizes reflections. Practically any wave spectrum and combination of wave spectra may be generated. Current is generated in the basin using a technique of entrainment. Water is pumped through high-pressure nozzles, located in a rack in front of the wave generators. Wind Load on vessels or structures can be simulated by computer-controlled wind fans.

The Shallow Water Basin for combined waves and current is 35 m long and 25 m wide with an overall depth of 0.8 m. The basin is ideal for model testing when the effects of combined waves and current are of major importance, for instance scour around structures, and loads on fixed or floating coastal and offshore structures. 3D wave generation with a new multi-directional segmented wavemaker. With a paddle height of 1.20m, the wavemaker is designed to operate at water depths between 0.2m and 0.8m. The wavemaker is equipped with DHI AWACS Active Wave Absorption which is a means of avoiding spurious reflection from a wavemaker. The technique allows for full control over the incident waves, even when testing highly reflective structures in a basin.

This basin provides the option of secondary uni-directional wave generation by movable piston type wavemakers. Current is generated by external recirculation of water. The additional moveable wavemakers provide the option of collinear wave-current generation by having the water injected underneath the wavemakers. Wind loading on vessels or structures can be simulated by computer-controlled wind fans.

ORTHOGONAL WAVE CURRENT INTERACTION OVER ROUGH BEDS: PRELIMINARY RESULTS OF THE WINGS HY+ TA PROJECT

Carla Faraci, Alessia Ruggeri, Giovanni Savasta (1), Rosaria E. Musumeci, Massimiliano Marino, Enrico Foti (2), Giuseppe Barbaro (3), Dag Myrhaug, Lars Erik Holmedal, Pierre-Yves Henry, (4), Paolo Blondeaux, Giovanna Vittori (5), Richard R. Simons (6), Bjarne Jensen, Bjorn Elsaβer (7)

(1) Department of Engineering, University of Messina, Italy, Email: cfaraci@unime.it
(2) DICAR, University of Catania, Italy, Email: rosaria.musumeci@unict.it
(3) Università Mediterranea di Reggio Calabria, Italy, Email: giuseppe.barbaro@unirc.it
(4) NTNU, Norway, Email: pierre-yves.henry@ntnu.no
(5) Università degli Studi di Genova, Italy, Email: blx@dicca.unige.it
(6) UCL, UK, Email: r.r.simons@ucl.ac.uk
(7) DHI, Denmark Email: bjj@dhi.dk

This paper reports some preliminary results obtained in the framework of the TA WINGS, funded by the EU through the Hydralab+ program. The project was aimed at gaining insights on orthogonal wave current interaction over rough beds. Velocity profiles were acquired within the DHI shallow water tank by means of several Vectrinos over sandy, gravel and rippled beds in order to investigate the effects of wave-current interaction on the bottom boundary layer and on the bed shear stresses.

1. INTRODUCTION

Wave-current interaction strongly affects the nearshore hydrodynamics, inducing changes both in the mean velocity profile and in the turbulent characteristics, in the structure of the bottom boundary layer and in the bed shear stress. Since the hydrodynamics at the bottom of the sea wave plays a fundamental role on many phenomena such as sediment transport, diffusion, mixing process, etc., the relevance of the topic in the coastal research community is unquestionable.

Following this consideration, in the last decades many experimental studies have been devoted to investigate wave-current bottom boundary layers in the case of currents following or opposing the waves (Kemp and Simons 1982,1983, Lodahl et al., 1998) or orthogonally interacting one with each other (Musumeci et al., 2006, Faraci et al., 2008, Lim et al., 2012). According to some of these studies, a key role in the wave current interaction seems to be played by the ratio between current and wave orbital velocity. Indeed, when the flow field is dominated by the current (current-dominated regime), a linear interaction occurs between the two forcing, while if the wave contribution prevails (wave-dominated regime) the nature of the boundary layer also play an important role.

Musumeci et al. (2006) found that when waves are added onto a current over a bed characterized by a small roughness, an increase of the current flow at the bed occurs; the contrary occurs in the case of large roughness.

The case of a rippled bed is also similar to a large roughness, causing the wave boundary layer to become turbulent and the bed roughness to increase up to an order of magnitude when waves are superimposed to a current (Fredsøe et al., 1999; Faraci et al., 2008). More recently, Faraci et al. (2018) shed also light on the statistical nature of the waves plus current near-bed velocities. They observed that the combined wave-current velocity distribution is double-peaked and can be decoupled in order to get single-peaked velocity distributions splitting the data in two classes according to the sign of the wave directed velocities.

In this work, both current and wave dominated conditions were investigated in order to understand the nature of the velocity distribution along the water column and the apparent bed roughness as well as the structure of the bottom boundary layers.

The effects of three different rough beds (sand, gravel, fixed ripples) on the velocity distribution along the water column were considered.

This task was accomplished within an experimental campaign carried out in the framework of the Transnational Access WINGS - Waves plus currents INteracting at a right anGle over rough bedS, funded by the EU Commission through the Hydralab+ program.

In this paper, some of the results of this campaign on the three different rough beds (briefly indicated as SB, GB and RB) are discussed and compared. The paper is organized as follows: first the experimental set up and instrumentation is presented, then the experiments are reported and the experimental results are discussed. The paper ends with some conclusions.

2.   EXPERIMENTAL SET UP

2.1 Shallow water basin

The experimental campaign was carried out at the Shallow Water Tank at DHI (Horsholm, Denmark). The tank dimensions are *35 m* by *25 m* (Figure 1). Along the longer side of the basin, the propagation of a current is generated by three submerged pumps, able to recirculate on the complex a flow rate of *1 m³/s*. The inlet section was reduced from *25 m* to *12 m*, in order to reproduce both current dominated and wave dominated regimes.

In Figure 1a*)* a sketch of the shallow water tank is reported. The origin of the reference system is located in the lower left corner of the basin and it is identified in Figure *1* with *O*; the *x*-axis follows the current direction, while the *y*-axis is directed as the wave propagation direction. *z*-axis has the origin at the bottom and points upward.

Waves are generated by a wavemaker 18 m wide, obtained by an array of 36 piston-type wave paddles, 1.2 m high and 0.5 m wide each.

Each paddle is controlled by an electric-servo motor through software DHI *WaveSynthesizer*, allowing the wave type (regular or random), the water depth, the wave characteristics and the test duration to be set up.

The *3D* wave generator is designed to operate at water depths *D* between *0.2 m* and *0.8 m*.

A C-shaped gravel beach with a slope of *1/5.6*, coupled with passive parabolic wave absorbers, provides energy absorption at the opposite end of the wave basin.

In this experimental campaign the tests were carried out with three beds with different roughness. In particular, several panels, each one measuring *1.25 x 2.5 m* were used to control bottom roughness over an area of *37.5 m²*. Namely a sandy bed (SB), a gravel bed (GB) and a rippled bed (RB) were installed in the wave-current interaction area of the basin.

The first two beds were obtained by gluing sand (d_{50}=0.9-1.6 mm) or gravel (d_{50}=16-32 mm) on wood tiles, which were thus drilled on the concrete floor in order to be fixed.

The rippled panels were built by fixing on the floor corrugated plastic panels having proper dimensions (height *1.85 cm* and wavelength *12.5 cm*) through screws of dimensions *4 x 3.5 mm*. Subsequently a homogeneous layer of glue was distributed and the ridges of the ripples were created with the use of a wooden template. Finally, they were sprinkled with the same sand of the sandy panels in order to reproduce proper surface roughness.

2.2 Instrumentation

A set of *24* resistive wave gauges, located in the central part of the basin where waves and currents interact orthogonally with each other, allowed the free surface to be recovered (Figure 1b). Five of them were placed along the same *x*-line and shifted along the *y*-axis by a fixed interval in order to measure the wave reflection inside the basin according to the method of Faraci et al. (2015).

Velocity profiles were acquired by means of several high resolution Acoustic Doppler Velocitimeters (Vectrino produced by Nortek As.). More in details, five Single-Point Vectrinos (*VS*), four of them down-looking and one side-looking, and one Vectrino Profiler (*VP*) were employed in the present experimental campaign.

Over the sandy and gravel bed, four *VS* were placed in a square shape, whose side was equal to *0.12 m*, while one *VS* occupied the centre of the square.

In the rippled bed tests, the cross configuration of the set of the Single-Point Vectrinos was modified and the instruments were displaced along the same line at a right angle with respect to the ripple crest. The Side Looking Vectrino was retreated by 5 cm with respect to the other four.
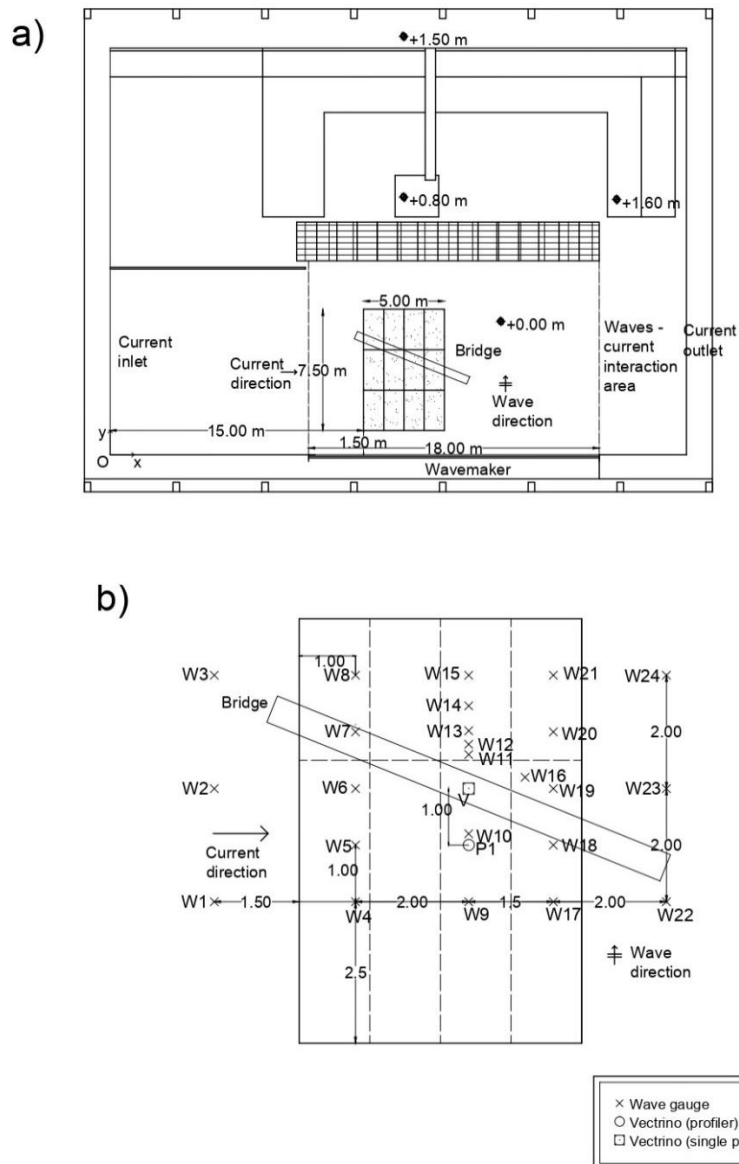
Figure 1. (a) Sketch of the DHI shallow water basin; (b) Zoom of the wave-current interaction area and instrument location inside the basin during the WINGS experiment.

Moreover, for rippled bed, in order to increase the number of vertical velocity profiles along the ripple profile including crest and trough, two different measurement positions were used by shifting the trolley of *1/8* of ripple wavelenght. The position of the Vectrinos for sandy or gravel bed and ripples bed is indicated in Figure *2*.

The whole system was held by a trolley mounted on a bridge and vertically moved by means of a micrometer.

The sampling volume of the VS probe is located 50 mm far from the transducer and its dimensions can be modified via the acquisition software in relation to the desired quality of the signal; the sampling rate is up to 200 Hz. The sampling volume of the VP probe extends from 40 mm down to 74 mm below the transducer, typically divided into 34 measuring cells with 1 mm resolution and sampling rate equal to 100 Hz.

The position of VSs and VP was set on the basis of preliminary tests focused on the definition of an area inside the basin where both waves and currents maintain a steady state, as it will be shown in the next section.
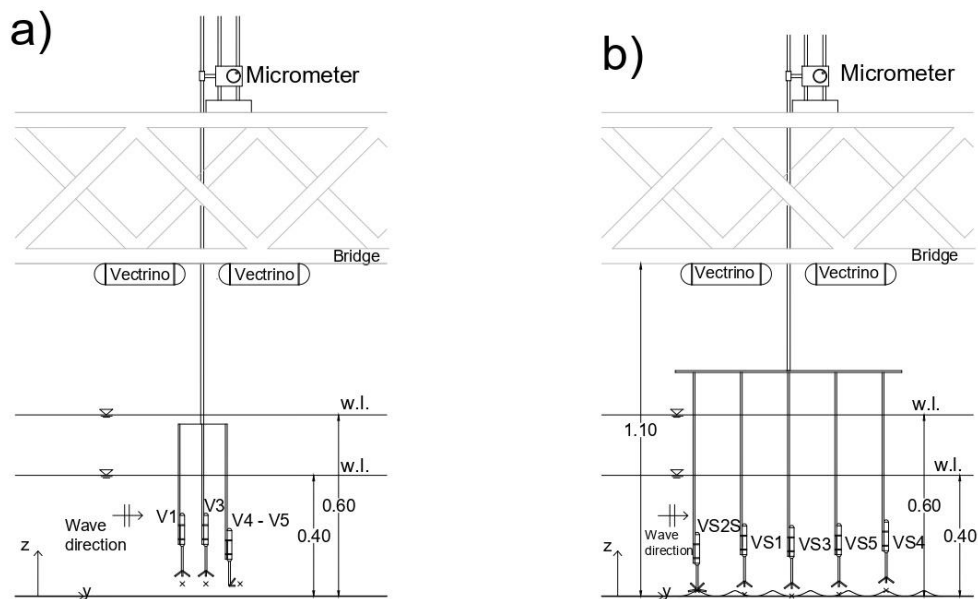
Figure 2. (a) plan view of the Vectrino Single Point position (SB and GB);
(b) plan view of the Vectrino Single Point position (RB).

The reliability of the measured velocities is related to two parameters namely Correlation (COR) and Signal to Noise Ratio (SNR), (see e.g.van der Zanden et al., 2017; Yoon and Cox, 2010). Two acceptance thresholds were adopted: *COR ≥ 90* and *SNR ≥30* near the sweet spot, i.e. from 50 to *65 mm* below the transceiver, *SNR ≥ 20* elsewhere. Non-reliable data were replaced by linear interpolation. Finally, data were despiked by means of the Goring and Nikora (2002) method.

Profiles acquired by the VP were obtained by vertically overlapping each measurement station by a certain amount. This is necessary in order to be able to remove the lower part of the sampling volume data, characterized by low SNR because of sound reflection from the bottom, without producing any gap in the profiles. When vertically moving from a position to another along the profile, the sensor position is shifted up by an amount *Δz* in each run. In order to get the proper overlap between two successive stations, *Δz* was kept equal to *2 cm*. For sake of brevity, data acquired by VP are not displayed in the present paper.

Wavemaker, wave gauges and Vectrinos are all synchronized by means of a TTL (*Transistor-Transistor-Logic*) and acquired by means of a data logger.

In Figure 1b a plan view of the position of the instruments inside the basin is reported.

In Table *1* the position of single point Vectrinos and Vectrino Profiler within the tank are reported for SB, GB and RB.

Table 1. Position of the Vectrinos for the sand, gravel and ripples bed.

Instrument name	Reference	SB and GB		RB	
		x [m]	y [m]	x [m]	y [m]
Vectrino profiler 1	VP1	18	5	18	5
Vectrino profiler 2	VP2	19	6	//	//
Vectrino single point 1	VS1	17,88	6	18	5,84
Vectrino single point 2	VS2	18	5,88	18,05	5,69
Vectrino single point 3	VS3	18	6	18	6
Vectrino single point 4	VS4	18	6,12	18	6,31
Vectrino single point 5	VS5	18,12	6	18	16

3.   EXPERIMENTS

Waves with periods between *1* and *2 s* and wave heights between *0.05 m* and *0.12 m* were propagated along the basin.

Two different water depths *d* were considered, *0.4* and *0.6 m*. In this way two different current conditions were generated within the flume keeping the flow rate equal to 1 m^3/s.

The combination of the wave and the current conditions led to reproduce both wave-dominated and current-dominated regimes.

Some preliminary tests were performed in order to check the regularity of the flow within the test area and to determine both the location of the rough panels inside the basin and the position of the instrumentation. First a Lagrangian particle tracking analysis, carried out using neutrally buoyant particles, allowed the large scale wave-current interaction to be monitored and secondary flows to be investigated by means of visual inspection. One water depth (*d=0.4 m*), i.e. one current condition, and one wave condition (*H=0.12 m* and *T=2 s*) were selected in order to run these preliminary tests. After that, a map of the flow conditions within the basin at one vertical position located *0.1 m* from the bed was carried out by means of one Vectrino single point. A current only case and a wave plus current one were taken into account. The main goal was to check to what extent the velocity in the outer flow could be influenced by the local coordinate. The measurements explored almost the entire area where the waves interact with the current; *14* measuring points in the current only case and *12* points in the wave plus current case (*5 m< x <30 m; 3.5 m< y < 8.5 m*) were acquired .

Moreover, before starting with the actual test programme, a time convergence test was performed, i.e. the velocity components were acquired at one point for *30* minutes and the convergence of the first and second order statistics were analysed by considering a different acquisition time. Moreover the comparison of the ensemble average with the single waves allowed to assess that no visible differences occurred within the acquisition time.

The results of these preliminary tests therefore allowed to define both the optimal position of the measurement point for the detailed investigations concerning the hydrodynamics generated by waves and currents on rough surfaces, as well as the time duration of the tests. As a result, it was decided to place the measuring point for the acquisition of the velocity profiles at the coordinate point *x = 18.5 m, y = 6 m.*

During the experimental campaign a total of 67 runs were performed, 18 of which for SB, 18 for GB and 31 for RB respectively (Table 2).

More in detail, for SB and GB cases, two runs of current only (CO) (*d=0.4 m and d=0.6 m*), 8 of waves only (WO) and 8 of waves and current (WC) were made, changing the period and the wave height (*T=1 s and T=2 s* and wave height between *H=0.12 m* and *H=0.05 m*).

For the rippled bed case, 18 runs were performed for the first trolley position, two of which were only current (CO), 8 of waves only (WO) and 8 of waves and currents (WC).

For the second position of the trolley, five runs of waves only (WO), two of only current (CO) and six of waves and current (WC) were carried out by changing wave height and period.

Table 2. Overview of the test conditions for respectively SB, GB and RB case.

Flow cond.	D(m)	Flow cond.	H(m)	T(s)	Flow cond.	H(m)	T(s)
CO	0,4	WO	0,05	1	WC	0,05	1
			0,08	1		0,08	1
			0,08	2		0,08	2
			0,12	2		0,12	2
	0,6		0,05	1		0,05	1
			0,08	1		0,08	1
			0,08	2		0,08	2
			0,12	2		0,12	2

4.   ANALYSIS OF THE EXPERIMENTAL RESULTS
4.1 Water surface

Regular waves were measured by the wave gauges during all the tests. An example of the acquired signal is reported in Figure *3*, where the ensemble average is plotted above each single recorded wave in the cases of different roughness: Run 16 (SB), Run 25 (GB) and Run 48 (RB) (*d=0.6 m; H=0.08 m; T=1 s*).

The wave signal seems to be fairly regular and with a good repeatability. Moreover, the comparison of overlapped waves for the three bed roughness shows a higher variability for the case of ripples. More in details, the average crest - trough variability estimated as the displacement of the maximum crest elevation or minimum trough position with respect to the ensemble average was found to be equal to 9.6%, 8.7% and 15.3% respectively for SB, GB and RB.

a)

b)

c)
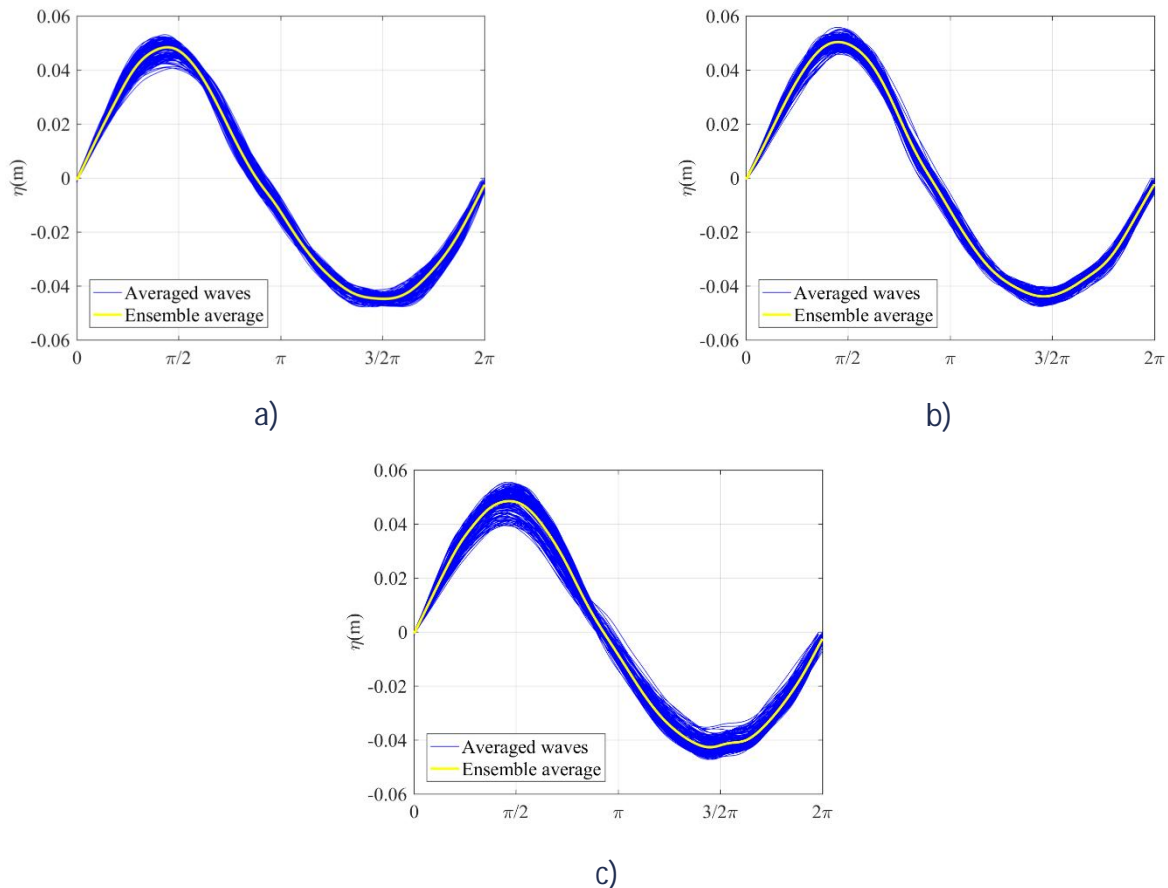
Figure 3. Wave series acquired during (a) Run 16 (SB), (b) Run 25 (GB) and (c) Run 48 (RB) (*d=0.6 m; H=0.08 m; T=1 s*)

4.2 Mean velocity profiles and shear stresses

In this section mean velocity profiles acquired by Single Point Vectrinos are shown.
As mentioned before, for each test the velocity was acquired by means of several Vectrinos, which were then averaged in order to obtain a spatially averaged velocity.
An example of this procedure is shown in Figure *4*, where the velocities acquired by each Vectrino in three current-only tests characterized by a water depth d=*0.4 m* and by different bed roughness are reported all together along with the spatially averaged profile. In particular, Figures 4a and 4b report respectively the x- and y- velocity component in Run *1* (SB), Figures 4c and 4d similarly indicate x- and y- velocity component in Run *32* (GB) and finally Figures *4e* and *4f* refer to the x-

and y- velocity component in Run *40* (RB). The velocity is made non-dimensional by means of the target current velocity, U_c, obtained by dividing the flow rate for the cross section.
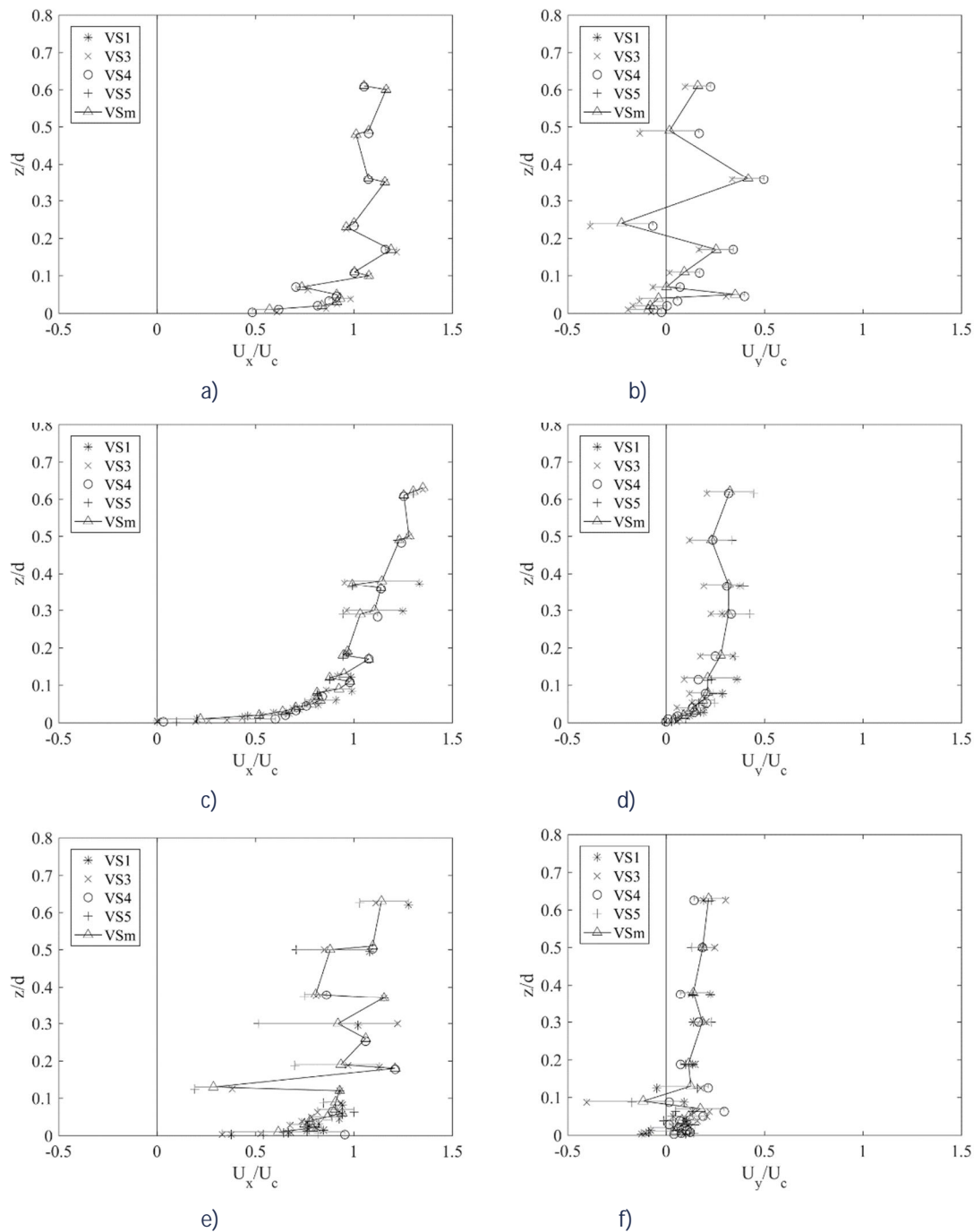

Figure 4. Mean velocity profiles acquired by the Vectrinos in the current only case (d=0.4 m): a) Run1 (CO, SB) Ux; b) Run1 (CO, SB) Uy c) Run32 (CO, GB) Ux; d) Run32 (CO, GB) Uy e) Run40 (CO, RB) Ux; f) Run40 (CO, RB) Uy.

It is possible to observe that in the SB case the measured U_x velocities are almost superimposed one over each other at all the measuring stations. The *y* component shows an irregular pattern which leads to argue the existence of transverse circulations inside the basin. In the GB case on the contrary, the scatter between each Vectrino Single Point is more relevant (up to 20% in the weak spot region), even though the averaged profile is less affected by abrupt changes.

The RB case shows an irregular pattern along the x component probably caused by a relevant transversal circulation maybe due also to the bed waviness close to bottom. Moreover, a significant variability among each Vectrino Single Point is also noted. For the y component of Run 40 the trend is more regular and the average profile shows a trend closer to each Vectrino Single Point.

In Figure 5 a current only, a wave only and a wave plus current conditions over three rough beds are plotted. Here respectively Run1, Run32 and Run40 (CO), Run3, Run36 and Run45 (WO), Run7, Run34 and Run41 (WC) are considered *(d=0.4 m, H=0.12 m, T=2 s)*. Each set of three velocity profiles refers to different bed roughness (SB, GB and RB).

While the wave only profile, as expected, shows only fluctuations around zero, the CO and WC profiles exhibit an increasing velocity from the bottom up to about *0.15-0.25 z/d.*

Here only the average profile is traced, while the spatial variability observed between the different Vectrino is represented in terms of an error bar. This variability is maximum at the bottom and is reduced far from the bed. It can be detected that, far from the bed, CO velocities are slightly higher than WC ones, while the opposite happens close to the bed. In the RB case however such behaviour is less clear.
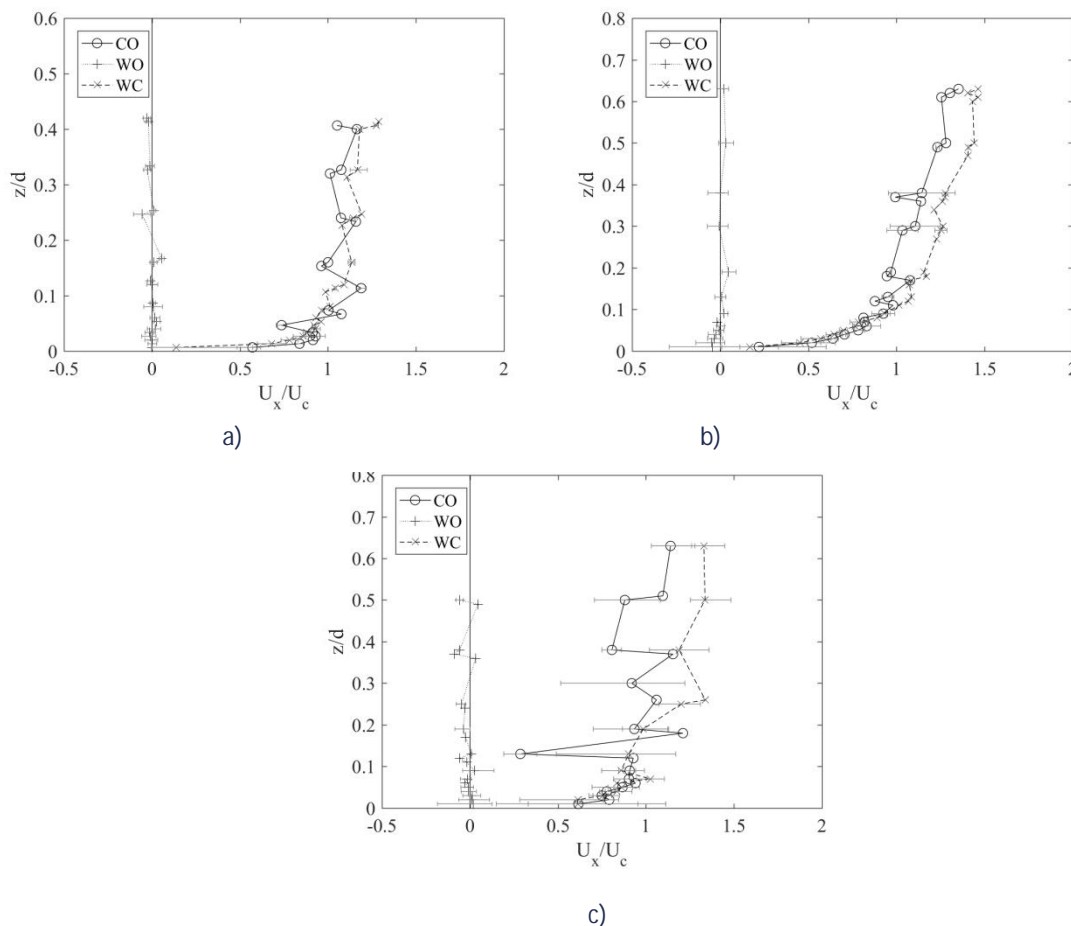

a)

b)

c)

Figure 5. Velocity profiles along the *x* direction: a) SB case Run1 (CO), Run3 (WO), Run7(WC), b) GB case Run32 (CO), Run36 (WO), Run34 (WC), c) RB case Run40 (CO), Run45 (WO), Run41 (WC) d=0.4 m, H=0.12 m, T=2 s.

Along the y-direction (Figure 6) time averaged profiles show that in the case of wave only the mean velocity is negative for all SB, GB and RB case for the majority of the vertical profile due to the setting of the undertow current. The addition of the current onto the wave tends to compensate these two opposite flows, with a mean profile that shows velocities smaller than in the current only case.

As before, the variability observed between the different Vectrinos is represented in terms of an error bar. This variability in the lower part is more evident in the RB case (Figure 6c). This is probably related to the type of bed as it involves a greater measurement displacement between a measurement point and another; indeed, a strong difference arise between measurements taken on the crest and the trough; this effect is greatly reduced far away from the bed.

Plotting on a semi-logarithmic scale the acquired profiles, it is possible to recover the equivalent roughness k_s and the friction velocity u^* respectively as 30 times the intercept and the angular coefficient of the log-layer. The latter quantity was used to determine the shear stress τ for the CO and WC conditions.

In Figure 7, the non-dimensional wall shear stress, obtained as the ratio of the wave-current shear stress to the current only one, is plotted versus the wave Reynolds number. Data are grouped on the basis of the rough bed condition. The nondimensional shear stress undergoes a reduction for Reynolds numbers lower than approximately 5.000, i.e. the flow relaminarizes, as already observed by Lodahl et al (1998). This behaviour is typical of current dominated conditions. Then, for Reynolds numbers higher than 10.000 and wave dominated conditions, wave-current shear stress increases more than linearly with respect to the current only one. A similar behaviour was also found in Musumeci et al (2006) and in Faraci et al. (2008).
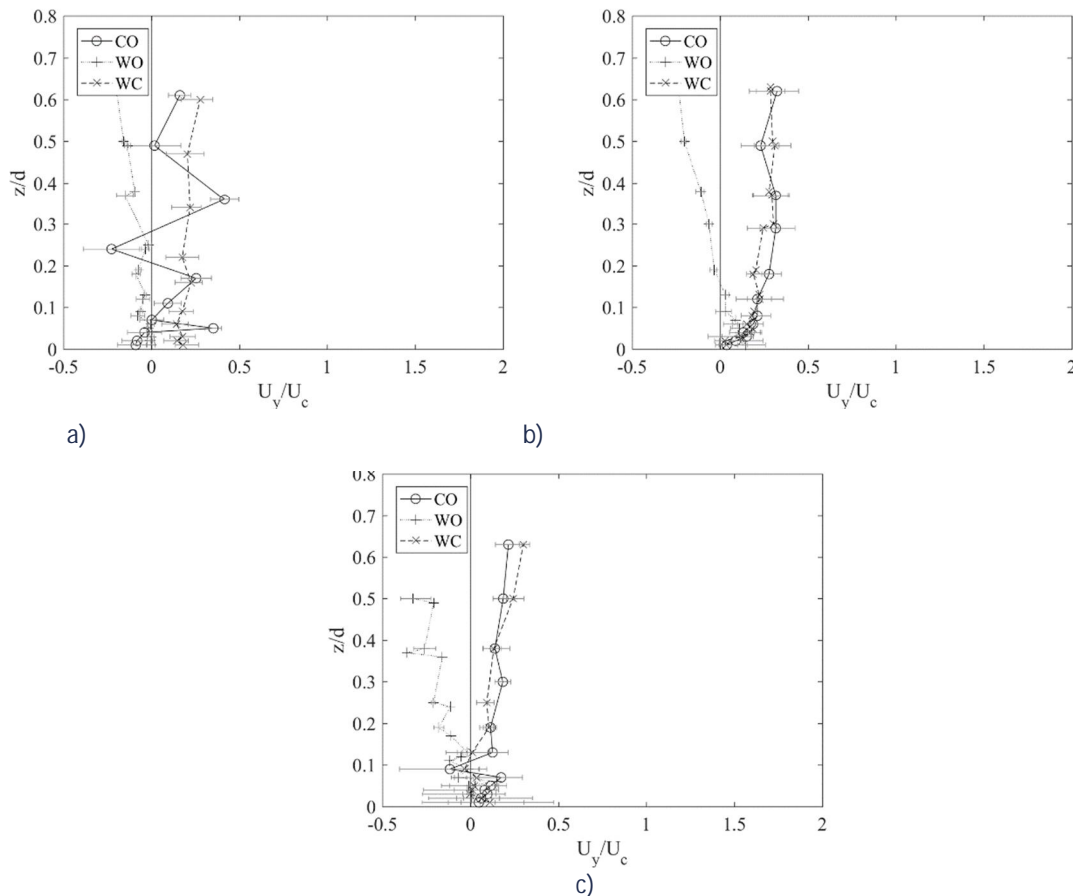

Figure 6. Velocity profiles along the *y* direction in the SB case, Run1 (CO), Run3 (WO), Run7 (WC) (a), GB case Run32 (CO), Run36 (WO), Run34 (WC), RB case Run40 (CO), Run45 (WO), Run41 (WC). d=0.4 m, H=0.12 m, T=2 s.
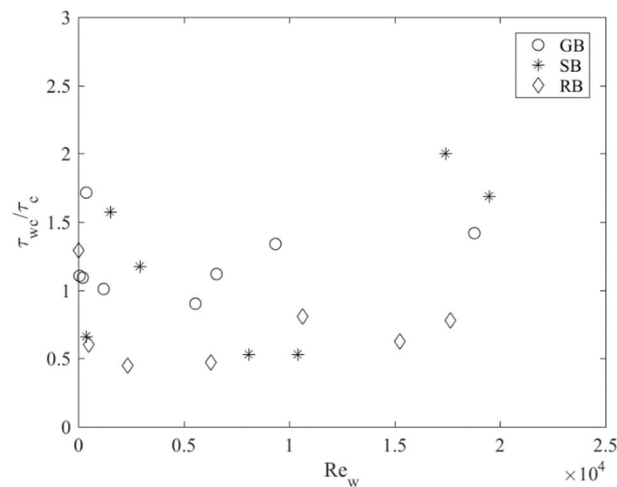
Figure 7. Non-dimensional wall shear stress as a function of wave Reynolds number.

5.   CONCLUSIONS

This paper reports an overview of the first results obtained in the framework of the TA WINGS, funded by the EU through the Hydralab+ program. The project was aimed at gaining insights on orthogonal wave-current interaction over rough beds in both wave dominated and current dominated conditions. A detailed experimental campaign was performed in order to gather flow measurements in WO, CO and WC conditions over sand, gravel and rippled beds. The analyses of the velocity profiles revealed that far from the bed CO current directed velocities are slightly higher than WC ones, while the opposite happens close to the bed, except for the RB case where such behaviour is less perceptible. In the wave direction in the WO case, the mean velocity is negative for all the rough beds for the majority of the vertical profile, due to the setting of the undertow current. The addition of the current onto the wave tends to compensate these two opposite flows, with a mean profile that shows velocities smaller than in the current only case.

Finally, the nondimensional shear stress was also investigated, and a reduction for Reynolds numbers lower than approximately 5.000 was observed, i.e. the flow relaminarizes, as already observed by Lodahl et al (1998). This behaviour happens in current dominated conditions. Then, for Reynolds numbers higher than 10.000 and wave dominated conditions, wave-current shear stress increases more than linearly with respect to the current only one. A similar behaviour was also found in Musumeci et al (2006) and Faraci et al. (2008).

REFERENCES

Faraci, C., Foti, E., and Musumeci, R. (2008). Waves plus currents crossing at a right angle: the rippled bed case. J. of Geophys. Res., 113(C07018):1{26. doi: 10.1029/2007JC004468.

Faraci, C., Scandura, P., and Foti, E., (2015). Reflection of sea waves by combined caissons. J. Waterway, Port, Coast. and Ocean Eng., 141(2).

Faraci, C., Scandura, P., Musumeci, R., and Foti, E. (2018). Waves plus currents crossing at a right angle: near-bed velocity statistics. J. of Hydraulic Research, 56(4):464{481. doi: 10.1080/00221686.2017.1397557.

Fredsøe, J., Andersen, K. H., and Sumer, B. M. (1999). Wave plus current over a ripple-covered bed. Coastal Engineering, 38:177-221.

Goring, D. G. and Nikora, V. I. (2002). Despiking acoustic doppler velocimeter data. Journal of Hydraulic Engineering, 128(1):117-126.

Kemp, P. H. and Simons, R. R. (1982). The interaction between waves and turbulent current: waves propagating with current. J. of Fluid Mech., 116:227-250.

Kemp, P. H. and Simons, R. R. (1983). The interaction between waves and turbulent current: waves propagating against current. J. of Fluid Mech., 130:73-89.

Lodahl, C. R., Sumer, B. M., and Freds_e, J. (1998). Turbulent combined oscillatory ow and current in a pipe. J. of Fluid Mech., 373:313-348.

Musumeci, R. E., Cavallaro, L., Foti, E., Scandura, P., and Blondeaux, P. (2006). Waves plus currents crossing at a right angle. Experimental investigation. Journal of Geophysical Research, 111(C07). doi: 10.1029/2005JC002933.

van der Zanden, J., O'Donoghue, T., Hurther, D., C_aceres, I., McLelland, S. J., Ribberink, J. S., et al. (2017). Large-scale laboratory study of breaking wave hydrodynamics over a fixed bar. Journal of Geophysical Research: Oceans, 122(4):3287-3310.

Yoon, H.-D. and Cox, D. T. (2010). Large-scale laboratory observations of wave breaking turbulence over an evolving beach. Journal of Geophysical Research: Oceans, 115(C10).

PHYSICAL MODEL TEST ON SPAR BUOY
FOR OFFSHORE FLOATING WIND ENERGY CONVERSION

Giuseppe Roberto Tomasicchio (1), Diego Vicinanza (2), Marco Belloli (3),
Claudio Lugni (4), John-Paul Latham (5), Gregorio Iglesias (6),
Bjarne Jensen (7), Axelle Vire (8), Jaak Monbaliu (9), Federico Taruffi (3), Luca Pustina (10), Elisa Leone (1), Sara Russo (2), Antonio Francone (11), Alessandro Fontanella (3), Simone Di Carlo (3), Sara Muggiasca (3), Griet Decorte (9), Irene Rivera-Arreba (8), Vincenzo Ferrante (2), Tommaso Battistella (12), Raul Guanche Garcia (12), Abel Martínez Díaz (6), Björn Elsäßer (7), Lluis Via-Estrem (5), Jiansheng Xiang (5), Morten Thøtt Andersen (13), Jens Peter Kofoed (13), Morten Bech Kramer (13),

(1) University of Salento, Italy, E-mail: roberto.tomasicchio@unisalento.it; elisa.leone@unisalento.it
(2) University of Campania, Italy, E-mail: diego.vicinanza@unicampania.it; ing.ferrante@gmail.com
(3) Polytechnic University of Milan, Italy, E-mail: marco.belloli@unimi.it; federico.taruffi@polimi.it; alessandro.fontanella@polimi.it; simone.dicarlo@mail.polimi.it; sara.muggiasca@polimi.it
(4) CNR (National Research Council), Italy, E-mail: claudio.lugni@cnr.it
(5) Imperial College London, England, E-mail: j.p.latham@imperial.ac.uk; j.xiang@imperial.ac.uk; l.via-estrem16@imperial.ac.uk
(6) University College Cork, Ireland, E-mail: gregorio.iglesias@ucc.ie; abel.martdiaz@gmail.com
(7) DHI Water & Environment, Denmark, E-mail: bjj@dhigroup.com; bje@dhigroup.com
(8) Delft University of Technology, Netherlands, E-mail: A.C.Vire@tudelft.nl; i.riveraarreba@tudelft.nl
(9) Catholic University of Leuven, Belgium, E-mail: jaak.monbaliu@kuleuven.be; griet.decorte@kuleuven.be
(10) Roma Tre University, Italy, E-mail: luca.pustina@uniroma3.it
(11) University of Calabria, Italy, E-mail: antonio.francone@unical.it
(12) University of Cantabria, Spain, E-mail: tommaso.battistella@unican.es; raul.guanche@unican.es
(13) Aalborg University, Denmark, E-mail: mta@civil.aau.dk; jpk@civil.aau.dk; mmk@civil.aau.dk

The present paper describes the experiences gained from the design methodology and operation of a 3D physical model experiment aimed to investigate the dynamic behaviour of a spar buoy (SB) off-shore floating wind turbine (WT) under different wind and wave conditions. The physical model tests have been performed at Danish Hydraulic Institute (DHI) off-shore wave basin within the European Union-Hydralab+ Initiative, in April 2019. The floating WT model has been subjected to a combination of regular and irregular wave attacks and wind loads.

1. INTRODUCTION

Nowadays, wind energy is said to account for 14% of Europe's total energy consumption, of which offshore wind has a share of 10% (WindEurope, 2019). This gives Europe a leading role in offshore wind energy. By moving offshore, wind energy gains many advantages compared to its onshore counterpart. Firstly, the social protest caused by visual pollution and noise is diminished and turbines can be made bigger. Secondly, at sea, winds are generally stronger and more stable which results in larger energy production. Due to new technologies, the turbines have increased in efficiency and so become viable from a financial point of view (Bilgili et al. 2011; Breton & Moe, 2009).

However, the added complexity due to the hostile offshore environment – waves, currents and salt – remains. Offshore wind has to cope especially with the severely limited installation depths of the commonly used bottom-founded structures, of which the majority are mono piles, which come relatively cheap, and gravity-based foundations. This is a major drawback as many densely populated areas worldwide are situated close to coastal areas characterized by huge wind potential, but too large depths for conventional foundations to be built. This is especially the case for North-Western America, but European countries, e.g. Norway and Portugal, face this problem as well (Breton & Moe, 2009).

This unused energy potential could be harvested by founding the wind turbines on floating platforms, thus reducing the increasing cost induced by using bottom-founded substructures. Three platform types are currently being considered as viable options; (1) the tension-leg platform

(TLP) which lends its stability to pre-tensioned mooring lines, (2) the spar-buoy (SB), which is stabilized by its large submerged volume and its deep-laying center of gravity, and (3) the semi-submersible (SS) which is stabilized by its large water plane area (Butterfield et al., 2007). Floating structures are already well established within the offshore industry. Especially, the SBs and the TLPs are frequently used in oil and gas applications.

Unfortunately, extrapolation to offshore wind applications is not justified, as the dynamic behavior of offshore wind turbines is radically different. The main differences are related to the slenderness of the wind turbine, the aero-elastic effects and the smaller submerged volumes, which increase the importance of viscous effects (Roald et al., 2013). Due to these differences, floating offshore wind turbines (FOWT) exhibit different behavior compared to their oil and gas ancestors. These differences need to be adequately assessed through lab testing in order to have sufficient understanding of the full-scale system as well as to validate numerical models for predicting this complex behavior.

Therefore, during this Hydralab+ project experiments were conducted on the spar-type floating offshore wind turbine. More specifically, these physical model tests were aimed at:

- to exploit the new large DHI wind-generator capable of generating wind speeds and to profit of the existence of the physical model from the Hydralab IV programme (Tomasicchio et al. 2017, 2018);
- to overcome most of the limitations from the adoption of an "approximate" systems to take into account the effect of the wind action when not in presence of a system to generate wind;
- investigating the coupling between a pitch-controlled rotor and the FOWT system rigid body hydrodynamics;
- create a reliable and accurate database for numerical modelling calibration and validation.

In the remainder of the present project DHI-09-SparBOFWEC, the physical model design of the FOWT will be discussed first. Next, the instrumentation is discussed and, subsequently, the test conditions are presented. To end with, conclusions are drawn and some future work based on these data is discussed.

2.   PHYSICAL MODEL DESIGN OF OFFSHORE FLOATING WT

The design of the FOWT model adopted during the Hydralab+ test campaign, shown in Figure 1, was based on the FOWT model developed as part of the OC3-Hywind (Offshore Code Comparison Collaboration) Phase IV project. The model consists of the NREL 5MW reference wind turbine (RWT) and the Hywind floating platform, a spar-buoy concept developed by Statoil of Norway. In the following, only the most relevant full-scale characteristics and their respective scaling used to define the scale model will be presented. For more details on the full-scale set-up, the reader is kindly referred to the NREL Technical Report (Jonkman, 2010). In the next paragraphs, the wind turbine and the rotor design, the spar-buoy platform and the mooring will be subsequently touched upon.

Wind turbine model
The NREL 5MW RWT is a typical utility-scale land and sea based multimegawatt wind turbine, suitable for deployment in deep waters (Jonkman et al., 2009). The turbine reaches the rated power of 5MW at 11.4 m/s and its operational phases are defined by a variable speed, collective pitch controller. As described in the OC3-Hywind report (Jonkman, 2010), the tower base is connected to the spar-buoy at an elevation of 10 m above the sea water level (SWL). The height of the tower is 87.6 m above SWL and the hub is located at 90 m. Table 1 summarizes the main characteristics of the full-scale reference wind turbine.

Two main changes were done to the full-scale NREL 5MW RWT during the OC3-Hywind project. Contrary to the 6 m diameter of the NREL 5MW RWT, the tower base diameter equals the diameter of the upper part of the spar-buoy platform, which amounts to 6.5 m. Another difference between the baseline NREL 5MW wind turbine and the turbine mounted on the Hywind platform concerns the controller setup. Because the reactivity of the baseline turbine would introduce negative damping under operational loads, in the OC3-Hywind project, the gains of the PI pitch controller where reduced and the generator torque controller was switched from constant power to constant

torque in operational conditions. Both adjustments were retained in the model of the FOWT system used in this test campaign.

The Hydralab+ wind turbine model was defined as a 1/40 Froude scale model of the NREL 5MW RWT. At present, the flexibility of the turbine tower is not considered and the tower is therefore considered as rigid. Some of the rotor dimensions were defined following the Froude scaling law as well. Although, in order to properly represent the rotor thrust response, the blade chord had to be scaled appropriately. The rotor is designed by upscaling the wind turbine model developed at Politecnico di Milano (PoliMi WTM), a 1/75 wind turbine model of the DTU 10MW RWT (Bak et al., 2013), designed and currently utilized for wind tunnel tests on FOWTs (Bayati et al., 2016; Bayati et al., 2017; Fontanella et al., 2018). The downscaled characteristics of the wind turbine tower and rotor-nacelle assembly are respectively shown in
Table 2 and
Table 3.

Figure *1*. Impression of the scaled spar-buoy wind turbine layout used during the Hydralab+ tests.

Aerodynamic properties of the rotor blades

Because the aerodynamic design of the rotor had to match the reference thrust and torque, the Hydralab+ rotor was designed as a geometrical upscale of the PoliMi WTM with its proper airfoil profiles. In order to improve the performance at low Reynolds numbers, which characterize the airfoil aerodynamics for wind tunnel tests, the SD7032 airfoil was chosen in favour of the one applied for the NREL 5MW and the DTU 10MW.

Table 1. Full-scale properties of the baseline NREL 5MW wind turbine (Jonkman et al., 2009).

Rating	5 MW
Rotor Orientation, Configuration	Upwind, 3 Blades
Control	Variable Speed, Collective Pitch
Drivetrain	High Speed, Multiple-Stage Gearbox
Rotor, Hub Diameter	126 m, 3 m
Hub Height	90 m
Cut-In, Rated, Cut-Out Wind Speed	3 m/s, 11.4 m/s, 25 m/s
Cut-In, Rated Rotor Speed	6.9 rpm, 12.1 rpm
Rated Tip Speed	80 m/s
Overhang, Shaft Tilt, Precone	5 m, 5º, 2.5º
Rotor Mass	110000 kg
Nacelle Mass	240000 kg
Tower Mass	347460 kg
Coordinate Location of Overall CM	-0.2 m, 0.0 m, 64.0 m

Table 2. Downscaled properties of the NREL 5MW wind turbine.

HYDRALAB+ *1/40 model of NREL 5MW*		λ_L=40 Froude
Length	[m]	1.86
Speed	[m/s]	6.325
Time	[s]	6.325
Frequency	[Hz]	0.158
Acceleration	[m/s^2]	1
Mass	[kg]	64000
Inertia	[kg.m^2]	1.02E8
Force	[N]	64000
Power	[W]	404771.5

Table 3. Downscaled properties of the rotor-nacelle assembly.

		NREL 5MW (Jonkman et al., 2009)	**HYDRALAB**
Rotor Orientation	[-]	Clockwise rotation - Upwind	Clockwise rotation - Upwind
Control	[-]	Variable speed - Collective Pitch	Variable speed - Collective Pitch
Number of blades	[-]	3	3
Rotor Diameter	[m]	126	3.15
Hub Diameter	[m]	3	0.075
Rated wind speed	[m/s]	11.4	1.8
Rotor speed (rated)	[rpm]	12.1	76.5
Ideal power (rated)	[W]	5.10^6	12.35

The blade section in the area near the blade root was determined through interpolation between this airfoil and a circular section, allowing for a smooth transition towards the blade root. The resulting airfoil is shown in Figure 2 and the original FFA airfoil is added to allow for comparison. In order to determine the rotor blade shape, first, a blade shape in terms of twist and chord was determined by geometrically upscaling the PoliMi WTM blade shape. Subsequently, the aerodynamic performance of this rotor was assessed through numerical simulations using FAST v8 (an aero-hydro-servo-elastic tool for wind turbines developed by NREL) with the NREL 5MW RWT as target (Jonkman & Buhl, 2005). The resulting Hydralab+ blade and PoliMi WTM blade airfoil chords and blade twists are shown in Figure 3.
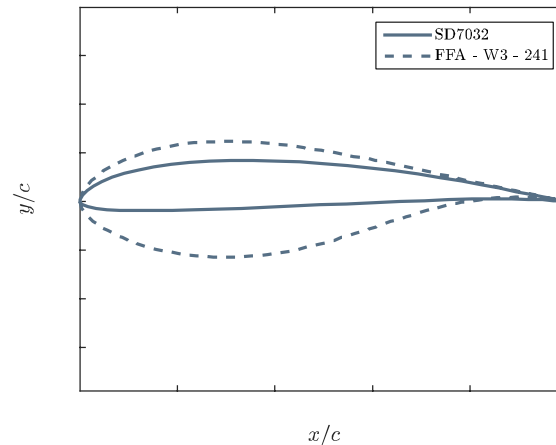
Figure 2. Comparison between the SD7032 low thickness profile and the FFA profile in the full-scale wind turbine.

The 3-D surface of the blade was obtained by 3-D B-Spline interpolation from a 721-points cloud generated by the 193 blade sections. A CNC machined mold was realized based on the blade surface. The wind turbine model blades are fabricated in prepreg CFRP (carbon fiber reinforced plastic) through a vacuum bag oven process. A 3-D view of the blade surface is shown in Figure 10.

The wind turbine model is equipped with a control and monitoring system and with actuators and sensors in order to ensure autonomous and continuous operation and to reproduce the reference full-scale turbine dynamics during experiments.

Four actuators characterize the mechatronics of the wind turbine model; a main shaft motor used to control the rotor angular speed and three dedicated motors allow to control the individual pitch angle of each blade in real-time. The wind turbine is also equipped with an encoder sensor measuring the generator speed used as controller feedback. An embedded system is able to control the actuators and acquire data from the sensors simultaneously.

The control system is designed based on the NREL 5MW, and the parameters are obtained applying the same scaling rules. The wind turbine controller resembles the standard variable-speed variable-pitch control strategy used by modern wind turbines to regulate power production and rotor speed throughout the machine operating range. Some modifications were introduced to the original controller to make the implementation on the scale model more effective (Fontanella et al., forthcoming).

The control strategy adopted is variable-speed variable-pitch. In this scheme, the turbine is programmed to operate at variable-speed and fixed-pitch below rated wind speed, to optimize the power extraction efficiency, and at variable pitch above rated wind speed, to regulate rotor speed and power.
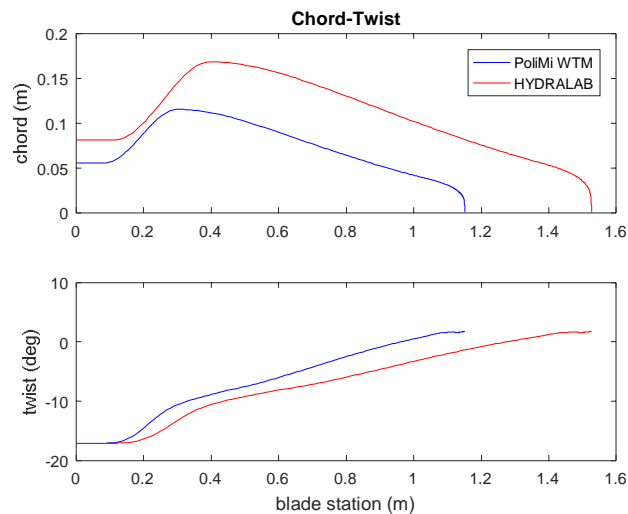
Figure 3. Dimensional chord and twist of the HYDRALAB model (red line) and the PoliMi WTM (blue line

The control system is characterized by three different regions of operation; (1) wind velocity range from start-up until cut-in speed, (2) the partial-load, operational velocity range in between cut-in and rated wind velocity – in this region the blade pitch is fixed at its minimum and the turbine is regulated at variable speed through the torque controller – , (3) the full-load, wind velocity range in between rated and cut-off wind velocity – in this region the generator torque is set at the rated value and the turbine operation is regulated by the blade pitch-to-feather PI controller.
The controller parameter set is obtained from the NREL 5MW coupled with the OC3-Hywind spar-buoy (Jonkman, 2010). The controller scheme is shown in Figure 4.

Hywind spar-buoy floating platform
The Hywind spar-buoy platform has a relatively simple geometry. The lower part of the platform has a diameter of 9.4 m. The upper part is tapered (between the depth of 4 and 12 m) in order to reach an upper part diameter of 6.5 m, which increases the transparency of the platform with respect to the hydrodynamic loads at the free surface. The main structural features of the Hywind platform are reported in Table 4. For additional information, the reader is referred to the OC3 report (Jonkman, 2010).
The OC3-Hywind spar-buoy platform scaling abides to a Froude similitude of 40. By doing so, both the geometry and the inertia between the scaled model and the full-scale structure where respected. The scaled down properties are given in Table 5, where the factor 1.025 takes into account the sea water.

Mooring system
Because the dimensions of the basin do not allow the full mooring lines to be modelled, the mooring line characteristics were approximated by a series of springs coupled to a mass placed at the bottom of the basin by an inelastic rope. The mass's and stiffness's of the various sections of the original mooring line were averaged in order to obtain the characteristics of a homogeneous mooring line. In designing the mooring, damping effects such as hydrodynamic drag and line-seabed drag were neglected (WindEurope, 2019). The scaled mooring system used in this project does not consider the yaw mooring rigidity and does not consider the damping related to hydrodynamic and friction effects. However, the system was modelled respecting the rigidity of the more relevant platform degrees-of-freedom, such as the sway and surge. The mooring layout is shown in Figure 1.
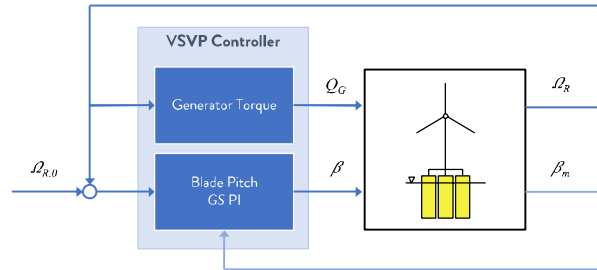
Figure 4. VS-VP controller scheme.

Table 4. Geometrical properties of the OC3-Hywind spar buoy.

Total draft	120 m
Elevation to Platform Top (Tower Base) Above SWL	10 m
Depth to Top of Taper Below SWL	4 m
Depth to Bottom of Taper Below SWL	12 m
Platform Diameter Above Taper	6.5 m
Platform Diameter Below Taper	9.4 m
Platform Mass, Including Ballast	7466330 kg
CM Location Below SWL Along Platform Centerline	89.9155 m
Platform Roll Inertia about CM	4229230000 kg m^2
Platform Pitch Inertia about CM	4229230000 kg m^2
Platform Yaw Inertia about Platform Centerline	164230000 kg m^2

Table 5. Froude similitude scaling factors.

Magnitude	Ratio	Scale
Geometry	λ	40
Time	$\sqrt{\lambda}$	6.32
Velocity	$\sqrt{\lambda}$	6.32
Acceleration	1	1
Mass	$1.025\,\lambda^3$	65600
Force	$1.025\,\lambda^3$	65600
Pressure	$1.025\,\lambda$	41
Reynolds Number	$\lambda^{1.5}$	253

3. INSTRUMENTATION

The deep-water basin at DHI is 20m long, 30m wide and 3m deep, with a 3m x 3m and 6m deep pit at the mid of the basin. Its wave maker is equipped with 60 individually controlled flaps, which are able to generate regular and irregular unidirectional and directional wave fields. To minimize reflection, a 6.5m long sloping wave absorber is located opposite the wave maker. The free surface elevation is captured by a row of three wave gauges at 1.5m before the spar-buoy and a row of six wave gauges placed at 1m behind the spar-buoy. Both sets of wave gauges are placed perpendicular to the wave direction. In addition, two more wave gauges are located at the back of the spar-buoy to allow for an array reflection analysis to obtain the incident and reflected waves (Mansard & Funke, 1980). These wave gauges are placed parallel with respect to the wave propagation. The far-field layout of basin and the wave gauge locations in the near-field area close to the FOWT are shown in Figure 5.
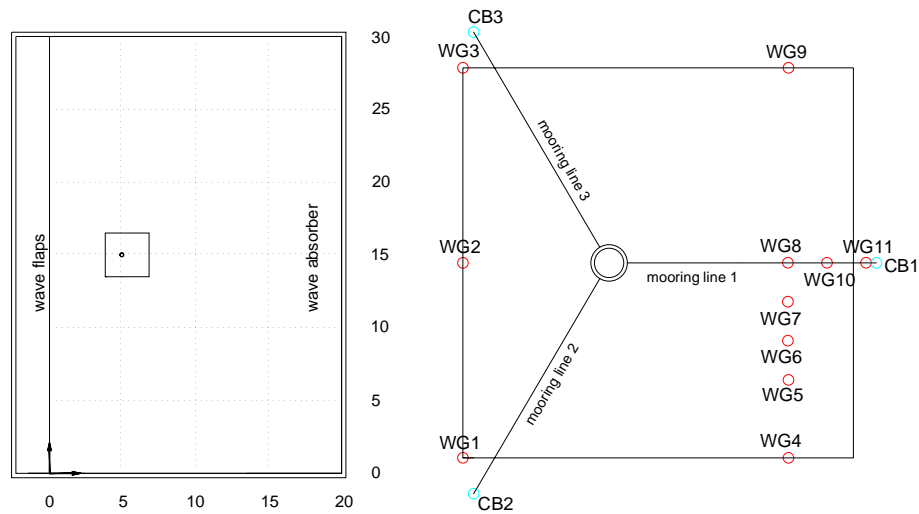
Figure 5. Wave basin layout (left) and wave gauge locations in the near-field area (right).

Wave elevation was sampled at 100Hz for regular and irregular waves. The duration for regular wave cases is about 3 minutes and 20-30 minutes for the irregular wave cases.

Furthermore, in case of large amplitude long waves, typically leading to Keulegan-Carpenter numbers larger than 7, vortex-shedding may occur in the small portion of the spar buoy just below the water level (Sumer & Fredsoe, 2006). In order to detect such vortex shedding effects, two Vectrino Acoustic Doppler Velocimeters were located close to each other at the back of the spar buoy. They were placed at an angle of 20 degrees with respect to the wave propagation.

To evaluate the vertical distribution of the dynamic pressures, three pressure transducers are located on the spar-buoy in the splash region. The wave impact forces are then obtained by spatially integrating these pressure measurements.

A Qualisys Tracking System was used to track the six-degrees-of-freedom motion of the FOWT. In addition, the model is equipped with four accelerometers. Two inertial frames measuring the translational and angular accelerations along three axes were used; one located at the top of the spar buoy and another one at the nacelle. Two uniaxial accelerometers were placed on the tower to capture the acceleration along the global x- and y-axis.

A load cell was placed at each mooring line connection to observe the tension force produced by the spar-buoy motion. An encoder placed in the wind turbine rotor allows measuring the angular velocity of the generator and, in addition, enables to track the reference for the blades' pitch. All observed data were synchronized by the DHI Wave Synthesizer.

4. PHYSICAL MODEL TEST CONDITIONS

Mmodel tests considered three conditions.: 1) the dynamic behaviour of the floating structure was investigated without wind conditions; 2) normal operational conditions have been simulated under combined rotation – rated wind speed conditions – and wave agitation; 3) extreme wave conditions were generated with the rotor stopped – cut-off wind speed. Preliminarily, a hammer test has been conducted in order to define the natural frequency of the tower.

Regular and irregular waves both orthogonal (0 degrees) and oblique (20 degrees) have been generated in presence of the floating structure composed by the spar buoy and the wind turbine. The selected wave conditions refer to typical storm conditions at both sea and ocean areas. In the following the characteristics of the adopted irregular wave attacks are given, where Hs and Tp represent the significant wave height and peak wave period (Table 6). Regular wave attacks considered the following wave height values: 0.05 m, 0.13 m, and 0.25 m. To each of these values, the wave period was assumed ranging between 0.8 and 2.2 s.

Free decay tests have been performed in order to define the natural frequency for displacements and rotations and the total damping; they have been carried out combining different conditions in presence or absence of mooring lines and wind load.

Table 7. Adopted irregular wave characteristics for "no wind" and "above rated" conditions.

	Test #	Hs [m]	Tp [s]	DD	Wind speed (m/s)
NO WIND	1	0,08	1,53	0	0,00
	2	0,06	1,12		
	3	0,10	1,15		
	4	0,15	1,44		
	5	0,20	1,69		
	6	0,08	1,53	20	
	7	0,06	1,12		
	8	0,10	1,15		
	9	0,15	1,44		
	10	0,20	1,69		

	Test #	Hs [m]	Tp [s]	DD	Wind speed (m/s)
ABOVE RATED	11	0,08	1,53	0	1,84
	12	0,06	1,12		
	13	0,10	1,15		
	14	0,15	1,44		
	15	0,20	1,69		
	16	0,08	1,53	20	
	17	0,06	1,12		
	18	0,10	1,15		
	19	0,15	1,44		
	20	0,20	1,69		

5. EXPECTED FUTURE WORK

For organizational reasons, planning of the present project got a relevant delay which induced the User group H+-DHI-09-SparBOFWEC to enter the Lab in the 3rd week of March 2019 with expected end of the model tests on the 12th of April, well before the preparation of the present manuscript. Consequently, it would be too ambitious to give some conclusions. It is more realistic to say about the expected future common work.

The experimental data obtained during the Hydralab+ project will improve the understanding of the integrated floating wind turbine spar-buoy model, and will be used to validate numerical models, such as computational fluid dynamics models (CFD) to be adopted for accurate predictions of the aerodynamic and hydrodynamic performance of a spar-type floating offshore wind turbine.

ACKNOWLEDGEMENTS

REFERENCES

Bak, C., Zahle, F., Bitsche, R., Kim, T., Yde, A., Henriksen, L. C., Natarajan, A. (2013). The DTU 10-MW reference wind turbine. *Danish Wind Power Research 2013*.

Bayati, I., Belloli, M., Bernini, L., Fiore, E., Giberti, H., Zasso, A. (2016). On the functional design of the DTU 10MW wind turbine scale model of LIFES50+ project. *Journal of Physics: Conference Series*, *753*(5).

Bayati, I., Belloli, M., Bernini, L., Mikkelsen, R., Zasso, A. (2016). On the aero-elastic design of the DTU 10MW wind turbine blade for the LIFES50+ wind tunnel scale model. *Journal of Physics: Conference Series*, *753*(2).

Bayati, I., Belloli, M., Bernini, L., Zasso, A. (2017). Aerodynamic design methodology for wind tunnel tests of wind turbine rotors. *Journal of Wind Engineering and Industrial Aerodynamics*, *167*, 217-227.

Bilgili, M., Yasar, A., Simsek, E. (2011). Offshore wind power development in Europe and its comparison with onshore counterpart. *Renewable and Sustainable Energy Reviews.*, *15*(2)

Breton, S. and Moe, G. (2009). Status, plans and technologies for offshore wind turbines in Europe and North America. *Renewable Energy*, 34(3), 646-654.

Butterfield, S., Musial, W., Jonkman, J., Sclavounos, P. (2007). Engineering challenges for floating offshore wind turbines. *National Renewable Energy Lab (NREL)*, Golden, CO, USA.

Fontanella, A., Bayati, I., Belloli, M. (2018). Control of Floating Offshore Wind Turbines: Reduced-Order Modeling and Real-Time Implementation for Wind Tunnel Tests. In: ASME 2018 37th International Conference on Ocean, Offshore and Arctic Engineering.

Fontanella, A., Taruffi, F., Bayati, I., Belloli, M. (forthcoming) Variable-speed Variable-pitch control for a wind turbine scale model. *Energy procedia*.

Jonkman, J. M. and Buhl, M. L. (2005). FAST user's guide. *National Renewable Energy Laboratory (NREL)*. Golden, CO, USA.

Jonkman, J., Butterfield, S., Musial, W., Scott, G. (2009). Definition of a 5-MW reference wind turbine for offshore system development (No. NREL/TP-500-38060). *National Renewable Energy Lab (NREL)*. Golden, CO, USA.

Jonkman, J. (2010). Definition of the Floating System for Phase IV of OC3 (No. NREL/TP-500-47535). *National Renewable Energy Lab (NREL)*. Golden, CO, USA.

Mansard, E. and Funke, E. (1980). The measurement of incident and reflected spectra using a least squares method. *Proceedings of the 17th International Conference on Coastal Engineering*, (pp. 154-172). Sydney, Australia.

Roald, L., Jonkman, J., Robertson, A., Chokani, N. (2013). The effect of second-order hydrodynamics on floating offshore wind turbines. *Energy Procedia*, 35, 253-264.

Sumer, B. M. and Fredsoe, J. (2006). Hydrodynamics around cylindrical structures. *World Scientific Publishing Co.*

Tomasicchio, G.R., Avossa, A.M., Riefolo, L., Ricciardelli, F., Musci, E., D'Alessandro, F., Vicinanza, D. (2017). Dynamic modelling of a spar buoy wind turbine. Proceedings of the 36th International Conference on Ocean, Offshore and Arctic Engineering (OMAE2017)

Tomasicchio, G.R., D'Alessandro, F., Avossa A.M., Riefolo, L., Musci, E., Ricciardelli, F., Vicinanza, D. (2018). Experimental Modelling of the Dynamic Behaviour of a Spar Buoy Wind Turbine. Renewable Energy Journal, RENE-D-17-02232

WindEurope. (2019). Offshore Wind in Europe. Key trends and statistics 2018. Retrieved March 28, 2019, from https://windeurope.org/about-wind/statistics/european/wind-energy-in-europe-in-2018/.

PLANT EFFECTS ON HYDRODYNAMICS AND SEDIMENTATION AT COASTAL WETLAND EDGES

Gillis LG (1), Maza M (2), Argemi M (3), Balke T (3), Folkard AM (4), Garcia-Maribona J (2), Geng L (5), Lanzoni S (5) , Meire D (6), Paul M (7), Sgarabotto A (5), Suzuki T (6), Lara JL (2)

(1) Mangrove Ecology Group, Leibniz Centre for Tropical Marine Research, Bremen, Germany

(2) Environmental Hydraulics Institute (IHCantabria), Universidad de Cantabria, Santander-Spain

(3) School of Geographical and Earth Sciences, University of Glasgow, Glasgow, UK

(4) Lancaster Environment Centre , Lancaster University, Lancaster, UK

(5) Department of Civil, Environmental and Architectural Engineering, University of Padova, Padova, Italy

(6) Flanders Hydraulics Research, Antwerp, Belgium

(7) Ludwig.Franzius-Institute for Hydraulic, Estuarine and Coastal Engineering, Leibniz Universität Hannover, Hannover, Germany

Coastal wetlands such as mangrove forests and salt marshes form the final terrestrial frontier facing the open sea. Wetlands attenuate wave energy, decelerate currents and affect turbulence, which can have profound implications for the morphological development of coastal wetlands such as coastal vegetation retreat or progradation. Offshore hydrodynamic forcing and mechanical (rigidity, buoyancy) and spatial (density) vegetation traits determine these processes. Using DHI's shallow water basin facility, we aimed to quantify how salt marsh and mangrove mimic vegetation attenuate wave and current energy, modify turbulent kinetic energy (TKE), and thus control sediment transport. These factors will determine wetland progradation rate or landward retreat. Combining densities of vegetation, mimic vegetation types (mangrove and salt marsh), waves and currents allows us to tease apart controlling factors of retreat and progradation in these environments. Sedimentation rates varied across mangrove and salt marsh vegetation, hydrodynamic conditions and densities. When only waves were deployed, both vegetation types showed accumulation of sediment, but for mangroves this was only at the patch front. The addition of currents did not change accumulation patterns for salt marshes but it did indicate erosion at the front of the mangrove mimic patch. Reducing mimic density caused erosion in both mimic patches, with salt marsh mimics characterised by erosion at the patch back whilst for mangroves erosion localised in the patch middle. The wave height decay observed along the two vegetation types relates to the accretion patterns observed within the meadow compared to the open channel. The erosion observed in both patches when their density was reduced is linked to an increase of TKE inside the meadow when it is sparser. Our results complement recent work by obtaining a better understanding of wave-current flow features at vegetation edges expanding our understanding of coastal wetland dynamics, and providing information used to increase coastal resilience and therefore protection.

1. INRODUCTION

Coastal ecosystem engineering dominated wetlands, i.e. mangrove forests and salt marshes, form the final terrestrial frontier facing the open sea. As such, they provide important ecosystem services for coastal protection by trapping sediments, attenuating waves and slowing currents (Moeller et al., 2014; Quartel et al., 2007; Temmerman et al., 2013). Together with their ability to adapt to sea-level rise through aggradation (vertical growth) and progradation (horizontal, seaward growth) [4], their ability to provide these services has led to increased interest in the use of coastal wetlands for defence against coastal flooding and tsunamis.

Despite this interest, little is known about the dynamics of coastal wetland progradation (and retreat), particularly under the effect of combined waves and currents [5-8]. The position of a wetland's seaward edge (Figure 1) is determined by the plants' tolerance to inundation and mechanical stresses, and sediment re-distribution caused by the hydrodynamic forces impacting upon them. Landward retreat is initiated by sediment erosion or drowning of ecosystem engineering plants (Morris et al., 2002), whereas progradation occurs when the tidal flat accretes to a height that is colonisable, or the physical conditions temporarily allow new vegetation establishment (Balke et al., 2014a; Balke et al., 2015). To understand progradation further information is required on wetland edge processes (Balke et al., 2013; Balke et al., 2014b) to enable managers to predict the progradation of coastal wetlands and thus use them to protect coastlines and infrastructures.
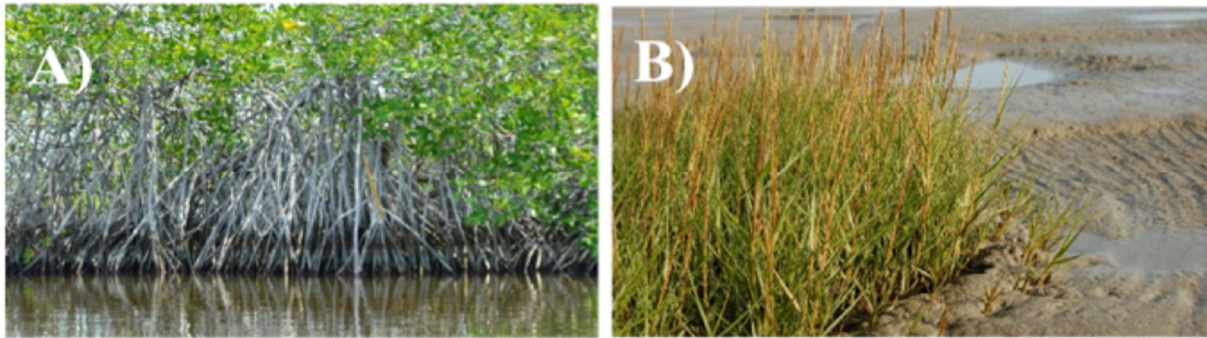
Figure 1 The seaward edge of A) *Rhizophora* mangrove forest, B) *Spartina* salt marsh.

Vegetation attenuates wave energy, decelerates currents and affects turbulence such that eddy length scales become dominantly governed by plant wake characteristics, rather than by the bed boundary layer (Nepf, 1999). For example, the quasi-discontinuous edges of *Spartina* salt marshes (Figure 1B) induce a sharp transition in hydrodynamic energy, potentially leading to cliff formation, whereas the transition at the seaward interface of mangrove forests is smoother, due to their lower density per surface area (Figure 1A). In general, the nature of this transition is determined by a) the offshore hydrodynamic forcing; and b) the mechanical (rigidity, buoyancy) and spatial (height, density) traits of the ecosystem engineers and can have profound implications for the morphological development of coastal wetlands.

In these experiments, we aim to quantify the way in which contrasting ecosystem engineers i.e. salt marsh and mangrove forest vegetation, attenuate incident wave and current energy, modify the nature of the turbulent kinetic energy (TKE), and thus control the sediment transport which determines the rate of progradation or landward retreat. Our results will complement recent work (Losada et al., 2016; Maza et al., 2013; Maza et al., 2016) in order to obtain a better understanding of wave-current flow features at vegetation edges. They will increase our understanding of coastal wetland dynamics, and deliver information that could be used for efforts to increase coastal resilience and therefore protection.

2. METHODHOLOGY

The flume experiment was completed using two different ecosystem-engineering mimics: *Spartina* – a common pioneer plant found at the seaward edge of salt marshes, and *Rhizophora* roots – a common fringing mangrove. Each mimic patch was composed of 12.25 m^2 (10 m in length and 1.25 m in width; Figure 2) plywood sheets upon which the different mimics were attached.
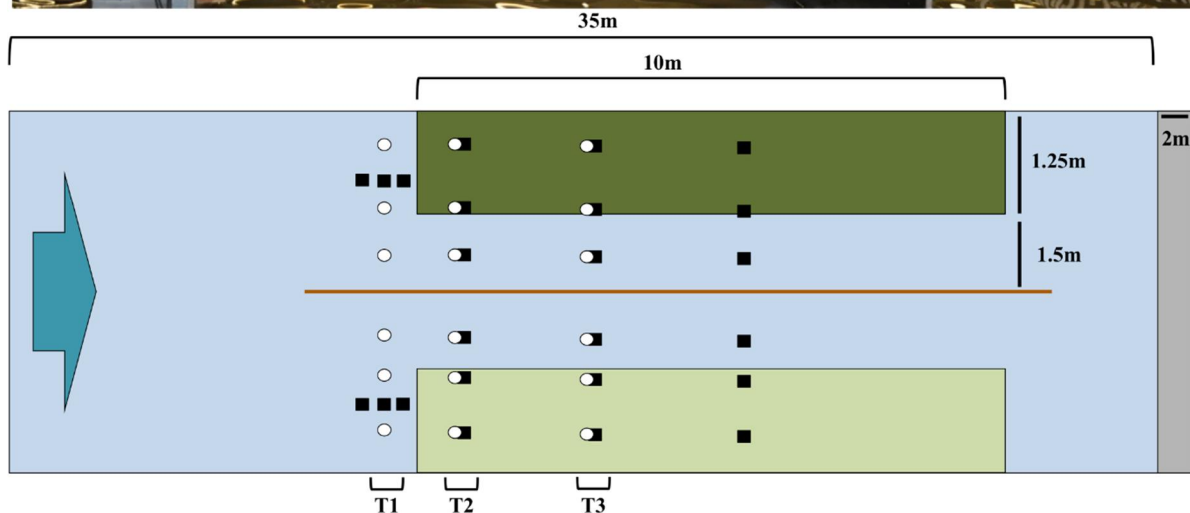
Figure 2. The top picture shows the flume in operation with mangrove mimics on the right hand side and saltmarsh mimics on the left hand side (not seen because of water depth). The bottom section shows a conceptualised experimental setup (not to scale). Depicting the set-up of the *Spartina* mimic patch (light green panel) and *Rhizophora* mimic patch (dark green panel) from an aerial perspective. White dots indicate the placement of the ADVs, which were fixed onto a traverse that moved down the flume. The black squares represent wave gauges, which were fixed in position. The large blue arrow indicates the wave and current maker. The grey patch indicates the beach to absorb waves and reduce reflection. The brown line is the wall between the two vegetation patches and the channel. The ADV's were placed at -0.75, 0.5, 2.0 m along the flume and at 0.75, 1.25 and 2.0 m across the flume. Whilst wave gauges were placed at -0.75, 0.5, 2.0 and 5.0 m along the flume and at 0.75, 1.25 and 2.0 m across the flume. T1 represents transect 1, T2 is transect 2 and T3 transect 3.

The *Rhizophora* root mimics were constructed using pine poles (0.03 m in diameter, 0.7 m long), and were pushed into holes in the plywood until the pine reached the concrete floor (Figure 3B). *Spartina* mimics were mimicked with straightened plastic tubing (0.006 m in diameter, 0.5 m long), which were pushed onto a nail (0.2 m) in the plywood (0.2 m of the *Spartina* mimics were buried in the sediment) (Figure 3A).
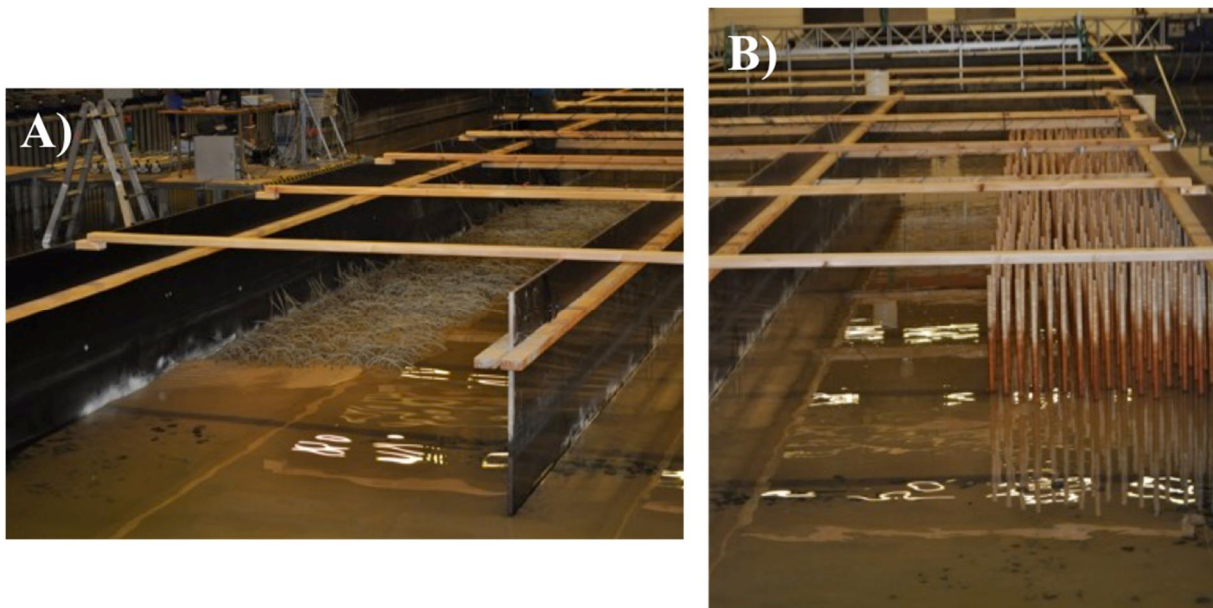
Figure 3. Showing salt marsh mimics on the left hand side (A) and mangrove mimics on the right hand side (B).

After mimics had been fixed, sediment (non-cohesive, 0.18 mm) to a height of 0.2 m was placed into the flume. In both cases, we had two separate patches of the same vegetation on either side of the flume with a wall and a 5 m dividing channel between them, so that the configuration covered the entire width of the flume (Figure 2).

To measure the hydrodynamics, we deployed 6 Acoustic Doppler Velocimeters (ADVs) across the flume, 3 on the *Rhizophora* mimic side and 3 on the *Spartina* mimic side (Figure 2). Waves were measured with fixed conductive wave gauges (Figure 4).
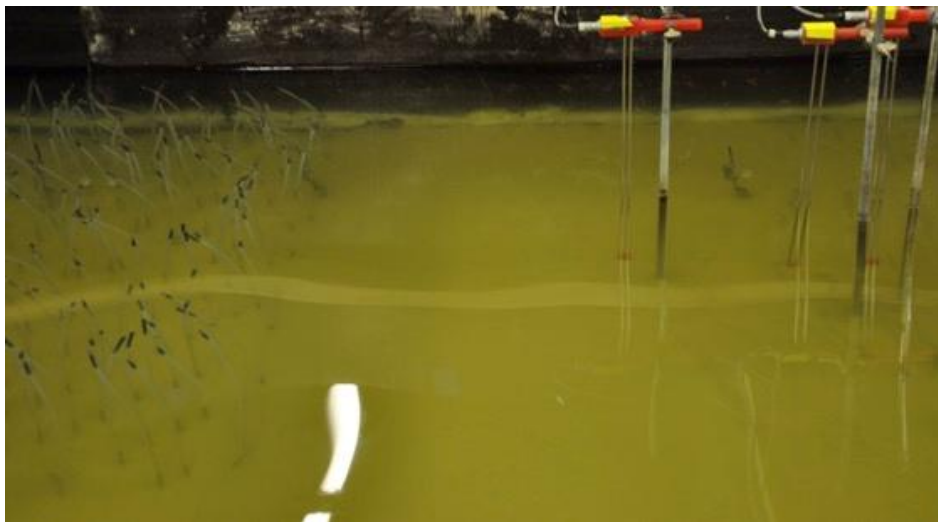
Figure 4. Showing the three waves gauges (right hand side) at the front of the salt marsh patch (left hand side).

The ADV's measured velocity profiles acquiring points every 5 cm in the vertical, except in the second transect where points every 2 cm were recorded. Surface elevation change at in the vegetation patches was measured using sedimentation erosion bars (SEBs), with elevation measurements at 5-10 cm intervals using metal pins lowered through the bar. The bars were moved along the flume taking measurements at -0.75, -0.1, 0.1, 0.5, 1.5, 2.5, 5, 7.5, 10 and 10.75 m. Behind the vegetation a perforated sloping beach was located, so that the waves were not

reflected back into the vegetation patches but the flow was maintained. After each hydrodynamic condition, the bathymetries of the vegetation patches were measured using the SEBs and then the sediment re-levelled. When we changed the density the flume was emptied, and half the mimics were taken from each vegetation patch. Runs were carried out using two different densities of each vegetation (*Rhizophora* roots low 42 roots m^{-2}, high 84 roots m^{-2} and *Spartina* stems low 210 plants m^{-2}, high 420 plants m^{-2}). We applied waves (H = 0.08 m and T = 0.8, 1.1, 1.4 s), currents (v = 0.3 ms^{-1}) and combined waves and currents (H=0.08 m, T= 0.8, 1.1, 1.4 s, v=0.3 ms^{-1}). We investigated current-only and waves-with-currents (in flood tide settings i.e. waves and currents propagating in the same direction) conditions, as in previous studies (Anderson and Smith, 2014; Hu et al., 2014; Jadhav et al., 2013). All these flow conditions were tested over a water depth equal to 0.30 m resulting in submerged (*Spartina* mimics) and emergent (*Rhizophora* mimics) vegetation conditions.

3. RESULTS AND DISCUSSION

Wave height evolutions along the two vegetation meadows were analysed. 50 waves were considered in the analysis and mean wave height was obtained. Figure 5 shows results for two wave conditions: H = 0.08 m and T = 0.8 and 1.1 s. Wave height values are divided by the incident wave height measured at 0.5 m offshore the meadow. Figure 5 shows a higher attenuation along the first 2 m for the mimic mangroves than for the saltmarshes.
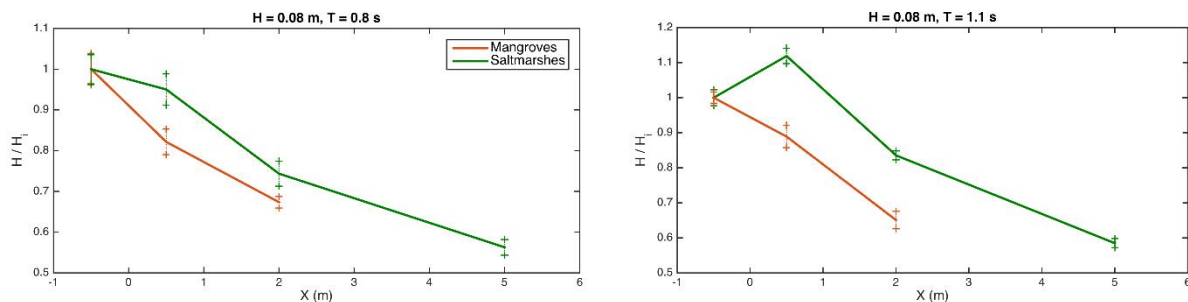
Figure 5. Wave height evolution along the mangrove (brown) and saltmarshes (green) meadow for two wave conditions: H = 0.08 m, T = 0.8 s and H = 0.08 m, T = 1.1 s. X = 0 shows the beginning of the meadows. Mean wave height values divided by the incident wave height (H$_i$) for 50 waves are displayed and standard deviation are shown in dotted lines.

Waves (H=0.08 m, T=1.1 s) showed sediment accumulation (≈2-4.5 cm) in the mimic *Spartina* patch at high densities. Whilst for mimic *Rhizophora* roots, sediment accumulation was only measured at the front of the patch, the remaining patch showed little or no change from the initial bed level. Previous research has found that shoot stiffness was the most significant plant trait involved in wave attenuation (Bouma et al., 2005). The sediment patterns and wave gauges agreed with this. The stiffer *Rhizophora* mimics significantly reduced attenuated wave height at the front of the patch causing sudden sediment deposition, whilst *Spartina* plants gradually attenuated wave height thus allowing for deposition through the entire patch.

When we combined currents (v=0.3 ms^{-1}) with waves (H=0.08 m, T=1.1 s), sediment movement was greater in both mimic *Rhizophora* roots and *Spartina* plants. *Spartina* plants in the initial patch edge showed erosion, but the majority of the patch showed accumulation (≈ 2-5.5 cm). *Rhizophora* mimics had widespread erosion across the entire patch and showed only two areas of accumulation, one at 2.5 m and the other at the 10 m point on the channel side. These points also were a hotspot for the *Spartina* mimic patch, which also showed accumulation at this point. Flexible canopies such as *Spartina* are more efficient at reducing erosion by reconfiguring their leaves with combined waves and currents (Peralta et al., 2008) so deflecting the flow, whilst the mimic roots had greater flow through. The greater erosion in the channel of the *Spartina* mimics also indicates higher lateral flow deflection from the *Spartina* mimics compared to the *Rhizophora* root mimics,

which had lower channel erosion. For salt marsh plants, increased sedimentation allows for the lateral expansion of their populations (Peralta et al., 2008).

When reducing the density of the plants and roots, we found that *Spartina* mimics again showed higher accumulation and lower erosion compared to *Rhizophora* root mimics, with combined waves and currents. Indicating that even at lower densities salt marsh plants accumulate more sediment and reduce greater erosion compared to *Rhizophora* roots. Although there was greater erosion within the *Spartina* patches compared to higher densities, this could be because lower density plants can sway within the water column causing turbulence thus increasing sediment erosion (Bouma et al., 2007). Additionally, higher salt marsh densities can cause skimming flows as described above, where flow is deflected around the patch. Occurrence of skimming flow protects sediments from erosion, by lifting the boundary layer and displacing the high Reynolds stresses to areas higher up in the water column (Bouma et al., 2007).

Interesting for low and high densities with combined waves and currents, an eroded area at the front of the patch can clearly be seen. *Rhizophora* root mimics showed higher levels of erosion (>10cm) compared to *Spartina* mimics (>5cm). Additionally, *Spartina* mimics showed a distinct edge of erosion whilst *Rhizophora* root mimics show a much more graduated erosion edge. The higher erosion in the *Rhizophora* is because the roots extend through the entire water column whilst the *Spartina* plants were deflected by the flow covering only part of the water column, and there is a higher density of stems in *Spartina* mimics than the *Rhizophora* mimics. The eroded sediment in both patches are trapped within the vegetation patches, as it can be seen that accumulation beyond the eroded patches is still high.

ACKNOWLEDGEMENT

REFERENCES

Anderson, M.E., Smith, J.M., 2014. Wave attenuation by flexible, idealized salt marsh vegetation. Coastal Engineering 83, 82-92.

Balke, T., Bouma, T.J., Herman, P.M.J., Horstman, E.M., Sudtongkong, C., Webb, E.L., 2013. Cross-shore gradients of physical disturbance in mangroves: implications for seedling establishment. Biogeosciences 10, 5411-5419.

Balke, T., Herman, P.M.J., Bouma, T.J., 2014a. Critical transitions in disturbance-driven ecosystems: identifying Windows of Opportunity for recovery. Journal of Ecology 102, 700-708.

Balke, T., Herman, P.M.J., Bouma, T.J., Nilsson, C., 2014b. Critical transitions in disturbance-driven ecosystems: identifying Windows of Opportunity for recovery. Journal of Ecology 102, 700-708.

Balke, T., Swales, A., Lovelock, C.E., Herman, P.M.J., Bouma, T.J., 2015. Limits to seaward expansion of mangroves: Translating physical disturbance mechanisms into seedling survival gradients. Journal of Experimental Marine Biology and Ecology 467, 16-25.

Bouma, T.J., De Vries, M.B., Low, E., Peralta, G., Tanczos, C., Van de Koppel, J., Herman, P.M.J., 2005. Trade-offs related to ecosystem engineering: A case study on stiffness of emerging macrophytes. Ecology 86, 2187-2199.

Bouma, T.J., van Duren, L.A., Temmerman, S., Claverie, T., Blanco-Garcia, A., Ysebaert, T., Herman, P.M.J., 2007. Spatial flow and sedimentation patterns within patches of epibenthic structures: Combining field, flume and modelling experiments. Cont. Shelf Res. 27, 1020-1045.

Hu, Z., Suzuki, T., Zitman, T., Uittewaal, W., Stive, M., 2014. Laboratory study on wave dissipation by vegetation in combined current–wave flow. Coastal Engineering 88, 131-142.

Jadhav, R.S., Chen, Q., Smith, J.M., 2013. Spectral distribution of wave energy dissipation by salt marsh vegetation. Coastal Engineering 77, 99-107.

Losada, I.J., Maza, M., Lara, J.L., 2016. A new formulation for vegetation-induced damping under combined waves and currents. Coastal Engineering 107, 1-13.

Maza, M., Lara, J.L., Losada, I.J., 2013. A coupled model of submerged vegetation under oscillatory flow using Navier–Stokes equations. Coastal Engineering 80, 16-34.

Maza, M., Lara, J.L., Losada, I.J., 2016. Solitary wave attenuation by vegetation patches. Advances in Water Resources 98, 159-172.

Moeller, I., Kudella, M., Rupprecht, F., Spencer, T., Paul, M., van Wesenbeeck, B.K., Wolters, G., Jensen, K., Bouma, T.J., Miranda-Lange, M., Schimmels, S., 2014. Wave attenuation over coastal salt marshes under storm surge conditions. Nature Geoscience 7, 727-731.

Morris, J.T., Sundareshwar, P.V., Nietch, C.T., Kjerfve, B., Cahoon, D.R., 2002. Responses of coastal wetlands to rising sea level. Ecology 83, 2869-2877.

Nepf, H.M., 1999. Drag, turbulence, and diffusion in flow through emergent vegetation. Water Resources Research 35, 479-489.

Peralta, G., van Duren, L.A., Morris, E.P., Bouma, T.J., 2008. Consequences of shoot density and stiffness for ecosystem engineering by benthic macrophytes in flow dominated areas: a hydrodynamic flume study. Mar. Ecol. Prog. Ser. 368, 103-115.

Quartel, S., Kroon, A., Augustinus, P.G.E.F., Van Santen, P., Tri, N.H., 2007. Wave attenuation in coastal mangroves in the Red River Delta, Vietnam. Journal of Asian Earth Sciences 29, 576-584.

Temmerman, S., Meire, P., Bouma, T.J., Herman, P.M.J., Ysebaert, T., De Vriend, H.J., 2013. Ecosystem-based coastal defence in the face of global change. Nature 504, 79-83.

V – LUH – WAVE AND CURRENT BASIN & LARGE WAVE FLUME

The Wave and Current Basin is a multidirectional wave and current basin (WB) with 2nd order wave generation and active wave absorption. The overall wave basin dimensions are 30 m in width and 15 m in length. It is equipped with a state-of-the-art multidirectional wave maker – consisting of 72 piston wave paddles (each 0.4 m wide and 1.8 m high) – and used to generate 1st and 2nd order regular waves and nature-like long and short crested wave spectra on a total length of 28.8 m. The wave maker can operate with a maximum stroke of 1.2 m and a maximum paddle velocity of 3.0 m/s. A high-class multilayer mesh screen absorber acts as a passive wave absorber East, West and South in the basin. By high-precision real-time analysis of the distinct surface elevation at each wave paddle the active absorption control enables properly experiments over long time frames including the following boundary conditions and features covering a wide range of needs:

- Directional waves with variable wave angles up to ±55° to the perpendicular line of the wave maker
- Maximum significant wave height: Hs = 0.25 m
- Up to 1.0 m water depth
- Active absorption of re-reflected signals up to 6 Hz
- Current generation (5.0 m3/s) parallel to the wave maker up to 0.3 m/s for 1m water depth over the entire basin width
- Extra large sand pit 7.0 x 5.0 x 1.2 m (LxWxD) in the center of the basin with circumferential sand trap on demand

.

The Large Wave Flume (Großer Wellenkanal, GWK) is the most important facility for basic and applied research on coastal engineering phenomena at Forschungszentrum Küste (FZK). FZK is a Joint Central Institution of Leibniz Universität Hannover and Technische Universität Braunschweig

With about 300m length, 5m width and 7m depth it is considered to be one of the largest facilities of its kind worldwide. The huge dimensions of GWK are necessary to perform unique large scale experiments for the investigation of certain phenomena that cannot be arbitrarily downscaled.

The piston type wavemaker of GWK has a maximum stroke of 4.2 m and is equipped with an active wave absorption system to avoid unwanted re-reflections of waves at the wave paddle. The standard implementation allows for the generation of regular waves, theoretical and measured natural wave spectra, focused waves and solitary waves. At a maximum water depth of 5 m the maximum wave height for regular waves is 2.1 m and for wave spectra 1.3 m significant wave height at the wave paddle.

The data acquisition system at GWK can record up to 120 channels simultaneously with a maximum digitising rate of 20 kHz per channel. Due to the large number of different measurement devices following physical parameters can be recorded: Water surface elevation, wave runup and overtopping, water velocities, water pressures, acceleration and deformation of structures, forces on structures, sediment concentration, survey of morphological processes. The obtained data can be visualized and analysed by comprehensive software tools immediately after the recording.

GWK represents a unique installation for European development of new integrated strategies to capture all processes associated with wave-induced seabed-structure interactions, wave-seabed interactions, dynamic structure-foundation interactions, wave-induced sediment transport and morphological changes.

MEASURING WAVE RUN-UP, OVERTOPPING AND DAMAGE OF RUBBLE-MOUND BREAKWATERS IN SCALE MODEL TESTS

João A. Santos (1), Rute Lemos (2), Julius Weimper (3), Oliver Gronz (3), Bas Hofland (4), José Sande (5), Liliana Pinheiro (2), Jan H. Spans (6), Enrique Peña (5), Maria Teresa Reis (2), Conceição Juana Fortes (2), Andrés Figuero (5), Emilio Laiño (5), Antje Bornschein (7), Nils B. Kerpen (8), Francisco Pedro (1), Mário Coimbra (1), Moritz Körner (7), Jeroen van den Bos (4), Bastien Dost (3), Rita Carvalho (9), Alberto Alvarellos (5) & Reinhard Pohl (7)

(1) ISEL – Instituto Superior de Engenharia de Lisboa, Instituto Politécnico de Lisboa, Portugal, E-mail: jasantos@dec.isel.ipl.pt, a32643@alunos.isel.pt, a39777@alunos.isel.pt
(2) LNEC, Portugal, E-mail: rlemos@lnec.pt, lpinheiro@lnec.pt, treis@lnec.pt, jfortes@lnec.pt
(3) UTrier, Germany, E-mail: weimper@uni-trier.de, gronz@uni-trier.de, s6jodost@uni-trier.de
(4) TU Delft, the Netherlands, E-mail: B.Hofland@tudelft.nl, J.P.vandenBos@tudelft.nl
(5) Universidade da Coruña, Spain, E-mail: jose.sande@udc.es, epena@udc.es, andres.figuero@udc.es, e.laino@udc.es, alberto.alvarellos@udc.es
(6) Saxion University of Applied Sciences, The Netherlands, E-mail: 444898@student.saxion.nl
(7) TU Dresden, Germany, E-mail: antje.bornschein@tu-dresden.de, reinhard.pohl@tu-dresden.de, koerner.moritz96@icloud.com
(8) Leibniz University Hannover, Germany, E-mail: kerpen@lufi.uni hannover.de
(9) MARE, UCoimbra, Portugal, E-mail: ritalmfc@dec.uc.pt

A set of scale-model tests was carried out at the wave basin of the Leibniz University Hannover to extend the range of wave steepness values analysed in run-up, overtopping and armour layer stability studies, focusing on oblique extreme wave conditions and on their effects on a gentler slope breakwater's trunk armour and roundhead. The paper describes the model set-up and operation concentrating on the measurement techniques used in those tests, namely on the innovative techniques for armour layer damage characterization.

1. INTRODUCTION

Wave breaking / run-up / overtopping and their impact on the stability of rubble-mound breakwaters (both at trunk and roundhead) are not adequately characterized yet for climate change scenarios. The same happens with the influence of high-incidence angles on such phenomena.

Several former investigations on wave run-up and overtopping of (impermeable and permeable) coastal structures aimed at quantifying the influence of oblique waves on mean overtopping discharge, water layer thickness and velocities through the development of empirical formulas of a reduction factor for wave obliquity (e.g. Nørgaard et al., 2013). However, most of the formulas did not consider very oblique wave approach.

Regarding the stability of armour layers, several authors have proposed guidelines on how to consider the effects of oblique waves (e.g. Van Gent, 2014). Especially for very oblique waves, for which the increase in stability is the largest, limited data are available.

Van Gent (2014) performed a set of physical model tests to assess the effects of oblique waves on the stability of rock slopes and of cube armoured rubble-mound breakwaters (single and double layers) mostly on a 1:1.5 slope. The tests included wave directions between perpendicular (0°) and parallel (90°) to the longitudinal structure axis, with long and short-crested waves. A series of tests was performed with an increasing wave height between 0.025 m to 0.274 m and constant wave steepness of 0.03 or 0.04 (only for a few tests).

Van Gent (2014) recommends the study of the influence of oblique wave attack on the stability of rubble-mound structures for: a) other slope angles, especially gentler rock slopes; b) other values of wave steepness, to cover values of the surf similarity parameter outside the range of 2.2-3.5 for rock and 3-3.5 for cubes; c) interlocking armour units.

The gaps in existing data and the R&D&I experience of the team members triggered the common interest in developing the present experimental work. Its main goal is to contribute to a new whole understanding of the phenomena to mitigate the effects of future sea-level rise on European

coastal structures, including the run-up and overtopping characterization on rough and permeable slopes, as well as to check and extend the validity range of the formulas developed for armour layer stability.

The key point is to expand the range of wave steepness values analysed in run-up, overtopping and armour layer stability studies, focusing on oblique extreme wave conditions and on their effects on gentler sloping breakwater's trunk armour and roundhead. By studying wave run-up and overtopping of porous armour layers, the present work covers Van Gent (2014) recommendations. This paper aims at describing this experiment, which involved people from eight different institutions and lasted for six weeks, starting with an empty wave tank at the Marienwerder facilities of the Leibniz University Hannover (LUH) and finishing with a rubble-mound again in an empty tank. The paper includes a brief description of the model construction as well as the equipment used in the experiments, the test plan and some preliminary results.

2. MODEL CONSTRUCTION

A stretch of a rubble-mound breakwater (head and part of the adjoining trunk, with a slope of 1(V):2(H)) was built in the wave basin of the LUH to assess, under extreme wave conditions (wave steepness of 0.055) with different incidence wave angles (from 40º to 90º), the structure behaviour in what concerns wave run-up, wave overtopping and damage progression of the armour layer. Two types of armour elements (rock and Antifer cubes) were tested.

Fig. 1 presents the plan view of the breakwater model as well as the cross section. The trunk of the breakwater was 7.5 m long and the head had the same cross section as the exposed part of breakwater. The model was 9.0 m long, 0.82 m high and 3.0 m wide. The reason for building such a large breakwater model is to reduce the scale effects associated to wave-induced flows across small models. The angle between the longitudinal axis of the breakwater and the tank wall was 70º.
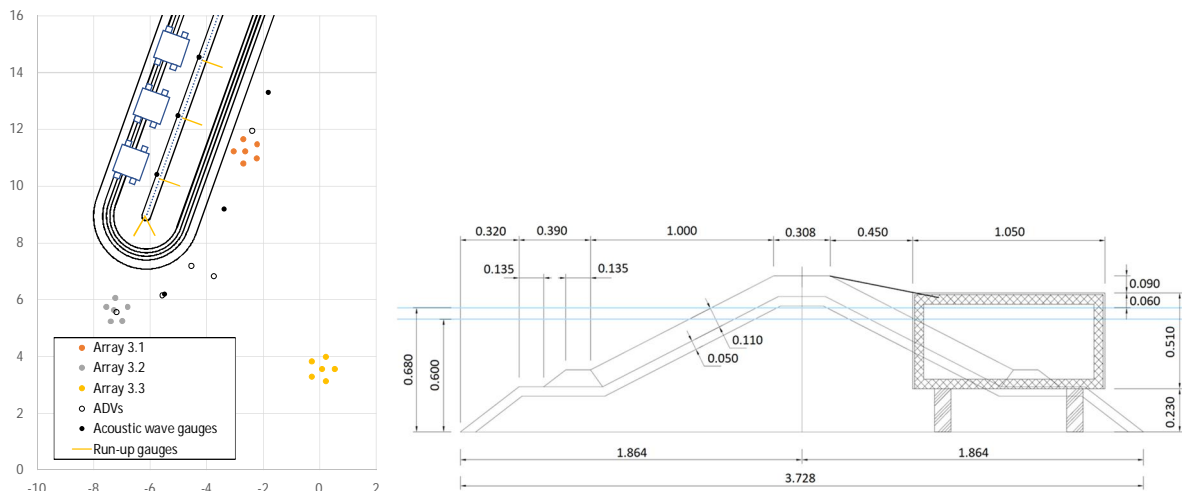
Figure 1. Plan view and cross-section of model breakwater

The model construction started with the assembly of a cage made of the core moulds for the breakwater trunk and connecting beams. Once the cage was complete, it was positioned at the wave tank bottom so that the desired alignment for the model axis was obtained. One extra mould was placed orthogonal to the end of the trunk, to help with the breakwater head construction.

Before starting to build the core by pouring the gravel (15 m^3 with a median weight of 6 gf), the three overtopping reservoirs were put in place. Once the core of the breakwater model was built, the moulds for the filter layer were placed on top of the core moulds and the filter layer material (gravel with a median weight of 59 gf) was poured in the remaining spaces and shaped as in the core.

After the shaping of the filter layer was complete, its moulds were removed from all trunk cross-sections. At the breakwater head, both the core and the filter layer moulds were removed to ensure nothing hampered the percolation across the core of the breakwater's head.

Then the moulds for the toe berm were placed on top of the filter layer. These moulds were held in place with small mounds of the toe material (gravel with a median weight of 260 gf) placed on both sides of each mould and then the rest of the toe was built along the breakwater.

The construction of the breakwater armour layer started at the breakwater head and at the 2.5 m wide adjoining strip. Here, 351 gf Antifer cubes were deployed in two layers, such that the porosity of the armour layer was 37%. Gravel with a median weight of 315 gf was employed both at the exposed and lee parts of the rock armour layer.

3.   EQUIPMENT DEPLOYED

Four different categories can be identified in the equipment deployed in the experiment according to the variables measured:
- Sea waves;
- Run-up;
- Overtopping;
- Armour layer damage.

A plan view of the key instruments for those variables (apart from "armour layer damage") is presented on the left of Fig. 1.

The sea waves generated by the wavemaker, as well as the incident sea waves on the structure and the ones reflected by it, were measured with arrays made of six acoustic wave probes (the vertices of an approximately regular pentagon and its centre of gravity). One wave gauge array was deployed in front of the wavemaker, another in front of the breakwater head, aligned with the breakwater crest, and one approximately at the middle of the breakwater trunk, in front of the entrance to the second overtopping reservoir.

In front of the entrance to the first and third overtopping reservoirs, two isolated acoustic wave probes were deployed. A third acoustic wave probe was deployed in front the breakwater head, approximately in the middle of the dihedral angle formed by the vertical plane that marks the end of the trunk and the plane that contains the middle of the breakwater crest.

Five acoustic Doppler velocimeters (ADV) were deployed close to the breakwater to characterise the wave-induced flow there. Three of them were deployed close to acoustic wave probes, to have an alternative source of information to compute the incident and reflected waves. The remaining two ADVs were placed approximately on the vertical plane that marks the end of the breakwater trunk. Despite the difference between the vertical positions of the acoustic transmitter of the several ADVs, the acoustic receiver that defines the x-axis was aligned with the breakwater crest in all ADVs.

Capacitive wave gauges, 0.87 m long, were deployed over the armour layer to measure wave run-up. Three were deployed at the breakwater trunk, close to the sections where wave overtopping was to be measured, and two at the breakwater head (one in the plane that contains the breakwater axis and the other was deployed perpendicularly to it).

A staff graduated with a chequered pattern was used close to the run-up gauge of the root overtopping reservoir, to get an alternative way of measuring run-up by processing the video frames obtained with a camera during the experiments. This staff was embedded in the armour layer and a column made of 20 black and white squares had a length of 0.328 m.

Each overtopping reservoir had a capacity of 500 l and was placed inside a watertight container. The water volume inside each overtopping reservoir was weighted with a load cell placed between the bottom of that reservoir and its container. A trapezoidal chute 0.60 m long and an entrance width of 0.60 m (and an exit width of 0.50 m) conveyed the overtopped water volume from the inner edge of the breakwater crest into the reservoir. An acoustic wave probe was deployed above the entrance of each chute to identify the occurrence of overtopping events. A capacitive wave gauge was placed inside each overtopping reservoir to have some redundancy in the measurement of the overtopping volume provided by the load cell. The cross-section in Fig. 1 includes the overtopping reservoir and the chute from the breakwater crest into the reservoir. In

Fig. 3 there is a picture from the entrance of the overtopping reservoir at the breakwater root. In addition to the chute, the acoustic wave gauge to identify overtopping events and the graduated staff deployed in front of that reservoir can be seen. During the tests, a video camera recorded the free-surface on the graduated staff. It is expected that run-up parameters can be extracted from such videos using the methodology of Bornschein et al. (2014).

Three different techniques were used to measure armour layer damage in the tests, in addition to the visual identification of rocking and displaced armour units.

Figure 3. General layout at the entrance of an overtopping reservoir (run-up wave gauge, acoustic wave gauge to identify overtopping events, graduated staff).

The first one is based in stereo photogrammetry. This means that two cameras have to hang above the breakwater model so that two simultaneous pictures of almost the same area can be taken by the two cameras. The procedures implemented to process the photo pairs enable the reconstruction of the scene corresponding to the submerged part of the breakwater without the need to remove the water from the wave basin, Pedro et al. (2015).

The second technique is based on the use of the Kinect motion sensor that travels over the study area. A reconstruction of the armour layer's above-water region can be made based on the collected information. Additionally, since it is possible "to see" below the water level, a first estimate of the armour layer's submerged region can also be made. Such rough estimate can be corrected with the information gathered with the Kinect motion sensor after the water is removed from the wave tank, Sande et al. (2018).

Since these two techniques implied the movement of the measuring equipment above the study region, an aluminium rail made of a straight stretch 7.85 m long and of a semi-circumference stretch with a diameter of 1.80 m was hung 2.00 m above the wave basin bottom. Fig. 4 shows the rail assembly as well as the special wagon that was moved along the rail and where the cameras ensemble or the Kinect motion sensor were hung.

A laser scan survey of the armour layer envelope established the ground truth for the measurements made with the other techniques. This was done at the second day of tests, just before the beginning of the test series and at the end of that test series. The same happened with the last test series.
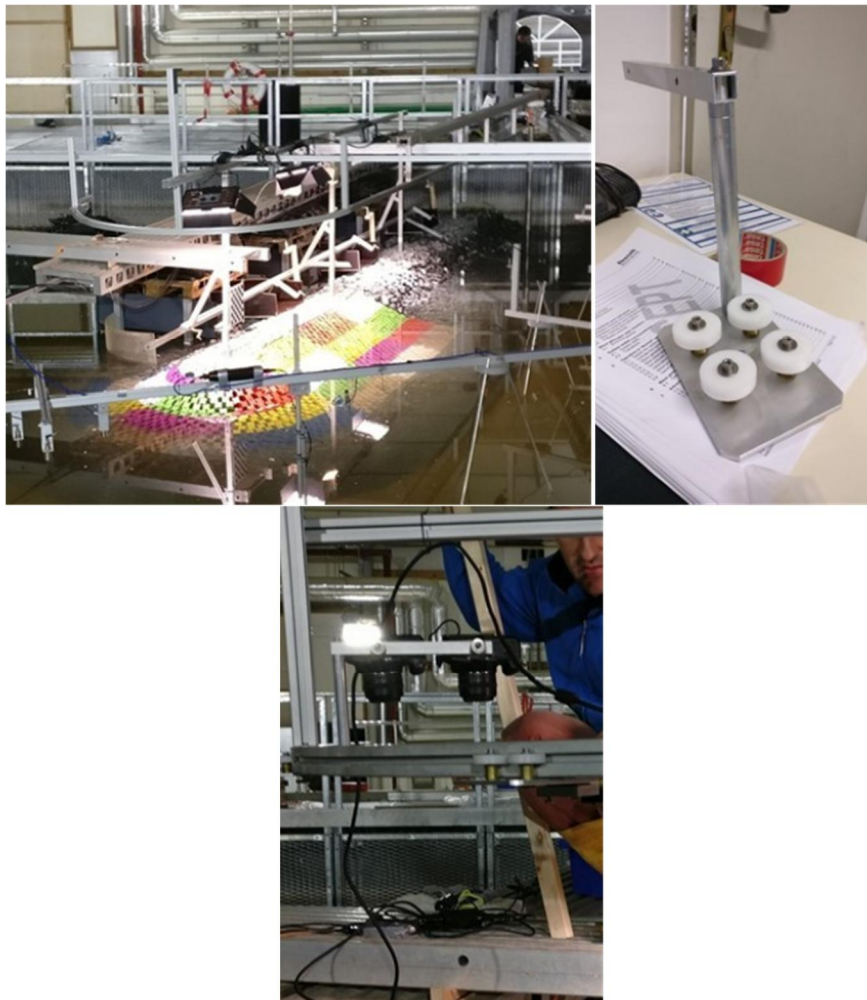
Figure 4. Left: rail to support the photographic cameras and the Kinect motion sensor; Middle: wagon to carry those cameras; Right: wagon on the rail with two cameras.

The third technique consists on the use of accelerometers inside a couple of armour layer elements, an extension of the Smartstones of Gronz et al. (2016). In these experiments 6 of such artificial armour elements were used, although there were not all working at the same time. Also, a second type was used. In these sensors open-source Arduino based hardware was used to obtain accelerations and rotations of the units (Hofland et al., 2018). These sensors were embedded in 3D-printed Antifer shapes that were weighted by lead to obtain the correct mean density. The main aim of using these sensors was to get experience in a project, to see whether this relatively cheap technology is developed enough to be used in an elaborate large-scale project like the present one. Two out of four functioned well for all tests. All smart Antifers were placed on the roundhead around the water line facing the incoming wave direction, as can be seen in Fig. 5.

Before and after each test, pictures were made from exactly the same position above the area where the smart armour units were deployed. From these picture sets small settlements can be detected (Hofland and Van Gent, 2016). These will be used to see whether the rocking of –and possible mechanical damage to– the Antifers can be linked to these small settlements.
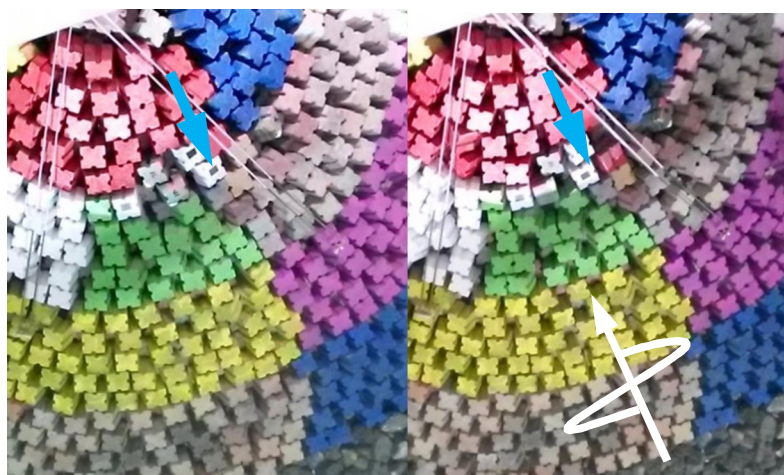
Figure 5. Three instrumented Antifer cubes in the roundhead, before (left) and after (right) test 23. Blue arrow points to the so-called "Cube 3"

4. TEST PLAN

For each incidence wave angle, at least 4 different wave conditions acted on the model (significant wave heights Hs=0.100 m, 0.150 m, 0.175 m and 0.200 m and the corresponding peak periods Tp=1.19 s, 1.45 s, 1.57 s and 1.68 s).

For long-crested waves and a water depth of 0.60 m, 5 incidence wave angles (40º, 55º, 65º, 75º and 90º) were considered. Since no major run-up, overtopping or damage were expected along the structure for high incidence angles, in the test series with a water depth of 0.68 m and long-crested waves, the number of incidence angles was reduced to 3 (40º, 55º and 65º).

The influence of the directional spreading of short-crested waves was investigated for the lowest water depth (0.60 m) and the incidence angles of 40º and 65º, the directional spreading being 50º. Finally, for the incidence angle of 40º results were also obtained for the highest water depth (0.68 m) and short-crested waves with a directional spreading of 50º.

5. RESULTS

Since some equipment was brought by the people from the institutions participating in the experiments and taken with them when they returned home, the first set of data chosen to be processed was for a water depth of 0.60 m and incident long-crested waves making an angle of 65º with the normal to the breakwater axis. This corresponds to a period when all equipment was available for the experiments. Moreover, for this set of experiments, it was possible to have a laser scan survey before it started and after its end.

5.1 Sea waves

The data collected at the acoustic arrays was processed for each array individually, using temporal and spectral analyses. Table 1 presents the averages of the significant wave heights and of the peak periods obtained for each array and test of the series.

Table 1. Wave characteristics. Average quantities obtained in the acoustic wave gauge arrays with temporal and spectral analyses.

Test	Goal		Array 3.3		Array 3.2		Array 3.1	
	Hs (m)	Tp (s)	Hs (m)	Tp (s)	Hs (m)	Tp (s)	Hs (m)	Tp (s)
17	0.100	1.19	0.108	1.19	0.100	1.19	0.107	1.19
18	0.150	1.45	0.147	1.47	0.143	1.46	0.150	1.47
19	0.175	1.57	0.168	1.58	0.162	1.60	0.171	1.57
20	0.200	1.68	0.189	1.65	0.177	1.67	0.185	1.69

The values for array 3.3, the one closest to the wavemaker, are quite similar to the test goal. Peak-period relative errors are smaller than 2% whereas the maximum significant wave height relative error is equal to 8% (it occurs for the smallest wave height).

The MATLAB toolbox DIWASP (Johnson, 2002) was employed to evaluate the directional spectrum of the waves at the location of the arrays made of acoustic wave probes. The six probes in each array were used to estimate the directional spectrum with the iterated maximum likelihood method of Pawka (1983). Since in this set of tests the wavemaker generated long-crested waves only, the estimated directional spectra are quite narrow, with most of the energy concentrated around the direction of 265° (this corresponds to waves propagating at an angle of 95° to the wavemaker and an angle of 65° to the normal to the breakwater). This can be seen in Fig. 6 with the estimated directional spectrum in front of the wavemaker for test 18.

Table 2 presents the wave characteristics obtained from the directional spectra estimated for the locations of the 3 arrays of acoustic wave probes. The column "Dir" contains the mean direction at the peak period. It can be seen in that table that the mean direction at the peak period in front of the wavemaker is almost 275°, which corresponds to the desired direction at the wavemaker.

Table 2. Wave characteristics. Quantities obtained from directional spectrum with IMLM.

Test	Goal		Array 3.3			Array 3.2			Array 3.1		
	Hs(m)	Tp(s)	Hs(m)	Tp(s)	Dir(°)	Hs(m)	Tp(s)	Dir(°)	Hs(m)	Tp(s)	Dir(°)
17	0.100	1.19	0.108	1.21	276	0.108	1.19	274	0.107	1.21	274
18	0.150	1.45	0.151	1.46	276	0.159	1.46	276	0.152	1.46	270
19	0.175	1.57	0.169	1.59	276	0.171	1.58	269	0.171	1.58	272
20	0.200	1.68	0.190	1.71	275	0.183	1.70	270	0.178	1.70	274

As the sea state propagates towards the breakwater model, there are some changes in the mean direction at the peak period, although not larger than 7°. Close to the wavemaker, the trend observed in table 1 can also be seen: as the wave height goal increases, so does the difference between target and measurement. One may conclude that the wavemaker has some difficulty to generate the highest waves. By comparing the values in Table 1 and Table 2, one may conclude that the significant wave height obtained from the temporal analysis is quite similar to the one obtained from the directional spectrum.
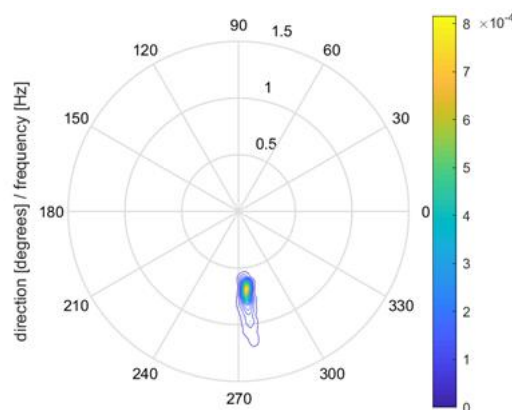
Figure 6. Directional spectrum estimated with the iterated maximum likelihood method. Data measured at the array of acoustic wave probes 3.3. Test 18: Hs = 0.150 m, Tp = 1.45 s.

One final test with the DIWASP toolbox was carried out with the free-surface elevation measured with the acoustic wave probe 3.2.6 (the central probe of array 3.2, the one in front of the breakwater head) and with the horizontal velocity components of the flow measured with ADV 2.3, the one closest to that acoustic wave probe. Since the ADV measurements did not start at the same time as the acoustic wave probes, the cross-correlation between the two signals was evaluated to find the time lag between them.

Fig. 7 presents the directional spectra obtained with such procedures for test 18 (Hs = 0.150 m Tp = 1.45 s). The agreement between the wave characteristics determined from the directional spectrum estimated from the probe + ADV data (Hs = 0.144 m Tp = 1,46 s Dir = 264°) with the

ones from the spectrum estimated with the array data (Hs = 0.159 m Tp = 1,46 s Dir = 276º) is a foreseen consequence of the similar shapes of the directional spectra shown in that figure.
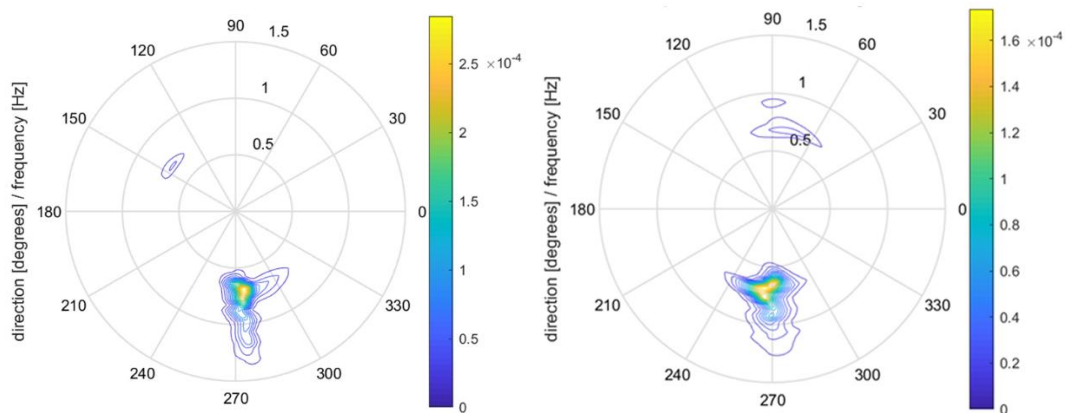

Figure 7. Directional spectra estimated with the iterated maximum likelihood method. Test 18: Hs = 0.15 m, Tp = 1.45 s. Left: data measured at the array of acoustic wave probes 3.3. Right: data measured at acoustic wave probe 3.2.6 and ADV 2.3.

5.2   Wave run-up and overtopping

Wave run-up and overtopping data analysis is still under progress.
Data from the capacitive gauges are used to determine the wave run-up height which is exceeded by 2 % of the incoming waves ($R_{2\%}$). The maximum wave run-up height for each run-up event is determined firstly. These values are than arranged with the highest first and the $R_{2\%}$ is determined. First attempts to analyse the video data led to the conclusion that this analysis will be very time consuming. The wave run-up on an armoured layer is characterised by a very turbulent and uneven water surface, which produces a lot of reflections. These reflections hinder a clear distinction of the upmost point of the water running up the slope. The use of different thresholds for converting the video frames into black-white pictures for data processing seems to be a promising way to overcome these difficulties.

5.3   Armour layer damage

A laser scan survey was carried out before the beginning of this set of tests (the second in a series of eleven) and before the eleventh set of tests. After each set of tests, the armour layer of the breakwater model had to be rebuilt, or at least some of the armour layer elements had to be put back in place. Before the last set of tests, the top layer of the armour with Antifer cubes (the breakwater roundhead and the adjoining trunk stretch 2.5 m wide) were completely rebuilt. Fig. 9 shows that despite all the rebuilding of the armour layer, no major differences were identified at one roundhead profile before the second set of tests and before the last set of tests.
Although photogrammetric data are still being processed, it is evident that the survey quality is highly dependent on the lighting conditions. Moreover, due to the rail height above the breakwater model, the surveyed area is limited to a strip 30 cm wide containing the still water level.
As to the Kinect surveys, preliminary results are quite interesting and innovative. In fact, to the authors' best knowledge, it is the first time that this sensor is used to measure damage in a breakwater head, with the sensor moving circularly along a rail.
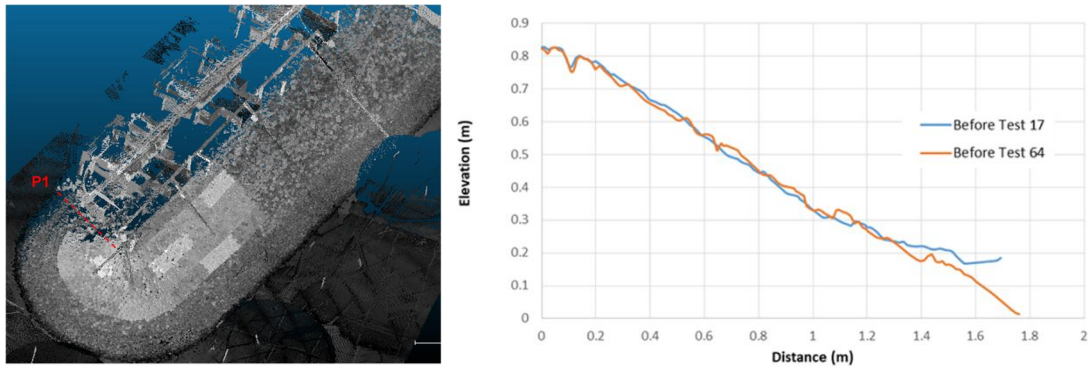
Figure 9. Roundhead profile at the beginning of the second and eleventh set of tests obtained from the laser scan survey.

The breakwater was correctly scanned, showing clearly the differences between the initial tests of the series with only movements between the armour units (increasing porosity) and tests with armour-unit extraction. Fig. 10 shows the initial state (before Test 17) and the final state (after Test 20) of the roundhead, whereas Fig. 11 presents the erosion and deposition data in mm. The density of area covered by the surface scanned was 0.50 points/mm^2. The analysis of the movements as a whole gave an estimation number of 19 pieces moved out of their initial position.

The scanning results enabled the detection of minor movements between the Antifer cubes with a displacement equivalent to 3 units and the evolution of the local porosity going from the initial value of 0.296 to the final value of 0.303. These results do suggest that Kinect can be used by laboratories and research groups to identify the different damage stages with a good resolution, not only in 2D cases, but also in 3D studies.
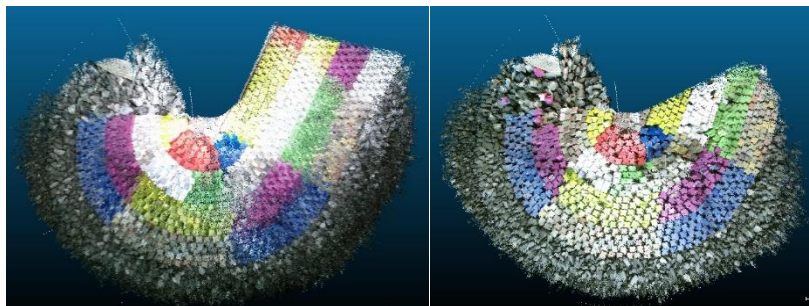
Figure 10. Roundhead scanned with Kinect. Left: before Test 17, Right: after Test 20.
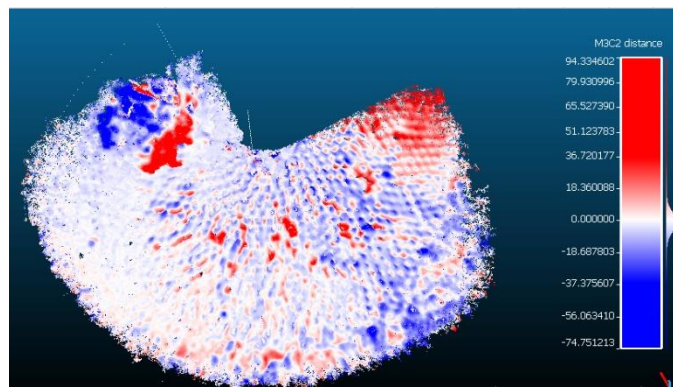
Figure 11. Movements of armour elements in the vertical direction. Red (erosion), blue (deposition.

For the Smartstone data, three approaches to detect the motions of Antifer cubes were tested:
(1) Local maxima above a certain threshold were obtained to calculate the number of peaks per number of waves. It was found that the obtained number of peaks per wave depends largely on

the threshold and results in much higher numbers compared to values from the literature (e.g. Hofland et al., 2018).

(2) Cross-correlation of a defined reference event, representing a typical rocking situation that was manually selected from the Smartstone data, resulting in a number of events per number of waves. Event detection based on correlation showed generally large differences to the visual estimation of the number of events, both in terms of the number and the temporal localization. The correlation technique appears to be more effective for gyroscope data, compared to the application for accelerometer data.

(3) A combination of high-pass and low-pass filters was applied and combined with a threshold also resulting in a number of events per number of waves. Events based on filtering were closest to the visual interpretation, but they were also influenced by the filter parameters.

The Arduino type smart Antifers did give signals over the duration of the test. A sampling frequency of 25 Hz could be obtained. This seems to be enough to obtain the rotational velocities directly from the gyroscopes. However, for obtaining the translation movements from integration of the accelerometer signals, this seemed to be insufficient.

Fig. 12 presents the recording of the motions of Cube 3 in test 29 (same water depth, long-crested waves with incidence angle of 40°, Hs = 0.175 m and Tp = 1.57 s). Cube 3 was one of the cubes that functioned during all tests. At the location of Cube 3 the regular packing of the Antifers opened up a little during testing. Moreover, the wave velocities are high. Hence, motion and rocking of the units can be expected. The location of Cube 3 before and after the test is indicated in Fig. 5. Cube 3 can be seen to have shifted during the test. In the top left graph of Fig. 12 the distribution over its components of the steady gravitational acceleration of 1G upward, can be seen to have shifted around t = 700 s. Hence, the cube's orientation relative to the horizontal plane has changed. Fig. 12 shows that Cube 3 rocked for nearly every wave, also around 700 s. As only one or two measurements are made during a rocking event, the accelerometer cannot be used to obtain a reliable estimate of the translation impact velocity, as that requires integration. As the gyroscope measured directly the rotational velocity θ, this rotational impact velocity is somewhat more reliable, and can be used for the structural analysis of the concrete Antifers. Since other cubes showed much less movement, this means that many cubes will have to be instrumented to obtain a good idea about the rocking motion of the entire armour layer. Hence it is of paramount importance that any such measurement technique is affordable.
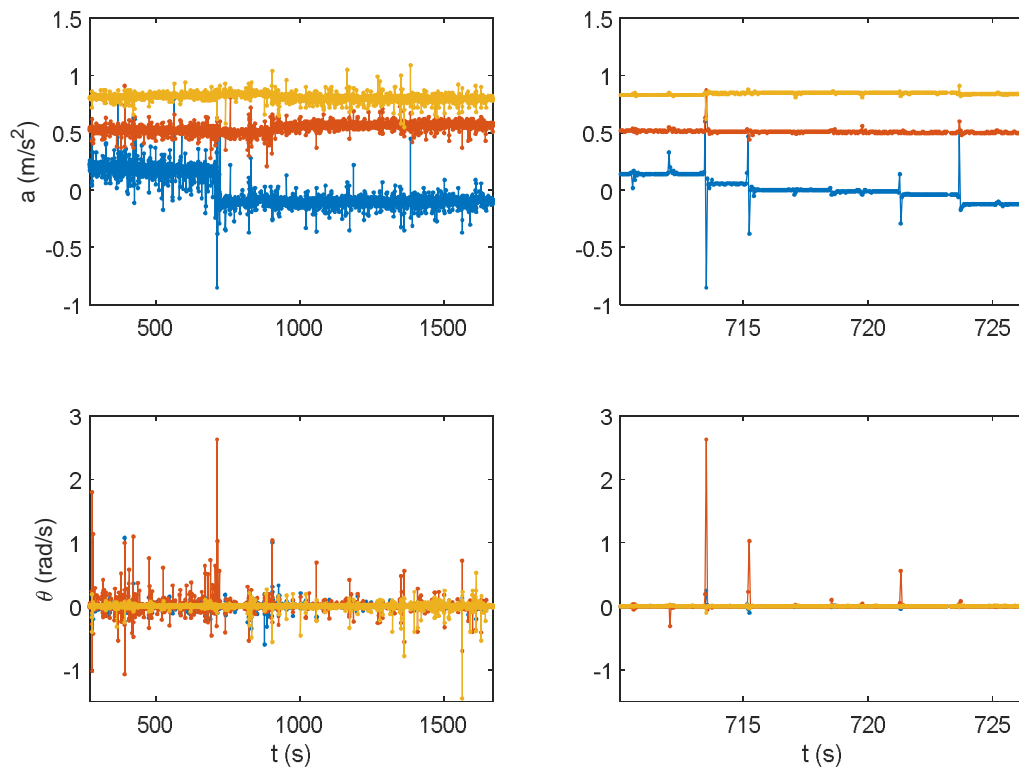
Figure 8. Time series of linear accelerations and angular velocities measured by Cube 3 in test 28.

6. CONCLUSIONS

The RODBreak experiment was a unique opportunity to characterize the influence of wave incidence obliquity on run-up, overtopping and damage evolution of the armour layer of rubble-mound breakwaters.

The incident waves produced by the wavemaker did comply with the plan, which means that the intended steepness of 0.055 was achieved.

This experiment also enabled the testing of several measuring procedures for armour layer evolution.

The two laser scan surveys before the beginning of the second and eleventh test series showed that, despite the wave action and the armour layer reconstructions, there was no significant settling of the breakwater model.

Although there is still a lot to process in the photogrammetry and Kinect surveys, it is clear that the results from the surveys of the armour layer envelope are relevant to understand the first stages and behaviour of the roundhead evolution, and to develop maintenance strategies before damage reaches failure.

The most effective technique to detect the motions from the Smartstone (Antifer cubes) data appears to be a filter-based technique applied to gyroscope data. Exemplary analysis of influencing factors for motions showed a generally higher number of events or peaks per waves for larger wave heights and positions close to the water level. However, these differences were mostly not significant.

The Arduino-based smart Antifer devices proved rather robust in use, although the sampling frequency needs to be increased. The number of impacts between Antifers (potentially leading to mechanical fracturing) and the extreme rotational velocities could be obtained.

ACKNOWLEDGEMENTS

REFERENCES

Bornschein, A., Pohl, R., Wolf, V., Schüttrumpf, H., Scheres, B., Troch, P., Riha, J., Spano, M. and Van der Meer, J. (2014). Wave run-up and wave overtopping under very oblique wave attack (CORNERDIKE-project). Proc. HYDRALAB IV Joint User Meeting, Lisbon, July.

Gronz, O., Hiller, P.H., Wirtz, S. and Ries, J.B. (2016) Smartstones: A small 9-axis sensor implanted in stones to track their movements, Catena, 142, 245-251.

Hofland, B., Arefin, S.S., Van der Lem, C. and Van Gent, M.R.A. (2018) Smart rocking armour units. Proc. 7th Int. Conf. on the Application of Physical Modelling in Coastal and Port Engineering and Science (Coastlab18), Santander.

Hofland, B. and Van Gent, M.R.A. (2016) Automatic settlement analysis of single-layer armour layers. Proc. 6th Int. Conf. on the Application of Physical Modelling in Coastal and Port Engineering and Science (Coastlab16), Ottawa.

Johnson, D. (2002) DIWASP, a directional wave spectra toolbox for MATLAB®: User Manual. Research Report WP-1601-DJ, Centre for Water Research, University of Western Australia.

Nørgaard, J.Q.H., Lykke Andersen, T., Burcharth, H.F. and Steendam, G.J. (2013) Analysis of overtopping flow on sea dikes in oblique and short-crested waves, Coast. Eng. 76, 43–54.

Pawka, S.S. (1983) Island shadows in wave directional spectra, J. Geophys. Research, 88(C4), 2579-2591.

Pedro, F., Bastos, M., Lemos, R., Fortes, C. and Santos, J.A. (2015) Toe berm damage progression analysis using a stereophotogrammetric survey technique, Proc. 7th SCACR - Int. Short Course/Conf. on Applied Coastal Research, Florence.

Sande, J., Laiño, E., Peña, J., Neves, M.G., Lemos, R., Figuero, A., Reis, M.T., Alvarellos, A. and Rabuñal, J. Application of scanning techniques for damage analysis in rubble mound breakwaters. Proc. 7th International Conference on the Application of Physical Modelling in Coastal and Port Engineering and Science (Coastlab18), Santander.

Van Gent, M.R.A. (2014) Oblique wave attack on rubble mound breakwaters, Coast. Eng. 88, 43-54.

DYNAMIC COASTAL PROTECTION: RESILIENCE OF DYNAMIC REVETMENTS (DYNAREV)

C.E. Blenkinsopp (1), P.M. Bayle (1), D. Conley (2), G. Masselink (2), E. Gulson (2), I. Kelly, (2), R. Almar (3), I.L. Turner (4), T.E. Baldock (5), T. Beuzen (4), R. McCall (6), Rijper, H. (7), A. Reniers (8), P. Troch (9), D. Gallach-Sanchez (9), A. Hunter (1), O, Bryan (1), G. Hennessey (1), P. Ganderton (2), S. Schimmels (10), M. Kudella (10)

(1) University of Bath, Bath BA2 7AY, UK.
(2) University of Plymouth, Plymouth PL4 8AA, UK.
(3) LEGOS, Toulouse, France.
(4) University of New South Wales, Sydney, NSW 2052, Australia.
(5) University of Queensland, Brisbane, QLD 4072, Australia.
(6) Deltares, 2600 MH Delft, Netherlands.
(7) Royal Boskalis Westminster N.V., 3356 LK Papendrecht, Netherlands.
(8) TU Delft, 2600 AA Delft, Netherlands.
(9) Ghent University, B-9000 Ghent, Belgium.
(10) Forschungszentrum Küste (FZK), Leibniz University Hannover & Technische Univeristät Braunschweig, 30167 Hannover, Germany.

A large-scale laboratory experiment was completed to investigate the performance of a dynamic cobble berm revetment designed to provide sustainable coastal protection under wave attack and a rising water level. The experiment demonstrated the inherent stability of the dynamic revetment, which was observed to be reshaped by every wave but retained its overall shape throughout the experiment with almost no loss of material. By comparing with a sand beach case, it was found that the revetment reduced shoreline retreat during an erosive wave condition and reduced runup excursions, thus eliminating erosion landward of the revetment. Overall the experiment provided significant new understanding of dynamic revetments and demonstrated the potential for dynamic revetments to provide low cost, robust coastal protection.

1.   INTRODUCTION

A recent study by Luijendijk *et al.* (2018) found that 24% of the world's beaches are eroding at rates exceeding 0.5 m/yr. The coastal zone has become heavily populated and developed, and in many countries is of key economic importance. Indeed, fifteen of the world's 20 megacities are located on the coast and, as such, ensuring the sustainability of coastal populations and infrastructure is of critical importance and will become ever more challenging and expensive as sea levels rise and wave conditions change due to the changing climate.

The typical coastal management approach in sensitive or developed areas is to hold the line, and coastal managers have two fundamental options to achieve this:

1. Hard structures (e.g. rock seawalls) which aim to reduce erosive wave energy, compartmentalise beach sediment or provide a barrier at the back of the beach to protect the land from inundation. As sea levels rise most such structures will need to be upgraded in order to maintain their level of protection.
2. "Soft engineering", typically beach nourishment, which aims to maintain the health of the sand buffer by artificially increasing the volume of the beach and/or dunes. This is a commonly used approach to maintain the sand buffer, particularly in areas of high recreational value where there is a desire to retain the natural character of the beach. Realistically, in many areas, the additional volumes of sand required to stabilise the shoreline as sea levels rise is likely to become unsustainable.

While hard engineering protection may well be required in highly developed areas where the economic and social implications of failure are disastrous, in some areas a lower level of protection may be acceptable. A relatively recent and little tested shore protection method is the use of what have been variously termed "dynamic revetments", "cobble berms" or "rubble beaches". This approach involves the construction of a gravel or shingle ridge around the extreme wave runup

limit. These structures aim to mimic composite beaches which consist of a lower foreshore of sand and a backshore ridge constructed of gravel or cobbles which stabilises the upper beach and provides overtopping protection to the hinterland. They contrast with static coastal defence structures as they are "dynamic" and are expected to reshape significantly under wave attack.

It is recognised that gravel beaches exhibit a remarkable degree of stability (e.g. Powell, 1988). As a result, the idea to use artificially constructed gravel barriers to provide shore protection can be traced to the 1970's when an artificial gravel beach was constructed along the entrance to Rotterdam Harbour. Since then, dynamic revetments have been installed in a small number of locations including Cape Lookout State Park, Oregon (Allan & Komar, 2002), Columbia River South Jetty, Oregon (Allan & Gabel, 2016) and North Cove, Washington. While very little information is available about dynamic revetments and composite beaches, the overall conclusion from these installations is that dynamic revetments perform well in terms of limiting wave runup, overtopping and erosion of the hinterland, continuing to provide robust coastal protection through high energy conditions. The major consideration for such structures is the loss of material alongshore and as such, just as with conventional beach nourishment, maintenance work should be expected on a multi-annual basis to maintain levels of protection.

Dynamic revetments potentially have a number of advantages over other forms of coastal protection. It is known that the berm crest of a gravel beach is generally formed just below the maximum level of wave runup (Bradbury and Powell, 1992) and studies have suggested that during severe storms material can be pushed up to or beyond the crest by extreme runup events, causing the berm to gain elevation and roll landwards (Carter and Orford, 1984). Dynamic revetments are expected to respond in a similar way, meaning that overtopping protection would actually improve during storm events as long as the crest is not breached and remains continuous. This process may also mean that the structure adapts to a rising sea level by increasing its crest height and rolling slowly landward, similar to gravel barriers. In addition to the potential adaptive nature of the structure, dynamic revetments are a relatively sustainable approach to coastal defence, suitable for community construction and use in developing nations as they require no foundation preparation, can be constructed through random placement of materials without the need for expensive plant, can make use of inexpensive, low grade, poorly sorted material, and are likely to provide a suitable habitat for beach invertebrates.

2.   METHODOLOGY

The DynaRev experiment was designed to investigate the resilience of a dynamic cobble berm revetment structure to wave attack and a rising water level. The experiment took place over a 2-month period from August to September 2017 in the Large Wave Flume (Großer Wellenkanal, GWK), Hannover, Germany. The GWK flume is 309 m long, 7 m deep and 5 m wide with a combined piston-flap type wavemaker. A schematic of the experimental setup is shown in Figure 1. All coordinates are given as the distance from the wave paddle rest position ($x = 0$ m), elevation above the horizontal flume bed ($z = 0$ m) and across-flume distance from the centreline ($y = 0$ m).
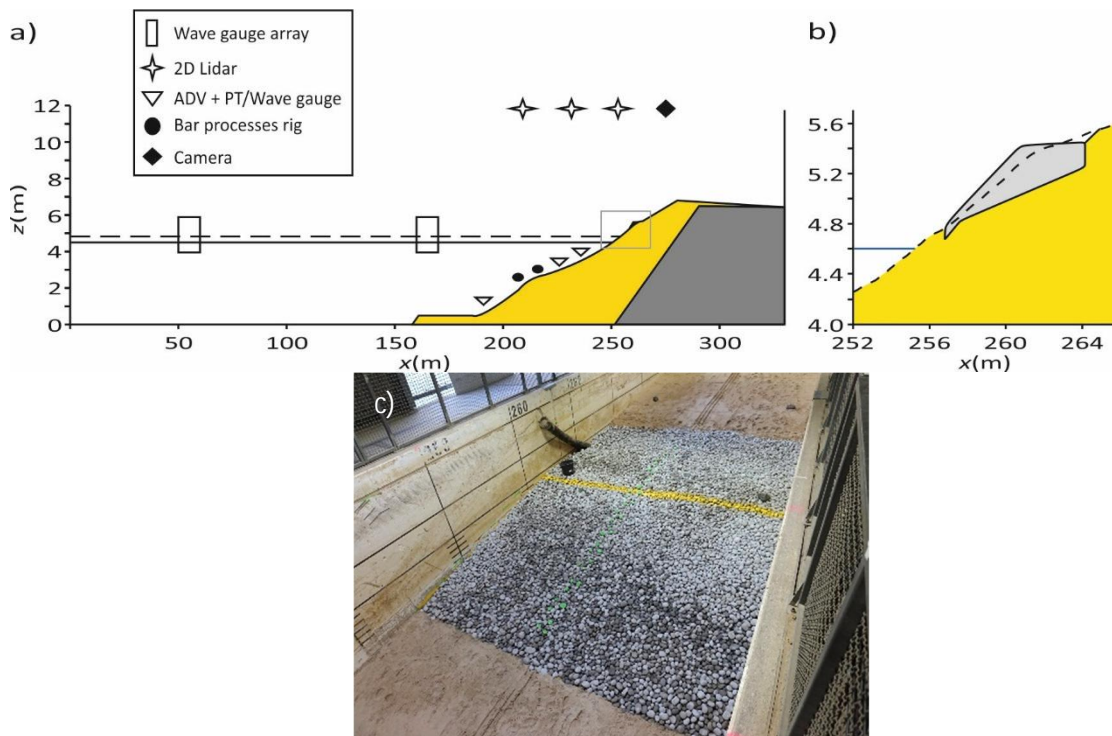
Figure 1. a) Schematic of flume setup showing primary locations (see Table 1). The yellow shaded area represents the sand volume and the dark grey shaded area is the permanent 1:6 impermeable slope. The black solid and dashed horizontal lines indicate the minimum ($h = 4.5$ m) and maximum ($h = 4.9$ m) water levels. b) Close up of the dynamic revetment geometry after construction prior to DR1, corresponding to the grey box in (a). The light grey region indicates the dynamic revetment and the dashed line shows the beach profile prior to revetment construction. c) Photograph of the constructed dynamic revetment. The yellow line indicates the line of the front of the crest at $x = 260.7$ m.

A total of 141.6 hours of testing was completed, divided into two "phases" as detailed below, with each phase being split into a series of "runs" (133 in total across both phases) varying from 20 minutes to 3 hours in duration. The full details of the test program are given in Table 1.

Phase SB - Unmodified sand beach response to a rising water level: Starting with a 1:15 plane slope, the evolution of the beach profile was measured under constant wave forcing ($H_s = 0.8$ m, $T_p = 6.0$ s). The mean water level in the flume was then raised by a total of 0.4 m in steps of 0.1 m. Following the completion of the water level rise increments, the short-term response of the beach was measured for a range different wave conditions expected to produce both erosion and accretion. Run names for this phase are given as SB<WL increment>_<Run No.>, where water level (WL) increments are numbered 0 for the initial water level of $h = 4.5$ m to 4 for $h = 4.9$ m and run numbering is started from 1 for each WL increment.

Phase DR - Dynamic revetment response to a rising water level: Again starting with a plane slope, a sand beach was measured as it evolved under the same constant wave conditions as used in Phase SB for 20 hours to provide a natural beach profile on which to construct the dynamic revetment. The cobble revetment was installed at the location of the sand beach berm prior to the first water level increment. The revetment was constructed using granite cobbles ($D_{50} = 66$ mm), had a 1:6.3 front slope and its crest height at the elevation of the $R_{5\%}$ runup level ($z = 5.42$ m) for the second water level increment to ensure significant overtopping as the water level increased. The sand foreshore and dynamic revetment were then reshaped under constant wave conditions over the remaining water level increments with the test durations at each water level mirroring those in Phase SB. Finally, higher energy storm waves were used at the end of the final water level increment to investigate revetment resilience to higher energy conditions. Run names for this phase are given as DR<WL increment>_<Run No.>. Note that the revetment was constructed prior to the start of DR1.

Table 1. Overview of the test program.

WL increment/Test	Duration (hr)	H_s (m)	T_p (s)	Water level h (m)	Number of Runs	Run Durations (minutes)
Phase SB - Morphological response of a sandy beach with a rising water level						
SB0	20	0.8	6	4.5	14	20,20,20,30,30,60,60,60,120,120,120,180,180,180
SB1	7	0.8	6	4.6	9	20,20,20,30,30,60,60,60,60,60
SB2	7	0.8	6	4.7	7	20,40,60,60,60,60,120
SB3	7	0.8	6	4.8	7	20,40,60,60,60,60,120
SB4	17	0.8	6	4.9	11	20,40,60,60,60,60,120,120,120,180,180
Phase SB – Resilience testing at the maximum water level h = 4.9 m						
SBE1	2	1	7	4.9	3	20,40,60
SBE2	4	1.2	8	4.9	5	20,40,60,60,60,60
SBA1	6	0.6	12	4.9	7	20,40,60,60,60,60,60
Phase DR – Morphological response of a sandy beach with a dynamic revetment to a rising water level						
DR0	20	0.8	6	4.5	14	20,20,20,30,30,60,60,60,120,120,120,180,180,180
Dynamic revetment installation						
DR1	7	0.8	6	4.6	9	20,20,20,30,30,60,60,60,120
DR2	7	0.8	6	4.7	7	20,40,60,60,60,60,120
DR3	7	0.8	6	4.8	7	20,40,60,60,60,60,120
DR4	17	0.8	6	4.9	11	20,40,60,60,60,60,120,120,120,180,180
Phase DR – Resilience testing at the maximum water level h = 4.9 m						
DRE1	2	0.9	6	4.9	3	20,40,60
DRE2	2	1	7	4.9	4	20,20,20,60
DRE3	1	1	8	4.9	3	20,20,20
DRA1	2	0.8	6	4.9	2	60,60
Phase DR – Resilience testing with recharged revetment at the maximum water level h = 4.9 m						
DRN1	2	0.8	6	4.9	2	60,60
DRN2	0.66	1.0	8	4.9	2	20,20
DRN3	2	0.8	6	4.9	2	60,60
DRN4	0.66	1.0	9	4.9	2	20,20
DRN5	0.33	1.2	8	4.9	1	20
DRN6	1	0.8	6	4.9	1	60

A large suite of instruments was deployed during the experiment to measure waves, morphology, sediment transport and hydrodynamics (see Figure 1). All instruments were logged to PCs connected to a local area network with a shared time-server to ensure time-synchronisation.

Wave measurements in the horizontal bed section of the flume were obtained using 2 x four wave gauge arrays. High resolution wave data through the surf and swash zones (see Figure 2) was obtained using an array of three roof-mounted (z = 11.8 m) SICK LMS511 2D Lidars (see Martins *et al.*, 2017). Additional runup data was obtained using a video camera mounted at z = 11.8 m above the subaerial beach.

Complete beach profile data was obtained intermittently between wave runs using a mechanical profiler. This was complimented by the Lidar array which was able to capture the subaerial beach profile continuously throughout the experiment by separating the stable "bed" from the "swash" using the variance-based method of Almeida *et al.* (2015) as the beach was inundated and exposed in the swash zone.

Hydrodynamics, sediment transport and morphological change during bar formation and migration were measured by two measurement rigs at x = 226.5 and 233.5 m on either side of the predicted

sand bar location. Each rig was equipped with a suite of instruments sampled at 25 Hz including 2 optical backscatter sensors (OBS) mounted at 5 and 10 cm from the bed, an acoustic backscatter sensor (ABS), 65 cm above the bed, two electromagnetic current meters at elevations of 5 and 10 cm above the bed, a Nortek Vectrino profiling ADV (Vectrino) mounted 6 cm above the bed and a pressure transducer (PT) mounted 45 cm above the bed. Finally, a ripple profile scanner (RPS) was mounted 75 cm above the bed to obtain local bed profile measurements. The RPS on each rig was sampled alternately for one minute to avoid cross-talk between instruments.

In addition to the rigs, a 3D sector scanning sonar (SSS) which provided measurements of the local bathymetry in a 1 to 2-m diameter circular region centred on the instrument which was located at x = 228.8 m. Two Nortek ADVs were located at x = 235 and 240 m and maintained at a height 150 mm above the bed.

The movement of individual cobbles within the dynamic revetment was monitored using an RFID tracking system similar to that used by Allan *et al*. (2006). A total of 97 cobbles were fitted with transponders and placed along the centreline of the revetment at the sand interface (20 cobbles), mid depth (30 cobbles) and top layer (47 cobbles). The cobble locations were detected before each water level increment using a radio-based detection system.

Finally, a multibeam echo-sounder was installed to obtain measurements of the bubble clouds generated by wave breaking. These measurements are described in Bryan *et al*. (2019).
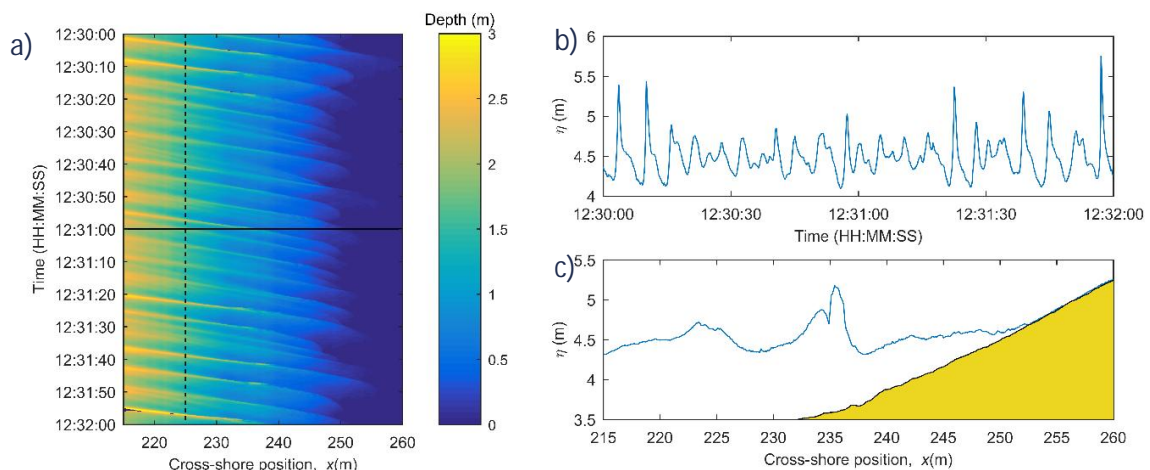
Figure 2. Example wave measurements. a) Timestack of water depth measured by the Lidar throughout the surf and swash zones. b) Timeseries of water surface elevation at x = 225 m as indicated by the vertical dashed line in panel a. c) Measured free- surface profile through the surf and swash zone at the time indicated by the horizontal solid line in a. Note that the measurements capture the splash-up generated by a breaking wave at x = 235.5 m.

3.   RESULTS

When installed for coastal protection, dynamic revetments are built above the typical wave runup limit to provide runup and overtopping protection during storms when water levels are super-elevated for an hour or two around high tide. By installing the revetment at the level of the natural berm and undertaking testing over tens of hours using a series of water level increments, it was possible to effectively carry out accelerated testing of the revetment performance at a series of raised water levels. This gives insight into how the revetment responds to a series of high energy events and also provides information about the rollover behaviour of the revetment as sea levels rise.

Figure 3 shows a series of profiles comparing the response of the beach with and without the revetment. It is clear that the evolution of the sandy part of the beach in Phase DR is similar to that for Phase SB. The offshore bar forms at the same location and grows to approximately the same height over the course of the water level increments. During this process, the defined trough and

inner bar evident landward of the bar at the start of the first water level increment (SB1, DR1) are smoothed out and becomes less pronounced. Between the shoreline and the sandbar, sand ripples with a wavelength greater than a metre are evident in all profiles. In Phase SB, the bed elevation in this region rises by approximately 0.25 m as the water level increases by 0.4 m. This is not the case for the Phase DR testing and the bed elevation between the revetment toe and the bar remains at approximately the same elevation.
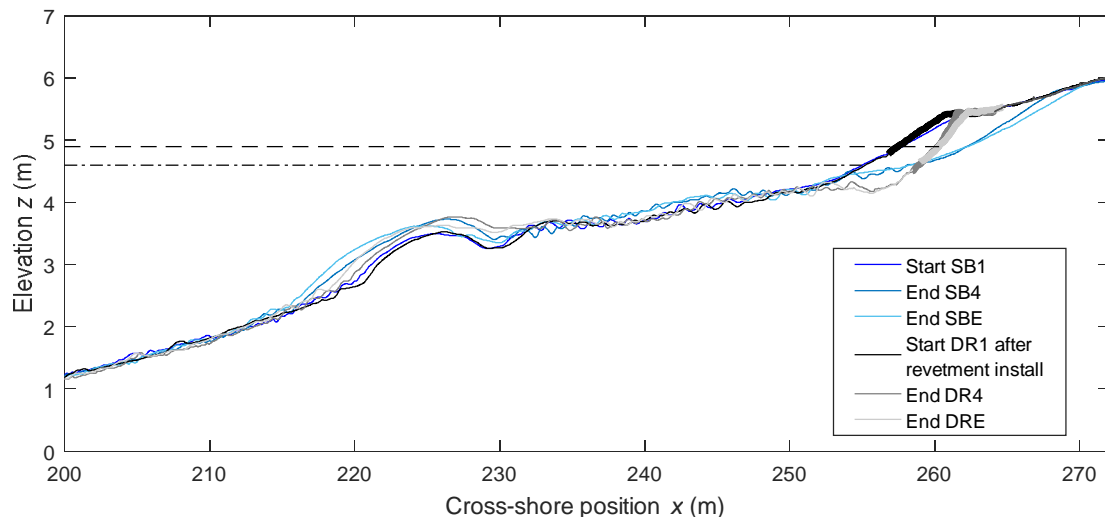
Figure 3. Beach profiles comparing beach response with and without the dynamic revetment. The revetment extent is shown by the thicker line. Phase DR runs are shown in greyscale while Phase SB runs are in blue colours. The dot-dash and dashed horizontal lines show the minimum (SB0, DR0) and maximum water levels (SB4, DR4) respectively.

Significant erosion of the sand beachface is observed during the Phase SB testing. The shoreline retreated (due to both water level rise and sand loss) by 7.5 m over the course of the water level increments and resilience testing, and erosion was observed up to $x = 270$ m. The presence of the revetment slowed this retreat considerably, with the shoreline retreating by approximately 5 m. Over the course of the water level increment testing, the toe of the revetment retreated by approximately 1.5 m and lowered by 0.3 m due primarily to a loss of sand from beneath the revetment and in front of the toe. This led to an overall steepening of the revetment from 1:6.3 to 1:3.5. The majority of this steepening occurred during DR4 when the percentage of waves overtopping the crest measured using the Lidar was around 50%. By comparison, the crest position was relatively stable throughout the testing. The front of the crest retreated by approximately 0.9 m, and the elevation increased by 0.07 m. Further gains in crest elevation were expected due to the rollover process which was observed throughout the testing; however it was observed that the rollover was approximately balanced by the rate of sand loss from beneath the revetment. As the experiment progressed, the rate of sand loss decreased as the revetment found a more stable configuration with the wave conditions, and crest elevation increase due to rollover became evident. Although the crest of the cobble structure was overtopped completely by multiple waves, the horizontal runup extent was greatly reduced when compared to the SB cases and no beach change is observable in the profile measurements landward of the back of the revetment crest at $x = 265$ m; thus, the revetment provided good erosion protection to the hinterland behind the structure.

A feature of the revetment performance was the loss of sand from beneath the structure. This is an inevitable consequence of constructing without a filter layer and is clearly a consideration when installing these structures for the purpose of coastal protection. Estimates of the sand beach elevation underlying the revetment through the experiment suggest that it forms a similar profile to the Phase SB case, and would be expected to approach a quasi-stable equilibrium shape in time. Support for this hypothesis comes from sediment balance calculations which showed that the rate

of sand loss was reducing with time throughout Phase DR, and observations of natural composite beaches which are known to be highly stable and show no evidence of episodic or continuous sand loss from beneath the cobble ridge. This is further supported by observations from a trial revetment structure at North Cove, Washington, where there was evidence that the sandy beach underlying and seaward of the revetment accumulated sand over time due to Aeolian processes and the armouring effect of the placed coarse material (P. Bayle pers comm.). It is thought that the rates of sand loss during the DynaRev experiment were enhanced due to the fact that the underlying sand profile had to be artificially modified to allow the full revetment volume to be placed at the correct location. This meant that the sand profile underlying the revetment was far from equilibrium and thus prone to rapid change. Despite the observed sand loss in the revetment case, the underlying sand profile was found to retreat at a lower rate during Phase DR than Phase SB as shown in Figure 4.
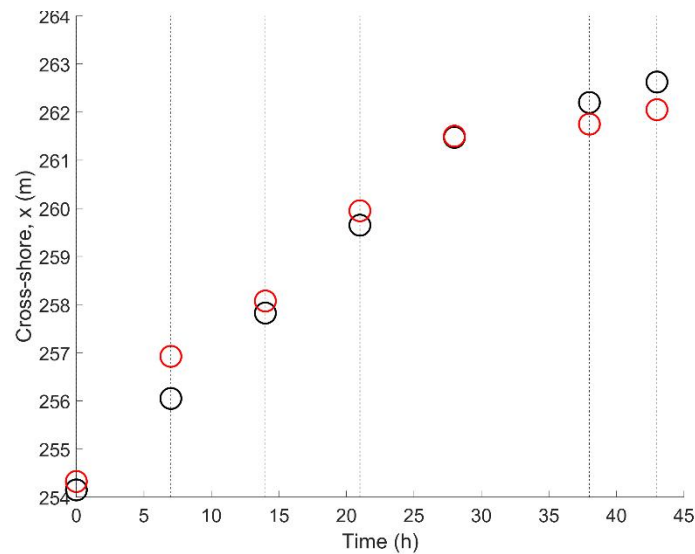
Figure 4. Shoreline position for Phase SB (black circles) and Phase DR (red circles) from the start of water level increment 1 (SB1, DR1). The vertical dashed lines indicate the times at which the water level was increased by 0.1 m and the start of erosive test (38 hours) and the start of recovery test (43 hours). Note that due to the need to artificially modify the underlying beach profile to enable placement of the full revetment volume, the initial sand beach shoreline in the Phase DR case is landward of that for Phase SB, however by the end of the testing it is approximately 1 m seaward.

Throughout all of the Phase DR testing it was evident that the revetment structure was dynamically stable and remained as a coherent structure with a defined toe through all test cases. Other than a few stones in a thin layer extending a few metres landward of the defined revetment toe, no material was lost from the structure throughout the testing, with at least 90% of the total volume of cobbles remaining within the body of the revetment at all times. It was noted that large individual waves could cause significant change to the shape of the revetment, particularly those that completely overtopped the structure. However, within a small number of subsequent waves, the majority of the change had been cancelled out. This observation of large gross change caused by sustained wave action, but minimal net change has also been observed on sand and gravel beaches (Blenkinsopp *et al.*, 2011; Masselink *et al.,* 2010).

The evolution of the revetment during the water level increment testing is shown in more detail in Figure 5. The figure demonstrates that the revetment retreats throughout the testing, with the maximum rate of retreat occurring during DR3 when the revetment starts to be overtopped (approximately 8% of waves overtop during DR3). This retreat is caused by loss of sand from beneath the revetment and the overall steepening of the front slope. It is evident that the revetment becomes steeper over time as the toe moves landward and lowers while the crest position only retreats slightly. Careful examination of the profiles indicates that the steepening occurs over the part of the revetment face being influenced by swash motion. During DR1, swash only occurs on the lower part of the revetment and leads to a change in slope at approximately $x = 258.5$ m with

the lower part of the slope having a gradient of 1:4, while the upper part of the slope is 1:6.3. As the water level rises and the runup limit moves landward, the position of the slope change moves up and landward, leading to a greater proportion of the revetment front slope becoming steeper.
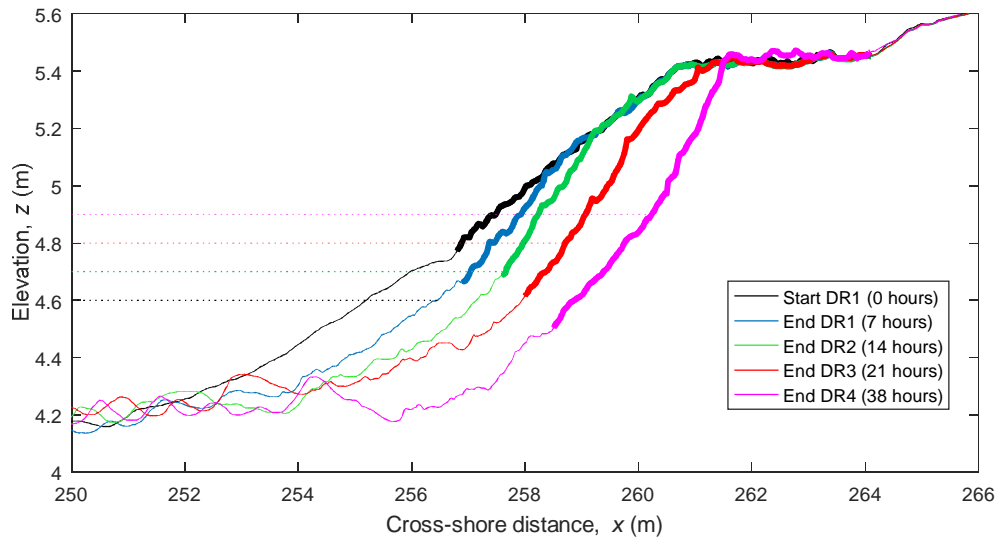

Figure 5. Revetment profiles at the end of each water level increment during Phase DR. The revetment extent is shown by the thicker line. Note that the duration of testing for DR1, 2 and 3 is 7 hours, while the duration of DR4 is 17 hours.

The steepening observed during the Phase DR testing leads to a change in reflection characteristics of the beach. Figure 6a shows the reflection coefficient measured by the wave gauge arrays as a function of time for both Phase SB and DR, starting from the beginning of SB0/DR0. Because Phase SB0 and DR0 both start from a planar sandy beach and use an identical wave time series, the reflection coefficient increases in a similar manner as sediment is transported from the beachface to the bar leading to a steepening of the bar and beachface. After construction of the dynamic revetment (20 hours in Figure 6), the reflection behaviour of the beaches diverges. For Phase DR, the value of K_r gradually increases as the slope of the revetment front face increases. Conversely, during Phase SB the reflection coefficient gradually decreases as the profile (separation between bar crest and shoreline) lengthens and mean surf/swash zone slope decreases with increasing water level. Figure 6b presents the reflection coefficient as a function of the deepwater Irribarren number for both phases. There is a clear relationship between Irribarren number and K_r as suggested by Battjes (1974), and the results for both phases demonstrate similar behaviour despite the complex nature of the beach profiles and the large differences in swash zone slope.
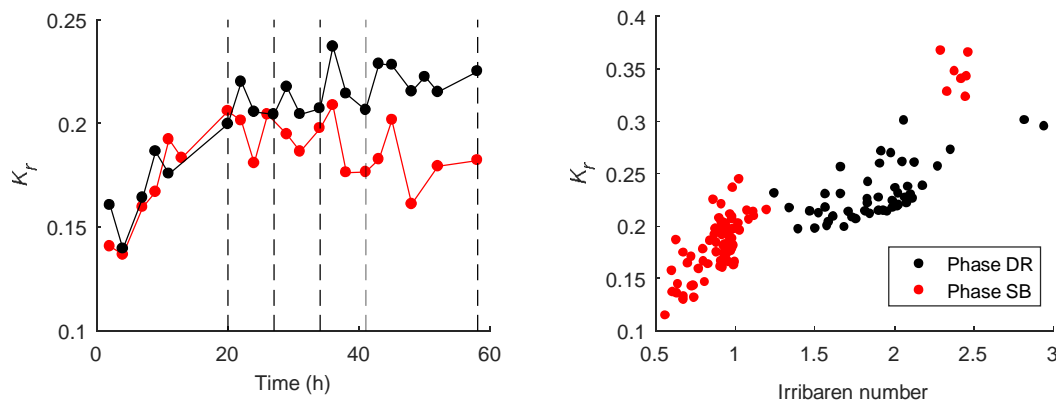
Figure 6. a) Reflection coefficient calculated every 2 hours as a function of time during Phases SB (red) and DR (black). The time axis starts at the beginning of SB0/DR0 unlike Figure 4 in which zero hours represents the time of revetment construction. b) Reflection coefficient for every run as a function of deepwater Irribarren number.

The results from the RFID cobble tracking give additional insight into the behaviour of the dynamic revetment during testing. Figure 7 presents the movement of the 97 instrumented cobbles throughout tests DR1 to DRR (Table 1). The main conclusion from this analysis is that the vast majority of the detected cobbles remain within the main body of the revetment, and only 4 of the 97 instrumented cobbles move seaward of the original revetment toe (x = 256.8 m). Of the remaining cobbles the majority finish landward of their original position and landward movements outnumber seaward movements by approximately 2 to 1. It is evident that the number of landward movements increases significantly during the first 7 hours of DR4 as the percentage of waves overtopping increases from approximately 8% during DR3 to 50% during DR4 and the rollover process becomes more obvious. As the revetment steepens and becomes narrower in cross-shore extent, it is evident that the instrumented cobbles bunch up between x = 260 m and x = 262.5 m by the end of DR4, with many of these cobbles having been transported onto the revetment crest. The majority of seaward movements occur during DR1, 2 and 3 as cobbles positioned in the upper swash zone are moved seaward by the backwash of the larger swash events, but there is insufficient energy in the uprush to move them back up the slope. The number of seaward movements decreases significantly during DR4 when the overtopping rate becomes large.
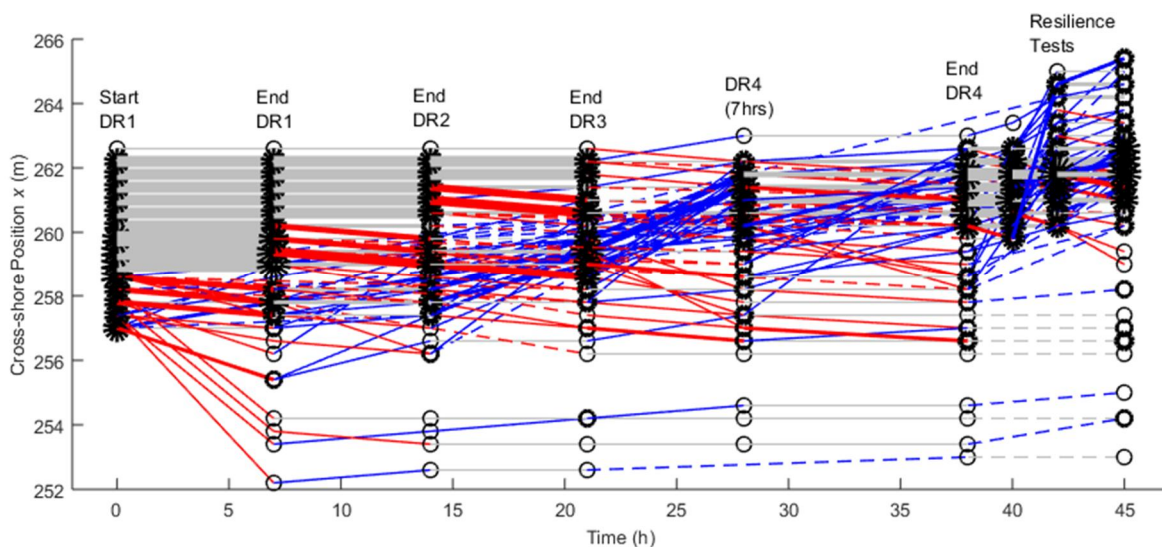
Figure 7. Cross shore position of the 97 tagged cobbles as a function of time. The position of the cobbles was measured to the nearest 0.4 m in the cross-shore direction at the end of every water level increment and after each resilience test. The black circles represent the instrumented pebbles at each 0.4 m cross-shore increment and the thickness of the circle is relative to the number of cobbles at each location. Plain red lines correspond to seaward transport. Plain blue lines correspond to landward transport. Plain grey lines correspond to no transport. The thickness of the lines is relative to the number of cobbles moving along a particular path. The dashed lines indicate that a cobble was not detected for at least one detection survey, but was found again later. The same colour and thickness principles apply for the dashed lines.

4.   CONCLUSIONS

A large-scale laboratory experiment was completed to investigate the performance of a dynamic revetment designed to provide sustainable coastal protection under wave attack and a rising water level. Testing was undertaken in 2 phases, first with an unmodified sand beach and subsequently with a cobble revetment constructed around the natural berm location. Long test durations were used in an attempt to approach profile equilibrium at each water level and to investigate the revetment resilience over many hours of wave attack.

Throughout all revetment testing, the revetment remained as a coherent cobble berm structure with minimal loss of cobbles. Thus, while the individual cobbles moved with every wave, continuously reshaping the revetment as overtopping rates increased with increasing water level, the overall structure was dynamically stable and overtopping and erosion protection to the hinterland was maintained. The movement of individual cobbles during the experiment was

monitored using an RFID-based cobble tracking system. This demonstrated that 95% of the tagged cobbles originally placed in the revetment remained within the structure throughout testing.

Comparison with the sand beach case demonstrated that the revetment structure led to a reduction in the rate of shoreline retreat and reduced runup excursions, thus eliminating erosion landward of the revetment. While the revetment slowed shoreline retreat compared to the sand beach case, the structure was observed to retreat continuously throughout the experiment due to a loss of sand from beneath and an overall steepening of the front face. The retreat of the revetment crest was significantly slower than the shoreline and the crest height was maintained throughout. Indeed, at the highest water level when around 50% of waves overtopped the crest, there was evidence of rollover transport leading to a small increase in crest elevation. The observations of rollover transport indicate that a sustained increase in crest height could be expected in the event of multiple large storms or a sea-level rise scenario.

The evolution of the sand beach profile was similar with and without the revetment, with the offshore bar forming in approximately the same location and growing to a similar height. In both cases, the bar crest elevation increased as the water level was increased in line with the Bruun Rule concept.

While the results of the experiment are promising, additional research will be required before dynamic revetments could be widely adopted. The loss of sand from beneath the revetment must be better understood because if the structure can only retreat, with no mechanism for the revetment to recover after a storm it may be unsustainable. Observations of composite beaches and a small number of dynamic revetments in the USA suggest that natural and artificial cobble berms are stable in the field with no evidence of continuous retreat. This suggests that once the beach/revetment system approaches an equilibrium condition, its stability greatly increases and the observed recession will slow or stop. Another consideration will be the influence of longshore transport which will inevitably require dynamic revetments to be regular inspected and maintained. With improved understanding of these issues, the testing presented here indicates that dynamic revetments could provide a feasible alternative to traditional hard engineering structures in some locations as they provide low cost, robust overtopping and erosion protection to the hinterland while maintaining some natural character.

ACKNOWLEDGEMENTS

REFERENCES

Allan, J.C. and Gabel, L.L. (2016). Monitoring the response and efficacy of a dynamic revetment constructed adjacent to the Columbia River South Jetty, Clatsop County, Oregon. Oregon Department of Geology and Mineral Industries, Tech. Rep., 2016.

Allan, J.C. and Komar, P.D. (2002). A dynamic revetment and artificial dune for shore protection. *Proceedings of the International Conference on Coastal Engineering. American Society of Civil Engineers, New York.*

Allan, J.C., Hart, R. and Tranquili, J.V. (2006). The use of passive integrated transponder (pit) tags to trace cobble transport in a mixed sand-and-gravel beach on the high-energy Oregon coast, USA, *Marine Geology*, vol. 232.

Almeida, L.P., Masselink, G., Russell, P.E. and Davidson, M.A. (2015). Observations of gravel beach dynamics during high energy wave conditions using a laser scanner, Geomorphology. 228 (2015) 15-27,

Battjes, J.A. (1974). Surf similarity, *Proceedings of 14th Coastal Engineering Conference, Copenhagen, Denmark, American Society of Civil Engineers, New York*, pp.466-480.

Blenkinsopp, C.E., Turner, I.L., Masselink, G. and Russell, P. (2011). Swash zone sediment fluxes: Field observations, *Coastal Engineering*, 59(1), pp. 28-44.

Bryan, O., Bayle, P.M., Blenkinsopp, C.E. and Hunter, A.J. (2018). Breaking Wave Imaging using Lidar and Sonar, *IEEE Journal of Oceanic Engineering, In Press.*

Luijendijk, A., Hagenaars, G., Ranasinghe, R., Baart, F., Donchyts, G. and Aarninkhof. S. (2018). The State of the World's Beaches. *Scientific Reports*, 8(1) DOI: 10.1038/s41598-018-24630-6

Martins, K., Blenkinsopp, C.E., Power, H.E., Bruder, B., Puleo, J.A. and Bergsma, E. (2017) High resolution monitoring of wave transformation in the surf zone using a LiDAR scanner array, Coastal Engineering, 128, pp. 37-43.

Masselink, G., Russell, P., Blenkinsopp, C.E. and Turner, I.L. (2010) Swash zone sediment transport, step dynamics and morphological response of a gravel beach, *Marine Geology*, 274, pp. 50-68.

Powell, K.A. 1988. The dynamic response of shingle beaches to random waves. *Proceedings of the 21st International Conference on Coastal Engineering,* ASCE. 1763-177

FORESHORE EVOLUTION AND HYDRAULIC PERFORMANCE OF A BEACH PROTECTED BY A NEARLY VERTICAL SEAWALL

Riccardo Briganti (1), Rosaria Ester Musumeci (2), Jentsje van der Meer (3), Alessandro Romano (4), Laura Maria Stancanelli (5), Matthias Kudella (6), Rizki Akbar (7), Ryard Mukhdiar (8), Corrado Altomare (9), Tomohiro Suzuki (10), Paolo De Girolamo (11), Giulia Mancini (12), Giovanni Besio (13), Nicholas Dodd (14), Stefan Schimmels (15)

(1) Department of Civil Engineering, University of Nottingham, United Kingdom
riccardo.briganti@nottingham.ac.uk
(2) Dept. of Civil Engineering and Architecture, University of Catania, Italy, rmusume@unict.it
(3) IHE Delft Institute for Water Education, The Netherlands
(4) Dept. of Civil, Building and Environmental Engineering (DICEA), "Sapienza" University of Rome, Italy
(5) Dept. of Civil Engineering and Architecture, University of Catania, Italy
(6) Forschungszentrum Küste (FZK), Hannover, Germany
(7) IHE Delft Institute for Water Education, The Netherlands
(8) IHE Delft Institute for Water Education, The Netherlands
(9) Universitat Politècnica de Catalunya, Barcelona, Spain
(10) Flanders Hydraulics Research, Antwerpen, Belgium
(11) Dept. of Civil, Building and Environmental Engineering (DICEA), "Sapienza" University of Rome, Italy
(12) Department of Civil Engineering, University of Nottingham, United Kingdom
(13) Department of Civil, Chemical and Environmental Engineering (DICCA), University of Genoa, Italy
(14) Department of Civil Engineering, University of Nottingham, United Kingdom
(15) Forschungszentrum Küste (FZK), Hannover, Germany

This work presents the results of an experimental investigation on the effects of a sequence of storms on wave overtopping at a nearly vertical battered seawall at the back of a sandy foreshore. The experiments were carried out in the Large Wave Flume (GWK) at Leibniz Universität Hannover (Germany), as part of the research project ICODEP (Impact of Changing fOreshore on flood DEfence Performance), within the European Union programme Hydralab+.
The layout consisted of a 10/1 battered seawall and a natural sandy foreshore with an initial 1:15 slope. The beach sand had a nominal diameter of 0.30 mm. Three sequences of individual storms were simulated. Each storm was divided into six steps in which the wave conditions and still water level were varied to represent the peak of an actual storm. Two storm profiles were considered, the first one with a lower level of energy and the second one with a higher one. These were combined in the three different sequences. All the tested wave conditions were designed to be erosive for the beach, with no recovery in between. Each sequence started from a plain beach configuration and the beach was not restored in between storms. The measurements included: the profile of the beach after each sea state tested, waves, wave pressure and forces at the sea wall, sediment concentrations, flow velocity, and wave overtopping.

1. INTRODUCTION

Coastal flood defence structures are often found at the back of a natural beach, and an interaction between the beach and the structure itself determines the joint performance of this system. With an increased emphasis on natural and mixed hard/soft coastal management approaches, the prediction of the performance of protected beaches received more attention by the coastal research community.
One important aspect that needs to be investigated is the influence of sequences of storms on the general behaviour of the system. Sequences of storms separated by intervals that are shorter than recovery time of the beach are often referred to as clusters. Existing investigations on this subject analyse natural beaches and very little research is available on the behaviour of engineered ones. The focus of the existing research is to understand if the cumulative impact of clusters is higher than the sum of the average impact of the individual events, as identified in the review by Senechal et al (2017), which presents a comprehensive overview of the literature on this topic.
The enhancement of the impact of storms of moderate intensity found for natural beach opens to the possibility that the same can happen for coastal defences. This occurrence has never been

investigated in depth. The project ICODEP (Influence of foreshore evolution on COastal DEfence Performance) aims at filling this gap in research.

Wave overtopping at a composite flood defence during a sequence of storms was investigated with a large-scale laboratory test in the Large Wave Flume (GWK) at Leibniz Universität Hannover (Germany).

2. EXPERIMENTAL LAYOUT

The experimental layout (Fig. 1) consists of a 10/1 sloped seawall and a sandy foreshore with an initial 1/15 slope. The natural sand of the beach has a nominal diameter (D_{50}) of 0.30 mm. The reference frame used in this work has the origin of x at the neutral position of the wave paddle and the origin of z is set at the bottom of the flume at the toe of the beach, which is at x=161.9 m. The y coordinate origin is located on the lateral instrumented wall of the flume, i.e. on the hydraulic right side of the wall (see Fig. 2). The coordinates of crest of the seawall are x=240.93 m and z=5.5 m (see Fig. 2).
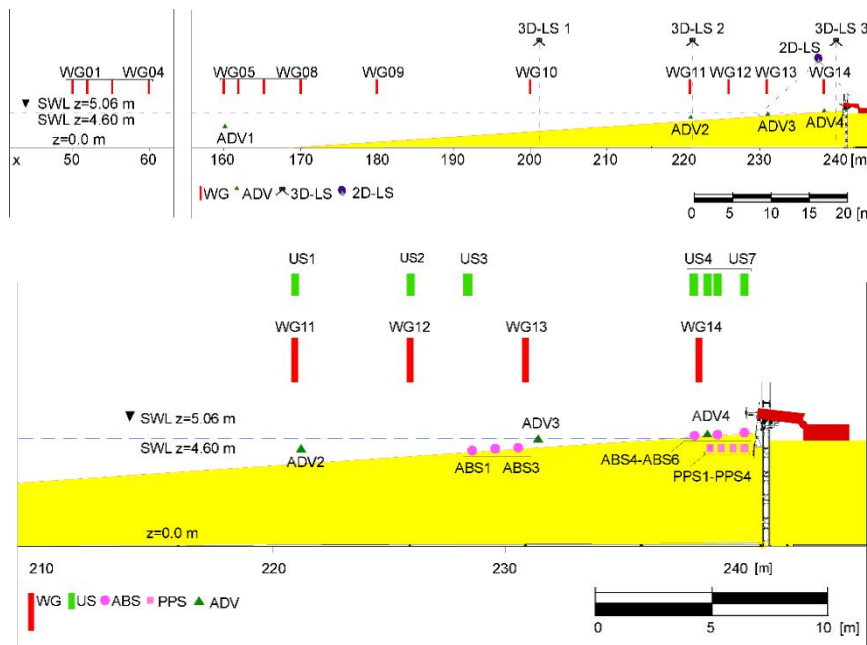
Figure 1: Layout of the ICODEP engineered beach and instruments. Upper panel: overview of the flume. Lower panel: detail of the structure
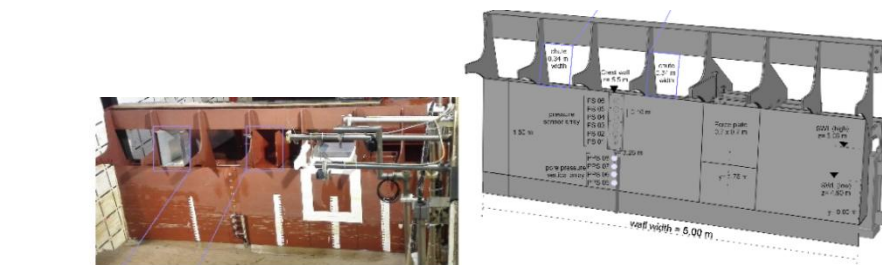
Figure 2: 3D view of the tested seawall with the position of the instruments installed.

The tested wave conditions have been chosen to be representative of those of typical storms in macro-tidal Northern European seas. However, in large scale laboratories, it is not feasible to replicate a sequence of complete storms, hence the focus was on the peak of each storm and the simultaneous peak of the sea levels.

Each storm profile was divided into six sea states, referred to as sea states T1 to T6. They were generated using the JONSWAP spectrum with a shape factor $\gamma=3.3$, consistent with the capability of the wave generator at the GWK. The duration of each sea state is $D_s=32$ minutes. Fig. 3 shows the target significant wave height (H_{m0}), peak period T_p and Still Water Level (SWL) in all trunks in S1 and S2. The sequence of individual waves for each sea state is kept the same throughout the tests, in order to remove the variability due to the particular sequence of waves at the boundary (Romano et al., 2015).

Two SWL conditions were applied during each storm; these were the same for storm S1 and S2. Sea states T3 and T4 were always tested with the SWL at 5.06 m from the bottom of the flume (referred as high SWL conditions hereinafter), and the rest of the storm was tested with the SWL at 4.60 m (low SWL hereinafter). As shown in Fig. 3 in both S1 and S2, H_{m0} increases from the first to the second segment of the storm (T1 and T2) at low SWL conditions, it reaches a maximum at T3 in high SWL conditions and decays afterwards from T4 to T6. The coincidence of maximum H_{m0} and maximum SWL was chosen because maximum overtopping is expected to occur when high tide and the maximum significant wave height occur at the same time. This was the case of the storm on the east coast of England (U.K.) that occurred from 5th to 6th December 2013, as discussed in Dissanayake et al. (2015), when the peak storm wave height coincided with high-water during spring-tide.
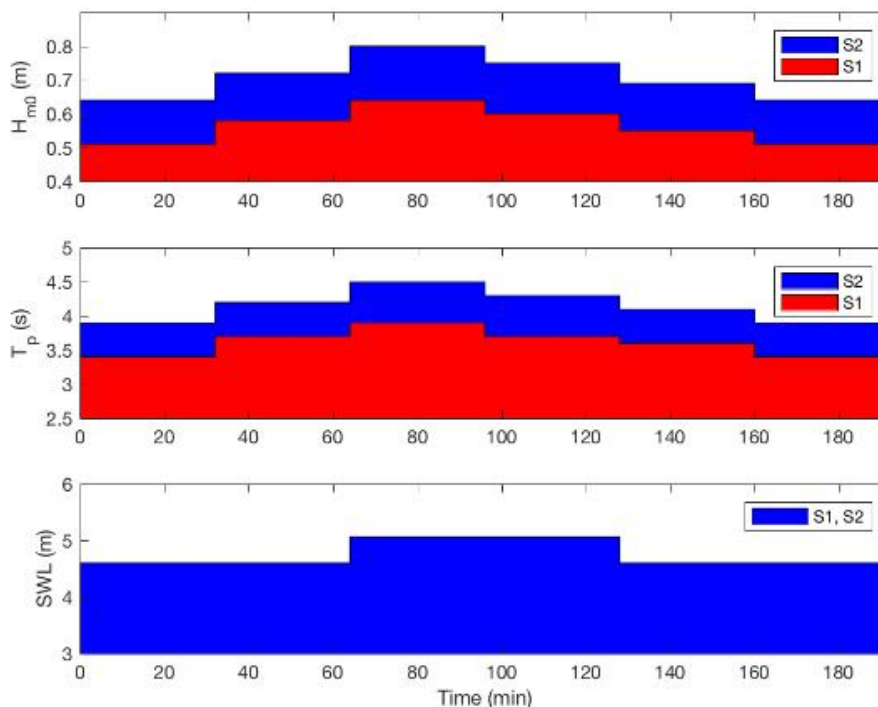
Figure 3: Characteristics of the simulated storms. Upper panel: Hm0; middle panel: Tp; lower panel: SWL

S1 and S2 have been combined into three sequences (see Table 1). Each sequence started from a 1/15 plain slope, while the beach profile after each storm was the initial one of the following storm. In C1 the repetition of the most energetic storm was tested, in order to measure the effects of previous bed evolution on the same storm. Conversely, C2 and C3 were meant to test the effects of storms of different energy levels alternating in a sequence.

Sequence	Position	Storm Profile	Initial beach profile
C1	1	S2	Slope 1/15
	2	S2	As evolved due to previous S2
	3	S2	As evolved due to previous S2
C2	1	S2	Slope 1/15
	2	S1	As evolved due to previous S2
	3	S2	As evolved due to previous S1
C3	1	S1	Slope 1/15
	2	S1	As evolved due to previous S1
	3	S1	As evolved due to previous S1

Table 1: Storms and initial bed conditions for the three sequences.

In this paper each storm sea state will be referred using the two character codes in a sequence, separated by "-", in which first the sequence is indicated, then a number from 1 to 3 is used to identify the position of the storm in the sequence, followed by the codes for the storm and that of the sea state. For example, C3-2-S2-T4 indicates sea state T4 of the storm S2 that was tested as second in sequence C3.

3.   HYDRODYNAMICS MEASUREMENTS

The measurement of the free surface was carried out using 14 resistive wave gauges (WG) and 7 ultrasonic wave gauges (US). The positions of these instruments are shown in Fig. 1.

An array of four WGs (WGs 01 to 04) was located at 50 m from the wavemaker and it was used to compute the actual incident wave conditions using the Mansard and Funke (1980) method at the paddle. A second array of 4 WGs (WGs 05 to 08) was located at the toe of the beach starting from x=160 m, WGs 05 to 07 were used to compute the actual incident wave conditions at the toe of the beach. Along the beach, WGs 08 to 14 were located in the shoaling and surf zone, while all seven USs are close to the structure. Note that US 1 and US 2 were co-located with WGs 10 and 11 respectively. It should be noted that WG 14 did not function properly during the experiments and it will not be included in the analyses.

An additional source of data for the free surface comes from one of the eight pore pressure sensors (PPSs) installed in the beach close to the toe of the structure (See lower panel of Fig.1). Four of these sensors (PPS 01 to 04) were installed along a horizontal array, always buried in the beach, while PPS 05 to 08 were located on a quasi-vertical array on the structure (see Fig. 2). These latter four sensors were exposed when erosion developed. In particular, it was observed in a series of preliminary tests that PPS 08 was exposed after a few waves when erosion started.

Four Acoustic Doppler Velocimeters (ADVs) were used to measure local flow velocity, these were located along the whole active part of the beach.

4.   BEACH PROFILE AND SEDIMENT TRANSPORT MEASUREMENT

The beach profiles were obtained by a combination of data gathered by a mechanical wheel profiler, a Sick LMS291-S14 Two-dimensional time of flight laser scanner (2D-LS hereinafter), and a Faro Focus 20/120 three-dimensional laser scanner (3D-LS hereinafter).

The mechanical beach profiler was run to measure the initial planar sloping beach and the profile after each sea state condition, from x=100m up to about x=240.3m, with a spatial resolution of ∆x=0.25m.

Point clouds of the bottom have been obtained by means of the 3D-LS, which was moved at three measuring stations along the flume (see upper panel of Fig. 1) and calibrated using the proprietary

Faro software and the known coordinates of several markers in the lab. The resolution of the point clouds was O(0.01 mm).

3D reconstructions of the entire sandy bottom (x>190 m) were obtained both at the beginning and at the end of each storm sequence, when the flume was drained before beach reshaping. Additional 3D-LS measurements of the region close to the wall, 231.5m<x<241.0m, were obtained in dry conditions in the upper part of the beach, i.e. at the end of every even sea state, except for T3, when a dry condition was not reached. In particular, the beach profile was extracted from the 3D point cloud by span-wise averaging the points gathered within a central stripe, 2.49m<y<2.51m. 2D-LS measurements running continuously during each test provided information on the foreshore evolution in proximity of the wall as well as a further measurement of the moving free surface. These measurements were calibrated using three metallic poles located at the center of the measurement region. The coordinates of the poles were known with topographic precision. The 2D-LS had an angle resolution of 0.1667° and a measuring angle of about 115°. The measuring range was 228.5m<x<243.5m.

Due to physical constraints, the mechanical wheel profiler could not reach the toe of the wall, located at about x=240.9m. The data on the near-wall bed profile obtained by the 3D scanner, for the initial condition and at the end of sea states T2, T4 and T6 were used to complete the beach profile for the last 60 cm. For sea states T1 and T5 the data of the 2D scanner were used for the same purpose.

Due to the presence of water, it was not possible to have data on the bottom morphology at the toe of the wall at the end of all the sea states T3, in high SWL conditions, and for some of the T5 sea states, as the scour was flooded notwithstanding the fact that the SWL was lowered.

Analysis of the data revealed that the profiles recovered by the wheel profiler were systematically lower, O(2 cm), than those recovered by the calibrated 2D and 3D laser scanners. On the other hand, the latter ones matched fairly well with each other. The mismatch is probably due to the burial of the wheel of the profiler in the sandy bottom. Therefore a correction was made of each bed profile measured mechanically.

The complete beach profiles were then obtained by joining the offshore part of the wheel profiler data and onshore part of the 3D/2D scanners data.

Finally, the scour evolution was also monitored by the same video camera used for wave overtopping. To this end, four rulers are attached to the sloping wall, in order to have a visual reference of the scour depth.

Sediment transport was measured by two Acoustic Backscattering Sensors (ABS), one located in correspondence of the surf-zone bar and the second close to the structure.

5. OVERTOPPING MEASUREMENTS

A gravimetric overtopping tank with a volume of approximately 1.40 m^3 was used to collect the volume of water due to overtopping. The mechanism consisted of two tanks (inner and outer) and a connection to the crest of the wall by means of one or two chutes, depending on the expected overtopping discharge.

The inner tank was placed on four force transducers (the positions of which are indicated in the additionally provided spreadsheet) that measured its weight during the tests. The outer tank provided a dry area around the inner tank to put the sensors. Also, a pumping system was used to pump the collected water during the experiment, which was activated manually, with the trigger signal of the pump being recorded to identify the intervals of usage.

The chute (0.34 m wide) was placed at the inner edge of the crest of the middle of the wall, connecting the structure and the inner tank. The number of chutes used depended on the water level. During low SWL sea states, two chutes were used, as opposed to high SWL conditions, in which only one was used (with the only exception of storm C2-1-S2-T3 in which two chutes were used).

A pressure transducer (PS), referred as PS 07, was installed at the crest of the sloping wall, in the central chute, in order to make an estimation of the number of wave overtopping events. Furthermore, two synchronised video cameras recorded the overtopping events. The first camera was located at x=225 m, at the level of the aisle along the flume, and the second one located close

to the roof, at x=238 m. Finally, in order to avoid problems due to the presence of the top beam of the structure, a plywood panel was installed on top of the beam that directed the entire overtopping volume within the chute.

6. FORCES AND PRESSURE MEASUREMENTS

In order to measure pressures on the wall, an array of six PSs (1 to 6) was installed on the wall (see Fig. 2). The PSs are spaced about 0.1 m from each other. Forces were measured on the wall using a plate at which 5 load cells were connected (see Fig. 2).

7. DYNAMICS OF THE PROTECTED BEACH

The foreshore evolution within a storm is studied by analysing the bed change after each sea state with respect to the initial bed profile $\Delta z_b = z_b(t_e, s) - z_b(t_0)$, where z_b is the bed level from the bottom of the flume, (t_e, s) is the end time of each sea state $(s=1,2,..,6)$ and t_0 is the start time of each sequence, when the beach had its 1/15 slope. The intra-storm evolution of the bed is qualitatively similar in all cases. Fig. 4 shows for Δz_b the first storm of C1 (i.e., C1-1-S2) as an example. At the start of the sequence, during T1, a bar started developing and grew in the subsequent sea states. At the same time erosion developed in the region between the bar and the wall, approximately between x=230 m and x=240.86 m. The evolution close to the structure is more complex as accretion occurred during the first storm of the sequence. During T2 the bar grew and migrated offshore, while the erosion of the region between the bar and the structure increased.

In the two high SWL sea states significant erosion developed near the toe of the structure. Also, it appears that partial backfilling occurred and Δz_b reached almost zero around x=236 m during T4. The backfilling in this region reversed to erosion in the subsequent T5, while partial filling of the scour at the toe of the seawall and continued in T6.
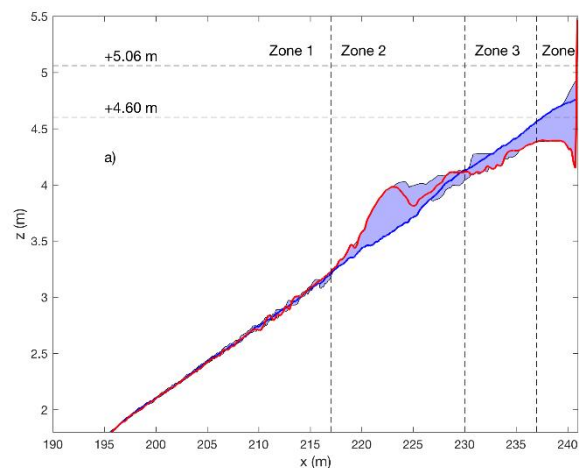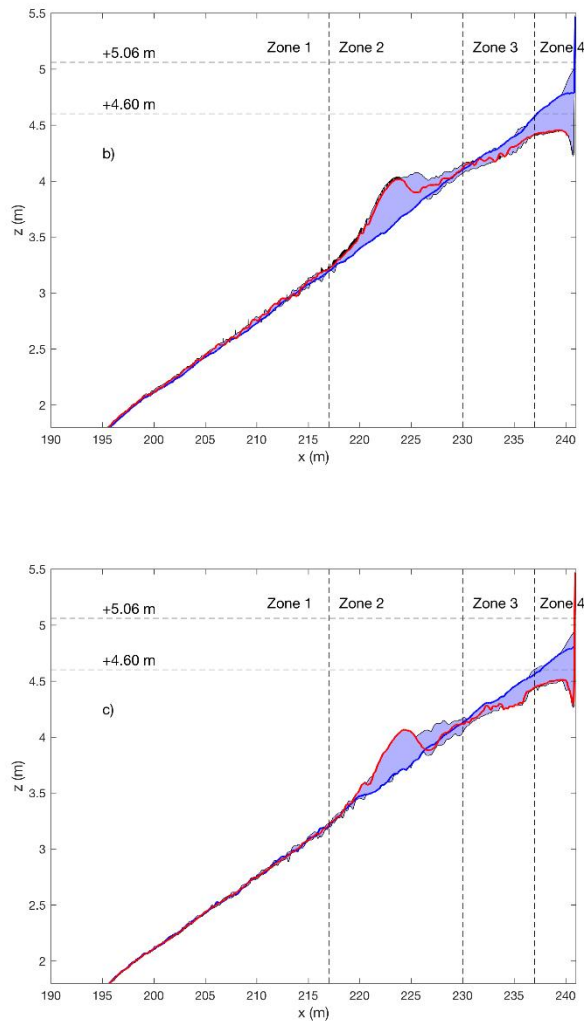
Figure 4: Zones of the beach evolution for sequence. Blue line: initial profile, red line: end profile. The blue shaded area is the range of the bed level at each position. a) C1 b) C2, c) C3.

The second storm of the sequence (i.e. C1-2-S2) started from a barred beach configuration. The bar continued to grow and migrates offshore, as shown in Fig. 4 Δz_b is negative overall close to the structure, however, during high SWL, the morphodynamics of the region between the bar and the seawall is more complex, with deposition occurring just offshore the scour area. Fig. 4 shows the initial and final profile for the three sequences together with the range of z_b reached. Results are consistent for all three sequences and the evolution of the beach can be described by dividing it into four zones. Zone 1 is the ripple region extending approximately from x=200 m and x=217 m. Zone 2 is the bar region extending approximately from x=217 m and x=230 m in C1 and C3; here the bar formed and migrated offshore during each sequence. The boundary between Zone 2 and 3 is a pivot around which the beach rotated. Zone 3 is characterised by overall erosion with respect to the initial profile, as the figure shows. However, in Zone 3 backfilling occurred at high SWL conditions as shown in Fig. 4; this could be large enough to establish a secondary bar above the original profile as the results for C1 (panel a of Fig. 4) show. The slope of Zone 3 was milder than the original 1/15 and appears to be almost zero in the upper part of this region in all sequences. This "terrace" formed at the position of the initial shoreline at the lower SWL. This is considered as the boundary with Zone 4. Here both swash motion and scour have an important role in modelling the beach.

7. DISCUSSION AND CONCLUSIONS

The ICODEP experiments investigated the evolution of an engineered beach during sequences of storms of different energy content. The analysis of the data reveals that the order of the storms has an important role in determining the beach profile. Further results (not shown here) show that, after the first storm of the cluster in which the bar rapidly forms, the bar offshore movement slowed down and its position only slightly changed during the rest of the sequence. The most active region, and the one in which the effect of the cluster is greater, is the one between the bar and the seawall itself. This region affects, in turn, the wave transformation after the passage of the bar, determining different levels of overtopping in different sequences.

This dynamics challenges existing predictive tools because of the need of knowing the initial beach profile and how this evolves during a storm. Therefore, an analysis of existing empirical and numerical prediction tools is a necessary step to support the improvement of natural/engineered coastal defence design.

ACKNOWLEDGEMENT

REFERENCES

Dissanayake, P., Brown J., Wisse, P., and Karunarathna, H. (2015). Effects of storm clustering on beach/ dune evolution. *Marine Geology*, 370:63–75, 2015.

Mansard, E.P.D. and Funke, E.R. (1980). The measurement of incident and reflected spectra using a least squares method. *Proceedings of the 17th Coastal Engineering Conference*, Vol. 1, pp. 154-172.

Romano, A., Bellotti, G., Briganti, R., and Franco, L. (2015) Uncertainties in the physical modelling of the wave overtopping over a rubble mound breakwater: The role of the seeding number and of the test duration. *Coastal Engineering*, 103:15–21.

Sénéchal, N., Castelle B., and Bryan K. R. (2017). Storm Clustering and Beach Response, chapter 8, pages 151–174. John Wiley & Sons, Ltd.

RESPONSE OF ECOLOGICALLY-MEDIATED SHALLOW INTERTIDAL SHORE TRANSITIONS TO EXTREME HYDRODYNAMIC FORCING (RESIST)

Möller, I.1, Bouma, T.J.2, Brendel, M.3, Brooks, H.1, Cao, H.2, Carr, S.4, Chirol, C.5, Christie, E.1, Dennis, R.2, Eggermond, A.9, Evans, B.1, Lustig, J.3, Miranda-Lange, M.6, Nolte, S.3, Paul, M.7, Reents, S.3, Rolfe, C.1, Royse, K.8, Schoutens, K.9, Spencer, K.5, Temmerman, S.9, Kudella, M.6

1Cambridge Coastal Research Unit, Department of Geography, University of Cambridge, United Kingdom, im10003@cam.ac.uk
2Royal Netherlands Institute of Sea Research (NIOZ), The Netherlands, tjeerd.bouma@nioz.nl
3Biocenter Klein Flottbek, University of Hamburg, Germany, stefanie.nolte@uni-hamburg.de
4Geography/Science, Natural Resources & Outdoor Studies, University of Cumbria, United Kingdom, simon.carr@cumbria.ac.uk
5School of Geography, Queen Mary University of London, United Kingdom, k.spencer@qmul.ac.uk
6Forschungszentrum Küste, University of Hannover, Germany, kudella@fzk.uni-hannover.de
7Ludwig-Franzius-Institut für Wasserbau, Ästuar- und Küsteningenieurwesen
Leibniz Universität Hannover, Germany, paul@lufi.uni-hannover.de
8British Geological Survey, Nottingham, United Kingdom, krro@bgs.ac.uk
9Ecosystem Management Research Group, University of Antwerp, Belgium, stijn.temmerman@uantwerpen.be

ABSTRACT

This paper reports on the preliminary results from a true-to-scale flume experiment carried out to better understand plant and sediment responses, as well as their interactions, under extreme hydrodynamic forcing in shallow coastal salt and brackish water marsh settings. We report here on bed level changes under individual plant seedlings and denser plant arrangements transplanted from seed and field sites on the Scheldt estuary and on the response of vertically extracted sediment cores from two UK field sites with contrasting sediment characteristics and plant species occupying the surface. Due to the relatively recent completion of the experiment in addition to time-consuming, complex data processing and analysis methods more time is required before definitive quantitative results can be reported. Initial insights into the general behaviour of salt marsh sediments under horizontal and vertical wave-driven hydrodynamic forcing, however, confirm marsh surfaces to be highly stable structures, at least during extreme storm surge events.

1. INTRODUCTION

A climate change induced acceleration in sea level rise and accompanying altered patterns of storm occurrence are set to affect shores globally throughout and beyond the 21st Century. Both sea level and wave climate have been shown to be key controls on coastal wetland evolution (i.e. phases of initiation, growth/stability, and erosion). At the same time, coastal wetlands have been shown to act as important buffers against sea level rise (by sediment accretion) and extreme storms (by wave and surge attenuation)(Möller et al., 2014). However, the risk of erosion of coastal wetland surfaces under extreme storms is yet poorly understood (Spencer et al., 2016). This leads to the need to determine the relative stability of these surface types when exposed to events of varying magnitude, particularly in the most seaward pioneer vegetation zone. Identifying what types of species and artificial protective measures are most effective in reducing erosion / increasing stability in a particular hydrodynamic setting will help identify which coastal management interventions are likely to be most successful in preventing (or at least significantly delaying) the loss of these valuable natural coastal buffers in the face of climate/environmental change.

Salt marshes are increasingly valued for their role in coastal defence, as they reduce the impact of waves and erosion on shorelines and engineered coastal defences behind salt marshes (Beaumont et al., 2008). Yet the response of salt marsh margins to extreme hydrodynamic forcing is complex and currently not well understood. The response of salt marsh and adjacent tidal flat

sediments to wave forcing is considerably more complex than that of sandy shores (Schuerch et al., 2019). This complexity arises largely due to (a) the large silt/clay fractions present and thus the cohesive nature of the sediment involved and (b) the presence of (partially mobile) biological 'structures' (plants and other organisms) within and on the surface (Bouma et al., 2005).

NW European macro-tidal shores have a negligible variation in water depth over short (< 2 m) distances and water depths over the upper intertidal zone rarely exceed 2 m such that significant wave-induced bed stress can only occur during high wave energy events. Direct observations of vegetation and sediment surface response to storm wave energy is rare (Cahoon, 2006). Establishing the impact of storms through detailed studies 'before' and 'after' is inherently difficult given the unpredictability of such events and few if any studies have been able to measure wave conditions over upper tidal flat surfaces during storms. The types of hydrodynamic conditions that lead to erosion of natural coastal features such as salt marshes, and the damage salt marsh plants sustain under wave forcing, are thus not well known. However, until we have such knowledge, it will not be possible to predict the way in which the future morphology of these systems, and thus the degree of natural coastal protection that they will provide, will alter with sea level rise and climate change. These issues are particularly critical in the early stages of marsh establishment and growth.

What is of particular concern in this context is that, while dense vegetation has been shown to protect the sediment bed from wave induced erosion (Spencer et al., 2016) (Fig. 1A), evidence suggests that a sparse vegetation cover can act as an active agent enhancing, rather than reducing, bed erosion. Such erosion occurs through bed scour around individual plant stems in relatively sandy soils (Fig. 1B) and mechanical action of flexible plant components (Fig. 1c) (Bouma et al., 2009; Feagin et al., 2009; Koppel et al., 2005) .

Figure 1: Examples of vegetation effects on fine-grained shores. A: protection by dense canopy; B: low-density plant cover with scour around individual stems; C: active scour through *Salicornia* plant movement on an eroding tidal flat (UK East coast; photos: I Möller)

This project thus aimed to quantify:

(1)   how extreme wave-forcing affects vegetation (both seedling survival of pioneer species and damage incurred by mature marsh plants);

(2)   how (and to what extent) vegetation typically present in the salt marsh pioneer zone affects erosion under extreme forcing conditions;

(3)   how vegetated salt marsh soils exposed in cliffs respond to high energy wave conditions;

(4)   how novel artificial erosion protection / stabilisation methods may be used to protect seedlings as a restoration measure (see 1) and reduce erosion as a conservation measure (see 3).

Here, we report specifically on results relating to aims (2) and (3) and focus specifically on surfaces adjacent to *Spartina* plants. Strong morphodynamic feedbacks exist between hydrodynamic forcing and the morphological characteristics of the tidal flat to salt marsh transition zone. By focussing on the most seaward salt marsh pioneer zone, exposed established dense canopies, and artificial erosion protection, we address key questions on how to manage vegetated tidal flats into the future.

2. METHODS

To achieve the above aims, we set up five separate 'experimental treatment zones' in the large wave flume (Grosser Wellenkanal, GWK), Hannover, Germany (see Figure 2 for experimental set-up).

All zones were exposed to a range of hydrodynamic conditions and were replaced with replicate marsh surfaces after four days of exposure, with three such four-day periods of exposure conducted overall (i.e. three replicate sets of marsh surfaces were exposed). Zones consisted of surfaces representing:

(A) Seedling establishment: individual seedlings of three species with different structures and stem flexibility and different associated substrates: *Scirpus* spp, *Spartina* spp, and *Puccinellia* spp;
(B) Pioneer zone plant tussocks: different densities of full-grown plants of the above species;
(C) Pioneer zone plant tussocks with erosion protection: a range of erosion protection/stabilisation measures applied to pioneer zone seedlings (same species above);
(D) Dense canopy with fronting tidal flat: pioneer and higher marsh species of contrasting flexibility/stiffness (*Spartina* spp and *Elymus* spp) as dense canopy with flat sediment surface in front; and
(E) Clifflet zone: Dense *Spartina* canopy on 10 cm high clifflet and alternative sculpted transitions to bare sediment (control) as well as with erosion reduction measures applied.

In addition, several meters behind the horizontal test section, sediment cores were mounted with an open side facing the approaching waves. They were deployed fully submerged during replicate 1 and 2. For replicate 3 they were elevated such that the still water level was at the core centre. Cores were sampled at Warton and Tillingham Flats in the UK prior to the experiments and transported to GWK in chilled conditions by car. The cores from Warton are characterised by sandy sediment while the Tillingham samples are dominated by silty sediment.
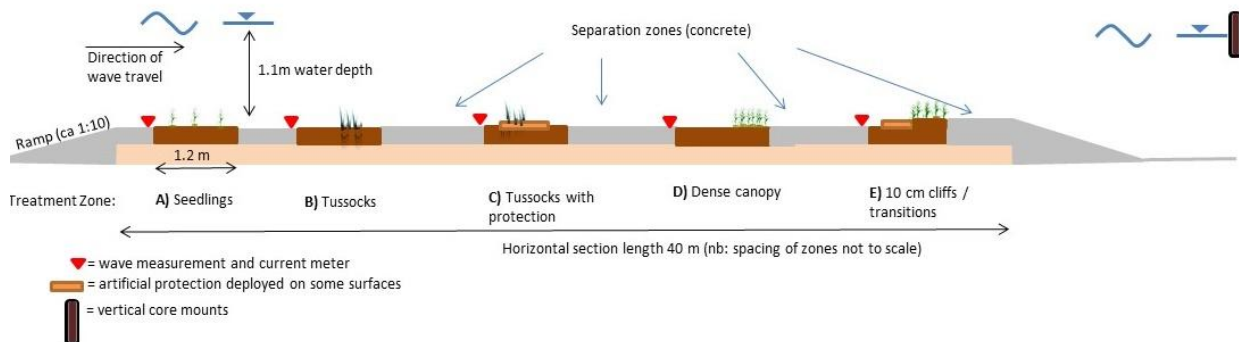
Figure 2: General setup of five experimental test sections and vertical core mount locations on cross-flume steel bar (nb: not to scale; zones A/B and C/D were swapped between wave runs 8 and 9)

Experimental Layout

A horizontal experimental platform was constructed on a sand base (Fig. 2), similar to that successfully deployed by Möller et al. (2014) in the GWK flume. The above zones stretched across the flume and consisted of 5 Europallets (0.8 x 1.2 x 0.3 m dimension, thus leaving a 0.5 m gap between the flume walls on either side and the marsh surfaces) with wooden frames. Each pallet was fully filled with substrate and transplanted seedlings or plant tussocks of varying arrangement according to zone layout excavated from sites in the Scheldt estuary. Fill sediment was flush with the sides of the wooden boxes and composed of 32% silt/clay (< 63 μm), and 31%, 11%, 24%, and 2% very fine, fine, medium, and coarse sand respectively. A previous experiment with similar material showed no significant edge-erosion effects at the juncture between soil and hard abutting

surfaces (Möller et al., 2014). The particle size distribution and shear strength of the fill sediment compares well with sediments found on north-west European salt marshes and tidal flats (see Table 1). With three replicates for replacement after each four days of flume-generated wave conditions, a total of 75 pallets were prepared in this way. Pallets were carefully transported into the flume by crane, after positioning them in their final zone layout on solid steel sleepers, such that no stress was placed on the soil surfaces prior to experimental wave runs.

Each of the replicate sets of pallets was exposed to one wave condition per day over the course of four days (Table 2) after which the replacement set of pallets was deployed. Wave conditions on day 1, 5, and 9 thus represent the first wave exposure of each of the three sets of replicates. Subsequent exposures to waves (on day 2-4, 6-8, and 10-12) then affected soils and plants that had already been affected at least once by prior conditions, although soil elevation change measurements took place before and after each wave run (see below).

Table 1: Fill sediment used in flume experiment compared to sediment at four salt marsh locations

Sediment source	Shear strenghth (kg/cm^2)		Mean size (µm)	% silt/clay (< 63 µm)
	Mean	Range		
Fill sediment (this experiment)	4.72	3.4-6.8	152.02	32.25
Tillingham, UK	4.56	0.8-9.6	70.26	73.16
Warton, UK			92.05	39.43
Zuidgors, NL	3.59	2.5-4.2		
Waarde, NL	4.81	4.1-5.5		
Rillard, NL	4.34	3.9-4.9		
Rattenkaai, NL	3.87	2.7-4.7		

Table 2: Wave conditions applied to all zones as forced by the wave maker during the three sets of simulations applied

	Wave run set S1				Wave run set S2				Wave run set S3			
Treatment set	Replicate 1				Replicate 2				Replicate 3			
Wave condition	1	2	3	4	5	6	7	8	9	10	11	12*
Hs (m)	0.3	0.40	0.6	0.7	0.7	0.7	0.8	0.8	0.7	0.8	0.8	0.5
Wave Period (s)	2.5	4.1	3.6	5.5	3.9	3.9	5.8	5.8	3.9	5.8	5.8	6.0

*monochromatic waves were run on this last day

To avoid the along-flume position of zones systematically affecting their wave exposure, zones C and D were swapped with zones A and B at the start of week 3 of the experiment, and wave conditions 6-8 were re-run as conditions 9, 10, and 11, with these zones in different positions within the flume.

Hydrodynamic measurements

Near-bed currents and waves were recorded immediately in front of each experimental zone using Accoustic Doppler Velocimeters (ADVs) mounted at a height of 15 cm above the concrete platform in the centre of the flume and flume wall mounted wave gauge arrays. With the exception of the final day of wave runs (wave condition 12), when monochromatic waves of the highest near-breaking condition were generated, waves were randomly generated in series of ca 1000 waves matching North Sea conditions (JONSWAP spectrum). Observed maxima/minima and mean forward and return wave currents alongside wave height and period were derived from the high-frequency (100 Hz) ADV measurements and wave gauge water level time-series. Wave reflection was negligible as determined using an array of three wave gauges in front of and behind the experimental platform.

Pre- and post-exposure bed elevation measurements

In addition to laser scanned bed levels, manual bed-level changes were recorded with a sedimentation-erosion table placed on fixed mounts on the concrete platform to provide locational accuracy (similar to the method described in Spencer et al.[2]) (Figure 3). The manual measurements allowed bed-level change to be determined at 27 locations per pallet (9 locations evenly spaced along 3 along-flume rows) at millimetre accuracy.
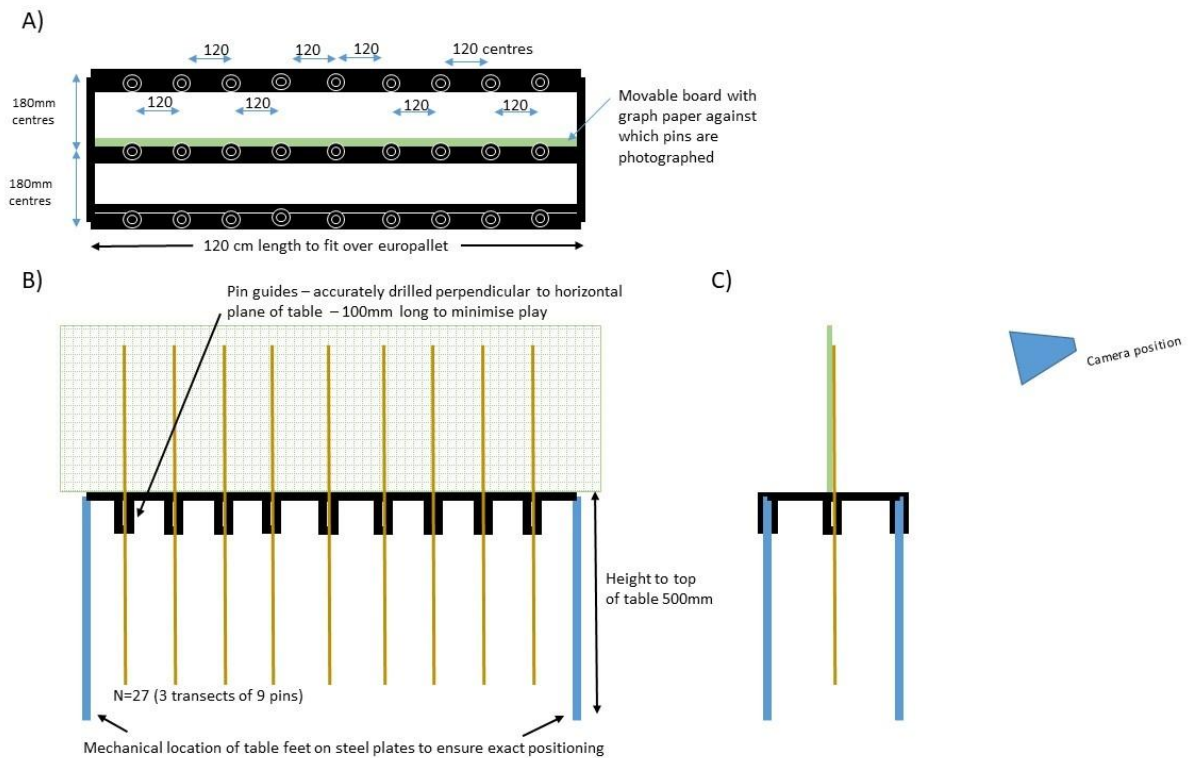

Figure 3: Manual bed-level measurements via purpose designed sedimentation/erosion table; A) top-down view of 27 pin locations positioned on three long-axis bars, B) side-view of pins and tops of pins against graph paper for quick deployment and subsequent transcribing from photographs, and C) view along the flume with pins inserted in central row.

3. RESULTS

Hydrodynamic forcing conditions

Wave heights and wave periods in the first week (Figure 4) produced a steady increase in mean and maximum wave-induced bed velocities (U_{max}), with some along-flume variability due to wave instabilities introduced as waves travelled over the test section (Figure 5). Maximum instantaneous currents were particularly variable (Figure 5B), with the highest currents overall reaching 2.33 ms^{-1} at the front of the platform during test no. 7. The average simulated random wave conditions were almost identical between test no. 7 and 11 (Hs of 0.73 and 0.72 m respectively, and Tp of 5.6 for both). The third replicate set of pallets in the front zone, however, experienced a much larger maximum stress than the second replicate on the third day of exposure (2.33 ms^{-1} compared to 0.89 ms^{-1}). As pallets were swapped between zones A/B and C/D when deploying the third replicate set of pallets, it was the plant tussock zone that experienced these conditions (see also Figure 2).

Bed level responses

Soil surface response to the hydrodynamic stress simulated in these extreme wave conditions was minimal, with average bed level change not exceeding 4 mm and both positive and negative bed level changes observed. The SET pin methodology resulted in n = 27 individual point measurements per pallet and variability of bed level change measured was high, with standard deviations larger than the average recorded bed level change per pallet.

There is no clear pattern of mean per-pallet bed level response to the applied hydrodynamic forcing and the greatest mean surface elevation changes occurred under conditions in which currents exceeded 0.8 ms^{-1} (i.e. after wave run 3) for most pallets that contained tussocks or dense canopies. Standard deviations are high and span zero change for all but two wave conditions applied to the *Spartina* seedling pallets: during the first wave run (maximum bed velocities 0.36 ms^{-1}) and test no. 11 (maximum bed velocities 1.21 ms^{-1}).
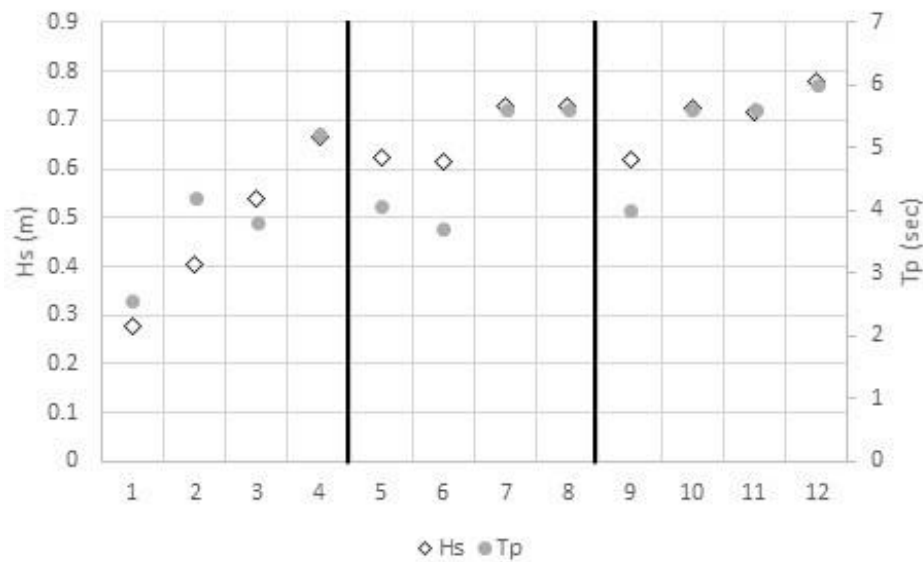
Figure 4: Significant wave height (Hs) and peak wave periods (Tp) as recorded immediately fronting the first zone (A) (nb: x-axis numbers represent exposure (day) number and exposure/day 12 conditions consisted of monochromatic waves); black lines indicate changeover of replicate pallet sets

In the case of the pallets planted with tussocks of *Spartina*, a tendency towards greater bed level change can be observed for the third replicate. They were exposed to current maxima exceeding 1 ms^{-1}, compared to the previous two, which were exposed to < 1 ms^{-1} on their first day of inundation (Figure 5B) . In addition, they were positioned in zones A and B during this replicate, which experienced higher current maxima than zones C and D where they were located during replicate one and two.

Overall, pallets covered with a dense canopy and/or cliff and fronting unvegetated soil showed comparatively higher variability in mean bed level change between consecutive wave runs and replicate pallet sets than those into which individual seedlings were planted. As mentioned above, however, per-pallet mean bed level changes overall were small compared to the variability amongst the 27 per-pallet pin measurements.

Vertical soil core responses

Figure 6 shows changes to the protrusion of the front face for both core types during replicate 2 exposure. During replicate 1 and 2, cores were fully submerged leading to higher velocities corresponding to areas of the core face located closer to the water level. For replicate 3, where still water level was at the midpoint of the core, the mean maximum velocities decrease above and below a maximum located just above still water level as a consequence of fewer waves reaching the higher portions of the core. The vertical soil cores showed a clear difference in response to the first exposure for each of the three replicates as well as between the two different extraction sites. Both cores behaved relatively similarly, with < 2 mm change along the length of the core during the first exposure, where mean orbital velocities remained below 0.1 ms^{-1} along the entire front face of the core. The second replicate set of cores exposed for the first time in run 5 , however, showed a clear difference in behaviour, particularly towards the top third of the core. In this run, orbital velocities exceeded 0.26 ms^{-1} along the length of the core, with > 0.28 ms^{-1} achieved at the top of the exposed core faces. The different sediment types responded differently to the wave forcing with the sandier core from Warton exhibiting sediment loss towards the top of the core which increased under the changed inundation level during replicate 3. The clay-rich cores from Tillingham Flats, on the other hand, even exhibited protrusion towards the top of the core for both inundation depths.
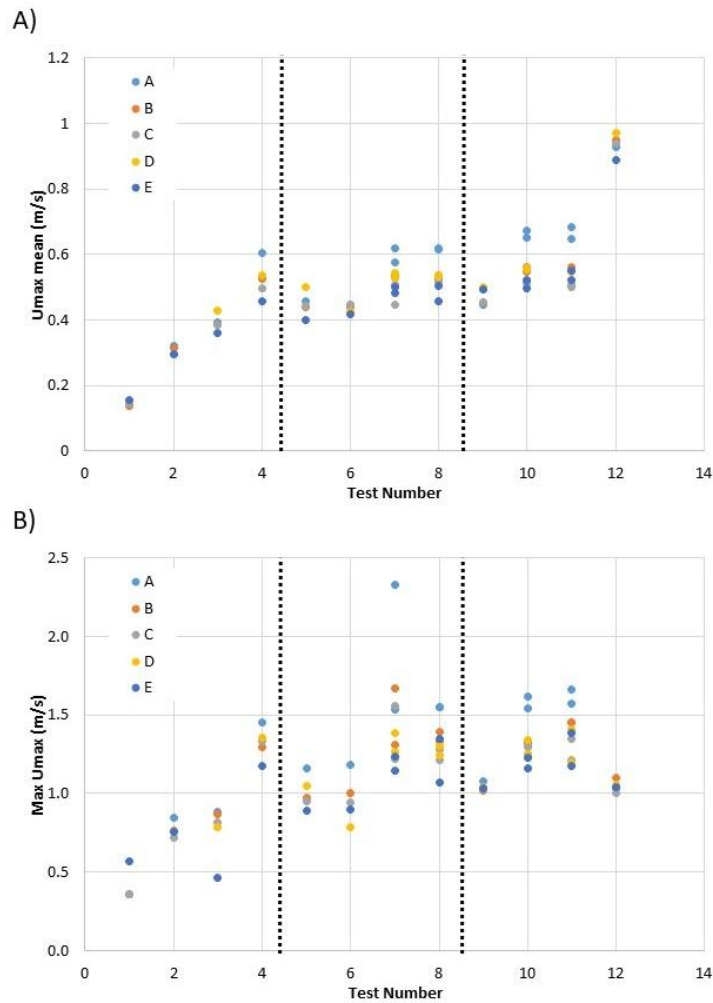
Figure 5: Mean (A) and maximum (B) wave-induced currents in the direction of wave travel for all 12 wave runs (see also Table 1 and Figure 4 for wave conditions); stippled lines indicate changeover of replicate pallet sets (nb: run number 12 consisted of monochromatic waves). Letters indicate zones at which the measurements were taken.

4. DISCUSSION

Response of horizontal surfaces to hydrodynamic forcing

The hydrodynamic forcing at the bed generated in this experiment exceeds that reported in other flume and field studies for comparable water depths. In Maza et al.'s (2015) large-scale experiment on wave damping by vegetation, for example, wave plus current generated velocities do not exceed 0.3 ms^{-1}. In the field, Shi et al. (2016) report velocities of just below 0.3 ms^{-1} from the upper tidal flats of the Jiangsu coast of China and Le Hir et al. (2000) report tidally driven maximum velocities of around 0.45 ms^{-1} on the Brouage mudflat, France. For the same location, Le Hir et al. (2000) suggest maximum wave-induced bed shear stress is achieved on the upper tidal flat at mid-tide level when the 'saturation' wave height is achieved, i.e. at the point at which the wave height to water depth ratio reaches its maximum, a value of 0.15 on the Brouage tidal flat. Wave height to water depth ratios in this experiment exceeded this value by some margin (> 0.26 in all wave runs), thus bed stresses would have far exceeded those observed in the field. The second and third replicate set of pallets deployed in the flume experienced bed velocities that, at > 1 ms^{-1}, clearly far exceeded these reported values from the literature.

The low per-pallet mean response of bed elevation to any of the wave runs and the high variability in bed level changes within each pallet (the maximum mean per-pallet bed level change observed was 3 mm with a standard error of +/- 13) suggests that no spatially uniform or consistent lowering of bed levels took place during the individual experimental runs.

Figure 6: Impressions of the vertical soil core faces before (left) and after (right). Top: sandy sediment from Warton (right); Bottom: clay-rich sediment from Tillingham (replicate 2 prior to exposure (left) and after exposure to conditions 5-8 (right)) (nb: structures from the slicing clearly visible in both)

Response of vertical core faces to hydrodynamic forcing

The two types of cores extracted from the field differed most clearly in terms of their sedimentology and vegetation growth. The greater responsiveness of the core from Warton (WS) compared to that of Tillingham (TF) when exposed to waves in the flume may thus be the results of either or both the lower cohesion / coarser grain size and/or the presence of the salt marsh grass *Puccinellia* with its fine root system instead of the more woody *Atriplex* shrub. The fact that the difference between the cores was markedly greater towards the top half of the core in spite of relatively small differences in wave driven orbital velocities with elevation, however, suggests that the vegetation may have been the dominant influence. This result can be seen in the context of other studies, e.g. Feagin et al. (2009), who suggested that roots protruding from exposed marsh cliffs can act as mechanical agents of erosion under wave action. Here, however, it is likely, that this mechanical action was assisted by the relatively less cohesive (and thus more porous nature) of the soil matrix, allowing material to be more easily 'washed out' from between the dense filamentous root mat that characterises this type of vegetation.

5. CONCLUSION

Improved knowledge of the stability of intertidal coastal habitats is not only an important consideration for flood and erosion prevention under climate change, but is essential for the successful conservation of these highly ecologically valuable ecosystems in their own right.

This paper provides the first in a series of analyses of the results of our large-scale flume experiment. It is clear from the results presented that the lack of larger spatial patterns of bed-level response to wave forcing apparent from the 27 pin readings within each pallet requires a finer spatial scale analysis of morphological change. Over the coming months we will conduct a more comprehensive analysis of the full results of bed level change derived from the deployment of a laser scanner and structure from motion photography. This should shed valuable insights into the highly spatially variable patterns of behaviour in response to the presence of different plant species and arrangements of plants within each pallet.

Our experiment has already, however, provided further proof alongside that of prior studies (e.g. Spencer et al., 2015), that exposed horizontal and vertical sedimentary surfaces typical of wetland-dominated intertidal shores are particularly resistant to wave forcing applied during single, extreme, inundation events. This in turn suggests that the importance of such individual events in terms of influencing the morphodynamic trajectory of salt marsh fringes is relatively low. We thus call for a re-evaluation of the role of extreme events versus more frequent events characterised by lower wave energy in terms of forcing morphological change.

REFERENCES

Beaumont, N. J., Austen, M. C., Mangi, S. C., and Townsend, M. (2008). Economic valuation for the conservation of marine biodiversity. *Mar. Pollut. Bull.* 56, 386–396. doi:10.1016/j.marpolbul.2007.11.013.

Bouma, T. J., De Vries, M. B., Low, E., Kusters, L., Herman, P. M. J., Tánczos, I. C., et al.

(2005). Flow hydrodynamics on a mudflat and in salt marsh vegetation: Identifying general relationships for habitat characterisations. *Hydrobiologia* 540, 259–274. doi:10.1007/s10750-004-7149-0.

Bouma, T. J., Friedrichs, M., Klaassen, P., van Wesenbeeck, B. K., Brun, F. G., Temmerman, S., et al. (2009). Effects of shoot stiffness, shoot size and current velocity on scouring sediment from around seedlings and propagules. *Mar. Ecol. Prog. Ser.* 388, 293–297. doi:10.3354/meps08130.

Cahoon, D. R. (2006). A Review of Major Storm Impacts on Coastal Wetland Elevations. *Estuaries and coasts* 29, 889–898.

Feagin, R. A., Lozada-Bernard, S. M., Ravens, T. M., Möller, I., Yeager, K. M., and Baird, a H. (2009). Does vegetation prevent wave erosion of salt marsh edges? *Proc. Natl. Acad. Sci. U. S. A.* 106, 10109–13. doi:10.1073/pnas.0901297106.

Koppel, J. Van De, Wal, D. Van Der, Bakker, J. P., and Herman, P. M. J. (2005). Self-organization and vegetation collapse in salt marsh ecosystems. *Am. Nat.* 165, E1–E12.

Le Hir, P., Roberts, W., Cazaillet, O., Christie, M., Bassoullet, P., and Bacher, C. (2000). Characterization of intertidal flat hydrodynamics. *Cont. Shelf Res.* 20, 1433–1459. doi:10.1016/S0278-4343(00)00031-5.

Maza, M., Lara, J. L., and Losada, I. J. (2015). Tsunami wave interaction with mangrove forests: A 3-D numerical approach. *Coast. Eng.* 98, 33–54. doi:10.1016/j.coastaleng.2015.01.002.

Möller, I., Kudella, M., Rupprecht, F., Spencer, T., Paul, M., van Wesenbeeck, B. K., et al. (2014). Wave attenuation over coastal salt marshes under storm surge conditions. *Nat. Geosci.* 7, 727–731. doi:10.1038/ngeo2251.

Schuerch, M., Spencer, T., and Evans, B. (2019). Coupling between tidal mudflats and salt marshes affects marsh morphology. *Mar. Geol.* 412, 95–106. doi:10.1016/j.margeo.2019.03.008.

Shi, B., Yu, Q., Gao, S., Wang, Y. P., and Wang, Y. (2016). Physical and sedimentary processes on the tidal flat of central Jiangsu Coast, China: Headland induced tidal eddies and benthic fluid mud layers. *Cont. Shelf Res.* 133, 26–36. doi:10.1016/j.csr.2016.12.015.

Spencer, T., Möller, I., Rupprecht, F., Bouma, T. J., van Wesenbeeck, B. K., Kudella, M., et al. (2016). Salt marsh surface survives true-to-scale simulated storm surges. *Earth Surf. Process. Landforms* 41, 543–552. doi:10.1002/esp.3867.

VI – HSVA – LIMB, AETB AND ICE LABORATORY

The Hamburg Ship Model Basin (HSVA) has been operating ice research facilities since 1972. The main feature is the 78 m long, 10 m wide and 2.5 m deep **Large Ice Model Basin (LIMB)**. At the end of the ice tank a deep water section of 12 m x 10 m x 5 m is available.

A mobile wave generator can be installed in the ice tank in short time when required and regular waves can be generated up to a wave height of 0.25 m.

A shallow water bottom covering the entire ice basin can be adjusted to simulate shallow water conditions (e.g. inland waterways). An air forced cooling system generates air temperatures as low as -20°C, by which the NaCl-doped water freezes at a rate of about 2 mm/hour. The mechanical ice properties of the model ice are correctly scaled in order to simulate the natural icebreaking processes. An advanced technique to improve the mechanical ice properties was developed and patented by HSVA. A motor-driven towing carriage spans the width of the tank and runs up to 3 m/s and provides a towing force of 50 kN.

A transverse carriage is installed as a sub-carriage to the towing carriage. Both carriages together make it possible to run fixed offshore structures or floating vessels in a combined and computer-controlled x-y-motion (planar motion) through the ice sheet. The new device gives the opportunity to simulate, for instance, ice drift scenarios with slow or rapid ice drift direction changes, whereby the model ice sheet is kept stationary.

The transverse carriage has a maximum static load capacity of 5 kN in any horizontal direction, and a load capacity of nearly 10 kN in vertical direction. The horizontal load can be applied on a vertical lever of up to 1.2 m length. A maximum driving force of about 3 kN is applied to the transverse carriage at speeds of up to 0.5 m/s by a geared electric motor.

Service carriages above water as well as underwater are available to carry experimental equipment, measuring devices e.g. a variety of load cells, dynamometers, accelerometers, and video cameras for surplus water and underwater.

These facilities are completed by an ice laboratory and the **Arctic Environmental Test Basin (AETB)**, an Ice tank (30 x 6 x 1.2 m) with minimum temperature of -16ŗC. Wave maker, current generators. Suitable for arctic marine biology and chemistry experiments, oil spill investigations

OVERVIEW OF THE RESULTS OF THE PROJECT 'LOADS ON STRUCTURE AND WAVES IN ICE' (LS-WICE)

Andrei Tsarau (1), Sukun Cheng (2), Hayley Shen (3), Agnieszka Herman (4), Hongtao Li (5) Karl-Ulrich Evers (6), and Sergiy Sukhorukov (7)

(1) SINTEF Ocean AS, Norway, E-mail: andrei.tsarau@sintef.no
(2) Nansen Environmental and Remote Sensing Centre, Norway. (3) Clarkson University, USA.
(4) University of Gdansk, Poland. (5) NTNU, Norway. (6) HSVA, Germany. (7) Kvaerner AS, Norway.

As an attempt to investigate several major research questions related to ocean wave-ice interaction, the HYDRALAB+ Transnational Access project '*Loads on Structure and Waves in Ice*' (LS-WICE) was conducted in the Large Ice Model Basin (LIMB) at the Hamburg Ship Model Basin (HSVA) from 24 October to 11 November 2016. The experimental data from this extensive project have been analysed in several research studies reported in other scientific papers. Here, an overall review of the obtained results is presented, and some recommendations for further work are given based on the collected experience.

1.   INTRODUCTION

As a result of climate change, Arctic sea-ice volume decreases opening northern waters for shipping and offshore engineering developments, which creates great future potentials. However, larger open-water areas in the Arctic are also associated with a less predictable environment, where storms and sparse ice features driven by large waves may create significant challenges for the safe navigation and sustainable developments. The reliable prediction of the new Arctic marine conditions requires wave models that can take into account the interaction between the dynamically changing ice cover and ocean waves, which is still an on-going research area. Understanding the ice-wave interaction mechanisms is also important for avoiding structural damage due to ice impacts on ships and structures operating in the marginal ice zone (Su et al., 2017). As an attempt to contribute to the research on several major topics related to wave-ice interaction, the LS-WICE project (Tsarau, 2017) was conducted in the Large Ice Model Basin (LIMB) at the Hamburg Ship Model Basin (HSVA) from 24 October to 11 November 2016 under the HYDRALAB+ program.

The main objective of the LS-WICE project was to collect unique experimental data which would be used for developing numerical models, validation analyses and further studies. Several series of experiments were performed to investigate linear monochromatic wave propagation under saline ice floes, including a test series in open water (series OW) to establish the baseline, Series 1000 for wave-induced ice fracture (Herman et al., 2017 and Herman et al., 2018), Series 2000 and 3000 for the wave dispersion and attenuation (Cheng et al., 2017, 2019) and for floe dynamics (Li & Lubbad, 2018), and Series 4000 and 5000 for ice-wave-structure interactions (Tsarau et al., 2017). This paper gives a brief overview of the results from the analyses of the LS-WICE experiments.

2.   INSTRUMENTATION AND EXPERIMENTAL SETUP

Fig. 1 shows the principal setup of the experiments in the LS-WICE project. At the left end of the basin, a wave maker consisting of four flap-type wave generators spans the width of the basin. The right end is a parabolic-shaped beach to reduce wave reflection. The wave basin is 72 m long and 10 m wide; the depth is 2.5 m in the first 61 m from the wave maker and increases to 5 m in the last 11 m near the beach.

For experiments with ice, first a continuous ice sheet was created overnight; then the prepared ice sheet was freed from the tank sidewalls and afterwards cut into uniform-size rectangular floes by using electrical saws. Different floe sizes were used in different test series, and an intact ice sheet was used in Series 1000.

In total, 12 pressure sensors were installed to study wave attenuation, wave dispersion relations and wave reflection. Two ultrasound sensors were deployed in the area free of ice to quantify waves reflected from the ice edge. The sampling rate of these sensors was 50 Hz. Two Inertial Measurement Units (IMUs) were installed to measure the three orthogonal translational accelerations of two ice floes in Series 3000, and one IMU was used in Series 4000 to measure the floe accelerations during its impacts on the structure. A set of load cells were installed inside the structure and fixed to a rigid carriage. Additionally, a non-contact motion tracking system, Qualisys, measured three-dimensional spatial positions of 12 reflectors (light weight balls painted with reflecting materials) at a fixed frame rate of 100 Hz. These reflectors were positioned longitudinally on upper surface of ice floes, aligning with incident wave propagation direction, with 50 cm in between.

All experiments were documented with several video cameras installed on the tank ceiling, sidewalls and the carriage.
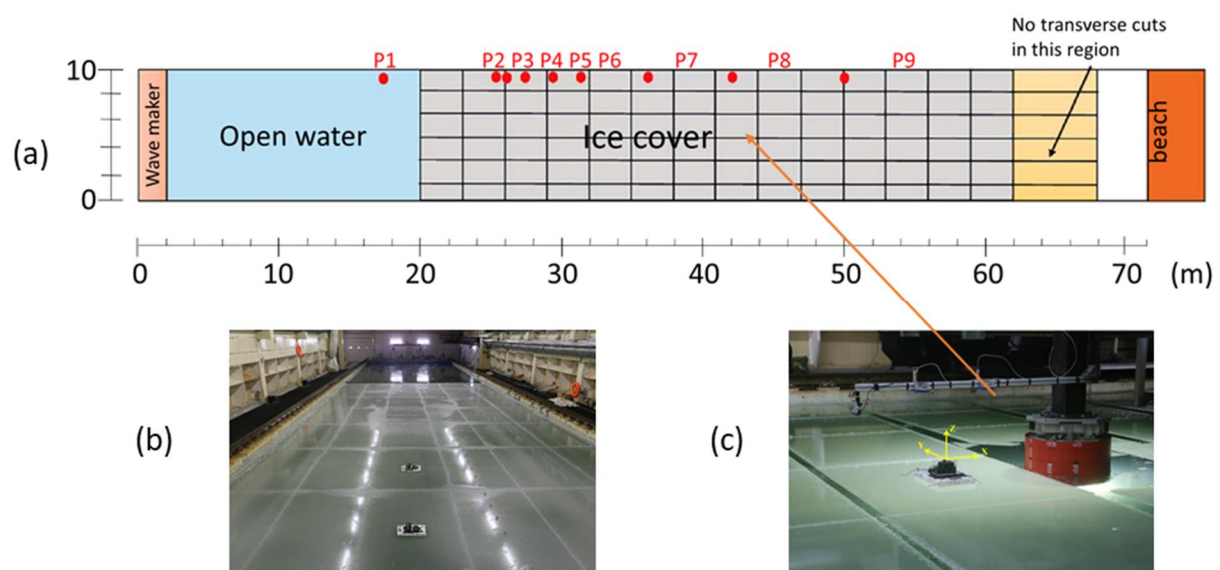
Figure 1. (a) Schematic of the experimental setup with broken ice shown as grey grids. Pressure sensors are numbered as P1 to P9. (b) Locations of the IMUs and the Qualisys reflectors. (c) Structure and its position in Series 4000.

3. WAVE-INDUCED ICE FRACTURE

Wave-induced ice fracture was analysed by Herman et al. (2018) based on the measurements and observations from Series 1000. They used digital images to obtain the floes' characteristics: surface area, minor and major axis and orientation of equivalent ellipse. This analysis shows that although the floe sizes cover a wide range of values (up to 5 orders of magnitude in the case of floe surface area), their probability density functions (PDFs) do not have heavy tails, but exhibit a clear cut-off at large floe sizes. Moreover, the PDFs have a maximum that can be attributed to wave-induced flexural strain, producing preferred floe sizes. It is also demonstrated that the observed floe size distribution (FSD) can be described by theoretical PDFs expressed as a weighted sum of two components, a tapered power law and a Gaussian, reflecting multiple fracture mechanisms contributing to the FSD as it evolves in time.

An example of a final result of the image analysis is shown in Fig. 2. As can be seen, the floe shapes are far from regular; most of floes are polygonal and elongated, and they tend to be longer in the across-tank direction than in the along-tank direction. Several processes were found to contribute to breaking and overall wear out of the ice: wave-induced flexural stress, overwash of the upper ice surface, floe-floe collisions and grinding of small ice fragments between larger ice floes. These processes might not be modelled the same as they are in the real world. Moreover,

laboratory-grown ice is typically softer, weaker, and thinner than real-world sea ice. Thus, it was not surprising that no regular breaking patterns similar to those repeatedly reported from the field were observed in this experiment. Nevertheless, the obtained laboratory data gave good insight into the processes governing ice fracturing by waves and can be used further to test alternative floe-size distribution models.
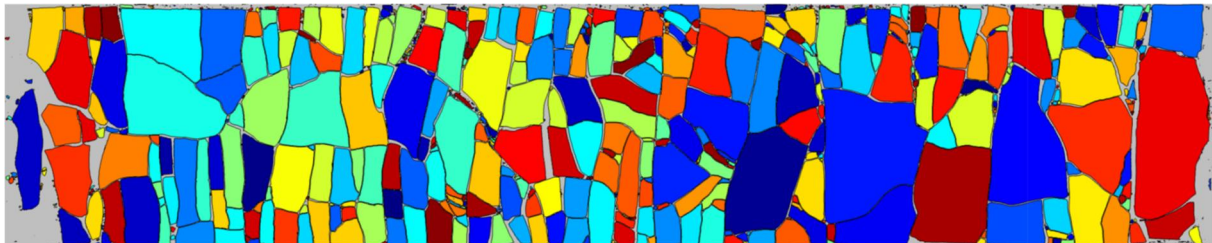

Figure 2. Results of the image analysis, where the identified ice floes are marked by black contours and randomly selected colours, and the open water is grey. The wave maker is to the left, and the beach to the right. The height of the image corresponds to the distance of 10 m (tank width).

4. WAVE DISPERSION AND ATTENUATION

Cheng et al. (2019) studied the effect of floe size on the wave dispersion and attenuation in Series 2000 and 3000. The wave number and amplitude for each run were calculated based on the pressure signals, which were first converted to meters of water using a calibrated pressure-depth relation. Fig. 3 shows the wave numbers obtained from the experimental data (in red) and also numerical results for floes with different sizes calculated based on the theory used by Cheng et al. (2019). Despite the scatter in the laboratory tests, both the experimental and theoretical results show that the wave number decreases when the floe size reduces.
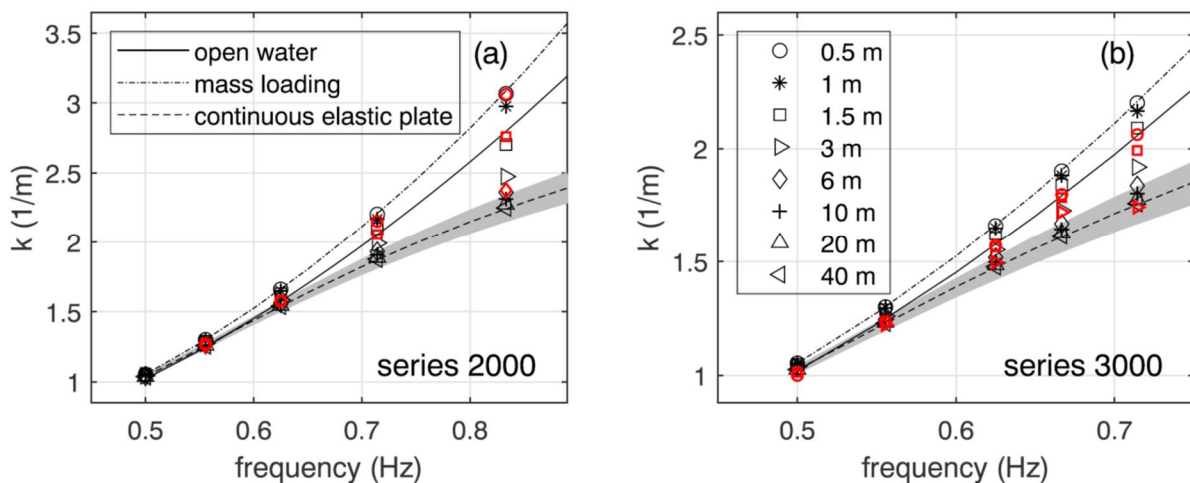
Figure 3. Wave number against frequency for Series 2000 (a) and 3000 (b): experiment (red) and theoretical results (black) for different floe sizes.

In the same study, the wave attenuation coefficient was identified by fitting the surface elevation with an exponential curve, that is, the snapshot method. The multiple modes that coexist due to the discontinuities in an ice cover create an undulating wave envelope, superimposed with an overall attenuating surface elevation. The result is an irregular amplitude variation, and therefore, the overall attenuation can be confidently measured only over a long distance. For each frequency and floe length, the measured attenuation coefficients are presented in Fig. 4.
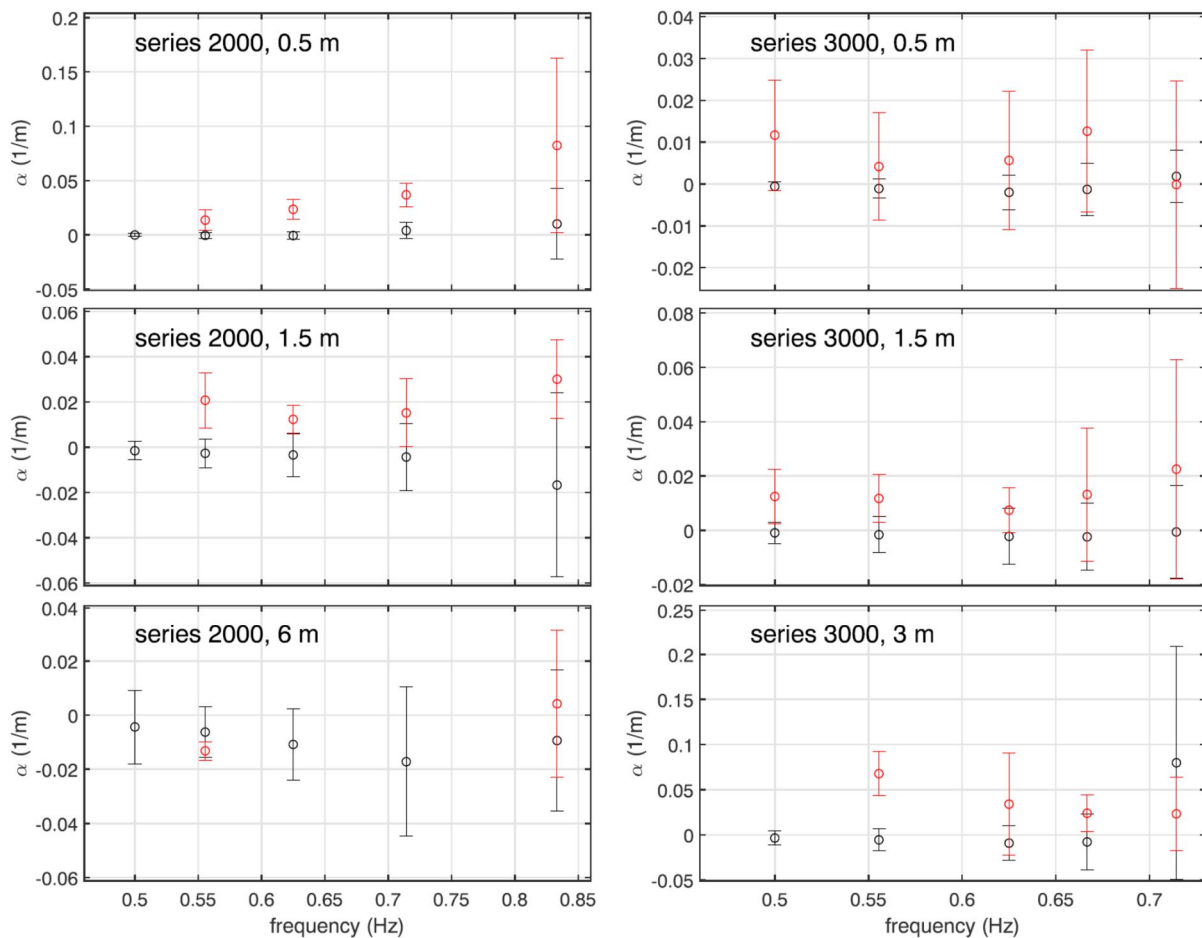
Figure 4. Attenuation coefficient α: experiment (red) and theoretical results (black) obtained by Cheng et al. (2019).

Fig. 4 shows both the large fluctuations and the discrepancy of the level of attenuation coefficients between the laboratory and theoretical results. These may indicate the presence of other damping mechanisms that were not revealed by this study, e.g., overwash, boundary layer effect under floes, floe-floe interactions and vortex shedding. An attempt to quantify the effect of floe-floe interactions on the overall damping was made in another study presented in the next section.

5. FLOE DYNAMICS

One experimental data set in the extensive LS-WISE project was analysed for investigating collisions between floes forced by regular incident waves and their effect on wave attenuation (Li and Lubbad, 2018). As the inelastic collisions between neighbouring floes dissipate wave energy, they contribute to the overall wave attenuation, which was discussed in the previous section. This contribution was quantified and the results are presented below.

Collisions between four neighbouring ice floes, instrumented with Qualisys reflectors and two IMUs while having pressure sensors deployed nearby, were examined by using both the positional and acceleration measurements (Fig. 5). The loss of wave energy due to a collision event was calculated as the difference between kinematic energy of floes before and after the collision, for which the pre- and post- collision velocities were identified first. Collision frequency, defined here as the number of collisions taking place on the same side of one ice floe in one second, was also estimated based on so-called collision signatures in the measured signals (e.g. peaks in the acceleration data). It was found that the collision frequency matched well the wave forcing frequency (1 / T = 0.5 Hz in the studied case). Finally, the energy loss because of collisions in this study was quantified to be approximately -0.025 J/m^2, which was approximately 3% of the incident

wave energy in open water and 10% of the total wave energy loss in the regions covered by the four neighbouring ice floes. Thus, this study implies that the wave energy dissipated by collisions were significant in the conducted experiment.
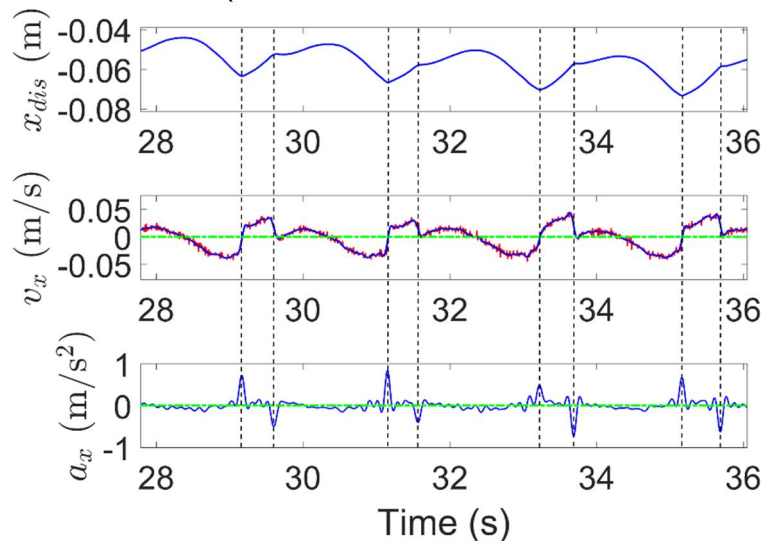
Figure 5. Displacement, velocity and acceleration of an ice floe in Series 3000 (Li and Lubbad, 2018).

6. FLOE IMPACTS ON THE STRUCTURE

In Series 4000 combined wave and ice actions on a fixed structure represented by a cylinder with a diameter of 0.69 m (in the model scale) were measured. Tsarau et al. (2017) presented an analysis of this experiment focusing on floe accelerations and forces during collision events. Some of the results from this study are highlighted here.

The cylindrical structure was located approximately in the middle of the ice tank at 43.7 m from the wave maker as shown in Figs. 1 (a) and (c). It was exposed to impacts from an adjacent ice floe, on top of which an IMU was installed to record accelerations (Fig. 1 c). Only accelerations along the surge direction (i.e., the direction of wave propagation) were studied, and the impact force was approximately estimated as $-m*a_{peak}$, where m is the mass of the ice floe (including the mass of the IMU, which is negligible) and a_{peak} is the peak acceleration. Although a set of force transducers was installed between the structure and the rigid carriage, a direct measurement of the impact forces was not possible due to the structural response. However, the forces obtained from these transducers were clearly showing the amplitudes of the wave loads and, together with the IMU measurements, helped identify the collision occurrence and impact loads. Fig. 6 shows an example of this identification for Series 4120. The impact forces due to ice-structure collisions appear as long vertical spikes with positive peaks; spikes with negative peaks mainly appear on the black curves and are attributed to floe-floe collisions. The initial sinusoidal signal shows the load due to only waves, as it took some time before the ice floe started to collide with the structure.

Fig. 6 demonstrates that the impact force on the structure was 2-5 times higher than the maximum wave load. However, as also found from this analysis, the impact occurrence in the experiments was not regular: in some tests impacts occurred almost at every wave cycle, in others impacts were rare, and in some tests no impacts were detected at all. There were several parameters influencing the impact force and its occurrence: wave height and period, ice-floe kinematics in waves, including momentum exchange due to floe-floe interaction, and the interaction area between the structure and the ice floe. The latter was found to increase after several wave cycles, which eventually led to the breaking of the ice floe. As discussed in the previous sections, wave heights and floe dynamics are interconnected and depend on the overall attenuation rate. Thus, the results from this analysis should be considered together with the results from Sections 4 and 5.
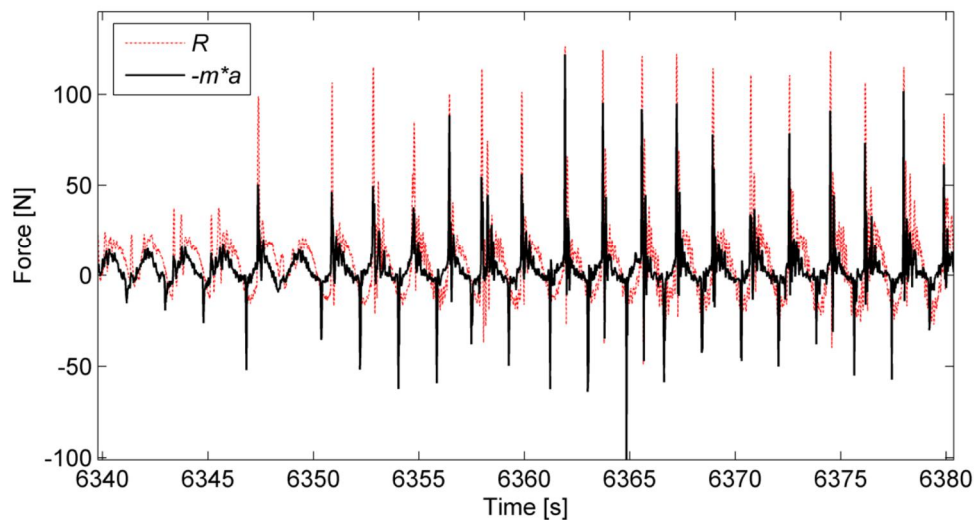
Figure 6. Time series of the impact force (black) on the structural response (red) during collision events in Series 4120.

7.   SUMMARY AND RECOMMENDATIONS

The experimental data from the extensive LS-WISE project have been analysed in several research studies reported in other scientific papers (see the reference list below). In this paper, we attempted to give an overall summary of the work related to this project, its main results and their relations to each other. Further, various recommendations to improve the experimental setup and analysis techniques for studying wave-ice-structure interactions are given based on the experience from the presented investigations.

The floe-size distribution from the LS-WICE experiments on wave-induced fracture of ice can be described by theoretical PDFs. However, these results may not be directly interpreted as the floe-size distribution in the marginal ice zone because of the difficulty to scale all the underlying processes that were identified in this laboratory study. For further work, it is recommended to try to re-examine the published floe-size data without commonly made a priori assumptions regarding the form of the PDFs and to test alternative floe-size distribution models.

The tests on wave propagation through broken-ice covers showed that the wave number decreases when the floe size reduces. The obtained attenuation rates indicate uncaptured damping mechanisms such as overwash, boundary layer effects under floes, vortex shedding and floe-floe interactions. Only the effect of the latter was estimated to be approximately 10 % of the overall damping, and the other mechanisms should be studied further.

The experiment with the structure in the LS-WICE is one of the very few laboratory studies on wave-ice-structure interaction described in the literature, and thus, the experience from this experiment may provide a useful guideline for further investigations. Both the IMUs and the optical system showed to be effective to capture floe dynamics, which was important for estimating floe-impact forces on the structure. As these loads are highly dynamic, to measure them with load cells installed on the structure, one may need to apply a load-identification model, which must be calibrated for structural response prior to tests with ice. This was not done in the LS-WICE, but instead the forces were identified based on the floe accelerations, which showed to be also a reasonable approach.

Finally, the LS-WICE project has already provided the basis for several high-level research papers, as the ones discussed here, and hopefully, there are more to come soon.

ACKNOWLEDGEMENT

REFERENCES

Cheng, S., Tsarau, A., Evers, K.-U., & Shen, H. (2019). Floe size effect on gravity wave propagation through ice covers. Journal of Geophysical Research: Oceans, 124. https://doi.org/10.1029/ 2018JC014094.

Cheng, S., Tsarau, A., Li, H., Herman, A., Evers, K. U., & Shen, H. H. (2017). Loads on Structure and Waves in Ice (LS-WICE) project. Part 1: Wave attenuation and dispersion in broken ice fields. Proceedings of the 24th International Conference on Port and Ocean Engineering under Arctic Conditions (POAC), June 11–16, 2017, Busan, Korea.

Herman, A., Tsarau, A., Evers, K. U., Li, H., & Shen, H. H. (2017). Loads on Structure and Waves in Ice (LS-WICE) project. Part 2: Sea ice breaking by waves. Proceedings of the 24th International Conference on Port and Ocean Engineering under Arctic Conditions (POAC), June 11–16, 2017, Busan, Korea.

Herman, A., Evers, K. U., and Reimer, N. (2018). Floe-size distributions in laboratory ice broken by waves. The Cryosphere, 12, 685–699, 2018 https://doi.org/10.5194/tc-12-685-2018.

Li, H. & Lubbad, R. (2018). Laboratory study of ice floes collisions under wave action. Proceedings of the twenty-eight International Ocean and Polar Engineering Conference (ISOPE), June 10–15, 2018, Sapporo, Japan.

Su, B., Aarsæther, K.G, and Kristiansen, D. (2017). Numerical Study of a Moored Structure in Moving Broken Ice Driven by Current and Wave. Proceedings of the 6th International Conference on Ocean, Offshore and Arctic Engineering (OMAE), June 25–30, 2017, Trondheim, Norway.

Tsarau, A. (2017). Data Storage Report of the Hydralab+ project "Loads on Structures and Waves in Ice (LS-WICE)" carried out at HSVA's Large Ice Model Basin (LIMB), 52 p. https://doi.org/ 10.5281/zenodo.1067169

Tsarau, A., Sukhorukov, S., Herman, A., Evers, K.-U., & Løset, S. (2017). Loads on Structure and Waves in Ice (LS-WICE) project, Part 3: Ice-structure interaction under wave conditions. Proceedings of the 24th International Conference on Port and Ocean Engineering under Arctic Conditions (POAC), June 11–16, 2017, Busan, Korea.

SEA ICE DYNAMICS: THE ROLE OF BROKEN ICE IN MULTI-SCALE DEFORMATION

Peter Sammonds (1) Sally Scourfield (1) Ben Lishman (2) Mark Short (1) Eleanor Bailey (3)
Aleksey Marchenko (4)

(1) UCL Institute for Risk and Disaster Reduction, UK, E-mail: p.sammonds@ucl.ac.uk
(2) London South Bank University, UK
(3) C-Core, Newfoundland, Canada
(4) UNIS, Svalbard, Norway

Realistic models of Arctic Ocean behaviour should capture the influence of broken ice acting as a fault gouge between sliding floes. We performed double-direct shear friction tests on floating saline ice floes in the HSVA ARCTECLAB, Large Model Basin, Hamburg. We have focused these experiments on angularity and size to determine fault gouge characteristics. In our experiments the displacements and deformation of ice gouge were characterized during on-going frictional slip for the first time. Both stable sliding and stick-slip behaviour were displayed. It appears that there are controls on behaviour according to gouge angularity. By measuring local stress, strain and acoustic emissions along the sliding interfacial fault we have captured the mechanics of the propagation of slip from slip initiation to dynamic propagation for the first time in the presence of broken ice.

1.   INTRODUCTION

As the Arctic warms, the extent of the Arctic Ocean sea ice cover is diminishing. But also the relative proportion of thick multi-year sea ice to thinner seasonal first-year sea ice is decreasing. The impact of the former will mean increased activity in the Arctic Ocean, particularly resource extraction and shipping (both freight and cruise liners), while posing challenges to indigenous people and to wildlife (Lishman, 2014). The impact of the latter will mean greater deformation of the sea ice cover as it is thinner, with generation of broken ice at all scales, which will influence the sea ice dynamics. Understanding the evolving sea ice thickness distribution and sea ice dynamics with on-going climate change is therefore crucial if the impacts of climate change are to be understood and adaptation strategies can be implemented.

Shear zones in the Arctic sea ice cover can be seen in Radarsat images as lineaments, often in sub-parallel sets (Kwok, 2001), of in-place sliding which may exert a strong control on the overall dynamics of Arctic sea ice cover (e.g., Hopkins, 1998; Schulson, 2004; Sammonds et al., 2005). Models of sea ice thickness are strongly dependent on the ratio of shear to compressive ice strength (Miller et al., 2005). Since shear deformation and slip is controlled by friction, a better understanding of the frictional behaviour is essential for a better understanding of overall Arctic sea ice dynamics. However, broken ice, acting like a fault gouge, can dramatically alter frictional properties (Scott et al., 1994). These may act at all scales (e.g., Marsan et al., 2004). Ice rubble consisting of broken ice is generated by Arctic vessels frequenting the same channel or as floes within a shear ice mass. At the local scale, accumulations of ice rubble provide resistance to repeated transits when it is both unconsolidated and consolidated (Mellor, 1980) and ultimately prevents transit through the channels. Understanding the frictional behavior and properties of consolidated rubble in this context could contribute to better management of these problems, and in future enable the use of Arctic shipping routes throughout the year. At the ocean scale, broken ice could exert a strong control on slip on cross-basin lineaments.

The frictional behavior of saline ice sliding in direct contact has already been described by empirical adaptations of Amonton's Law. Fortt and Schulson (2009). Lishman et al., (2011, 2013) have developed rate and state laws to describe this behaviour, and Hatton et al. (2011) and Schulson and Fortt (2013) describe sliding in terms of ice micromechanics and thermodynamics. What is not known is how the presence of broken ice between the sliding surfaces affects friction, and our work aims to address this
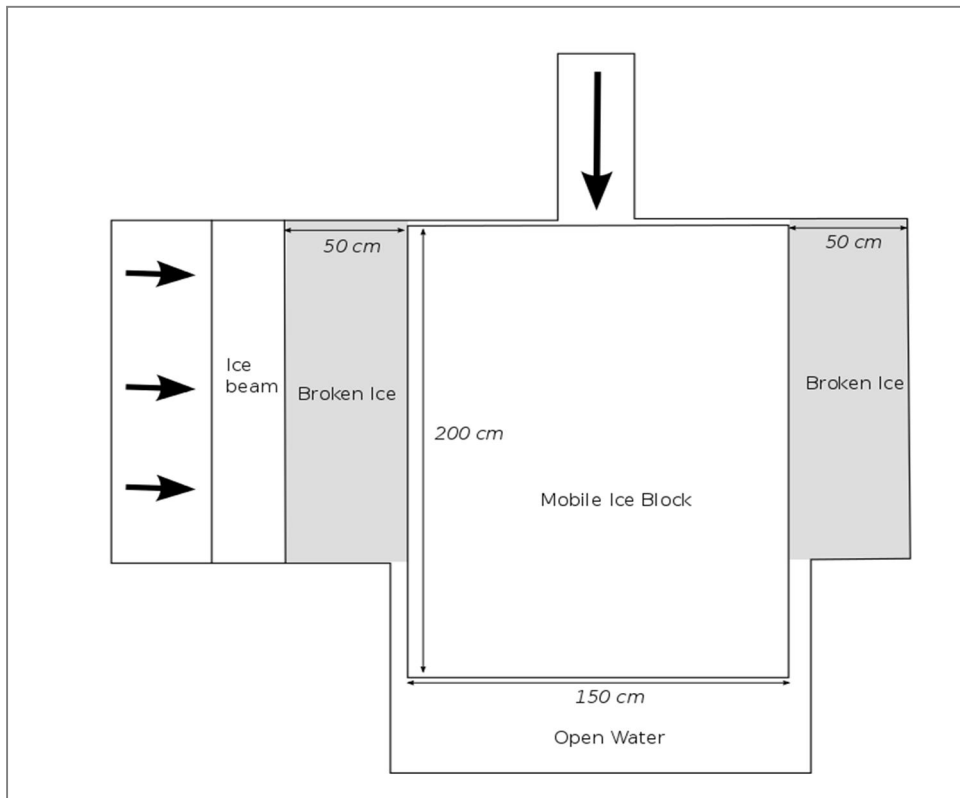
2. METHODS

Figure 1. The experimental setup. A mobile, floating ice block is surrounded on two sides by regions of ice rubble. Side load is applied throughout the slide-hold-slide experiments by hydraulic jacks housed within a specially designed frame, denoted here by the three horizontal arrows.

Our method was to perform ice basin experiments in which a saline ice blocks, representing sea ice floes, with broken ice gouge are deformed by a pusher plate and confined by side loading panels (Figure 1). The experiments required the use of the HVSA ARCTECLAB Model Ice Basin (e.g. Lishman et al., 2009, 2011). The HSVA basin offered a controlled environment in which to conduct experiments, which contrasted with previous experimental field work in the Barents Sea in 2014 and 2015 (Scourfield et al., 2015). The ability to control variables such as temperature (which has been found to influence friction between saline ice blocks sliding in direct contact), ice thickness, applied shear stress and velocity greatly enhanced the quality of the results produced which could then be used for comparison with the aforementioned field experiments. A less challenging working environment also allowed the deployment of acoustic emissions sensors, which had previously been used to monitor fracture in ice. The advantage of using HSVA is that it allowed the use of saline water, which other comparable facilities do not.

Experiments simulated slide-hold-slide experiments (Sammonds et al., 2005; Lishman et al., 2011) (Fig. 1). A mobile, floating ice block surrounded on two sides by broken ice was held for specified "hold times" ranging from 1 second to hours. Following this, a direct load was applied to the central floating ice block and the force needed to reinitiate its movement recorded. Side load panels designed and built at UCL applied a normal force throughout. We used ice floes of up to 30cm thickness. The acoustic emissions produced during deformation was captured. Filming the ice rubble region during shear allowed analysis of the mechanisms involved during deformation (for example, the role of force chains and fracture), and where shear occurs within the rubble region. We carried out a new investigation the effect of ice rubble angularity on frictional behavior such as sliding stability and frictional strength, and the response to the application of high and low normal

stresses. Experiments were performed to investigate the behavior of fracturing of ice bonds under tension, to complement the shear tests.

3. RESULTS
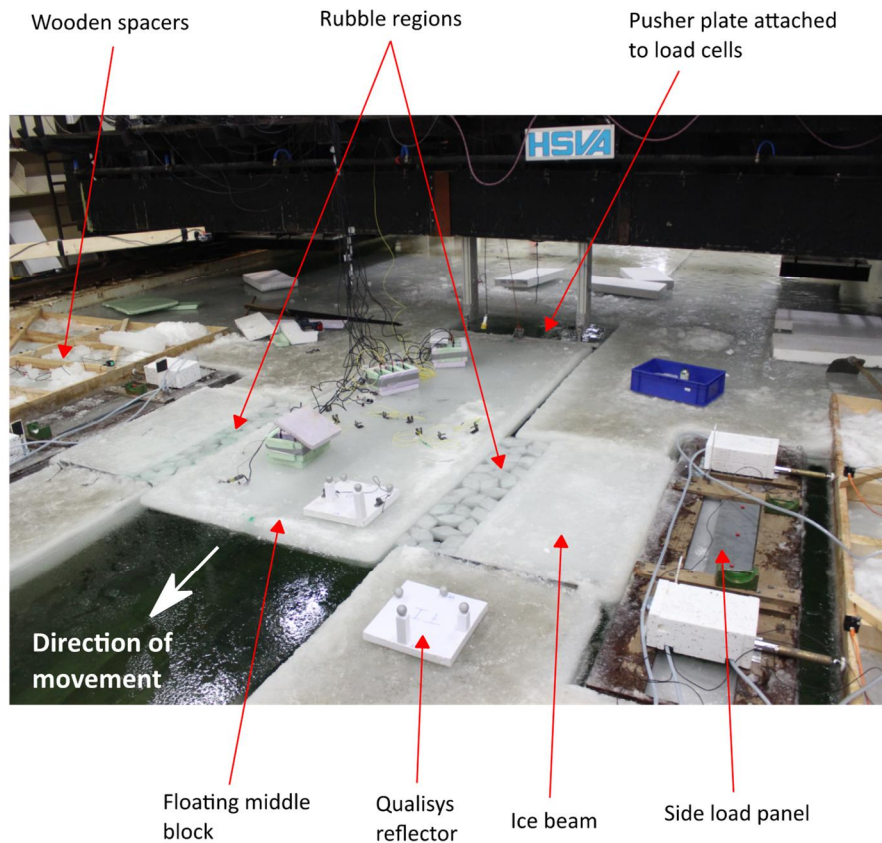
Figure 2. A labelled photograph showing an experimental run in the HSVA ice tank.

A novel set of 4 double-direct shear experiments were performed with 4 velocity steps and 4 hold times steps. 4 fault gouges were used: flat pancakes and regular parallelepipeds of ice, each of two uniform sizes. Global loads pushing and side loads were measured by load cells and slip displacements by reflector tracking image capture. Local stresses, strains and acoustic emissions along the sliding fault interface were measured by embedded instruments. Dilatancy of the gouge was measured by laser range-finders. The experiments were recorded by a global view camera and a local view camera on the gouge. Experiments on ice-ice friction (with no gouge) and free-floating ice were also done to provide baseline data.

The level ice and stacked ice blocks were characterized by thickness measurements, temperature and salinity profiles, compression and four-point bend tests, thin sections and surface profiles (of the sliding faults and the layered ice)

Here we address the relationship between the maximum effective friction coefficient when sliding commences, μ_{peak} and hold time. Values for μ_{peak} were extracted by identifying the time at which the maximum load occurred when sliding commenced and taking the corresponding value for μ at that time (Fig. 3). Two regimes appeared to exist, before and after a hold time of approximately 10^4

seconds. In the first regime, after shorter hold times, μ_{peak} changed very little. After longer hold times, in the second regime, μ_{peak} increased significantly. We believe that in the first regime (at short hold times) μ_{peak} was low because the contribution of consolidation to resistance was minimal, and the rubble pieces were free to move around. In the second regime (at long hold times) consolidation, or the shear strength of the consolidated rubble region, was the primary cause of

high resistance. As such, friction was not a suitable way of describing resistance in this regime as the processes of consolidation took over. We also noted that increased acoustic emissions signals are recorded when sliding recommences after long hold times. These suggested the occurrence of fracture and supports our assumption that at long hold 2 times, the shear strength of the consolidated rubble region is responsible for the 1.5 resistance to sliding.
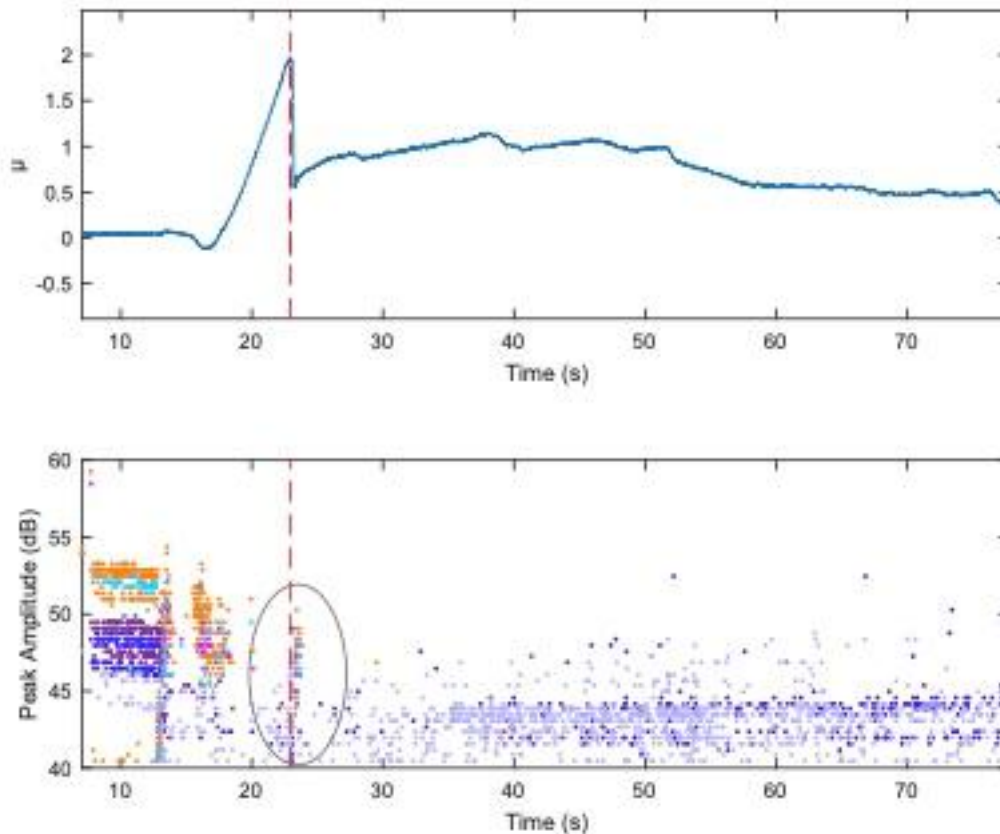
Figure 3. Experimental results showing how the effective coefficient of friction and acoustic emission activity vary during an experimental run. The peak in μ after a hold time of 10,000s is shown. (The increased acoustic emission activity at 22s in an artifact.)

4. DISCUSSION

Realistic models of Arctic Ocean behaviour should capture the influence of broken ice acting as a fault gouge between sliding floes. We have focused here in these experiments on angularity and size to determine fault gouge characteristics.

In our experiments the displacements and deformation of ice gouge were characterized during on-going frictional slip for the first time. Both stable sliding and stick-slip behaviour were displayed. It appears that there are controls on behaviour according to gouge angularity. By measuring local stress, strain and acoustic emissions along the sliding interfacial fault we have captured the mechanics of the propagation of slip from slip initiation to dynamic propagation for the first time. By measuring friction under conditions of stepped velocities and hold times we are able to incorporate the influence of fault gouge into a modified rate and state friction law. This will be developed on the full analysis of the experimental results. The advantage of a rate and state law is that it is a relatively simple empirical law, but captures much of frictional behaviour.

The effect of hold time on the effective peak coefficient of frictions, μ_{peak}, falls into two distinct regimes - before approximately 10^4 seconds (where μ_{peak} is low), and after (where μ_{peak} increases dramatically) (Fig. 4). This trend is common to all rubble types. In the first regime, friction is controlled primarily through rubble dynamics - the contribution of consolidation is minimal. In the

second regime, consolidation, or the shear strength of the consolidated rubble region, is the primary cause of high resistance. As such, at long hold times friction may not be a suitable way of addressing this problem

Novel experiments on stacked ice blocks, free floating and submerged, with both a liquid interfacial layer and none, have for the first time characterized the development of the consolidated layer under these conditions in the controlled environment of an ice tank. These will be used to test a thermal and mechanical consolidation model.

We have trialed a new experiment local strain measurement system. Difficulties we encountered included the loading pusher plate breaking under high loads and there was insufficient loading capacity for ice consolidated beyond 10,000s. We overcame this by separate consolidation experiments on stacked ice blocks and measuring the interfacial shear strength. We used one test temperature of -10 deg C. The experiments were of such complexity and duration that repeats at a different temperature were not practical. The environmental test tank at HSVA was unavailable. We used the large ice basin which has lower salinity water. These did not detract from the overall findings from the experimental programme.
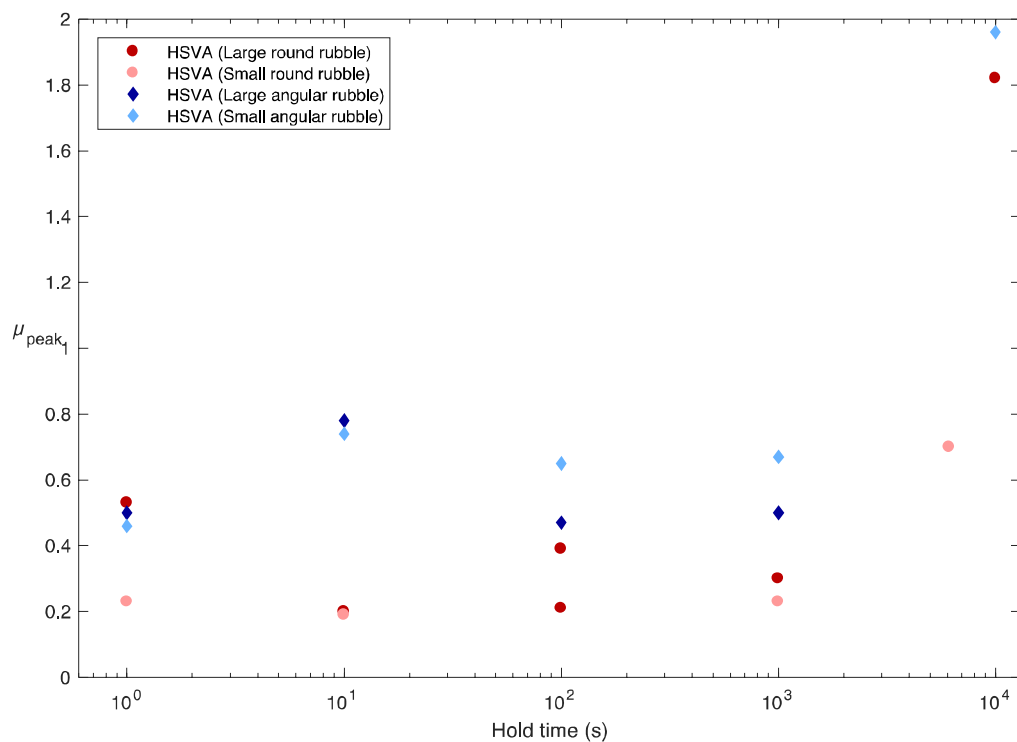
Figure 4. The relationship between μ_{peak} and the hold time for four rubble types. It should be noted that the μ_{peak} for the large angular rubble type at the longest hold time of 10,000s is not shown due to insufficient load capacity to move the ice floe under these conditions. But the lower bound limit is 7 kN. Force.

REFERENCES

Fortt, A.L. and Schulson, E.M. (2009). Velocity-dependent friction on Coulombic shear faults in ice. *Acta Materialia*, 57(15), 4382–4390.

Hatton, D.C., Sammonds, P.R. and Feltham, D.L. (2009). Ice internal friction: Standard theoretical perspectives on friction codified, adapted for the unusual rheology of ice, and unified. *Philosophical Magazine*, 89(31), 2771–2799.

Hopkins, M.A. (1998). Four stages of pressure ridging. *J. Geophys. Res.* 103(C10), 21883.

Kwok, R. (2001). Deformation of the Arctic Ocean sea ice cover between November 1996 and April 1997: A qualitative survey. *In IUTAM Symposium on Scaling Laws in Ice Mechanics and Ice Dynamics* (ed. J. P. Dempsey & H. H. Shen), pp 315-322, Kluwer Academic Publishers.

Lishman, B., Sammonds P. and Feltham, D.L. (2009). The Rate- and State- Dependence of Sea Ice Friction. *POAC*'09.

Lishman, B, Sammonds, P. and Feltham, D. (2011). A rate and state friction law for saline ice. *J Geophys Res*, 116, 1–13.

Lishman, B., Sammonds, P. and Feltham, D. (2013). Critical slip and time dependence in sea ice friction, *Cold Reg Sci & Tech*, 90-91, 9-13.

Lishman B. `and Sammonds, P.R. (2013). Memory in sea ice friction, *POAC'13*.

Lishman, B. (ed) (2014). Arctic Risk: A Discussion of the Possible Outcomes of Two Disaster Scenarios, *IRDR Special Report 2014-02*, UCL Institute for Risk and Disaster Reduction

Mair, K., Frye, K. and Marone, C. (2002). Influence of grain characteristics on the friction of granular shear zones, *J. Geophys. Res.*, 107(B10), 2219

Marson, D., Stern, H., Lindsay, R. and Weiss, J. (2004). Scale dependence and locatization of the deformation of Arctic sea ice, *Phys. Rev. Letts*, 93, 178501.

Mellor, M. (1980). Ship resistance in thick brash ice. *Cold Reg Sci & Tech*, 3(4), 305–321.

Miller, P.A, Laxon, S.W. and Feltham, D.L. (2005). Improving the spatial distribution of modeled Arctic sea ice thickness. *Geophys Res Lett*, 32(18)

Sammonds, P. et al. (2005). Experimental study of sliding friction and stick-slip on faults in floating ice sheets, *POAC'05*.

Schulson, E.M. (2004). Compressive shear faults within arctic sea ice: Fracture on scales large and small, *J Geophys. Res*, 10.1029/2003JC002108.

Schulson, E.M. and Fortt, A.L. (2013). Static strengthening of frictional surfaces of ice. *Acta Materialia*, 61(5), pp.1616–1623.

Scott, D.R., Marone C.J. and Sammis, C.G. (1994). The apparent friction of granular fault gouge in sheared layers, *J Geophys. Res* 10.1029/93JB03361.

Scourfield, S. et al. (2015). The effect of ice rubble on ice-ice sliding. *Ports and Oceans Under Arctic Conditions (POAC).*

ACKNOWLEDGEMENTS

INTERNAL SOLITARY WAVE PROPAGATION IN ICE-COVERED WATER

Magda Carr (1), Andrea Haase (2), Karl-Ulrich Evers (3), Ilker Fer (4), Peter Sutherland (5), Atle Jensen (6), Henrik Kalisch (4), Jarle Berntsen (4), Emilian Părău (7), Øyvind Thiem (8) & Peter. A. Davies (9)

(1) Newcastle University, UK, E-mail: magda.carr@ncl.ac.uk
(2) Hamburg Ship Model Basin, Germany, E-mail: Haase@hsva.de
(3) Solutions4Arctic, Hamburg, Germany, Email: kueham@gmail.com
(4) University of Bergen, Norway, E-mail: ilker.fer@uib.no henrik.kalisch@uib.no jarle.berntsen@uib.no
(5) IFREMER, University of Brest, France, E-mail: peter.sutherland@ifremer.fr
(6) University of Oslo, Norway, E-mail: atlej@math.uio.no
(7) University of East Anglia, UK, E-mail: e.parau@uea.ac.uk
(8) Norwegian Public Roads Administration, Bergen, Norway, E-mail: oyvind.thiem@vegvesen.no
(9) University of Dundee, UK, E-mail: p.a.davies@dundee.ac.uk

Internal solitary waves (ISWs) propagating in a stably-stratified two layer fluid in which the surface condition changes from open water to different ice types namely, nilas ice, grease ice and level ice are studied. Experiments are conducted in a cold laboratory at the Hamburg Ship Model Basin (HSVA). A customized flume is designed and built. Specific objectives are to obtain accurate measurements of (i) wave amplitude, (ii) wave-induced velocity field, and (iii) wave speed. In addition, measurements of ice thickness and wave-induced ice floe speed are made. The main questions to address are (i) what is the dissipation of ISW energy under different ice conditions and (ii) what is the effect of ISW energy on the ice dynamics?

1.   INTRODUCTION

Oceanic internal solitary waves (ISWs) propagate along density interfaces and are ubiquitous in stratified water. Their properties are strongly influenced by the nature of the sea surface above the waves, and by the geometry of the containing basin below. As the Arctic Ocean evolves to a seasonally more ice-free state, the internal wave field will be affected by the changes at the surface. The relationship between ISW dynamics and ice is crucial in understanding (i) the general circulation and thermodynamics in the Arctic Ocean and (ii) local mixing processes that supply heat and nutrients from depth into upper layers, especially the photic zone. This, in turn, has important ramifications for sea ice formation processes and the state of local and regional ecosystems.

It is known that ISWs cause flexure of sea ice (Czipott *et al.*, 1991; Marchenko, Morozov, Muzylev, & Shestov, 2010) and theoretical studies suggest that they are responsible for the formation of ice bands in the marginal ice zone. However, the effect of diminishing sea ice cover on the ISW field (and vice versa) is not well established. A better understanding of ISW dynamics in the Arctic Ocean and, in particular, how the ISW field is affected by changes in both ice cover and stratification, is central in understanding how the rapidly changing Arctic will adapt to climate change.

While field observations have provided insight into ISW dynamics in the Arctic Ocean, none to date isolate the effects of individual ice, ocean and wind parameters. Satellite imagery has provided valuable new insight but its use is restricted to areas of open water and to climatic conditions being favourable for the observations to be made. There is a clear need, therefore, to supplement field work with modelling studies. In this campaign, a laboratory investigation of ISWs in a two-layer stratified flow propagating from open water to under different ice features is performed. The ice type is varied and the interaction between the ISW and ice investigated. This is the first time that ISWs have been generated under ice in a laboratory setting.

This paper presents the experimental set-up, the model ice production and some key findings. The data processing and data analysis is under review in *Geophysical Research Letters* (Carr *et al.*, 2019).

2. EXPERIMENTAL SET UP AND PROCEDURE

2.1 GENERAL DESCRIPTION

The experiments were performed in the Arctic Environmental Test Basin (AETB) at the Hamburg Ship Model Basin (HSVA). The AETB is a cold room which houses a basin of 30m length, 6m width and 1.5m depth and has a volume of 270m^3. The room can be cooled to a temperature of -15°C. For this study, the basin was emptied and an internal wave flume was designed and custom-built within the AETB. The wave flume had dimensions of 6m in length, 0.5m in width and 0.6m in depth and consisted of rectangular aluminium profiles (type Bosch-Rexroth 45/45; 90/90 and 90/180mm) with corner connections and 15 mm thick transparent Plexiglass® plates (*Fig. 1*). The Flume was composed of 2 Plexiglass® elements (length=3000m, width=470mm and height=600mm) which had a total length of 6000mm and was based on a foundation that also consisted of rectangular aluminium profiles (12 supports). The Plexiglass® construction allowed visualisation from the side and illumination from below. The total height of the experimental set-up was approximately 1.7m.
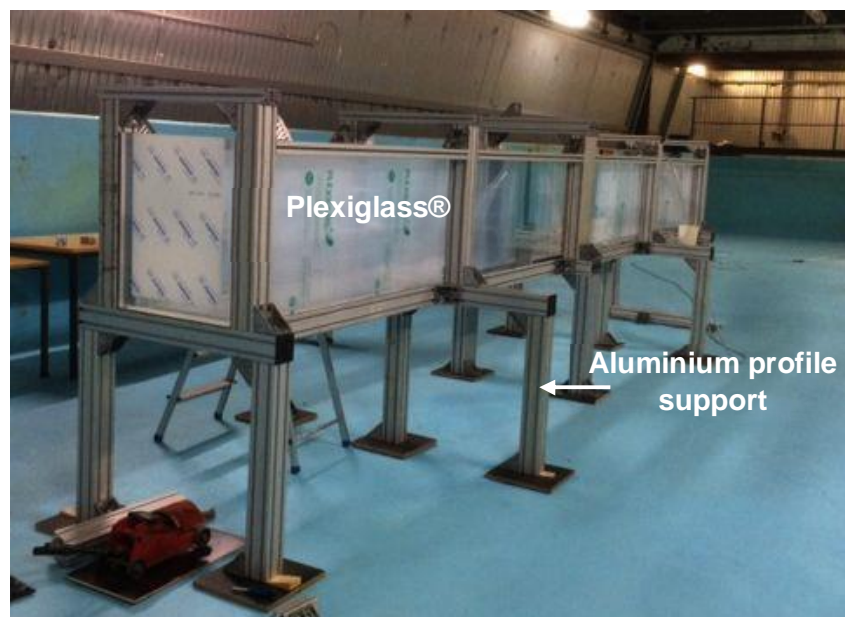
Figure 1. Plexiglass® flume (6m x 0.47m x 0.6m) installed within HSVA's (blue) Arctic Environmental Test Basin.

2.2 STRATIFICATION OF THE WATER COLUMN

The flume was filled with homogeneous salt water of prescribed density ρ_3 = 1045 kg/m^3 to a depth h_3. Less dense brine solution of density ρ_1 = 1025 kg/m^3 was then slowly added to the top of the dense salt water layer via an array of floating surface sponges (*Fig. 2*). Consequently, an interface (pycnocline) between the two fluids formed in which the density, varied as a linear function of depth z. After the flume was stratified, ice was then made or added at the surface such that half the surface was ice-covered and the other half was ice-free. *Figure 3* shows a schematic diagram of the flume arrangement.
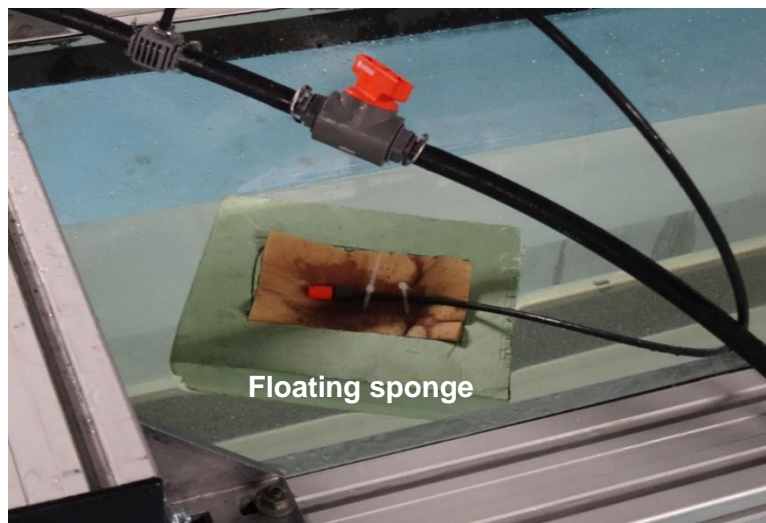
Figure 2. Brine solution of density ρ_1 = 1025 kg/m^3 was added via an array of floating surface sponges.
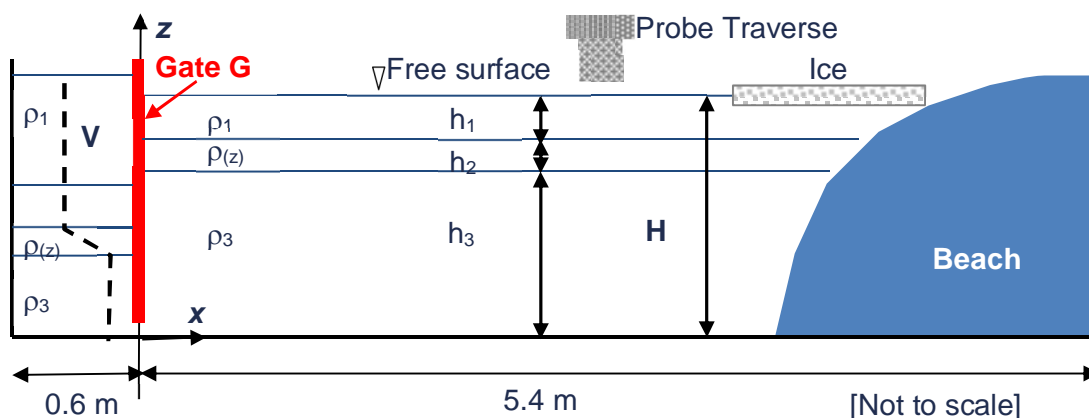
Figure 3. Schematic diagram of the flume arrangement.

2.3 ICE PRODUCTION

Different ice types were frozen on the surface of the water column or produced in the Large Ice Model Basin (LIMB) at HSVA and then added to the water surface in the flume.

(i) **Level ice** was made in the LIMB. The model level ice was frozen from a 0.7% sodium chloride solution in the natural way, i.e. the water/ice surface was exposed to cooled air. The preparation of the ice sheet was started by a seeding procedure. For this purpose water was sprayed into the cold air of the ice tank. The droplets froze in the air forming small ice crystals which settled on the water surface. By this method the growth of a fine-grained ice of primarily columnar crystal structure was initiated. Tank water which had been pressure-saturated with air was uniformly discharged along the tank bottom during the entire freezing process. Immediately after discharging, the surplus air segregated from the water and formed tiny air bubbles. These air bubbles whose diameter ranged from 200−500 microns rose to the ice sheet, where they were embedded into the growing ice crystals. An advantage of the air content in the ice is the possibility to adjust the ice density so that the density difference between ice and water is within the natural range. The embedded air bubbles gave the model ice a white appearance (Evers & Jochmann (1993); Evers,

2015). When the ice sheet reached a certain thickness, sections were cut and removed from the LIMB, and then kept in a cold storage unit on boards of wood until required. The floes of level ice, sitting on wood, were carefully lowered into the stratification and then the wood slid out from beneath them (*Fig. 4*).
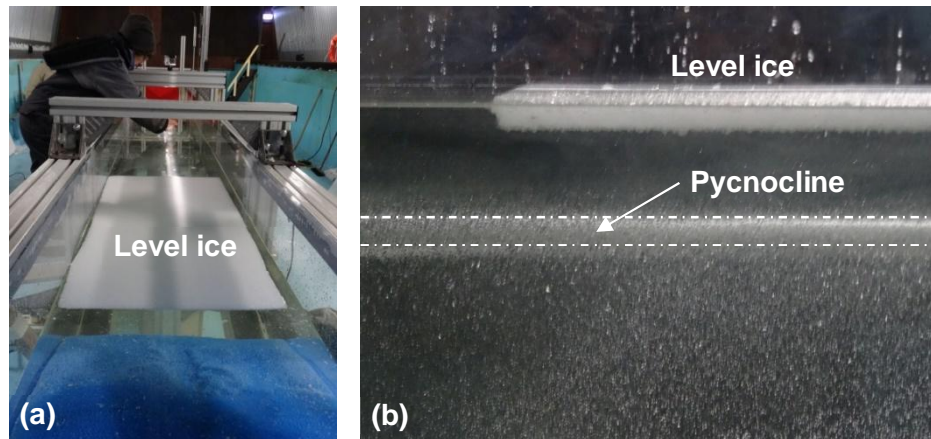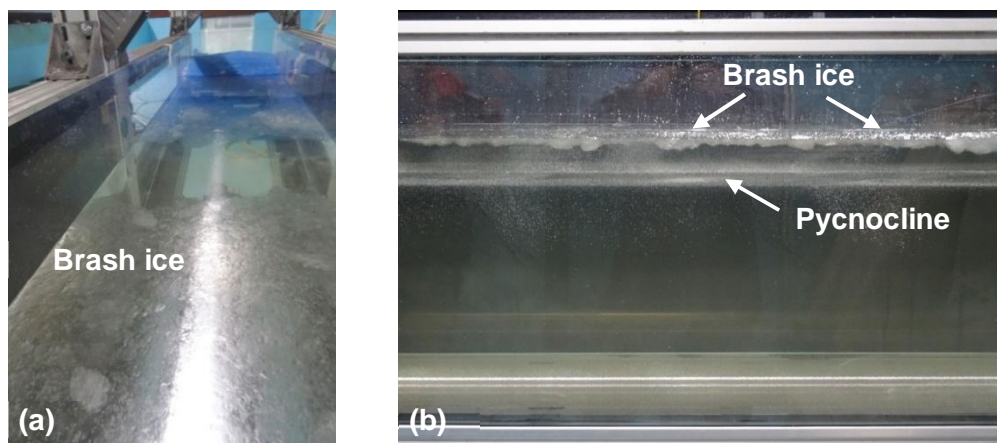

Figure 4. Level ice floe in the stratified flume (a) viewed from above and (b) viewed from the side; the pycnocline is shown in (b).

(ii) **Grease ice/brash ice** was made in buckets by crushing model level ice. The grease ice was then carefully added to the surface of the water column using a grate and hand shovel (*Fig. 5*). The grate was placed in the top layer of the water column; care was taken not to disturb the pycnocline and the grease ice was slowly poured over the grate using the hand shovel. The grate was then removed from the water column.

Figure 5. Brash/Grease ice in the stratified flume (a) viewed from above and (b) viewed from the side; the pycnocline is shown in (b).

(iii) **Nilas ice** was made by reducing the temperature in the AETB so that the surface of the water column in the flume froze (*Fig. 6*). Open water sections were maintained by placing styrofoam at the surface during the freezing process. The styrofoam lids were removed just prior to an experiment commencing.
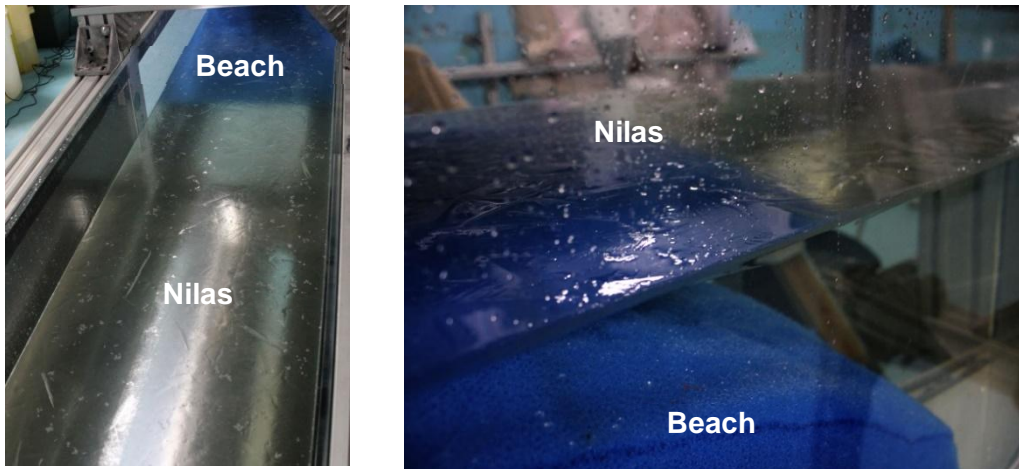
Figure 6. Nilas ice in the stratified flume.

A gate was inserted at the upstream end of the flume (*Fig. 7a*) and lowered approximately 1 cm above the bottom of the flume. A beach consisting of polyether filter foam (*Fig. 7b*) was placed at the downstream end of the flume and absorbed some of the ISW energy. A fixed Volume V, of water density ρ_1 was then added behind the gate. Due to hydrostatic balance, fluid of density ρ_3 flowed under the gate into the main section of the flume. After the Volume, V, was added, the entire fluid depth H, in the main section of the flume was measured using a pre-set tape on the Plexiglass® window. During filling the air temperature was kept just above $T= 0°C$.
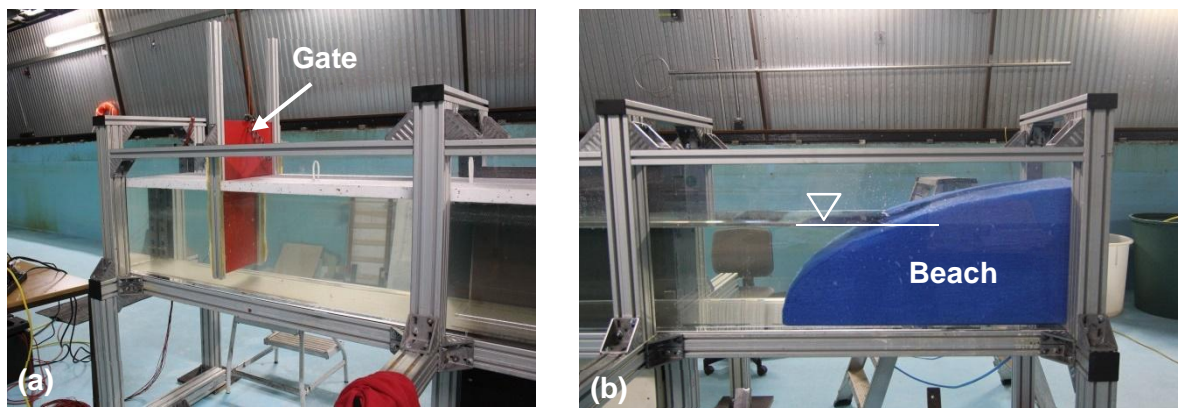
Figure 7. Arrangement of (a) gate and (b) beach within the flume.

2.4 WAVE GENERATION

ISWs were generated by removal of the gate which was lifted quickly and smoothly in the vertical direction. After a sorting distance of about 1 m, an ISW of depression propagated along the pycnocline into the main section of the flume. Once an experiment was finished and the water column stationary, the gate, was reinserted and a fixed volume of fluid of density ρ_1 was again added behind the gate so that a second (and sometimes third) wave could be generated.

2.5 FLOW MEASUREMENT AND VISUALISATION

The stratification was measured using MSCTI high precision micro-conductivity sensors (Precision Measurement Engineering). The sensors were mounted on a rigid rack and pinion traverse system fitted with a potentiometer. The sensors were moved vertically through the water column and density profiles were obtained by calibrating the potentiometer output and conductivity data against known values of height and fluid density respectively. The micro-conductivity probes sampled at 10 k Hz and profiles were acquired just prior to a given experimental run commencing.

A light source (intensive LED strip passing through a double slit) was placed beneath the transparent base of the flume. This generated a thin vertical column of light illuminating a 2D-slice of the flow field in the mid-plane of the flume. In order to make the streamlines of the flow visible, the water column was seeded with neutrally-buoyant, light-reflecting tracer particles of "Pliolite" having grain diameter in the range 150 – 300 microns.

Three UNIQ UP-1830CL-12B 2/3" 1024 x 1024 Mono 12 bit digital cameras attached to R64-PCE-CL-D R64e PCI Express frame grabbers were used to record the fluid motion. The cameras were set up outside of the flume and viewed the flow field orthogonally from the side. Video capture took place throughout an experiment. The cameras were arranged so that they had overlapping fields of view and a light source was used such that the cameras were synchronised in time (*Fig. 8a*). The *UNIQ* cameras sampled at 30 frames a second.
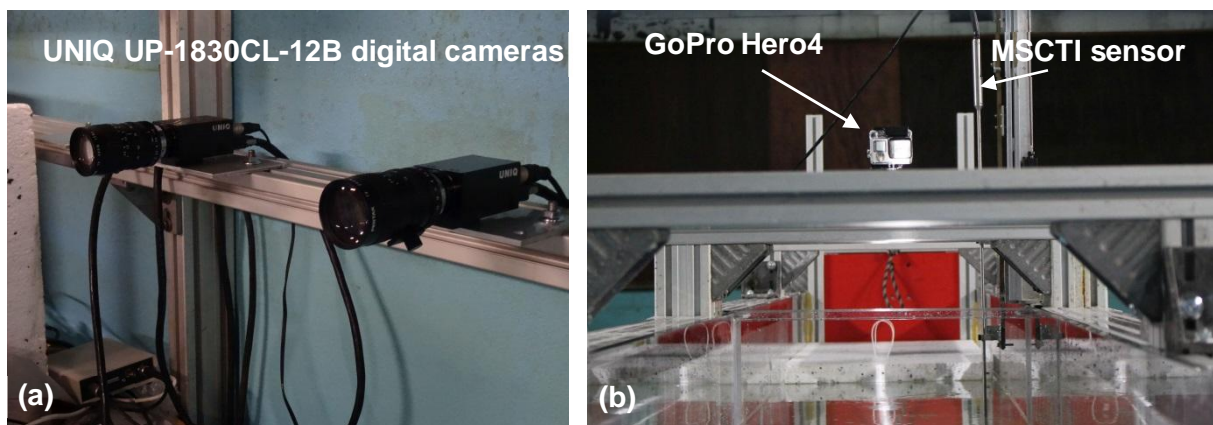
Figure 8. The photo shows (a) 2 of the 3 UNIQ cameras used and (b) the position of the *GoPro Hero 4* camera and the *MSCTI* conductivity sensor.

The video records were processed using the software package *DigiFlow*. From the time series function of *DigiFlow* the wave speed, wave amplitude, wave length and wave-induced ice floe speed were measured. The PIV-function of *DigiFlow* was used to calculate continuous synoptic velocity and vorticity field data along the illuminated cross-section in the middle part of the flume.

A *GoPro Hero 4* camera was set up above the flume (just upstream of the ice edge) and viewed the surface of the water column from above (*Fig. 8b*).

2.6 ICE AND TEMPERATURE MEASUREMENTS

Calipers were used to determine ice thickness. To measure the temperature and the salinity of the water in the reservoirs before and during the experiment a Type *WTW Multi 3310 IDS* device equipped with a conductivity cell of type *WTW TetraCon 925* was used. To measure ice core temperature a thermometer of type *Testo 720* was used and a generic hydrometer was used to measure the density of the water.

The room temperature at different locations of the AETB was recorded continuously during the campaign as was water temperature in the flume by means of a *PT100* sensor chain. A photo of the arrangement is given in *Figure 9.*

Channel	Height above base of flume [mm]
Ch 1	550 (air)
Ch 2	500 (air)
Ch 3	425 (air, sometimes water)
Ch 4	375 (water usually top layer)
Ch 5	275 (water usually bottom layer)
Ch 6	175 (water bottom layer)
Ch 7	100 (water bottom layer)
Ch 8	50 (water bottom layer)

Figure 9. *PT 100* sensor arrangement

Ice was sampled from the flume and the ice density was determined. The results from a given test day (18-04-2018) are summarized in *Table 1.*

Table 1. Results of ice density measurements

Run [-]	Length L [m]	Breadth B [m]	Thickness H [m]	Weight G [kg]	Volume V $1*10^{-04}$ [m3]	Density ρ_{ice} [kg/m3]
1	0.098	0.089	0.014	0.980	1.22108	803
2	0.098	0.100	0.015	0.115	1.47000	782

3. EXPERIMENTAL PROGRAMME

Table 4 provides a summary of the experimental runs. "Date" is the date of the experiment, "Run" is the run number for a given day, "Ice type" provides a summary of the ice type, "h3", "h2", "h1" are the stratification layer thicknesses. H is the total fluid depth and V is the wave generating volume of fluid added behind the gate.

Table 2. Experimental programme. "h3", "h2", "h1" are the stratification layer thicknesses, "H" is the total fluid depth and "V" is the wave generating volume of fluid added behind the gate.

Date	Run	Ice type	h_3	h_2	h_1	H	V
[ddmmyyyy]	[-]	[-]	[mm]	[mm]	[mm]	[mm]	[$1*10^6$ mm^3] resp. litres
10-04-2018	1	Nilas smooth & thin - whole surface covered	322	35	43	399	31
	2	Nilas thick & rough - wholesurface covered	307	37	68	412	31
	3	Grease - whole surface covered	276	57	90	424	31
12-04-2018	1	Grease - surface partially covered	323	31	44	399	31
	2	Grease - surface partially covered	330	35	55	420	60
17-04-2018	1	Nilas - surface partially covered but fixed in x	321	35	44	400	31
	2		332	30	57	420	60
18.04.2018	1	Thin level ice - surface partially covered, free to move	316	38	47	401	30
	2		323	42	55	421	60
19-04-2018	1	Thick level ice - surface partially covered, free to move	302	60	45	406	31
	2		314	59	53	426	61
	3	Thick level ice and double length	313	56	83	452	60

4. MAIN RESULTS

The experiments showed that the ISW-induced flow at the surface was capable of transporting ice floes in the horizontal direction. It is anticipated that the results will allow the transport speed of the ice to be parameterised in terms of the wave induced horizontal velocity, the wave length, the floe thickness, the floe ice type and the floe length respectively.

In thick ice cover cases, in which the thickness of the ice was comparable to the depth of the top layer in the stratification, the ice significantly damped the ISW signal causing the wave to break and even be destroyed in some cases.

The roughness associated with different ice types caused varying degrees of vorticity and turbulence in the wave-induced boundary layer beneath the ice. It is hoped that the velocity data obtained (via PIV) can be used to analyse wave dissipation rates for different wave properties and ice types.

5. CONCLUSION

The objective of the study was to generate ISWs under different ice types, namely, nilas, grease, and level ice. The main focus of the experiments was to (i) obtain accurate measurements of the wave induced velocity field under the ice and (ii) get a qualitative understanding of how different ice conditions affect the ISW field.

ISWs were generated using a sluice gate and the surface condition was varied. Measurements of wave speed, wave amplitude and wave induced velocity under the ice were obtained in the mid-plane of the tank. Difficulties in visualisation very close to the bottom side of the ice were encountered due to (i) reflection of the light source off the underside of the ice and (ii) ice at the front of the tank obstructing the field of view.

The range of investigated parameters was limited by the duration of the experimental campaign and the scale of the flume. The experiments are original and unprecedented; combining stratified ISW flow with ice.

Preliminary results and observations indicate the need for further more detailed investigations and show clearly that the physical interactions of ISWs with ice have significant implications for ISW energy dissipation and mixing processes in polar oceans.

REFERENCES

Carr, M., Haase, A., Evers, K.-U., Fer, I., Sutherland, P., Jensen, A., Kalisch, H., Berntsen, J., Părău, E., Thiem, Ø. and Davies, P. A. (2019). Laboratory Experiments on Internal Solitary Waves in Ice-Covered Waters. *Submitted to American Geophysical Union (AGU) - Geophysical Research Letters*

Czipott, P.V., Levine, M.D., Paulson, C.A, Menemenlis; D., Farmer, D.M, & Williams, R.G. (1991). Ice flexure forced by internal wave packets in the Arctic Ocean. *Science*, 254, 832-835.

Evers, K.-U., Haase, A. and Carr, M. (2019). Physical experiments of internal solitary waves (ISWs) under various ice conditions in a cold laboratory, Proceedings 25th International Conference on Port and Ocean Engineering under Arctic Conditions, Delft, The Netherlands, 9 – 13 June 2019, *submitted to POAC on March 15, 2019*

Evers, K.-U. (2015). Modeling ice processes in laboratories and determination of model ice properties. In P. Langhorne (Ed.), Cold regions science and marine technology. EOLSS Publishers

Evers & Jochmann (1993). An Advanced Technique to Improve the Mechanical Properties of Model Ice Developed at the HSVA Ice Tank. Proceedings POAC'93

Marchenko, A.V., Morozov, E., Muzylev, S.V., & Shestov, A.S. (2010). Interaction of short internal waves with ice cover in an Arctic fjord. *Oceanology, 50,* 18-27

LABORATORY INVESTIGATIONS OF THE BENDING RHEOLOGY OF FLOATING SALINE ICE AND WAVE DAMPING INT THE HSVA ICE TANK

Aleksey Marchenko (1), Andrea Haase (2), Atle Jensen (3), Benjamin Lishman (4), Jean Rabault (5), Karl-Ulrich Evers (6), Mark Shortt (7), Torsten Thiel (8)

(1) The University Centre in Svalbard, Aleksey Marchenko, Norway, E-mail: Aleksey.Marchenko@unis.no
(2) Hamburg Ship Model Basin, Andrea Haase, Germany, E-mail: Haase@hsva.de
(3) University of Oslo, Atle Jensen, Norway, E-mail: Atlej@math.uio.no
(4) London South Bank University, Benjamin Lishman, UK, E-mail: Ben.Lishman@lsbu.ac.uk
(5) University of Oslo, Jean Rabault, Norway, E-mail: Jean.Rblt@gmail.com
(6) Solutions4arctic, Karl-Ulrich Evers, Germany, E-Mail: kueham@gmail.com
(7) University College London, Mark Shortt, UK, E-mail: Mark.Shortt.12@ucl.ac.uk
(8) Advanced Optics Solutions GmbH, Torsten Thiel, Germany, E-mail: thiel@aos-fiber.com

An experiment on the propagation of flexural-gravity waves was performed in the HSVA ice tank. Physical characteristics of the water-ice system were measured in different locations in the tank during the tests, with a number of sensors deployed in the water, on the ice and in the air. Water velocity was measured with an acoustic doppler velocimeter (ADV) and an acoustic doppler current profiler (ADCP); wave amplitudes were measured with ultrasonic sensors and the optical system Qualisys; in-plane deformations of the ice and the temperature of the ice and water were measured by fiber optic sensors, and acoustic emissions were recorded with compressional crystal sensors. All together 61 tests were performed, with ice thicknesses of 3 cm and 5 cm. The experimental setup and selected results of the tests are discussed in this paper. We show that the formation of cracks in the ice, caused by the action of waves, increases wave damping.

1.   ORGANIZING OF EXPERIMENT

The experimental programme was focused on the investigation of surface wave propagation below solid ice. Therefore, 38 tests were performed with solid ice, 1 test with the ice split into square blocks manually, and 2 tests with the ice broken by waves. Two groups of tests (TGI and TGII) were conducted during the test programme. The ice thickness was 3 cm in TGI and 5 cm in TGII. Measurements were performed with the sensors listed in Table 1. A Qualisys™ motion capture system is used to detect the rigid body motions of the ice in all six degrees of freedom (6-DOF). The system uses four cameras, installed on the main carriage, to detect markers which are located at different positions on the model. In this paper only experiments of TGII are considered. Locations of the installed sensors are shown in Fig. 1.

Table 1. List of sensors, their short names and symbols.

Sensors (Full names)	Abbreviated name	No. of sensors	Symbol in Fig.1
Acoustic Doppler Current Profiler	ADCP	3	☐
Acoustic Doppler Velocimeter	ADV	2	☐
Acoustic Emission Transducers	AE	8	■
Fiber Bragg Grating Strain Sensors	FBGS	8	☐
Fiber Bragg Grating Thermistor String	FBRGT	2	☐
Qualisys™	Q	6	●
Ultrasonic sensors	US	24	▬
Water pressure sensor	WP	8	☐

TGI and TGII included similar tests performed with varying wave frequencies in the range from 0.7 Hz to 1 Hz and varying open water wave heights in the range from 0.5 cm to 1.5 cm. These tests were repeated on (a) steady ice and (b) ice cyclically moving along the x-direction with an

amplitude of about 1 m. Cyclic motion of the ice was produced manually by two persons pushing and pulling the entire ice sheet along the tank using two poles with hooks. TGI finished with tests performed on manually broken ice with rectangular floes (1.8x1.8 m). TGII finished with tests on the ice after it had been broken by waves.

The model ice cover has salinity of 2.8-3.2ppt and consists of two layers. During the experiment campaign from 15 January to 18 January 2018 the salt content in the ice decreased from about 3.2ppt to 1.6ppt due to drainage of brine. The upper layer, of about 5 mm thickness, consisted of granular crystals as a result of the seeding process. The average grain diameter is about 1 mm. Thereafter, the ice continues to grow, forming relatively long columnar crystals. These crystals reach a diameter of about 2-4 mm at the bottom of the 50 mm thick ice sheet. Air is pumped into the water during the ice growth, such that micro air bubbles of 200-500μm diameter are trapped by the ice crystals and are distributed homogeneously in the ice cover.
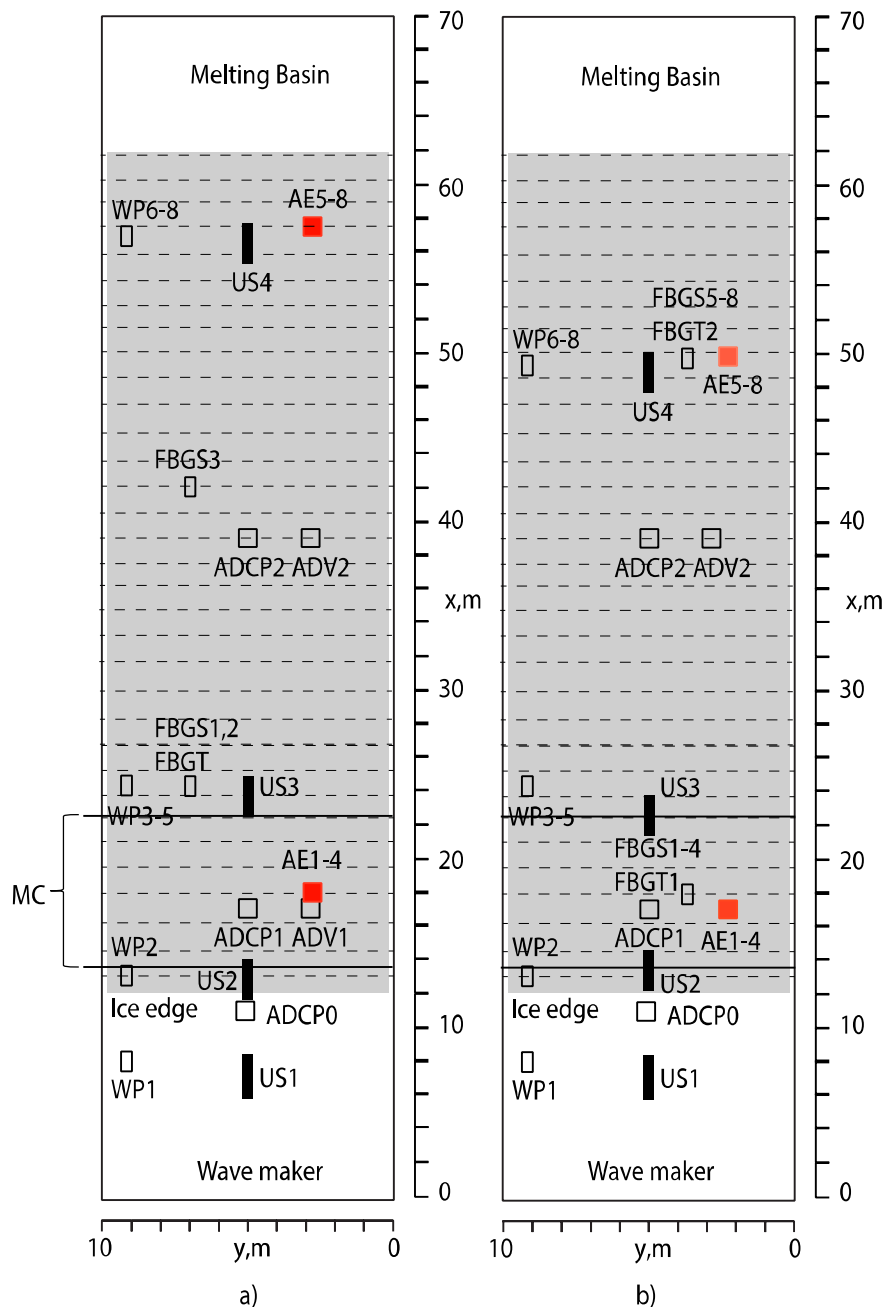

Figure 1. Locations of the sensors in TGI (a) and TGII (b). Designations are given in Table 1.

The elastic modulus and flexural strength of model ice was measured each day using a point loading method and flexural strength tests with floating cantilever beams. The mean values of the elastic modulus and flexural strength measured in TGI and TGII are shown in Table 2. 'AT' and 'BT' denote values measured before and after the tests. There is a reduction of flexural strength during TGII.

Table 2. Elastic moduli and flexural strengths measured during TGI and TGII

TGI		TGII			
E, MPa	σ_f, kPa	E, MPa (BT)	E, MPa (AT)	σ_f, kPa (BT)	σ_f, kPa (AT)
43	92	250	245	118	86

These wave heights were programmed before the wave maker starts to work. The ice sheet affects actual wave heights in the tank due to damping in the ice covered region (8 m < x < 62 m) and due to reflections from the ice edge in the region with open water (0 < x < 8 m). Wave reflection from the end of the tank can be ignored in the tests because of the small wave amplitudes at the end of the tank and the relatively small wave lengths.

2. SIMILARITY CRITERIA AND SCALING

Scaling laws for model tests with waves in ice are formulated in order to interpret the test results. Specifically, this helps to clarify which naturally-occurring wave-ice interactions are comparable to those in the tests described in this paper. In addition to the Froude ($Fr = V/\sqrt{gh}$) and Cauchy ($Ch = \rho_w V^2/E$) numbers, and wave slope (ak) used for the scaling of water-ship interaction, a set of dimensionless parameters includes

$$\rho_i/\rho_w, \; \nu V/gh^2, \; \sigma_f/\rho_w gh, \; E/\sigma_f, \; \kappa V/\nu h, \tag{1}$$

where ρ_i and ρ_w are the water and the ice densities, a and k are the amplitude and wave number, ν is the kinematic viscosity of water below the ice, V is either phase either group wave velocity, g is the acceleration due to gravity, h is the ice thickness, E is the effective elastic modulus of ice, σ_f is ice flexural strength, and κ is the permeability of ice. For broken ice, the ratio l_f/h, where l_f is a representative diameter of floes, should be added as geometrical scaling parameter. Another geometrical parameter, h/H, is added when the water depth H influences wave properties. Additional parameters proportional to rheological constants should be added to set (1) when the influence of viscous and anelastic properties of ice is important. In the experiments where the ice doesn't fail, the use of the dimensionless parameters which include flexural strength is not necessary.

The dispersion equation describing flexural-gravity waves, ignoring ice inertia, has the form

$$\omega^2 = gk \tanh(kH)(1 + Dk^4), \; D = \frac{Eh^3}{12(1-\nu_p^2)\rho_w g}, \tag{2}$$

where ν_p is the Poisson's ratio, which for sea ice is typically between 0.3 and 0.4 (see, e.g., Timco and Weeks, 2010). For the estimates, here it is assumed that $1 - \nu_p^2 \approx 1$. Equation (2) gives the dispersion equation of gravity waves when $D = 0$. Dispersion curves of flexural-gravity waves (FGW1 and FGW2) and gravity waves (GW) are shown in Fig. 2. Curves FGW1 and FGW2 are calculated with minimum ($E = 43$ MPa, $h = 3$ cm) and maximum ($E = 250$ MPa, $h = 5$ cm) values of the elastic modulus and ice thickness measured during the tests, and a water depth of $H = 2.5$ m, equal to the water depth in HSVA tank. The gray rectangle shows the region where most of the tests were performed. Figure 3 shows that ice elasticity is not important for wave dispersion with 3cm thick ice when the wave frequency is smaller than 0.7 Hz. The deep-water approximation is valid throughout, since $kH > 2.5$ inside the gray region in Fig. 2.

Further, the phase velocity of gravity waves in deep water is used for the calculation of $V = g/\omega$, where ω is the wave frequency in rad/s, in formula (1). The Froude number, calculated with the formula $Fr = \omega^{-1}\sqrt{g/h}$, changes from 2.2 to 5.7 in the tests described here. From dispersion equation (1) it follows that the number Dk^4 gives an estimate of the influence of elasticity on wave dispersion (instead of the Cauchy number). We consider the range of wave frequencies where $Dk^4 \approx \mathbf{1}$ (i.e. wave lengths are not very short) so that we can ignore the influence of the gravity force. Expressing the wave number from the dispersion equation for gravity waves in the deep-water approximation ($\omega^2 = gk$) we find that the number $\alpha_{fg} = Eh^3\omega^8/(\mathbf{12}\rho_w g^5)$ can be used instead of Dk^4. Numerical values of the dimensionless coefficients E/σ_f and α_{fg} are shown in Table 3 for the ice characteristics in TGI and TGII.
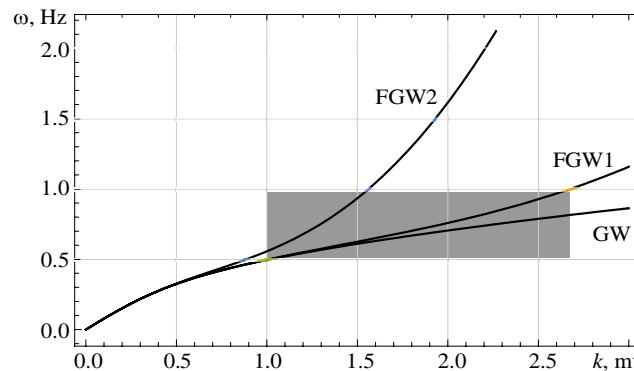
Figure 2. Dispersion equations of flexural gravity waves (FGW1,2) and gravity waves (GW).

Table 3. Dimensionless numbers characterizing the bending failure of ice and the influence of elasticity on wave dispersion in TGI and TGII.

	TGI	TGII	
$E/\sigma_f \cdot \mathbf{10}^{-3}$	0.47	2.1	2.8
α_{fg}	0.01-2.6	0.27-70	0.26-68

The effective elastic modulus of sea ice measured in full-scale tests with cantilever beams is $E \approx \mathbf{3}$ GPa and flexural strength is $\sigma_f \approx \mathbf{0.3}$ MPa (Marchenko et al, 2017). The ratio $E/\sigma_f \cdot \mathbf{10}^{-3} \approx \mathbf{10}$ is higher in full scale tests than it was TGI and TGII. Figure 3 shows dimensionless numbers Fr and α_{fg} calculated with the characteristics of natural sea ice and natural wind waves and swell. One can see that similarity by Froude number (2.2-5.7 in our tests) can be reached for wind waves with frequency 0.2 Hz (5 s period), swell or local waves with frequency 0.1 Hz (10 s period) in relatively thick ice ($h > \mathbf{1}$ m), and almost reached for low frequency swell in thick ice (30 s period and 0.033 Hz frequency). Similarity by α_{fg} (0.01-70 in our tests) can be reached only for waves with frequencies close to or higher than 0.1 Hz (10 s period) propagating in relatively thick ice. The ratio ρ_i/ρ_w is similar for the model and natural ice. Similarity by the number $\alpha_{\sigma h} = \sigma_f/\rho_w gh$, characterizing the influence of hydrostatic pressure on bending failure, is not fulfilled, since $\sigma_f/\sigma_{f,exp} \approx \mathbf{3}$, while $h/h_{exp} > \mathbf{10}$.
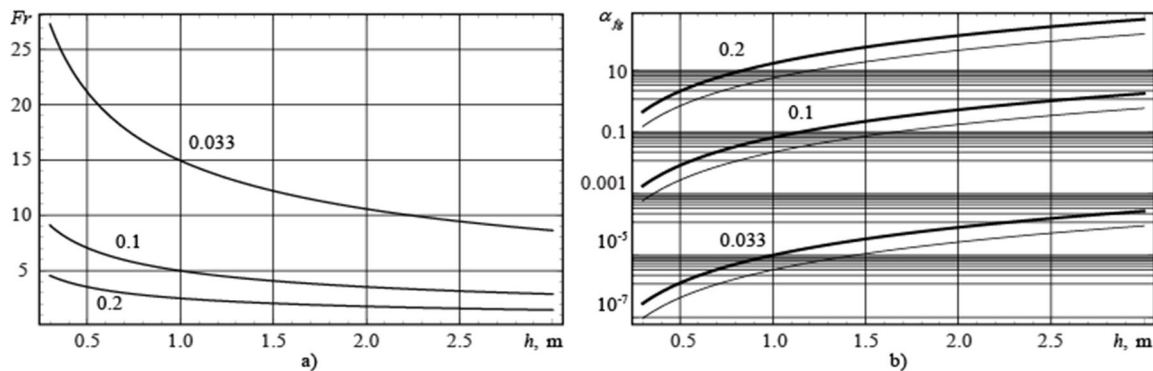
Figure 3. Dimensionless numbers Fr (a) and α_{fg} (b) versus ice thickness, calculated with the characteristics of natural sea ice. Wave frequency (Hz) is marked on the individual curves. Thick and thin lines in (b) are constructed with $E = 3$ GPa and $E = 1$ GPa respectively.

The amplitude of the wave-induced velocity of surface water particles, calculated with standard formulae following from the potential theory of surface waves with small amplitude, equals ωa. The wave amplitudes varied within 0.5 – 1.5 cm, and the wave frequencies varied within 0.5-6 rad/s in the experiment. Therefore, the velocity amplitude is estimated as varying from 1.5 cm/s to 10 cm/s in the tests. At full scale, the velocity amplitude is estimated in the same range when the wave frequency is of about 0.6 rad/s and wave amplitude is of about 10 cm. The decay distance of wave induced motion in the vertical direction is given by k^{-1}. According to Fig. 3, this decay distance extends below the ice by 0.4-1 m in the experiment, which excludes any influence of the tank bottom on the waves.

3.   INSTALLATION OF FBG SENSORS

The FBG sensors were used in the experiments to measure in-plane strains in the ice (excited during propagation of surface gravity waves below the ice) and to record a vertical profile of the temperature (in the water layer below the ice, in the ice and above the ice) over a distance of 12 cm (with spatial resolution of 1 cm). A schematic of the installation of the strain and temperature sensors is shown in Fig. 4a. Each strain sensor (FBGS sensor) measures strain (FBG strain) between two points where the fiber is fixed to bolts, which in turn connect the working length of the fiber (including the FBGS sensor) to the fiber which transmits optical signal. The bolts are fixed onto brackets with nuts and washers, and each bracket is mounted on the ice with four screws. It is evident that FBG strain consists of a sum of the in-plane strain in the ice and the strain due to the bracket tilts caused by ice bending. Four FBGS sensors were deployed to measure longitudinal (x-direction) strains in the ice at distances (x-direction) of 19 m (2 sensors) and 50 m (2 sensors) from the ice edge. Another four FBGS sensors measured strains in the transversal direction to the tank axis (y-direction) in similar locations. Two FBG temperature strings (FBGT sensors) were supported by foam plastic holders so that 3 thermistors were above the ice surface. These FBGT sensors were then placed inside holes of 2 mm diameter drilled through the ice. The diameter of FBGT sensors is slightly smaller than 2 mm. Therefore, FBGT sensors were tightly held inside the holes without visible gaps. Photographs of the sensors, installed in position, are shown in Fig. 5. Measurements of strain and temperature were recorded at a frequency of 40 Hz. Strain records show a periodic dependence on time, with a dominant period equal to the wave period.
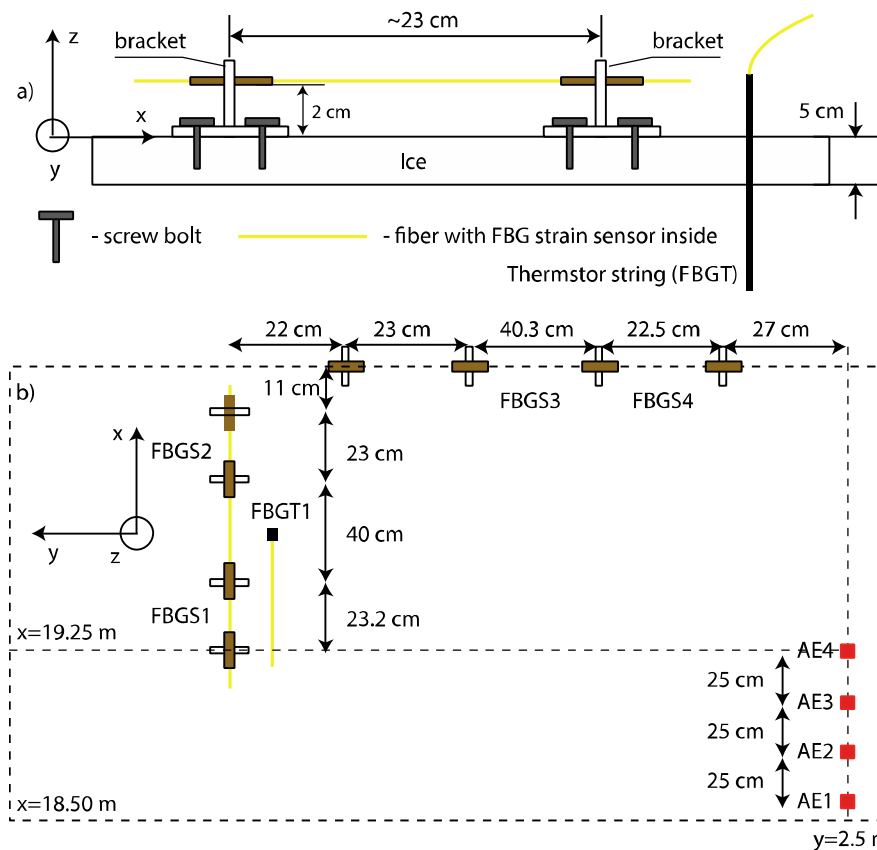
Figure 4. Scheme of the installation of FBG sensors on the ice by $x < 20$ m.

Figure 5. Mounting of FBG strain sensor on the ice (a). Four FBG strain sensors (FBGS) and thermistor string (FBGT) mounted on the ice near AE sensors (b).

4.   WAVE DISPERSION AND ELASTIC MOSULUS

Data analysis of sensors FBGS1 and FBGS2 (Fig. 4b) was performed to calculate wave speeds and elastic modulus of ice. Longitudinal deformation $\epsilon = \Delta L / L$, where $L = 23$ cm (Fig. 4a), measured by FBGS sensor is calculated by the formula

$$\frac{\Delta \lambda}{\lambda} = GF \cdot \epsilon, \tag{3}$$

where the variation of the peak wavelength $\Delta\lambda$ is measured with a spectrometer that receives the reflected signal from the FBGS sensor, and GF **= 0.719** is the gauge factor obtained from a calibration cycle for the FBGS sensors in standard SMF fiber. Influence of the air temperature of the strain is ignored because the temperature changes during one tests are assumed to be small.
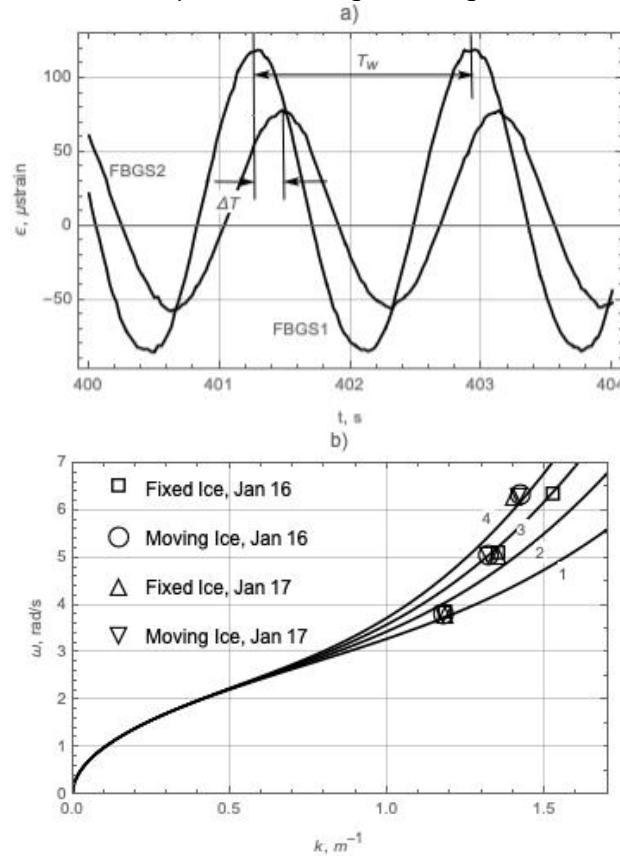
Figure 6. Example of the records of FBGS1 and FBGS2 sensors (a). Waves frequencies versus wave numbers calculated from the experiment TGII. Dispersion curves 1, 2, 3, and 4 are constructed with elastic moduli of 100, 200, 300 and 400 MPa respectively.

Figure 6a shows an example of the records of FBGS1 and FBGS2 sensors versus the time. Both of the signal show periodic dependence from the time and their period T_w coincides with the period of waves made by the wave maker. Distance between the brackets used for the mounting of the FBGS sensors is l **=** 63.2 cm. Each wave crest runs this distance during the time ΔT, therefore,

$$\frac{\omega}{k} = \frac{l}{\Delta T}. \tag{4}$$

From dispersion equation (2) written in deep water approximation ($kH \rightarrow \infty$) it follows

$$E = \frac{12\rho_w(1-\nu_p^2)}{h^3}\frac{\omega^2 - gk}{k^5}. \tag{5}$$

It is assumed $1 - \nu_p^2 \approx$ **1** since typical value of the Poisson's ratio for ice is about 0.33. The water density is assumed equal to ρ_w **= 1000** kg/m3. Formulas (4) and (5) are used to calculate wave number k and elastic modulus E from the experimental data. Values of ΔT were calculated for each period of the FBGS1 and FBGS2 records in 6 tests with fixed ice and 6 tests with moving ice with wave frequencies of 0.6 Hz, 0.8 Hz and 1.0 Hz. The tests were performed on January 16 and 17 within TGII (h **= 5** cm). Then, the mean values of ΔT averaged over 250 s interval were used to calculate k and E from formulas (4) and (5).
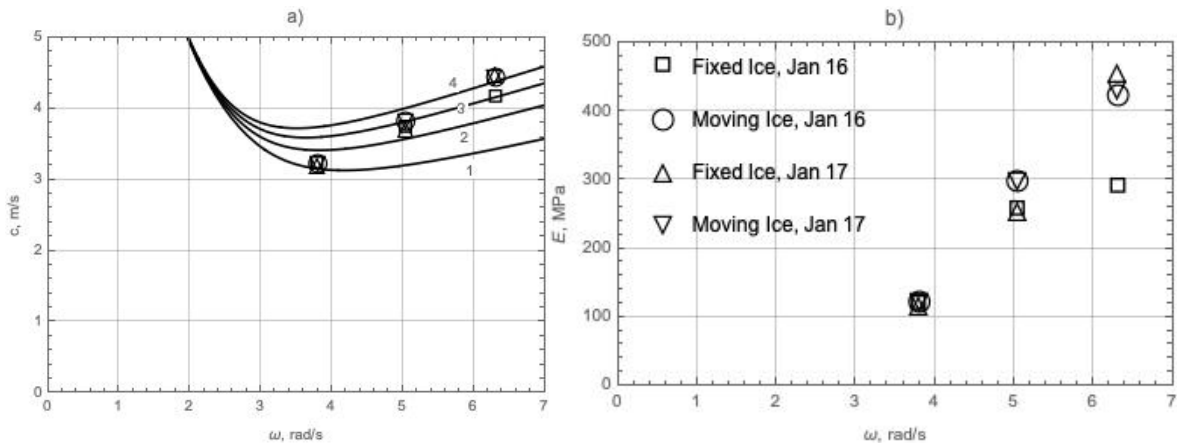
Figure 7. Wave speeds calculated from experimental data TGII (a). Lines 1, 2, 3, and 4 are constructed with elastic moduli of 100, 200, 300 and 400 MPa respectively. Elastic moduli of ice calculated from the experiment (b).

Figure 6b shows that the calculated values of ω and k are located within dispersion curves constructed with elastic moduli of 100, 200, 300 and 400 MPa. Figure 7a shows that the calculated wave speeds $c = \omega/k$ are close to the phase velocities of waves constructed with the same values of elastic modulus. Figure 7b shows that elastic moduli of ice calculated from the tests with wave frequency of 0.6 Hz, 0.8 Hz and 1 Hz are of about 100 MPa, 300 MPa and 400 MPa respectively.

5. INFLUENCE OF ICE CRACK ON WAVE DAMPING

The ice located in the tank with $x > 30$ m remained undestroyed in all tests. The first crack extending across the tank at the distance of 1-2 m from the ice edge and providing effective wave damping was discovered during TGII on January 17 in the next test after the tests described in the previous section. The crack was clearly visible from a distance, due to its cyclic opening and closing during wave propagation. Cycling pumping of the water or brine through the crack was also clearly visible (Fig. 8). It was not possible to locate crack at the bottom of the ice by manual inspection near the tank wall, while it was clearly visible at the upper ice surface.

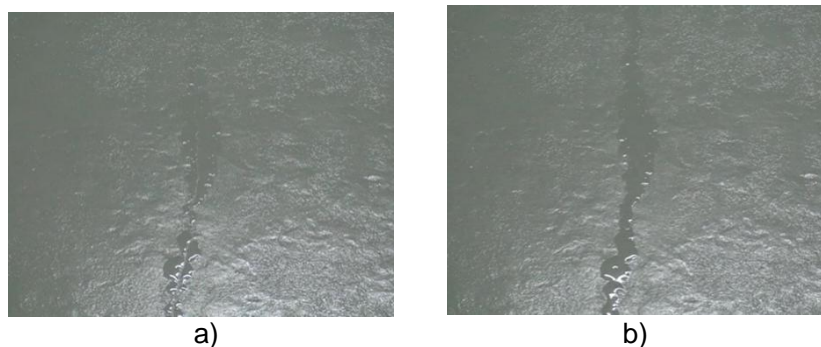a)   b)

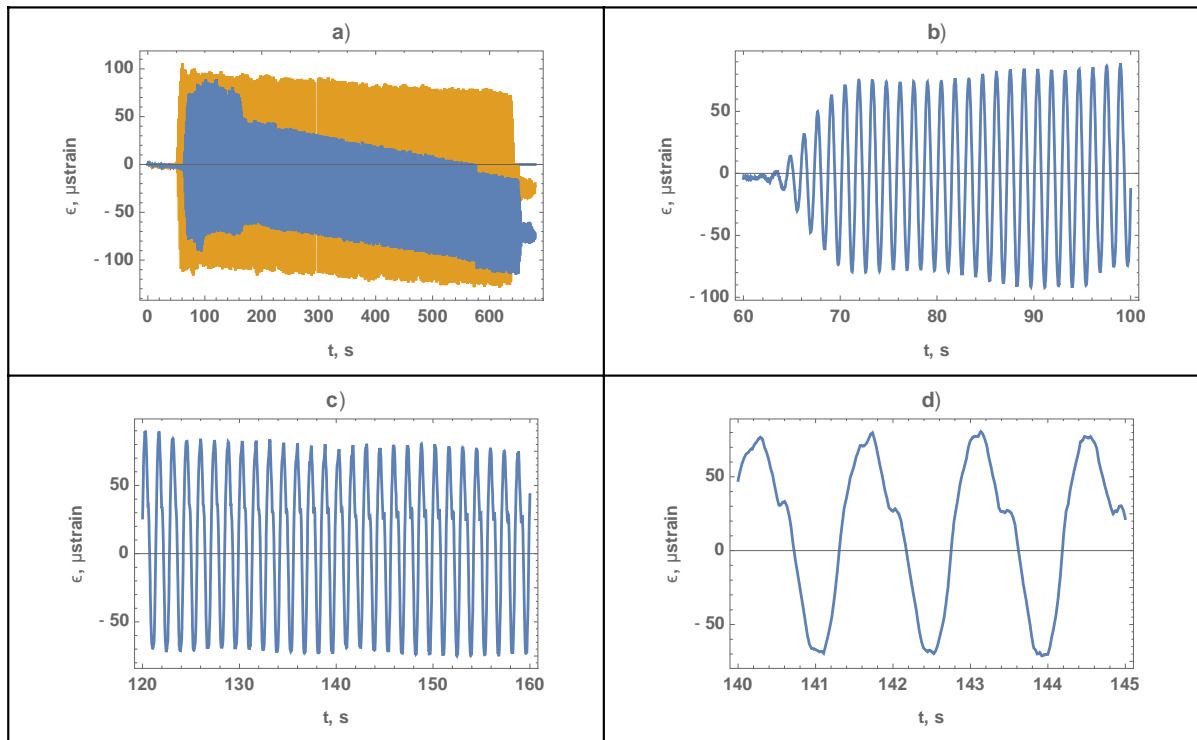Figure 8. Photographs of (a) closed, and (b) open and brine-filled crack.

Figure 9. Strain records of FBGS1 in the test when the first crack was registered are shown by blue lines. Yellow line shows record of FBGS1 in the test before the crack formation.
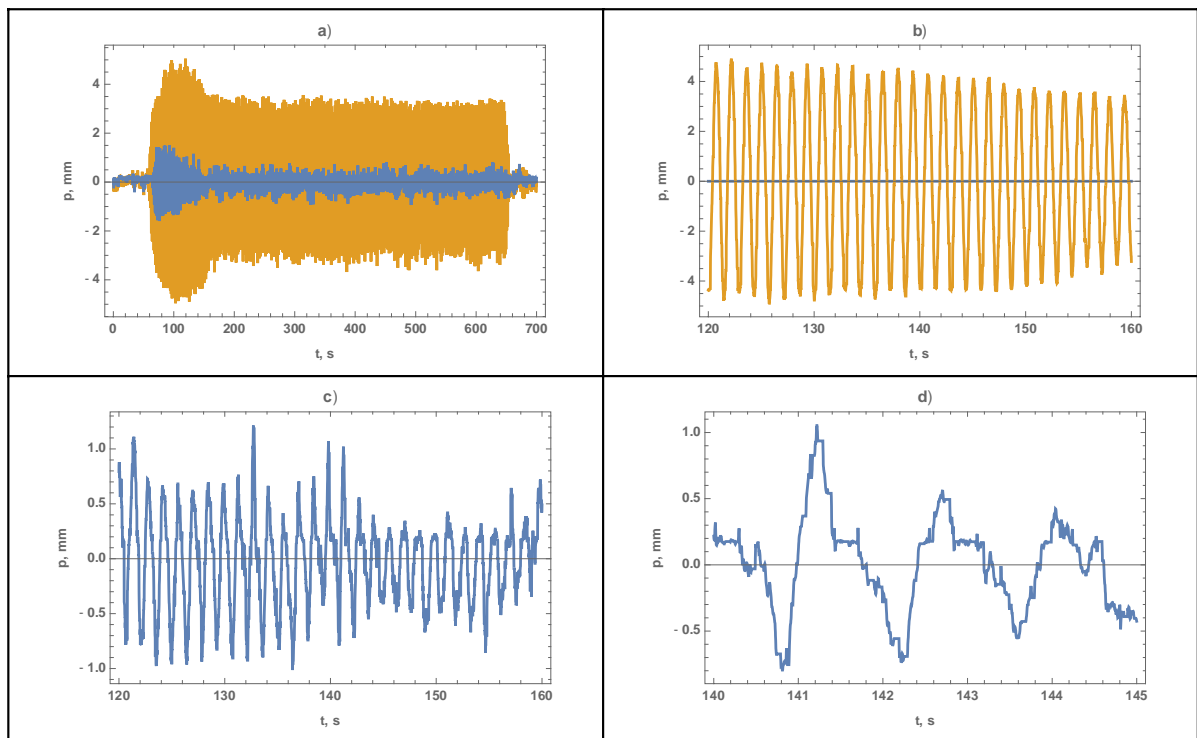

Figure 10. Strain records of pressure sensors WP1 (yellow lines) and WP3 (blue lines) in the test when the first crack was registered.

Figure 9 shows that the crack formation influenced the amplitude and shape of strains recorded by FBGS1. The strain amplitude became smaller in comparison with similar test performed before the crack formation (Fig. 9a). Strain signal changed from sinusoidal signal registered by $t < 120$ s (Fig. 9b) to the signal with two peaks in one wave period (Fig. 9c,d). Figure 10 shows the same effect registered by water pressure sensors WP1 and WP3 mounted on the tank wall at the depth of 15 cm below the water (Fig.1). Sensor WP1 was mounted in ice free are near the wave maker, and sensor WP3 was mounted below the ice at the distance of about 12 m from the ice edge. Yellow line in Fig. 10a shows that wave amplitude created by wave maker in the beginning of the test was higher than in previous tests. It was probably the reason for the ice crack formation. Figure 10b shows that pressure record of WP1 has sinusoidal shape before and after the crack formation. Figure 10c shows a transformation of the pressure recorded by WP3 from sinusoidal signal to a signal with several maxima in one wave period. Pressure signals are not very smooth in comparison with FBGS signals because of the resolution of the pressure sensors.

6. INFLUENCE OF ICE MOTION ON WAVE DAMPING

Five markers from a Qualisys–Motion Capture System were used to record ice movements at 5 points. The data includes the records of the three coordinates of each marker as a function of time, with sampling frequency of 200 Hz. An example of the record of the ice motion along the tank in the test with moving ice is shown in Fig. 11a. Periods of the cyclic motion varied within 40-50 s. Representative speed of the cyclic motion is of 0.04 m/s.
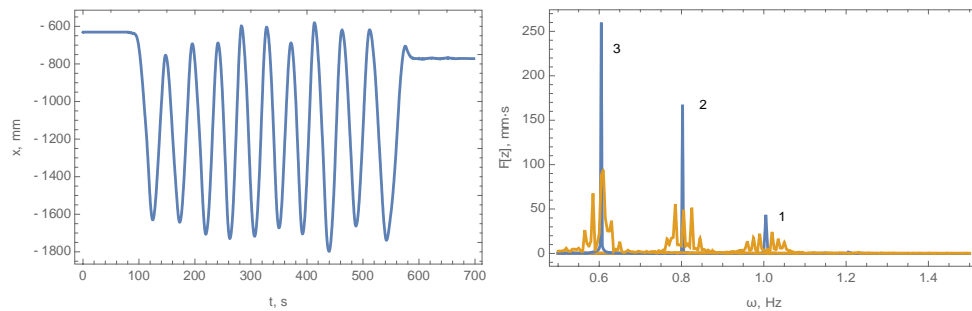

Figure 11. Records of the ice marker motion along the tank (left panel). Fourier spectrums of vertical oscillations of the ice in the tests (TGII) with fixed (blue lines) and moving (yellow) ice (right panel).
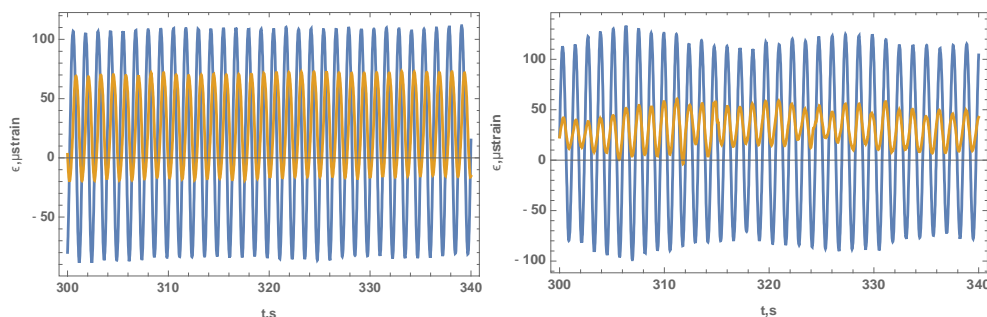

Figure 12. Examples of the records of FBGS1 (blue lines) and FBGS5 (yellow lines) in the tests (TGII) with fixed ice (left panel) and moving ice (right panel). Wave frequency is 0.8 Hz.
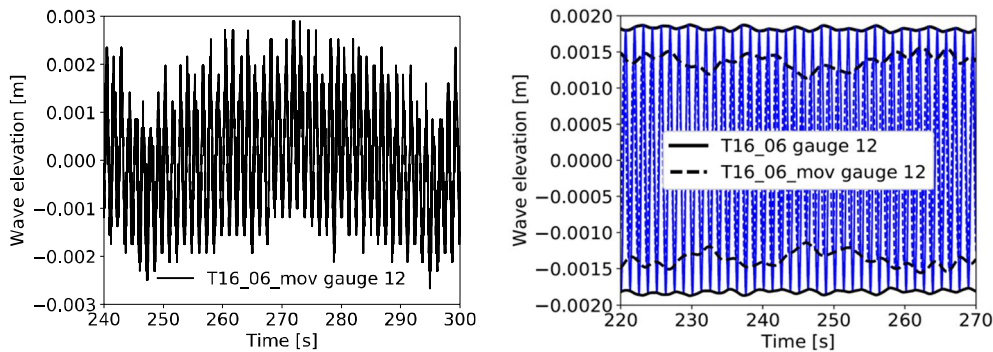
Figure 13. Wave modulation registered by US sensors in the test (TGII) with moving ice (left panel) and effect of wave modulation on the wave amplitude below the ice in the test with moving ice in comparison with the test with fixed ice (right panel). Wave frequency is 0.6 Hz.

Figures 11b, 12-14 show the influence of the ice motion on an increase of wave damping registered by different sensors. Yellow lines in Figure 11b show the decrease of spectral amplitude of the vertical motion of the ice and spectral spreading in the experiments with moving ice in comparison with the spectrum (blue lines) calculated from the experiments with fixed ice. Figure 12 shows the decrease of strain amplitudes recorded by FBGS sensors in the tests with moving ice in comparison with the strain amplitudes recorded in the tests with fixed ice. Figure 12b shows also the effect of low frequency wave modulations registered in the tests with moving ice. Figure 13 shows similar effects in the records of US sensors. Figures 14 shows the reduction of hits amplitudes recorded by AE sensors in the tests with moving ice in comparison with the hit amplitudes recorded in the tests with fixed ice.
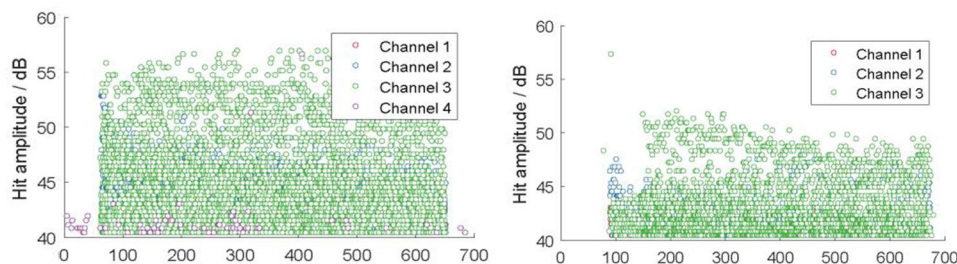

Figure 14. Hit amplitudes as a function of time, across three channels, for the tests (TGII) with fixed ice (left panel) and moving ice (right panel). Wave frequency is 0.8 Hz.

6. CONCLUSIONS

Analysis of wave speeds performed with FBGS sensors showed an increase of elastic modulus of ice with increasing of wave frequency in the tests of TGII with ice thickness of 5 cm. Calculated from the experiment dynamic value of elastic modulus varied from 100 MPa to 400 MPa when the wave frequency changed from 0.6 Hz to 1 Hz, while static value of elastic modulus measured by vertical displacements of ice loaded in the point was of around 250 MPa.

Several physical effects causing wave damping below the solid ice were observed in the experiments including perforation of the ice edge, formation of non-through cracks, ice break up by waves and under-ice turbulence generated by cyclic motion of the ice sheet along the ice tank. Not extended cracks, produced in the ice by waves, caused strong damping due to the cyclic pumping of the brine or water up and down through the ice. Wave damping in the region where the ice was broken by the waves and in the region with a net of non-through cracks prevented ice failure in the end of the tank in all experiments. Results from the Qualisys system, FBGS, US and AE sensors show stronger wave damping in experiments with moving ice. Thus, the experimental results confirm the importance of ice drift and under-ice turbulence for wave damping.

ACKNOWLEDGEMENT

REFERENCES

Marchenko, A., Karulina, M., Karulin, E., Chistyakov, P., Sakharov, A., 2017. Flexural Strength of Ice Reconstructed from Field Tests with Cantilever Beams and Laboratory Tests with Beams and Disks. *Proceedings of the POAC17,* POAC17-177.

Timco, G.W. and Weeks, W.F. (2010). A review of the engineering properties of sea ice. Cold Regions Science and Technology. 60, 107-129.

VII – U.Hull – TES

The Total Environment Simulator (TES) is a unique hydraulic infrastructure for environmental, hydraulic and morphological research due to its flexibility and integrated high-resolution measurement systems. The facility is ideally suited to ecological research and modelling aquatic system responses to climate change because of the environmental control (light and water salinity) and flexibility to change boundary conditions. The TES is rare in its capability to provide an adaptable physical modelling space that can be configured for a wide range of environmental conditions. This enables efficient use of resources since many different types of experiment can be undertaken within this single facility.

Modelling capabilities include: turbulent boundary layers up to 1m deep; transport of homogeneous and heterogeneous sediment mixtures; variable channel widths and planform configurations, normal and oblique wave directions with regular or irregular wave forms; and spatially distributed rainfall from an array of 50 nozzles. In addition, the researchers working at the TES have world-leading experience in physical modelling using natural and surrogate vegetation including the use of nutrient-rich saline water recycled from the adjacent aquarium tanks to enable modelling of estuarine and coastal ecology. To maximise the output from experiments, the flexible physical modelling capability is coupled with a unique set of state-of-the-art instrumentation that enables high-resolution measurements of flow field characteristics, sediment transport dynamics and morphologies. For flow measurement we use high-resolution submersible Particle Image Velocimetry which can measure at frequencies of up to 100Hz and image areas up to 30cm x 40cm in clear waters and an array of profiling acoustic Doppler velocimeters for sediment-laden flows. Bed morphology and morphodynamics can be quantified both during and after experiments using acoustic profilers and a high-resolution 3D laser scanner.

The flexibility of the TES makes the facility ideal for investigating problems relating to climate change adaptation and the TES particularly suited to providing new opportunities for experiments to investigate the interactions between ecology and sediment transport dynamics under changing or extreme hydraulic conditions.

.

THE EFFECT OF RAINFALL SEQUENCING ON EROSION DYNAMICS: A LARGE SCALE RAINFALL SIMULATION EXPERIMENT

Jantiene Baartman (1), Niels Lake (1), Bart Verschaeren (1), Hannah Williams (2), Stuart McLelland (2), Dan Parsons (3) & Martine van der Ploeg (1)

(1) Soil Physics and Land Management Group, Wageningen University, the Netherlands, E-mail: jantiene.baartman@wur.nl

(2) Department of Geography, Geology and Environment, University of Hull, UK Hull University

(3) Energy and Environment Institute, University of Hull, UK Hull University

Climate change is expected to result in more extreme rainfall events, which may impact soil erosion rates and patterns. Adaptation is difficult if the effects are unknown, especially as the magnitude-frequency relationship is highly non-linear and may also depend on connected pathways within a landscape. Both were investigated in the Total Environment Simulator at Hull University in a large-scale rainfall simulation experiment. Erosion effects on plots with two grain sizes, and five different rainfall events in varying order were combined for a total of 10 sequences. The results show highly variable responses. Further work will focus on quantifying DEMs of difference to determine the connectivity of the two plots in relation to the different sequences of rainfall events.

1. INTRODUCTION

Although research and interventions have aimed at soil and water conservation (Panagos et al. 2015), erosion by water is still a large threat to soils globally (EU 2006, Pimentel 2006). The effects of soil and water conservation efforts are difficult to estimate, because of the non-linearity in the relationship between rainfall, runoff and erosion (Boardman et al. 1999, Philips 2003, Cerdà et al. 2013) and differences across scales (Cammeraat 2004, Cantón et al. 2011 Vanmaerke et al. 2011). This non-linearity is known from field and model studies of catchments; precipitation events with higher amounts of rainfall do not necessarily produce greater amounts of eroded material, similarly lower amounts of rainfall do not necessarily produce less eroded material (Gonzalez-Hidalgo 2007, Hungr et al. 2008, Van de Wiel et al., Baartman et al. 2013a). Even if low amounts of rainfall produce less erosion, these low amounts of rainfall may occur more frequently compared to extreme events, potentially leading to a higher net amount of soil loss (Marques et al. 2007). This so-called magnitude-frequency relation is not yet established, since data and information on this relation is limited.

One of the reasons the magnitude-frequency relationship is not clear, is the lack of repeatability in real landscapes. Once a rainfall event has occurred, the landscape has changed, and therefore no consistent testing of the magnitude-frequency relationship is possible.

Hence, the most pressing issue currently is the lack of data on both rainfall event information and the response of a landscape in terms of soil loss to sequences of rainfall events (González-Hidalgo et al. 2009). Nonetheless, in numerical modelling studies it is possible to recreate the exact same landscape. A modeling study by Baartman et al. (2013a) showed no particular trends for 50 varying rainfall events. Possibly, the lack of particular trends is caused by another factor, namely the change in connectivity in a landscape (Appels et al. 2011, Baartman et al. 2013b, Bracken et al. 2013). If pathways in a landscape suddenly connect during a particular rainfall event, sediment may leave a catchment as a sudden pulse (Schoorl et al. 2014).

As a result of climate change, it can be expected that the frequency-magnitude of rainfall events will change, most likely extreme rainfall events will become more intense and frequent in many regions (IPCC, 2014), leading to accelerated erosion and flooding. However, adaptation to such changes is not possible, if their effects are unknown. Therefore, analysis of the possible effects of rainfall event sequence with different magnitude-frequency occurrence on landscape dynamics, including erosion and sediment dynamics is an urgent research task (Boardman, 2006). This

research aimed to improve our understanding of the effects of different sequences of rainfall events on erosion and sediment dynamics. The Total Environment Simulator at the University of Hull was ideally suited for this research, offering a large experimental area in which a small 'landscape' could be imitated and recreated to test the effects of varying rainfall event sequences.

2.　　　MATERIALS AND METHODS

The 'Total Environment Simulator' (TES, at Hull University, UK, was used for the rainfall simulation experiments. The TES consists of a surface area of ~40 m^2 and is equipped with a rainfall simulation system containing 40 rainfall nozzles arranged in a regular grid above the experimental area (Fig. 1).
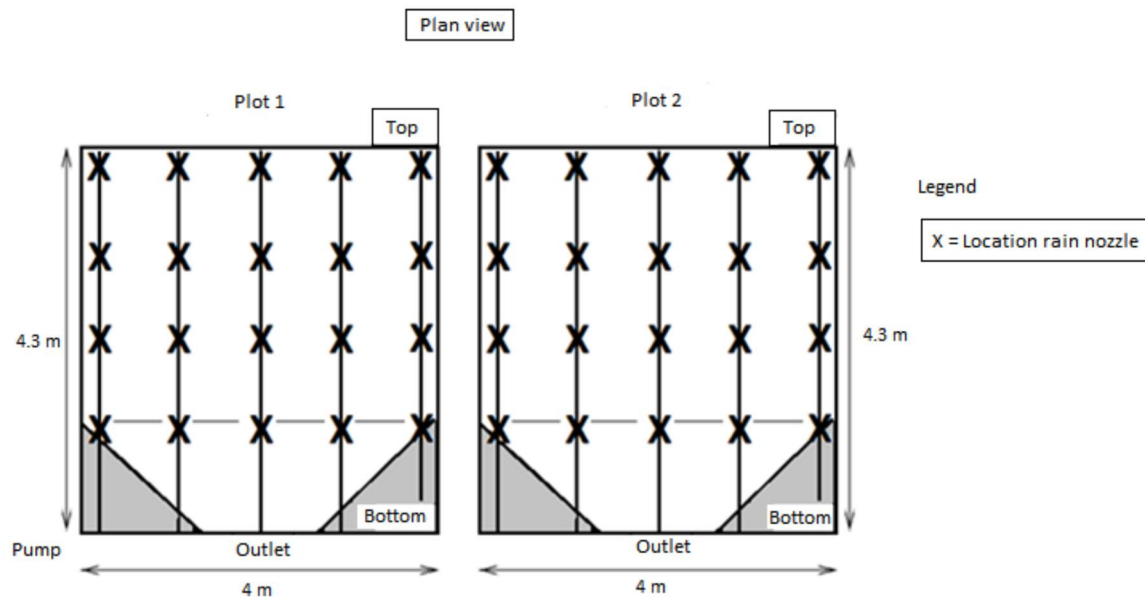

Figure 1: Schematic overview of the rainfall nozzle system over the experimental plots in the TES.

The experimental design consisted of two plots (plot 1, left hand and plot two, right hand in Fig. 1) of 4 by 4.3 m. Each plot was filled with different size sand: plot 1 contained fine sand (D50 = 215 µm) and plot 2 contained medium coarse sand (D50 = 458 µm). Grainsize distribution within the plots was uniform. The base of each plot was sealed with an impermeable plastic layer to avoid leakage of infiltrating water. The plots had the same morphology with a V-shape in the upper part, resulting in an inward flow direction towards the middle of the plot and an almost straight (very slightly V-shaped) slope downwards towards the outlet in the lower part of the plot. Dimensions and slopes are given in Fig. 2a and b for plot 1 and 2 respectively.
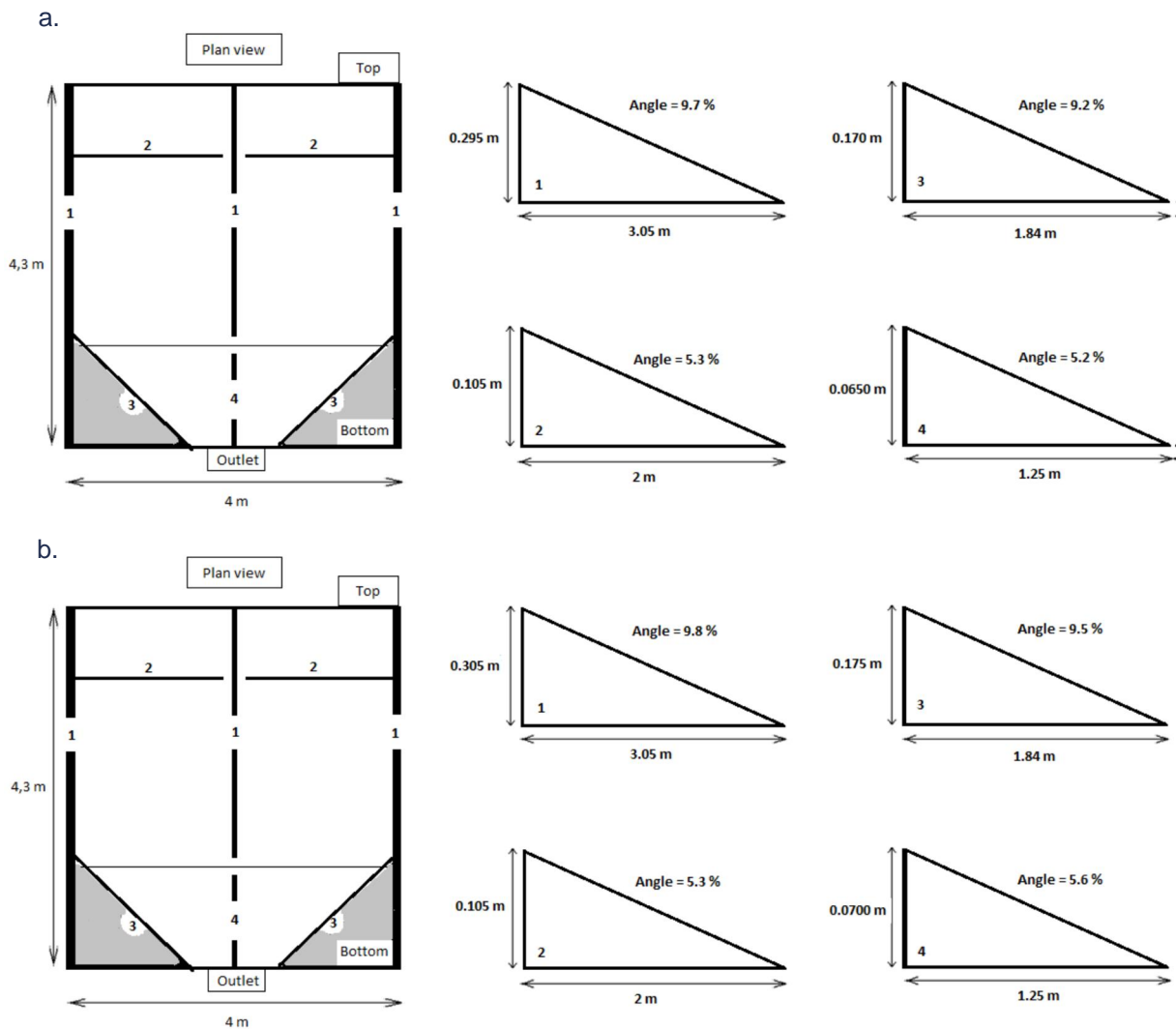
a.

b.

Figure 2: Design of plots 1 (a) and plot 2 (b) including dimensions and slopes.

Before the rainfall sequences could be designed, the rainfall simulation system was tested and calibrated. To calibrate the rainfall intensities and to investigate the spatial variation of the rainfall within each plot, 22 rain gauges and 27 boxes were installed on each plot (Fig. 3a). As shown in Fig. 3b, the rainfall was not spatially uniformly distributed.
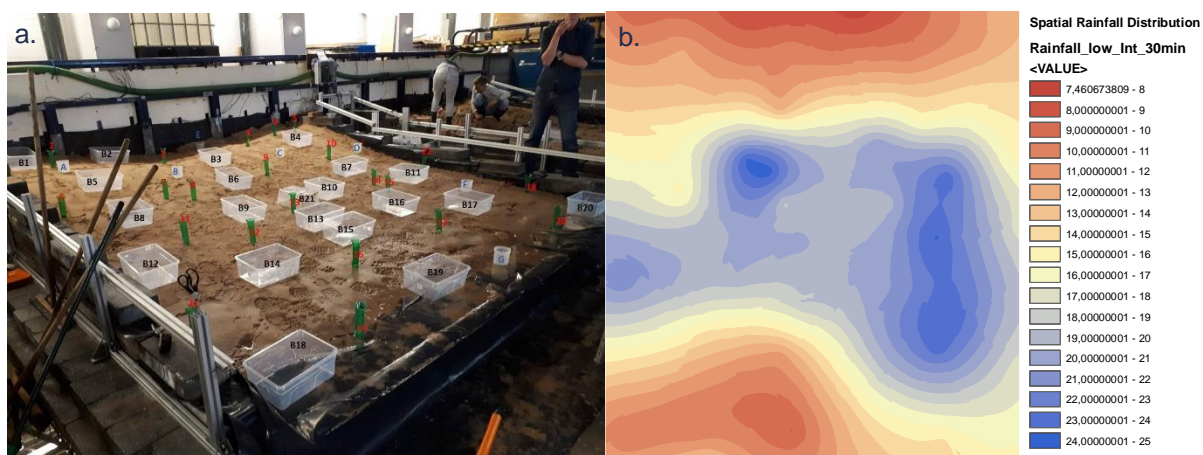
Figure 3: a) Calibration set-up to calibrate the rainfall distribution over the experimental plot, b) interpolated spatial distribution of rainfall of the low intensity rainfall event (Photo: Niels Lake / Bart Verschaeren).

From several tests, eventually it was decided to use three rainfall intensities (Table 1) of significant difference: Low (35 and 33 mm/h), Medium (92 and 78 mm/h) and High (126 and 117 mm/h for plot 1 and plot 2 respectively). Higher intensities were not possible due to the pumping capacity of the system, while lower intensities led to dripping of the system, with unwanted large drops being produced by the nozzles. The spatially averaged rainfall intensities are consistently lower for plot 2 as compared to plot 1, due to a slightly decreasing water pressure with increasing distance from the water pump, which was located closer to plot 1.

Table 1 Calibrated average rainfall intensities for plot 1 and plot 2

Rainfall Intensity	Low (mm/h)	Medium (mm/h)	High (mm/h)
Plot 1	35.1	92.1	126
Plot 2	33.0	79.4	117

A total of 10 sequences of rainfall events were applied to both plots. Rainfall sequences consisted of the same 5 individual rainfall events (Table 2), but applied in different order (Table 3). One of the sequences was the so-called 'base sequence' which consisted of 5 events of the same intensity and duration. To ensure an equal total amount of rainfall being applied as in the other sequences, the duration of each event was 19 minutes.

Table 2: Rainfall events: intensity and duration.

Rainfall event code	Intensity			Duration (min)
		Plot 1 (mm/h)	Plot 2 (mm/h)	
1 - L30	Low	35	33	30
2 - L60	Low	35	33	60
3 - M15	Medium	92	78	15
4 - M30	Medium	92	78	30
5 - H15	High	126	117	15

Table 3: Sequences of rainfall events applied to the plots, codes as in Table 2.

Sequence	1	2	3	4	5	6	7	8	9	10
event.ID	Increasing	Decreasing	Hill	Valley	Stabilizing	Destabilizing	Base run	Random1	Random2	Random3
A	L30	H15	L30	M30	H15	L30	M19	L30	M15	L60
B	L60	M30	M30	L60	L30	L60	M19	M30	L30	L30
C	M15	M15	H15	L30	M30	M30	M19	M15	L60	H15
D	M30	L60	M15	M15	L60	L30	M19	H15	H15	M15
E	H15	L30	L60	H15	L30	H15	M19	L30	M30	M30

To be able to compare the effects of the different rainfall sequences, the starting landscape needed to be the same. Therefore, the plots were (re)built each time to the same morphology as much as possible. The topsoil was loosened with a rake to remove channels and patterns formed by a previous sequence. The soil was then compacted, while care was taken to do this as homogeneously as possible over the plot surface. Finally, a scraping board specifically made for this experiment was used to recreate the same slope and landscape form. To minimize differences in the effects of the rainfall events due to differences evolving from the tramping and scraping phase, a spin-up rainfall event was applied before each rainfall sequence. The spin-up event was a low intensity, one-hour rainfall event. Figure 4 and 5 show the difference in the plot surface before and after applying the spin-up event.

Figure 4. Smooth landscape after scraping phase (plot 1).

Figure 5. Starting landscape after spin-up rainfall event (plot 1).

At the outlet of each plot, a large box was placed to collect the runoff water and sediment during each rainfall event. The runoff water was automatically measured by directing it into large containers placed on scales. The sediment was manually collected from the boxes after each rainfall event and weighted. A conversion factor from wet to dry sediment was calibrated and applied to convert the weighed wet sediment to dry sediment weight. From three starting landscapes, bulk density samples were taken at top, middle and low positions in the plot using 100 cm^3 sample rings. These were used to check if rebuilding of the plots leads to differences in bulk density. Soil moistures sensors (EC5) were installed in the plots to check the spatial distribution and temporal evolution of soil moisture during the experiment. Finally, after each rainfall event, the surface was scanned using a FARO X330 high-resolution laser scanner.

3.   RESULTS & DISCUSSION

During the experiment surface runoff caused by field saturation was observed for both grain sizes. Spatial differences in erosion patterns between both plots were clearly visible (Fig. 6).

Figure 6. Typical erosion pattern for plot 1 with fine sand (left) and plot 2 with medium sand (right).

Figure 7 and 8 show the erosion amounts for the two plots generated by each rainfall event within each sequence executed in the experiment. Sequences are indicated by the different colors. Rainfall event size (Table 2), is indicated from small to large with increasing circle size. The order of occurrence of events 1-5 in a sequence is indicated as A to E on the x-axis. As can be seen, the results for this experiment were very heterogeneous.

From the overview of plot 1 (Fig. 7), clear differences can be distinguished in the amount of erosion between the lower three rainfall event numbers (events 1, 2 and 3) and the two higher rainfall event numbers (events 4 and 5). The highest erosion value of these first three event numbers is 8.19 kg, while the lowest erosion value of event 4 and 5 is 11.57 kg. Furthermore, when event 1 or event 5 is the first event in a sequence, the subsequent amount of erosion generated by this event is the lowest for this specific rain event. When events 1 and 5 are run later in the sequence, e.g. on timestep B, C, D or E, the amount of erosion is always higher. Also, event 1 generates the lowest amount of erosion in all sequences; erosion generated by the other events is always higher.

Plot 2 shows (Fig. 8) that event 1 and event 5 generate, similar to plot 1, the lowest erosion amounts when located as the first event in a sequence. There is one exception for event 5 in sequence 5, which has a higher erosion output compared to some other rainfall events of event 5. Also, event 1 is for all sequences generating the lowest amount of erosion. Other deviations can be seen from event 5 of sequence 2, which has less erosion compared to event 2 (sequence 10) or event 3 (sequence 9). For all other sequences, event 4 and 5 have the highest erosion amounts. Also, ranges in erosion are increasing from event C onwards, where maximum erosion reaches to around 15 kg compared to maximums of 9.35 kg for event A and 11.19 kg for event B.
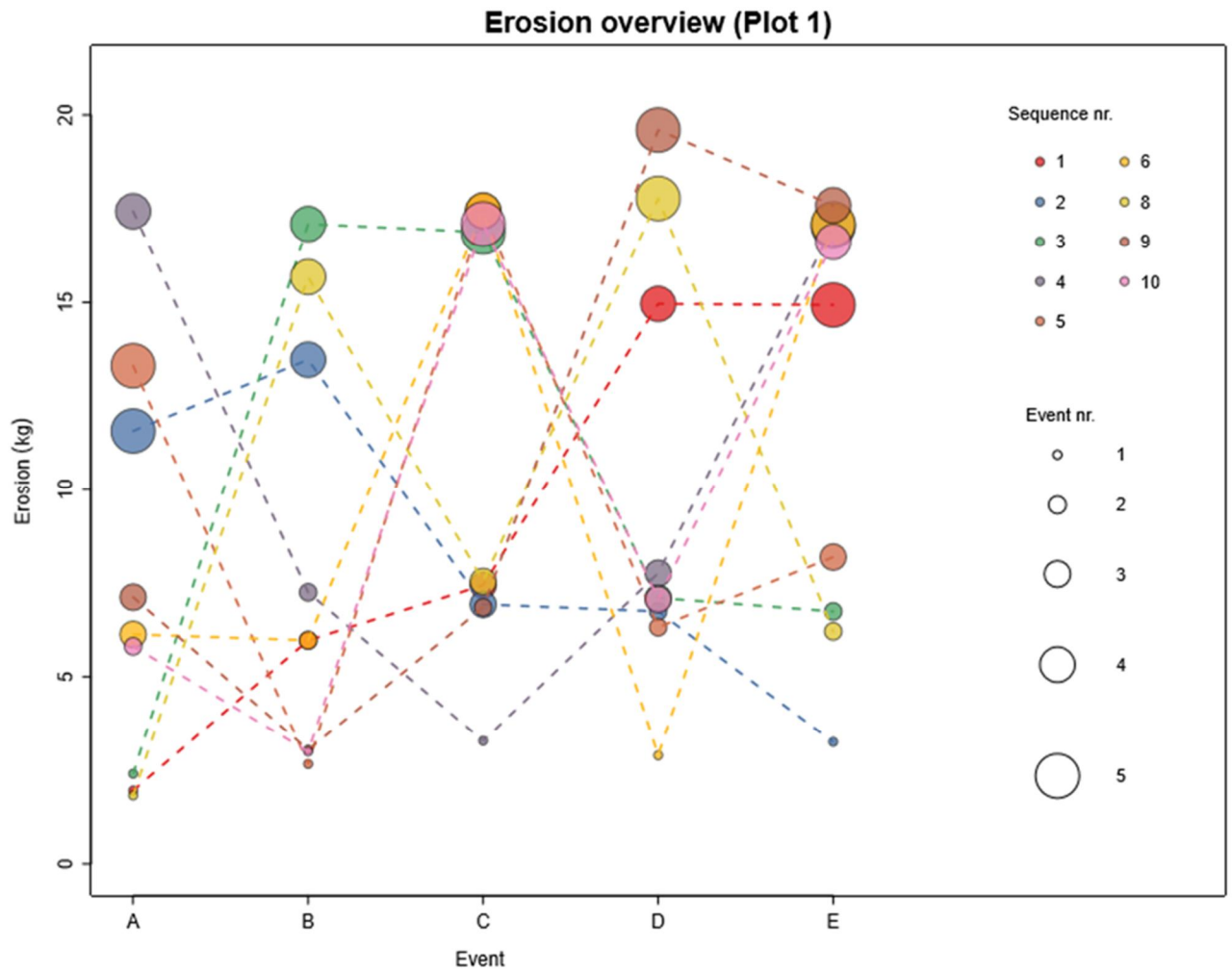
Figure 7. Erosion overview plot 1. Each color indicates one of the 10 sequences. Each circle size indicates one of the five rainfall events, where rainfall event 1 has the smallest circle and event 5 is indicated by the largest circle size.
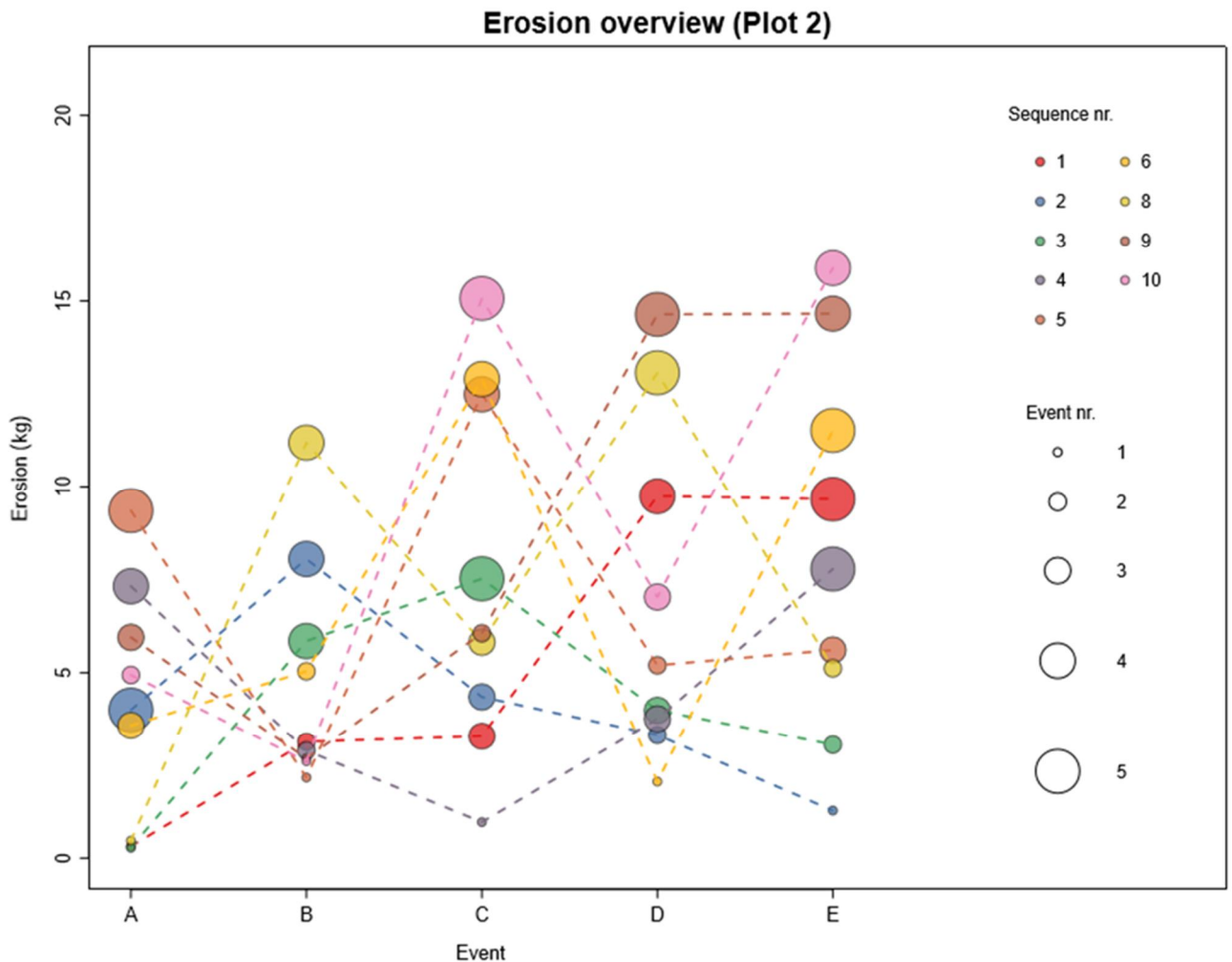
Figure 8. Erosion overview plot 2. Each color indicates one of the 10 sequences. Each circle size indicates one of the five rainfall events, where rainfall event 1 has the smallest circle and event 5 is indicated by the largest circle size.

Figures 9 and 10 show some first results of the analysis of the laser scan data for plot 1 and plot 2 respectively. The left-hand column of the figures (Fig. 9abc and 10abc) show results from after the spin-up event, so before application of a particular rainfall sequence, the right hand column (Fig. 9def and 10def) show results after the last event of a sequence of rainfall events. The figures show results of sequence 10. As can be seen from the pictures, and also from the slope patterns and flow accumulation patterns, a drainage pattern clearly developed due to the rainfall events. The slope maps show that rills developed in the upper part of the plot and the flow accumulation maps show that the drainage pattern development was mainly in the lower part of the plot. Comparing Figures 9 and 10, the flow pattern development in plot 2 (medium coarse sand) was somewhat wider as compared to the flow pattern development in plot 1 (fine sand), which is a bit more confined, especially in the middle of the plot. These differences in pattern development need to be analyzed in further detail.
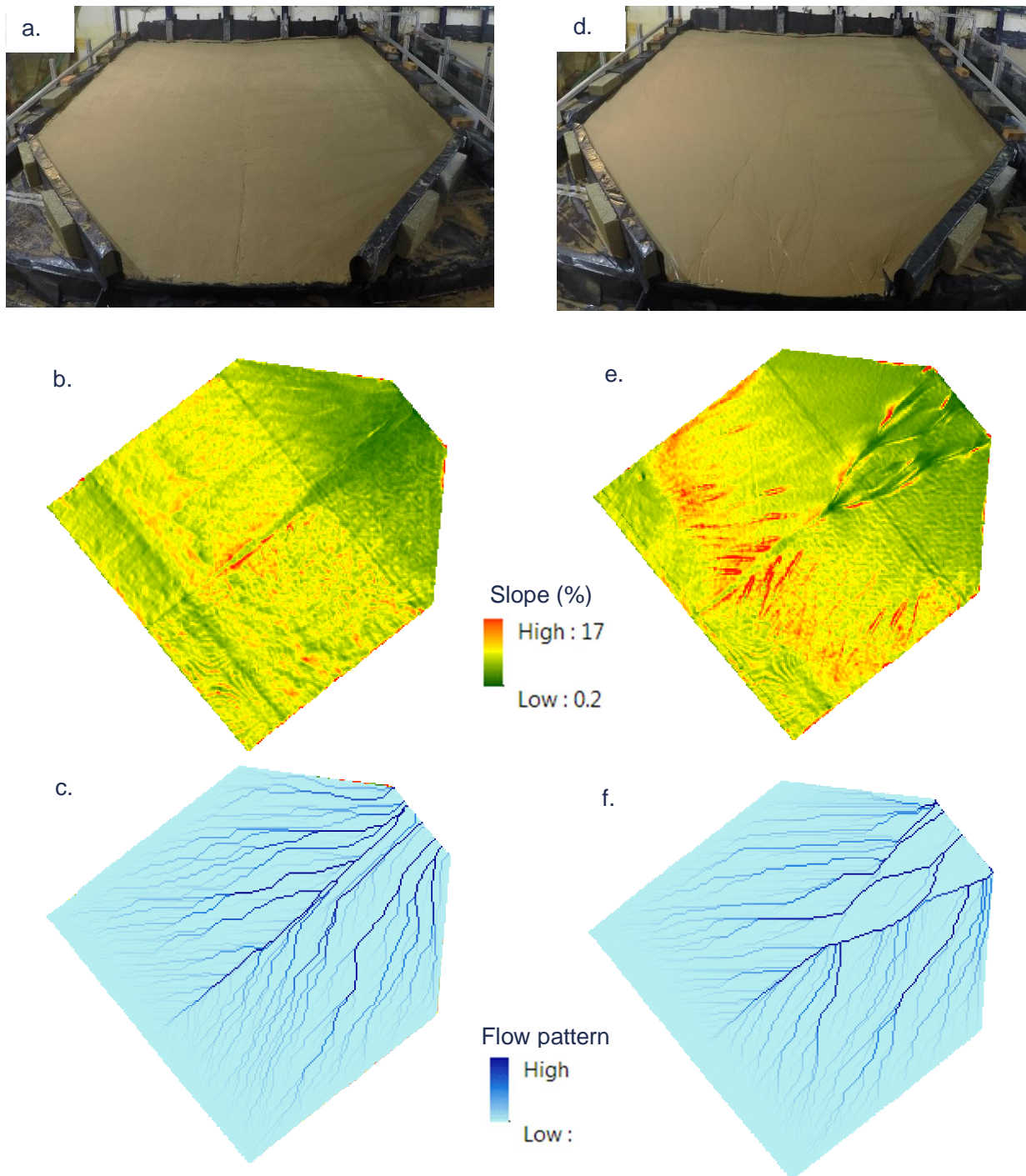
Figure 9. Pictures, slope maps and flow accumulation maps showing slope and flow pattern development between the beginning of sequence 10 (i.e. after spin-up; a,b,c) and at the end of sequence 10 (d,e,f) for plot 1.
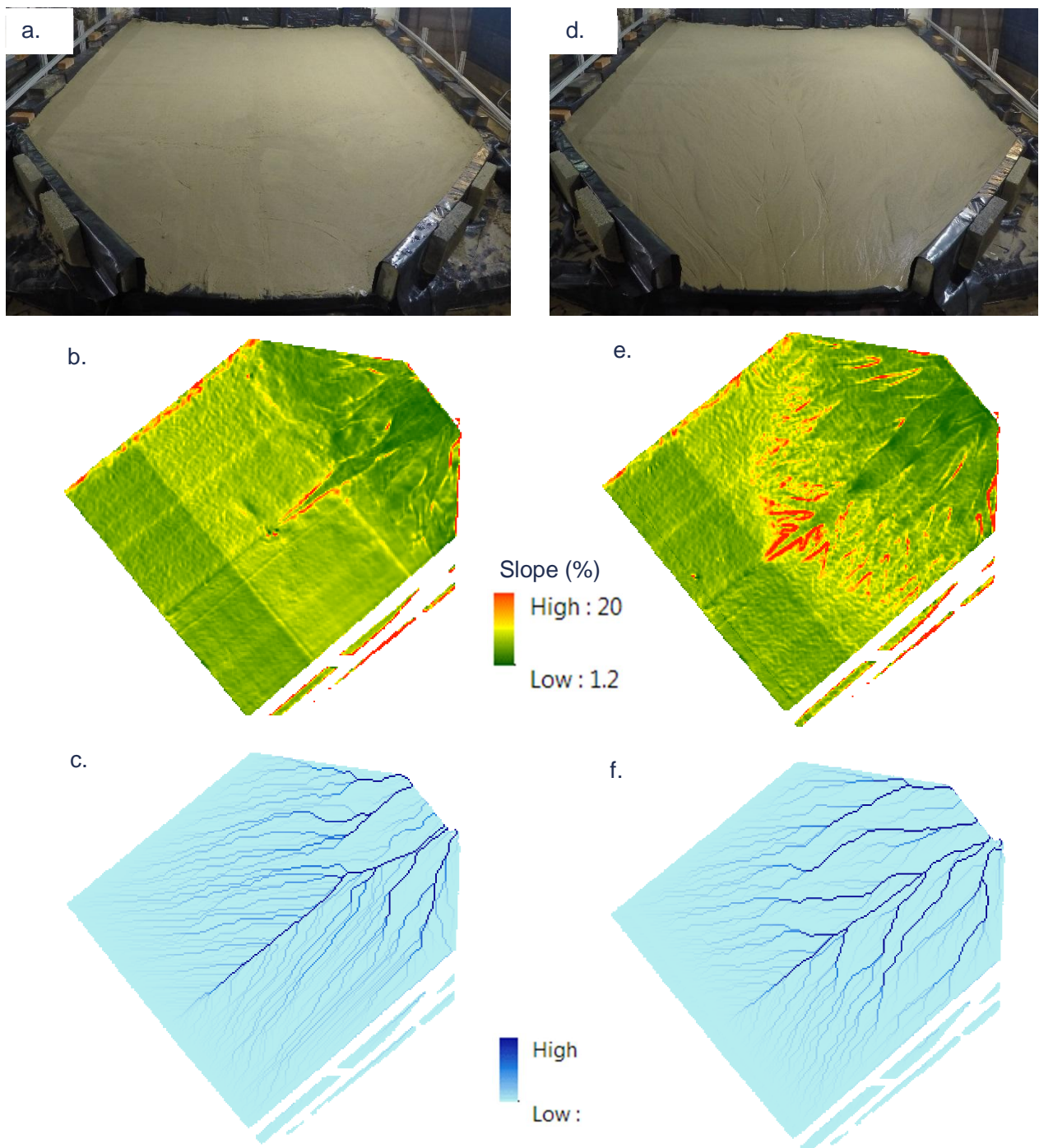
Figure 10. Pictures, slope maps and flow accumulation maps showing slope and flow pattern development between the beginning of sequence 10 (i.e. after spin-up; a,b,c) and at the end of sequence 10 (d,e,f) for plot 2.

4.   OUTLOOK

In section 3, the current results of the project are presented. Further data processing and analysis is ongoing Some challenges have been encountered with post-processing of the laser scan data into reliable DEMs and DEMs of Difference (DoDs). When these challenges are solved, this data will be used to quantify connectivity development in the catchments. Subsequently, differences in connectivity development and patterns will be related to differences in erosion and sediment yield as measured from the different rainfall sequences. Furthermore, the data can be used to parameterize, calibrate and validate erosion and/or landscape evolution models (e.g. LAPSUS or

CEASAR). These can then be used to evaluate erosion dynamics for different landscapes and (climate) scenarios.

ACKNOWLEDGEMENT

REFERENCES

Appels WM, Bogaart PW, van der Zee SEATM. 2011. Influence of spatial variations of microtopography and infiltration on surface runoff and field scale hydrological connectivity. *Advances in Water Resources* 34: 303-313. http://dx.doi.org/10.1016/j.advwatres.2010.12.003.

Baartman JEM, Temme AJAM, Veldkamp T, Jetten VG, Schoorl JM. 2013a. Exploring the role of rainfall variability and extreme events in long-term landscape development. *CATENA* 109: 25-38. http://dx.doi.org/10.1016/j.catena.2013.05.003.

Baartman JEM, Masselink R, Keesstra SD, Temme AJAM. 2013b. Linking landscape morphological complexity and sediment connectivity. *Earth Surface Processes and Landforms* 38: 1457-1471. 10.1002/esp.3434.

Boardman J. 2006. Soil erosion science: Reflections on the limitations of current approaches. *Catena* 68: 73-86.

Boardman J, Favis-Mortlock D. 1999. Frequency-magnitude distributions for soil erosion, runoff and rainfall – a comparative analysis. *Zeitschrift für Geomorphologie, Supplement band* 115: 51-70.

Bracken LJ, Wainwright J, Ali GA, Tetzlaff D, Smith MW, Reaney SM, Roy AG. 2013. Concepts of hydrological connectivity: Research approaches, pathways and future agendas. *Earth-Science Reviews* 119: 17-34. http://dx.doi.org/10.1016/j.earscirev.2013.02.001.

Cammeraat ELH. 2004. Scale dependent thresholds in hydrological and erosion response of a semi-arid catchment in southeast Spain. *Agriculture, Ecosystems & Environment* 104: 317-332.

Cantón Y, Solé-Benet A, de Vente J, Boix-Fayos C, Calvo-Cases A, Asensio C, Puigdefábregas J. 2011. A review of runoff generation and soil erosion across scales in semiarid south-eastern Spain. *Journal of Arid Environments* 75: 1254-1261.

Cerdà A, Brazier R, Nearing M, de Vente J. 2013. Scales and erosion. *CATENA* 102: 1-2. http://dx.doi.org/10.1016/j.catena.2011.09.006.

European Commission. 2006. Soil protection - the long story behind the strategy. Technical report. Office for Official Publications of the European Communities, Luxembourg.

Fryirs K. 2013. (Dis)Connectivity in catchment sediment cascades: a fresh look at the sediment delivery problem. *Earth Surface Processes and Landforms* 38: 30-46. 10.1002/esp.3242.

Gonzalez-Hidalgo JC, Pena-Monne JL, de Luis M. 2007. A review of daily soil erosion in Western Mediterranean areas. *Catena* 71: 193-199.

González-Hidalgo JC, de Luis M, Batalla RJ. 2009. Effects of the largest daily events on total soil erosion by rainwater. An analysis of the USLE database. *Earth Surface Processes and Landforms* 34: 2070-2077. 10.1002/esp.1892.

Hungr O, McDougall S, Wise M, Cullen M. 2008. Magnitude–frequency relationships of debris flows and debris avalanches in relation to slope relief. *Geomorphology* 96: 355-365. http://dx.doi.org/10.1016/j.geomorph.2007.03.020.

IPCC. 2014. *Climate Change 2014: Synthesis Report. Contribution of Working Groups I, II and III to the Fifth Assessment Report of the Intergovernmental Panel on Climate Change*. IPCC, Geneva, Switzerland:

Marques MJ, Bienes R, Jiménez L, Pérez-Rodríguez R. 2007. Effect of vegetal cover on runoff and soil erosion under light intensity events. Rainfall simulation over USLE plots. *Science of The Total Environment* 378: 161-165. http://dx.doi.org/10.1016/j.scitotenv.2007.01.043.

Panagos P, Borrelli P, Robinson DA. 2015. Common Agricultural Policy: Tackling soil loss across Europe. *Nature* 526: 195-195.

Phillips JD. 2003. Sources of nonlinearity and complexity in geomorphic systems. *Progress in Physical Geography* 27: 1-23. 10.1191/0309133303pp340ra.

Pimentel D. 2006. Soil erosion: A food and environmental threat. *Environment, Development and Sustainability* 8: 119-137. 10.1007/s10668-005-1262-8.

Schoorl JM, Temme AJAM, Veldkamp T. 2014. Modelling centennial sediment waves in an eroding landscape – catchment complexity. *Earth Surface Processes and Landforms* 39: 1526-1537. 10.1002/esp.3605.

Van De Wiel MJ, Coulthard TJ. 2010. Self-organized criticality in river basins: Challenging sedimentary records of environmental change. *Geology* 38: 87-90. 10.1130/G30490.1.

Vanmaercke M, Poesen J, Verstraeten G, de Vente J, Ocakoglu F. 2011. Sediment yield in Europe: Spatial patterns and scale dependency. *Geomorphology* 130: 142-161.

SMELLING VORTICES: ANIMAL TRACKING OF CHEMICAL SCENTS IN TURBULENT, UNIDIRECTIONAL FLOWS

Elena Tricarico[1], Matthew Johnson[2], Jan Kubec[3], Miloš Buřič[3], Iva Johovic[1] Stuart J. McLelland[4], Thomas Breithaupt[5]

(1) Department of Biology, University of Florence, Italy, E-mail: elena.tricarico@unifi.it; iva.johovic@gmail.com
(2) School of Geography, University of Nottingham, Nottingham, UK, E-mail: M.Johnson@nottingham.ac.uk
(3) Faculty of Fisheries and Protection of Waters, University of South Bohemia, Vodňany, Czech Republic, E-mail: kubecj@frov.jcu.cz; buric@frov.jcu.cz
(4) Department of Geography, Geology and Environment, University of Hull, Hull, UK, E-mail: S.J.McLelland@hull.ac.uk
(5) Department of Biological and Marine Sciences, University of Hull, Hull, UK, E-mail: T.Breithaupt@hull.ac.uk

Aquatic animals rely on chemical scents to identify food, conspecifics and potential predators. Climate change can alter the conditions in rivers, affecting the ability to track chemical scents. We conducted laboratory experiments at the Total Environment Simulator, University of Hull (UK) to assess the reception by the American signal crayfish *Pacifastacus leniusculus* of chemical signals in a range of ambient velocities and substrate roughnesses (also simulating the effects of climate change). Experiments showed that *P. leniusculus* was more successful tracking the odour on gravel substrate, at low velocity conditions (0.16 m/s), irrespective of low or high-water depth (0.15 m and 0.26 m). Results highlight the ability of this species to detect chemical scent in lower velocity but not flood conditions.

1.   INTRODUCTION

In aquatic animals, chemical scents can come from a food-source or a predator or a conspecific, and can be used to attract a mate or deter a competitor (Aquiloni & Gherardi, 2010; Breithaupt & Thiel, 2011; Tricarico et al., 2011). They are transmitted, diluted and filtered by the flow. Consequently, the characteristics of the flow can exert a control over the structure of the chemical plume and its dispersal and, therefore, the response of receiving organisms (Webster & Weissburg, 2009). However, research on this phenomenon has been primarily conducted in marine environments where conditions are different from river environments. Experiments with low roughness and low velocities (< 10 cm/s) have shown that turbulent mixing dilutes waterborne chemical stimuli, creating an intermittent distribution of chemical patches and filaments that are interspersed with scent-free water (Weissburg et al., 2000). This affects the ability of animals to track odour plumes to their source. However, there is a lack of studies that have assessed plume tracking behaviour with velocity, roughness or turbulence levels that correspondent to river environments, even during low flows, or assessed the distance over which animals can find scent sources.

Climate change is expected to impact rivers in severe and pervasive ways, altering water levels and changing the frequency and magnitude of drought and flood conditions in Europe (Vörösmarty et al., 2000). In particular, alterations in water depth and velocity during summer drought conditions are likely to affect the ability of animals to distinguish and interpret chemical signals because of the role of the flow in mixing, transporting and diluting signals. Ecohydraulics has the potential to inform us about these issues and, more specifically, about the relationships between animals and habitats to better inform how we can manage aquatic animals, particularly if they are species introduced by humans, i.e. alien species (Johnson & Rice, 2014).

The American signal crayfish (*Pacifastacus leniusculus*, Dana 1852) is a widespread invasive alien species across Europe, Japan and localities in the USA outside its original distribution, inhabiting a variety of aquatic environments, and exerting relevant impacts on local biodiversity (Lodge et al.,

2013). In this study we use signal crayfish as a model to understand how hydrological conditions (simulating the effects of climate change) affect the reception of chemical scent by freshwater organisms.

2.   METHODS

The work was carried out in July-September 2018 at the Total Environment Simulator, University of Hull (UK). The first three weeks were devoted to the construction of the flume set-up (building four channels, two with sand, two with gravel, insertion at the substrate surface of an airstone attached to a peristaltic pump to diffuse the odour), to the conditions deployed in the flume for the experiments (e.g. flow, velocity, lighting, camera set-up, odour type, release, testing crayfish). Flow conditions were set up for all experimental configurations used in the following behavioural essays (see below). Animals were collected from Gaddesby Brook, Leicesterhire, UK, permitted by the Environment Agency of England. During the first week, crayfish were acclimated in cages (100x60x39cm; water temperature: 16°C) downstream of the experimental area in two channels of the flume. A total of 39 crayfish were measured, sexed, marked with a numbering code and reversibly blindfolded to ensure that they do not respond to visual cues. We discarded crayfish with missing claws or antennules (used for chemo-reception). Various sources of odour and set up's were tested during week 2 and 3. Week 4 was dedicated to testing crayfish tracking behaviour: after some trials, cat food was used as the source of food odour and was placed in a porous bag (made from a dishcloth), within a mesh cube and placed 70 cm from the crayfish (Figure 1). Two water depths (15 cm and 26 cm), two velocities (16 cm/s and 26 cm/s), two different substrates (gravel, sand) were used in the presence or absence of odour, for a total of eight configurations. In the control (=no cat food), the porous bag was filled only with stone. Ten crayfish were tested per condition. Crayfish were allowed two minutes to acclimate in a Perspex enclosure that enabled water flow through the chamber. After the two minutes, the porous bag with cat food or with only stone was placed into the channel and the whole enclosure was removed immediately afterwards. Behaviour, movements and directions of test crayfish were video-recorded for 15 minutes. For each environmental combination, the physical environment was characterised (surface roughness, velocity with depth and spatially) and a detailed hydraulic assessment was made using an array of Vectrinos. Here, we present the main results related to successful detection of scent in different conditions.
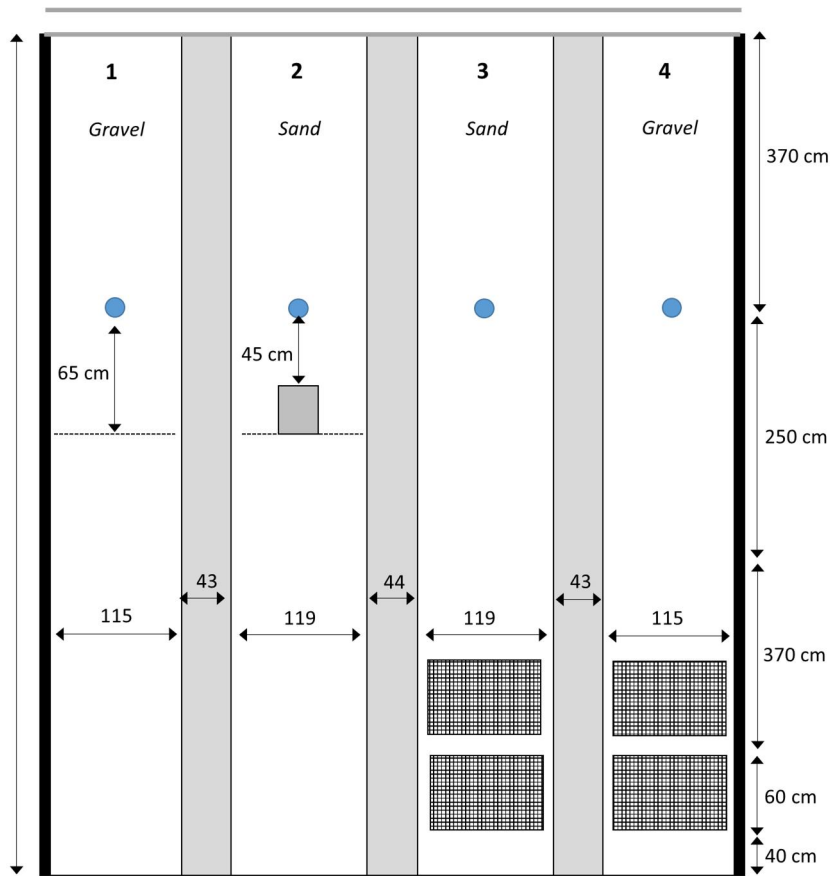
Fig. 1. The experimental set-up: crayfish were acclimatized at the end of the channels 3 and 4; experiments were carried out in the channels 1 and 2. Blue dots indicate the location of the odour source.

3.   RESULTS AND DISCUSSION

Crayfish did not find the bag in the absence of odour, while in the presence of cat food more successful attempts were recorded in the channel with gravel (overall, 8 vs 2, χ^2=4.12, p=0.04; Figure 2), in the presence of low velocity conditions (overall, 7 vs 3, not statistically significant, χ^2=1.83, p=0.18) and in both water depths (overall, low 4 vs 6 high, χ^2=0.46, p=0.50).
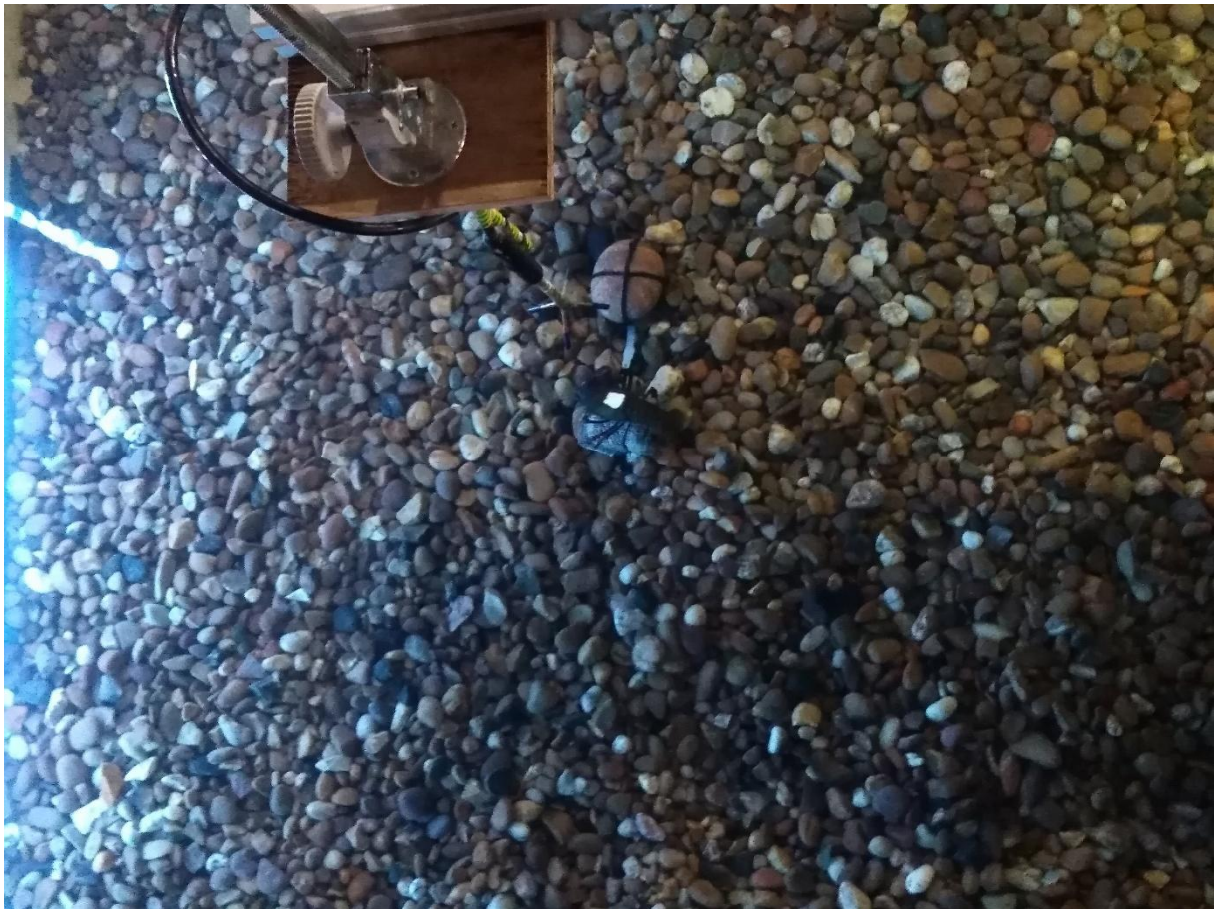
Fig. 2. A test crayfish successfully reached the porous bag with cat food in the gravel substrate.

Table 1. Number of test crayfish that successfully reached the porous bag with cat food in different conditions. LD=Low Depth, LV= Low Velocity, HD= High Depth, HV=High Velocity.

	LD, LV	LD, HV	HD, HV	HD, LV
Gravel	2	1	2	3
Sand	1	0	0	1

Signal crayfish are found in a variety of aquatic environments, ranging from still-water lakes, rapid upland streams and gravel shelves in large rivers (e.g. Lewis, 2002). However, they tend to favour and be active on relatively stable substrates and in areas of low velocity, because at higher velocities crayfish activity can become impeded (e.g. Johnson et al., 2014) with animals seeking shelter in macrophyte stands, marginal areas or burrows to prevent entrainment into the flow.

In our experiments, odour detection seems to be more successful in the presence of gravel substrate, corroborating the findings by Moore & Grills (1999) on rusty crayfish (*Orconectes rusticus*): in their experiments crayfish located food quicker in artificial streams (velocity: 5 cm/s) when cobbles were placed on uniform, planar sand substrates, which the authors state to be because turbulence generated by cobbles spread the plume further than when cobbles were not present. Finally, different water depths seem not to affect significantly the successful detection of odour by *P. leniusculus*.

Overall, successful detection was low across all treatments, with a maximum success rate of 30% on gravel substrates with high depth but low flow velocity. We hypothesis that this may be due to

two factors. The first is that the complexity of the hydraulic environment in the flume makes plume tracking challenging for animals. Given that the experiments represent a more complex hydraulic environment than many previous experiments, but still a simplified environment relative to a river, this has important implications for our understanding of how animals in small, gravel-bedded streams, may use chemo-reception. Certainly, our results suggest that chemoreception is likely to be significant only over short distances (> 10 cm) in shallow, gravel-bedded streams. The second is that crayfish may have felt exposed in the channels, preferring to remain at the margins, in areas of shadow rather than venturing into central areas. Therefore, it is possible that animals did perceive the scent but chose to not track it because of a fear of predation. Future work investigating the behaviour and movement pathways of crayfish will enable us to develop these hypotheses further. The fact that animals did not track as successfully on sand is also likely to relate to the threat of expose, as well as impeded movement because near-bed flows were higher over smoother substrates.

In conclusion, our experiments show that, as expected, gravel is a more suitable substrate to spread the chemical scent and to favour its detection that high velocity impedes the normal movement of crayfish (thus in case of floods the species is not able to successfully reach the odour source), while in case of droughts, here represented by low level of water, we can expect that the species would be able to detect and reach the food.

ACKNOWLEDGEMENT

REFERENCES

Aquiloni, L. and Gherardi, F. (2010). Crayfish females eavesdrop on fighting males and use small and sight to recognize the identity of the winner. Animal Behaviour 79: 265–269.

Breithaupt, T. and Thiel, M. (2011) Chemical communication in crustaceans: research challenges for the twenty-first century. In: T. Breithaupt, M. Thiel (eds.) Chemical communication in crustaceans. Springer.

Johnson, M.F. and Rice, S.P. (2014). Animal perception in gravel-bed rivers: Scales of sensing and environmental controls on sensory information. Canadian Journal of Fisheries and Aquatic Sciences 71: 945–957.

Johnson, M.F., Rice, S.P. and Reid, I. (2014). The activity of signal crayfish (*Pacifastacus leniusculus*) in relation to thermal and hydraulic dynamics of an alluvial stream, UK. Hydrobiologia 724: 41–54.

Lewis, S.D. (2002). *Pacifastacu*s. In Holdich, D.M. (ed.) Biology of freshwater crayfish, pp. 511-540.

Lodge, D.M., Deines, A., Gherardi, F. et al. (2012). Global introductions of crayfishes: Evaluating the impact of species invasions on ecosystem services. Annual Review of Ecology, Evolution, and Systematics 43: 449–472.

Moore, P. and Grills, J.L. (1999). Chemical orientation to food by the crayfish *Orconectes rusticus*: influence of hydrodynamics. Animal Behaviour 58: 953–963.

Tricarico, E., Breithaupt, T. and Gherardi, F. (2011). Interpreting odours in hermit crabs: a comparative study. Estuarine, Coastal and Shelf Science 91: 211–215.

Vörösmarty, C.J., Green, P., Salisbury, J. and Lammers, R.B. (2000). Global water resources: vulnerability from climate change and population growth. Science 289: 284–288.

Webster, D.R. and Weissburg, M.J. (2009). The hydrodynamics of chemical cues among aquatic organisms. Annual Review of Fluid Mechanics 41: 73–90.

Weissburg, M.J. (2000). The fluid dynamical context of chemosensory behavior. The Biological Bulletin198: 188–202.

MOMENTUM BALANCE OF A GLASS-PLATE PATCH IN SHALLOW FLOW

O. Eiff, V. Dupuis, M. Trevisson, S. Wunder, D. Hettmann, A. Zygouli (1)
L. Chagot, F. Moulin (2)
B. Murphy, & S. McLelland (3)

(1) KIT, Karlsruhe, Germany, Email: olivier.eiff@kit.edu; victor.dupuis@kit.edu
(2) IMFT, Université de Toulouse, CNRS-INPT-UPS, Toulouse, France, Email: fmoulin@imft.fr
(3) University of Hull, Hull, Great Britain, Email: S.J.McLelland@hull.ac.uk

The resistance to flow of aqueous vegetation patches is a challenge to model due to their complex geometry and topological adaption under hydrodynamic loading. Patches not only influence the water level and mean velocities due to the drag they exert, but they also affect the turbulence and hence the processes such as the sediment deposition and erosion within and around the patch. Existing studies dealing with the interaction of flow and vegetation mostly measured the drag of individual plants or focused on the flow through and above homogeneous canopies. Studies of the flow around and within isolated patches are scarce and restricted to arrays of cylindrical elements. For leafy plants or surrogates there is only limited if any information and understanding of how the flow evolves through and around the plants. In this access project, the aim was to fill this gap via complementary physical lab-scale and numerical experiments of the flow through and around a surrogate leafy vegetation patch. The measurements were also performed around a real plant in the same flow configuration. Here, we focus on the momentum budget based on the measurements around the surrogate plant performed via stereoscopic particle image velocimetry (SPIV).

1. INTRODUCTION

The prediction of flow velocities and water levels during flood events is a challenge due to the need to account for the flow resistance or drag of complex emergent and/or submerged obstacles. The flow resistance due to vegetation patches is particularly difficult to quantify due to their complex geometry and topological change under hydrodynamic loading and seasonal conditions. Vegetation also affect locally the flow field including the turbulence and associated mass transfer processes. The flow resistance and interactions depend on the allometric characteristics of the vegetation patch itself. These are generally described by frontal density, solid volume fraction, leaf area index (LAI), shape and flexibility, with major uncertainties both in their flow-dependent determination and parameterization, necessary for implementation in larger-scale numerical models (Aberle & Järvelä, 2013; Boothroyd et al., 2015; Jalonen et al., 2013; Marjoribanks et.al., 2014).

Existing investigations on the vegetation drag were mostly performed by direct force measurements using the classical one-parameter drag force equation for solid bodies to parameterize the effects of the allometric plant characteristics by modifying the velocity dependence with additional parameters (Aberle & Järvelä; Armanini et al., 2005; Wunder et al., 2011). However, as recent studies on the flow through emergent single vegetation patches (Nicolle & Eames, 2011; Rominger & Nepf, 2011) have shown, the use of such parameterization of the drag force equation is questionable when the plant is significantly penetrated by the flow. To avoid these parametrizations, studies have started to investigate the flow itself around emergent patches constructed by arrayed cylinders, to better characterize the flow pattern and turbulence structures in the wake zone (Tanino & Nepf, 2008; Thomas & McLelland, 2015). In these studies the flow was characterized by instantaneous and local velocity measurements. Yet, most of the local flow investigations did not focus on the question of the drag parametrization but on the morphodynamic processes within and downstream of the emergent patches (Chen et al., 2012; Kim et al., 2016). PIV-measurements around patches have so far only been performed in the wake zone of a single and submerged artificial fractal tree (Bai et al, 2012, 2013). Numerical (RNG and LES)

investigations of the flow field within and around a patch have also been performed and have so far considered emergent arrays of solid cylinders (Chang et al., 2017; Marjoribanks, 2014a, 2014b) or artificial plants (Boothroyd et al, 2015; Stoesser et al., 2010; Zong & Nepf, 2011). In summary, for leafy plants there is still very limited information and understanding of how the flow through them and the resulting drag evolves. This paper proposes to start filling these gaps by performing PIV-measurements around an artificial leafy patch made of glass plates. The PIV measurements were performed in a stereoscopic configuration in order to be able to include the necessary transverse planes as well as the out-of-plane components, necessary for a full momentum balance. The artificial plant meets the allometric characteristics of a real leafy plant. The project also included measurements around a real leafy plant and measurements within the artificial plant. Here, the focus is on the momentum balance of the artificial plant for one flow configuration and includes an analysis of the turbulent flow structure in the near-wake of the patch.

2.   EXPERIMENTAL SET-UP

The experiments were performed in the recirculating Total Environment Simulator of Hull University, Great Britain, a glass-walled flume 6 m wide and 10 m long. The effective flume width was symmetrically reduced to a width B = 3 m in order to use a side-looking submersible stereo PIV set-up described below. This effective width still enabled to minimize side wall effects in a shallow-water configuration with water depth h = 20 cm, while retaining a large enough patch for Reynold number similarity. The patch, consisting of a geometrically ordered structure, designed with 35 vertical glass plates, t = 1 mm thin, l = 4 cm long and h_p = 20 cm high, arranged in a staggered configuration (cf. **Figure 1a**), was installed in the centre of the flume. The bed of the flume was covered by gravel with mean diameter of d_g = 2 cm (cf **Figure 1b**). The bed was not water-worked but levelled manually to obtain a flat bed. The levelling is expected to lower the roughness. To cover the allometric parameters of a real leafy plant, the design of the geometry (number of plates per base area) met the natural values of solid volume fraction, i.e. porosity (ϕ = 0.98), and the leaf area index (LAI = 4.0) of a real shrubby willow. The layout of the 35 glass plates spaced at distance s = 33 mm apart is given in **Figure 2**. The patch has a total width b = 27.3 cm so that B/b > 10 and length a = 34.2 cm and was positioned 7 m downstream from a set of grids to homogenize the flow and to reduce inlet turbulence intensities. The coordinate origin is fixed at the middle of the upstream edge of the patch, with x the longitudinal direction, y the transverse and z the vertical directions.

Figure 1. Design of the artificial patch (**a**), meeting the allometric characteristics of a natural willow plant, installed in the flume (**b**), and during experiments (**c**).
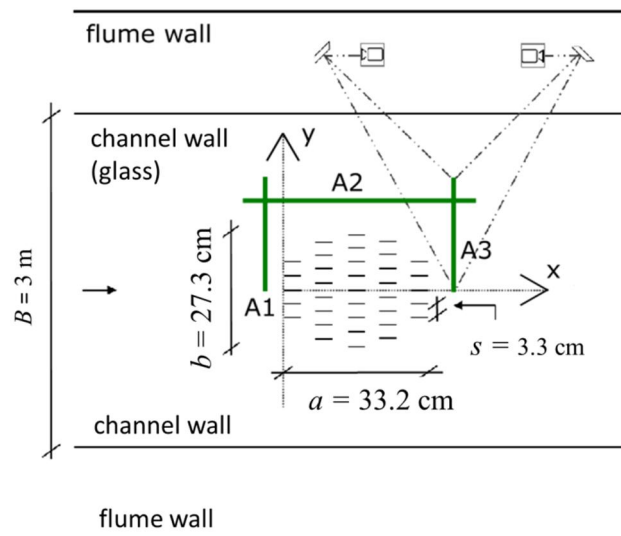
Figure 2. Set-up of the stereoscopic PIV (SPIV). The green lines refer to SPIV measurement planes. Not to scale.

The flow field around the patch was characterized by stereoscopic 2D-3C PIV measurements in two transverse vertical planes and a longitudinal plane (**Figure 2**). The transverse planes were positioned upstream of the patch 3.4 cm upstream to the first row of glass sheets ($x = -3.4$ cm and 3.4 cm downstream of the patch last row of glass plates ($x = 36.6$ cm). The longitudinal plane was position at $y = 25$ cm. On the basis of upstream ADV measurements, it can be reasonably assumed that the flow field behaves symmetrically with respect to the centreline in flow direction. Measurements were performed for relative submergence of plant-height to water-depth $h_p/h = 1$, a bulk flow velocity of $U_b = 0.3$ m/s and a flow depth of $h = 0.2$ m. The Reynolds-number of the channel flow is $Re_f = U_b\, h\, /v = 6.0$ x 10^4 and the leaf Reynolds-number $Re_l = U_b\, l\, /v = 1.2$ x 10^4. The transverse plane measurements were also performed with the patch.

The instrumentation consisted of a 2 x 120 mJ pulsed laser from Dantec Dynamics producing a 10 mm thick laser sheet synchronized with two CMOS cameras with a resolution of 2320 pixels x 1726 pixels and mounted with motorized 65 mm lenses. The cameras were positioned in a 1.5 m long underwater-torpedo from Dantec in the side-channel which recorded the images via adjustable mirrors. The seeding used was PLASCOAT TALISMAN 20 with a mean density of $\rho = 0.99$ g/cm^3 and a particle size of about 180 μm. To converge statistically, 5000 image pairs with a sampling rate of 4 Hz were collected for each camera and each measurement plane. The data was processed with the Davis software from Lavision.

3. RESULTS AND DISCUSSION

Comparison of the longitudinal velocity contours without the patch in the two transverse planes 1 and 3 shown in Figure 3a-b suggests that the flow was developed. Also, the turbulent shear stress $-\rho \overline{u'w'}(z)$ (not shown) can be seen to be essentially linear except near the bed, suggesting developed and 2D flow. Yet, the velocity contours also reveal relatively strong lateral variations. This non-uniformity does not appear to be associated with secondary circulations but with non-uniformity at the inlet. The friction velocity evaluated from the linear extrapolation of the fitted turbulent shear stress down to the top of the gravel bed yielded a value of 2.5 cm/s. The velocity profiles were fitted with the logarithmic law with a van Karman constant of 0.41 and yielded an equivalent sand-roughness of the manually-levelled gravel bed $k_s = 3$ mm, resulting in $k_s^+ \cong 70$, i.e. fully rough flow.

Figure a-b show the longitudinal velocity component with the patch in the upstream and downstream transverse planes, respectively. In the downstream plane, vertical bar-like structures of lower velocity can be identified which are clearly the signatures of the upstream glass plates. This suggests that the individual wakes of the plates have not merged. Also, except close to the

ground, the wake velocities are relatively uniform in strength. The non-uniformity of the flow outside of the wake region is relatively well correlated with the no-patch flows shown in **Figure 2** and therefore do not represent a wake or patch effect.
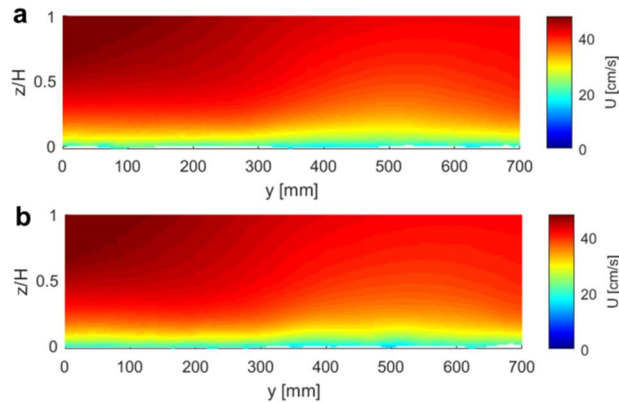

Figure 3. Gravel bed flow without patch. Contour plot of the longitudinal velocity at x = -3.4 cm (**a**) and at x = 36.6 cm (**b**).
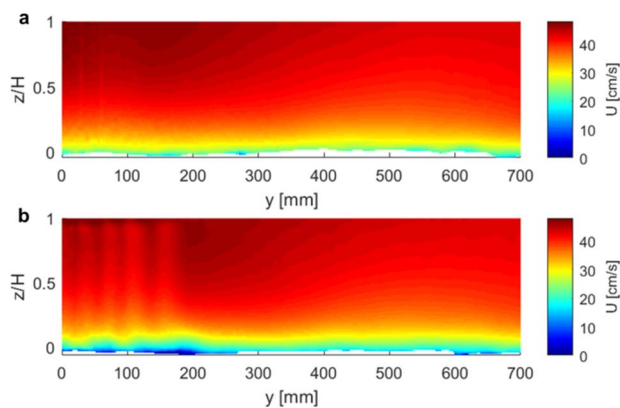

Figure 4. Gravel bed flow with patch. Contour plot of the longitudinal velocity upstream of the patch at x = -3.4 cm (**a**) and downstream at x = 36.6 cm (**b**).

Figure 5 shows, from measurement plane A3 downstream of the patch, the lateral profiles of the time-averaged longitudinal velocity $\bar{u}$, the time averaged lateral velocity $\bar{v}$, the normal turbulent stress $\overline{\rho u'^2}$, the lateral turbulent shear stress $\overline{\rho u'v'}$, all at **z/h** = 0.39 and **z/h** = 0.88. The green lines show the position of minimum $\bar{u}$, i.e. the centre of the wakes. The black solid and dashed lines indicate the position of the glass blades. The black solid lines correspond to positions for three rows of blades (rows 1, 3, 5), while the black dashed lines to two rows (2, 3). For $y = 0$ the green and black lines overlap. For higher **y**'s, the separation increases with increasing y suggesting that the wakes are deviating. Interesting, rows 2 and 3 (dashed lines) do not appear with minimum $\bar{u}$ signature. There are only five green lines or $\bar{u}$ minima, as seen in Figure 4b. Minimum $\bar{u}$ do not quite correspond to $\bar{v} = 0$ which again suggests a deviation of the wakes. It should also be noted that the mean velocity profiles are in phase at the two heights plotted, again in agreement with the columnar iso-contours seen in Figure 4b. The normal stress does not reveal an evident phase relationship and is in fact slightly lower in the wake than in the free stream, suggesting that the blades are reducing the turbulent kinetic energy of the flow. The lateral turbulent shear stress again reveals a strong variation in the wake. Maximum negative values are expected at the strongest positive gradient of $d\bar{u}/dy$, which the profiles mostly corroborate, again suggesting that the wakes generated by the separating boundary layers retain their identities, at least for the dominant rows 1, 3 & 5. The measurements within the patch should be able to shed more light on this.
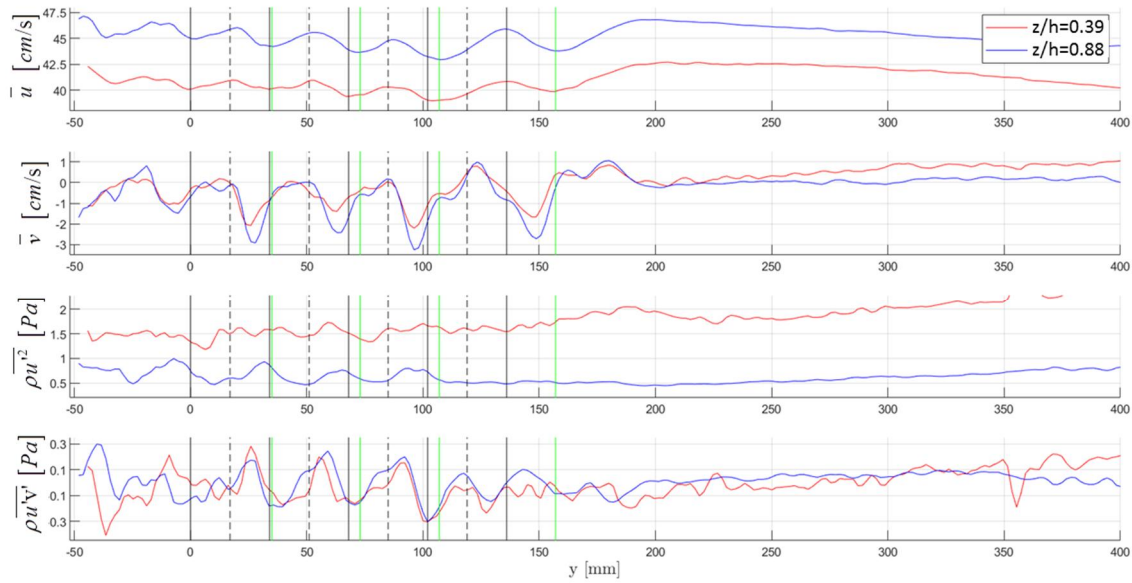
Figure 5. Lateral profiles of the time-averaged longitudinal velocity $\overline{u}$, the time averaged lateral velocity $\overline{v}$, the normal turbulent stress $\rho\overline{u'^2}$, the lateral turbulent shear stress $\rho\overline{u'v'}$, all at z/h = 0.39 and 0.88. x = 36.6 cm, downstream of the patch. The black solid and dashed vertical lines indicate the positions of the glass blades and the green vertical lines indicate the position of the minimums of $\overline{u}$.

The three measurement planes including allow a momentum balance to be performed to estimate the drag exerted on the patch. For a control volume given by the three planes and assuming a hydrostatic pressure distribution at the control surfaces upstream and downstream, the momentum balance over half the patch along the symmetry line writes as:

$$D_x = \underbrace{-\rho \int_{A_1} \overline{uu}\,dA}_{Adv_1} + \underbrace{\rho \int_{A_3} \overline{uu}\,dA_3}_{Adv_3} + \underbrace{\rho \int_{A_2} \overline{uv}\,dA_1}_{Adv_2} - \underbrace{\rho \int_{A_1} \overline{u'u'}\,dA_1}_{Turb_1} + \underbrace{\rho \int_{A_3} \overline{u'u'}\,dA_3}_{Turb} + \underbrace{\rho \int_{A_2} \overline{u'v'}\,dA_2}_{Turb_2}$$

$$\underbrace{-\rho\,gI\cdot V_{cv}}_{Gravity} - \underbrace{\tau_{bed}A_b}_{Bed\ Shear\ Stress} - \underbrace{\rho\,gB\left(\frac{h_1^2 - h_3^2}{2}\right)}_{Press.\ Grad}$$

Here, D_x is the total force exerted by the blades on the fluid due to viscous and pressure forces (i.e., it should be negative). The indices 1, 2 & 3 of the integration areas A_i and water depths h_i refer the portions of the measurement planes A1, A2 & A3, respectively, which intersect to give the control surface of the control volume V_c. A_b is the surface area of the control volume adjacent to the bed and I is the bed-slope. Bed friction τ_{bed} (here negative) is estimated via the friction velocity measured with the patch and the water depths h_i were determined from the PIV images. **Figure 6** shows the resulting terms. It can be seen that the pressure term given by the water depths is the leading order term followed by the net streamwise advection of streamwise momentum across the transverse planes. Momentum loss through the side is about a third as that through the transverse sections but of opposite sign, reducing the drag force which the patch exerts. The turbulent stress terms play no significant role and the gravity term is also small. The drag coefficient defined with the frontal area of the patch $C_D = \dfrac{-2D_x}{bh_p\rho U_b^2}$, yields $C_D = 0.42$.

The wake analysis suggests that the boundary layers developing on the glass blades dominate the wake. To pursue this, the frictional drag force acting on both sides of the glass blades was

216

estimated with a standard turbulent boundary layer relationship $C_f = 0.032\,\mathrm{Re}_l^{-1/7}$ with l the length of the blades in Re_l and taking U_b as the reference velocity for simplicity. The resulting frictional force for the half-patch considered in the control volume is -0.38 N, compared to -1.95 N for $D_{s,}$, i.e., about 20%. Accordingly, the drag coefficient reduces to $C_D = 0.34$ when subtracting the estimated frictional force exerted by the blades. This suggests that the interaction of the individual wakes plays an important role, more than the direct frictional effects. Of course, the frictional drag estimation also assumes free-stream potential flow and can therefore underestimate the frictional drag.
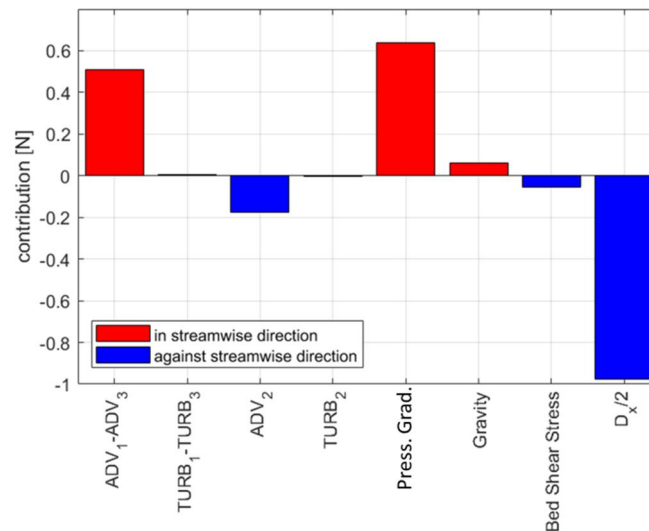

Figure 6. Contribution of the different terms to the drag D_x in the momentum balance.

CONCLUSION

The flow field around a patch made of thin glass plates aligned with the flow was measured via stereoscopic PIV in order to estimate the drag exerted by the patch on the flow. The patch was designed to meet the allometric characteristics of a real leafy floodplain plant (willow), with a leaf-area index (LAI) of 4 and a porosity of 98%. The patch was positioned on a manually-levelled gravel bed and the plates extended up to the free surface ($h/h_p = 1$), while the width of the patch was less than one-tenth of the flume width ($b/B < 10$) to be a shallow water configuration without side-wall effects. Analysis of the longitudinal mean velocity and the lateral turbulent shear stress profiles in the transverse plane of the near wake revealed the signatures of vertically aligned wakes generated by the glass sheets. These wakes appear to interact and to deviate sideways and dominate the wake-behaviour of the patch. In other words, the patch does not generate a single dominant large-scale wake behaviour. The momentum balances yields a drag coefficient of $C_D = 0.42$. A rough estimate of the frictional force acting on the glass plates as if each plate was isolated in uniform and potential flow yields a frictional-resistance to total-drag ratio of 0.2 so that the drag coefficient without this estimated frictional resistance is reduced to 0.34 – still relatively high. This estimate suggests that the pressure losses and interactions between the separating boundary-layer wakes is nevertheless rather significant, despite an LAI of 4 and a porosity of 98%, but needs to be confirmed with measurements and LES simulations within the patch. 2D-PIV data of the flow within the artificial patch should help to elucidate the interaction of the wakes as well as the actual bed shear stress in the presence of the patch. Furthermore, other measured flow velocities and depths still need to be analysed and compared to the real-plant equivalent.

REFERENCES

Aberle, J., Järvelä,J. (2013). Flow resistance of emergent rigid and flexible flood plain vegetation. *J. Hydr. Res., 51(1)*, S. 33-45.

Armanini, A., Righetti, M., Grisenti, P. (2005). Direct measurement of vegetation resistance in prototype scale. *J. Hydr. Res., 43(5)*, S. 481-487.

Bai, K., Meneveau, C., Katz, J. (2012). Near-wake turbulent flow structure and mixinglength downstream of a fractal tree, 143,. *Boundary Layer Met.*, S. 285–308.

Bai, K., Meneveau, C., Katz, J. (2013). Experimental study of spectral energy fluxes in turblence generated by a fractal treelike object. *Phys.Fluids, 25*, S. 110810.

Boothroyd, R.J., Hardy, R.J., Warburton, J., Marjoribanks, T.I. (2015). The importance of accurately representing submerged vegetation morphology in thenumerical prediction of complex riverflow. *Earth Surf. Process and Landf.*

Chang, W.-Y., Constantinescu, G., Tsai, W. F. (2017). On the flow and coherent structures generated by a circular array of rigid emerged cylinders placed in an open channel with flat and deformed bed. *J. Fluid Mech., 831*, S. 1-40.

Chen, Z., Ortiz, A., Zong, L., Nepf, H. (2012). The wake structure behind a porous obstruction and its implications for deposition near a finite patch of emergent vegetation. *Water Res. Res. 48(9)*.

Jalonen, J., Järvelä, J., Aberle, J. (2013). Leaf area index as a vegetation density measure for hydraulic analyses. *J: Hydr. Eng., 139(5)*, pp. 461-469.

Kim, H.S., Kimura, I., Shimizu, Y. (2015). Bed morphological changes around a finite patch of vegetation. *Earth Surf. Process. Landf., 40* , S. 375-388.

Liu, C., Nepf, H. (2016). Sediment deposition within and around a finite patch of model vegetation over a range of channel velocity. *Water Res. Res., 52*.

Marjoribanks, T. I., Hardy, R. J., Lane, S. N., Parsons, D. R. (2014). The hydraulic description of vegetated riverchannels: the weaknesses of existing formulations and emerging alternatives. *Wiley Interdisciplinary Reviews: Water 11/2014, 1(16)*.

Marjoribanks, T. I., Hardy, R. J., Lane, S. N., Parsons, D. R. (2014a). High-resolution numerical modelling of flow–vegetation interactions. *J. Hydr. Res. 52(6)*, S. 775-793.

Marjoribanks, T. I., Hardy, R. J., Lane, S. N., Parsons, D. R. (2014b). The hydraulic description of vegetated riverchannels: the weaknesses of existing formulations and emerging alternatives. *Wiley Interdisciplinary Reviews: Water 11/2014, 1(16)*.

Nicolle, A., Eames, I. (2011). Numerical study of flow through and around a circular array of cylinders. *J. Fluid Mech., 679*, S. 1-31.

Rominger, J. T., Nepf, H. M. (2011). Flow adjustment and interior flow associated with a rectangular porous obstruction. *J. Fluid Mech., 680*, S. 636-659.

Stoesser, T., Kim, S. J., Diplas, P. (2010). Turbulent flow through idealized emergent vegetation. *J. Hydr. Eng. 136(12)*, S. 1003–1017.

Tanino, Y., Nepf, H. M. (2008). Laboratory investigation of mean drag in a random array of rigid emergent cylinders. *J. Hydr. Eng., 134(1)*, S. 34–41.

Thomas, R.E, McLelland, S.J. (2015). The impact of macroalgae on mean and turbulent flow fields. *J. Hydrodyn., 27(3)*, S. 427-435.

Wunder, S., Lehmann, B., Nestmann, F. (2011). Determination of the drag coefficients of emergent and just submerged willows. *J. River Basin Management, 9(3-4)*, S. 231-236.

Zong, L., Nepf, H. (2011). Vortex development behind a finite porous obstruction in a channel. *J. Fluid Mech. 691*, S. 368–391.

MORPHOLOGICAL DIFFUSION EXPERIMENT: SEDIMENT SPREADING UNDER WAVE, CURRENT AND MIXED ENERGY FORCINGS

Matthieu de Schipper (1), J. Hopkins (1), M. Wengrove (2), M. Kleinhans (3), N. Senechal (4), B.Castelle (4), F. Ribas (5), B.G. Ruessink (3) & S. McLelland (6)

(1) Delft University of Technology, the Netherlands, M.A.deSchipper@TUDelft.nl, J.A.Hopkins@TUDelft.nl
(2) Oregon State University, USA, meagan.wengrove@oregonstate.edu
(3) Utrecht University, the Netherlands, M.G.Kleinhans@uu.nl, B.G.Ruessink@uu.nl
(4) Université de Bordeaux, France n.senechal@epoc.u-bordeaux1.fr , b.castelle@epoc.u-bordeaux1.fr
(5) Universitat Politècnica de Catalunya, Spain francesca.ribas@upc.edu
(6) University of Hull, United Kingdom, S.J.McLelland@hull.ac.uk

Understanding the dispersal of sand from submerged mounds is key to evaluate coastal protection strategies. Most of the work on the evolution of submerged mounds, however has been based on currents only and neglecting the effects of waves. This contribution introduces the laboratory MOrphological Diffusivity EXperiment (MODEX) aimed at examining morphological diffusivity under different forcing conditions: waves, currents and waves with currents. The experiment particularly addresses the linkages between small scale effects (e.g. bed slope, bedforms) on the larger scale adjustment of the sandy mounds. For this experiment the Hydralab+ scheme provided a unique opportunity to investigate morphological diffusivity while fostering collaborations between different institutes.

1. CONTEXT

Coastal protection is of prime importance for the upcoming century as the majority of the world population and economic value depends on beach and dune strength. Beach replenishments (also referred to as nourishments), where sand from offshore is disposed on or near the beach, are the principal mitigation measure in adaptive coastal maintenance during times of climate change for many locations. Recently, concentrated nourishments have been proposed as an innovative alternative to traditional smaller scale nourishments, using natural forces to spread the sand and feed the surrounding sand-starved coasts. A first pilot study of this type of replenishment scheme is the Sand Engine (Stive et al., 2013; de Schipper et al., 2016; see Figure 1).
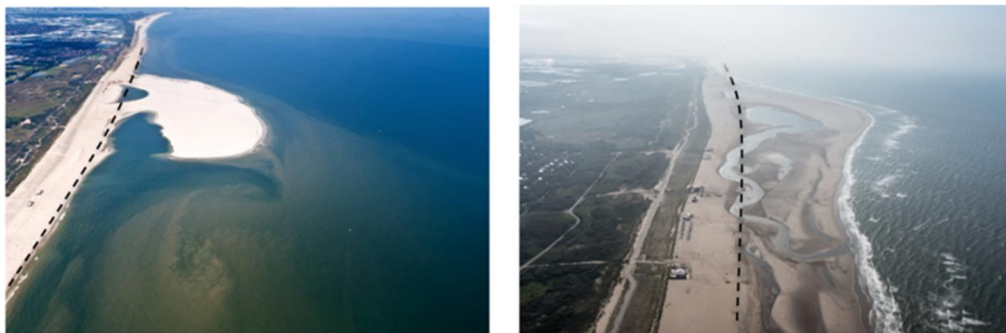

Figure 1 The evolution of a concentrated nourishment. Aerial photographs of the Sand Engine after completion in 2011 (left) and in 2015 (right). The location of the land/water interface prior to the project is given by the dashed lines. Photos adjusted from: Rijkswaterstaat/Joop van Houdt (left) and Jurriaan Brobbel (right)

To apply maintenance schemes, it is paramount to have knowledge and a good prediction skill of morphological diffusivity (i.e. the spreading characteristics) and its driving processes. However, an accurate prediction of this mechanism remains one of the great challenges in present day coastal engineering. For example, Arriaga et al. (2017) modelled the long-term evolution (30 year) of the Sand Engine and the simulated diffusivity was almost 3 times smaller than the prediction of the classical 1-line diffusion equation.

Moreover, though sand is sometimes placed on the beach for a nourishment, it has become more common to dispose sand in 3 to 8 m of water depth (Stive et al., 2013). The dispersal of sand from submerged sandy bodies in the nearshore is driven by the interplay of processes such as

converging and recirculating flows, changing roughness, bed slope effects and wave focusing/refraction. This morphological diffusivity is key to understanding sand bars in shallow seas, tidal inlets, estuaries, and the nearshore response to human interventions such as nourishments and dredging. Most of the work on the evolution of submerged mounds has been based on fluvial studies, focusing on flow without waves (e.g. de Vriend et al., 1987). In these cases, circular mounds tend to deform to crescentic (barchan) shapes. In contrast, observations of sandbars and berms in the nearshore subjected to waves show much more complex translation and deformation behavior (e.g. Rutten et al., 2018; Huisman et al., 2019).

This contribution introduces the laboratory MOrphological Diffusivity Experiment (MODEX). This Hydralab experiment was focused on morphological diffusivity under different forcing types. MODEX is a collaboration between Delft University of Technology, Utrecht University, Oregon State University, CNRS, Université de Bordeaux, Universitat Politècnica de Catalunya and the University of Hull. The proposed experiment and concurrent numerical model development are meant to improve the prediction of concentrated nourishments in the near future and coastal response to human interventions in general.

2.   EXPERIMENT

A detailed description of the experiment and instrumentation is given in de Schipper et al. (2019), while details on setting up the experiment are given below.

MODEX was executed at the Total Environment Simulator (TES) in Hull, United Kingdom for a total of 7 weeks in spring 2018. The TES is a facility that can run both waves and currents. The size of the flume, 6 by 12 meters, making it an ideal lab facility to execute the project goals. It is large enough such that flow easily diverges around the mound, yet small enough such that the sandy bed can be flattened and reconstructed in a single day.

For the experiment, the TES is filled with a layer of 0.1 m of sand with a D50 of 215 µm (Figure 2, middle). After two weeks preparation of the experiments, 9 different forcings were tested. In between each of these 9 tests the flume bed was flattened and a Gaussian mound was constructed using a mold.

Figure 2 Total Environment Simulator Laboratory setup in Hull, United Kingdom. Photos of the flume prior (left) to the experiment, after filling with sand (middle) and after a test (T4) was run (right). Blue panels on the back wall are the HR Wallingford wave paddles.

Experiments with combined flow and waves require a particular downstream beach-like structure. At this downstream end waves need to dissipate to prevent reflection, while flow needs to be diverted to the recirculation system below the flume. A permeable beach was therefore constructed with slopes of ~1:5. The beach panels are based on plywood with an artificial grass layer on top. Water flows into the recirculation system through 1) overtopping of the beach plane, 2) flow through the holes in the beach, and 3) a gap between the beach and the bed below the wave through level (Figure 3, left)

Figure 3 Beach like structure on the downstream side of the flume (left) and the mound prior to a test (right)

Nine different forcing conditions were tested on identical mounds (Figure 3, right). Test conditions are designed to span different energy levels, while exploring the waves, currents and combined forcings. The combined forcing tests (T7, T8 and T9) are particularly designed to have similar combined shear stress estimates with different ratios of wave to current forcing (Table 1).

Table 1. Forcing conditions used during different tests of the experiment. Θ refers to the expected non-dimensional shear stress (Shields parameter) for waves Θ_w or currents Θ_c used to create a dominance of either of the two. Currents follow from the imposed flow rate divided by the wet cross-section (6 by 0.4 m). Values are the imposed values, observed values near the centre of the mound given in bold.

Tests date	Wave forcing	Flow rate	Total time (intervals)
T1 Waves only (low) 16 & 17 May (day of year 136 &137)	T=1s, H=0.11 m **(0.10 m)**	-	150 min (10 x 15)
T2 Waves only (medium) 21 & 22 May (141 & 142)	T=1.2s, H=0.14 m **(0.12 m)**	-	90 min (9 x 10)
T3 Waves only (high) 24 & 25 May (144 & 145)	T=1.3s, H=0.16 m **(0.12 m)**	-	60 min (9 x 6.66)
T4 Current only (large) 30 May (150)	-	900 l/s, 0.38m/s	35 min (10 + 5 x 5)
T5 Current only (medium) 1 June (152)	-	700 l/s, 0.29m/s	40 min (8 x 5)
T6 Wave+Currents (low energy) 5 June (156)	T=0.85s, H=0.07 m **(0.055m)**	400 l/s, 0.17m/s	125 min (5+5+10+15+30+30+30)
T7 Wave+Currents ($\Theta_w \approx \Theta_c$) 7 June (158)	T=1.2s, H=0.14 m **(0.10 m)**	500l/s, 0.21m/s	45 min (9 x 5)
T8 Wave+Currents ($\Theta_w < \Theta_c$) 11 June (162)	T=1.0s, H=0.11 m	580 l/s, 0.24m/s	47 min (2 + 9 x 5)
T9 Wave+Currents ($\Theta_w > \Theta_c$) 13 June (164)	T=1.3s, H=0.16 m	420 l/s, 0.18m/s	45 min (9 x 5)

During the experiment waves were in the non-breaking regime. Visually, wave shape altered as waves passed over the mound (Figure 4), which is to be explored further using the data.

Figure 4 Sideview of waves passing over the mound during testing (May 10) The mound is positioned below the vertical aluminum bar.

The morphological evolution showed a clear diffusion of the mound, while also showing the creation of bedforms (Figure 5). Observed diffusion and bedform type (symmetrical, linguoid) varied substantially between the different forcings tested.
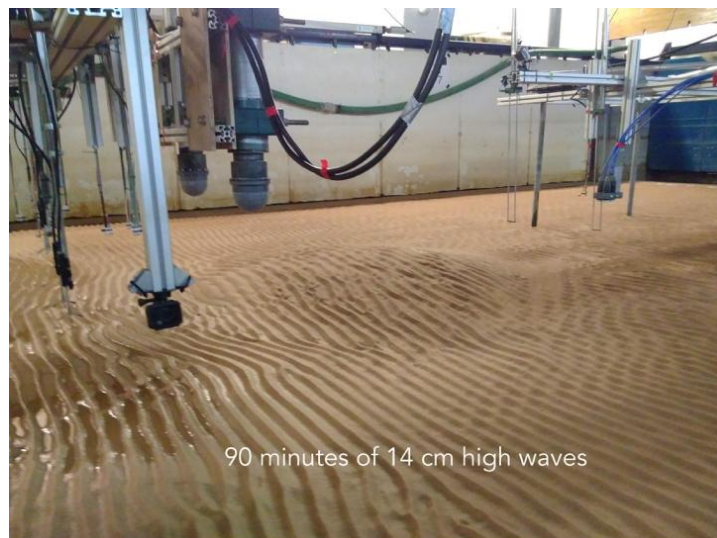

Figure 5 Photo of the bed level after test T2. Paddles of the wavemaker (blue) are visible on the right.

For the analyses, the morphological evolution of the bed was recorded using terrestrial laser scanning, ripple scan sonar and altimeters (Schipper et al., 2019). The combination of the three techniques enables a detailed view of the bed changes during the test with high temporal and spatial resolution. Hydrodynamics are mapped using ADVs, Vectrino's and wave gauges.

First results of the experiment analyses will be discussed at the conference and in future publications.

3.   CONCLUDING REMARKS

MODEX (MOrphological Diffusivity EXperiment) was conducted in May/June 2018 with the aim to establish a link between the imposed hydrodynamic forcing and observed morphodynamic

response of a sandy mound in shallow water. The experiment successfully brought together a group of (European) scientists from different institutes and background. It included a large group of young academics on site which were provided a unique opportunity to learn.

The data is made available on a repository to facilitate a wide use and interested parties are encouraged to contact the MODEX scientist for further details.

In the coming decades, many coastal locations will have to evaluate their coastal protection strategy in light of the projected climate change. With the data of the experiment and the analyses, we aim to support this decision making by providing a better understanding of the effect of anthropogenic interventions in the coastal zone.

ACKNOWLEDGEMENT

REFERENCES

Arriaga, J., Rutten, J., Ribas, F., Falques, A., Ruessink, G., (2017). Modeling the long-term diffusion and feeding capability of a mega-nourishment. *Coastal Engineering* 121, 1–13.

Huisman, B., Walstra, D. J., Radermacher, M., De Schipper, M., & Ruessink, G. (2019). Observations and modelling of shoreface nourishment behaviour. *Journal of Marine Science and Engineering,* 7(3), 59.

Rutten, J., B. G. Ruessink, and T. D. Price. (2018). Observations on sandbar behaviour along a man-made curved coast. *Earth Surface Processes and Landforms* 43.1 134-149.

de Schipper, M.A., Hopkins, J., Wengrove, M, Saxoni, I, Kleinhans, M. Senechal, N, Castelle, B, Ribas, F, Ruessink, B.G., Murphy, B, McLelland, S. (2019). Modex: Laboratory Experiment Exploring Sediment Spreading Of A Mound Under Waves And Currents P*roceedings of the Coastal Sediments Conference 2019.*

de Schipper M.A., de Vries, S., Ruessink G., de Zeeuw, R.C., Rutten J., Gelder- Maas, C. and Stive, M.J.F. (2016). Initial spreading of a mega feeder nourishment: observations of the Sand Engine pilot project. *Coastal Engineering*

Stive, M.J., de Schipper, M.A., Luijendijk, A.P., Aarninkhof, S.G., van Gelder- Maas, C., van Thiel de Vries, J.S., de Vries, S., Henriquez, M., Marx, S. and Ranasinghe, R., (2013). A new alternative to saving our beaches from sea-level rise: The sand engine. *Journal of Coastal Research,* 29(5), pp.1001-1008.

de Vriend, H. N. (1987). 2DH mathematical modelling of morphological evolutions in shallow water. *Coastal Engineering*, 11(1), 1-27.

VIII – NTNU – Sletvik Field Station

The Sletvik Field Station is set around the semi-enclosed lagoon of Hopavågen, situated west of Trondheim (100 km drive) and about 20 km west of the outlet of the Trondheimsfjord. The Sletvik field station is located 300 m from the lagoon and has a laboratory space of 250 m2, kitchen facilities, nearby catering possibilities and dormitories for about 50 persons. It has also a pier and a small laboratory at the shore of Hopavågen.

The lagoon is sheltered from wind and waves and is a mesocosm by itself. It has an area of 370.000 m2 and an average depth of 18 m (max 32 m). Due to tidal forcing, about 14% of its water is exchanged per day. The field experiments within the landlocked bay can be conducted from a small boat. Hopavågen is ideal to study interrelations between physical, chemical and biological processes, ecohydraulics and transport processes.

Available hydraulic instrumentation: acoustic Doppler velocimeters, ADCP, current meters and water level loggers

Water quality parameters can be determined in collaboration with the Department of Hydraulic and Environmental Engineering

STRATIFICATION-INDUCED MODIFICATION OF FOOD WEB DYNAMICS IN A MARINE PELAGIC ENVIRONMENT

Herwig Stibor (1), Maria Stockenreiter (1), Luna Benítez-Requena (1), Sabine Schultes (1), Claudia Alexandra Forster (1)
(1) Department of Biology II, Aquatic Ecology, Ludwig-Maximilians-Universität München, LMU Großhaderner Straße 2, 82152 Planegg-Martinsried, Germany,
E-mail: stibor@zi.biologie.uni-muenchen.de

Patrick Fink (2, 3), Maja Ilić (2),
(2) University of Cologne, Cologne Biocenter, Workgroup Aquatic Chemical Ecology, Zuelpicher Strasse 47b, 50674 Cologne, Germany
(3) Helmholtz Centre for Environmental Research, Department River Ecology and Department Aquatic Ecosystem Analysis, Brueckstrasse 3a, 39114 Magdeburg, Germany,
E-mail: patrick.fink@uni-koeln.de

Olav Vadstein (4),
(4) Department of Biotechnology and Food Science, NTNU, N-7491 Trondheim, Norway,
Email: olav.vadstein@ntnu.no

Nicolas Djeghri (5), Rudolph Corvaisier (5), Anne Donval (5) Philippe Pondaven (5)
(5) Université de Brest, UBO, Institut Universitaire Européen de la Mer, IUEM, Laboratoire des Sciences de l'Environnement Marin, LEMAR-UMR 6539, Technopôle Brest Iroise, rue Dumont d'Urville, 29280 Plouzané, France,
Email: philippe.pondaven@univ-brest.fr

ABSTRACT

Global warming is expected to increase water column stratification, thereby affecting the dynamics of plankton communities. In this context, experimental manipulations allowing mechanistic insights into the general relationship between the depth of the mixed layer and ecological dynamics are scarce and mainly limited to freshwater systems. Here, a mesocosm experiment was carried out in the Bay of Hopavågen (63°36' N, 9°33' E, Norway) on Aug-Sept 2017. Stratification was experimentally manipulated in 18 enclosures, and the responses of different trophic groups of marine plankton were determined. Preliminary analysis suggests that the total phytoplankton biomass did not change significantly between treatments during the experiment. However, disparities within and between trophic groups were recorded, and changes in the depth of the mixed layer resulted in a reorganization of food web structure and dynamics. Reasons for the observed effects are still under study; they may combine direct effects of mixing, and light exposure, and associated indirect effects through biotic interactions.

INTRODUCTION

Stratification is one of the most important physical characteristics of pelagic water columns with large effects on the suspended biota (Sommer et al. 1986; Peeters et al. 2007; Berger et al. 2010). Stratification depth will influence essential resource levels such as the daily amount of light within the upper mixed layer to which phytoplankton is exposed, or the amount of dissolved nutrients, thereby having large influence on phytoplankton growth (Diehl et al., 2002; Winder and Hunter 2008; Winder and Sommer 2012). However, strength of mixing also affects sedimentation of suspended phytoplankton – a significant aspect of phytoplankton mortality (Ptacnik et al., 2003). Besides the growth of phytoplankton, its composition might be also strongly affected by mixing depth. Large, heavy algae such as diatoms may be favored by deep mixing whereas motile phytoflagellates may benefit from lower mixing depths (Winder and Hunter 2008). Additionally, phytoplankton thin layers frequently occur at the physical discontinuities associated with stratification and create hot spots of biological activity (Durham & Stocker 2012). It is therefore not surprising that two iconic theoretical concepts of biological oceanography are linked to stratification

and mixing depth: Sverdrup's principle of critical depth is dealing with effects of mixing depth for phytoplankton development and Margalef's Mandala is describing the interaction of mixing and nutrients on phytoplankton community composition. Sverdrup's principle states that the vertical mixing of the surface layer must stay above a critical depth beyond which phytoplankton has negative growth because of light limitation (Sverdrup 1953). The concept has been re-visited in recent years taking into consideration the role of turbulence and of temporal decoupling from grazing pressure by grazers (review by Fisher et al. 2015). Margalef's Mandala is a guide to the description of phytoplankton assemblages based on combining the interactive effects of habitat mixing and nutrient conditions and basically describes the succession between major algal groups, diatoms and dinoflagellates, in water columns with different mixing depth (Margalef 1978; Margalef et al.,1979).

The above mentioned concepts clearly point towards the relevance of mixing depth for biological oceanography. Hence, as shifts in mixing depth affect phytoplankton, which is the base of pelagic food webs based on photosynthesis, it is realistic to assume that these effects will have further influence within food webs. Consequences for herbivorous zooplankton and probably even higher trophic levels such as fish or jellyfish can be expected. Beside potential positive effects of phytoflagellates on jellyfish growth via food web effects (Parsons and Lalli 2002; Colin et al. 2005) increasing stratification may additionally favor jellyfish by direct effects such as warmer temperatures in shallow mixed water layers (Richardson et al. 2009).

However, stratification and mixing depth of water columns are very sensitive to climate change. Increasing sea surface temperatures will decrease mixing depth and indirect consequences for biological and ecological dynamics might be larger than physiological effects of just temperature increases alone. Hence, most of the concepts dealing with mixing depth and its effects on plankton rely on theoretical considerations and purely observational data. For example, increasing stratification of water columns is discussed as one major factor that can contribute to further extending jellyfish blooms (Purcell et al. 2001; Richardson et al. 2009); however, this concept was until now never tested experimentally.

Experimental manipulations allowing more mechanistic insights into the general relationship between water column stratification and ecological dynamics are scarce and mainly limited to freshwater systems (Berger et al. 2010). Experiments are needed to contribute to a better insight into how global change might affect marine plankton communities via changes in the physical environment. To further increase such knowledge is a necessity to improve models and predictions how global change will affect European coastal waters and to foresee potential remediation measures to be taken in the future.

Here, the effects of increasing water column stratification on plankton dynamics were investigated experimentally by performing mesocosm experiments in the Bay of Hopavågen (Norway). Mixing depth of the water column was manipulated in enclosures, and consequences of the manipulations for the plankton community dynamics were followed. Three research questions related to food web dynamics and stratification were tested:

  (1) Decreasing mixing depth of a water column will favor phytoflagellates over diatoms and thereby change phytoplankton communities.
  (2) Decreasing mixing depth therefore decouple prevalent phytoplankton – zooplankton dynamics by changing food quantity and quality (biochemical composition) for different zooplankton groups.
  (3) Decreasing mixing depth will favor jellyfish growth.

In this report, we present the experimental design and some preliminary results related to the observed food web dynamics induced by our experimental manipulations.

METHODS

The mesocosm experiment was carried out during August-September 2017 in the semi-enclosed bay of Hopavågen (63°36' N, 9°33' E), located west of Trondheim (Norway). Mixing depth was manipulated based on previous experiments performed in lakes (Diehl et al. 2015). A total of 18 enclosures were moored with a three times replicated gradient of depth of 2, 4, 6, 8, 10 and 12 m. Enclosures consisted of transparent polyethylene tubes, with a diameter of 0.9 m. They were

filled on the day before the start of the experiment (Day 0) by lifting them from the depth to the surface. After filling, enclosures were daily mixed (every 12 hours; 7:00 AM and 7:00 PM) with short pulses (5 min) of compressed air; thereby ensuring a well mixed water column during the experiment.

A full sampling program was performed in all enclosures on 26/08, 31/08, 07/09 and 10/09 (end of experiment). For this purpose, the entire water column was sampled (around 7:00 AM) with an opaque integrated tube sampler (tube Ø 40 mm x 200 cm, ®KC Denmark). In addition, a lighter daily sampling program was conducted to check for short-term changes in the physical environment and plankton dynamics. This daily program included measurements of temperature, salinity, and phytoplankton biomass; temperature and salinity were determined using a CTD to verify the mixing depth and degree of stratification of the water column (inside the enclosures and inside the bay, next to the experimental raft); phytoplankton biomass was estimated from a measurement of chlorophyll *a* fluorescence using a fluorometer (see below).

Nutrient concentrations - Nutrient samples were collected in all 18 mesocosms on a weekly basis. Samples were pre-filtered (®Millex, Ø 0.2 μm) before analysis. Concentrations of soluble reactive phosphorus (SRP, PO_4^{3-}) and orthosilicic acid ($Si(OH)_4$) were measured using standard methods (Strickland and Parsons 1972). Each separate assay run was calibrated along a standard curve (range 0-1 μM-P, and 0-5 μM-Si). Standard solutions of SRP and orthosilicic acid were prepared from anhydrous potassium dihydrogen phosphate (KH_2PO_4) and sodium fluosilicate (Na_2SiF_6), respectively, diluted in deionized-water. To determine particulate organic carbon (POC), nitrogen (PON) and phosphorus (POP), 250 mL of seawater were filtered onto precombusted and acid-washed glass-fiber filters (GF/F ®Whatman). POC and PON, as well as their isotopic signatures $^{15}\delta N$ and $^{13}\delta C$, were then measured with an elemental analyzer (CE Instruments, Milan, Italy), coupled with a mass spectrometer. POP was measured after sulfuric acid digestion followed by molybdene-blue reaction (Wetzel & Likens, 1991).

Phytoplankton & microbial community composition - Phytoplankton samples were fixed with a Lugol's iodine solution, and analyzed on an inverted microscope following Utermöhl's (1958) method. Phytoplankton were identified to the species or genus level whenever possible, or merged into generic groups such as "unidentified nanophytoplankton". In addition, the composition of the phytoplankton community was characterized by the analysis of photosynthetic pigment concentrations. For this purpose, 750 mL of seawater were collected from each enclosure and filtered onto precombusted and acid-washed glass-fiber filters (GF/F ®Whatman). Pigments were extracted at -20°C in 3 mL of ethanol (95%), filtrated, and determined via high performance liquid chromatography (HPLC; ®Agilent 1200), according to Van Heukelem and Thomas (2001). External pigment standards (®DHI, Denmark) were used to calibrate the system. The software CHEMTAX (Mackey *et al*., 1996) was used to estimate the relative abundances of various algal classes from pigments concentrations ratios. Flow cytometry provided additional information on the composition of microbial communities. Samples were fixed with glutaraldehyde (0.5% final conc.) prior to analysis. Abundances of bacteria, *Synechococcus spp.*, picoeukaryotes, nanoeukaryotes, and heterotrophic nanoflagellates (HNF) were determined with a flow cytometer, according to Vadstein (2000). A multispectral Algal-Lab Analyser (®*PSI Photons Systems*) was also used for a daily survey of phytoplankton community composition. This fluorometry system is able to differentiate between the main "optical algal groups" (diatoms, cryptophytes, green algae and cyanobacteria). Aquapen fluorometers (®*PSI Photons Systems, Brno*) were used for analyses of the phytoplankton biomass (from a measure of the 'Fix Area' value: i.e. the area under the induction curve of fluorescence during a saturating light flash), and photosynthetic efficiencies of the algal communities. The net growth rates (μ; d^{-1}) of phytoplankton and other microorganism taxa were calculated as follows:

$$\mu = \ln(N_{t2}/N_{t1})/\Delta t \qquad\qquad (Eq.1)$$

where N_i is the abundance of a taxon "i", and Δt is the time step (t_2-t_1).

Zooplankton community and food web interactions - The initial composition of the zooplankton community in Hopavågen Bay was determined on day 0 using a zooplankton net (Ø 200 µm) lifted

vertically from the depth to the surface, just beside the mesocosm raft. At the end of the experiment, the zooplankton community was sampled in all enclosures using the same procedure. Crustacean zooplankton samples were stored in a solution of formaldehyde (4%) before analysis. Gelatinous zooplankton (appendicularia, ctenophores, hydromedusae) were sampled using an identical net, but with a plastic bag collector to preserve the integrity of the organisms; the different taxa were then identified and counted immediately after sampling, using a microscope. Finally, lipid contents were determined by extraction of polyunsaturated fatty acids (PUFAs) with dichloromethane:methanol (2:1) and transesterified to FAME before GC-FID analysis (Fink, 2013).

Statistical Analyses- The above measurements were used to link stratification manipulations to responses in nutrient levels, light and the composition and dynamics of the different plankton communities within the mesocosms. In the present manuscript, only first preliminary analyses are presented.

PRELIMINARY RESULTS

Nutrient concentrations- Orthosilicic acid concentrations ranged from 0.12 μM-Si to 2.25 μM-Si. SRP concentrations ranged from 0.01 μM-P to 0.06 μM-P, i.e. ≤ to the precision of the method used here (Strickland and Parsons, 1972). A decrease of nutrient concentrations was recorded in all enclosures at the beginning of the experiment (from 26/08 to 31/08; Figure 1 a-b). Additionally, preliminary results suggest that changes in mixing depth had no clear influence on the dynamics of dissolved inorganic nutrient concentrations (not shown).
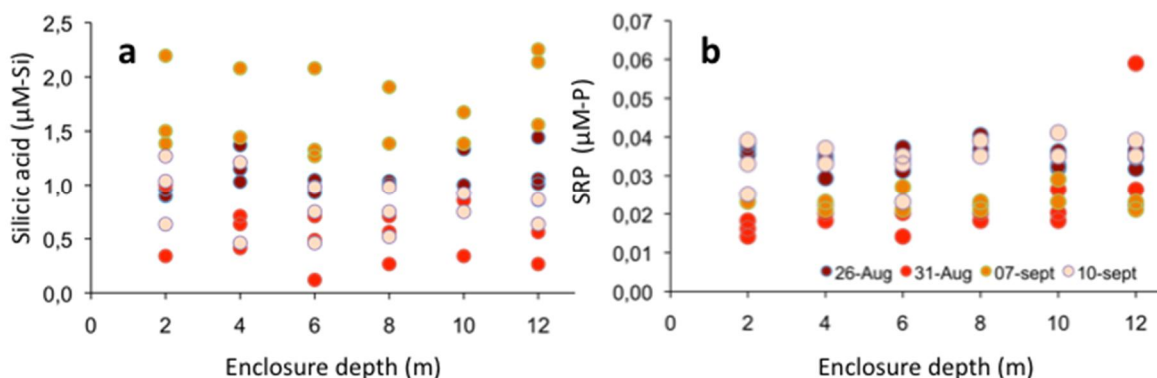

Figure 1: Concentrations of **(a)** orthosilicic acid (μM-Si) **and (b)** orthophospate (SRP, μM-P) on 26/08/17, 31/08/17, 07/09/17 and 10/09/17, in 18 enclosures moored with a three times replicated gradient of mixing depth of 2, 4, 6, 8, 10 and 12 m.

Phytoplankton community composition- Phytoplankton biomass, shown as chlorophyll *a*, ranged from 1.5 to 3.5 µg L^{-1}. Transient dynamics were recorded in all enclosures with a decrease at the beginning of the experiment (from 26/08 to 31/08; Figure 2 a), followed by a net increase from 26/08 to 10/09. At the end of the experiment (day 16), the phytoplankton biomass was close to that observed at the beginning (day 0; figure 2a).
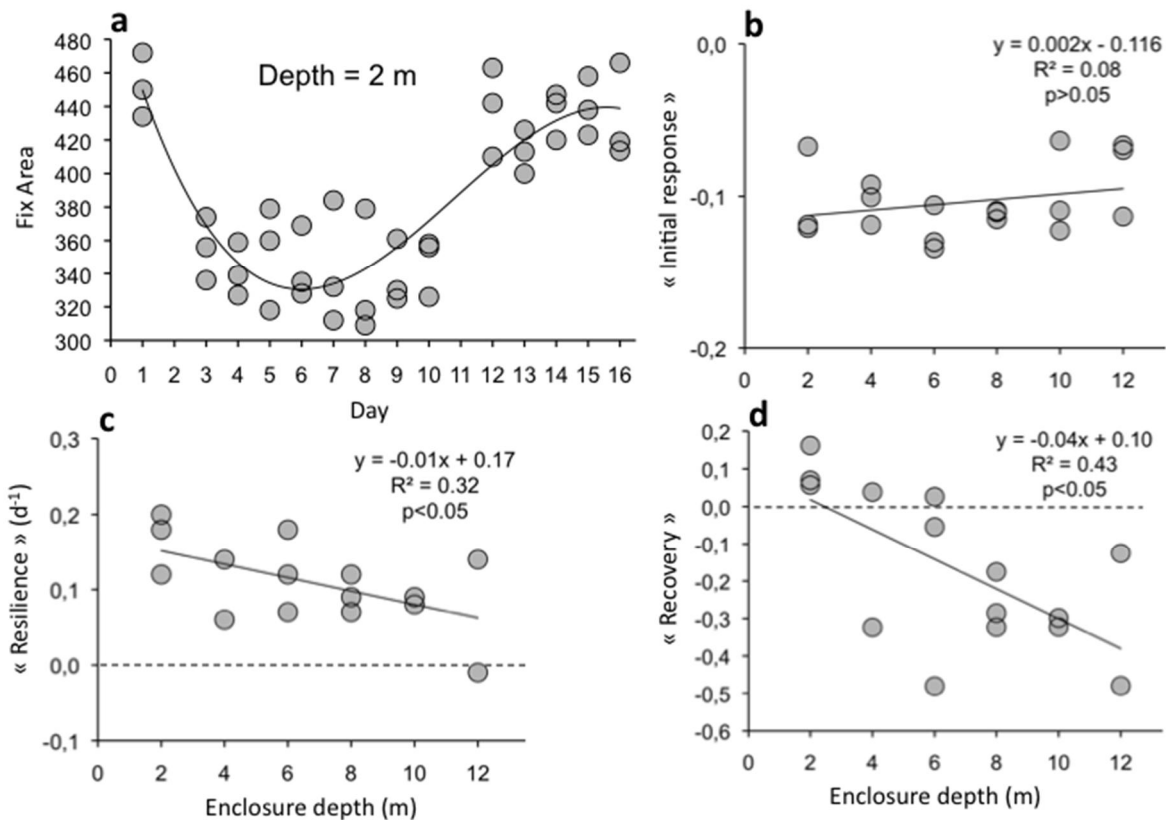
Figure 2: (a) Example of the evolution over time of the "Fix Area" (proxy of the chlorophyll *a* content) in three enclosures (depth = 2 m); (b) Initial response of the phytoplankton community, calculated using the formula $\ln(N_{t5}/N_{t1})$, where N is the biomass of chlorophyll *a* at time t_1 (26/08) or t_5 (31/08); (c) Index of "resilience": phytoplankton Net Growth Rate (NGR, d^{-1}) from t_5=31/08 to t_{16}=10/09; (d) Index of "recovery", calculated as $\ln(N_{t16}/N_{t1})$; for details on (b), (c) and (d) see Hillebrand et al. (2018).

The fact that the total phytoplankton biomass did not change substantially during the experiment is probably due to the low concentrations of dissolved nutrients at the beginning of the experiment, regardless of the depth of the enclosure. However, this apparent lack of response masks disparities within and between trophic groups.

We first explored how the response of phytoplankton communities to changes in mixing depth could be described using variables such as "resistance", "resilience" or "recovery" (see Hillebrand et al, 2018). Using these concepts in the case of the Hopavågen experiment, it was found that resilience and recovery of the phytoplankton community were significantly lower in deeper enclosures (Fig. 2 c-d).

In addition, a more detailed analysis of the structure of phytoplankton communities suggests that, although the total biomass varied little between the beginning and end of the experiment (Figure 2), a proliferation of prymnesophytes (probably calcifying coccolithophores) occurred in shallow mesocosms (Figure 3).
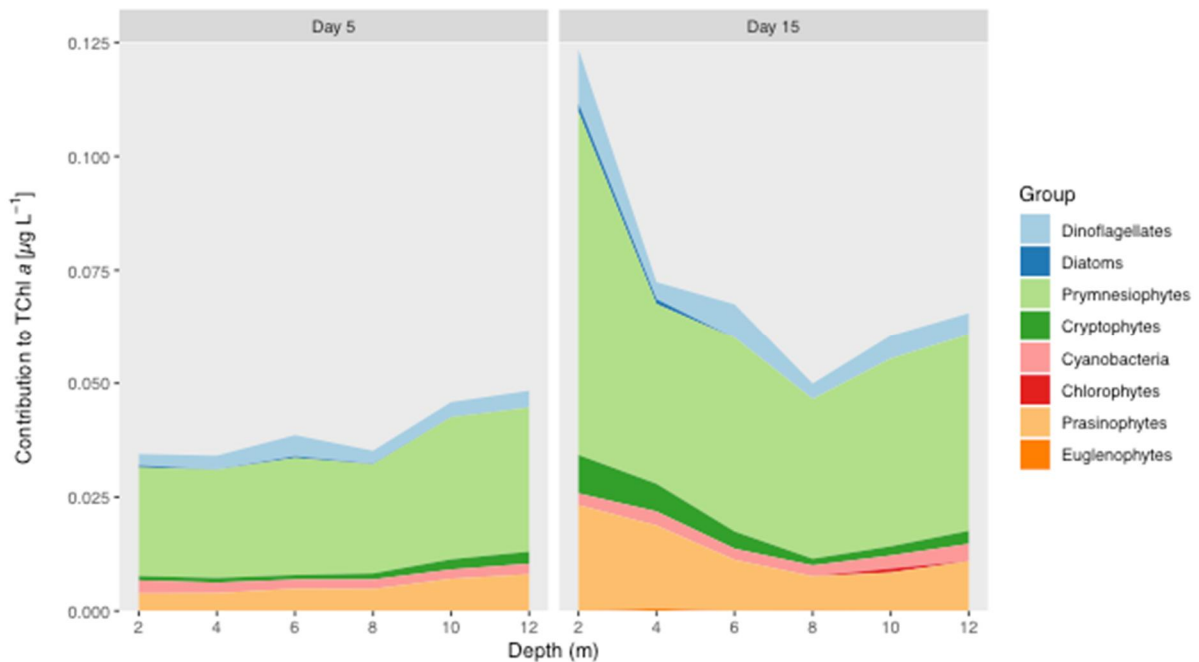
Figure 3: Evolution over time (day 5 and day 15) of the abundance of different algal groups (contribution to total Chlorophyll *a* estimated from pigments analysis and CHEMTAX; see text), along a gradient of mixing depth of 2, 4, 6, 8, 10 and 12 m.

Conversely, analysis of flow cytometry data revealed that the abundance of small prokaryotes belonging to the genus *Synechococcus spp.* was higher in deeper enclosures (p<0.05; Figure 4a).
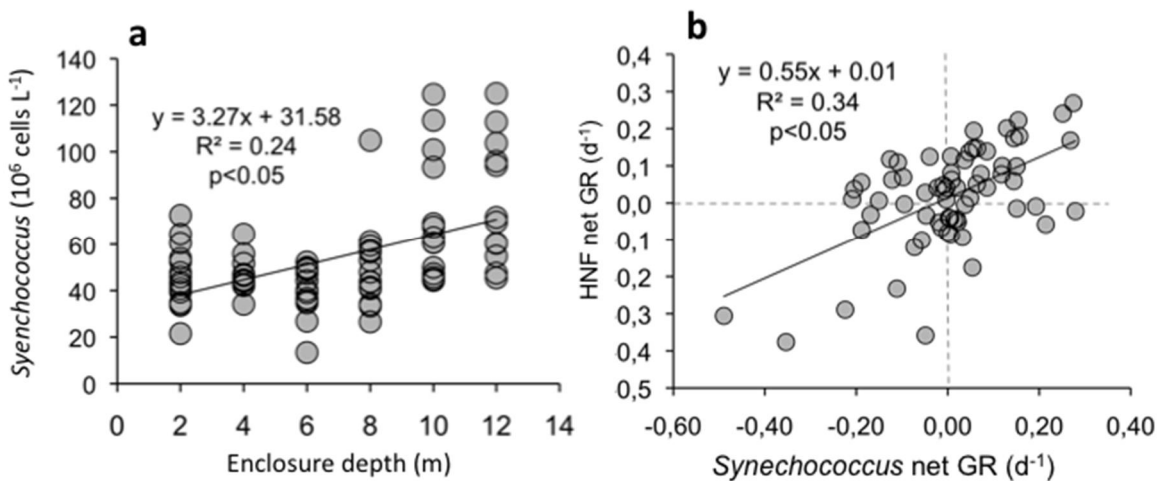

Figure 4: Preliminary results from flow cytometry; **(a)** Abundance of *Synechococcus* spp along a gradient of mixing depth of 2, 4, 6, 8, 10 and 12 m; **(b)** net Growth Rate (GR, d^{-1}) of heterotrophic nanoflagellates (HNF) *versus* net GR of *Synechococcus* in all 18 enclosures.

A preliminary conclusion that can be drawn from Figures 3 and 4a is that, all other things being equal, changes in the depth of the mixing layer may have resulted in a reorganization of the structure of the phytoplankton community. Ongoing analyses of stored phytoplankton samples will verify this pattern.

Heterotrophic nanoflagellates (HNF), micro- and mesozooplankton- A stratification-induced change in the dynamics of the zooplankton community was also recorded during the experiment (Figure 5).
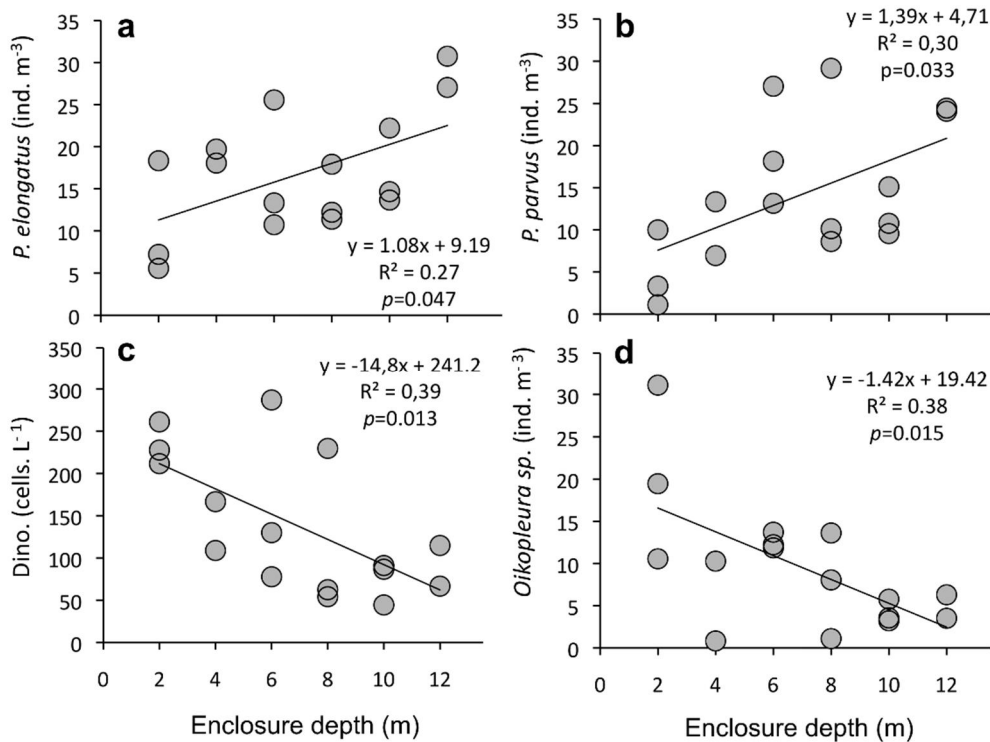
Figure 5: Abundances of **(a)** *Pseudocalanus elongatus,* **(b)** *Paracalanus parvus,,* **(c)** *large dinoflagellates*, and **(d)** *Oikopleura sp* along a gradient of mixing depth.

For example, the net growth rate of HNF was significantly related to that of *Synechococcus spp.* (Figure 4b), suggesting direct or indirect trophic relationships between these organisms (e. g. Sundt-Hansen et al., 2006). With respect to micro- and mesozooplankton abundance, changes in the depth of the mixing depth had also contrasting impacts across taxa (Figure 5a-d). On the one hand, the abundance of some species of small sized calanoid copepods, such as *Pseudocalanus elongatus* and *Paracalanus parvus*, was significantly lower in shallow mesocosms compared to deep mesocosms at the end of the experiment (Figure 5a-b). On the other hand, the abundance of large dinoflagellates and *Oikopleura sp.* was higher in shallow mesocosms than in deep mesocosms at the end of the experiment (Figure 5c-d). The higher abundance of *Synechococcus* in deeper mesocosms (Figure 4a) could then be partly explained by a decrease in mortality due to a lower abundance of their potential consumers, heterotrophic dinoflagellates or *Oikopleura* sp. (e. g. Sundt-Hansen et al., 2006). This is at least suggested in Figure 6, where *Synechococus* abundance is negatively correlated with that of large dinoflagellates and Oikopleura sp. at the end of the experiment.

The causal links that may explain the observed stratification induced change in the dynamics of the zooplankton community probably combine bottom-up and top-down effects (Diehl et al., 2002; Stibor et al., 2004; Stibor et al., 2006; Sundt-Hansen et al., 2006; Diehl et al., 2015). For instance, differences among zooplankton taxa regarding starvation tolerance, metabolic efficiency to use the available food, or feeding mode may play a role. Further analyses, such as zooplankton isotopic signatures or changes in fatty acids contents, may help to disentangle the relative importance of these effects.
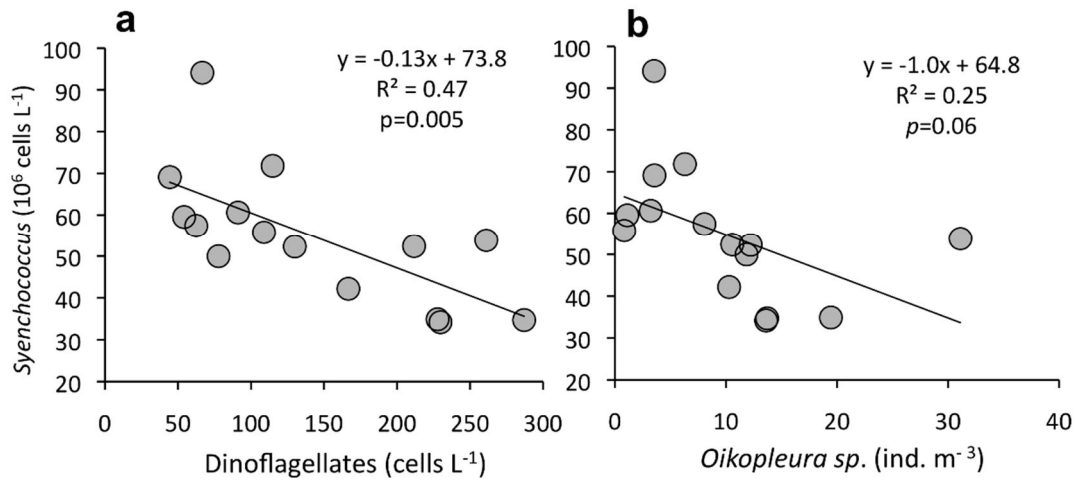
Figure 6: Abundances of **(a)** *Synechococcus versus* Dinoflagellates and **(b)** *Synechococcus versus Oikopleura sp.* at the end of the experiment, along a gradient of mixing depth of 2, 4, 6, 8, 10 and 12 m.

PRELIMINARY CONCLUSIONS AND PERSPECTIVES

In this study, water column stratification was experimentally manipulated in a mesocosm experiment carried out in the Bay of Hopavågen (63°36' N, 9°33' E, Norway). A total of 18 enclosures were moored, with a three times replicated gradient of mixing depth of 2, 4, 6, 8, 10 and 12 m. Responses from different trophic groups of marine plankton were determined over a 16-day period. Preliminary results suggest that the total phytoplankton biomass did not change significantly, possibly due to the low dissolved nutrient concentrations at this time of year (August-September 2017). However, disparities within and between trophic groups were recorded, and it was observed that changes in the depth of the mixed layer lead to a reorganization of the structure and dynamics of the food web. The mechanisms underlying these reactions are still under study and ongoing analyses (such as phytoplankton taxonomy) should provide further insights on how changes in the stratification of the upper surface layers can influence food web dynamics.

ACKNOWLEDGEMENTS

REFERENCES

Berger, S. A., Diehl, S., Stibor, H., Trommer, G., and Ruhenstroth, M. (2010). Water temperature and stratification depth independently shift cardinal events during plankton spring succession. *Global Change Biology*, *16*, 1954-1965.

Colin, S. P., Costello, J. H., Graham, W. M., and Higgins, J. (2005). Omnivory by the small cosmopolitan hydromedusa *Aglaura hemistoma*. *Limnology and Oceanography*, *50*, 1264-1268.

Diehl, S., Berger, S., Ptacnik, R., and Wild, A. (2002). Phytoplankton, light, and nutrients in a gradient of mixing depths: field experiments. *Ecology*, *83*, 399-411.

Diehl, S., S.A. Berger, Q. Soisson, D. Giling, and Stibor, H. (2015). An experimental demonstration of the critical depth principle. *ICES Journal of Marine Science,* 72, 2051–2060.

Durham, W.M., and Stocker R. (2012). Thin Phytoplankton Layers: Characteristics, Mechanisms, and Consequences. *Annual Review of Marine Science*, 4, 177-207.

Fink, P. (2013). Invasion of quality: high amounts of essential fatty acids in the invasive Ponto-Caspian mysid *Limnomysis benedeni. Journal of plankton research*, 35, 907-913.

Hillebrand, H., Langenheder, S., Lebret, K., Lindström, E., Östman, Ö., Striebel, M. (2018). Decomposing multiple dimensions of stability in global change experiments. Ecology letters, 21, 21-30.

Margalef, R. (1978). Life-forms of phytoplankton as survival alternatives in an unstable environment. *Oceanologica Acta, 1*, 493-509

Margalef, R., Estrada, M., and Blasco, D. (1979). Fuctional morphology of organisms involved in red tides, as adapted to decaving turbulence. In Tylor, D. and Seliger, H (eds). Toxic dinoflagellate blooms. Elsevier New York, 89-94.

Parsons, T.R., and Lalli, C.M. (2002). Jellyfish population expolsions: revisting a hypothesis of possible causes. *La mer, 40,* 111-121.

Peeters, F., Straile, D., Lorke, A., and Livingstone, D. M. (2007). Earlier onset of the spring phytoplankton bloom in lakes of the temperate zone in a warmer climate. *Global Change Biology*, *13*, 1898-1909.

Ptacnik, R., Diehl, S., and Berger, S. (2003). Performance of sinking and nonsinking phytoplankton taxa in a gradient of mixing depths. *Limnology and Oceanography*, *48*, 1903-1912.

Purcell, J. E., and Arai, M. N. (2001). Interactions of pelagic cnidarians and ctenophores with fish: a review. *Hydrobiologia*, *451*, 27-44.

Richardson, A. J., Bakun, A., Hays, G. C., and Gibbons, M. J. (2009). The jellyfish joyride: causes, consequences and management responses to a more gelatinous future. *Trends in Ecology Evolution*, *24*, 312-322.

Sommer, U*.,* Gliwicz, Z.M*.,* Lampert, W.*,* and Duncan, A. (*1986). The PEG-Model of seasonal succession of planktonic events in fresh waters. *Archiv für Hydrobiologie, 106,* 433–471.

Stibor, H., Vadstein, O., Diehl, S., Gelzleichter, A., Hansen, T., Katechakis, A., Lippert, B., Løseth, K., Peters, C., Roederer, W., Sandow, M., Sundt-Hansen, and L. Olsen, Y. (2004). Copepods act as a switch between alternative trophic cascades in marine pelagic food webs. *Ecology Letters,* 7, 321-328.

Stibor, H., Gelzleichter, A., Hantzsche, F., Sommer, U., Striebel, M., Vadstein, O., and Olsen, Y. (2006). Combining dialysis and dilution techniques to estimate gross growth rate of phytoplankton and grazing by micro-and mesozooplankton *in situ. Archiv für Hydrobiologie,* 167, 403-419.

Strickland, J. D. H. and Parsons, T. R. (1972). A practical handbook of seawater analysis. Second Edition, Bulletin 167. Fisheries Research Board of Canada, Ottawa.

Sundt-Hansen, L. E., Olsen, Y., Stibor, H., Heldal, M., Vadstein, O. (2006). Trophic cascades mediated by copepods, not nutrient supply rate, determine the development of picocyanobacteria. *Aquatic microbial ecology*, 45, 207-218.

Sverdrup, H.U. (1953). On conditions for the vernal blooming of phytoplankton*. Journal du Conseil International pour l'Exploration de la Mer, 18,* 287-295.

Vadstein, O. (2000). Heterotrophic, planktonic bacteria and cycling of phosphorus. In Advances in microbial ecology (pp. 115-167). Springer, Boston, MA.

Wetzel, R. G., and Likens, G. E. (1991). Limnological analyses, 2nd ed. Springer Verlag.

Winder, M., and Hunter, D. A. (2008). Temporal organization of phytoplankton communities linked to physical forcing. *Oecologia*, *156*, 179-192.

Winder, M., and Sommer, U. (2012). Phytoplankton response to a changing climate. In *Phytoplankton responses to human impacts at different scales* (pp. 5-16). Springer Netherlands.

IX – UPC – CIEM

The Canal d'Investigació i Experimentació Marítima (CIEM), a large-scale wave flume at the Laboratori d'Enginyeria Marítima (LIM) of the Universitat Politècnica de Catalunya (UPC), is an international research facility for controlled hydraulic experiments in coastal, harbour and oceanographic engineering, and in other fields such as aquaculture and the study of wave energy.

The CIEM wave flume, which is 100 m long, 3 m wide and up to 7 m deep inside the current generator's wells, is a facility of excellence for scaled tests and studies under close-to-real conditions. Typical working scales are between 1:2 and 1:20, although it is also possible to work at other scales. The larger scale ratios enable the scale effects inherent to all scaled experiments to be reduced.

Waves and currents are generated by a wedge-type wave generator, which is particularly suitable for generating waves in intermediate water conditions, and a bidirectional pumping system whose capacity is 2,000 l/s. The system is hydraulically actuated and PC-controlled, and is capable of reproducing waves with heights up to 1.6 m.

The generation of waves can be used to study the influence of sea swell on beach profiles and coastal defence structures. Tests can be carried out to assess projects and to identify innovative solutions to a given problem. The generation of currents allows their interaction with waves and sediments to be studied, and enables experiments to be carried out with submersible vehicles and energy devices

HYDRODYNAMICS AND TURBULENCE DYNAMICS UNDER LARGE-SCALE BICHROMATIC BREAKING WAVES

Dominic van der A (1), Joep van der Zanden (2), Bjarke Eltard Larsen (3),
Pietro Scandura (4) and Ming Li (5)

(1) University of Aberdeen, United Kingdom, E-mail: d.a.vandera@abdn.ac.uk
(2) MARIN, the Netherlands, E-mail: J.v.d.Zanden@marin.nl
(3) DTU, Denmark, E-mail: bjelt@mek.dtu.dk
(4) University of Catania, Italy, E-mail: pietro.scandura@unict.it
(5) University of Liverpool, United Kingdom, E-mail: M.Li@liverpool.ac.uk

Experiments were conducted in a large-scale wave flume involving a bichromatic wave group breaking over a fixed barred beach profile. Velocity profiles were measured using optical and acoustics instrumentation at 22 cross-shore locations ranging from the shoaling zone to the inner surf zone. The measurements show that turbulence in the shoaling region is primarily bed-generated and decays almost fully within one wave cycle, in contrast, in the surf zone the breaking-generated turbulence, decays over multiple wave cycles, leading to a gradual increase and decay of Turbulent Kinetic Energy (TKE) during a wave group cycle. The measurements are compared to a two-phase RANS model based on a new stabilized k-ω turbulence closure. The model accurately predicts the water surface elevation, and outperforms standard non-stabilized model in predicting the undertow profile and TKE levels in the shoaling zone and outer surf zone.

1. INTRODUCTION

Predicting cross-shore sediment transport remains a difficult task since the net sediment transport is affected by various hydrodynamic processes such as undertow, wave skewness and asymmetry, and various forms of boundary layer streaming. In the surf zone additional complexities arise from wave breaking-induced turbulence and the horizontal and vertical flow non-uniformities. In many practical applications for predicting cross-shore sediment transport, empirical/semi-empirical transport formulas are coupled with numerical hydrodynamic models based on the non-linear-shallow water (NLSW) equations. These models have difficulties in predicting cross-shore sediment transport, particularly in the surf zone, which can be largely attributed to a limited quantitative understanding of the near-bed hydrodynamics and sediment transport processes in the surf zone.

This study focusses on plunging breaking waves, which are characterized by the forward curling front of the overturning wave, which transforms into a jet that impinges the water surface and invades the water column. Under plunging breakers, breaking-generated turbulence is transported more quickly down to the bed and mixing rates are higher than for spilling breakers, therefore plunging waves may be expected to have a stronger and more direct effect on surf zone sediment transport than spilling breakers. The spatial and temporal distributions of turbulence under plunging waves have been measured extensively in laboratory wave flumes at small scale, mostly over plane-sloping beds (e.g. Ting & Kirby, 1995; De Serio & Mossa, 2006; Govender et al., 2011), and at large scale over barred bed profiles (e.g. Yoon & Cox, 2010; van der A et al., 2017). These studies revealed strong spatial variation with highest turbulent kinetic energy (TKE) in the breaking region near the water surface, from where turbulence spreads vertically and horizontally due to diffusion, wave-related advection, and current-related advection. The flow non-uniformity, in the presence of wave breaking turbulence, can also further enhance turbulence production in the water column (van der Zanden et al., 2018). The time-dependent transport and production rates lead to a strong temporal variation in TKE, with peaks during the wave crest cycle or the wave trough cycle and may take multiple wave cycles for breaking generated turbulence to decay. The magnitude and direction of these transport processes and the timing of peak TKE depend strongly on cross-shore location, breaking process, and bed geometry.

Computational fluid dynamics (CFD) either through a RANS approach or using a LES approach can potentially handle the breaking processes and boundary layer dynamics naturally. Various studies have applied RANS models to reproduce time-varying TKE, as well as spatial distributions of time-averaged TKE at outer flow levels (e.g. Jacobsen et al., 2014) and inside the wave bottom boundary layer (Fernandez-Mora et al., 2016). Although qualitatively successful, RANS approaches report a consistent overestimation of the modelled TKE in the pre-breaking and the wave breaking regions. A recent study by Larsen and Fuhrman (2018) shows how the overestimation of turbulence pre-breaking comes from an instability problem for RANS models when applied to free-surface waves. An improved model that eliminates the problem was analytically derived and numerically tested, showing significant improvements in modelled turbulence levels as well as in undertow profiles in the pre-breaking and initial breaking regions.

The main aim of the present project was to study the spatial and temporal distribution under a bichromatic wave group, which resemble better natural waves which tend to arrive in groups, and allows use to study the wave-to-wave variation of turbulence better compared to regular waves. Moreover, using a repeatable wave group enables ensemble averaging to determine the turbulence statistics. The secondary aim of the project was to generate a high-resolution dataset to test the new stabilized RANS model's ability to accurately simulate the hydrodynamics and turbulence under a bichromatic wave group breaking over a barred profile.

2.   EXPERIMENTAL SET-UP

The experiment were conducted in the 100 m long, 3 m wide and 5 m deep wave flume at the Polytechnic University of Catalonia in Barcelona. The bed profile was generated in a previous experiment (van der A et al., 2017) and consisted of an offshore slope with a breaker bar and trough (Figure 1a). The bed profile was fixed by replacing the top 0.2m layer of sand with a layer of concrete. To increase the bed roughness and ensure that the wave bottom boundary layer was in the rough turbulent regime similar to natural beaches, a single layer of gravel with $d_{50} = 9.0$mm was glued to the concrete bed surface. The experimental conditions involved two wave conditions: a bichromatic condition, with short wave frequency components $f_1 = 0.25$ Hz and $f_2 = 0.22$ Hz, resulting in a wave group with group period $T_{gr} = 31.5$ s that consisted of 7.5 short waves with mean period $T_m = 4.2$ s and maximum wave height at the paddle of $H = 0.58$m, and a regular wave with period $T = 6$s and $H = 0.55$m. In this paper we focus on the bichromatic wave condition only, results of the regular wave experiment are presented in Scandura et al. (2018).
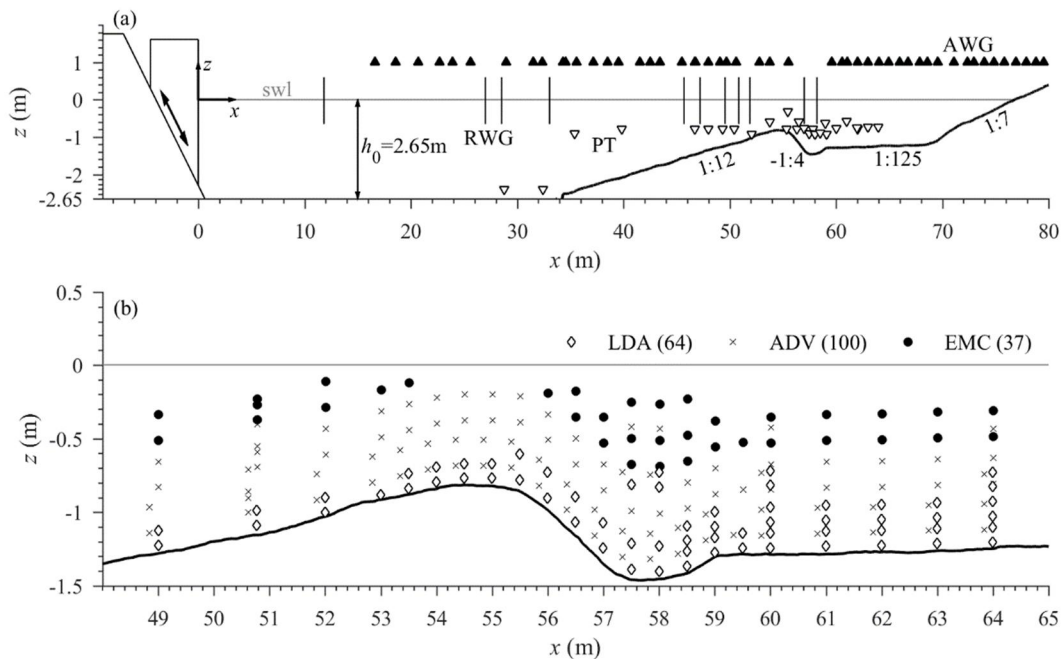
Figure 1. Experimental set-up (a) beach profile including locations of the water surface measurements (RWG = resistive wave gauges; AWG = acoustics wave gauges; PT = pressure transducers); (b) locations of the velocity measurements (LDA = laser Doppler anemometry; ADV = acoustic Doppler Velocimeter; EMC = electromagnetic current meter)

The water surface elevation was measured at a sampling frequency f_s = 40 Hz, with resistive wave gauges (RWGs) at 12 cross-shore locations and with acoustic wave gauges (AWGs) at 52 locations (Figure 1a). In addition, pressure transducer (PT) measurements of the dynamic pressure at 28 cross-shore locations were used to retrieve the water surface level by applying the non-linear weakly dispersive approach by Bonneton et al. (2018). The PTs were primarily deployed in the breaking region, where the RWGs and AWGs suffer from spurious measurements due to bubbles and splash-up of water.

Velocities were measured using two laser Doppler anemometers (LDAs), two acoustic Doppler velocimeters (ADVs), and two electromagnetic current meters (ECMs), deployed from a measurement frame attached to a carriage on top of the flume (**Error! Reference source not found.**). This "mobile frame" could be repositioned at any elevation (with mm accuracy) and cross-shore location (with cm accuracy). Velocities in cross-shore, transverse and vertical direction are defined *u*, *v* and *w*, respectively. The LDAs were two identical Dantec two-component backscatter systems, consisting of a 14 mm diameter submersible transducer probe with 50 mm focal length. The instantaneous LDA sampling frequency depends on seeding particle density and flow velocity, but was about f_s = 300 Hz on average for the present experiment. The lower ADV ("ADV1" in what follows) was a side-looking Nortek Vectrino, while the upper ADV ("ADV2" in what follows) was a downward-looking Nortek Vectrino+. The two ADVs measured the three-component velocity at f_s = 100 Hz. The two disc-shaped ECMs, custom-built by Deltares, measured the *u* and *w* component at f_s = 40 Hz.

The flow velocity was measured at 22 cross-shore locations ranging from *x* = 49-64 m. For each cross-shore position, the frame was positioned at three different elevations, which after discarding spurious data resulted in approximately 200 velocity measurement locations (Figure 1b). Additional detailed measurements of the WBL flow were obtained in the shoaling zone *x* = 50.78 m. These velocities were measured with the LDA at 16 vertical positions, starting from 0.005 m up to 0.125 m from the top of the bed roughness and logarithmically spaced to capture the velocity distribution within the boundary layer. For the regular waves measurements were obtained for a duration of 12 min at each elevation, corresponding to approximately 120 waves, while for the bichromatic waves

the measurement duration was 58 min at each elevation, corresponding to approximately 100 wave groups.

Due to the repeatability of the regular waves and the wave groups the phase-averaged quantities could be determined, which enabled decompositions of the velocities into a time-averaged component, a periodic component and the turbulent fluctuation. The periodic component was separated into a low-frequency (long wave) and high-frequency (short wave) component, by separating the signal with a cut-off frequency of 0.1 Hz.

3.   WATER SURFACE ELEVATION

Time series of the phase-averaged water surface elevation η at three cross-shore locations are shown in Figure 2a-c. To facilitate a good inter-comparison, the time series in these figures were time-referenced such that $t/T_{gr} = 0$ corresponds to the passage of the front of the group at each location. Note that the grey contours around the lines mark +/- one standard deviation - the contours are barely visible, which indicates the excellent repeatability of the wave groups.

Figure 2a shows that after generation, the short waves forming the wave group are slightly skewed (crests higher than troughs) and approximately symmetric. As the wave group propagates over the slope, the short waves become higher, more skewed, and more asymmetric ('sawtooth-shaped'). At $x = 50.9$ m (Figure 2b), which is in the shoaling region before wave breaking, the wave group consists of seven well-defined short waves. The five highest short waves broke over the bar as plunging-type breakers, with the "plunge point", i.e. the location where the plunging jet first strikes the water surface, for waves two to six located at $x = 58.5, 57.5, 56.5, 57.5$ and 57.5 m, respectively. The first and seventh short waves broke at the shoreline. The "break point" (where the wave starts to overturn) of the most offshore breaking wave was measured at $x = 54.0$ m, while the "splash point" (where the bounced jet strikes the water surface a second time) of wave two was located at $x = 60.0$ m. Based on these visual observations we define the shoaling region ($x < 54$ m), breaking region (54 m $< x < 60$ m), and inner surf zone ($x > 60$ m). Hence, Figure 2c ($x = 66.0$ m) corresponds to the inner surf zone where waves two to six have broken and have transformed into surf bores. These five surf bores have similar wave heights, are highly skewed, and are significantly lower in wave height than at $x = 50.9$ m.
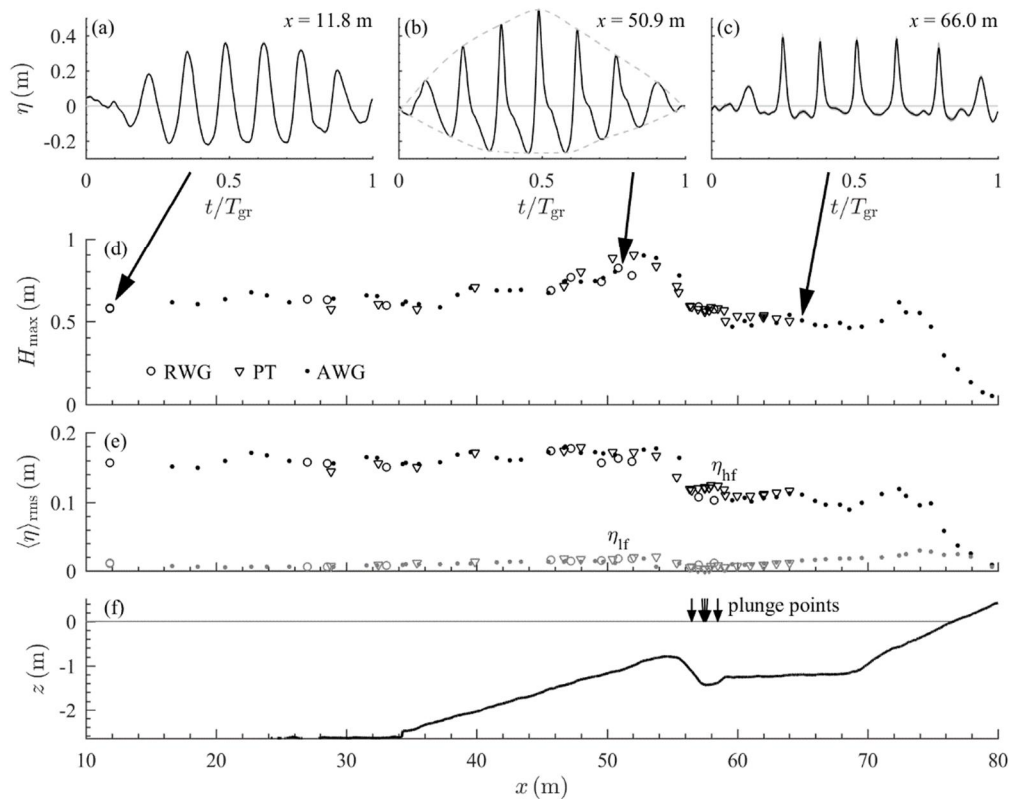
Figure 2. (a-c) Time series of phase-averaged water surface, measured by RWG (a, b) and AWG (c) (solid), with dashed lines in (b) marking the upper and lower bounds of the wave group envelope; (d) Maximum wave height $H_{max} = \langle\eta\rangle_{max} - \langle\eta\rangle_{min}$, measured by RWGs (circles), PTs (triangles) and AWGs (dots); (e) Root-mean-square water surface elevation, high-frequency (black symbols) and low-frequency (grey symbols) components; (f) bed profile including locations of the five plunge points.

Figure 2d shows the cross-shore distribution of the maximum wave height $H_{max} = \langle\eta\rangle_{max} - \langle\eta\rangle_{min}$. The three instruments yield generally consistent results, although the PTs tend to underestimate the wave height in the breaking region, where waves are strongly skewed and asymmetric, due to strong pressure attenuation of the higher harmonics of the wave. The wave heights are approximately constant over the horizontal, deeper part of the flume ($x < 34$ m), except for some modulations that are attributed to wave reflection at the beach and at the offshore slope. As waves shoal over the offshore slope, the wave height increases up to $H_{max} = 0.90$ m at $x = 52.8$ m. The maximum wave height decreases by about 50% between $x = 53.8$ m and 59.6 m due to wave breaking. Between $x = 60$ and 70 m the wave height remains approximately constant, while over the sloping beach ($x > 70$ m) the waves shoal and break a second time.

The water surface elevation was decomposed into a high-frequency (η_{hf}) and low-frequency (η_{lf}) component. Figure 2e shows the cross-shore distribution of $\langle\eta\rangle_{rms}$ for both components. It can be seen that $\langle\eta_{hf}\rangle_{rms}$ is approximately uniform over the offshore slope, which indicates that the increase in H_{max} (Figure 2b) is primarily due to an increasing skewness of the waves. The low-frequency component $\langle\eta_{lf}\rangle_{rms}$ gradually increases between the wave paddle and the bar crest, which relates to shoaling of the long wave and to energy transfer from the short waves to the wave group as shown in several other studies. Both $\langle\eta_{lf}\rangle_{rms}$ and $\langle\eta_{hf}\rangle_{rms}$ decrease in the wave breaking region around the bar crest ($x \approx 55.0$ m). Such decrease at both high and low frequencies near the break point is consistent with several other laboratory studies (see Baldock, 2012, for an overview). The low-frequency wave energy increases across the inner surf zone towards the shoreline ($x = 55$ to 75 m) as the wave groups shoal for the second time.

4.   FLOW VELOCITIES

Time series of the phase-averaged horizontal and vertical velocities $\langle u \rangle$ and $\langle w \rangle$ in the free-stream ($z - z_{bed} \approx 0.4$ m) at four cross-shore locations are shown in Figure 3. The time series reveal the strongly skewed-asymmetric shape of the short-wave-induced velocity at all locations. The orbital amplitude increases from $x = 49.0$ to 54.0 m (shoaling region to bar crest). At $x = 54.0$ m, the highest velocities in both onshore (1.3 m/s) and offshore (-1.1 m/s) direction occur. The orbital amplitude decreases strongly between $x = 54.0$ and 58.0 m (bar crest to trough) due to a combination of wave energy dissipation and an increasing water depth. At the same time the magnitude of the undertow increases, leading to increasing durations of the negative (seaward-directed) flow half cycles. At $x = 62.0$ m the undertow has weakened and the duration of the positive (shoreward-directed) flow half cycles increases again.

Figure 3 further includes the low-frequency velocity $\langle \tilde{u}_{lf} \rangle$ (dashed lines). The amplitude of the low-frequency velocity shows a clear variation with cross-shore location. The amplitude of $\langle \tilde{u}_{lf} \rangle$ is small in the shoaling region (e.g. $x = 49.0$ m), but its magnitude increases in the breaking region at the bar crest ($x = 54.0$ m) and reaches a maximum at $x = 58.0$ m, which corresponds to the bar trough and is located about 1 m shoreward from the plunge point of the largest breaking waves. At $x = 62.0$ m, the amplitude of $\langle \tilde{u}_{lf} \rangle$ has decreased again. This cross-shore variation of $\langle \tilde{u}_{lf} \rangle_{rms}(x)$ differs from the variation of $\langle \eta_{lf} \rangle_{rms}(x)$ (Figure 2e), which indicates that the low-frequency velocity variations are not directly driven by the water surface level variations at the wave group frequency. Instead, the large $\langle \tilde{u}_{lf} \rangle$ values for $x = 57$ - 59.5 m are explained by time variations in the return flow induced by the successive breaking waves: the return flow, averaged over a short wave cycle, is relatively low under the non-breaking waves and relatively high under the highest breaking waves, hence yielding a periodic velocity oscillation at the wave group time scale (see also, e.g., Alsina and Caceres, 2011). The $\langle \tilde{u}_{lf} \rangle$ oscillations in the surf zone can thus be interpreted as a wave to wave variation in "undertow" velocity, although it should be stressed that the term "undertow" is used in the present study for the longer-term (i.e., wave-group-averaged), and not for the short-wave-averaged, cross-shore velocity.
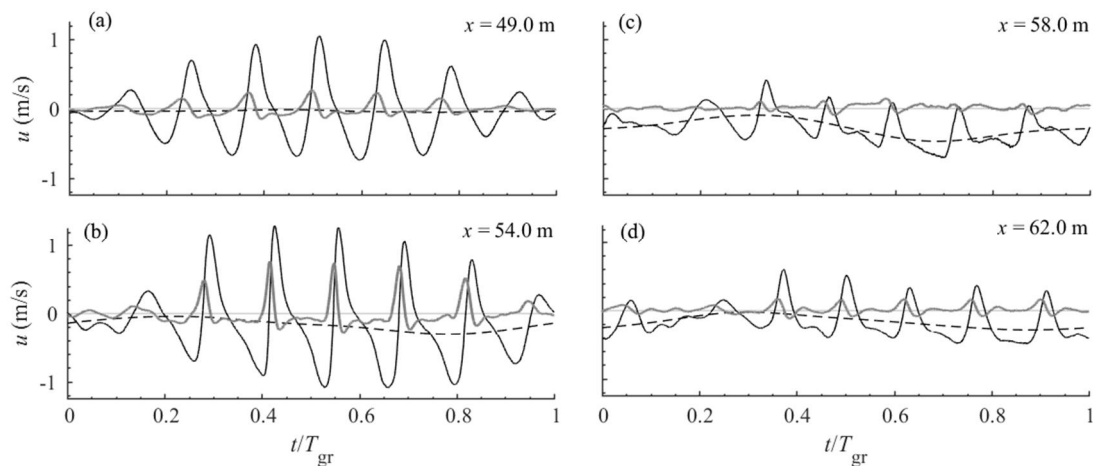

Figure 32. Time series of phase-averaged velocities $\langle u \rangle$ (solid black), $\langle \tilde{u}_{lf} \rangle + \bar{u}$ (dashed black), and $\langle w \rangle$ (solid grey) at eight locations and at $z - z_{bed} \approx 0.40$ m.

The spatial distribution of the time-averaged cross-shore velocity $\bar{u}$ is shown in Figure 4. The time-averaged cross-shore velocity magnitude increases from -0.05 m/s in the shoaling region to a maximum of -0.3 m/s in the breaking region over the bar trough, followed by a decrease to -0.2 m/s in the inner surf zone. Mass continuity requires these cross-shore variations in time-averaged cross-shore velocity to be balanced by a time-averaged velocity in vertical direction ($d\bar{u}/dx = -d\bar{w}/dz$), which the measurements do indeed confirm (not shown for brevity).

The undertow profiles in Figure 4 differ strongly in shape: around the bar crest ($x = 53$ to 56 m, i.e. under wave break points) $\bar{u}(z)$ distributions tend to convex shapes, while $\bar{u}(z)$ over the bar trough ($x = 58$ to 61 m, i.e. under splash points) increases strongly within the first few cm above the bed

and tends to a concave shape at higher elevations. The variation of these undertow shapes, and their spatial occurrence relative to break and splash points, is consistent with previous observations of regular (e.g. Govender et al., 2011) and irregular (Boers, 2005) breaking waves over a bar.
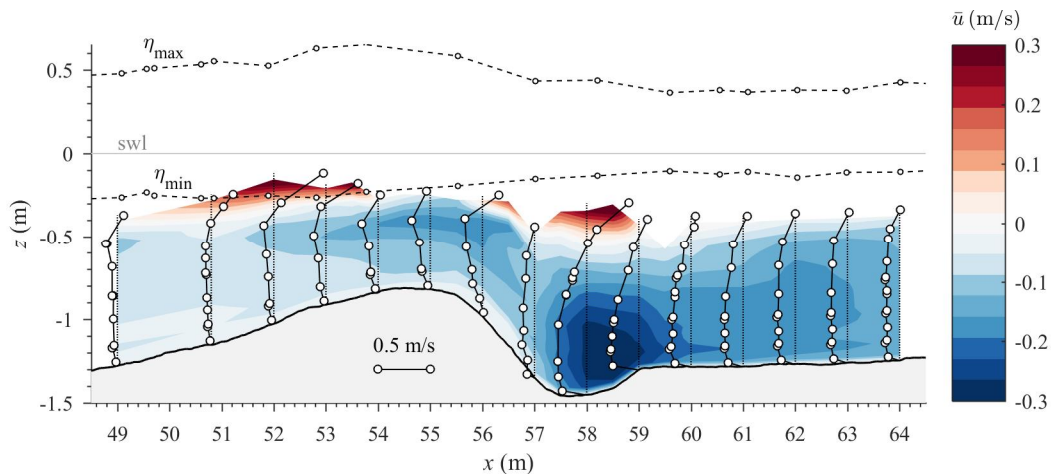

Figure 4. Spatial distribution of time-averaged cross-shore velocity $\bar{u}$.

5.   TURBULENCE

Figure 5 shows time series of phase-averaged TKE, $\langle k \rangle$, at four cross-shore locations and at two elevations: $z - z_{bed} = 0.40$ m (free-stream) and 0.025 m (in the WBL). In the shoaling region at $x = 49.0$ m $\langle k \rangle$ shows pairs of short-duration peaks within the boundary layer (Figure 5b, grey line), that lag the maximum offshore- and onshore-directed velocity by approximately $0.2 T_m$ (Figure 5a). These TKE peaks relate to turbulence that is produced at the bed during each half-cycle and that subsequently spreads upward. During the relatively long interval between the maximum onshore and maximum offshore velocity, i.e. under the rear side of the wave, $\langle k \rangle$ decays to nearly zero until the maximum velocity in offshore direction is reached and the process repeats as described.

At the bar crest ($x = 55.0$ m), near-bed $\langle k \rangle$ shows six well-defined peaks that are approximately in phase with the maximum onshore free-stream velocity (Figure 5c,d). The fact that only one peak in $\langle k \rangle$ appears per wave cycle, instead of two peaks such as at $x = 49.0$ m, can be explained by the increased wave asymmetry, leading to a shorter time interval between the maximum offshore and maximum onshore velocity and which merges the turbulence peaks into one peak. At the same location at $z - z_{bed} = 0.40$ m (Figure 5d, black line), $\langle k \rangle$ is substantially higher than at $x = 49.0$ m (same elevation) which can be explained by wave breaking turbulence that is advected in offshore direction by the undertow.

Figure 5f shows $\langle k \rangle$ over the bar trough ($x = 59.0$ m). At this location $\langle k \rangle$ is continuously higher at $z - z_{bed} = 0.40$ m than at 0.025 m, due to the injection of turbulence from the breaking waves. The TKE does not dissipate within one wave cycle, leading to a gradual build-up of TKE during the wave group cycle ($t/T_{gr} = 0.50$ to 0.80). Consequently, $\langle k \rangle$ shows a pronounced asymmetry at wave group time scale, with substantially higher TKE under the last three waves in the group ($t/T_{gr} = 0.75$ to 0.05) than under the first three waves ($t/T_{gr} = 0.20$ to 0.50). Three evident peaks in $\langle k \rangle$ are observed at $t/T_{gr} \approx 0.65$, 0.80, and 0.90. These peaks occur consistently under the rear of the short waves, i.e. around crest to trough reversal, when orbital velocities are downward-directed. Therefore, the occurrence of the peaks in $\langle k \rangle$ likely relates to an advective influx of TKE by the combined downward-directed time-averaged and periodic velocity. $\langle k \rangle$ is maximum at $t/T_{gr} \approx 0.8$, shortly after the fifth short wave in the wave group has passed. Note that the highest wave upon breaking is the fourth wave (passing $x = 59.0$ m at $t/T_{gr} = 0.6$) and the maximum $\langle k \rangle$ thus lags this wave by about 1.5 short wave cycle. Near the bed (grey line) $\langle k \rangle$ shows a similar time variation at wave group scale, although less pronounced than at 0.40 m. Finally, Figure 5h shows the time

series of $\langle k \rangle$ in the inner surf zone ($x = 64.0$ m), showing that TKE at both elevations is continuously small with minor temporal variation at short-wave and wave-group time scales.
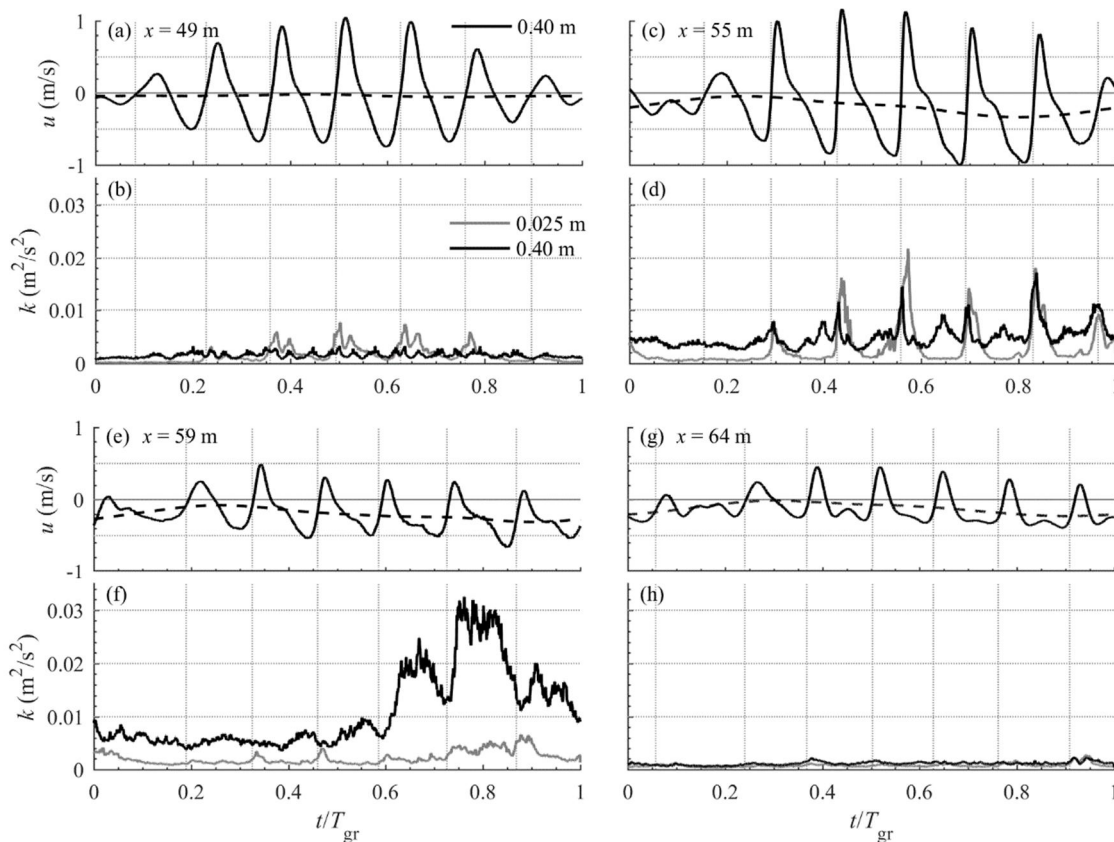

Figure 5. Time series of phase-averaged velocity and TKE at $x = 49.0$ (shoaling region), 55.0 m (bar crest), 59.0 m (bar trough), and 64.0 m (inner surf zone). (a, c, e, g) Cross-shore velocity $\langle u \rangle$ (solid) and $\langle \tilde{u}_{lf} \rangle + \bar{u}$ (dashed) at $z - z_{bed} \approx 0.40$ m; (b, d, f, h) TKE at $z - z_{bed} \approx 0.40$ m (black) and at $z - z_{bed} = 0.025$ m (grey). The vertical grid lines mark the zero-up crossings of $\langle \tilde{u}_{hf} \rangle$ at $z - z_{bed} = 0.40$ m at each location.

6. NUMERICAL MODELLING

The simulations are performed using the two-phase volume-of-fluid (VOF) model *waves2foam* developed by Jacobsen et al. (2012), using the new stabilized *k-ω* turbulence closure model described by Larsen & Fuhrman (2018). The simulations are performed in two dimensions, on a bathymetry following grid composed of 2250x188 points (*x* and *z* direction), resulting in 423,000 cells in total. Wave generation is based on a second order bichromatic bidirectional solution, with amplitudes chosen to match the maximum experimental wave height in the flat part of the domain. In total 20 wave groups were simulated and the last 10 groups used to phase-average the model results.

Figure 6a shows the measured and modelled maximum and minimum phase-averaged surface elevations along the flume. The model captures both the highest crest and trough levels in the flat part of the flume (x < 34 m) and during shoaling ($x \approx 34$ m - 53 m). The model accurately captures the point where the wave heights decrease due to breaking ($x \approx 53$ m). In the inner surf-zone (x > 60 m) crest heights are slightly overestimated, compared to the AWG measurements, but this might be due to the applied de-spiking routine that slightly smoothens the wave crests, as also mentioned by van der Zanden et al. (2019). Closer to the swash zone the second decay in wave height is also captured. The largest difference between the modelled results and the experiments can be seen in the swash zone where the modelled results show an additional small peak. This

peak comes from the splash up of one of the waves in the group breaking a second time in the swash zone. In the experiments the waves also shoaled and broke again in the swash zone, but a distinct splash-up as in the model was not measured.
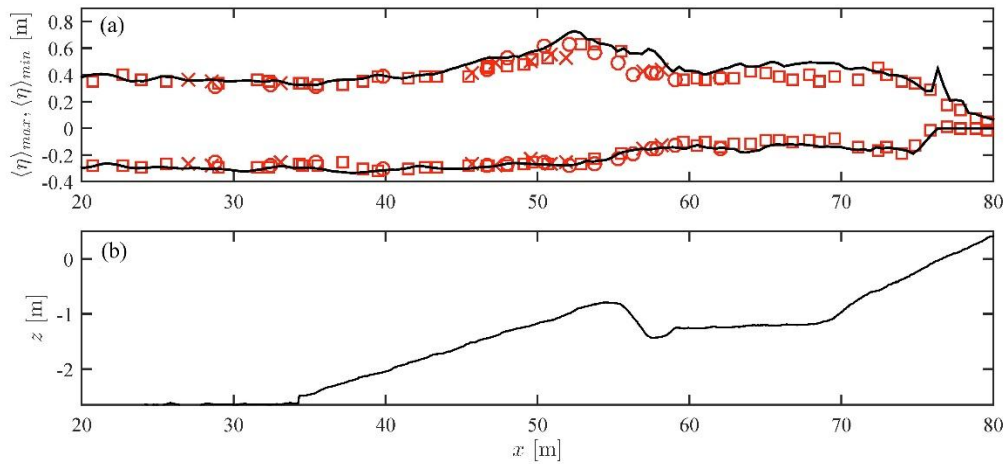

Figure 63. (a) Comparison between measured and modelled water surface envelope; (b) beach profile

Figure 7 shows the spatial distribution of the time-averaged cross-shore velocity (the undertow) of both the model (small circles and colored velocities) and the experiments (large circles). For reference, the figure also includes the results from using a standard non-stabilized two-equation turbulence model (green lines). The experiments showed two distinct different undertow profile shapes in the shoaling region and the surf zone. In the shoaling region ($x < 56$ m) the magnitude of the undertow is largest far away from the bed, whereas in the surf zone ($x > 58$ m) the undertow is strongest near the bed. This qualitative difference in the undertow profile as well as the transition in profile shape from one region to the other is well captured by the model. The non-stabilized turbulence model, on the other hand, does not capture the difference in profile shape nor the transition in the shape of the undertow structure between $x = 56 - 58$ m and instead, returns a similar profile shape from shoaling to inner surf zone. In Larsen and Fuhrman (2018) this behaviour was attributed to the overproduction of turbulence in the pre-breaking region which increases the flow resistance in the upper part of the flow and forces the undertow to maintain the same shape as in the surf zone.
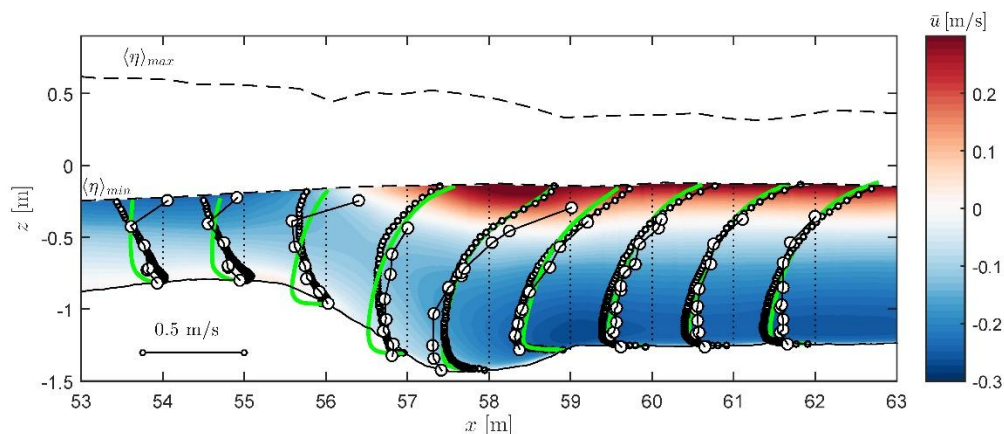

Figure 74. Spatial distribution of the time-averaged cross-shore velocity of the experiments (large circles), from the model (small circles and colored velocities) and using a non-stabilized model (green lines)

The overproduction of turbulence is illustrated in Figure 8, which presents a comparison of the measured time-averaged TKE with the model results based on the new model (Figure 8a) and based on the non-stabilized k-ω turbulence closure (Figure 8b). Using a formally stabilized

turbulence model, the TKE levels at shoaling and wave breaking locations (x = 50.7 - 56 m) are generally low and correspond well with the measured TKE (Figure 8a). In contrast, using a non-stabilized k-ω turbulence model (Figure 8b) yields TKE levels in these regions that are of similar magnitude as in the surf-zone and that are several orders of magnitude larger than the measured levels. In the inner surf zone both the stabilized and non-stabilized model show an overestimation of the TKE. The overestimation is significantly larger for the non-stabilized model which can be explained by the wave arriving at the surf-zone with severely over-estimated turbulence levels, hence advecting additional turbulence into the surf zone.
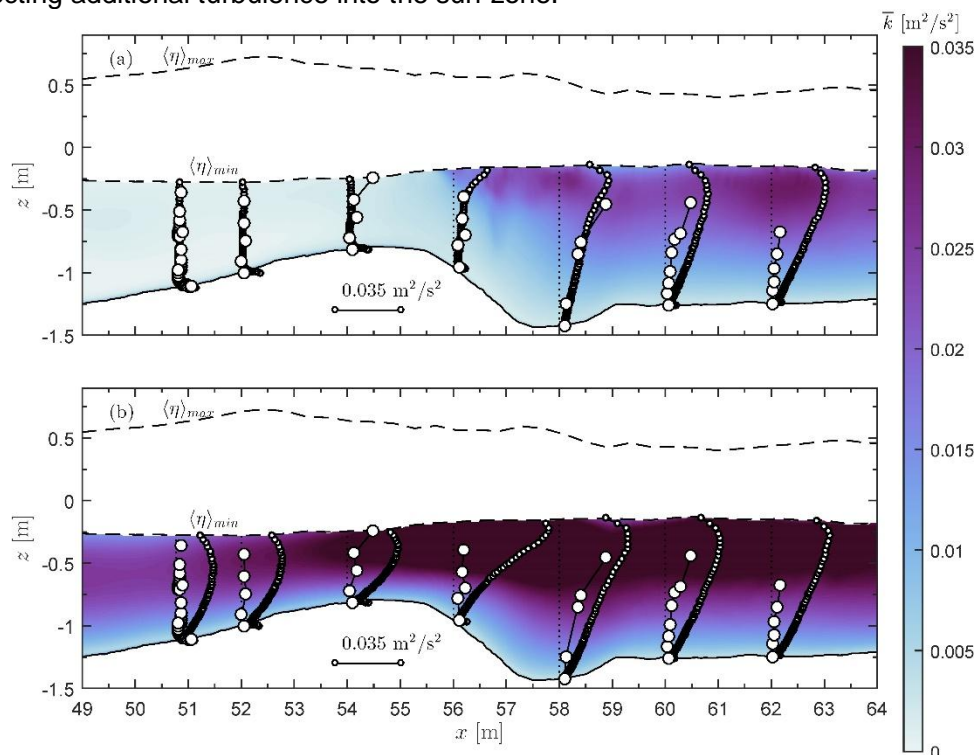

Figure 8. Snapshot of the spatial distribution of TKE upon wave breaking using (a) a formally stable turbulence model and (b) a standard two-equation turbulence model.

7.   CONCLUSION

Velocity and turbulence profiles were measured under a bichromatic plunging breaking wave in a large-scale wave flume over a fixed barred profile. The measurements covered 22 cross-shore locations that covered part of the shoaling region, the full wave breaking region, and part of the inner surf zone. The bichromatic wave produced a wave group with seven incident short waves, of which the highest five waves were plunging breaking over the bar.

The temporal dynamics of TKE vary strongly across the profile. In the shoaling region, where turbulence is primarily bed-shear generated, turbulence decays within one wave cycle, leading to time-varying TKE at the short wave frequency. In contrast, the wave breaking-generated turbulence between plunge and splash points requires multiple wave cycles to decay fully, leading to a gradual increase in TKE during the group and to variations of TKE at the wave group frequency.

The measurements are compared to a two-phase RANS model based a new stabilized k-ω turbulence closure. Very good agreement is obtained between measured and modelled water surface elevations, meaning that the model handles the wave propagation, shoaling and breaking of the wave group. The model predicts the undertow well and captures the correct shape of the undertow profile and the shape transition between shoaling and surf zone. Standard non-stabilized RANS models are unable to capture this shape transition, due to the inherent overestimation of

turbulence in the shoaling zone. The present model still overestimates TKE levels and undertow magnitude in the inner surf zone, similar to many other RANS models, which will be the focus of future research.

ACKNOWLEDGEMENT

REFERENCES

Alsina, J. M., and Cáceres, I. (2011). Sediment suspension events in the inner surf and swash zone. Measurements in large-scale and high-energy wave conditions. *Coastal Engineering*, 58(8), 657-670.

Baldock, T. E. (2012). Dissipation of incident forced long waves in the surf zone—Implications for the concept of "bound" wave release at short wave breaking. *Coastal Engineering*, 60, 276-285.

Bonneton, P., Lannes, D., Martins, K., and Michallet, H. (2018). A nonlinear weakly dispersive method for recovering the elevation of irrotational surface waves from pressure measurements. *Coastal Engineering*, 138, 1-8.

De Serio, F., and Mossa, M. (2006). Experimental study on the hydrodynamics of regular breaking waves. *Coastal Engineering*, 53(1), 99-113.

Fernandez-Mora, A., Ribberink, J. S., van der Zanden, J., van der Werf, J. J., and Jacobsen, N. G. (2016). RANS-VOF modeling of hydrodynamics and sand transport under full-scale non-breaking and breaking waves. *Proceedings of the 35th ICCE*, Antalya, Turkey.

Govender, K., Michallet, H., and Alport, M. J. (2011). DCIV measurements of flow fields and turbulence in waves breaking over a bar. *European Journal of Mechanics B-Fluids*, 30(6), 616-623.

Jacobsen, N. G., Fuhrman, D. R., and Fredsøe, J., 2012. A wave generation toolbox for the open-source CFD library: OpenFOAM (R). *Int. J. Numer. Meth. Fluids*, 70, 1073–1088.

Larsen, B. E., and Fuhrman, D. R. (2018). On the over-production of turbulence beneath surface waves in Reynolds-averaged Navier–Stokes models. *Journal of Fluid Mechanics*, 853, 419-460.

Scandura, P., van der A, D.A., van der Zanden, J., Petrotta, C., Faraci, C., Cooper, J., Clark, S., Eltard Larsen, B., Carstensen, S., Fuhrman, D.R., Caceres, I., McLellands, S., Fromant, G., Hurther, D., Ruessink, G., Brinkkemper, J., Li, M. (2018). Hydrodynamics under large-scale breaking waves over a barred beach. *Poc. 7th Coastlab Conference,* Santander, Spain.

Ting, F. C. K., and Kirby, J. T. (1995). Dynamics of surf-zone turbulence in a strong plunging breaker. *Coastal Engineering*, 24(3-4), 177-204.

van der A, D. A., van der Zanden, J., O'Donoghue, T., Hurther, D., Cáceres, I., McLelland, S. J., and Ribberink, J. S. (2017). Large-scale laboratory study of breaking wave hydrodynamics over a fixed bar. *Journal of Geophysical Research: Oceans*, 122(4), 3287-3310.

van der Zanden, J., van der A, D. A., Cáceres, I., Hurther, D., McLelland, S. J., Ribberink, J. S., and O'Donoghue, T. (2018). Near-bed turbulent kinetic energy budget under a large-scale plunging breaking wave over a fixed bar. *Journal of Geophysical Research: Oceans*, 123(2), 1429-1456.

van der Zanden, J., van der A, D. A., Cáceres, I., Eltard Larsen, B., Fromant, G., Petrotta, C., Scandura, P., and Li, M. (2019). Spatial and temporal distributions of turbulence under bichromatic breaking waves, *Coastal Engineering*, 146, 65-80.

Yoon, H. D., and Cox, D. T. (2010). Large-scale laboratory observations of wave breaking turbulence over an evolving beach. *Journal of Geophysical Research-Oceans*, 115.

INFLUENCE OF STORM SEQUENCING AND BEACH RECOVERY ON SEDIMENT TRANSPORT AND BEACH RESILIENCE (RESIST)

Sonja Eichentopf (1), Tom E. Baldock (2), Iván Cáceres (3), David Hurther (4),
Harshinie Karunarathna (5), Matteo Postacchini (6), Nicola Ranieri (7),
Joep van der Zanden (8) & José M. Alsina (3)

(1) Imperial College London, UK, E-mail: sonja.eichentopf16@imperial.ac.uk
(2) University of Queensland, Australia, E-mail: t.baldock@uq.edu.au
(3) Universitat Politècnica de Catalunya, Spain, E-mail: i.caceres@upc.edu, jose.alsina@upc.edu
(4) LEGI, CNRS, University Grenoble Alpes, France, E-mail: david.hurther@legi.cnrs.fr
(5) Swansea University, UK, E-mail: h.u.karunarathna@swansea.ac.uk
(6) Università Politecnica della Marche, Italy, E-mail: m.postacchini@staff.univpm.it
(7) Università degli Studi dell'Aquila, Italy, E-mail: nicola.ranieri1@student.univaq.it
(8) University of Twente, the Netherlands, E-mail: j.vanderzanden@utwente.nl

Large-scale experiments on beach profile evolution and detailed sediment transport processes under varying wave conditions were performed within the HYDRALAB+ transnational access project 'RESIST'. Five wave conditions were tested, of which two presented high energy wave conditions and three presented low energy wave conditions (including one very low energy condition that was run for a long duration (24 h)). These five wave conditions were combined into three sequences of alternating high-low energy conditions, with similar total power of each sequence. Each sequence departed from an initial 1/15 sloped profile. The experiments resulted in a large data set comprising measurements of high temporal-spatial resolution of the beach profile, water surface elevation, velocity field, sediment concentrations as well as the collection of sediment samples and observations of wave breaking and runup/rundown. The analysis of the beach profiles in the context of storm sequence forcing has highlighted the evolution of the beach towards an equilibrium state for each wave condition. The analysis of sediment transport and bed level changes under high energy, alternating swash events has provided new insights into sand transport processes, including the influence of small differences in wave-swash interactions on transport rates, and the mobilisation of sediment in the swash.

1.   INTRODUCTION

Research on beach evolution and sediment transport has largely focussed on erosive processes with only little emphasis on processes under recovery conditions or alternating wave climates. In line with that, most of the existing data sets obtained under controlled, large-scale morphodynamic conditions have focussed on high energy (storm) wave conditions, of which some were followed by one low energy (recovery or accretive) event. Normally, no long sequences of alternating high-low energy conditions have been performed (Eichentopf et al., 2018). Reasons for the large focus on high energy conditions can be related to the strong effects and related threats that a storm poses onto the beach, large efforts (costs and time) for long sequences of wave conditions in physical modelling, potentially long recovery times, and difficulties in measuring flow velocities and sediment concentrations under low energy conditions.

Conditions of alternating, or cyclic, periods of high and low energy conditions ('storm sequences') have increasingly been regarded to become more relevant in a climate change scenario (e. g. Webster et al., 2005; Knutson et al., 2010). In terms of beach evolution, recent research indicated more severe erosion of beaches under storm sequence forcing compared to isolated storm events at specific field sites (e. g. Karunarathna et al., 2014). This implies an important responsibility for coastal researchers to investigate the subject of beach evolution under storm sequence conditions in more detail and to work towards recommendations on how to react to potentially more severe beach changes under storm sequence forcing (Eichentopf et al., 2019b). Therefore, an important step to improve our understanding of beach response to cyclic wave conditions as well as the

underlying processes is to perform controlled, large-scale morphodynamic experiments comprising cyclic high-low energy wave conditions and to investigate their effect on beach evolution.

For storm sequences, low energy wave conditions and associated beach recovery are of particular interest as they might present the key to avoid long-term beach erosion. However, especially for low energy wave conditions, beach profile evolution and sediment transport patterns are not well understood. This becomes evident through the limited number of available (large-scale) morphodynamic data sets comprising low energy conditions (Eichentopf et al., 2018) and the poor performance of numerical models under low energy compared to high energy conditions (van Rijn et al., 2011). Recent advances in the development of state-of-the-art instrumentation to acquire high-resolution sediment transport data have opened new possibilities to improve our understanding on sediment transport dynamics (Hurther et al., 2011; van der Zanden et al., 2015). The developed instrumentation has, however, primarily been applied to the study of sediment transport under high energy conditions (e. g., van der Zanden et al., 2015, 2017).

Consequently, research on the short-term processes of beach evolution and sediment transport processes has provided only limited understanding of beach erosion and recovery patterns under alternating wave conditions. The existing simplistic erosion-recovery approach of high-low energy wave conditions does not provide the level of detail required for coastal management and for the development of numerical modelling capabilities. This paper focusses on the design and performance of new, large-scale morphodynamic experiments that were performed within the HYDRALAB+ transnational access project 'RESIST' and hence, the paper provides a comprehensive overview of the methodology in the measuring campaign and the acquired data. A considerably large amount of high-quality data with high temporal-spatial resolution has been acquired in the experiments and is being analysed. Recent results on the beach profile evolution under alternating wave conditions (Eichentopf et al., 2019a) and on sand transport dynamics under a high energy alternating swash event (van der Zanden et al., 2019) are resumed.

This paper is organised as follows: In section 2 the experimental setup and the data acquisition is described. Section 3 describes the evolution of the beach profile under the performed storm sequence conditions. Section 4 focusses on the analysis of sediment transport data and detailed bed level measurements obtained in the swash zone. A discussion and conclusions follow in section 5.

2.   EXPERIMENTS

The experiments were performed within the EU funded HYDRALAB+ Transnational Access project RESIST ('Influence of storm sequencing and beach REcovery on SedIment tranSporT and beach resilience'). This project had two major objectives:

- obtain large-scale morphodynamic data on beach profile evolution under sequences of alternating high-low energy wave conditions; and
- obtain sediment transport data of high temporal-spatial resolution under both erosive and accretive wave conditions in the surf and swash zone.

In this section, the experimental set-up is presented, including a description of the wave flume and the measurements as well as the wave conditions that made up the storm sequences.

2.1.   WAVE FLUME

The experiments within the RESIST project were performed in the Canal d'Investigació I Experimentació Marítima (CIEM) at Universitat Politècnica de Catalunya (UPC) in Barcelona, Spain. This is a large-scale wave fume which measures 100 m, 3 m and 4.5 m in length, width and height, respectively. The water depth of the still water level in the deep water part of the flume was 2.5 m throughout the measuring campaign.

The beach consisted of commercial fine to medium size sand with a narrow grain size distribution ($d_{50} = 0.25$ mm, $d_{10} = 0.15$ mm, $d_{90} = 0.37$ mm). Before the start of each sequence of wave

conditions (see section 2.2.), the beach was manually shaped to an initial, plane profile with a slope of 1/15. Following Baldock et al. (2017), two thin metal plates of 6 m length and 0.7 m height ('dividers') were placed in the swash zone (see right photo in figure 1) in order to reduce cross-tank asymmetries generated by the interactions of the runup and rundown. These dividers were placed parallel to the flume walls and divided the flume in three equal widths of 1 m (0.75 m, 1.5 m and 0.75 m in the beginning of the measuring programme).

Figure 15: Preparation of the beach profile (view towards the wave paddle). Left photo: manually shaped beach. Right photo: filling the wave flume (dividers in the front).

2.2. WAVE CONDITIONS AND SEQUENCES

In the RESIST experiments, different wave conditions were performed to generate three sequences of varying wave conditions. The wave conditions with their target values of wave height, wave period and dimensionless sediment settling velocity Ω (-) (Gourlay, 1968; Dean, 1973) are summarised in table 1.

Table 1: Details of the performed benchmark and bichromatic wave conditions (target values).

Wave condition		Observations	H_s (m)	T_p (s)	Ω (-)
B	Benchmark	Random waves	0.42	4	
E1	Erosive 1	Highly energetic storm	0.64	3.7	5.09
E2	Erosive2	Lower energy storm	0.49	3.7	3.90
A1	Accretive1	Low energy condition	0.32	4.7	2.00
A2	Accretive 2	Intermediate low energy condition	0.27	5.3	1.50
A3	Accretive 3	Very low energy condition	0.20	5.7	1.03

Condition B refers to the benchmark condition which was run for one test at the beginning of each sequence to homogenise the profile. Condition B presented a random wave condition with a Jonswap spectrum ($\gamma = 3.3$). The other wave conditions presented repeatable wave groups (bichromatic waves) allowing for ensemble averaging which is essential for the analysis of sediment concentration and velocity data obtained by means of ACVP and CCM+ (see section 2.3.) as well as for the detailed analysis of the effect of individual waves within the groups on beach profile evolution. Bichromatic waves were previously reported to have a similar effect on beach profile change as random wave conditions (Baldock et al., 2011).

Details of the bichromatic wave conditions are shown in table 2. T_p refers to the mean primary frequency ($T_p = (f_1+f_2)/2$), T_g is the group frequency ($T_g = f_1-f_2$) and T_R presents the period after which the defined number of groups repeats exactly ('repetition period'). For erosive conditions, T_R comprised two wave groups and the waves were fully modulated ($N = 1$), i. e. the amplitude at the two primary frequencies was the same. The accretive wave conditions repeated every three wave groups and were partly modulated where the amplitudes at the two frequencies differed by a factor of two ($N = 0.5$).

Table 2: Details of the performed bichromatic wave conditions (target values).

Condition	Component 1		Component 2					
	H_1 (m)	f_1 (Hz)	H_2 (m)	f_2 (Hz)	T_p (s)	T_g (s)	T_R (s)	$N = H_1/H_2$
Erosive 1	0.320	0.3041	0.320	0.2365	3.7	14.80	29.60	1
Erosive 2	0.245	0.3041	0.245	0.2365	3.7	14.80	29.60	1
Accretive 1	0.101	0.2276	0.202	0.1979	4.7	33.68	101.05	0.5
Accretive 2	0.085	0.2018	0.171	0.1755	5.3	37.98	113.95	0.5
Accretive 3	0.063	0.1877	0.126	0.1632	5.7	40.85	122.55	0.5

The presented wave conditions were combined into three sequences of alternating high-low energy conditions (see table 3). In sequences 1 and 2, the same set of wave conditions was performed but with varying order of the high energy (erosive) conditions. Sequence 3 comprised the same order of high energy conditions as sequence 1 but with different low energy (accretive) conditions.

Table 3: Combination of wave conditions into storm sequences.

Sequence 1		Sequence 2		Sequence 3	
Case	Duration (min)	Case	Duration (min)	Case	Duration (min)
B	30	B	30	B	30
E1	240	E2	120	E1	240
A1	600	A1	600	A2	780
E2	120	E1	240	E2	120
A1	600	A1	600	A3	1440

2.3. INSTRUMENTATION AND DATA ACQUISITION

A large number of measurements was performed throughout the measuring programme, including measurements of the beach profile, water surface elevation, velocity field, sediment concentrations, the collection of sediment samples and observations of the location of outmost and innermost breaking as well as maximum runup and rundown.

The beach profile was measured along a central line of the wave flume by means of a mechanical profiler that is capable of measuring the profile depth in both the emerged and the submerged part of the beach. The spatial resolution of the profile measurements was 2 cm. The beach profile was measured before the start of each sequence and after each performed wave run resulting in a total of 119 beach profile measurements.

At the end of the measuring programme (after completion of sequence 3 (after condition A3)), the flume was drained, and sediment samples were collected from the top of the bed at 20 cross-shore locations with a spatial resolution of 0.5 m or 1 m (see figure 2 for locations of bed samples collected from the evolved profile after A3). The cross-shore region from which the samples were collected extended from offshore of the bar to the top of the berm. The sediment samples were later analysed regarding their grain size distributions in the soils lab at Imperial College London by means of a laser-based particle detection instrument (QicPic).
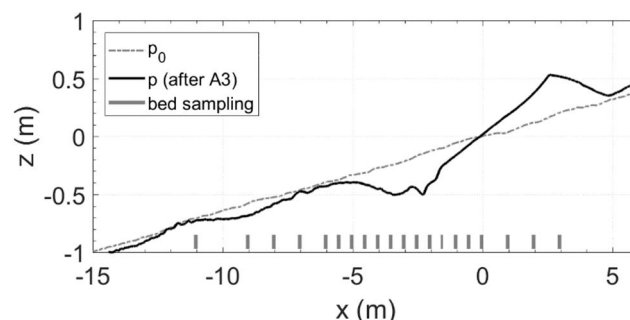

Figure 2: Locations of bed sediment samples collected after completion of the measuring programme (after condition A3).

A variety of instrumentation to measure water surface elevation, flow velocities and sediment concentration was deployed at fixed locations before the start of the measuring programme. The locations of the fixed instrumentation are shown in table 4.

Table 4: Locations of fixed instrumentation at the start of the measuring programme.

Instrument	N°	Cross-shore location (in m) with respect to shoreline of initial profile; in parenthesis, vertical elevation with respect to bed (where applicable)
RWG	13	-63.40, -63.40, -48.22, -46.71, -42.32, -35.23, -31.16, -27.12, -23.18, -19.21, -17.42, -15.66, -11.30
AWG	20	-61.77, -56.04, -44.94, -21.85, -20.55, -14.66, -13.26, -9.57, -7.38, -5.57, -3.44, -1.57, -0.52, 0.47, 1.25, 2.31, 3.5, 4.55, 5.56, 6.51
PPT	12	-54.49, -51.94, -50.22, -43.52, -40.75, -39.11, -37.21, -33, -28.9, -24.5, -8.71, -4.68
ADV	6	-4.72 (0.10), -1.54 (0.03), -0.52 (0.03), 0.27 (0.03), 1.28 (0.03), 2.26 (0.03)
OBS	5	-1.68 (0.03), -0.45 (0.03), 0.38 (0.03), 1.28 (0.03), 2.36 (0.03)
CCM+ tanks	2	-0.52 m (tank 2), 1.28 m (tank 1)

Water surface elevation data were usually acquired at 45 fixed cross-shore locations by means of Resistive Wave Gauges (RWG), Pore Pressure Transducers (PPT) and Acoustic Wave Gauges (AWG) which were (primarily) deployed in the offshore, the breaking and the surf/swash region, respectively. Water surface elevation data were measured at a sampling frequency of $f_s = 40$ Hz. Acoustic Doppler Velocimeters (ADV) were deployed in the inner surf and swash zone to acquire data on the three-dimensional velocity field. Optical Backscatter Sensors (OBS) were co-located with the ADVs to measure sediment concentrations at the same elevation as velocities. ADVs and OBSs were deployed at 3 cm from the bed. This vertical position was controlled and, if necessary, adjusted before each test. ADVs and OBSs acquired data at $f_s = 100$ Hz and $f_s = 40$ Hz, respectively. Figure 3 shows examples of deployed ADVs, OBSs and AWGs.
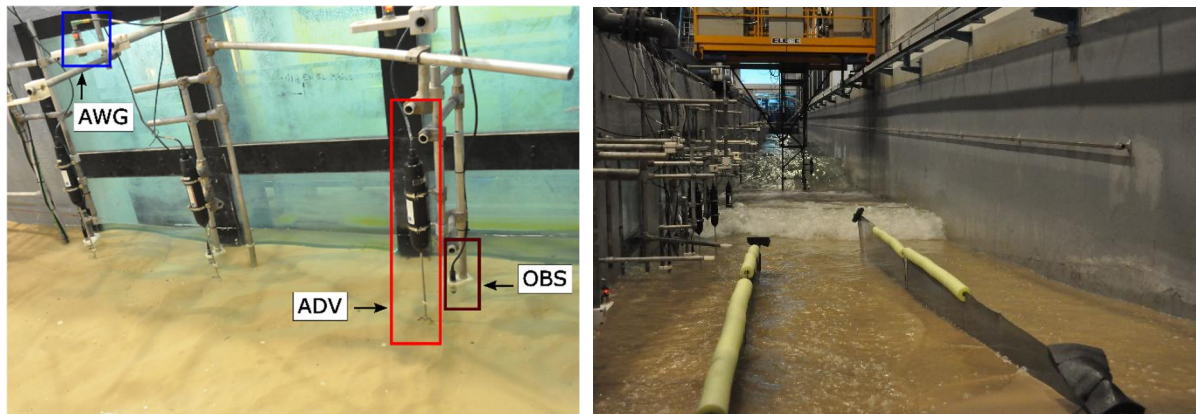

Figure 36: Measurements in the CIEM. Left photo: deployed ADV, OBS and AWG. Right photo: waves arriving on the beach (dividers in the front).

Two conductivity-based concentration measuring tanks (CCM+ tanks) were installed in the inner swash zone for measurements of bed level motions and sediment concentrations in the sheet flow layer (see van der Zanden et al. (2015) for detailed information on the CCM+ technology). The two tanks were buried into the beach before the start of the experiments and hence, took measurements from below in order to minimise flow disturbances (see figure 4). Both CCM+ tanks were deployed close to the shoreline of the initial beach profile: tank 1 at circa 1 m onshore, tank 2 at circa -0.5 m (see table 4). Tank 1 (70 kg tank) has three probes (a single and a twin probe), where the single probe tracked the continuous bed level and the twin probe was used to measure particle velocities in the sheet flow layer (by alternating between concentration measurement and bed level tracking mode). Tank 2 (50 kg) has one single probe that alternated between concentration measurement and bed level tracking mode (as the twin probe of tank 1). The CCM+ data were sampled at $f_s = 1000$ Hz.

Figure 47: CCM[+] instrumentation. Left photo: Moving CCM[+] tank 2. Right photo: Probes of CCM[+] tank 1 (in red square) measuring within the bed.

Further instrumentation was deployed at the mobile frame (see left photo in figure 5) which, together with the movable trolley, allows positioning of instrumentation in the vertical and horizontal direction, respectively. The position of the mobile frame and hence, of the deployed instrumentation, was varied between tests in order to cover a wide range of locations around the outer breaker bar (i. e. in the shoaling to inner surf zone). On the mobile frame a variety of instruments was deployed, namely ADVs, OBSs, PPTs as well as an Acoustic Concentration and Velocity Profiler (ACVP). The ACVP allows the acquisition of sediment concentration and velocity profiles with high temporal-spatial resolution in proximity to the bed (see Hurther et al. (2011) for detailed information on the ACVP technology).

Figure 5: Instrumentation on the mobile frame. Left photo: mobile frame. Right photo: ACVP and the three nozzles of the TSS.

A transverse suction system (TSS) was installed at the mobile frame with three nozzles at three different vertical elevations within 20 cm from the bed (see right photo in figure 5). The nozzles were connected to pumps which were started circa 10 min after the beginning of each test and which were run for 10-12 min for collection of the sediment-water mixture. Following design criteria by Bosman et al. (1987), the nozzles were positioned normal to the direction of wave propagation with a ratio of the intake to the ambient velocity beyond three so that the measurements were insensitive to inversion of the flow direction. Through the TSS, sediment samples were obtained which allow the investigation of the time-averaged concentration profile of each test as well as the investigation of the sediment grain size distribution of the samples. All samples, including the 20 bed samples collected after A3, were dried, stored in plastic bags and shipped to Imperial College London for further analysis.

In addition to the data acquired by the presented high-quality, specialised instrumentation, information on the outmost and innermost breaking location as well as the maximum runup and the maximum rundown location were acquired by means of visual observations within the first 5-10 min of each test.

3. BEACH PROFILE EVOLUTION UNDER STORM SEQUENCE FORCING

In the RESIST experiments, a very large number of beach profiles was measured which allowed the investigation of beach evolution under the performed storm sequence wave climate. Results on this part of the analysis comprising data of beach profile measurements, wave breaking observations as well as data from the 20 sediment bed sampled (collected after completion of condition A3) are presented in Eichentopf et al. (2019a) and most important aspects are resumed here.

The influence of storm sequencing and beach recovery was studied in terms of shoreline and breaker bar evolution. Both indicators evolve towards an equilibrium with the breaker bar reaching its equilibrium location much faster than the shoreline suggesting differences in the transport processes involved in the bar and shoreline evolution. The final equilibrium configuration is specific for each wave condition and, for the present experiments, does not depend of the previous morphological beach configuration. Overall, storm sequencing did not produce increased beach erosion and the final beach configuration after a sequence of storms seems controlled by the last wave condition in the sequence.

However, the sequence of storms is important when determining the sediment transport processes as the initial beach configuration controls the sediment dynamics producing the equilibrium state. Therefore, when the beach profile is not yet fully recovered before being disrupted by the following storm, further erosion is not necessarily caused by the storm, but it can move sediment onshore and be part of the recovery of the shoreline (compare condition E2 in figure 6a-c).
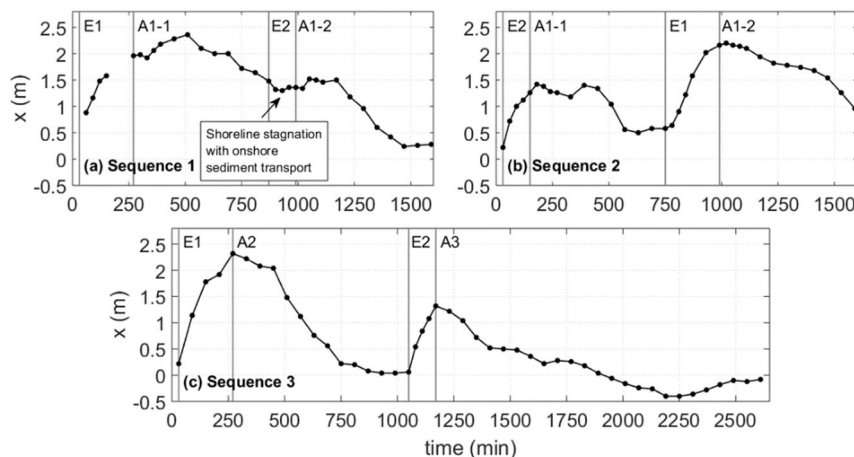

Figure 68: Shoreline evolution during RESIST experiments in the three performed sequences of wave conditions.

Examination of the beach profile evolution during the long-duration recovery wave condition (condition A3) shows cases of full beach recovery and the development of a reflective beach state with no plunging wave breaking and the formation of a steeply sloped berm (see figure 2).

4. SAND TRANSPORT PROCESSES AND BED EVOLUTION IN THE SWASH ZONE

Detailed intra-wave sediment transport was measured for wave condition E1 in the inner surf and swash zones using conductivity probes (CCM+ tanks) and results were analysed and discussed in van der Zanden et al. (2019) (see figure 7). The intra-wave mobilisation of sand increases both as

sheet flow and suspended load from the inner surf zone to the mid swash zone. Large quantities of sediment are mobilized during the uprush and backwash within the swash zone, but the amount of sediment exchanged with the inner surf zone is comparably small within the period of one swash event and becomes increasingly important for longer time scales.

Strong instantaneous bed level changes occur in the low swash region especially during the early uprush and during instants of strong wave-swash interactions. The net bed level change in the swash zone induced by single events is primarily explained by sediment redistribution within the swash zone. The sediment transport along the swash zone is strongly influenced by horizontal sediment advection during the uprush and backwash whereas in the inner surf zone, the vertical sediment exchanges in the water column seem more important.
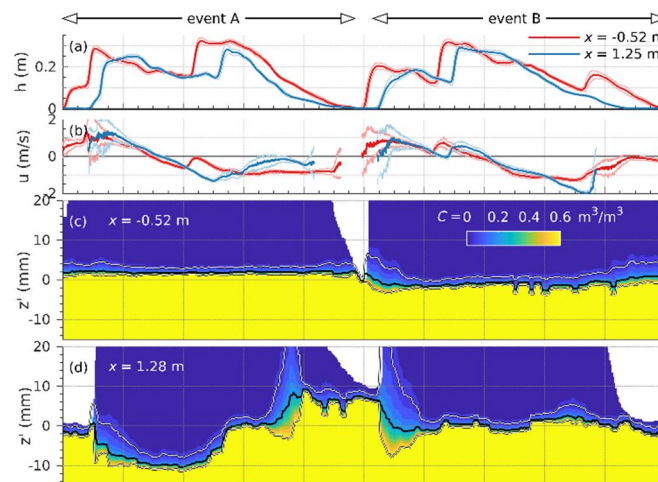

Figure 79: Ensemble-averaged water depths (a), velocities (b) and sediment concentration profiles (c,d) measured at the two CCM+ locations. The concentration profiles cover the sheet flow layer, white lines mark the bottom and top of the sheet flow layer.

The use of controlled bichromatic wave conditions with controlled wave phasing modulation produced two alternating swash events with similar offshore statistics but with different wave-swash interactions. Small differences in the wave-wave phasing and wave-swash interactions produced large differences in the observed sediment transport and bed evolution.

5.   DISCUSSION AND CONCLUSIONS

Large-scale experiments, that were performed within the HYDRALAB+ transnational access project 'RESIST', have been presented. These experiments have resulted in a unique, high-quality data set which comprises measurements of high resolution in space and time of the beach profile, water surface elevation, velocities and sediment concentrations. In addition, visual observations of locations of wave breaking and runup/rundown as well as sediment samples were obtained.

The presented experiments involved the generation of controlled wave sequences with similar cumulative wave power but varying storm chronology as well as variations in the duration and wave conditions of the recovery phases. Consequently, based on these experiments the beach profile evolution under both storm and recovery conditions and the influence of isolated influencing factors, such as storm chronology and varying recovery conditions, and potentially enhanced erosive effects due to storm sequencing can be studied.

Observations of the wave breaking and runup/rundown locations have been very valuable for the data analysis as they provide information on the extent of the breaking region and swash zone, respectively. The collection of sediment samples from the bed after draining the wave flume was important for the investigation of sediment sorting by means of sediment grain size analysis. An

increased collection of bed samples in large-scale wave flume experiments would be desirable in future experiments to advance the study of graded sediment transport. The acquisition of data on water surface elevation and velocity with high cross-shore resolution provides a detailed picture of the wave height and velocity transformation which can be linked to the profile evolution. In addition, the use of conductivity probes (CCM⁺ tanks), ACVP and the performance of controlled, repeated wave conditions allow the analysis of detailed sediment transport processes in the breaker bar region and the swash zone.

Two journal papers are currently under review focusing on the influence of storm sequence forcing on the evolution of the breaker bar and the shoreline (Eichentopf et al, 2019a) and sediment transport processes in the swash zone during high energy wave conditions (van der Zanden et al., 2019). Further aspects from the performed experiments are currently being analysed. This analysis includes the investigation of hydrodynamic and sediment transport patterns that result in the described beach profile evolution under varying wave conditions as well as the analysis of sediment transport data obtained by means of the ACVP under both high and low energy wave conditions.

ACKNOWLEDGEMENT

REFERENCES

Baldock, T.E., Alsina, J.M., Cáceres, I., Vicinanza, D., Contestabile, P., Power, H. and Sánchez-Arcilla, A. (2011). Large-scale experiments on beach profile evolution and surf and swash zone sediment transport induced by long waves, wave groups and random waves, *Coastal Engineering*, 58, 214-227.

Baldock, T.E., Birrien, F., Atkinson, A., Shimamoto, T., Wu, S., Callaghan, D.P. and Nielsen, P. (2017). Morphological hysteresis in the evolution of beach profiles under sequences of wave climates – Part 1; observations, *Coastal Engineering*, 128, 92-105.

Bosman, J.J., van der Velden, E.T.J.M. and Hulsbergen, C.H. (1987). Sediment Concentration Measurements by Transverse Suction, *Coastal Engineering*, 11, 353-370.

Dean, R.G. (1973). Heuristic Models of Sand Transport in the Surf Zone, *Proceedings of the 1st Australian Conference on Coastal Engineering, Engineering Dynamics in the Coastal Zone, Sydney*, 208-214.

Eichentopf, S., Cáceres, I. and Alsina, J.M. (2018). Breaker bar morphodynamics under erosive and accretive wave conditions in large-scale experiments, *Coastal Engineering*, 138, 36-48.

Eichentopf, S., van der Zanden, J., Cáceres, I., Baldock, T.E. and Alsina, J.M. (2019a). Influence of storm sequencing on breaker bar and shoreline evolution in large-scale experiments, *submitted for publication*.

Eichentopf, S., Karunarathna, H. and Alsina, J.M. (2019b). Morphodynamics of sandy beaches under the influence of storm sequences – current research status and future needs, *submitted for publication*.

Gourlay, M.R. (1968). Beach and Dune Erosion Tests. Delft Hydraulics Laboratory, Delft, The Netherlands, Report No. M935/M936.

Hurther, D., Thorne, P.D., Bricault, M., Lemmin, U. and Barnoud, J.-M. (2011). A multi-frequency Acoustic Concentration and Velocity Profiler (ACVP) for boundary layer measurements of fine-scale flow and sediment transport processes, *Coastal Engineering*, 58, 594-605.

Karunarathna, H., Pender, D., Ranasinghe, R., Short, A.D. and Reeve, D.E. (2014). The effects of storm clustering on beach profile variability, *Marine Geology*, 348, 103-112.

Knutson, T.R., McBride, J.L., Chan, J., Emanuel, K., Holland, G., Landsea, C., Held, I., Kossin, J.P., Srivastava, A.K. and Sugi, M. (2010). Tropical cyclones and climate change, *Nature Geosci.*, 3, 157-163

van der Zanden, J., Alsina, J.M., Cáceres, I., Buijsrogge, R.H. and Ribberink, J.S. (2015). Bed level motions and sheet flow processes in the swash zone: Observations with a new conductivity-based concentration measuring technique (CCM$^+$), *Coastal Engineering*, 105, 47-65.

van der Zanden, J., van der A, D.A., Hurther, D., Cáceres, I., O'Donoghue, T. and Ribberink, J.S. (2017). Suspended sediment transport around a large-scale laboratory breaker bar, *Coastal Engineering*, 125, 51-69.

van der Zanden, J., Cáceres, I., Eichentopf, S., Ribberink, J.S., van der Werf, J.J. and Alsina, J.M. (2019). Sand transport processes and bed level changes induced by two alternating laboratory swash events, *submitted for publication*.

van Rijn, L.C., Tonnon, P.K. and Walstra, D.J.R. (2011). Numerical modelling of erosion and accretion of plane sloping beaches at different scales, *Coastal Engineering*, 58, 637-655.

Webster, P.J., Holland, G.J., Curry, J.A. and Chang, H.-R. (2005). Changes in Tropical Cyclone Number, Duration, and Intensity in a Warming Environment, *Science,* 309(5742), 1844-1846

LARGE SCALE MODEL TEST ON SAND-FILLED GEOSYSTEMS FOR COASTAL PROTECTION (GEOS)

Adam Bezuijen (1), Luciana Das Neves (2), Ivàn Caceres (3), Altomare Corrado (4), Tomohiro Suzuki (5)

(1) Ghent University and Deltares, E-mail: adam.bezuijen@ugent.be
(2) IMDC and UPorto – Faculty of Engineering. E-mail: luciana.das.Neves@imdc.be
(3) Universitat Politècnica de Catalunya. E-mail: i.caceres@upc.edu
(4) Flanders Hydraulics Research. Email: corrado.altomare@upc.edu
(5) Flanders Hydraulics Research, E-mail: tomohiro.suzuki@mow.vlaanderen.be

Large scale model tests have been performed on a scale 1:5 in the ICTS-CIEM to test the stability of sand-filled geosystems, both tube and bags, and their effect on the morphological evolution of a beach profile. Tube and bags were buried in sand at the upper part of a beach profile with a slope 1:15 in the area where it was transitioning to a beach berm (horizontal flat section). Erosion of the beach during the experiment exposes the tube and bags to direct wave attack. Tests were done under the action of irregular waves with a significant wave height of 2.5 m in prototype, also the effect of two different water levels was considered. Under these conditions the erosion at the seaward side of the tube and bags was limited. Remarkable there was more erosion around the bags. As a consequence of the limited erosion the stability of the structure was never a problem.

1. INTRODUCTION

Flooding, erosion, inundation and extreme weather events affect hundreds of millions of people, important infrastructure, tourism and trade, causing significant human suffering and losses to national economies (World Bank, 2016). The predicted sea level rise and increased storminess in the coming decades is a great threat for the low-lying coastal regions. Existing coastal defences are often insufficient to protect these regions against extreme storms, thus it is mandatory to design and build protective countermeasures. For example, the Coastal Safety Master Plan (Afdeling Kust, 2011) from the Flemish government in Belgium is currently being implemented to provide better protection against extreme storm events. As a counter measure for an extreme storm, it recommends using a combination of a storm wall and beach nourishment. However, the build (and often the rebuild) of more traditional coastal protection measures is showing that many coastal stretches worldwide are still vulnerable to coastal storms and flooding. On top of that are additional restrictions, including costs, and environmental challenges.

Natural and nature-based features can enhance the resilience of coastal areas challenged by sea level rise (Borsje, 2011) and coastal storms (Gedan, 2011). A dynamic coastal protection as dunes is more resilient against sea level rise than fixed structures. This is proven by history: the dune system of the Netherlands and Belgium has adapted itself to the sea level rise in the past although sometimes with considerable erosion and loss of land. The much larger sea level rise that is predicted in the near future, and the need to stabilise the coastline will make human intervention in this natural process necessary. The advantage of a dynamic system is that for example beach nourishments can be continuously adapted to the circumstances (sea level, expected storms). A disadvantage is that significant changes in the coastline may occur in one storm due to erosion. The sand-filled geotextile tubes and bags (further abbreviated as Sand-Filled Elements, SFE) tested in this study have the advantage of a dynamic coast line but limits the erosion of the coast during large storm events because it provides some structural reinforcement. Furthermore, they are easy adaptable to sea level rise by installing new SFE above the first ones without the need to remove the old ones, while a traditional hard structure, normally has to be removed to build a new one.

2.   STATE OF THE ART

In recent decades, SFE have been studied intensively (e.g. Oumeraci et al., 2002; Van Steeg and Breteler 2008; Oumeraci and Recio, 2009; das Neves et al., 2015; Van Steeg and Vastenburg 2010; Dassanayake, 2013; and das Neves et al., 2015) as an additional or alternative coastal protection measure. The SFE concept has been tested through physical modelling in both large and small-scale fixed-bed model set-ups and proven its usefulness for coastal protection under certain circumstances. Most of the existing references focus on the stability of the bags; only das Neves (2011) also studied the morphological changes around geosystems, in a small-scale (scale 1:12) movable-bed model set-up. This means that although there are available design guidelines for the stability of these structures (Bezuijen and Vastenburg, 2013), still knowledge gaps can be identified. For instance, *(i)* the sediment transport mechanisms around the SFE; *(ii)* the amount of erosion in the leeside when the system is overtopped; *(iii)* quantitative contribution the SFE for the wave overtopping reduction; and *(iv)* failure mechanisms of the SFE under extreme conditions. Those questions can only be partly answered by using numerical models. There are in general substantial uncertainties and limitations (not only limited to one particular numerical model) for estimating aspects such as (but not limited to) wave-structure interaction and sediment transport, large scale physical model testing was necessary to develop the understanding of coastal processes around the SFE and to predict beach morphological change.

3.   AIM OF TESTS

The main objective of the present project is: to evaluate the SFE concept as proposed herein with respect to coastal protection and risk reduction by studying its influence on morphological changes in the coastal zone under storm wave conditions through large scale physical model testing. In addition, physical model results can be further used for the calibration of numerical models. In order to achieve that objective, the following research questions have been defined:

(i)   How do nearshore coastal processes (wave transformation, and sediment transport) and wave structure interactions during extreme events differ from those during more usual big storm conditions for situations with and without the SFE?

(ii) How do feedbacks between the hydrodynamics and morphology of natural and nature-based features affect flooding, erosion, and recovery of coastal areas when erosion is limited by the SFE?

(iii) How to conceive a dynamic coastal protection that can easily adapt to climate change in areas experiencing coastal squeeze (i.e. dense urban environment and human infrastructure with sea encroaching land) and vulnerable to coastal erosion and flooding risks?

4.   TESTS PERFORMED

Tests were performed in the CIEM wave flume of Barcelona (Universitat Politècnica de Catalunya), a large-scale wave flume of 100 m in length, 3 m in width and 4.5 m in depth.

The initial beach profile (Figure 1) is an idealised bathymetry consisting of a 1:10 approach slope starting at x-coordinate 36 m up to 43 m, measured along the flume from the wave paddle and going positive towards the shoreline. This initial slope is followed by a foreshore 1:25 slope for another 20 m (from x-coordinate 43 m up to 63 m). The beach profile continues for another 14.6 m on a 1:15 slope followed by a beach berm at 2.5 m crest elevation up to the other end of the wave flume opposite to the wave paddle.
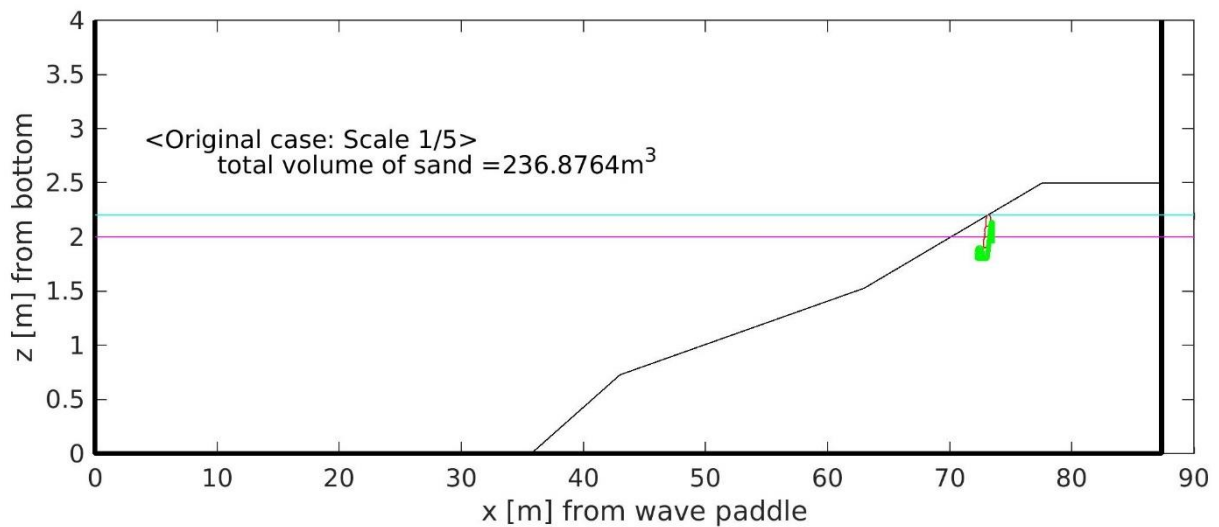
Figure 1. Theoretical initial bed condition. The geobags and geotubes were deployed at the same location (x around 72,42 m where the red and green construction present the geobags buried at that position). In cyan and magenta the SWL to be tested at 2.2 and 2 m

The experimental programme included four different test-series with varying protection and water level conditions (Table 1 *Table*).

Table 1. Experimental programme and sequence of the tests done during GEOS testing programme (in model dimensions)

Test-series	Protection	SWL (m)	H_s (m)	T_p (s)
1	none (benchmark)	2.2	0.5	4
2	Tube	2.2	0.5	4
3	Tube	2.0	0.5	4
4	Bags	2.2	0.5	4

Test-series were run under a unique wave time series for the whole experimental programme that consisted of an irregular wave train of 1000 waves with significant wave height of 0.5 m and peak wave period of 4 s, both in model dimensions, according to a JONSWAP spectrum (peak enhancement factor of 3.3).

As indicated in Table 1, test-series 1 was performed without protection as a benchmark for the other test-series. Test series 2 and 3 were run with a sand-filled geotextile tube protecting the beach profile, but with two different water levels being 2 and 2.2 m in the model. The last test-series, test-series 4, was run with the bags protecting the beach profile and the highest water level. Tube and bags location are sketched in Figure 2 and picture after construction of the tube and during construction of the bags is shown in Figure 3.
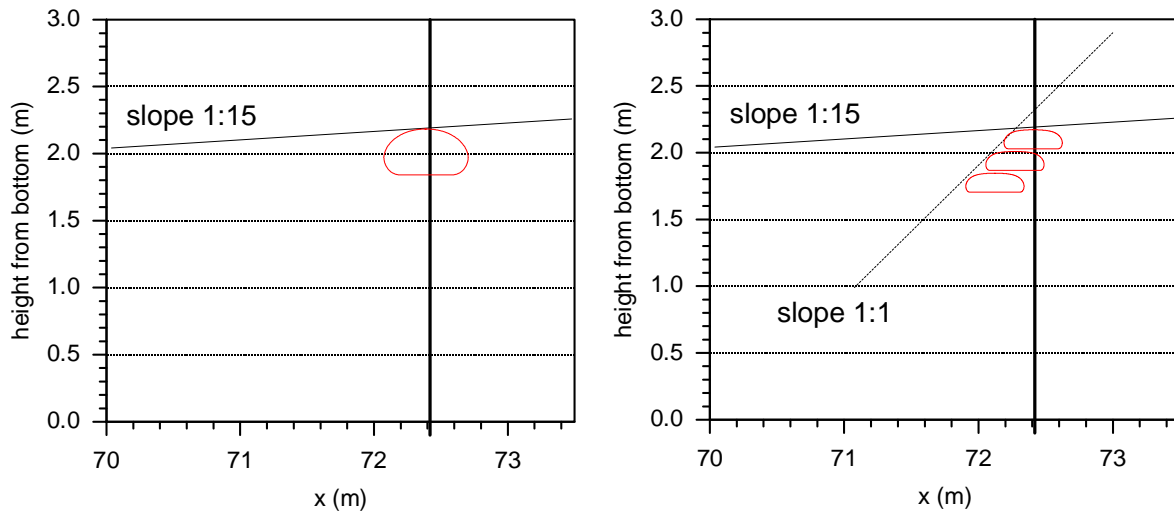
Figure 2. Theoretical position of tube and bags

Figure 3. Images of the a) geotube installed in the beach and b) geobags during installation in the beach

A median sediment grain size of 250 μm was used during the experiments. It should be noted here that this is the sand available at the wave flume, no active choice was made on this. The grain size distribution of the sand was determined in the past and is determined before the tests by sieving. The results are shown in Figure 4. The two recent test samples taken on different locations along the flume evidence almost the same grain size distribution.

The four test-series were produced by 14th repetitions of the same time series (1000 waves with H_s=0.5 m and T_p=4 s), which a duration of around 56 minutes. Before and after each time series, the initial beach profile was recorded for reference. Further measurements of surface elevation, flow velocity and sediment concentrations were recorded and monitored continuously. This paper focus on the morphological evolution of the beach profiles, specifically on the erosion in front of the sand-filled geosystem structures and profile changes within the breaking zone, for the various configurations tested.
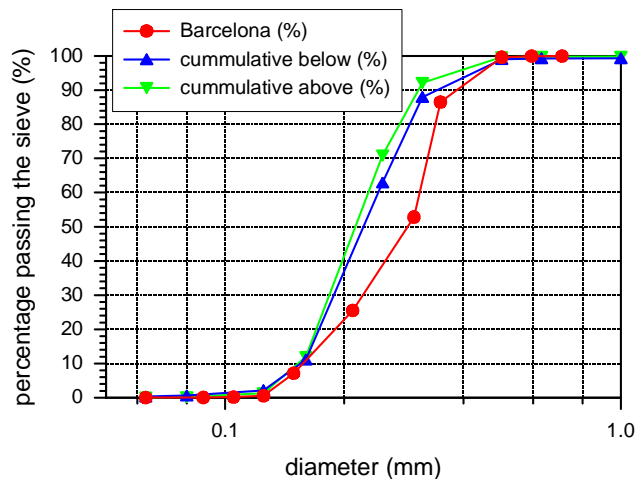
Figure 410. Grain size distribution of the sand used in the tests. The result marked Barcelona was an older determination, and the other two are from just before the tests

5. RESULTS

The developed erosion profile for Test 1, benchmark case, where the beach profile is not protected by SFE, after 14 hours testing is shown in Figure 5. Since there is no well-defined prototype all dimensions are given in model dimensions. The eroded volume is calculated from the upper part of the slope and starts at x-coordinate 86 m from the wave paddle through around 50 m, being at maximum in the area of the profile just above the submerged bar that develops within the profile.

Since the total volume of sand did not change the sum of erosion and accretion should be zero. This is not always the case, which may be justified by some offset in the measurements observed in some test-series. If this was the case, the data is corrected. In some cases, it appears not to be an offset and there may be some compaction of the sand. The difference is clear from the data. In the tests where this happened, the calculated eroded volume does not go back to zero. This may have an influence on the maximum eroded volume calculated from the test results (depending where the compaction occurs).
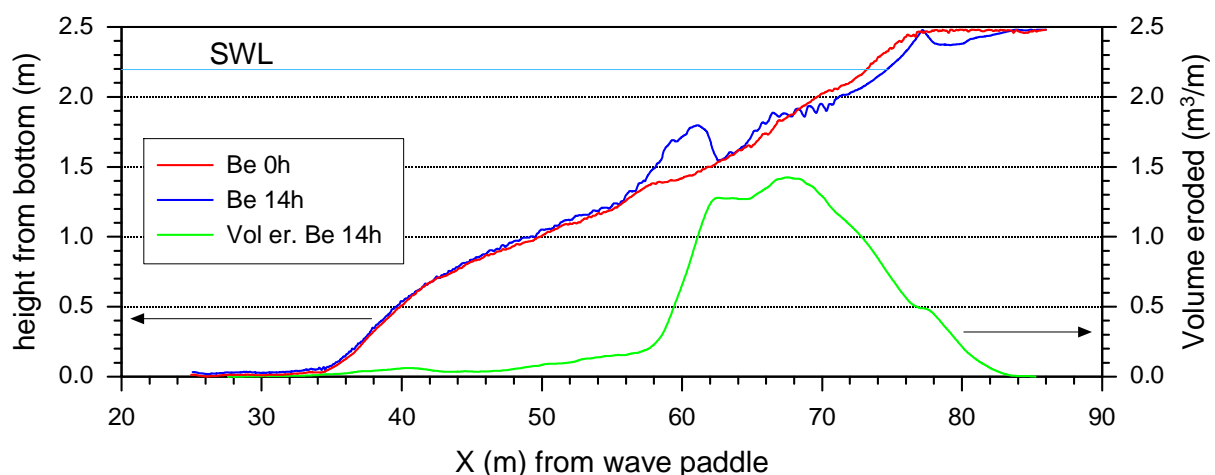

Figure 511. Benchmark test without SFE. Initial slope (Be 0h) and slope after 14 hours of testing (Be 14) and the eroded volume (Vol er. Be 14h)

As described in Van Rijn et al. (2011), the volume of the eroded sediment increases slowly and after 15 hours of testing there is not yet an equilibrium.

The expected influence of the sand-filled geotextile tube was to hold the sand on the landward side of the tube at the expense of more erosion on the seaward side. This appeared hardly the case, see Figure 6 and Figure 7. Only a localised small scour area developed just in front of the tube on the seaward side immediately in front of the geosystem. The erosion at 2 m water level was even less than at 2.2 m water level.

The erosion around the bags and the tubes is compared in Figure 8 and Figure 913. It appeared that the total erosion along the slope is quite comparable. However, there is significantly more scour developing just in front the bags, compared to that area around the tubes. Also, the line of the eroded volume does not reach 0 m^3/m close to the wave paddle. It can be that during the installation of the bags the sand was loosened and was compacted by wave action afterwards.
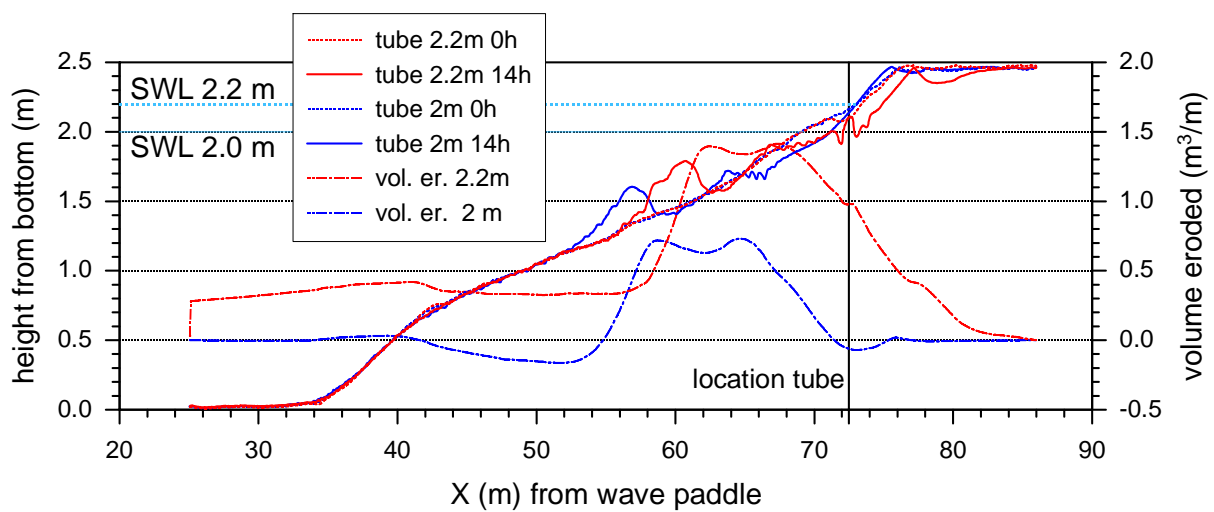

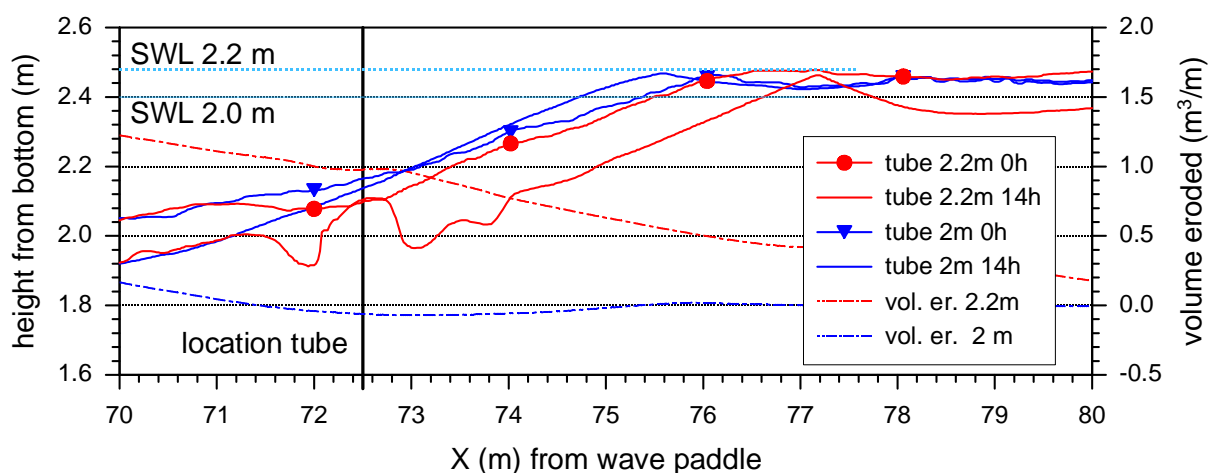*Figure 6. Measured erosion with tube installed in the beach for 2.2 and 2 m water level*

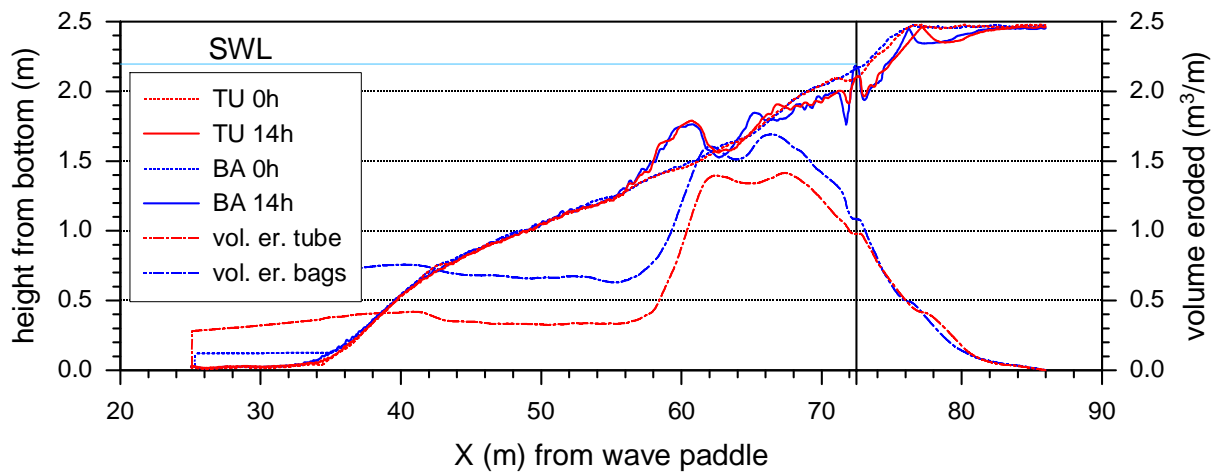*Figure 7. As Figure 6. Upper part of slope*

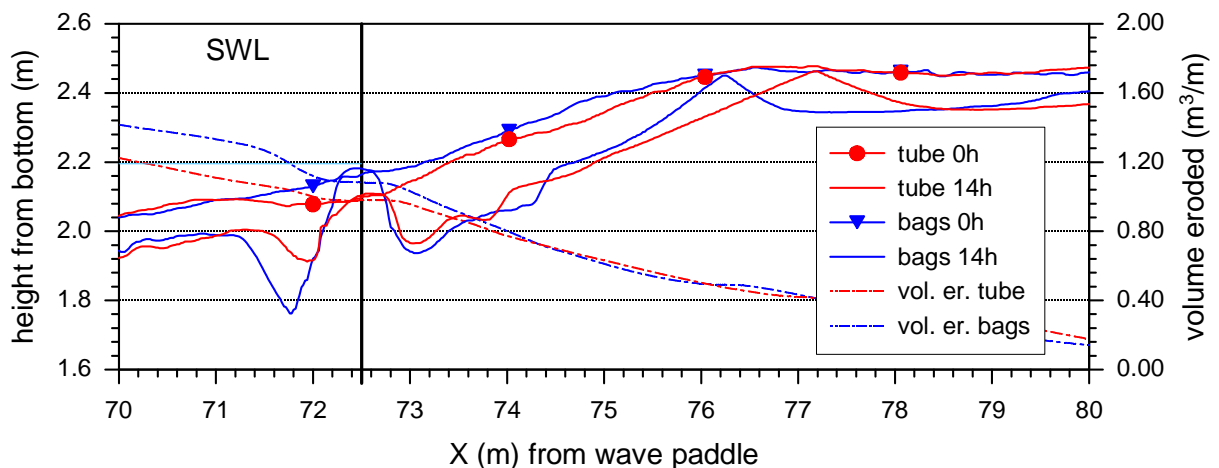*Figure 815. Erosion on beach with tube and bags compared.*

Figure 913. As Figure 9, upper part of slope

5. DISCUSSION AND CONCLUSION

The measured erosion is rather limited in all tests. According to the scaling laws given by Van Rijn (2011), the 250 μm sand in an undistorted 1:5 scale test corresponds to 616 μm in prototype. This is rather course sand, which explains to some extend the limited erosion. The measured erosion with respect to the eroded volume is in agreement with XBeach simulations. However, the submerged bar that develops within the breaking zone along the beach profile has a shape that is completely different from that predicted with XBeach,

The limited influence of the tubes and the bags on the erosion results, means that these elements can be applied as a dune toe protection, although it is advisable to check the results for circumstances where more erosion can be expected (for a situation with, scaled to prototype, smaller grains). Remarkable was that there was hardly any deformation for both the tube and bag structure during the tests, which indicates that these structures are internally sufficiently stable under wave heights of 0.5 m and the position on the beach tested here.

The difference in erosion around the structure between the tube and the bag is a remarkable result. This indicate that small differences in the structure already have quite an influence on the erosion results. This result needs further investigation, since this result can be rather important for necessary maintenance on these structures.

The tests indicate that a SFE dune toe protection is feasible. However, the tests described here are only a first indication. As mentioned, the erosion was limited, also the influence of tide and longshore current was not tested. However, the stability of the SFE structures and that, within the limits of testing, the influence of the water level is limited are promising results.

ACKNOWLEDGEMENT

REFERENCES

Afdeling Kust (2011). Masterplan Kustveiligheid.
http://www.afdelingkust.be/Userfiles/pdf/110628_RL_Rappor_%20KustveiligheidWEB4.pdf

Bezuijen, A., Vastenburg, E.W. (Editors), Geosystems, Design Rules and Applications, The Netherlands, Taylor & Francis/Balkema, ISBN 978-0-4156-2148-9

das Neves, L. (2011). Experimental Stability Analysis of Geotextile Encapsulated-sand Systems Under Wave-loadingPhD Thesis University of Porto, Faculty of Engineering, Portugal (290 pp.).

das Neves, L., A. Moreira, F. Taveira-Pinto, M.L. Lopes, F. Veloso-Gomes (2015). Performance of submerged nearshore sand-filled geosystems for coastal protection, Coastal Engineering, Volume 95, Jan. 2015, Pages 147-159, ISSN 03783839, http://dx.doi.org/10.1016/j.coastaleng.2014.10.005.

Borsje, B.W., B.K. van Wesenbeeck, F. Dekker, P. Paalvast, Tj. J. Bouma, M. M. van Katwijk, M.t B. de Vries (2011). How ecological engineering can serve in coastal protection (2011). Ecological Engineering, Volume 37, Issue 2, February 2011, Pages 113122, ISSN 09258574, http://dx.doi.org/10.1016/j.ecoleng.2010.11.027.

Dassanayake, D. (2013). Experimental and Numerical Modelling of Hydraulic Stability of Geotextile sand Containers for Coastal Protection PhD Thesis Fakultät Architektur, Bauingenieurwesen und Umweltwissenschaften der TU CaroloWilhelmina zu Braunschweig, Germany (182 pp.).

Gedan, Keryn B., Matthew L. Kirwan, Eric Wolanski, Edward B. Barbier, and Brian R. Silliman (2011). The present and future role of coastal wetland vegetation in protecting shorelines: answering recent challenges to the paradigm. Climatic Change Vol. 106, Issue 1, May, pages 729, ISSN 01650009, http://dx.doi.org/10.1007/s1058401000037

Oumeraci, H., Hinz,M., Bleck,M., Kübler, S. (2002). Großmaßstäbliche Untersuchungen zur hydraulischen Stabilität geotextiler Sand container unter Wellenbelastung. Leichtweiß Inst. for Hydr. Eng. and Water Resources, Braunschweig, Germany: Research Report no. 878, (in German).

Sánchez-Arcilla, A., Cáceres, I., Van Rijn, L., Grüne, J. (2011). Revisiting mobile bed tests for beach profile dynamics. Coastal Engineering, volume 58, Pages 583–593.

Van Rijn, L.C.; Tonnon, P.K.; Sánchez-Arcilla, A; Cáceres, I; Grüne J. Scaling laws for beach and dune erosion processes. Coastal Engineering 58 (2011) 623–636.

Van Steeg, P., and Breteler, K. (2008). Large scale physical model tests on the stability of geocontainers. DELTARES.

Van Steeg, P., and Vastenburg, E. (2010). Large scale physical model tests on the stability of geotextile tubes. DELTARES.

World Bank (2016). Managing Coasts with Natural Solutions: Guidelines for Measuring and Valuing the Coastal Protection Services of Mangroves and Coral Reefs. M. W. Beck and G-M. Lange, editors. Wealth Accounting and the Valuation of Ecosystem Services Partnership (WAVES), World Bank, Washington, DC.

X – HRW – FAST FLOW FACILITY

The Fast Flow Facility allows investigation into the complex way waves, currents and sediments interact at a larger scale and in more detail than has previously been possible, helping optimise designs more effectively and minimise the water based risks inherently involved in projects.

We can study sediment transport, scour and morphology for a wide range of subsea, coastal, estuarine and fluvial engineering projects, as well as the combined impact of waves and currents on structures in a fast flow environment.

The 75 m long, 8 m wide Fast Flow Facility holds a million litres of water, can generate waves up to 1 m high and flows of over 2 m/s. The size of the facility allows us to model complex structures and arrays without compromising on scale. The main working channel has a 60 m long test section, giving the space to look at array effects, long wakes behind structures and the relative placement of structures and devices.

In the marine renewable energy sector, developments in exposed marine environments are high risk: fast currents, deep water and energetic waves present significant technical challenges. The ability to model large structures and arrays, without compromising on scale, means that we can help our clients plan, install and maintain their assets in the most efficient way possible.

Instrumentation within the facility includes Nortek Vectrino II profiling ADV's, a Nortek HR Aquadopp, pressure transducers and an underwater laser scanner capable of measuring and monitoring the flume bathymetry with millimeter accuracy.

LARGE SCALE EXPERIMENTS TO IMPROVE MONOPILE SCOUR PROTECTION DESIGN ADAPTED TO CLIMATE CHANGE

Carlos Arboleda Chavez(1), Vasiliki Stratigaki(1), Minghao Wu(1), Peter Troch(1), Alexander Schendel(2), Mario Welzel(2), Raúl Villanueva(2), Torsten Schlurmann(2), Leen De Vos(3), Dogan Kisacik(4), Francisco Taveira Pinto(5), Tiago Ferradosa(5), Paulo Rosa Santos(5), Piet Haerens(6), Viktoria Szengel(6), Leen Baelus(6), Richard Whitehouse(7), David Todd(7).

(1) Ghent University. Department of Civil Engineering; vicky.stratigaki@ugent.be; minghao.wu@ugent.be; peter.troch@ugent.be.
(2) Ludwig-Franzius-Institute for Hydraulic Estuarine and Coastal Engineering; schendel@lufi.uni-hannover.de; welzel@lufi.uni-hannover.de; villanueva@lufi.uni-hannover.de; schlurmann@lufi.uni-hannover.de.
(3) Geotechnics Division, Department of Mobility and Public Works, Flemish Government; leen.devos@mow.vlaanderen.be
(4)   Dokuz Eylül University. Institute of Marine Sciences and Technology; dogankisacik@gmail.com.
(5)   Universidade do Porto. Faculty of Engineering; tferradosa@fe.up.pt; pjrsantos@fe.up.pt; fpinto@fe.up.pt.
(6)   International Marine & Dredging Consultant N.V.; piet.haerens@imdc.be; viktoria.szengel@imdc.be; leen.baelus@imdc.be.
(7)   HR Wallingford Ltd; r.whitehouse@hrwallingford.com; d.todd@hrwallingford.com.

This study aims to improve the design of scour protection around offshore wind turbine monopiles, as well as future-proofing them against the impacts of climate change. A series of large scale experiments have been performed in the context of the PROTEUS (PRotection of Offshore wind Turbine monopilEs against Scouring) project in the Fast Flow Facility in H.R. Wallingford. These experiments make use of state of the art optical and acoustic measurement techniques to assess the damage of scour protections under the combined action of waves and currents.

1.   INTRODUCTION AND OBJECTIVES

A series of large scale experiments have been performed in the context of the PROTEUS (PRotection of Offshore wind Turbine monopilEs against Scouring) project in the Fast Flow Facility in H.R. Wallingford in the United Kingdom. The PROTEUS testing campaign is a collaborative effort between the Department of Civil Engineering at Ghent University (Belgium), HR Wallingford (UK), the Ludwig-Franzius Institute for Hydraulic, Estuarine and Coastal Engineering at the University of Hannover (Germany), the Faculty of Engineering at the University of Porto (Portugal), the Geotechnics division of the Belgian Department of Mobility and Public Works (Belgium), and the International Marine and Dredging Consultants (IMDC nv) (Belgium). PROTEUS is performed in the context of the European Hydralab+ programme and funded by the EU's Horizon 2020 Research and Innovation Programme.

De Vos et al. (2012) studied the disintegration failure mode of an armor layer over a geotextile under different hydrodynamic conditions. Static and dynamic stability of the armor layer were tested in a model scale of 1:50 (all the scale factors consider a prototype monopile diameter of 5 m) under different waves, currents and a combined action of both flows. Loosveldt & Vannieuwenhyuse (2012) extended the test dataset of De Vos et al. (2012) by including larger grain sizes, by varying the water depth and by performing a parametric analysis of the pile diameter (scales of 1:100, 1:50, 1:40) on the scour protection damage. Nielsen et al. (2013) focused on the winnowing of scour protection under different waves and currents. The testing scales used for the current experiments were 1:35.7, 1:9 and 1:5. Nielsen et al. (2013) provided an answer to the sinking of the scour protections in the "Horns Rev 1" wind farm and gave improved guidelines for the design of filter layers through the mobility parameter. Whitehouse et al. (2014) evoked an optimization of scour protection design taking into account rock size, density, number of layers and width of the cover. Finally, Petersen et al. (2014) performed experiments using physical models with a scale 1:100 to 1:50 for the study of edge scour under waves and currents.

Schendel et al. (2014, 2016) presented large scale experiments of scour protection design under waves and currents. The scale used for wave tests which included a monopile was 1:5, whereas,

the scale for current tests without a monopile was 1:1. In the latter case, the material tested as scour protection was the actual prototype material. This work introduced a single armor layer composed of a wide-graded material. 'Wide-graded' refers to a large geometric standard deviation of the granular material composing the scour protection (D84/D16 > 1.5, for wide graded material and D84/D16 >2.5 for very wide graded material, where D84 and D16 account for the diameter larger than 84 % and 16 % of the mass of the material, see Rock Manual (2007) Table 3.4). The usage of this novel technique could show itself easier to install, as well as cost effective compared to a traditional two-layer scour protection design (filter and armor). Nevertheless, it is concluded that more experiments should be carried out to fully understand the stabilizing process of using wide-graded materials as scour protection. In this direction, Petersen et al. (2018) studied different compositions of scour protection material in small scale experiments (scales of 1:100 – 1:45.45) under a unidirectional current.

Deterministic design criteria exist for the classic narrow graded two-layer scour protection (De Vos et al. (2012), Nielsen et al. (2013)) but none has been established for wide-graded materials. Fazeres Ferradosa et al. 2018 proposed a reliability analysis of the scour protection failure and proposed a probabilistic design, without considering the gradation of the scour protection material. The aim of this manuscript is to present the PROTEUS project, and specifically to present the experimental setup, the methodology followed throughout the study and quality of the unique dataset acquired during the testing campaign, which addresses the data and knowledge gaps in scour protection studies. The novel PROTEUS experiments, presented further in this paper, test the static and dynamic stability of different scour protection designs including monopiles at two different large scales 1:16.66 and 1:8.33, under the combined action of waves and currents.

2. EXPERIMENTAL SET-UP

The FFF experimental facility is a race-track shaped flume (illustrated in Figure 1). It comprises a main working channel, 4.0 m wide and 57.0 m long, and a secondary channel, 2.6 m wide and 50.0 m long. The hinge flat type multi-element wave generator with active wave absorption (located at the left in Figure 1) can deliver significant wave heights up to 0.5 m and a maximum wave height up to 1.0 m, depending on the water depth. The water depth can be set in the range of 0.85-2.00 m. At the opposite side of the wave generator (at the right in Figure 1), a beach made of sponge material passively absorbs the generated wave trains. The axial pumps (located in the secondary channel) can deliver a discharge of up to 3.5 m3/s and their reversible nature can provide a current propagation following or opposing the waves.
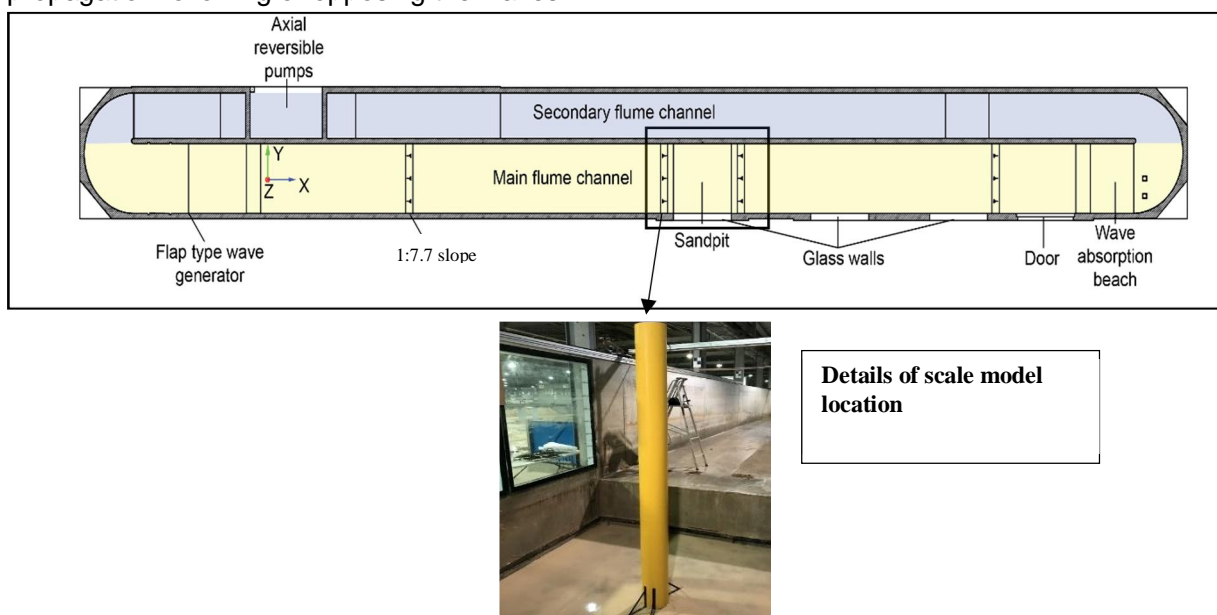

Figure 1. Sketch of the FFF flume channels presenting the position of the scale models.

A local reference system was established with the origin being at the front of the wave maker, in the middle of the channel on the flume floor. The positive x-axis points into the wave propagation direction (from left to right in Figure 1), the positive y-axis points upwards in the top view in Figure 1 and the positive z-axis follows the gravity vector. In the sketch of the main channel (Figure 2), the position of the resistive Wave Gauges (abbreviated as WGs), the Acoustic Doppler Velocity meters (ADVs) and the scale model of a monopile are indicated.

There are two variants of monopile scale models with two different diameters, $D_p = 0.3$ and $D_p = 0.6$ m, and are constructed from thin-walled metal (Figure 2). Each monopile model is placed in the wave flume with its center at x=30 m and y = 0 m, following the local reference system presented in Figure 1. The sand pit consists of a 4.0 m long, 4.0 m wide and 1.0 m high box. This sand pit size provides the necessary area for testing large scale scour protection models over a sand bed, which is composed of uniform sand, $d_{50} = 0.21$ mm, for all tests.
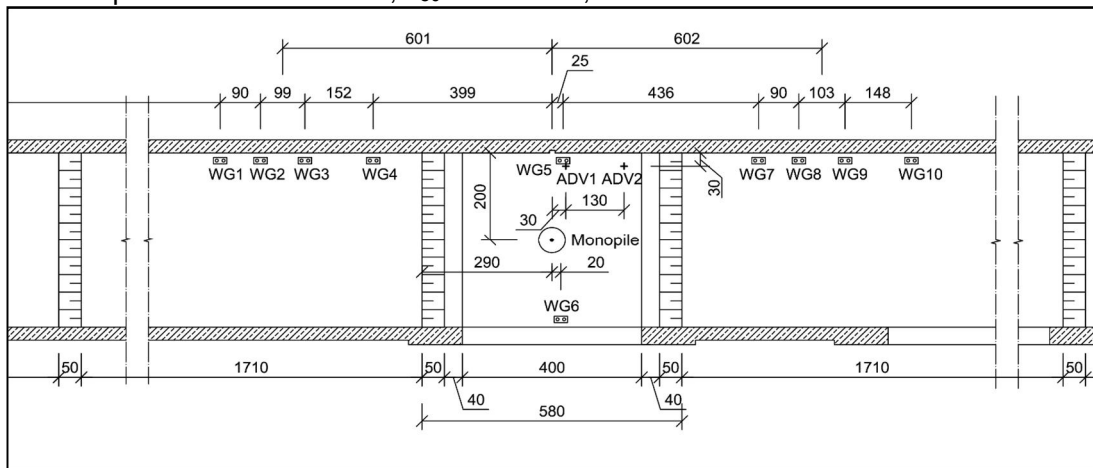

Figure 2. Positions of the 10 resistive wave gauges (WG1-WG10) and the 2 Acoustic Doppler Velocity meters (ADV1 and ADV2) in the main flume channel. Dimensions are in mm.

During the testing campaign data is recorded in both the main and the secondary flume channels. In the main flume channel, in order to characterize the flow in the vicinity of the monopile, the free surface elevations and 3D flow velocities are recorded at ten and two (point velocity measurements) locations, respectively (see Figure 2). In the secondary channel, in order to characterize the current characteristics in the facility, profile of horizontal flow velocities and free surface elevation are measured at one location, respectively. Before the onset of motion test and after every damage development tests, the topography of the scour protection model is measured. The topography measurements provide the initial, intermediary and final state of the scour protection model. Photographic material is produced before the filling and after the draining of the flume. These measured quantities, the instruments used and the sampling frequency of the instruments are presented in Table 1.

Table 1. Measured parameters and instrumentation

Measured parameter		Instrumentation	Sampling frequency
Free surface elevation		Resistive Wave Gauges (WGs)	100 Hz
Flow velocities	3D point measurements	Acoustic Doppler Velocity meters (ADVs)	100 Hz
	Profile measurements of the horizontal velocity	Aquadopp profiler	1 Hz
Scour protection model topography		ULS-200 laser scanner	7 Hz (7mm/s)
Photographic material		Cameras	-

4. EXPERIMENTAL TEST PROGRAMME

Two types of tests are carried out during this testing campaign, namely, onset of motion and damage development tests for each of the scour protection models. The testing programme objectives are (i) to compare the performance of single-layer wide-graded material used against scouring with current design practices, and (ii) to verify the stability of the scour protection designs under extreme weather conditions. Hereafter, the experimental conditions are presented and summarized in Table 6, Table 7 and Table 8. In Table 6 and Table 7, the experiments' basic hydrodynamic conditions and the hydrodynamic variants are included. The variants of a test are performed successively, for which the wave height and wave period are modified for onset of motion tests, and the number of waves changes for damage developments tests.

4.1 Onset of motion tests

Onset of motion experiments assess the stability of the scour protection from a statically stable design point of view. From this perspective, failure is considered if armoring material is removed over a minimum area of four armor units ($4 \times D_{50}^2$, D_{50} is the mean stone diameter of the scour protection model). Such design of the scour protection allows very little motion of the scour protection material. During onset of motion tests, when the desired current velocity is reached and stable, short regular wave trains (12 waves) are generated. The scour protection is observed throughout the propagation of the wave train in order to spot motion of the scour protection material. Motion of scour protection material (stones) refers to the displacement of a stone which size, d_s, is larger or equal to the mean stone diameter ($d_s > D_{50}$) for a distance at least equal to two times the mean stone diameter De Vos et al. (2012). Once it has been established if motion of the stones occurred, new wave conditions are tested, while the current generation is not interrupted in-between applying different wave conditions. The test conditions for the onset of motion tests are shown in Table 6.

Table 6. Onset of motion test conditions. The highlighted conditions are the ones where motion of scour protection material is spotted.

Test no.	Water depth	Monopile diameter	Current Velocity	Test variant	Wave height	Wave period
S/N	d [m]	Dp [m]	Uc [m/s]	S/N	H [m]	T [s]
03	1.2	0.3	-0.25	A	0.22	2.94
				B	0.28	2.94
				C	0.27	2.94
				D	0.33	2.47
				E	0.39	2.47
05	1.5	0.3	0.27	A	0.20	2.91
				B	0.22	2.93
				C	0.28	2.98
				D	0.32	2.94
				E	0.35	2.94
				F	0.32	2.51
				G	0.37	2.48
07	1.2	0.3	-0.23	A	0.25	2.94
				B	0.29	2.94
				C	0.33	2.46
				D	0.31	2.46
09	0.9	0.3	-0.23	A	0.20	2.46
				B	0.22	2.06
				C	0.26	2.08
11	1.8	0.6	-0.39	A	0.50	3.50
				B	0.37	3.48
				C	0.42	3.48
				D	0.54	3.48
				E	0.41	2.84
				F	0.46	2.85
				G	0.50	2.83
				H	0.56	2.85

4.2 Damage development tests

Damage development assess a dynamically stable design of scour protections. Such design allows some motion of the scour protection material. The criteria for considering the failure of the scour protection is the global damage number, S3D. Following the methodology De Vos et al. (2012), the scour protection model is subdivided into subsections with an area equal to the area of the monopile as shown in Figure 3.
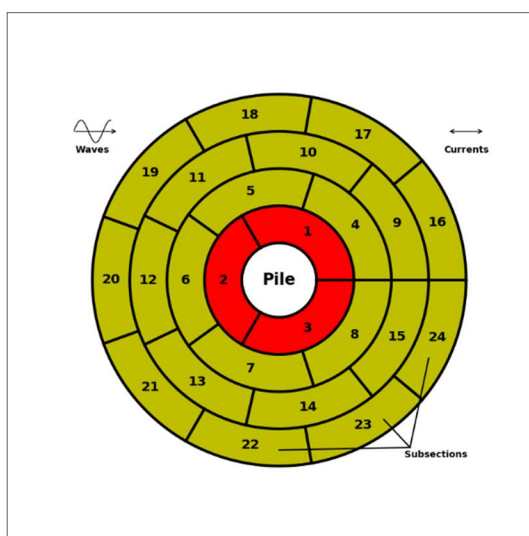
Figure 3. Sketch of the scour protection model around the monopile divided in subsections as in De Vos et al. (2012), with the inner ring in red. The wave and current propagation directions are also indicated.

The damage number of each of the subsections is calculated from the eroded volume, V_e, the nominal mean diameter, D_{n50}, and the monopile diameter, D_p, using the formula:

$$S_{3D,sub} = \frac{V_e}{D_{n50} \, \pi \, \frac{D_p^2}{4}} \qquad (1)$$

The global damage number is obtained by considering the maximum damage number of the subsections:

$$S_{3D} = \max(S_{3D,sub}) \qquad (2)$$

Damage development tests are performed in a similar way as the onset of motion test; when the current has reached the desired velocity, a long wave train is generated (1000 irregular waves). The current is stopped and a topography laser scan takes place. Then, a longer wave train of 2000 irregular waves is generated and, finally, the last laser scan is performed. Test 14 has an additional 2000 waves wave train, followed by a laser scan (Table 7). V_e will be determined by the comparison of the topography laser scans. The test conditions for the damage development tests are shown in Table 7.

Table 7. Damage development test conditions

					Test Variant	A	B	C
	Water depth	Monopile diameter	Significant wave height	Peak wave period	Current mean velocity	Number of waves		
Test no.	d [m]	Dp [m]	Hs [m]	Tp [s]	Uc [m/s]	N [-]	N [-]	N [-]
04	1,2	0,3	0,225	2,46	-0,5	1000	2000	
06	1,5	0,3	0,37	2,2	0,34	1000	2000	
08	1,2	0,3	0,17	2,46	-0,5	1000	2000	
10	0,9	0,3	0,175	2	-0,34	1000	2000	
12	1,8	0,6	0,35	2,83	-0,49	1000	2000	
13	1,5	0,6	0,37	2,2	-0,58	1000	2000	

| 14 | 1,8 | 0,6 | 0,35 | 2,83 | -0,49 | 1000 | 2000 | 2000 |
| 15 | 1,8 | 0,6 | 0,35 | 2,83 | -0,49 | 1000 | 2000 | |

Other than the hydrodynamic conditions, the properties of the scour protection material are tested. The intrinsic properties of the scour protection material the mean stone diameter, D50, geometric standard deviation of the material composition, D84/D16, are stated in Table 8.

Table 8. Properties of scour protection composition and indication of usage

Scour protection Mixture no.	Test no.	Mean diameter	Geometric standard deviation of the material
S/N	S/N	D50 [mm]	D84/D16 [-]
1	03/04	12.5	2.48
2	05/06	6.75	2.48
3	07/08/09/10	6.75	2.48
4	11/12/13	13.5	2.48
5	14	13.5	6
6	15	13.5	12
7 (Geotextile)	03/04/07/08	-	-

Mixture 1 is the scale model of a standardize grading 2-80 kg. A wide-graded material with a mean diameter of 110 mm in prototype scale is studied at intermediate model scale by Mixture 2 and 3 and at large scale model by Mixtures 4, 5 and 6. The variable between Mixtures 4, 5 and 6 is the geometric standard deviation of the material. Figure 4 presents the grain size distribution of the mixtures, as obtained from the fabrication of the mixtures.
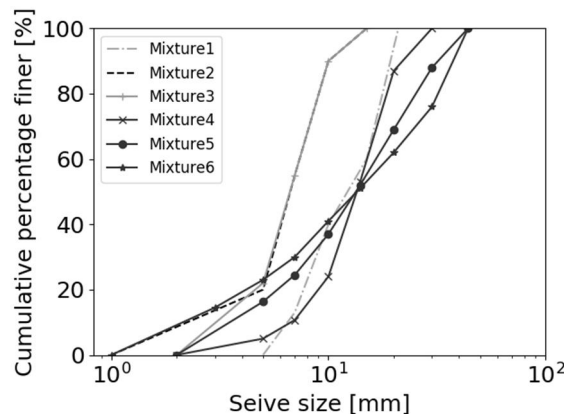

Figure 4. Percentage finer against the sieve size for the 6 tested mixtures

The use of geotextile as an installation method was studied in tests 03/04/07/08 at intermediate model scale.

5. RESULTS AND DISCUSSION

Results from Test 04 are presented in the present manuscript. During Test 04, the hydrodynamic conditions represent an extreme climate change driven condition of a current with a velocity U_c = 2 m/s at prototype scale. The scour protection model is subjected to considerable hydrodynamic loads. The visual assessment of the damage is of "Level 3" (damage without failure) following the criteria presented in by De Vos et al. (2012) used for visual assessment of the damage levels:

- Level 1: no movement of the stones
- Level 2: very limited movement of stones
- Level 3: significant movement of stones, without failure of the protection
- Level 4: failure of the protection

The static stability of the scour protection models are assessed in the onset of motion test shown in Table 6, where tests where motion of the scour protection material (stones) was spotted, are highlighted. The visibility in the facility was not appropriate when the current was established, once the wave generation started, the sediment transport was enhanced and the turbidity of the water increased substantially. Therefore, the results of the onset of motion test need to be considered with care because of their qualitative nature.

Scour protection damage development tests, such as Test 04, are composed of at least two wave trains. In the Section 3, it has been stated that optical material is collected before and after the tests. In Figure 5, the merged optical material is shown for Test 04. The initial state of the scour protection model can be seen in the left panel (Figure 6a), and the final state on the right panel (Figure 6b). In Figure 5b the displacement of the scour protection material of the inner ring (red stones) can be clearly be observed in the direction of the current propagation. Furthermore, deposition of sediment material is seen on top of the scour protection, outside of the inner ring region.
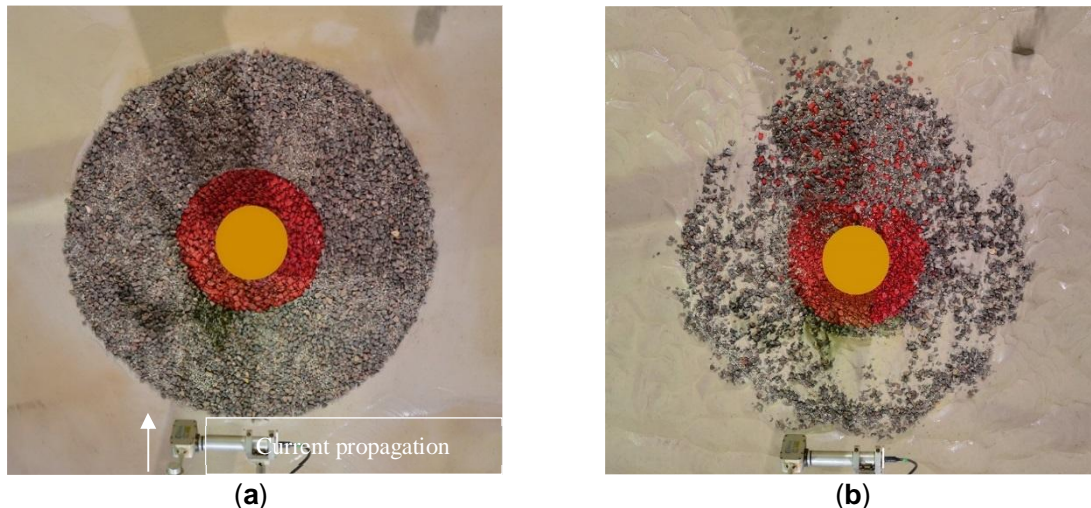

(**a**)   (**b**)

Figure 5. Merged picture of the scour protection scale model Tests 0 4 before (left) and after (right) the test.

This initial visual assessment of the damage of the scour protection is corroborated by the topographic laser scans shown in Figure 6. In Figure 6 topography of the scour protection material at the initial state, after 1000 waves (Test 04_A) and after 3000 waves (Test 04_B) are shown. Regions with higher elevation are shown in red color, while the lower elevation regions are shown in blue color. Through Test 04, in Figure 6, the development of two symmetrically eroded zones can be observed in the wake of the monopile, in the direction of the current. Upstream, just in front of the monopile in Figure 6, the development of scour is clear and shown by an increasing dark blue region. Furthermore, upstream of the monopile, the sedimentation outside the inner ring is clearly progressing from the middle laser scan (Figure 7b) to the right scan (Figure 7c).
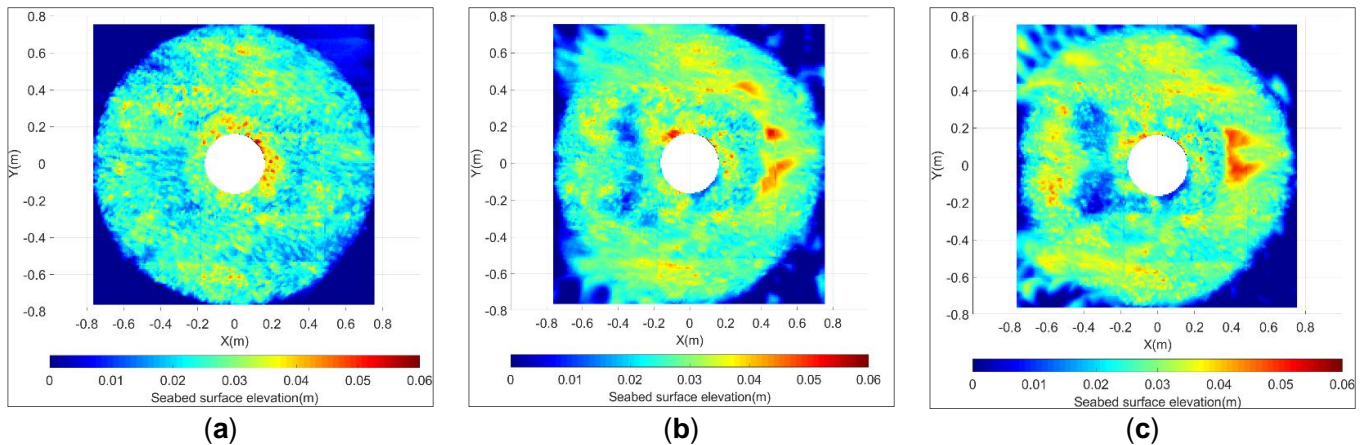
(**a**)　　　　　　　　　　　(**b**)　　　　　　　　　　　(**c**)

Figure 6. *Topography of the scour protection material and of the sand pit measured by the laser scanner before Test 03 (a), after the first 1000 waves of Test 04_A (b*) and after 3000 waves at the end of Test 04_B (c). The current propagation in this set of figures is from right to left.

From Figure 5 and Figure 6 it is clear that the scour protection material has undergone damage caused by the hydrodynamic action of the flow. This damage development becomes even clearer when each subsection considered separately, in Figure 7.
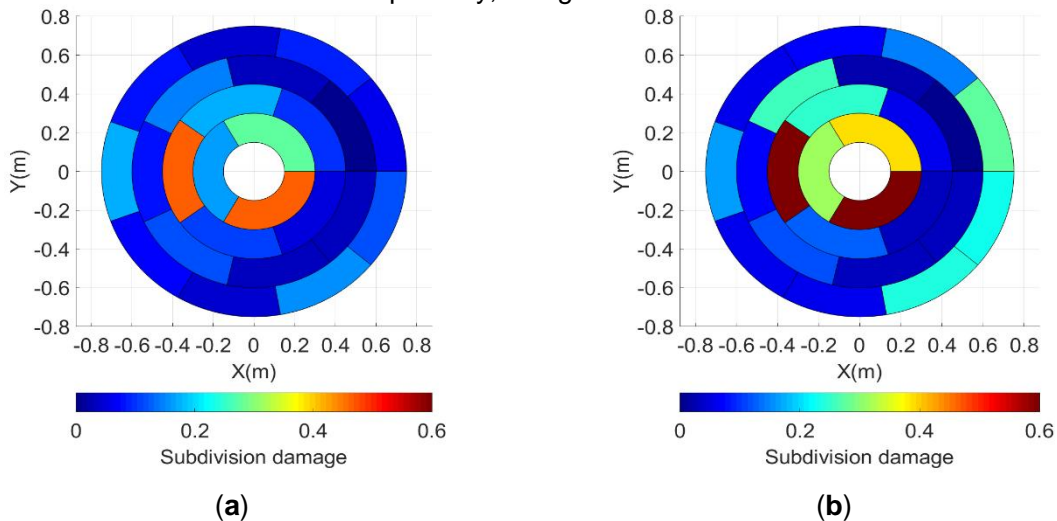

(**a**)　　　　　　　　　　　　　　(**b**)

Figure 7. Test 04 subdivision damage number: after 1000 waves Test 04_A (a) and after 3000 waves Test 04_B (b). The current propagation in this set of figures is from right to left.

From the tested hydrodynamic conditions, the measured damage and the predicted damage of the scour protection material are presented in Table 9. The S_{3D} number is the indicator that characterise the scour protection material damage. The predicted damage of the scour protection material is obtained from the damage prediction formula (Equation 3) presented by De Vos et al. (2012):

$$\frac{S_{3D}}{N^{b_0}} = a_0 \frac{U_m^3 T_{m-1,0}^2}{\sqrt{gd}(s-1)^{\frac{3}{2}}D_{n50}^2} + a_1 \left(a_2 + a_3 \frac{\left(\frac{U_c}{w_s}\right)^2 (U_c + a_4 U_m)^2 \sqrt{d}}{gD_{n50}^{3/2}} \right) \tag{3}$$

More information on Equations 3 can be found in De Vos et al. (2012). A significant deviation in magnitude of the predicted and the measured S3D for the scour protection material can be seen from Table 9. It is important to note that the damage prediction formula, Equation 3, was established for a scale 1:50 while the scale of Test 04 is 1:16.667. This deviation can be accounted for the scale effects introduced by the present testing campaign.

Table 9. Measured and predicted S3D number for Test 04_A and 4_B

	Mean grain size	Geometric standard deviation	Number of waves	Pile diameter	Water depth	Significant wave height	Peak period	Mean current velocity	Predicted damage number	Measured damage number
Test no.	D50 [mm]	D84/D16 [-]	N [-]	Dp [m]	d [m]	Hs [m]	Tp [m]	Uc [m/s]	Predicted S3D	Measured S3D
Test 04_A	12.5	2.48	1000	0.3	1.2	0.25	2.45	-0.461	1.834	0.465
Test 04_B	12.5	2.48	2000	0.3	1.2	0.24	2.48	-0.462	2.141	0.675

6. CONCLUSIONS

The experiments performed at the FFF at HR Wallingford have yielded a large dataset that provide a benchmark for large scale experiments of scour protection designs around monopiles. The full extent of the obtained results will be made available in future studies that will focus in more detail on the impact of specific parameters and methodologies of damage assessment. The comparison of the basic analysis of the damage development results and the predicted damage, shows that scale effect are not accounted by the prediction formula, Equation 3. Further analysis of the acquired data will provide valuable insight in scale effects and the performance of wide-graded materials.

ACKNOWLEDGEMENT

REFERENCES

Whitehouse R. *Scour at marine structures*. Telford, London, UK, 1998.

Sumer, B.; Fredsoe, J. The Mechanics of Scour in the Marine Environment. Advanced series on ocean engineering. World Scientific, River Edge, N.J., USA, 2002.

De Vos, L. ; De Rouck, J. ; Troch, P. ; Frigaard P. Empirical design of scour protections around monopile foundations. Part 2: Dynamic approach. *Coastal Engineering* 2012, 60, 286-298.

Loosveldt N.; Vannieuwenhyuse K. Experimental validation of empirical design of a scour protection around monopiles under combined wave and current loading. MSc thesis, Ghent University, Ghent, Belgium, 2012.

Nielsen A. W.; Liu X.; Sumer B. M.; Fredsoe J. Flow and bed shear stresses in scour protections around a pile in a current, Coastal Engineering, 2013, 72, 20-38

Whitehouse, R.; Brown, A.; Audenaert, S.; Bolle, A.; de Schoesitter, P.; Haerens, P.; Baelus, L.; Troch, P.; das Neves, L.; Ferradosa, T.; Pinto, F. Optimising scour protection stability at offshore foundations. Proc. 7nd International Conference on Scour and Erosion (ICSE-7), 2014.

Petersen, T.U. Scour around Offshore Wind Turbine Foundations. 2014, PhD Manuscript, Technical University of Denmark.

Schendel, A; Goseberg, N.; Schlurmann, T. Experimental study on the performance of coarse grain materials as scour protection. *Coastal Engineering Proceedings* **2014**, 1(34), 58.

Schendel, A; Goseberg, N.; Schlurmann, T. Erosion Stability of Wide-Graded Quarry-Stone Material under Unidirectional Current. *Journal of Waterway, Port, Coastal, and Ocean Engineering*, **2015**, 142

CIRIA, CUR, CETMEF, *The Rock Manual. The use of rock in hydraulic engineering*, 2nd ed. C683, CIRIA, London, UK, 2007, ISBN 978-0-86017-683-1

Petersen, T. U.; Nielsen, A; Hansen, D. A.; Christensen, E.; Fredsoe, J. Stability of single-graded scour protection around a monopile in current. Scour and Erosion IX: Proceedings of the 9th

International Conference on Scour and Erosion (ICSE 2018), November 5-8, 2018, Taipei, Taiwan, CRC Press, October 10, 2018.

SPLITTING NATURE AT ITS SEAMS: MORPHODYNAMIC STABILITY OF RIVER AND TIDAL BIFURCATIONS

Maarten Kleinhans (1), Kaspar Sonnemans (1), Michele Bolla Pittaluga (2),
Maarten van der Vegt (1), Lisanne Braat (1), Jasper Leuven (1), Stefano Lanzoni (3),
Alessandro Sgarabotto (3), Manuel Bogoni (3), Zheng Bing Wang (4),
Nicoletta Tambroni (2), Giovanni Coco (5) & David Todd (6)

(1) Utrecht University, the Netherlands, E-mail: m.g.kleinhans@uu.nl
(2) University of Genova, Italy, E-mail: michele.bollapittaluga@unige.it
(3) University of Padua, Italy, E-mail: stefano.lanzoni@dicea.unipd.it
(4) Delft University of Technology, Netherlands, E-mail: Z.B.Wang@tudelft.nl
(5) University of Auckland, New Zealand, E-mail: g.coco@auckland.ac.nz
(6) HR Wallingford, England, E-mail: D.Todd@hrwallingford.com

Channel bifurcations split flow and sediment around fluvial and tidal bars in rivers and estuaries and at junctions in river deltas and tidal deltas. Their long-term development depends on the balance between sediment partitioned at the bifurcation and the transport capacity in the bifurcated channels. For unidirectional flow, theory predicts that stability depends on channel width-to-depth ratio and sediment mobility, but this has not been tested under high sediment mobility and in tidal conditions. Here we report on nine unidirectional and bidirectional flow experiments on a sand bed with a splitter plate wherein bed development and flow partitioning were monitored. Results show that fluvial and tidal experiments develop unstable bifurcations for intermediate and high sediment mobility and channel width-to-depth ratio in agreement with theory.

1. INTRODUCTION

Multithread rivers such as the Jamuna and Mekong have networks of channels separated by bars that change with every flood. Likewise, tidal systems such as the Scheldt, Humber and Columbia estuaries and short tidal basins in the Wadden Sea and in Florida, have interacting channels and shoals formed by ebb and flood currents. Main channels are economically important shipping fairways, whilst shoal areas that emerge and submerge daily are ecologically valuable habitats. Channel bifurcations are critical elements that partition flow and sediment through the channel network, govern bar merging and splitting and are locations where bed steps form in shipping lanes, as in river bifurcations. Stability and equilibrium configurations are mostly unknown for tidal bifurcations except for one recent theory (Jeuken & Wang 2010). In particular, we have a fair understanding of the tidal flow dynamics, but understanding of the morphodynamics, especially related to the sediment division at the bifurcation, is mostly lacking. Here we begin to build on the better but as yet incomplete understanding of river bifurcations.

The stability of river bifurcations has been studied for two decades in fieldwork, experimentation, linear stability theory and numerical modelling (e.g., Wang et al. 1995, Bolla Pittaluga et al. 2003, Kleinhans et al. 2013). A recent theory (Bolla Pittaluga et al. 2015) synthesises many of the earlier results as follows. For the case of a symmetrical bifurcation with a minor water depth perturbation in one of the bifurcates, the nonlinear relation between flow and sediment transport leads to higher transport in the deeper bifurcate, while the upstream sediment division is symmetrical. This tends to cause runaway channel incision in the deeper channel, and more so close to the beginning of sediment motion or high suspension where the nonlinear effects are more important. However, as one channel deepens and the other shallows, a transverse bed slope develops around the bifurcation. This leads to downslope sediment deflection, causing a transverse flux towards the deeper channel. For low aspect ratios, i.e. width-to-depth ratio, the slope effect is sufficient to counteract the incision of the deeper channel, with the result that the bifurcation stabilises. The theory assumes that the slope effect also affects the suspended bed material load for lack of better understanding of the lateral diffusion processes. In brief, bifurcation stability depends mainly on channel aspect ratio and sediment mobility.

As a result, symmetrical bifurcations in bedload-dominated rivers of modest and larger aspect ratios are predicted to be unstable and shift, when perturbed, towards a highly asymmetrical division of discharge and sediment. In the case of suspended sediment-dominated rivers the theory predicts stable bifurcations for intermediate sediment mobility. However, there is very little data for conditions intermediate between low and high mobility rivers.

Moreover, we have no idea whether bifurcations in reversing tidal flow are unstable for configurations and conditions similar to those of rivers. Here we consider configurations that are entirely free of topographic forcing on the flow, namely straight channels split into two branches over some length, with one perturbed in depth. Any form of topographic forcing and channel curvature will cause deviations in bifurcation stability (van Veen 1950, Kleinhans et al. 2008) and are disregarded here. Our objective is therefore to experimentally investigate bifurcation stability under a range of sediment mobility and channel aspect ratio in unidirectional flows and reversing tidal flows.

2.   METHODS AND MATERIALS

The methodology is to study the development of initially symmetrical, but perturbed bifurcations in the idealised condition of a straight flume with a splitter plate that schematize a central bar without any planimetric, topographic forcing. Creating reversing tidal currents in large morphodynamic experiments is challenging. Here we use the novel Fast Flow Facility at HR Wallingford (UK, http://www.hrwallingford.com/facilities/fast-flow-facility). The flume has a main working channel of length 70.00 m and width (W) 4.00 m and water depths (h) in the range of 0.85 m to 2.00 m. The facility is equipped with two pumps with a combined discharge of up to 4.9 m^3/s.

The initial bathymetry was created on a mock bed by screeding a freely erodible sand bed of length 31.3 m. The well-sorted sand had a median diameter of about 0.2 mm to maximise mobility, suppress dunes in favour of ripples, and avoid cohesion. The length of the centered splitter plate was 16 m. A perturbation, necessary to initiate bifurcation instability, was made by setting a 5 cm sediment hump in one of the channels over a given length and height.

Selected conditions (Table 1) were based on the theory of Bolla Pittaluga et al. (2015). Low mobility was impossible to test because of run time limitations and higher mobility experiments were run as briefly as possible to be able to investigate a larger number of conditions. In addition, there are already experimental data for low mobility unidirectional flows and most tidal systems are suspension-dominated. Tidal flows were run for comparable conditions to test stability. The test duration was assessed on the basis of sediment transport rate estimated by a predictor and the time required to either remove the perturbation on the bed or to assure a measurable growth. The Shields mobility number for unidirectional flow was calculated from measured flow velocity and skin friction, while for the reversing flow was calculated from the peak flow velocities in both directions.

Table 1. Approximate experimental conditions.

exper	run-time (hr)	depth (m)	dis-charge (m3/s)	(peak) veloc (m/s)	target Shields	aspect W/h	uni-directional / tidal	tidal period (s)	target bifurcation
4	13	0.14	0.22	0.39	0.5	29	uni		Unstab
5	35.24	0.50	0.85	0.42	0.5	8	uni		Stable
6	18	0.50	0.85	0.42	0.5	8	tidal	216	Stable
7	18.5	0.14	0.22	0.39	0.5	29	tidal	280	Unstab
8	19.5	0.50	0.85	0.42	0.5	8	tidal	216	Stable
9	2.24	0.25	0.77	0.77	2	16	uni		Unstab
10	18.5	0.50	0.85	0.42	0.5	8	uni		Stable
11	38	0.14	0.22	0.39	0.5	29	tidal	280	Unstab
12	0.9	0.80	2.60	0.81	1.5	5	uni		Stable

The following instruments were used for monitoring purposes (see Data Storage Report, Kleinhans and Sonnemans 2018):

- two line-laser scanning systems for bed elevations in both parallel channels, used to scan the initial bed, the developing bed about halfway through the experiment and the final bed.
- two Nortek Vectrino ADVs for velocity measurements in both parallel channel branches, both upward looking and at an elevation of about 0.1 m above the bed
- six pressure sensors for measuring water levels along the flume
- one Nortek HR Aquadopp acoustic device for discharge measurements related to pump control frequency

The bifurcation development was quantified by data analysis of bed scans and velocity measurements. The spatially-averaged difference in bed level height between the perturbed channel and unperturbed channel quantifies the overall morphological asymmetry. As the bed level data has a high spatial resolution over a reach much longer than the bedform length, this leads to highly accurate averages for the initial, perturbed bed and the two development stages (i.e., halfway and at the end of a run). On the other hand, the velocity measurements were taken at only a few points even though with high time resolution, allowing quantification of the development. Velocity was measured at a fixed elevation, while water depth varied especially in tidal conditions because the pump in the racetrack flume was not centered to equal distance from the splitter plate, which requires correction to depth-averaged velocity in future analyses. The combination was used to interpret the stability of each condition.

3.   RESULTS

The main results are that all experimental conditions, including the tidal conditions, behave as predicted by the theory (see in Table 1). Lower aspect ratios and lower mobilities lead to stable bifurcations with disappearing bed perturbation and flow asymmetry. Conversely, higher aspect ratios and higher mobilities lead to unstable bifurcations, with increasing bed elevation in the perturbed channel and increasing flow through the unperturbed channel branch (example in Figure 1,2). The development towards symmetry observed in the stable bifurcation experiments also demonstrates that the flume setup did not lead to significant topographic forcing on the bifurcations.
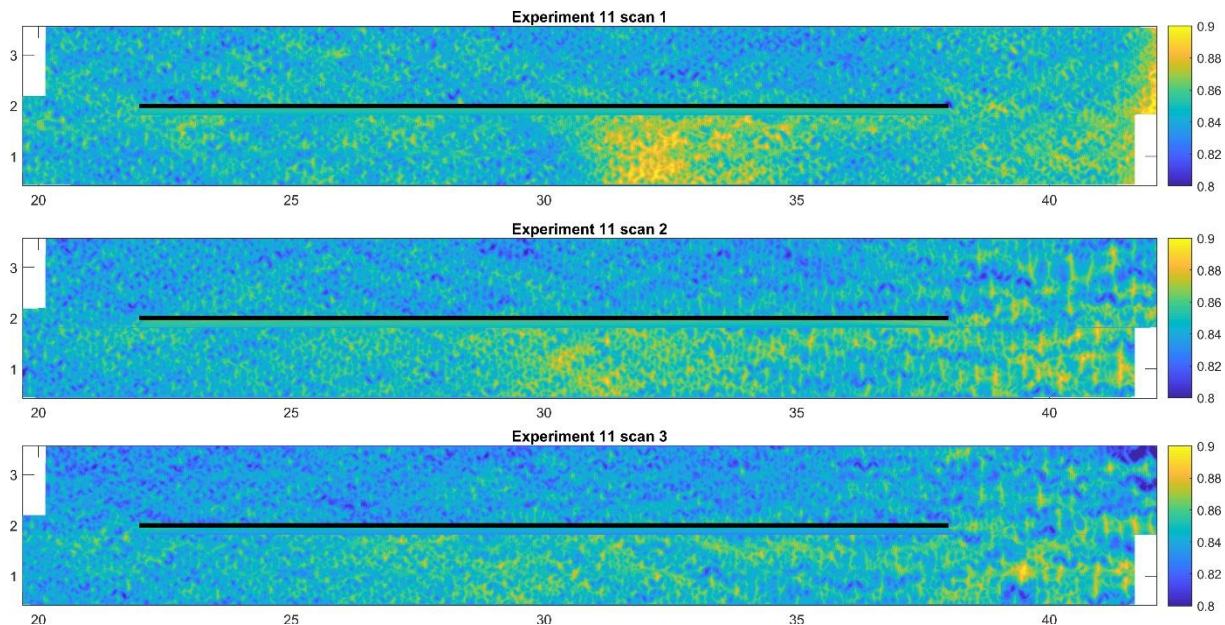

Figure 1. Bed scans of tidal experiment 11 which was interpreted as unstable.
Bottom channel was perturbed; net sediment transport to the left. All dimensions in m.
The splitter plate position is indicated by the bold black line. Microrelief are ripples resolved in the scans.
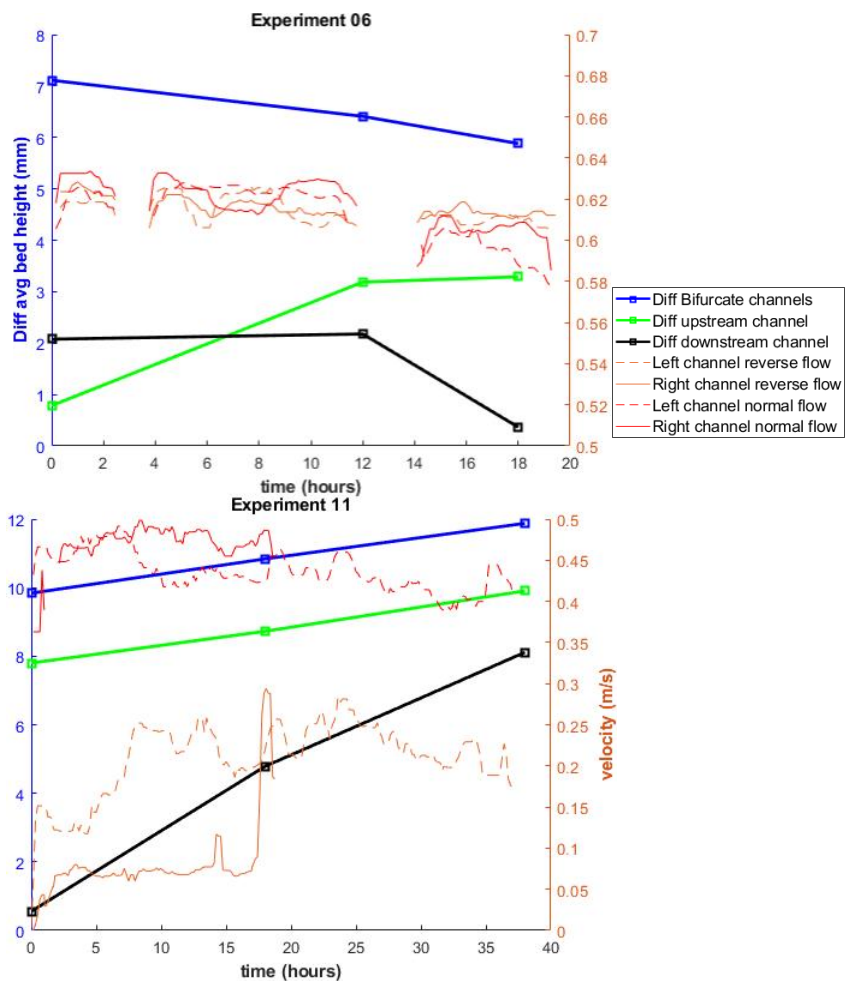
Figure 2. Timeseries of two tidal experiments with intermediate Shields number and low (left) and high (right) channel aspect ratio. Bold lines show bed level difference between perturbed and unperturbed sides averaged upstream of the splitter plate (green), downstream (black) and in the split section (blue). Detailed timeseries are median-filtered flow velocities for left (orange lines) and right (red lines) channel branches (showing gaps in the data). Difference in water depths explains difference in velocity measured at fixed elevation.

The bed scans (see, e.g., Fig. 1) required some interpretation as the morphological development is the result of superimposed development of the perturbation, the bedforms, and, for the highest mobility, the development of a bed wave intiated on the gentle bed ramp. However, the development of stable bifurcations in which the perturbation disappeared and the channels became symmetrical within the measurement accuracy (examples in Fig. 2) showed that topographic forcings were avoided despite the race track setup of the recirculating flume.
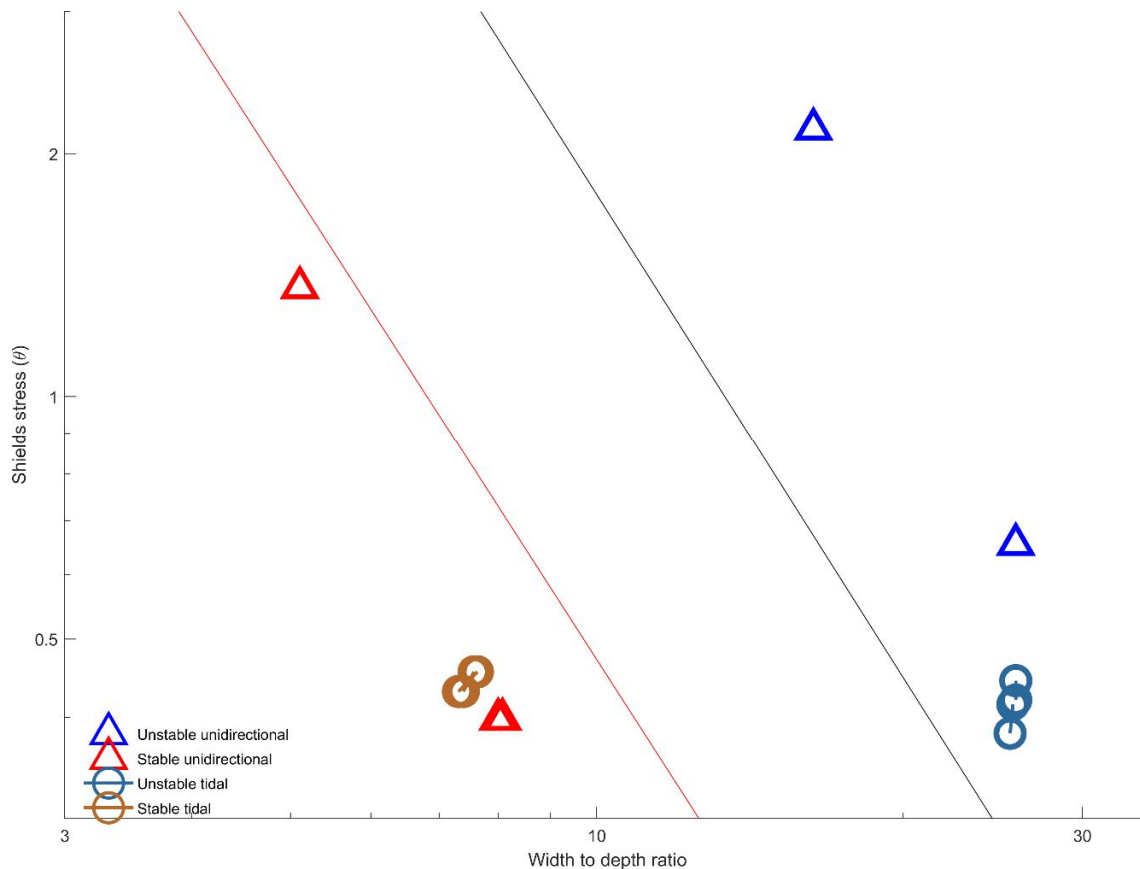
Figure 3. Summary of all experiments plotted in the bifurcation stability space for suspension-dominated conditions (Bolla Pittaluga et al. 2015), where the range between the two lines represent the uncertainty in the transition from stable to unstable bifurcations due to model parameter choices. Connected double symbols show tidal experiments with slight difference between peak ebb and flood conditions.

All experiments plot in agreement with the theory in the channel aspect ratio and sediment mobility parameter space. The agreement is found for both intermediate mobility and high mobility in the fluvial setup, and for the tidal setup under intermediate mobility conditions. The theory thus appears to hold for intermediate and high sediment mobility conditions as well as for tidal conditions. Furthermore, as many channels in nature have aspect ratios far above 10, theory and data suggest that the majority of bifurcations in nature are unstable.

Because of the limited amount of time available for the tests no runs in the transition zone between stable and unstable bifurcations. Therefore, we cannot draw conclusions about the predicted sensitivity of the transverse bed slope effect over a certain length in the undivided channel, which requires further experiments. Overall, the agreement of the experiments with the theoretical predictions suggests that the physical framework of the theory is sufficient to explain general bifurcation stability in idealised conditions, notably the lack of topographic forcing.

4. CONCLUSIONS

We conclude that, in the absence of topographic forcing, channel bifurcations in fluvial and tidal systems are unstable in relatively wide and shallow channels and intermediate to high mobility.

ACKNOWLEDGEMENTS

REFERENCES

Bolla Pittaluga, M., Repetto, R. and Tubino, M. (2003). Channel bifurcation in braided rivers: Equilibrium configurations and stability, Water Resour. Res., 39(3), 1046, doi:10.1029/2001WR001112.

Bolla Pittaluga, M., Coco, G. and Kleinhans, M.G. (2015). A unified framework for stability of channel bifurcations in gravel and sand fluvial systems, Geophys. Res. Lett., 42, 7521–7536, doi:10.1002/2015GL065175.

Jeuken, M.C.J.L., Wang, Z.B., (2010). Impact of dredging and dumping on the stability of ebb–flood channel systems. Coast. Eng. http://dx.doi.org/10.1016/j.coastaleng.2009.12.004.

Kleinhans, M.G., Jagers, H.R.A., Mosselman, E. and Sloff, C.J. (2008). Bifurcation dynamics and avulsion duration in meandering rivers by one-dimensional and three-dimensional models, Water Resour. Res., 44, W085454, doi:10.1029/2007WR005912.

Kleinhans, M.G., Ferguson, R.I., Lane, S.N., and Hardy, R.J. (2013). Splitting rivers at their seams: Bifurcations and avulsion, Earth Surf. Processes Landforms, 38, 47–61, doi:10.1002/esp.3268.

Kleinhans, M.G. and Sonnemans, K. (2018). Data Storage Report; Splitting nature at its seams: morphodynamic stability of river and tidal bifurcations. Hydralab+, http://dx.doi.org/10.5281/zenodo.1456622.

van Veen, J. (1950). Ebb and flood channel systems in the Netherlands tidal waters, J. Roy. Dutch Geographical Soc., 67, 303–325.

Wang, Z.B., Fokkink, R.J., De Vries, M. and Langerak, A. (1995). Stability of river bifurcations in 1D morphodynamics models, J. Hydraul. Res., 33(6), 739–750.

Appendix A

Hydralab Transnational Access

Introduction

HYDRALAB is an Integrated Infrastructure Initiative, financially supported by the EC, to optimise the use of unique facilities for laboratory experiments in the field of Hydraulics, Geophysical Hydrodynamics, Environmental Fluid Dynamics and Ice Engineering. One of the three main activities of Hydralab was enabling international groups of researchers to conduct hydraulic research in selected large and unique facilities, which is called 'transnational access'. Ten partners within Hydralab participated in this programme by making their facilities available to external user groups:

- Deltares, the Netherlands (Delta Flume and Delta Basin)
- Leibniz University Hannover, Germany (Large Wave Flume and Multi-directional Wave and Current Basin)
- CNRS, France (CoriolisII Rotating Platform)
- HSVA, Germany (Arctic Environmental Test Basin and Large Ice Model Basin)
- NTNU, Norway (Marine Ecohydraulics Field Station, Sletvik)
- Aalto University, Finland (Ice Tank)
- Universitat Politècnica de Catalunya, Spain (CIEM)
- DHI, Denmark (Offshore Wave Basin and Shallow Water Basin)
- University of Hull, UK (Total Environment Simulator)
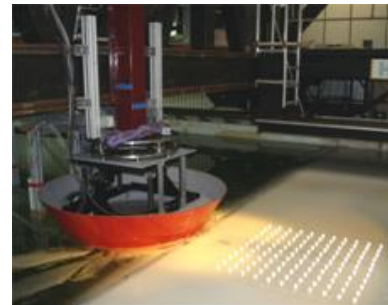- HR Wallingford, UK (Fast Flow Facility)

The objective of this programme was to stimulate co-operation between European researchers by providing the opportunity to undertake novel research in unique hydraulic experimental facilities which they do not normally have access to. The focus of Hydralab+ was Climate Change Adaptation.


Leibniz University Hannover   NTNU, Sledvik Field Station   HSVA, Hamburg

The programme provided groups of researchers with access, free of charge, to the facilities for the duration of their research project and also covered their travel and subsistence costs. The programme was intended for short access periods, not exceeding 3 months. State-of-the-art measuring instruments, data-acquisition and processing systems were at their disposal, as well as a supportive research environment, from access to facilities through to assistance and guidance from experts at the host institute. Previous background in laboratory methods and techniques was

not a prerequisite with all the necessary technical support and training being provided by the host institute.
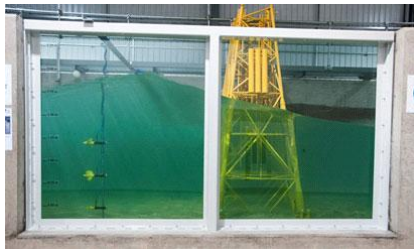
HR Wallingford, Fast Flow Facility
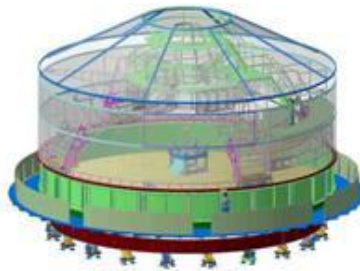
CNRS, Grenoble

Delta Flume Deltares, Netherlands

Project selection procedure

A common user selection procedure (USP) was followed throughout Hydralab+ to select the best projects to be granted access to the facilities. The proposals for access projects were firstly reviewed by the facility provider to check their feasibility. The facility provider then supported the proposers (User Groups) while they improved their draft proposals to compensate their lack of experiences with the facilities. This was of particular benefit to first-time users.

The Access proposals for the various Infrastructures in the same field (e.g. Hydraulics, Geophysical Fluid Dynamics or Ice Engineering) were selected in 3 common sessions of a joint USP-meeting, thus achieving an optimal and co-ordinated access for the various Infrastructures and User Groups. Each User Selection Panel consisted of 4 to 8 independent members, and a minority of dependent members coming from one of the HYDRALAB Participants. Representatives of the facility providers were present at each User Selection Panel meeting with an advisory role only.

For the acceptance of a proposal, a majority agreement of the USP-members was required in addition to the confirmation of the relevant facility manager that the research was feasible in their specific installation. Sometimes the possibility of moving a project to another facility within HYDRALAB was discussed by the User Selection Panel, where this may have enabled better utilisation of resources.

UPC, Barcelona

Aalto University, Helsinki

DHI, Denmark

Joint User Meeting

A total of 31 projects have been carried out in the framework of Transnational Access of Hydralab+, in which more than 300 researchers from across Europe participated. At least one researcher of each of these projects was present during the final closing event of Hydralab+ in Bucharest, during which a mini conference was organised on May 23, 2019. This mini conference, in which each

project was presented, is called the Joint User Meeting. The group of researchers from each project also prepared a paper, summarising the most interesting highlights of results.